

# Robustness Assessment of Deployable Gossamer Structural Space Systems

Von der Fakultät für Maschinenbau  
der Technischen Universität Carolo-Wilhelmina zu Braunschweig

zur Erlangung der Würde

eines **Doktor-Ingenieurs (Dr.-Ing.)**

genehmigte Dissertation

von: **Dipl.-Ing. Martin Eckhard Zander**

aus (Geburtsort): Wolmirstedt

eingereicht am: 03.09.2020

mündliche Prüfung am: 11.01.2021

Gutacher: Prof. Dr.-Ing. Michael Sinapius

Prof. Dr.-Ing. Andreas Rittweger

## ABSTRACT

The growing interest of science and industry in space, especially for commercial use in communications, climate and earth observation, as well as space exploration, is leading to the demand for increasingly efficient and lighter technical systems. For economic use, weight savings and the associated development of alternative and advanced designs are necessary, such as deployable, ultra-light weight structural systems, so-called Gossamer structures that enable a wide variety of space applications to be realized.

To this end, the thesis will investigate one of the most important aspects of deployable ultra-light-weight structural space systems, their robustness. This is investigated on different levels of complexity and finally quantified for the Gossamer structural space system as a whole. Although such structural systems are characterized by their very large outer dimensions, with a filigree design featuring very thin walls, and have a superior mass-area or mass-length ratio, thus offering great advantages in terms of economy and mission technology, they are at the same time more susceptible to disturbances, variation and imperfections, compared to traditional designs.

The analysis of robustness, understood as a quantifiable metric, as well as the integration of robustness considerations and corresponding methods, can identify and determine these vulnerabilities and reduce them already during the development and design process by countermeasures. As a result, a structural system with minimized vulnerabilities and increased structural performance in the form of robustness can be achieved.

In order to provide a first overview a general classification of existing Gossamer structural space systems and existing approaches for robustness assessment and quantification are analyzed. However, very different approaches are reported in the various fields of technology and engineering, with some highly theoretical and some only partially transferable. For this reason, a new methodology is developed and discussed in this thesis, which considers the characteristics of two-dimensional deployable Gossamer structural space systems and allows for a technical assessment of individual subsystem and overall system robustness. This is mainly shown by the example of the DLR solar sail demonstrator Gossamer-1.

With the focus on quantification, it is essential to determine influencing variables and parameters, such as disturbances and deviations, which characterize the robustness of such structural systems. In practical experiments geometrical changes, such as shape and form deviations, caused by the manufacturing process, tooling and long-term stowage, changes in material properties due to environmental influences in space, as well as load changes due to interaction of components are investigated.

Based on this, the here presented thesis investigates the effects of the determined influences on the robustness of deployable fiber composite booms and its subsystem, in mechanical bending tests as well as in numerical calculations. The resulting robustness parameters are subsequently used to quantify subsystem and overall system robustness facilitating the here developed method. Consequently, this thesis enables direct comparability and assessment of ultra-light weight Gossamer structural space systems based on their robustness as quantified metric.

## KURZFASSUNG

Ein wachsendes Interesse der Wissenschaft und Wirtschaft an der Raumfahrt, vor allem zur kommerziellen Nutzung für Kommunikation, Klima- und Erdbeobachtung, sowie der Erforschung des Weltalls führen zur Notwendigkeit von immer effizienteren technischen Systemen. Zur wirtschaftlichen Nutzung sind Gewichtseinsparungen und die damit verbundene Entwicklung von alternativen und fortschrittlichen Bauweisen notwendig, wie zum Beispiel entfaltbare, ultra-leichte Struktursysteme, sogenannte Gossamer-Strukturen, mit denen verschiedenste Raumfahrtanwendungen realisiert werden können.

Zu diesem Zweck soll in dieser Arbeit einer der wichtigsten Aspekte bei entfaltbaren, ultra-leichten Weltraumstruktursystemen untersucht werden, deren Robustheit. Diese soll auf verschiedenen Komplexitätsebenen analysiert und letztendlich für das Gossamer-Struktursystem als Ganzes quantifiziert werden. Obwohl sich solche Struktursysteme durch ihre sehr großen äußeren Abmessungen, bei filigraner Bauweise mit sehr dünnen Wandstärken, auszeichnen, ein überlegenes Masse-Flächen- bzw. Masse-Längen-Verhältnis aufweisen und damit wirtschaftlich sowie missionstechnisch große Vorteile bieten, sind sie zugleich anfälliger gegenüber Störungen, Abweichungen und Imperfektionen, im Vergleich zu herkömmlichen Bauweisen.

Die Analyse von Robustheit, verstanden als quantifizierbare Größe, sowie die Einbindung von Robustheitsbetrachtungen und entsprechenden Methoden, kann diese Anfälligkeiten identifizieren, bestimmen und bereits während des Entwicklungs- und Konstruktionsprozesses durch Gegenmaßnahmen reduzieren. Als Ergebnis kann somit ein strukturelles System, mit minimierten Anfälligkeiten und erhöhter struktureller Leistung, in Form von Robustheit, erzielt werden.

Nach einer allgemeinen Einordnung von bestehenden Gossamer-Weltraumstruktursystemen in Klassen werden bestehende Vorgehen zur Robustheitsbestimmung analysiert. Dabei zeigt sich ein sehr unterschiedliches Vorgehen in den verschiedenen Bereichen aus Technik und Ingenieurwesen, mit teils hoch theoretischen sowie nur teilweise übertragbaren Ansätzen. Aus diesem Grund wird in dieser Arbeit eine neue Methodik entwickelt und diskutiert, die die Eigenheiten von zweidimensionalen, entfaltbaren Gossamer-Weltraumstruktursystemen berücksichtigt sowie eine technische Bewertung von Einzel- und Gesamtr robustheiten ermöglicht. Dies wird hauptsächlich an dem Beispiel des DLR Sonnensegeldemonstrators Gossamer-1 aufgezeigt.

Mit dem Ziel der Quantifizierung ist es besonders essentiell Einflussgrößen und Parameter, wie Störungen und Abweichungen, die die Robustheit solcher Struktursysteme charakterisieren, zu bestimmen. In praktischen Versuchen werden dazu geometrische Änderungen wie Form- und Gestaltabweichungen, unter anderem durch Herstellungsprozess und -werkzeug oder Langzeitstauung verursacht, Änderungen von Materialeigenschaften aufgrund von Umwelteinflüssen im Weltraum, sowie Laständerungen durch Interaktion von Bauteilen untersucht.

Aufbauend darauf, werden in dieser Arbeit die Auswirkungen der ermittelten Einflüsse auf die Robustheit von entfaltbaren Faserverbundmasten bzw. dessen Subsystem, in mechanischen Biegeversuchen sowie in numerischen Berechnungen untersucht. Die daraus resultierenden Robustheitsparameter können anschließend genutzt werden um Subsystem- und Gesamtsystemrobustheiten mithilfe der zuvor erarbeiteten Methode zu quantifizieren. Somit wird eine direkte Vergleichbarkeit und Bewertung von ultra-leichten Gossamer Weltraumstruktursystemen, basierend auf deren Robustheit als quantifizierter Wert, ermöglicht.





## ACKNOWLEDGMENTS

The here presented doctoral thesis is the result of my work as a researcher and engineer in the area of deployable space structures at the DLR Institute of Composite Structures and Adaptive Systems in Braunschweig (Germany), at the Institute of Adaptionics and Function Integration of the Technical University Carolo Wilhelmina (Germany), and at the European Space Research and Technology Centre (ESTEC) in Noordwijk (The Netherlands) of the European Space Agency (ESA). It has gratefully been funded by the European Space Agency - ESA and the German Aerospace Center - DLR in the framework of the co-sponsored Networking/Partnering Initiative (NPI): “Robust and Tolerant Gossamer Structures”, NPI Proposal Reference Number: 193-2011.

Many people have contributed to the development of this thesis through scientific discussions, advice, the introduction of different viewpoints and often by practical support. I would like to take this opportunity to thank those who have supported my journey in a special way.

Firstly, I would like to thank Prof. Dr.-Ing. Michael Sinapius for his continuous support of my research, his guidance and for the many discussions about the scientific aspects of this thesis. Moreover, I would like to thank him for bringing me into the space community thru DLR and giving me the opportunities for my research stays at NASA LaRC and ESA ESTEC.

Furthermore, I would like to thank Prof. Dr.-Ing. Christian Hühne, the head of the department of Composite Design, in which I was able to do the many fascinating projects, for his support over many years and for providing the resources and opportunities necessary to carry out this work. I also would like to thank Prof. Dr.-Ing. Andreas Rittweger for his agreement to provide the second opinion to this thesis and Prof. Dr.-Ing. Enrico Stoll for chairing my defense.

My special thanks go to Martin Hillebrandt for the numerous scientific discussions, the valuable suggestions and the entertaining philosophical conversations we had in off-work topics, as well as for the lunchtime runs that helped us to refocus. I would also like to thank Marco Straubel, who was always available for assessments and support in many ways.

Moreover, I would like to mention and acknowledge the manifold support I received from the members of our deployable space structures team at the Institute of Composite Structures and Adaptive Systems in Braunschweig and from colleagues in other departments especially Carmen Westphal and Ary Zipfel for their advice and practical support in the many tests performed within this thesis.

During my research stays at ESTEC I was welcomed and supported by a lot of ESA staff members that were sharing their impressive expertise with me and always open for exchange and discussions. Here in particular I would like to thank Daniele Teti, Torben Henriksen, Rafeal Bureo Dacal, Tiziana Cardone, Julie Rocks and the many others I had the chance to work with.

I would like to address my special gratitude to my former mentor at NASA LaRC and friend, Keith Belvin. Keith introduced me to the field of Gossamer space systems and sparked in me the fascination for the extreme lightweight designs and the highly innovative approaches for such systems. Throughout my work on this thesis he encouraged me to pursue this topic further and always offered valuable advice, professionally as well as personally.

In addition, this PhD thesis would have not been possible without the many students that supported me during their internships, Bachelor’s, Master’s or semester theses, directly or indirectly in the many side projects. I want to thank Joffroy Grangladien, Dina Früh, Andreas Wilkens, Marcel Hillebrandt, Johannes Schlegel, Nils Gerrit Kottke, Frank Schmidt, Diego Miranda de Leon, Yannick Hoven, Jannic Völker, Daniel Müller, Niels Hagmeister and Dominic Jost for their countless contributions.

Apart from the professional support I received, I would like to thank my friends for their support and believe in me and their recurring, mostly motivating, questions about the status of my thesis.

I would especially like to thank my partner Alexandra, who encouraged me in specific during the final compilation of my thesis and who supported me with the most understanding for the many weekends full of work.

I am especially grateful to my parents Ute and Eckhard who have always encouraged me to strive for my goals and who unconditionally supported me and believed in me during my entire project PhD thesis and long before. They provided me with the foundation and opportunities without which this thesis would not have been possible.

*Thank you,  
Martin*

*This work is dedicated to my dad.*

## CONTENTS

NOMENCLATURE	IV
FIGURES	VII
TABLES	X
1. INTRODUCTION	1
2. AIM OF THESIS AND HYPOTHESES	4
3. STATE OF THE ART GOSSAMER STRUCTURAL SPACE SYSTEMS, DESIGN PHILOSOPHIES & ROBUSTNESS	7
3.1 Gossamer Structural Space Systems & Applications .....	7
3.1.1 Definition and Heritage.....	7
3.1.2 Classification and Examples.....	8
3.1.3 Deficiencies in Robustness & Resulting Damages on GosSSS Applications .....	9
3.1.4 Basic Structural System Design, Elements & Functions.....	15
3.1.5 System Requirements & Characteristics .....	17
3.2 Standard Design Approach, Principles & Allocation of Robustness Assessment .....	18
3.2.1 Allocation in Standard Design Approach and Life Cycle Phases .....	18
3.2.2 Design Philosophies and related Principles.....	21
3.3 Robustness and present Approaches .....	25
3.3.1 Robustness .....	25
3.3.2 Robust Design .....	26
3.3.3 Robustness Metrics .....	27
3.4 Chapter Conclusion.....	35
4. ROBUSTNESS ASSESSMENT — METHODOLOGY	37
4.1 Requirements & Extent .....	37
4.2 Conditional System Robustness Considerations.....	39
4.3 System Robustness — Bottom-up versus Top-down .....	40
4.4 Mathematical Robustness Approach.....	42
4.4.1 Composition of Overall System Robustness .....	42
4.4.2 Weighting Factors for System Robustness.....	46
4.4.3 Visualization of overall Robustness Composition .....	47
4.4.4 Subsystem & Component Robustness Metrics .....	48
4.5 Framework of Robustness Assessment and Quantification .....	59
4.6 Implementation in the Design Process .....	65
4.7 Chapter Conclusion.....	68
5. SENSITIVITY, RISK AND SYSTEM ANALYSIS – CASE STUDY	69
5.1 The selected Gossamer Structural Space System.....	69
5.1.1 Mission envelope and objectives.....	69

5.1.2	Overall Structural System Architecture of Gossamer-1 .....	71
5.1.3	Boom Subsystem.....	72
5.1.4	Membrane Subsystem.....	77
5.1.5	Mechanism Subsystem .....	79
5.1.6	Interface (I/F) Subsystem .....	82
5.1.7	Realized Gossamer-1 Hardware .....	83
5.2	Identification of Functions, Robustness Parameters and associated Weighting Factors.....	84
5.2.1	System Structure and Functions Analysis .....	85
5.2.2	Derived Robustness Parameters and Determination of Partial Robustness Weighting Factors .....	89
5.3	Mission Phases & Relevance .....	95
5.4	Identification of Influence Factors and Detrimental Effects.....	98
5.4.1	Environment related Influences.....	98
5.4.2	Measurements related Influences .....	103
5.4.3	Methods related Influences .....	104
5.4.4	Materials related Influences.....	104
5.4.5	Manufacturing related Influences.....	104
5.4.6	Gossamer Technology related Influences .....	105
5.4.7	Overview of Influences on Gossamer-1 Subsystems and System.....	107
5.5	Application of Influence Factors – An Example .....	109
5.6	Subsystem Weighting Factors – Conditions and Determination.....	113
5.7	Chapter Conclusion.....	116
6.	<b>EXPERIMENTAL DETERMINATION OF INFLUENCE FACTORS ON THE BOOM SUB-SYSTEM</b>	<b>117</b>
6.1	Geometric Dimension Changes induced Influence Factors.....	117
6.1.1	Stowage induced Influences – on short Boom Specimens.....	117
6.1.2	Manufacturing & Stowage induced Influences – on a full-size Gossamer-1 Boom.....	130
6.1.3	Manufacturing induced influences – on a 10 m Gossamer-2 Boom.....	134
6.1.4	Long term Stowage induced Influences – on Boom material specimens .....	137
6.1.5	Interaction induced Influences – caused by Interfaces .....	139
6.2	Mechanical Property Changes induced Influence Factors.....	141
6.2.1	Material Property Variations .....	141
6.2.2	Atomic Oxygen exposure induced Influences .....	143
6.2.3	MMOD induced Influences .....	145
6.2.4	Test Equipment induced Influences .....	147
6.3	Chapter Conclusion.....	148
7.	<b>METHOD APPLICATION – CASE STUDY</b>	<b>150</b>
7.1	Assessment in mechanical Boom Tests.....	150
7.1.1	Boom Test Stand & Test Principle.....	150
7.1.2	Testing Gossamer-1 Boom Subsystem and Boom Component.....	153
7.1.3	Robustness Assessment of Experimental Results.....	166
7.2	Finite Element Analysis of Case-Study Structural System.....	169
7.2.1	FE-Model, Cases and Results.....	170

---

7.2.2 Robustness Assessment of FEA results and comparison to Experiments .....	175
7.3 Chapter Conclusion.....	178
<b>8. SUMMARY, CONCLUSION AND OUTLOOK</b>	<b>180</b>
<b>REFERENCES</b>	<b>185</b>
<b>APPENDIX A EXAMPLE LIST OF GOSSSS APPLICATIONS</b>	<b>200</b>
<b>APPENDIX B SURVEY OF ASSESSMENT METHODS</b>	<b>208</b>
<b>APPENDIX C FUNCTIONS, PARAMETERS AND WEIGHTING FACTORS</b>	<b>225</b>
<b>APPENDIX D ANALYTICAL CALCULATION OF BOOM SECOND MOMENT OF AREA</b>	<b>231</b>
<b>APPENDIX E RESULTS OF INFLUENCE MEASUREMENTS</b>	<b>237</b>
<b>APPENDIX F RESULTS OF MECHANICAL BOOM TESTS</b>	<b>242</b>
<b>APPENDIX G INPUT VALUES – ROBUSTNESS ASSESSMENT</b>	<b>246</b>

## NOMENCLATURE

## ABBREVIATIONS

ACOS	Attitude and Orbit Control System
AO	Atomic oxygen (abbreviation according to ECSS standard)
ARTP	Advanced Radar Technology Program (NASA)
ATOX	Atomic oxygen
BSDU	Boom and Sail Deployment Unit
BSFR	Boom-Sail-Fixation-Ring
BSI	Boom and Spacecraft Interface
CBSU	Central Boom and Sail Unit
CFRP	Carbon fiber reinforced plastic
CME	Coronal Mass Ejections
COTS	Commercial off-the-shelf
CS	Convex side of a boom's cross section
CSCU	Central Spacecraft Unit
CTE	Coefficient of thermal expansion
DL1	Displaced Libration point 1 (Displaced Lagrange point 1)
DLR	Deutsches Zentrum für Luft und Raumfahrt e.V. (German Aerospace Center)
ECSS	European Cooperation for Space Standardization
ESA	European Space Agency
FDIR	Fault Detection, Isolation and Recovery).
FMEA	Failure Modes and Effects Analysis
FMECA	Failure Modes, Effects and Criticality Analysis
FMEDA	Failure Modes, Effects, Criticality and Detection Analysis
FoS	Factor of Safety
FS	Flange side of a boom's cross section
FTA	Fault Tree Analysis
GEO	Geosynchronous Orbits (Clarke Orbits, orbits with a revolution of exactly one day at an altitude of 35,786 km; When the orbit is circular and the rotational period has zero inclination, the platform is considered to also be "geostationary"; according to NASA Global Change Master Directory)
GPS	Global Positioning System
GTO	Geostationary Transfer Orbit
HEO	High Earth Orbits/Highly Elliptical Orbits (High Earth Orbit is any orbit above geosynchronous orbits < 35,786 km; a Highly Elliptical Orbit is an orbit of low perigee, about 1000 km, and a high apogee over 35,786 km; according to NASA Global Change Master Directory)
IOD	In-Orbit Demonstration
L1	Libration point 1 (Lagrange point 1)
L1	Libration point 1 (Lagrange point 1)
L2	Libration point 2 (Lagrange point 1)
LEO	Low Earth Orbit (altitudes between 80 km and 2000 km, according to NASA Global Change Master Directory)
MAR	Mission Analysis Report (according ECSS-E-ST-70, req. 5.2.2.1c)
MEO	Medium Earth Orbit (Intermediate Circular Orbits; altitudes between 2000 km to 35,786 km, but most commonly at 20,200 km or 20,650, with an orbital period of 12 hours; Note that the Van Allen Belts of high energy protons lie within the MEO orbital range; according to NASA Global Change Master Directory)
MGSE	Mechanical Ground Support Equipment

MMOD	Micrometeoroids and Orbital Debris
NASA	National Aeronautics and Space Administration (United States of America)
NPI	Networking/Partnering Initiative
NWA	Nutzwertanalyse
PCB	Printed Circuit Board
RBD	Reliability Block Diagram
RPN	Risk Priority Number
SAR	Synthetic Aperture Radar
SEP	Solar Electric Propulsion
SSM	Sail-Spool-Mechanism
STA	Success Tree Analysis
TA	Technology Assessment
VDI	Verband Deutscher Ingenieure - Association of German Engineers
Vega	ESA Launcher (Vettore Europeo di Generazione Avanzata - Advanced Generation European Carrier Rocket)
VUV	Vacuum Ultra violet radiation
WP	Work package

## SYMBOLS

$Ro_{SRMS}$	-	Shape-accuracy-based partial robustness
$b_B$	[mm]	Width of boom cross section
$c$	[N/mm]	Bending stiffness
$CL$	[N]	Collapse load
$d$	[mm]	Diameter of reeled boom
$E$	[MPa]	Young's modulus
$e_B$	[mm]	Width of flattened boom
$EI$	[ $\times 10^6$ Nmm <sup>2</sup> ]	Flexural rigidity
$F$	[N]	Force
$F_s$	[mm]	String force measured
$FuN$	-	Functionality number
$GB$	[N]	Global buckling load
$h_B$	[mm]	Height of boom cross section
$HN$	-	Failure number
$I$	[mm <sup>4</sup> ]	Second moment of area
$L$	-	Quality loss
$l$	[mm]	Free boom length
$LL$	[N]	Limit load
$r_1$	[mm]	Radius 1 of boom cross section
$r_2$	[mm]	Radius 2 of boom cross section
$RN$	-	Redundancy number
$RO_{Booms}$	-	Boom Subsystem robustness
$RO_d$	-	Packaging-based partial robustness
$RO_{FS}$	-	Spool-off-force-based partial robustness
$RO_{GosSSS}$	-	Gossamer Structural Space System robustness
$ROI_{FS}$	-	Interface Subsystem Robustness
$ROL$	-	Load-based partial robustness
$RO_{MechS}$	-	Mechanism Subsystem robustness

---

$RO_{Mem-braneS}$	-	Membrane Subsystem robustness
$RO_{Subi}$	-	Subsystem robustness (general)
$RO_{Sys}$	-	System robustness
$RO_u$	-	Displacement-based partial robustness
$RO_{\Delta l}$	-	Length-change-based partial robustness
$RO_{\kappa}$	-	Stiffness-based partial robustness
$RO_{\tau}$	-	Torque-based partial robustness
$RO_{\tau}$	-	Torque-based partial robustness
$S$	[mm]	Boom sag
$s_x$	[mm]	Boom tip displacment in x-direction of test stand coordinate system
$t_r$	[mm]	Boom flange thickness
$t_s$	[mm]	Boom shell thickness
$u_i$	[mm]	Boom tip displacment (general)
$WN$	-	Weighting number
$w_{si}$	-	Weighting factor for subsystem robustness
$\alpha$	[°]	Angle of attack in-plane of the test stand coordinate system
$\alpha_1$	[rad]	Subtended angle 1 of boom cross section
$\alpha_2$	[rad]	Subtended angle 2 of boom cross section
$\beta$	[°]	Angle of attack out-of-plane of the test stand coordinate system
$\Psi_i$	-	Influence factor for parameter i



FIGURES

**Figure 3.1.** Classification of Gossamer Structural Space Systems by application .....8

**Figure 3.2.** ISS’ solar arrays – damages due to lacking robustness .....11

**Figure 3.3.** Hubble’s flexible Solar Arrays– damages and sensitivities .....14

**Figure 3.4. a)** The deployed Roll-Out Solar Array (ROSA), during on-orbit testing, attached to ISS’ robotic arm (SPDM) of ISS [32] (image cropped); Blanket flap mode (FEM) causing anomalies [31] .....15

**Figure 3.5.** Main configurations a) to c), with a combined configuration d), and main elements (① Booms, ② Membrane(s), ③ Interfaces, ④ Mechanism(s), main spacecraft in white) of Gossamer structural Space Systems.....16

**Figure 3.6.** Summarized allocation of robustness assessment within the Space Flight Project Life Cycle according to ECSS standards.....19

**Figure 3.7.** Allocation of robustness assessment in general procedure of systematic development and design according to VDI 2221:2019-11 (adapted image from [40]).....21

**Figure 3.8.** Robustness based on insensitivity to variations .....26

**Figure 3.9.** Deriving measurements and metrics.....27

**Figure 3.10.** Classification scheme for robustness metrics (adopted from Göhler et al. [61]) and assessment .....29

**Figure 3.11.** Robustness metric based on feasible design space (adopted, edited from Göhler [61]) .....32

**Figure 4.1.** Multidisciplinary approach for robustness quantification.....38

**Figure 4.2.** Exemplary cases of Conditional System Robustness on GosSSS applications .....40

**Figure 4.3.** System robustness composition – Bottom-up versus Top-down .....42

**Figure 4.4.** Conservatism heat map of example robustness using the investigated approaches...43

**Figure 4.5.** Determination of subsystem weighting factors.....46

**Figure 4.6.** Visualization of robustness composition for two example cases A and F.....48

**Figure 4.7.** Load introduction into boom subsystem (boom bending test) .....51

**Figure 4.8.** Comparison of characteristic parameters as measure of robustness (c - stiffness, u - boom-tip displacement, LL - limit buckling load, GB - global buckling load, CL - collapse load)51

**Figure 4.9.** Symmetric membrane/tension loads of different applications.....56

**Figure 4.10.** Main tasks of the robustness assessment method (sub-tasks are denoted with sub-numberings).....60

**Figure 4.11.** Parameter-Diagram (P-Diagram).....62

**Figure 4.12.** GRID-Analysis in a portfolio scheme .....63

**Figure 4.13.** Strategy for robustness quantification – exemplary on the boom subsystem .....65

**Figure 4.14.** Design process with the implemented robustness assessment methodology – over all levels of complexity.....67

**Figure 5.1.** Considered mission design envelope (CME- coronal mass ejection, L1- Lagrange point 1, DL1-Displaced Lagrange point 1) .....70

**Figure 5.2.** Overall design of Gossamer-1 .....72

**Figure 5.3.** Deployment sequence of Gossamer-1 .....72

**Figure 5.4.** Boom subsystem of Gossamer-1 .....73

**Figure 5.5.** Gossamer-1 boom cross sectional dimensions and principle .....75

**Figure 5.6.** Sensors and equipment of the boom subsystem.....76

**Figure 5.7.** Boom spacecraft interface (BSI).....77

**Figure 5.8.** Membrane Subsystem of Gossamer-1.....78

**Figure 5.9.** Features of the membrane subsystem .....79

**Figure 5.10.** Mechanism Subsystems and components .....81

**Figure 5.11.** Interface subsystem of Gossamer-1 .....83

**Figure 5.12.** Built and tested Gossamer-1 system model (EQM).....84

**Figure 5.13.** System structure breakdown and coding of Gos-1.....86

<b>Figure 5.14.</b> Partial robustness weighting factors determined for the Boom Subsystem.....	94
<b>Figure 5.15.</b> Mission phases of Gossamer-1 .....	97
<b>Figure 5.16.</b> Categorized causes for occurring influences on GosSSS.....	98
<b>Figure 5.17.</b> Atomic oxygen flux in Low Earth Orbits according to Rooij [96].....	99
<b>Figure 5.18.</b> Illustration of tracked debris objects in LEO and GEO (image source: NASA ODPO 2019 [107]).....	103
<b>Figure 5.19.</b> Identified influence types in GosSSS.....	106
<b>Figure 5.20.</b> Influences and consequences on subsystem and system level of Gossamer-1 .....	108
<b>Figure 5.21.</b> Load cases on boom example for analytical influence factors application .....	109
<b>Figure 5.22.</b> Cross sectional geometry of the studied boom example .....	110
<b>Figure 5.23.</b> Conditional physical connections and interactions of the Gossamer-1 structural system.....	113
<b>Figure 5.24.</b> Determination of failure numbers $FN$ .....	115
<b>Figure 5.25.</b> Determination of functionality numbers $F_{uN}$ .....	115
<b>Figure 5.26.</b> Determination of subsystem weighting factors for Gossamer-1 .....	116
<b>Figure 6.1.</b> Process of specimen surface scanning and model preparation for analysis .....	118
<b>Figure 6.2.</b> Change of boom cross section caused by stowage.....	119
<b>Figure 6.3.</b> Centroid boom sag of 500 mm specimens for 23°C and 80°C temperature regime (approx. radius displayed for day 98).....	121
<b>Figure 6.4.</b> Curvature and sag of tensioned side of the 500 mm specimens for 23°C and 80°C temperature regime .....	123
<b>Figure 6.5.</b> Curvature and sag of compressed side of the 500 mm specimens for 23°C and 80°C temperature regime .....	125
<b>Figure 6.6.</b> Averaged sag and curvature over both sides (tensioned, compressed) .....	127
<b>Figure 6.7.</b> Sag, curvature and buckles of the flange of two 500 mm boom specimens stowed at 23°C and 80°C and over different periods of stowage.....	129
<b>Figure 6.8.</b> Scanned and analyzed 4300 mm Gossamer-1 boom and tool halves.....	131
<b>Figure 6.9.</b> Sag, curvature and waviness – 4300 mm boom and tool .....	132
<b>Figure 6.10.</b> Resulting boom curvature and sag of boom in pristine and stowed conditions ...	133
<b>Figure 6.11.</b> Scanned Gos-2 10 m boom and 14 m tool .....	135
<b>Figure 6.12.</b> Sag, curvature and local buckling of 10 m boom specimen and 14 m tool .....	136
<b>Figure 6.13.</b> Creep testing of boom material specimens for estimating long-term stowage behavior .....	139
<b>Figure 6.14.</b> Boom transition zone and its change with changing deployed length.....	140
<b>Figure 6.15.</b> Influence comparison of boom-I/F-interaction on load carrying capability and failure mode under lateral bending .....	141
<b>Figure 6.16.</b> Determining material property influences – Tensile testing.....	142
<b>Figure 6.17.</b> Microscopic images of ATOX exposed specimens.....	144
<b>Figure 6.18.</b> Impact, optical analysis and compression after impact (CAI) testing of boom specimens .....	146
<b>Figure 6.19.</b> Determining influence factor and error of the boom bending test stand with a reference aluminum profile beam .....	148
<b>Figure 7.1.</b> Boom test stand and conventions .....	150
<b>Figure 7.2.</b> Boom test stand – Sensor & Load Rack (load string marked red; visual load adapter on boom tip not displayed).....	151
<b>Figure 7.3.</b> Boom test stand – Scheme.....	152
<b>Figure 7.4.</b> Dimensions of tested configurations .....	153
<b>Figure 7.5.</b> Boundary conditions of ideal and real test configurations .....	154
<b>Figure 7.6.</b> Orientation of angles of attack for each tested boom side.....	155
<b>Figure 7.7.</b> Observed buckling behavior in ideal (clamped) and real (spacecraft) configurations under lateral bending .....	157

---

<b>Figure 7.8.</b> Failure modes of ideal (clamped) and real (spacecraft) configuration under lateral bending .....	158
<b>Figure 7.9.</b> Observed buckling loads of subsequent and repeated testing, exceeding collapse..	160
<b>Figure 7.10.</b> Residual load carrying capacity of assessed cases.....	162
<b>Figure 7.11.</b> Flexural rigidity (stiffness) and standard deviation (whiskers) of assessed load cases under lateral bending .....	163
<b>Figure 7.12.</b> Failure modes of ideal (clamped) and real (spacecraft) configuration under quasi-axial compression .....	164
<b>Figure 7.13.</b> Comparison of averaged maximum buckling loads under quasi-axial loading (standard deviation represented by whiskers).....	165
<b>Figure 7.14.</b> Residual load carrying capacity of tested booms under axial compression (angles given as $\alpha/\beta$ ) .....	166
<b>Figure 7.15.</b> Comparison of Boom Subsystem robustness for exemplary cases .....	169
<b>Figure 7.16.</b> Finite Element Analysis – Procedure and implementation of influenced parameters .....	170
<b>Figure 7.17.</b> Boundary and load conditions on the boom model.....	171
<b>Figure 7.18.</b> Imperfections applied to the FE boom model.....	172
<b>Figure 7.19.</b> Resulting buckling patterns at failure.....	173
<b>Figure 7.20.</b> Principle strain at local buckling failure at convex side loading .....	174
<b>Figure 7.21.</b> Comparison of Boom Subsystem robustness for exemplary cases simulated in FEA .....	178

## TABLES

<b>Table 4.1.</b> Exemplary values of subsystem robustness and weighting factors.....	43
<b>Table 4.2.</b> Exemplary scale of robustness metrics associated with the severity of possible failure.....	46
<b>Table 5.1.</b> Overview determined partial robustness weighting factors .....	94
<b>Table 5.2.</b> Comparison of nominal and influenced robustness parameter results .....	112
<b>Table 6.1.</b> Cross sectional changes of boom specimens .....	120
<b>Table 6.2.</b> Results of discrete curvature and sag measurements .....	122
<b>Table 6.3.</b> Overview curvature results – tensioned specimen side.....	124
<b>Table 6.4.</b> Overview curvature results – compressed specimen side .....	126
<b>Table 6.5.</b> Overview curvature results – Averaged curvature .....	128
<b>Table 6.6.</b> Flange curvature and sag.....	129
<b>Table 6.7.</b> Flange waviness .....	130
<b>Table 6.8.</b> Gossamer-1 boom curvature and sag.....	134
<b>Table 6.9.</b> Determined Gossamer-1 boom tip displacements.....	134
<b>Table 6.10.</b> Gossamer-2 boom and tool curvature and sag.....	137
<b>Table 6.11.</b> Determined Gossamer-2 boom tip displacements .....	137
<b>Table 6.12.</b> Result comparison of 3D- and 2D-setup.....	143
<b>Table 6.13.</b> Mass loss due to ATOX exposure .....	144
<b>Table 6.14.</b> Result comparison – shear modulus of ATOX-exposed vs. reference (pristine) ....	145
<b>Table 6.15.</b> Buckling load of impacted Gos-1/ADEO boom specimens .....	147
<b>Table 6.16.</b> Result overview aluminum beam - Measured vs. analytical bending stiffness .....	148
<b>Table 7.1.</b> Quantified Boom Subsystem robustness from experiments.....	168
<b>Table 7.2.</b> Acquired results from FEA .....	175
<b>Table 7.3.</b> Resulting Robustness based on FEA .....	177

## 1. INTRODUCTION

As interest in space rises for scientific and commercial use, especially in recent years, a one field is Earth observation with the goal to obtain data on weather, climate, vegetation, as well as on the impact of natural disasters like forest fires, volcano eruptions, earthquakes, flooding or other extreme weather conditions. Furthermore, in the increasingly connected world with many businesses, services and daily tasks based on the digital world and digital exchange, space is utilized intensively for communication and navigation. When imagining a future with autonomous transportation and digital industry, this aspect will likely gain even more importance. With the growing reliance on electronics and complex power grids in daily life, space weather warning, has gained attention as solar flares impose damaging electro-magnetic charging to satellite electronics, electronics on ground or even cause power outages on Earth. Besides manned spaceflight in low Earth orbits and around moon, utilization of space is more scientific driven the farther away from Earth. Science of outer space is often set to researching our galaxy, other planets or other celestial bodies like moons, comets and asteroids. However, as private companies already show interest in further commercial utilization of space e.g. space mining and colonization of Mars, as well as space tourism on space stations, such activities may emerge in the future.

All space activities, science based or commercial driven, facilitate space systems like satellites, probes, landers, rovers, transport systems for cargo and crew, orbiters and space stations. These however usually need some kind of secondary system to generate power, achieve signal transmission, perform measurements or other operations. For some standard functions, large secondary systems are needed like large solar arrays to generate enough power, large areal antennae for signal transmission and beam focusing, or long antennae for undisturbed measurements. Some applications are requiring even larger functional areas e.g. solar sails using mainly solar pressure for propulsion, solar shades that shade instruments like cryogenic telescopes, or drag sails that decelerate satellites in order to be removed from its low Earth orbit after decommissioning.

These systems share the difficulty of being very large when in operation but having to fit in the limited volume of available launchers. They therefore are either assembled in space or folded to small volumes on ground and deployed to full size in space. The latter category, known as Gossamer systems, usually features delicate structures with thin walls and low areal densities, and are in the focus of the here presented thesis. Gossamer systems are used in a variety of types in 2D-shape formats featuring deployable structural elements that span membranes, or spin-deployed and -stabilized membrane systems, and types in 3D overall formats like inflatable systems.

Although Gossamer structural space systems provide the opportunity for new and more efficient applications as they feature a very low relative mass at large dimensions, it also leads to delicate build with small structural wall thicknesses and therefore to increased vulnerability and sensitivity.

With the goal of reducing costs while increasing performance, a low mass and lighter design is pursued to lower launch costs, costs of propulsion in space, and to lower power consumption of a spacecraft. Gossamer systems are therefore striving for low areal densities, determined by the systems average functional area and its mass, while increasing relative payload capability at the same time as found.

However, challenging here is in most applications the requirement of providing a low mass coupled with a reasonable stiffness, while being able to bear certain load amplitude. As stiffness is provided through tensioning thin membranes with ultra-light deployable booms or tethers and tendons by spinning, using centripetal forces, new designs, materials and mechanisms must therefore be engaged.

When packaging the functional area or membrane and the support structure in order to meet stringent volume constraint of the launcher fairing, the highest possible packaging rates are aimed for. At same time membranes must not be punctured or torn, thus preventing permanent damage or

total loss, as well as structural elements must be stowed in such a way that damage due to overstraining is avoided. Nevertheless, all elements of such a system must withstand long-term storage in stowed state without degradation in functionality or performance.

Thus, such requirements and the harsh environmental conditions in space demand a certain resistance and durability of Gossamer systems. Hence, the used advanced materials, mostly plastics and composites, must sustain space environment like electro-magnetic radiation, large temperature gradients, vacuum, highly reactive atomic oxygen and particle impacts. Furthermore, the extreme transformations that take place during deployment from the highly compacted and stowed structure to the very large dimensions are very challenging to withstand, and vice versa for packaging.

Of similar importance is a reliable mechanical performance. This is challenging especially in terms of obtaining accurate performance values from tests and making accurate predictions and simulations based on test results, since practical experiments of such large structural systems can only be performed upon gravity acting, thus influenced by its own weight, or on a smaller scale.

In order to withstand noise, influences, environmental and technological induced conditions, a structural system must be designed featuring certain robustness. Commonly, safety factors in place provide margins in terms of structural over-performance. However this usually and inevitably introduces an increase in mass, which contradicts the inherent ultra-light weight approach of Gossamer structural space systems. Therefore, a balance between providing low but large enough performance margins and reserves, and extreme mass savings should be accounted for by the assessment of robustness as an integral part of the design process. In order to enable an objective comparison in this type of assessment, the quantification of robustness is considered essential.

This is done within this thesis by developing a methodology for robustness assessment specific to Gossamer structural space systems, a framework for its integration into the design process, as well determining quantifiable metrics and values in case studies, as proof of concept. The thesis is therefore structured as follows:

Chapter 2 points out the aims and developed hypothesis that are used as guides to develop a method for robustness assessment, applying to Gossamer structural space systems.

In chapter 3 the state of the art of Gossamer structural space systems in existence are analyzed and categorized into classes. Exemplary deployable Gossamer structure applications are scrutinized towards deficiencies in robustness, experienced in operation, in-orbit. In order to address robustness methodically existing approaches and principles of robustness assessment and related design principles are analyzed and reviewed. Furthermore, it is iterated on the diverse robustness metrics that are used in different fields, advantages and disadvantages are compared and discussed against the backgrounds of their applicability to Gossamer structures.

Following in chapter 4 is the methodical development. Here the necessary requirements, considerations and extend of the robustness assessment method are developed and approaches of top-down and bottom-up methods are discussed in the light of Gossamer structures. By elaborating on the methodical core of the thesis, a mathematical robustness approach is developed and discussed on a simplified example, thus finding the composition of the overall system robustness, weighting factors as well as relations between robustness of different levels of system complexity. Moreover, with a framework developed, a guideline is given on how and when to assess robustness in the design process, as well as which methods of assessment and evaluation ought to be used.

Chapter 5 is investigating the sensitivity and risks of a Gossamer space structural system in a case study, on the solar sail demonstrator Gossamer-1, developed, built and qualified at DLR. Its mission and architecture is analyzed in order to identify main structural subsystems and associated essential functions. Following this, the functions and necessary degree of fulfillment are further scrutinized, from which robustness parameters and their impact on the overall system and robustness in terms of weighting factors are derived. As deemed necessary for the assessment, influences, noise and detrimental effects are identified and categorized in types, while their associated causes are elaborated. With the purpose of demonstration, the effect of induced influences affecting parameters that determine robustness and reducing performance is shown on a simplified example of a carbon fiber

composite boom in a characteristic load case. Moreover, differences in importance of single subsystems and their robustness related to the overall system is analyzed and quantified in terms of subsystem weighting factors.

With the focus on the identified Boom Subsystem as case study, in chapter 6 the influences and influence factors that impact robustness by external and internal deviations, noise, imperfections and disturbances are quantified in experiments. The effects of long term storage in stowed state, under different temperatures, is analyzed on short CFRP boom samples, full size Gossamer-1 booms and a large scale boom of a larger solar sail. Here impacts by stowage and manufacturing are quantified in terms of influence factors that e.g. change cross sectional dimensions, impose straightness and surface shape deviations. Furthermore, changes of mechanical properties specific to the solar sail demonstrator Gossamer-1 and its envisioned operational environment in space are analyzed. This includes determining the degradation of structural performance e.g. by the influence of atomic oxygen eroding material properties, high velocity impacts by micro meteoroids and orbital space debris, or test equipment itself.

In order to validate the findings made in this thesis, mechanical experiments are performed in chapter 7 on a case study on the Boom Subsystem of Gossamer-1 and its boom component, with the goal to quantify performance parameters that determine robustness for a subsystem (robustness parameters). Furthermore, the test stand and principle, that have been developed for this purpose is described, and the generated results from lateral bending and quasi-axial compression loading are compared discussing their impact on robustness. In a finite element analysis the tests are simulated with the aim to predict and generate characteristic mechanical parameters of a boom influenced e.g. by atomic oxygen degradation, weightlessness, shape deformations, impact damage or thermal conditions, and can therefore not be tested in full size in a lab environment. Finally, robustness is quantified and compared for different load cases using the obtained results in a combination of robustness parameters and weighting factors, as developed within this thesis.

Conclusively chapter 8 provides a summary of the findings and developments, and addresses issues that arose during this thesis. It furthermore gives an outlook and suggestions for future work in this field.

## 2. AIM OF THESIS AND HYPOTHESES

Gossamer Structural Space Systems (GosSSS) are delicate and ultra-light weight structural systems that deploy large functional areas, and are designed for very low loads utilized under zero gravity environments in space. As the demand for efficient and affordable solutions for space exploration, communication and observation, power generation and debris mitigation increase with the emerging market of the space industry, Gossamer Structural Space Systems are experiencing a rising interest in. They are comparably cheap in production, low in maintenance, while saving mass and volume during launch.

However, as broader application is anticipated making use their full potential, an increased acceptance with more flight opportunities rely on the question of their performance while being influenced e.g. by being stored in stowed configuration for an extended period of time and operated under harsh conditions in space afterwards. This consequently raises the question about robustness, as customers and agencies demand a proof of robust performance of GosSSS, albeit being very weight efficient. The here presented thesis seeks to answer this question and further addresses a methodical assessment of robustness, while also elaborating on how to quantify robustness in a most suitable manner. Designed to save structural mass and volume by being foldable and deployable, Gossamer Structural Space Systems provide large functional areas or length at the same time. This leads to structural elements with ultra-thin wall thicknesses and large dimensions, like deployable thin shell CFRP booms, thin membranes or delicate interfaces. However, this induces also difficulties when designing, building, testing and qualifying such structural system, as they are prone to deviations in loading, geometry or material imperfections and external influences. Until now, robustness for GosSSS has not been investigated or systematically considered in methodology or design procedures. It is further assumed that robustness and performance of GosSSS can only be significantly increased if its characteristics are known, understood and quantifiable, as this is generally true for technical systems. This can most efficiently be done in terms of quantified values of robustness, representing performance under existing influences [1–4].

As it is necessary to determine how well a deployable Gossamer system performs under e.g. space environment, external influences and deviating loads, robustness should already be considered the design process. Nevertheless, the characteristics of GosSSS and their robustness are not addressed in present design guide lines for space systems and structures as given with [5–7]. Furthermore, only a brief description of Gossamer Structural Space Systems in terms of thin walled structures, mainly referring to inflatable structures, is outlined. Nevertheless, Hillebrandt [8] developed a conceptual design methodology, based on a system analysis, that aims to generating GosSSS consisting of a deformable structure and a deployment mechanism. With the goal of identifying design drivers and specific characteristics, he determined analytic sizing expressions for several deployable masts and their deployment mechanism components. While this approach is complementary to an overall GosSSS design methodology by providing indicators for functional and mechanical performance, robustness has not been considered. In literature, robustness is defined and approached very differently in different fields of engineering, and mostly determined theoretically on greatly simplified system models. However, in order to provide realistic robustness statements, practical approaches complying with the characteristics of GosSSS are necessary. It is further assumed advantageous to determine overall system robustness from constituents like subsystem robustness using a bottom-up approach instead of a top-down approach. This may reduce the effort of determining robustness and provide robustness for each subsystem, as they are usually developed by different parties. For increased system robustness, it is necessary to provide quantified data of imperfections, environmental effects or material behavior as well as resulting consequences, since GosSSS with their delicate structures are prone to those impacting influences. While current standards do not provide data at all, valuable experiences in designing, testing and operation from more than 1000 launched deployable booms and 38 missions are analyzed and summarized in a NASA guideline in [9]. However, this guideline only provides information in a qualitative form and is limited to a single application type using open profile metallic stem booms. This underlines even more the need for quantified



values that should be considered in order to achieve a robust design of deployable Gossamer Structural Space Systems. Thus, a precise and dedicated framework facilitating a realistic and appropriate methodology for robustness assessment should be developed.

Additionally, to these goals, the thesis further aims for developing the necessary robustness metrics, complying with the specific characteristics of GosSSS, while being measurable. The idea of robustness considered as a composition of several robustness components, that contribute in a varying extend as functions differ, even at different phases of a mission, is therefore followed. Moreover, it is essential to include acting influences and interactions when deriving such metrics. It is further aimed for developing a framework that incorporates the robustness assessment methodology into the design process of such structural systems. Consequently, this thesis shall provide an improvement in structural system robustness, performance and their prediction, by offering a methodology for technical decisions on the commercial and scientific use of GosSSS.

To do so existing Gossamer systems need to be analyzed for deficiencies, lacking robustness, detrimental effects and affecting influences. Existing robustness approaches need to be investigated in order to derive new specific robustness metrics that can apply to the characteristics of Gossamer systems. Furthermore, mathematical relations need to be established that determine the robustness assessment methodology. While those relations are assumed conditional, interactions within a Gossamer system as well as their dependence on different phases of a mission must be scrutinized. Here quantifiable and measurable robustness parameters and acting influences for each subsystem shall be identified and implemented in terms of metrics and factors. Determining such influences in practical experiments is therefore inevitable in order to provide quantified and realistic robustness values. Finally, the developed robustness methodology shall be applied on a practical example.

In order to achieve the set aims, the thesis follows a basic hypothesis and four work hypotheses that have been derived from the anticipated goals and are used as guiding pillars along the process of investigation, study and research as follows:

### **Basic Hypothesis**

“If all connections, interactions, functions and influences on subsystem level of a deployable Gossamer Structural Space System are known, overall system robustness can be quantified as a composite of single subsystem robustness.”

### **1. Work Hypothesis**

“Connections and interactions of subsystems can be captured sufficiently in robustness by using weighting factors, while simple addition or multiplication of partial robustness values does not suffice.”

### **2. Work Hypothesis**

“Realistic robustness determination demands parameters that are measurable values and related to the fulfillment of essential subsystem and system functions.”

### **3. Work Hypothesis**

“Influences, impacting geometry, loads, material, mechanical behavior, test and simulation results of components and subsystems, regarded as factors, contribute to a realistic structural robustness quantification of subsystems and system.”

### **4. Work Hypothesis**

“Robustness of Gossamer Structural Space Systems is conditional to the mission phase for which it is determined for and its application.”

In chapter 3 the state-of-the-art Gossamer Structural Space Systems and applications is analyzed for deficiencies and damages in regard to robustness. Further the state-of-the-art in robustness approaches that had been developed for different fields are analyzed and discussed, while existing design approaches are studied on how and at which point in development robustness assessment is most beneficial for GosSSS. Necessary requirements to be regarded for the development of a robustness methodology and metric are defined in chapter 4 and approaches of bottom-up and top-down strategies in terms system composition, thus evaluating the **2. Work Hypothesis**, and discusses conditional robustness relations with the **4. Work Hypothesis**. Along with this consideration, a mathematical robustness approach is developed and discussed, thus scrutinizing the **1. Work Hypothesis**. The chapter closes with the developed framework for robustness assessment and quantification as well as with an implementation into the design process. In chapter 5, in a case study, a Gossamer Structural Space System is analyzed on the example of a solar sail spacecraft, further scrutinizing the **2. Work Hypothesis** and **1. Work Hypothesis**. Moreover, a system and function structure for this example is synthesized and analyzed for applicable and quantifiable parameters that can be used as partial measure of robustness. It is further worked on the **3. Work Hypothesis** as influences and their according quantifiable factors are identified, and weighting factors, representing subsystem interactions and functions, are developed. Chapter 6 focuses on the experimental determination of values for the most important influence factors that affect e.g. subsystem robustness and therefore addresses the **3. Work Hypothesis**. In a case study based on the Gossamer system analyzed in chapter 5, the developed robustness assessment methodology is applied to a boom subsystem in chapter 7. In here, methodology, weighting factors and influences are applied in simulations and experiments in order to achieve and compare its robustness, thus assessing the **3. Work Hypothesis**. Chapter 8 is giving a summary, outlook and conclusions.

### 3. STATE OF THE ART GOSSAMER STRUCTURAL SPACE SYSTEMS, DESIGN PHILOSOPHIES & ROBUSTNESS

This chapter discusses the state of the art of Gossamer Structural Space Systems, further termed GosSSS, and methods related to structural robustness. Starting with their definition, application as well as a classification and an extended list of advanced applications, the discussion about robustness in GosSSS begins with examples of damages and failures, based on deficiencies in robustness, on advanced and flying GosSSS in service today. This is followed by the description of basic design elements and requirements of GosSSS. Following is a review of the standard design process, while discussing the allocation of application of robustness assessment within the development and design process. Then definitions of robustness as well as robust design are discussed and transferred to Gossamer Structural Space Systems. The chapter ends with a review of existing design metrics and a discussion related to their application on GosSSS as well as their deficiencies.

#### 3.1 Gossamer Structural Space Systems & Applications

##### 3.1.1 Definition and Heritage

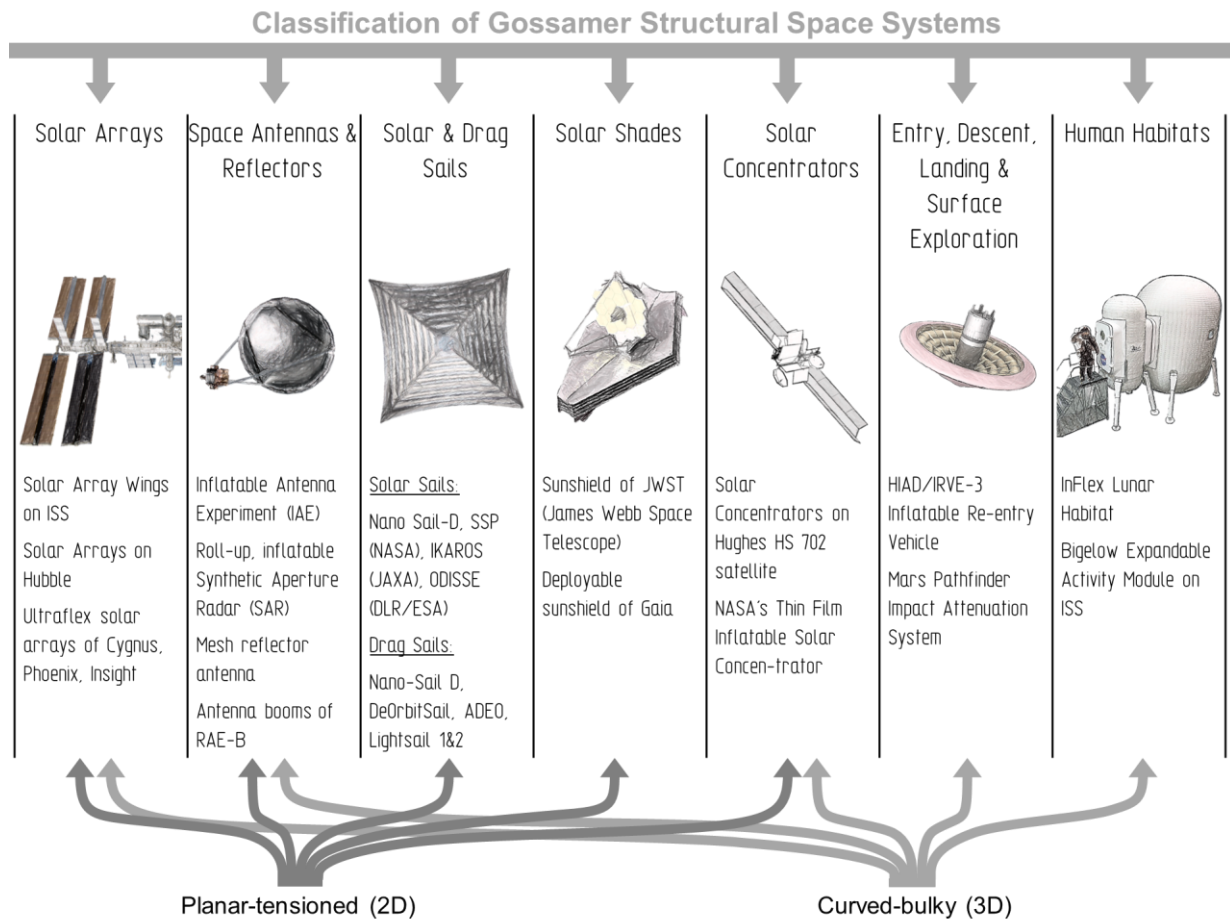
The definition of the term Gossamer is not very well known and only found in a few literature sources. One definition derives from the Middle English term *goose summer* and “signifies something tenuous and insubstantial such as a cobweb floating in the air” [3]. *Goose summer* was used to refer to geese sold at the end of summer fairs as a traditional meal on Michaelmas (September 29). In this time of the year spiders ballooning, mainly linyphiid or money spiders, was at its greatest because of perfect atmosphere conditions. Huge amounts of gossamer, or “angel hair”, descended from the air covering very large areas. According to Jenkins in [3] however, Gossamer structures in engineering are defining a general category of ultra-low-mass space structures, that are expandable, deployable or inflatable in some way to large areal or length dimensions. Space applications of this kind are mostly using functional areas (membranes) that are deployed by a supporting and stiffening structure in combination with some actuator or deployment mechanism. The membrane itself is comprised of highly flexible two-dimensional plate elements made of thin, low modulus materials, such as polymer films or some kind of mesh material. They provide very little inherent bending stiffness and are unable to carry compressive loads. Regarding these circumstances this type of space structures is usually found in planar-tensioned and in curved-bulky (mostly inflated) configurations. Recent technological advancements in ultra-light-weight, deployable space structures pose new technological possibilities to the space community with a low-cost, low-mass, low-volume alternative to conventional mechanical space structures or propulsion system. Gossamer structures have the potential to provide many benefits and advantages over current mechanical systems. While lower in mass and packaged into smaller volumes, they can potentially reduce the overall space mission costs by reducing the launch vehicle size requirements. Thus, reducing total system mass and deployment complexity an increase in system reliability is another advantage.

Many Gossamer Space applications are using membranes in order to provide large functional areas and are developed with different aims and goals. Yet most applications share the most significant characteristics: low packaging volume (high packaging efficiency), large area at low mass (low areal density, low specific mass) and flexibility. Additionally, all applications are deployed in some way and strive for the lowest mass possible while providing the necessary stiffness to keep functional areas taught. This is achieved through some combination of low modulus and thin materials, typically thin polymer sheets, films, mesh or thin-walled polymer tubes and by lightweight metal or fabric booms, trusses or inflatable structural elements, which span out one or more functional membranes and provide the necessary structural support.

In the following sub sections, different Gossamer Structural Space System applications are listed by type of application while most advanced and flown examples are explained in more detail.

### 3.1.2 Classification and Examples

As the previous section describes the specific characteristics of Gossamer structures, this sub section gives an overview of the most relevant applications of such structural systems. These can be classified in different ways, by application, by structural elements used or by build type. Here these structural systems are classified by type of application, as depicted in Figure 3.1. This is considered beneficial regarding the purpose of informing about their function and the possibilities provided. Besides providing the derived classes, Figure 3.1. further contains representative images of typical applications of each class as well as some example applications below. The determined classes are: *Solar Arrays*, used for power generation; *Space Antennas & Reflectors*, used for communication and earth observation; *Solar & Drag Sails*, used for propulsion with sun light and deorbiting via drag augmentation respectively; *Solar Shades*, used for shading instruments; *Solar Concentrators*, used for concentrating sunlight to increase power generation efficiency; *Entry, Descent, Landing (EDL) & Surface Exploration*, used for atmospheric entry, re-entry and descent as well as extraterrestrial surface exploration; and *Human Habitats*, used for housing for manned mission in space and extraterrestrial surfaces. However, the sub categories *planar-tensioned (2D)*, generally flat and tensioned membrane structures with large two-dimensional expansion, and *curved-bulky (3D)*, voluminous and curved structures, mostly inflated, with large three-dimensional expansion, are introduced in order to distinguish different build types within a class of GosSSS applications. Nonetheless, single structural elements of structure in a sub category might feature characteristics of the other sub category e.g. inflatable booms for planar sails. The build type that is discussed in this thesis fall within the sub category of planar-tensioned structural systems. Nevertheless, general findings and methods as discussed e.g. in chapter 4 can also be applied to other sub categories.



**Figure 3.1.** Classification of Gossamer Structural Space Systems by application

A comprehensive list of existing GosSSS applications featuring the most advanced examples for each class is given in Table A. 1, in Appendix A. These examples represent the most widely known and advanced ones. Here images of the applications, their most significant specifications and technological status, as well as references are provided for further interest. While this overview gives an impressive extend of GosSSS applications already or about to be brought into service in commercial aerospace, unpublished, confidential or potentially ongoing developments are not described due to inaccessibility.

Some examples and their encountered deficiencies in robustness during their flight mission are discussed in the following section (section 3.1.3).

### 3.1.3 Deficiencies in Robustness & Resulting Damages on GosSSS Applications

This section gives examples of existing and advanced GosSSS in in-orbit service that encountered damages and failures throughout their service life. The resulting damages and encountered failures are assumed to have their origin in lacking robustness, as proposed. However, there are also incidence given in which a sufficient robustness can be assumed. Nevertheless, mostly no quantitative data of the degree of function loss in case of a damage is given, while all examples have in common that robustness was not determined. These issues might show in many different types of failures, damages, influences and impacts encountered by ultra-light weight and delicate space structures such as: material degradation and change of chemical and physical properties due to UV light or ATOX; damage due to particle impacts; mechanical misbehavior and changed kinematics; changed mechano-dynamical behavior due to large temperature gradients and vacuum, unknown and unpredicted interactions due to insufficient on ground validation available; and others. Eventually resulting in degradation of the application's intended function, dramatic cost increases due to additional servicing, replacements or even to total loss have been encountered.

#### *Encountered Deficiencies on the Solar Array Wings of the International Space Station ISS*

The most visible and impressive example of Gossamer Structural Space Systems in operation is the deployable array phalance presently in use on the International Space Station (ISS), depicted in Figure 3.2 a). Each of the Solar Array Wings (SAW) extends about 34 m in length and 12 m in width from the ISS to a wingspan of 73 m, using 262,400 solar cells that produce 32 kW of electricity [10]. A wing consists of two rectangle and retractable blankets with solar cells held by a deployable FAST truss mast (ATK Aerospace Systems, formerly ABLE Engineering, Inc., U.S.) between them [11]. When stowed, each wing z-folds into a solar array blanket box just 51 cm high and 4.57 m in length, while the masts fold into canisters.[12] Currently the ISS uses its full complement of eight solar array wings for power generation [13].

Although ISS' solar arrays have been on duty for many years, some critical situations with damages and failures occurred during that time, all attributable to lacking robustness. The still image in Figure 3.2 b) was taken by a crewmember aboard the Space Shuttle Discovery on Shuttle Mission STS-116. It depicts a kink that occurred on the portside P6 of the solar array of the ISS during the first attempt to retract that array on December 13 2006, leading to a potential major failure. The crew later extended the array again, cleared the kink and successfully resumed retraction with a slower retraction rate without any issues this time [14].

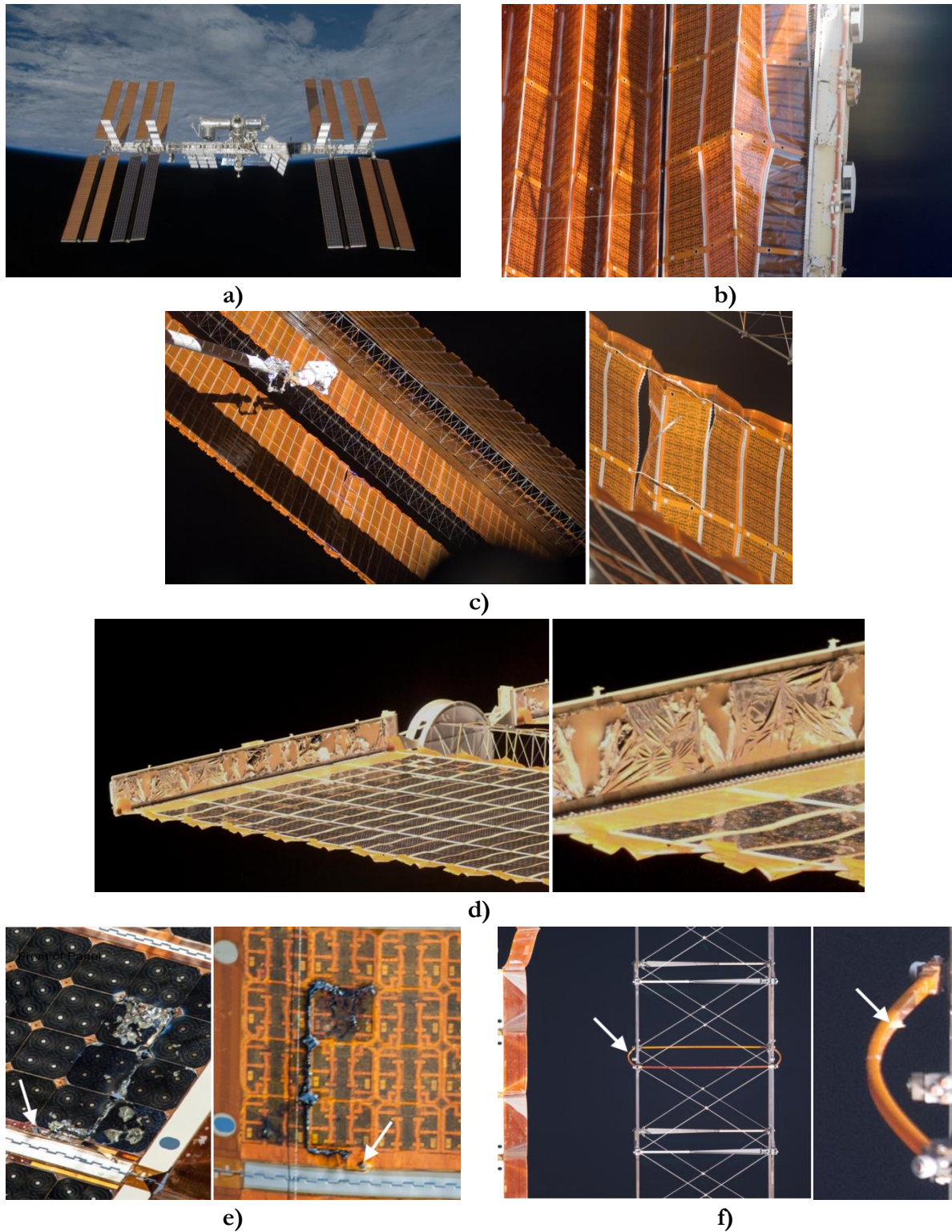
Another incident occurred in November of 2007 during Space Shuttle Mission STS-120. With the goal to finalize the installation and repositioning of the P6 solar wings in its permanent home at the end of the port side of the station, the two wings had to be extended. While the first went smoothly, on the second wing, a guide wire snagged, causing tears in two of the panels. With the wing only 80 % extended, the operation was halted after seven hours. The partially deployed array was producing power, but an unplanned and untrained spacewalk repair was needed to allow it to fully extend. Using strips of aluminum, a hole punch, a bolt connector and about 20 m of wire, the astronauts constructed hinge stabilizers that would strengthen the damaged hinges on the solar array. Not only was this increasing the risk for two astronauts outside in space, it also demanded about seven

additional hours of crew time, an hour and a half alone to reach the worksite, located about 50 m down the station's truss and 27 m out on the damaged the solar wing. Images of the damage, the repaired panel, as well as the repair spacewalk itself are displayed in Figure 3.2 c). After the successful repair, flight controllers on the ground successfully completed the deployment of the array [15, 16]. A further weak spot in terms of robustness shows in damages caused over a large period of time. Defects in the vapor deposited aluminum coatings on both surfaces of a Kapton covering, on ISS' solar array blanket box cushions allowed atomic oxygen to become trapped, completely oxidizing the underlying Kapton. This resulted in torn and partially detached protective aluminum film, leaving the structural surface unprotected as depicted in Figure 3.2 d). Atomic oxygen interacts readily with many materials especially hydrocarbon polymers. It is highly reactive, breaks chemical bonds, oxidizes and erodes materials. In the here described case an undercutting has occurred allowing oxygen to attack the polymer film and eroding it [17]. Delicate Gossamer Structural Space System like solar array blankets, thermal control polymers, and fiber-reinforced plastics (composites) are at high risk since oxidization causes these structures to become thinner and less capable of supporting the loads imposed upon them. Fortunately, the solar array blankets of the ISS themselves have a double-sided, protective coating of 1300 Å of sputter deposited SiO<sub>2</sub>, showing a higher resistance towards oxidation than aluminum coatings [18]. However, they may show similar effects of erosion over time as simulations and experiments indicate.

Another incident attributable to lacking robustness was documented by astronauts. Impacts caused by micrometeoroids and orbital space debris (MMOD) led to critical damages on the solar array wings of the ISS. Being initially a tiny hole in the solar array blanket one impact broke a bypass diode causing an overheat damage, eventually leaving a larger area of the array inoperable, as reported by NASA [19] and images of the front and back panel in Figure 3.2 e) indicate. Yet another critical MMOD damage was observed on the deployable solar array truss mast of ISS' solar arrays. One of the delicate but vital and stability providing elements of the mast (flexible batten) had been damaged from MMOD impacts as depicted in Figure 3.2 f). In order to access the residual strength and to ensure a safe operation of the International Space Station, on-ground hypervelocity impact test had to be performed for validation. [20] However, MMOD impact damages are not specific to Gossamer Structural Space Systems, but their effect can be much more severe, as impact probability increases with increasing dimensions and damage severity with thinner materials and less protective structures. However, this is the case for Gossamer Structural Space Systems and should be considered by robustness considerations.

Further effects from space environment among other aspects are discussed in greater detail in section 0.





**Figure 3.2.** ISS' solar arrays – damages due to lacking robustness  
**a)** Fully deployed solar array wing configuration [10], **b)** Kink forming during retraction, **c)** Damage due to ripping during deployment of solar array and repaired area [16], **d)** Erosion damage by ATOX on solar array blanket box cushion after one year in LEO [17], **e)** Impact damage on ISS pv of solar array (impact puncture marked with arrow) shown on front (left) and back side (right) [19], **f)** Impact damage on a structural part of ISS' solar array deployable truss mast (impact marked with arrow) [20]

### *Encountered Deficiencies on Hubble's flexible Solar Arrays*

Another example of flown and in space operated GosSSS is the Hubble Space Telescope (HST), more precisely its first two sets of solar arrays. Designed by ESA and other European partners, they were flexible and ultra-light weight roll-out arrays, similar to roller blinds, arranged in two identical wings with a size of 2.9 m x 12.9 m each [21]. The main driver to use flexible, rollable and retractable solar arrays was the original plan to roll them back up for maintenance of HST by the Space Shuttle every 2.5 years, and returning the entire telescope with rolled up arrays to Earth for major overhauls every five years. Therefore, the arrays needed to fit between the hull of the telescope and the round cargo bay of the Shuttle. However, maintenance was eventually only carried out in-orbit [22].

The solar array wings were lightweight, however still somewhat complex. Each wing consists of two flexible solar cell blankets (a composite of Glass fiber, Kapton™ layers, adhesive and a silver mesh) that are rolled up on a drum, and are attached to a spreader bar that is held by two stainless steel Bi-STEM booms at their tips (see Figure 3.3 a). These booms are made from thin metal strips of stainless steel formed into circular cross sections, each of 6.4 cm in diameter, 0.13 mm thick, with a 30° slit opening oriented 180°. For storage they are flattened and rolled up on spools or cassettes. While being rolled out and pushed out of their mechanisms they are unfurling the blankets synchronously and keeping them taut [21].

Already early in operation, the advanced flexible solar arrays of Hubble encountered some problems simply because of their flexibility, the lightweight, delicate design and the harsh space environment, and consequently a lack of robustness. Soon after deployment detrimental vibrational disturbances were observed, which were thermally induced during orbital sunlight/eclipse transition. The caused oscillations were estimated to be two to three orders of magnitude greater than the allowable jitter for the telescope and large enough to hinder focusing on distant objects, thus negatively affecting Hubble's very-high angular resolution imaging [21]. Two main causes were identified according to Foster [21] as boom vibrations due to thermal gradients and a possible stick/slip behavior in the blanket tension mechanism (drums and spreader bars). The open cross section Bi-STEM booms of the flexible solar arrays caused some problems in resonant frequencies. Because of these open cross section elements were overlapping each other the same temperature was expected by default design, but due to a poor thermal contact when one side was in sunlight and one in shadow they expanded at differential rates, causing a clicking against each other [21]. The second failure on a compensation mechanism on one of the arrays caused one boom bent like a bow and Hubble's solar arrays were flexing every time they passed through the day-night terminator. Images taken after deployment, during the first Hubble mission (STS-31), indicate that a significant boom curvature resulted in a twist at the spreader bar as much as 12° out of plane [21]. Figure 3.3 b shows these images with a close up on the left images and a comparison of twisted and unaffected array with the two right images. Additionally, when the crew of the first servicing mission (Shuttle Mission STS-61) tried to retract that array, the bent boom split and could not fully be hauled. Instead astronaut Kathy Thornton released it into space in order for it to burn up into the atmosphere. Later a close-up examination of the solar array that had been brought back to Earth showed one of the array compensator springs had broken, caused by a micrometeoroid impact [22]. Furthermore, the temperature has cycled between +60 °C to -85 °C and back 45000 times during the lifetime of the second set of arrays causing cracks due to thermal cycling on different areas [30].

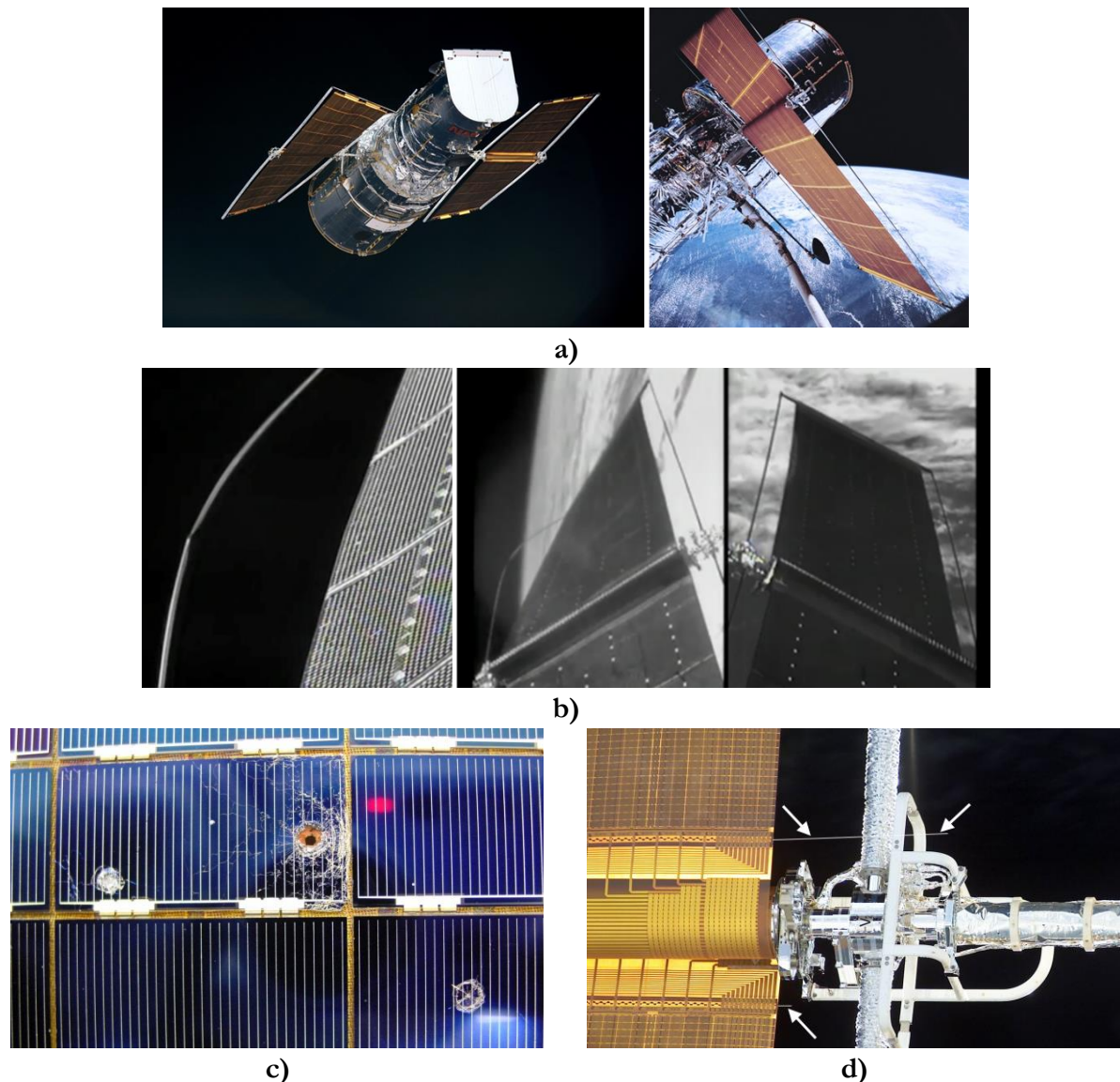
In recognition of the severe damage micrometeoroids and orbital space debris (MMOD) might cause post-flight impact investigations, initiated by ESA, were undertaken on the one retrieved solar array of the first and on both solar arrays of the second set. Over their total surface area of roughly 120 m<sup>2</sup>, including 42 m<sup>2</sup> covered with solar cells, exposed over 8 years to space environment, the retrieved solar array wings exhibited thousands of craters [23, 24]. About 80000 particle impacts of varying sizes were found, many of which are visible to the naked eye according to Moussi et al [25]. A few hundred impacts have completely penetrated the 0.7 mm thin blankets while the largest impact features are about 7–8 mm in diameter [23, 24]. The impact survey revealed 400 craters larger than 3.7 mm and about 175 clear holes. One of the severe penetration damages is depicted in Figure 3.3



c), showing a clear hole. Surprisingly, the total cratered solar cell area was  $<0.2\%$ , barely exhibiting any power degradation and thus indicating good robustness in this regard [22, 23].

However, insufficient robustness can be assumed for another incident seen on other mechanical parts of the solar arrays. Several of the 2.4 m long pins of the piano hinge like connections that hold the segments of solar cells together were protruding from one of the sides of the arrays, as depicted in Figure 3.3 d). Engineers believed that these pins wander back and forth due to differences in the thermal expansion between the solar blanket and the pins themselves when Hubble comes in and out of the Sun [25]. Extending up to 50 cm out from the array edge, the wire-like hinge pins holding different segments of the solar blankets together had come loose. Emergency testing on ground showed that the astronaut's spacesuits were not in danger to be damaged, nor would the solar panels fall apart. Fortunately and not designed for, the array's power bridge pieces were strong enough to hold the structure together for the remaining mission life and for the planned retraction during the Servicing Mission 3B retraction, thus showing some unplanned local robustness [22].

Moreover, space environment itself demands high robustness as seen on the effects of UV radiation as well as atomic oxygen. Analyzing Hubble's solar arrays showed strong evidence for chemical degradation e.g. the found severe darkening of the silicone adhesive due to UV radiation exposure [22]. Another effect that illustrates lack of robustness was seen during a Space Shuttle servicing mission. A delamination of the solar array bus bars was observed. However, while silver material for the interconnectors of the solar array blankets had to be dropped from the design due to severe oxidation, revealed on a test flight of a shuttle mission, the flown interconnectors were made of molybdenum-based metals, which were oxygen safe, while the Kapton was protected by a silicone coating. Solving these issues and thus increasing robustness was addressed by updating the control system to attenuate the disturbances and by enclosing the bi-stem boom in a foil bellow as thermal shielding to reduce the disturbances in the first place. Additionally the initial blanket compensation mechanism was replaced by a kind of bedspring system with a set of limit straps as back up (passive redundancy) to ensure the blanket is held together and functioning [25]. Although delivering even 10 % above the required 4 kW of power and lasting 8 years instead of the 5 years it was designed for, the flexible solar arrays were replaced on orbit by the third set of US-made models (rigid, mechanically and thermally new designed) during the 2002 Servicing Mission. Replacing the flexible solar arrays was mainly owed to the degradation of this structural system and consequently due to insufficient robustness. Furthermore, the fact that the idea of retrieving the solar arrays of Hubble on the Shuttle had been abandoned made the foldable and flexible features of the solar arrays obsolete. The last set of solar wings now possessed a rigid architecture, derived from Iridium satellites, and had a higher output at twice the weight of the first two set [22].



**Figure 3.3.** Hubble's flexible Solar Arrays— damages and sensitivities

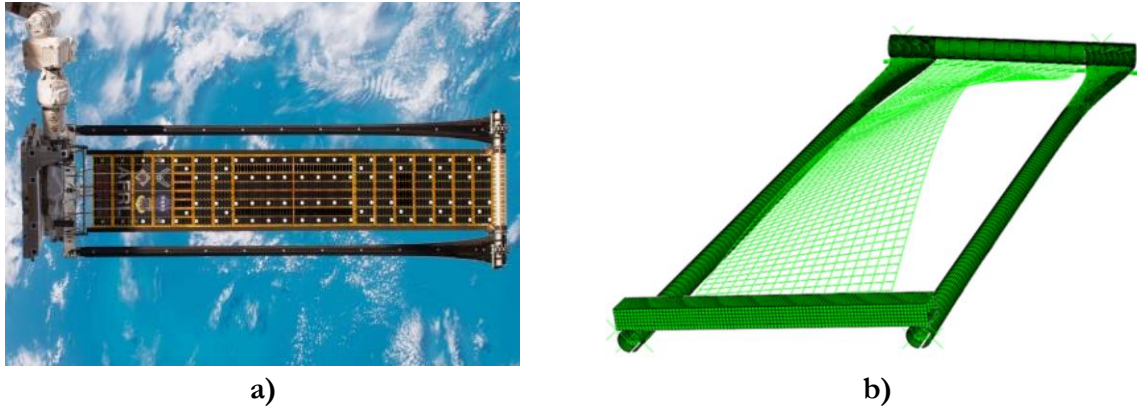
**a)** Flexible roll-out solar arrays on Hubble [26, 27], **b)** Deformed solar array panel due to kinked metal STEM boom observed during the 1<sup>st</sup> servicing mission STS 61 (left: kinked boom, middle and right: comparison of deformed and intact solar array) [28], **c)** Debris impact damages observed on the first set of Hubble's solar arrays [29], **d)** Displaced pins reaching out of the solar array piano wire hinges [30]

### *Anomalies encountered by the Roll-Out Solar Array ROSA*

An example that faced some anomalies during testing is the Roll-Out Solar Array (ROSA), developed by the Air Force Research Laboratory (AFRL), the National Aeronautics and Space Administration (NASA), and Deployable Space Systems, Inc. (DSS), as a lightweight alternative to conventional rigid panel solar arrays. The 5.40 m x 1.67 m experimental ROSA wing, using composite slit tubes as structural frame, was launched to the International Space Station (ISS) on the SpaceX Falcon 9 Commercial Resupply Services mission (CRS-11) in 2017, inside the unpressurized trunk of the Dragon spacecraft. Two anomalies occurred [31]: First, the fundamental system bending mode was measured to be 20 % lower than predicted by finite element models, seemed highly damped and was far more difficult to excite than during testing in vacuum on ground prior to flight. Moreover, an unexpected motion of ISS' Special Purpose Dexterous Manipulator (SPDM), the robotic arm it was attached to, could be clearly seen. Indicating that ROSA was driving motion into the robot arm, pre-

flight analysis suggested otherwise, assuming that the small lightweight solar array could not impart any motion in the large robot arm when its joints were locked.

A second anomaly observed was that the right edge of the solar array blanket seemed to vibrate at greater amplitude and lower frequency than the left edge. As analyses indicate an uneven blanket tension may be the source of this anomaly according to Chamberlain [31].



**Figure 3.4.** a) The deployed Roll-Out Solar Array (ROSA), during on-orbit testing, attached to ISS' robotic arm (SPDM) of ISS [32] (image cropped); Blanket flap mode (FEM) causing anomalies [31]

### 3.1.4 Basic Structural System Design, Elements & Functions

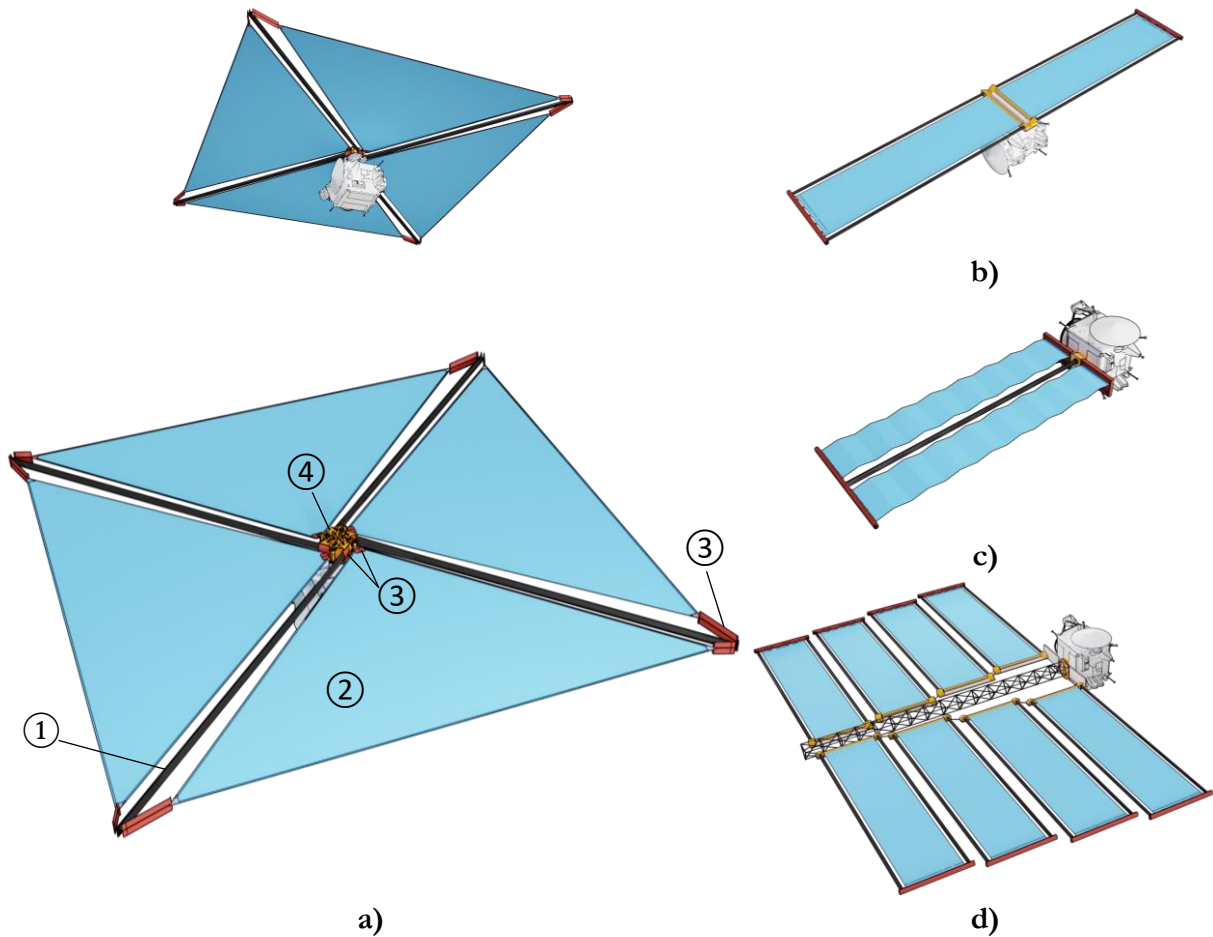
Although many of the aspects discussed in this thesis apply to Gossamer Structural Space Systems in general, the focus is put on systems using booms to deploy and stretch functional membranes, thus falling into the sub class of planar-tensioned, two-dimensional systems (cf. section 3.1.2). With the plethora of designs and applications for such structural systems as revised in the previous section 3.1.2., main elements and main configurations can be synthesized. At this point it is worth noting that the satellite main structure, the bus and electronics are not considered elements of a Gossamer structural space system, within this thesis. Nevertheless, the main structure is necessary to direct and transfer loads from the GosSSS into the spacecraft, while requirements based on e.g. the main structure or spacecraft adapter might bias the GosSSS design.

The main elements of GosSSS considered here are:

- 1) *Booms/Trusses*: such as rollable, collapsible, telescopic or inflatable booms made of CFRP, metal alloy or polymer film, supporting and stabilizing the tensioned system.
- 2) *Functional membrane(s)*: film like material for solar sails, drag sails, photovoltaic blankets, substrate membranes for antennas, or mesh material for such applications; to reflect and/or transmit electromagnetic radiation or to provide drag.
- 3) *Interfaces (I/F)*: that connect boom(s) and membrane(s) to one another, to the main structure, transfer loads, and/or to provide boundary conditions e.g. guiding booms towards a certain direction or enforcing certain cross-sectional dimensions.
- 4) *Mechanisms*: can be active and passive mechanisms that deploy and/or retract the booms or membranes, control movement, force and speeds, while inhibiting uncontrolled deployments.

In Figure 3.5, these elements (numbered 1 to 4) are depicted in the three main configurations of planar-tensioned GosSSS. In the first configuration, as depicted in Figure 3.5 a), the booms are arranged in a cross like manner in order to stretch triangular membrane segments, mostly in a symmetrical manner, resulting in a squared overall shape. The second main configuration comprises

parallel booms, stretching rectangular membranes (rolled or z-folded), thus providing an elongated rectangular shape. This is depicted in Figure 3.5 b). The third main configuration synthesized consists of a central single boom deploying two parallel membranes with a cross beam as seen e.g. on ISS' solar arrays. This results in an elongated rectangular shape as well, as illustrated in Figure 3.5 c). Additionally, more complex configurations combining two or more main configurations e.g. using several booms deployed from a central boom or truss as depicted in Figure 3.5 d) are possible as well.



**Figure 3.5.** Main configurations a) to c), with a combined configuration d), and main elements (① Booms, ② Membrane(s), ③ Interfaces, ④ Mechanism(s), main spacecraft in white) of Gossamer structural Space Systems

According to ECSS standards, the defined elements are classified, depending on their complexity, into certain levels. These levels are defined by the ECSS standard ECSS-E-ST-10-03C, Space engineering – Testing, to: system level, considering space segment system, space segment elements as stand-alone or embedded space segment elements; sub system level, considering space segment sub-systems or equipment; and component level, considering components and materials. Additionally, a sub level of components is used for coupons if this granularity is needed. For example, in this thesis a boom alone is considered as component, while a boom cross (comprising of four booms) or a boom in conjunction with interfaces, sensors or other parts is considered as sub system. Consequently, a complete assembly of booms, membranes, interfaces and mechanisms is considered a system, and is further referred to as structural system, Gossamer Structural Space System (GosSSS) or just system, throughout this thesis. Further considerations of complexity levels, especially concerning robustness are discussed in chapter 4.

### 3.1.5 System Requirements & Characteristics

Generally, when compiling a requirements-list for a design mission requirements are translated into technical requirements for system, subsystem and components at the beginning of the concept phase. However, considering the many different applications and designs as described in section 3.1.3, it becomes obvious that requirements in a quantitative manner are not feasible to compile. Nonetheless, requirements and characteristics can be composed in a qualitative way for such ultra-light weight structures.

The specific requirements (not regarding requirements for space structures in general) and characteristics (see also section 3.1) that are based upon them are:

<i>Requirement</i>	<i>Characteristics</i>
Large dimensions in operation (length, area, volume)	– low areal density ( $\text{g}/\text{m}^2$ ); large area at low mass
Small dimensions when stowed (during launch & transfer)	– low specific mass ( $\text{g}/\text{m}$ ); large length at low mass
Minimal mass	– deployable (foldable & unfoldable)
	– high packaging ratio; low stowage volume
	– high flexibility
Deployment controllability & reliability	– low Eigen frequencies
	– thin wall thickness of structures
(Scalability)	– can take only very small loads compared to conventional space structures
	– lowest mass possible while providing the necessary stiffness to keep functional areas taut

The requirement for large dimensions when deployed and in operation is based on the need for large functional areas e.g. to maximize power generation, propulsion, drag, shading and others, depending on the applications. In contrast, small dimensions are required when stowed leading to a small stowage volume accounting for the comparably small payload capacity (volume wise) of launchers and costs for transport. For example, will the James Webb Space Telescope be launched on an Ariane 5 rocket. The actual dimensions of the Gossamer structural space system on JWST, the sun shield, are about 21 m x 14 m [33] in operation. However the Ariane 5 usable payload volume offers only cylindrical dimensions of 4.5 m in diameter and a height of 10 m, with a conical volume on top of 5.6 m in height leading to a tapered diameter of about 1 m according to the Ariane 5 user's manual [34]. This makes the necessity of small stowage dimensions well visible. Minimal mass is required many times for cost reasons of transport. Additionally, a minimally achievable mass is also needed when maneuvering and controlling attitude of a spacecraft equipped with such structural system, or when propelling with very small forces as found in solar sail and drag sail applications. Deployment controllability and reliability are important requirements. In order to prevent dynamic loads, that can be harmful and cause damage on the structural system, deployment controllability must be provided. This is usually realized in terms of controlling deployment speed, deployed length and deployment forces. Providing save and repeatable deployment on the other hand is realized with an appropriate reliability of the deployment process, usually validated by extensive testing. Depending on the application scalability is not necessarily required for all Gossamer Structural Space Systems. In many cases the development process along the levels of technical readiness starts with a proof of principle or concept on a smaller scale. This is mostly done for cost and schedule reasons. In order to provide



the same behavior in later designs for the final application in space with larger dimensions, as found in smaller test or bread board versions, scalability is required to be considered already from the beginning e.g. in the concept phase.

Listing even further requirements Sickinger [35] provides several sources of specific requirements for e.g. inflatable systems or solar sails as well as criteria for requirement evaluation, that are valid for all structures dedicated for operation in space, not only Gossamer Structural Space Systems. Such general criteria are: robustness of design, system complexity and redundancy, energy demand, level of technology readiness, costs of development, (including verification, manufacturing and integration), capability of on ground verification, stow ability, thermo-elastic stability, geometric accuracy, withstanding space environment, demanded life cycle time, mitigation of space debris. As good practice for all technical systems, the necessary technical specifications as well as costs and risks must be evaluated and traded off throughout the entire design process.

### **3.2 Standard Design Approach, Principles & Allocation of Robustness Assessment**

This section briefly reviews the standard design approach in space product engineering, with its life cycle, as well as applicable standards in regard to the implementation of robustness. Further the allocation of the proposed robustness assessment and quantification within the standard design process and the different levels of abstraction are given. Additionally, this section reviews the established design philosophies and principles in regard to GosSSS.

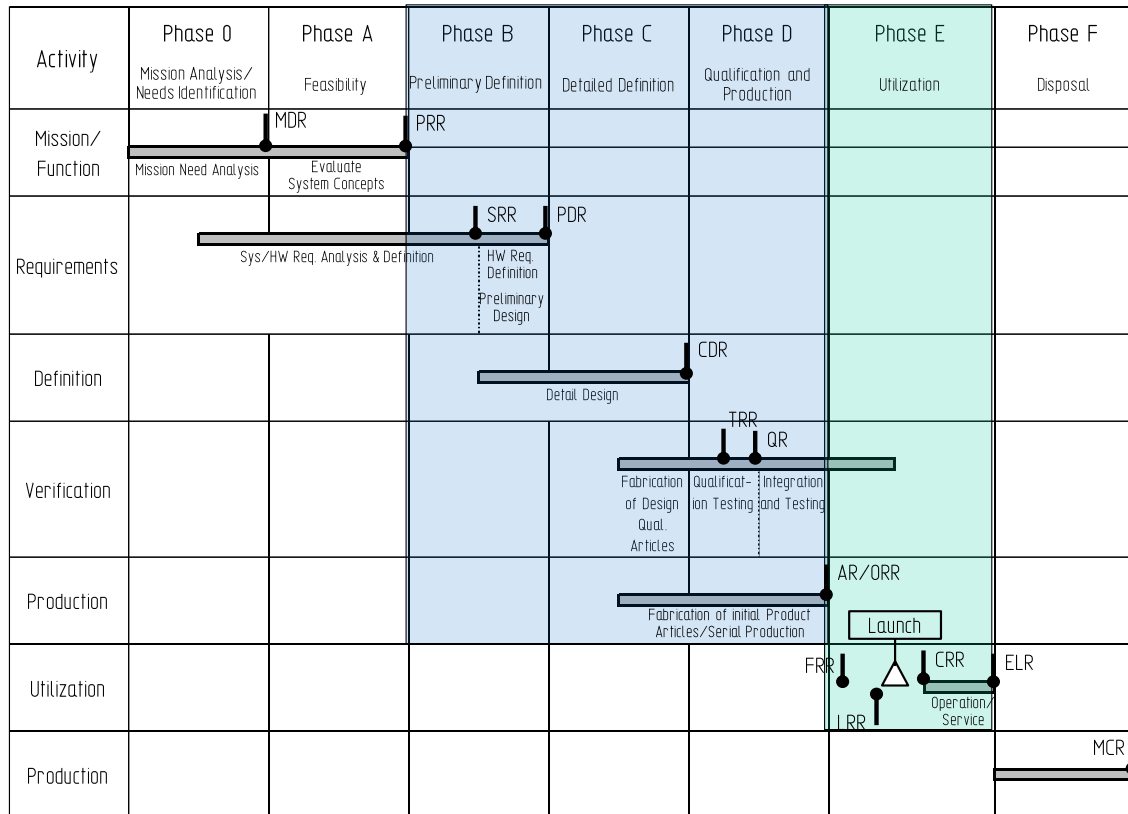
#### **3.2.1 Allocation in Standard Design Approach and Life Cycle Phases**

The most followed design standards in space engineering for Europe and North America are ESA's ECSS (European Cooperation for Space Standardization) technical standards system and NASA's NTSS (NASA's Technical Standards System), including their provided technical standards, center standards, specifications and handbooks. Design and development processes are thus guided in successive manner thru the according standards and handbooks, to which contractors working for ESA or NASA must adhere. Further, current developments and needs are constantly implemented. This thesis mainly refers to ESA's ECSS standards, due to the environment this work was generated in. However, NASA standards are mentioned and whenever providing more information applied or discussed. With regard to applying robustness assessment, it is necessary to know where in the development and design process it is most beneficial to be performed. The development and design process itself is guided successively thru seven phases of the so-called Space Flight Project Life Cycle according to ECSS-M-ST-40C [36] and ECSS-M-ST-10C Rev. 1 [37]. NASA is defining similar phases in their systems handbook [38] and NASA Procedural Requirements (NPR) specific to a certain area.

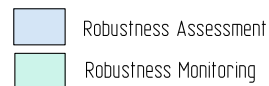
The phases, as summarized in Figure 3.6, are: *Phase 0/Pre-Phase A*, in which a mission analysis is performed and needs are identified; *Phase A*, in which system concepts are evaluated and their feasibility is investigated, and system and hardware requirements are derived by analysis. In *Phase B* hardware requirements are derived, definitions are set and preliminary designs are generated, while the detail design is concurrently started. *Phase C* is focusing on the detail design, while test articles for the design qualification as well as initial product articles are already fabricated. *Phase D* concentrates on qualification testing of test articles and hardware, integration into the final system (assembly) and system testing, while the hardware or product is fabricated in its final design. *Phase E* contains after several reviews the launch and spacecraft operation and service in orbit/space. With *Phase F* follows the final and last phase, that marks the end of life with the disposal (closeout) of the decommissioned spacecraft. Figure 3.6 further shows the most relevant key points (reviews) and the main activities during each phase, which are not further discussed at this point.

By reviewing the space flight project life cycle it is apparent, that robustness aspects as well as all influences that might affect robustness itself should be considered as early as possible. However,

robustness assessment requires a certain quantity of data and knowledge about the structural system e.g. of design, material, loads, and should mainly be performed within the phases, B, C and D, as indicated with a blue mask in Figure 3.6. Additionally, in order to improve future robustness predictions and gain valuable data, monitoring robustness is considered beneficial in phase E, during operation, and whenever possible (indicated with a green mask in Figure 3.6). This enables a direct comparison of achieved robustness in weightlessness (in space, under operational conditions) and the robustness determined on ground (by simulation and/or testing). Nonetheless, this thesis focuses on robustness assessment, and touches monitoring only in minor extend in chapter 4.



- AR Acceptance Review
- CDR Critical Design Review
- CRR Commissioning Result Review
- ELR End-of-Life Review
- FRR Flight Readiness Review
- LRR Launch Readiness Review
- MCR Mission Close-out Review
- MDR Mission Definition Review
- ORR Operational Readiness Review
- PDR Preliminary Design Review
- PRR Preliminary Requirements Review
- MCR Mission Close-out Review
- QR Qualification Review
- SRR System Requirements Review
- TRR Test Readiness Review



**Figure 3.6.** Summarized allocation of robustness assessment within the Space Flight Project Life Cycle according to ECSS standards

*Allocation of robustness assessment within Technology Readiness Levels*

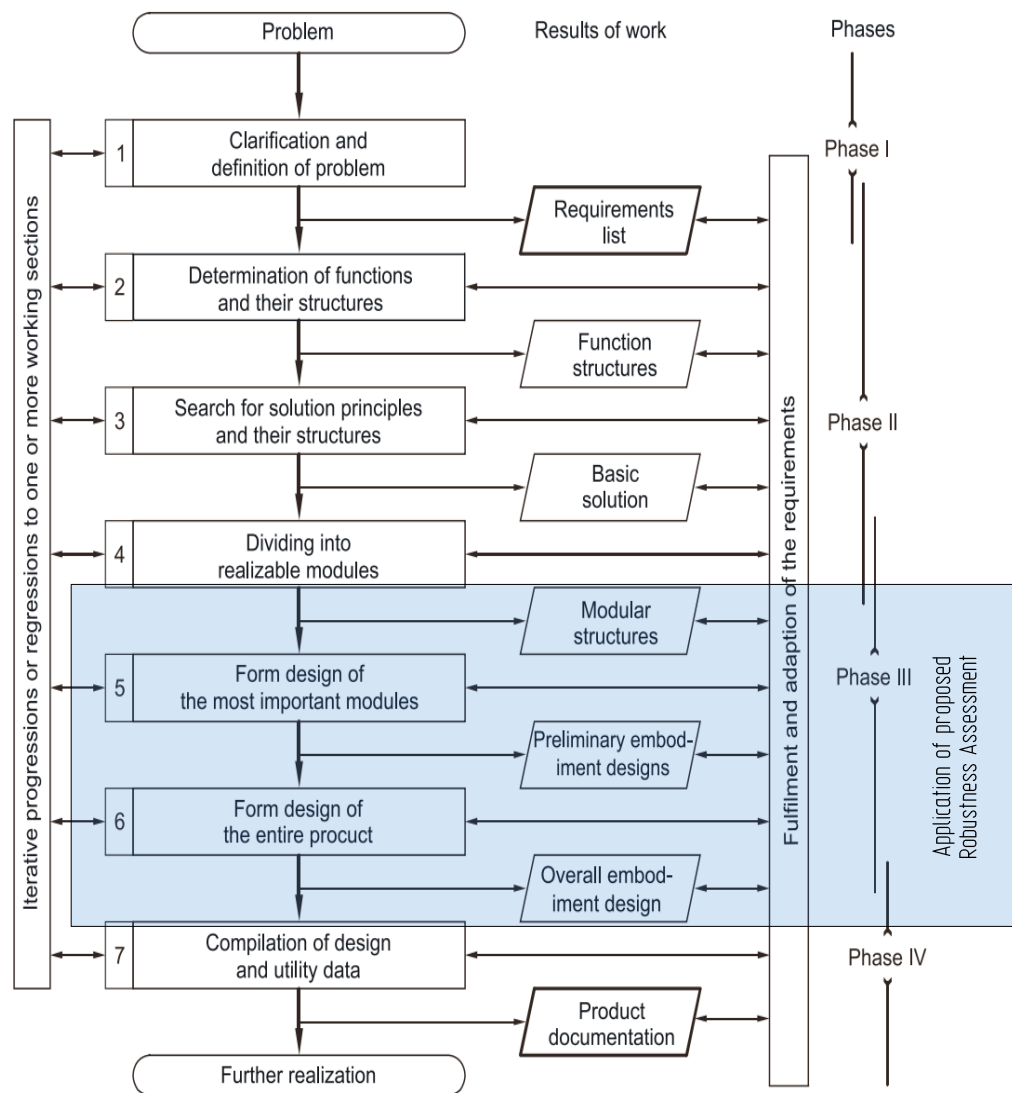
Allocating the application of robustness assessment within levels of technological maturity, the so called Technology Readiness Levels (TRL, 9 levels), according to ECSS [39] and similarly to NTSS [38] is suggested to be performed from at least TRL 3 (component and experimental critical function and/or characteristic proof-of-concept) up to TRL 9. Due to lacking information, data and knowledge about the structural system and the preliminary design on lower TRL, and thus inhibiting a profound robustness assessment at this low state of maturity.

*Allocation of Robustness Assessment in the Engineering Design Process*

Allocating robustness assessment on the more detailed level within the design process itself, as part of the space flight project life cycle, is visualized in Figure 3.7. Here the standards for engineering and systematic design VDI 2221:2019-11 [40] part 1 and part 2 are used for illustration, due to their widespread recognition and application within industry (in Europe). These industry standards provide the most comprehensive and detailed procedure information on designing and development of technical systems in a systematic manner, and are not specific to any industry and rather generic, concentrating on methodology.

The design process is here further detailed into four phases: Phase I: Clarification of the task, Phase II: Conceptual design, Phase III: Embodiment design (Preliminary Design) and Phase IV: Detail design. Without going into detail for each phase as they are more or less self-explanatory and can be studied in VDI 2221 [40], robustness assessment, as discussed here exceeding just quality control, is seen most beneficial in Phase III and Phase IV of VDI 2221, thus executed along the core processes of designing. Generating preliminary (preliminary embodiment design) and detail designs (overall embodiment design) in these phases give the opportunity to increase robustness right from the beginning, in terms of integrating robustness assessment and quantification, followed by an optimization. This is not done so far in a standardized or regular basis. Nevertheless, robustness assessment applied early in the design phase can only be performed insofar that sufficient information about the product, influences or knowledge from previous similar systems is available. However, robustness considerations e.g. setting requirements or limits should already be incorporated as early as phase I, with being part of acquiring the requirements list.





**Figure 3.7.** Allocation of robustness assessment in general procedure of systematic development and design according to VDI 2221:2019-11 (adapted image from [40])

### 3.2.2 Design Philosophies and related Principles

#### *Redundancy, Alternative Load Paths and Segmentation*

The principle of *redundancy* provides means of increasing both the safety and the reliability of systems. Commonly redundancy means superfluity or excess. In information theory, it refers to that fraction of transmitted data that may be eliminated without loss of essential information. Redundant structural arrangements lead to an increase in safety and are believed to increase robustness as well. However, this is only true, provided that the breakdown of a particular element of the system is not dangerous in itself, and that other elements, arranged in parallel or in series, can take over its function fully or at least in part [41]. The provision of several identical elements in a structural system all ensure that, should a particular element break down, the function is not completely impaired. In this case active redundancy, in which all the elements/components are actively involved, is provided. Passive redundancy exists if reserve elements (for instance alternative boiler feed pumps) –usually of the same type and size– are provided and put into operation during breakdowns. In a third type of redundancy, principle redundancy, an arrangement of elements, is to be equal in function but

different in working principle. Depending on the situation and system, elements can be arranged in parallel, for instance pillars of a building, or in series, for instance filter installations. Although redundancy in systems is closely related to the concept of robustness and redundant systems are generally believed to provide a higher robustness, structural robustness tends to decrease as redundancy increases over a certain degree as found by Biondini [42] when investigating truss structures for buildings. Further the conflict between optimization (minimizing mass) and the requirement for sufficient redundancy was demonstrated on the example of a three-dimensional truss by Frangopol and Klisinski [43]. This conflict is also apparent in Gossamer Structural Space Systems, as mass reduction plays an even more essential role here.

*Alternative load paths*, according to Starossek [44] and the standard UFC Design of Buildings to Resist Progressive Collapse (UFC 4-023-03, 2009) [45] –here termed alternate load paths– is a further principle to enhance robustness of a structural system. This principle provides alternative paths for a load to be transferred from a point of application to a point of resistance, thus enabling redistribution of forces originally carried by failed components. This eventually prevents a failure from spreading and the system from failing. Alternative load paths can form through load-transfer mechanisms, as e.g. listed by Starossek [44] with the examples of the inversion of flexural load transfer (from hogging to sagging above a failing column), the transition from flexural to tensile load transfer (catenary action), or other transitions.

*Segmentation*, also known as crack arrest, is another design principle to enhance the robustness of a structural system. This principle prevents a spreading of failure following an initial damage or limits it by isolating the failing part of a structure from the remaining structure by so-called segment borders as explained by Starossek [44]. This can be realized by three mechanisms: With the first, segment borders are formed by strong components or features, designed to provide high local resistance to accommodate large forces, thus arresting an incipient collapse and damage propagation. The second mechanism works inversely by weak components at which failing parts can safely disconnect from the structural system. Such components work similarly to predetermined breaking points or structural fuses, thus eliminating continuity or reducing stiffness to accommodate large deformations and displacements. Thirdly, the usage of segment borders with high ductility and large energy dissipation capacity, accommodating large forces and large displacements at the same time, is thought to enhance robustness.

In GosSSS, redundancy is utilized in motors or interfaces with parallel elements. Due to the strong mass and volume restrictions that are specific to GosSSS, redundancy for the main structural elements like booms or membranes is commonly not realized. While a doubled number of elements would increase, overall mass somewhat, the additional mass by the necessary larger or doubled number mechanisms, guides or similar items would increase overall mass significantly. Nevertheless, redundancy as an integral part of robustness considerations is regarded within this thesis. Segmentation however is a common principle to facilitate in the design of GosSSS. It is utilized a crack arrest, the so called rip-stop in membranes, as each membrane is made up of several segments and provide strong borders at the fused edges, integrated lines or applied rip-stop structure as applied by Belvin and Zander in [46, 47].

### *Safe-Life*

According to [41] the *Safe-Life* philosophy demands that a system, all its components and their connections be constructed in such a way as to allow them to operate without failure, breakdown or malfunction throughout their anticipated design live. The basis is given by detailed life span and durability calculations of each component, so called life-limited parts, thus determining their limits of safe operation, until overloaded (load levels and/or running time) or subjected to adverse environmental influences. Once the calculated end of life is reached, components and parts are replaced, regardless of the component exhibiting damage or not. A continuous monitoring of the state of components is herein demanded. However, an occurring damage under the safe-life philosophy means system failure. This philosophy is commonly applied on systems that are difficult to repair or

highly safety relevant i.e. in structures exposed to fatigue like airplane landing gears. Since this design philosophy is known for generating very safe designs, it is also known for “overdesigning” thus leading to designs with low weight efficiency. This however is not suited for GosSSS except for specific components e.g. bolts on mechanisms.

### *Fail-Safe*

The design philosophy *Fail-Safe*, as applied in engineering [41], allows for some malfunctions or damage of a system or component within the design life, as long as no total failures/severe consequences occur and the system function or at least an acceptable, limited functionality can be provided. In this philosophy, such limited functionality must be provided by the damaged component or taken over by another component until: the system can be shut down safely and put out of order for repair or replacement; the failure and its cause can be detected and identified; and/or the failure site can be evaluated regarding its state of total safety. Furthermore, the principles of redundancy (active or passive), alternative load paths and segmentation (compartmentation, crack arrest) are commonly applied within this design philosophy. The Fail-Safe principle is also applied in current design approaches of GosSSS.

### *Damage Tolerance*

Tolerating and accepting damage to a certain extent is the main characteristic of systems or structures designed under the philosophy of *Damage Tolerance*. According to literature [41], it proclaims the ability to sustain defects safely until repair can be carried out or as defined by Lind [48] the ability of a system to withstand damage or perturbations that are unforeseen or not considered in the design, without undesirable response. Damage tolerance is further considered the reciprocal of vulnerability (sensitivity) – with vulnerability understood as the ratio of failure probability of the damaged system to the failure probability of the undamaged system, or as defined by Agarwal [49] “a structure is considered to be vulnerable if damage from any exposure results in consequences which are disproportionate to the original damage event”. Additionally, it is assumed that flaws can exist in any structure and such flaws propagate with usage. This design approach demands a highly accurate analysis of damage, failure modes and effects for possible scenarios. Additionally, implementing a maintenance program that enables detection and repair of accidental damage, corrosion and fatigue cracking before such damage reduces i.e. the residual strength of the structure below an acceptable limit, renders a structure to be damage tolerant, thus considering it damage tolerant. Overall, this philosophy aims for precise design for the necessary loads and given environment, tries to omit overly dimensioned structures or redundancy, thus leading to lower system mass and less maintenance. Due to the high potential to save weight with utilizing this design philosophy, it seems rewarding, especially when designing ultra-light-weight GosSSS.

### *Safety Factor*

Expressing how much stronger a system is than it needs to be for an intended load, the Safety Factor (SF), also known as Factor of Safety (FoS), is widely used in engineering design. According to the aerospace standard NASA-STD-5001B W/CHANGE 2 SF are: “Multiplying factors to be applied to limit loads or stresses for purposes of analytical assessment (design factors) or test verification (test factors) of design adequacy in strength or stability.” [50]. Many systems are intentionally built much stronger than needed for normal usage to allow for all kinds of uncertainties like emergency situations, unexpected higher loads, worse properties of the material than foreseen (degradation), imperfect theory of the failure mechanism, possibly unknown failure mechanisms, and human error (e.g. design, misuse,) as reported by Doorn & Hansson [51]. According to literature, like Elishakoff [52], a safety factor can generally be defined as the ratio between the failure load and the allowed load (exchangeable used with design load; or stress ratio), while the first is the minimum value of the load that would cause failure, and the second is the maximum load that a component is allowed to

experience during its service life. This relation is expressed in equation (3.1), with a safety factor greater than 1 for safety to some degree.

A *Safety Factor SF (FOS)* is generally defined as:

$$SF = \frac{\text{Yield Stress}}{\text{Working Stress}} = \frac{\text{Failure Load}}{\text{Allowable Load}} \quad (3.1)$$

Using detailed analysis to calculate safety factors is many times necessary, since comprehensive testing is impractical on many complex systems. Nevertheless, the magnitude is often determined based on the observation of past failure events of similar designs and validated through physical tests in case of critical structural systems. The principle of safety factors is based on the faith that the design is safe under any circumstances if the design requirements on safety, namely the design safety factors, are satisfied. Thus, high safety factors are presumed to provide high safety, while providing structures of high load carrying capability. However, for ultra-light-weight GosSSS applications, safety factors should be as small as possible due to the predominant mass constraints. This is in large contrast to the general and conservative requirement in aerospace engineering to provide high structural safety via SF, leading many times to overly heavy designs. Since safety factors are considered in all design philosophies (safe-life, fail-safe and damage tolerant designs), Elishakoff [52] explored the coexistence and combination of deterministic safety factors and non-deterministic structural reliability. With the outcome of several probabilistic interpretations of the safety factor Elishakoff concluded that structural reliability and the safety factors can peacefully coexist and are useful to combine in order to allow for more rational allocation of the safety factors. This notion is adopted to GosSSS robustness considerations, with the combination of deterministic and non-deterministic concepts as explained in section 4.1.

### *Reliability*

Reliability is defined as the probability that a given item will perform its intended function for a given period of time under a given set of conditions. As stated by Woo [53] it is defined by four parts, namely probability (likelihood that some given event will occur); the intended function of the system, subsystem or component; time (mission time), and conditions (i.e., the operating and environmental conditions). In NASA [54] also refers to the “probability of success” for reliability in the success space and of “probability of failure” in the failure space. The according fundamental math theory is expressed in equations (3.2) and (3.3).

The *Reliability R* is generally defined as: the reliability function:

$$\text{Reliability} = 1 - \text{Probability of Failure} \quad (3.2)$$

$$R(t) = P\{T > t\} = \int_t^{\infty} f(x)dx \quad (3.3)$$

where  $f(x)$  is the failure probability density function and  $t$  is the length of the period of time (starting at time zero).

In aerospace engineering the importance of system risk and reliability analysis to assess safety is acknowledged in the Fault Tree Handbook, NUREG-0492 [147], issued by the US Nuclear Regulatory Commission (NRC) and in a adopted version by NASA’s Fault Tree Handbook with Aerospace Applications [54]. Some of the risk assistant and quantification methods are revised and discussed in terms of applicability to robustness in section Appendix B, while the assessment and relations within system reliability (e.g. composition of system reliability from components in series; Lusser’s law) are discussed and compared to system robustness of GosSSS in section 4.3.

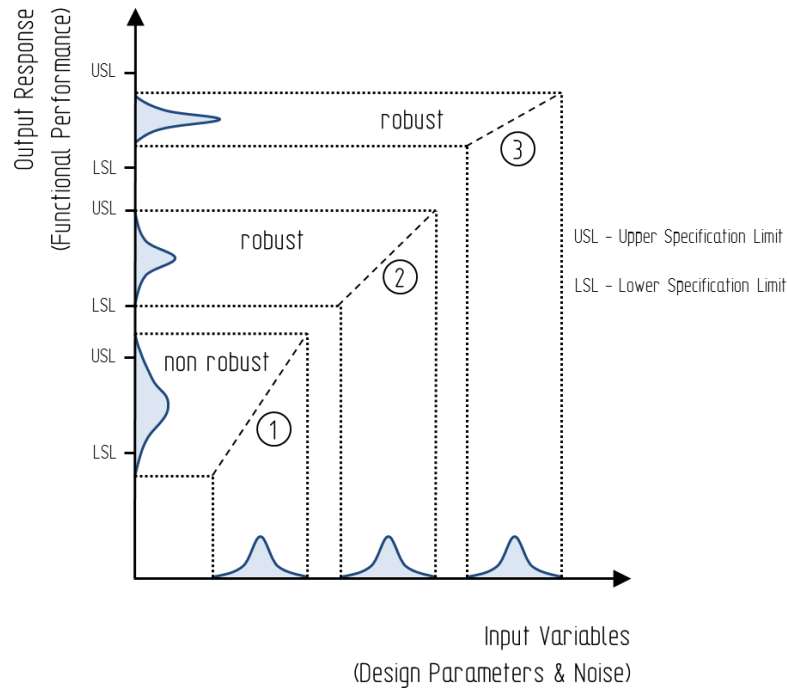
### 3.3 Robustness and present Approaches

#### 3.3.1 Robustness

Robustness is being investigated and determined in different fields of research and interest, as well as under different aspects and understandings of robustness itself. These areas can be identified as: Structural Engineering (Structural Standards), Software Engineering, Product Development and Quality Control, Ecosystems, Control Theory, Statistics, Design Optimization, Bayesian Decision Making and Language Science. A categorized and synthesized list, from several authors, of the different understandings of robustness in regard to the area of its application is given by Faber et al. [55]. Although many definitions are given in diverse fields of industry and science, the classical definition, originated in the pioneering work of Genichi Taguchi in statistical methods, as cited by Stewards [56] is: “Robustness is the state where the technology, product or process performance is minimally sensitive to factors causing variability (either in manufacturing or user’s environment) and aging at the lowest unit manufacturing cost”. This definition has been derived in the context of quality control under varying parameters. The variation can generally be caused by inherent uncertainties (noise factors), that are reducible by tolerance design and tightening the tolerances on product or process parameters, and by design variables according to Park et al. [57]. In other fields, somehow different interpretations of robustness have found their way into practice. In structural robustness assessment in civil engineering, in the context of investigating truss bridge structures and buildings like the Empire State Building, Starossek [58] defines robustness as the insensitivity of a structure to local failure. He defines a structure to be robust if an initial damage does not lead to an extent of collapse/disproportionate collapse [44]. However, he demands insensitivity and local failure must be quantified by design objective, thus setting measurable limits in which robustness is considered. Similarly, in civil engineering, Brett [59] defines structural robustness as the ability of a system to withstand abnormal circumstances without disproportionate failure, while Slotine and Li [60] define structural robustness as the degree to which a system is insensitive to effects outside the design considerations. In the field of technical systems Göhler [61] interprets robustness as a property that reduces variability. In a similar fashion Faber [55] interprets robustness in the context of civil engineering of offshore jacket type steel structures. Here robustness is related to the acceptable behavior of certain performance characteristics or properties of a system and considered as a measure of sensitivity of certain qualitative features in a system in regard to changes in system composition, system state, fundamental assumptions and general unexpected systematic disturbances.

Although in different areas of research definitions and interpretations may vary due to different characteristics and goals of the applications, a common and simplified core meaning can be excerpted with: *Robustness is the insensitivity of a system function towards variations.*

Figure 3.8 illustrates this principle on three examples. Here input variables (design parameters and noise) are displayed as similar distribution curves on the abscissa. In relation to different model transfer functions (displayed as dashed lines 1, 2 and 3), the according output responses on the ordinate show significant differences in their distribution. Note that each model transfer function represents a different system behavior for a parameter and can be linear or non-linear, although they are displayed in a simplified manner in Figure 3.8. Thus, applying the principle of robustness, all output responses within a prior defined upper and lower specification limit (USL, LSL respectively) can be considered robust, while output responses exceeding these limits renders the system behavior as non-robust. However, this only gives a qualitative indication of the robustness of a system. Quantitative assumptions can be derived using robustness metrics as described in section 3.3.3.



**Figure 3.8.** Robustness based on insensitivity to variations

### 3.3.2 Robust Design

Robust Design is a design approach based on the underlying principles invented and developed by Taguchi (1924 - 2012), the so-called Taguchi Method. This method developed for the design of experiments or simulation calculations in multi-parameter systems, strives for developing robust products and processes. It is defined as “a methodology for designing products, devices and product equipment to perform as intended, despite variation in manufacturing, assembly, material properties, ambient conditions, loading scenarios or time related factors” [62]. A similar definition is given by Phadke, who was working closely with Taguchi in robust design techniques, as methodology “to make a product’s performance insensitive to variations in material, geometry, manufacture and operating environment” [63].

*The aims of Robust Design are summarized by Klein [64] as follows:*

- making quality measurable by defining a Quality Loss Function
- Formulating the quality goal as an achievable extremum
- Searching robust parameter constellations for products and processes using a matrix experiment (DoE – Design of Experiment strategy) under the influence of external parameters (noise)
- Optimizing settings for all parameters (factors) as well as quantifying main influences in order to raise awareness of sensitivities and deviations
- Preventing quality loss and waste of time, money, prototypes or warranty

Thus, Robust Design can generally be acknowledged as a design methodology to increase a product or process performance already in early design phases, with the goal to develop high quality products at short terms and low costs. Furthermore, quality in terms of robustness and gain in robustness are quantified in comparable metrics that are reviewed and discussed in the following sections.

As Robust Design has been applied and categorized by several authors, Göhler et al. [61] gives an overview of all types, classified by their level of complexity:

<i>Type I</i>	Addressing variations in noise factors (uncontrollable)
<i>Type II</i>	Addressing variations in Design Parameters (DP) (controllable)
<i>Type III</i>	Include variability and uncertainty in the system model
<i>Type IX</i>	Addressing uncertainties concerning the fulfillment of constraints the design variables must obey”

Clearly, Robust Design considers uncertainties in its approach. This can be deterministic or probabilistic and a major influencing factor for the decision-making. Nevertheless formal decision making necessitates that all uncertainties are considered and treated in the same manner and differentiated in the types (according to Baker [65]): uncertainties due to inherent natural variability, model uncertainties and statistical uncertainties. Thus, it becomes obvious that it overlaps with the discipline of Sensitivity Analysis (“the study of how the uncertainty in the output of a model can be apportioned to different sources of uncertainty in the model input”, Lee [66]). This circumstance will be regarded as the methodology of measuring robustness in GosSSS is laid out in chapter 4.

### 3.3.3 Robustness Metrics

This sub-section reviews the existing robustness metrics applied mostly in similar areas as the here discussed structural system. However, due to the interchangeably use of terms like “quantification”, “metric” and “measure”, and an overlap in meaning for some areas, these terms are clarified for better understanding and indisputable use in the following sections.

#### *Quantification*

Quantification is generally understood as the process of mapping human observations and experiences into numbers with the result of a measure.

#### *Measurement*

As the result of quantification, a measurement is defined, according to the Oxford English Dictionary as system or scale of units expressing size, amount, or degree of something or as a systematic way to assign a number to each suitable subset of set intuitively, interpreted as its size.

#### *Metric*

In general, understanding a metric is a function that defines a distance between each pair of elements of a set. It is widely understood as a derivative of a measure. It can be derived from one or more measures, representing a relation, while a measure itself is a fundamental or unit-specific term.

**Figure 3.9** illustrates exemplary a process of deriving a metric for quantification the observation of a moving object.



**Figure 3.9.** Deriving measurements and metrics

#### *Classes of Robustness Metrics*

Many different approaches have been developed to quantify robustness with a metric, pursuing different goal, thus varying along with the specific understanding of robustness over the range of disciplines. An overview of mainly sensitivity based robustness metrics are given by McPhail et al. [67], with the background to compare performance of decision alternatives in environmental decision making. The regarded robustness metrics consider local uncertainty (reliability, vulnerability, and resilience) while applied within a framework for robustness calculation using three major transformations that execute: a performance value transformation, a scenario subset selection and a

robustness metric calculation. However, robustness here is mainly assessed by sensitivity and uncertainty, thus giving the relation between input (expectations) and output variables. Structural robustness is also an addressable entity in this field. Nevertheless, the proposed approach of transferring information via different metrics from level to level along the quantification process is considered also applicable in this work.

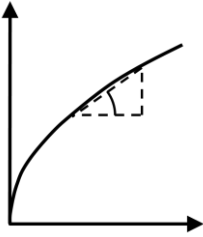
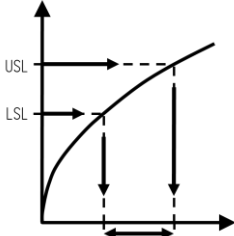
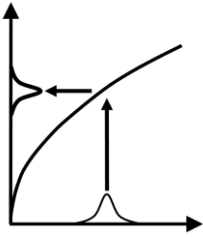
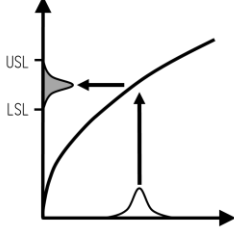
A thorough review of robustness metric applied to find structural robustness is given by Göhler et al. [61]. With the goal to classify existing robustness metrics, in the context of product development and engineering design, the authors studied 90 relevant publications and identified 38 different robustness metrics. The found robustness metrics were categorized in four classes according to their need for information about the model, functional limits, expected variation, and the level of complexity given as an overview in Figure 3.10. The four classes are defined as:

Class 1 – *Sensitivity robustness metrics*, Class 2 – Metric describing the *Size of feasible design space*, Class 3 – Metrics that evaluate *Functional Expectancy and dispersion*, and Class 4 – metrics that evaluate *Probability of functional compliance*. The *Sensitivity robustness metrics* are well established and the simplest form of robustness metric, relating the change of an independent variable (design parameters & noise) to the change of one or more dependent variables (output), thus correlating the input to the functional requirements. This metric class evaluates robustness via sensitivity of a function with respect to one (or more) independent variable and is favorable in early design phases.

Metrics describing the *Size of feasible design space* (Class 2) are quantifying the design feasibility taking all functional requirements into consideration. They allow analysis of robustness of a function towards single and a set of independent variables, as well as robustness of a product or system consisting of multiple functions that need to be fulfilled simultaneously. By putting sensitivities into perspective to requirements on the associated function two principles can be distinguished: the “distance to closest constraint”, addressing how much variation (across all independent variables) can be allowed ensuring that the function will always be within the limits, and the “entire feasible design space” (distance, area, volume) measuring the entire design space as metric for robustness. Although these robustness metrics can be used for comparison of designs or to determine the influence of a constraint, interactions and additive effects are not considered.

The class 3 metrics that evaluate *Functional Expectancy and dispersion*, measure the spread of the performance of functions resulting from variation in the influencing factors, thus quantifying robustness of a function. They further indicate if a functional performance is on target, based on the two statistical moment measures expectancy (mean) and dispersion (variance, standard deviation). However, the needed probabilistic information of the stochastic variation of independent variables (DP, noise factors) are mostly impossible to be analytically calculated (except large empirical data sets are available from past and similar systems) and have to be approximated, thus lowering the information quality. Metrics that evaluate the *Probability of functional compliance* (class 4) measure the robustness of a product and reflect the sum of sensitivity, requirements and ingoing variation. This is done by using the probability of fulfilling the functional requirements under the influence of stochastic variation of the independent variables. Advantageous is the fact that in case of coupling between functions is known, conditional probabilities can be derived to calculate joint a probability. However, it is always assumed that output variables are normally distributed, which might not always be the case. In order to give a brief outlook for the usability of the robustness metrics a brief rating of the applicability of each class to GosSSS is added in Figure 3.10. Here class 1 and 2 are considered to be well applicable, since all necessary information to determine these types of robustness metrics for a GosSSS are available or can be determined. Class 3 and 4 are rated with a medium applicability. This is due to the effort of generating large empirical data sets or in case of approximation a lower information quality (less precise) for the information of variation of independent variables (probability density functions). Nevertheless, all classes are considered to be applicable to a Gossamer Structural Space System.



Class of Robustness Metric	Necessary Information	Level of Complexity (No. Dependent Variables/ No. of Independent Variables)	Applicability to GosSSS
<p>Class 1 Sensitivity</p> 	<p>Model/Experiment</p>	<p>single/single (single/multiple)</p>	<p>●●●</p>
<p>Class 2 Size of feasible Design Space</p> 	<p>Model/Experiment Functional limits</p>	<p>single/single single/multiple multiple/multiple</p>	<p>●●●</p>
<p>Class 3 Functional Expectancy &amp; Dispersion</p> 	<p>Model/Experiment - Expected/measured Variation</p>	<p>single/single single/multiple multiple/multiple</p>	<p>●●</p>
<p>Class 4 Probability of functional Compliance</p> 	<p>Model/Experiment Functional limits Expected/Measured Variation</p>	<p>single/single single/multiple multiple/multiple</p>	<p>●●</p>
<p>● low applicability; ●● medium applicability; ●●● high applicability</p>			

**Figure 3.10.** Classification scheme for robustness metrics (adopted from Göhler et al. [61]) and assessment

Nonetheless, other robustness metrics that were not considered in the review by Göhler [61] can be categorized into this class system as well. The most promising of all found robustness metrics are briefly described and discussed in the following section. Here mainly structural and product related metrics were brought into focus.

### Quality Loss Function & Signal-to-Noise Ratio

In the field of quality engineering Taguchi (cited by Klein [64] and Ruefer [68]) introduced two robustness metrics with the aim to improve and quantify product quality and robustness. In order to measure the loss in quality as a result of lacking robustness, Taguchi defined a quadratic Quality Loss Function (QLF). Using the monetary loss of a manufacturer due the reduced robustness, this function penalizes the deviation of a parameter from the specification value that contributes to deteriorating the performance of the product. Thus, determining the sensitivity of a product towards deviation from parameter tolerance it can be categorized as metric of Class 1 – *Sensitivity robustness metrics*.

The Quality Loss Function follows:

$$L(y) = k \cdot (y - m)^2 \quad (3.4)$$

with

$$k = \frac{A_0}{\Delta_0^2} \quad (3.5)$$

where  $L$  is the loss associated with parameter  $y$ ,  $m$  is the nominal value of the parameter specification, and a constant  $k$ , given with equation (3.5), depending on the cost  $A_0$  (e.g. for repair, replacement or rejects) at the specification limits  $\Delta_0$  (parameter tolerance).

The QLF is defined for three main cases: The “nominal the best” (NTB) case has a form as given in equation (3.4) and is chosen when the input parameter  $y$  is a targeted value ( $\neq 0$ ) with a symmetric loss of quality. A special form of this case is the asymmetric NTB, when the deviation of a parameter is significantly more detrimental to quality in one direction than in the other. The second case is the “smaller the better” (STB) case as given with equation (3.7), with the nominal value of a parameter  $m = 0$  (e.g. undesired characteristics). It is applied when a parameter cannot become smaller than zero, and an increase in value  $y$  results in a decrease of product quality, as the loss raises, thus representing a “Minimizing” case. In contrast to this, in the third case “larger the better” (LTB) the aspired nominal value of a parameter  $m > 0$ , while the parameter values cannot be negative. With an increasing parameter  $y$  the product performance increases as quality loss decreases. As the optimal value of  $y \rightarrow \infty$ , the quality loss becomes zero, thus representing a “Maximizing” case. This case is resembled by equation (3.8). While only one quality characteristic can be put into relation with one model transfer function within one QLF, an average of several QLF can be derived as given in equation (3.9). As this is suitable to apply for e.g. a badge of produced component of one type, a system made up of different components or subsystem like a GosSSS demands another approach. Furthermore, the application of cost is for research systems are hard to be estimated and are not seen to be precise enough nor suited for the structural aspects of a GosSSS. Nevertheless, the factor cost may be substituted by another more applicable measure.

Nominal the best QLF (NTB):

$$L(y)_{NTB} = \frac{A_0}{\Delta_0^2} (y - m)^2 \quad (3.6)$$

Smaller the better QLF (STB):

$$L(y)_{STB} = \frac{A_0}{\Delta_0^2} \cdot y^2 \quad (3.7)$$

Larger the better QLF (LTB):

$$L(y)_{LTB} = A_0 \cdot \Delta_0^2 \left(\frac{1}{y}\right)^2 \quad (3.8)$$

Average Quality Loss for nominal the best (NTB):

$$\bar{L}(y) = \frac{1}{n} \sum_{i=1}^n L(y_i) = \frac{A_0}{n \cdot \Delta_0^2} [(y_1 - m)^2 + (y_2 - m)^2 + \dots + (y_n - m)^2] \quad (3.9)$$

Taguchi introduced the second robustness metric, the Signal-to-Noise ratio (SNR or S/N), within his work with orthogonal arrays in the field of Design of Experiment (DoE) [64, 68]. This metric assesses the real system behavior that is better, the smaller the deviations are and the better a given target is being hit, thus fulfilling the intended function more robust. As given with equation (3.10), the SNR represents the ratio of the target value of a function to be fulfilled (counter) and the numerical value that attenuates or disturbs the intended function (denominator) as described by Ruefer [68].

$$SNR = 10 \cdot \log_{10} \left( \frac{Signal}{Noise} \right) \quad (3.10)$$

Akin to the cases of the QLF mentioned before, three optimal ratios can be used for the SFR depending on the output response that is required.

That is the “nominal the best” case to achieve an SNR (see equation (3.11)) where variability about a mean is to be reduced:

$$SNR_{NTB} = 10 \cdot \log_{10} \left( \frac{\bar{y}^2}{\sigma^2} \right) \quad (3.11)$$

with the mean response  $\bar{y}$  of an input parameter and the standard deviation  $\sigma$ .

The “smaller the better” case (equation (3.12)) to achieve the smallest SNR ratio where the smallest response is desired:

$$SNR_{STB} = -10 \cdot \log_{10} \left[ \frac{1}{n} \sum_{i=1}^n y_i^2 \right] \quad (3.12)$$

and the “larger the better” case (equation (3.13)) to achieve an SN ratio where the largest SN ratio is required aiming for the largest response to be obtained:

$$SNR_{LTB} = -10 \cdot \log_{10} \left[ \frac{1}{n} \sum_{i=1}^n \frac{1}{y_i^2} \right] \quad (3.13)$$

As the SNR is generally applicable to any system, it is assumed to be well adoptable for GosSSS. However, an SNR is lacking the ability to combine or connect different types of variables. Furthermore, it is rather general and needs to be adapted to the specific characteristics of a GosSSS. However, once adapted to the specific independent and dependent variables of a GosSSS, these robustness metrics are considered to work for design parameters as well as for outputs like stiffness, deflection, buckling failure load or reflectivity.

*Robustness radius and feasible Design Space*

A robustness metric reviewed by Göhler [61], that puts sensitivities into perspective to the requirements on the associated function is the “Robustness Radius”  $r_R$  (Euclidean distance). It addresses the question of how much variation across all independent variables can be allowed ensuring that the function will always generate responses within the upper and lower specification limits (USL and LSL respectively). This measure determines the closest distance to the most constraining limit, as given with equation (3.14).

Another, similar metric for robustness, reviewed by Göhler [61], is the “Feasible Volume”  $Vol$ , measuring the entire feasible design space. It relates in terms of parameters of a design space to a distance, area, volume, or polyhedron volume in 1D, 2D, 3D, and nD, respectively and is independent of the nominal value (see equation (3.15)).

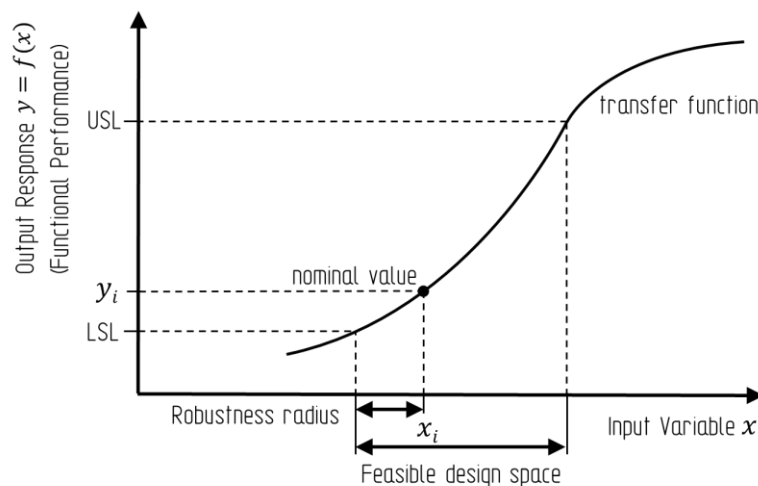
The “Robustness Radius”  $r_R$  is calculated as follows (for 1D case):

$$r_R = \min(|(x|f(x) = f_{\max}) - x_{nominal}|; |(x|f(x) = f_{min}) - x_{nominal}|) \tag{3.14}$$

The “Feasible Volume”  $Vol$  is calculated as follows (for 1D case):

$$Vol = |(x|f(x) = f_{\max}) - (x|f(x) = f_{min})| \tag{3.15}$$

In Figure 3.11 a one-dimensional case, in which the size of the feasible design space is derived for one independent variable  $x$  toward one output response (functional requirement)  $y = f(x)$  with an upper and lower specification limit, is shown. As each metrics is considered to show high robustness with high values, they should be most expressive when using in combination. This is seen well applicable for GosSSS in early design phase when for example tolerances for geometry is set for acceptable boom tip deflections under load.



**Figure 3.11.** Robustness metric based on feasible design space (adopted, edited from Göhler [61])

Another sensitivity based robustness metric is proposed by Lee et al. [66] evaluating how the responses are influenced by the design parameters (inputs) and inherent uncertainties with the “Robust Index”  $R.I.^1$  as given in equation (3.20). Herein are  $B_{xi}$  the scaled sensitivity and  $\rho_{xi}$  the “influence”, determined with the Spearman correlation coefficient. Scaling of the sensitivity, as given with

equation (3.20), is realized by factoring the sensitivity of output to the input variables  $\beta_i$  (linear regression slope determined with the least-squares method) by the sample mean  $\mu_i$ .

$$R.I.^1 = \text{Min} \left| \frac{1}{\rho_{xi} B_{xi}} \right| \quad (3.16)$$

$$B_{xi} = \beta_i \mu_i \quad (3.17)$$

This measure is suitable for the comparison of design concepts, and might be applicable in the early design phase of a GosSSS. However, since it does not measure the insensitivity of a structure due to a local failure event, it should only be complementing the overall assessment of robustness. It further does not allow for verification of robustness requirements.

### *Stiffness-, Damage-, Energy- and Risk/Probability based Robustness Metrics*

In the field of civil engineering Starossek & Haberland [58] developed different approaches, based on stiffness, energy and damages measures, to determine structural robustness of buildings and bridges. Assuming damage has been occurred, all three approaches are based on either comparing the properties of the damaged and undamaged structures by deterministic or probabilistic comparative values or on examining the response of the structure to such an initial damage.

The *stiffness-based metric* of robustness  $R_s$  is calculated as follows:

$$R_s = \min_j \frac{\det K_j}{\det K_0} \quad (3.18)$$

with the system stiffness of the intact structure  $K_0$  in relation to the system stiffness of the structure after removing a structural element or connection (damaged structure)  $K_j$ . According to Starossek [58] verification on ultimate load of a simple frame structure showed that  $R_s$  does not correlate very well with reduction in load carrying capacity due to removal of an element, simulating a damage. Nevertheless, GosSSS are stiffness driven and relying on ultimate load as well, thus at least considering this approach in specific cases in which stiffness plays a dominant role is regarded viable. Alternatively Starossek [58] suggests to substitute stiffness by other structural properties like strength, load capacity utilization, ductility or mass distribution.

The *damage-based robustness metric*  $R_d$  is based on the maximum total damage  $p$  resulting from the assumable initial damage  $i_{lim}$  in relation to the acceptable total damage  $p_{lim}$ , and calculated as follows:

$$R_d = 1 - \frac{p}{p_{lim}} \quad (3.19)$$

The necessary analysis of damage and its quantification can become intractable or very complex while  $R_d$  does not adequately reflect the relative larger importance of the effect of small initial damage according to Starossek & Haberland [58]. To remedy this weakness the authors suggest modifying the damage-based robustness metric e.g. by weighting. However, the quantification of damage for a complete GosSSS seems to be very complex and unprecise, since it would have to be carried out as simulation or simplified test at ground conditions on Earth, not resembling the real physical behavior in space.

The energy-based robustness metric developed by Starossek & Haberland [58]  $R_e$  is based on  $E_{r,j}$ , the energy released during the initial failure of a structural element  $j$  and contributing to damaging a

subsequently affected structural element  $k$ , and  $E_{f,k}$  the energy required for the failure of the subsequently affected structural element  $k$ .

The *energy-based robustness metric* by Starossek & Haberland [58] is as follows:

$$R_e = 1 - \max_j \frac{E_{r,j}}{E_{f,k}} \quad (3.20)$$

According to the authors the metric  $R_e$  is especially applicable to structures composed of similar elements and with the failure of the subsequently affected element  $k$  resulting in complete collapse. Such structures are rows of overhead transmissions line towers or high-rise buildings that show a domino or pancake type collapse. This approach is also interesting for GosSSS, since its elements can be considered to fail successively as well. However, such a structural system comprises of very different elements, thus rendering this approach applicable for groups of similar elements, like the boom system or the membrane system including the rigging.

A modified energy-based robustness metric is introduced by Da Cunha [69] and applied on stiffened composite shells made up of skin and stringers (CFRP panels of an airplane fuselage). As a panel is considered a structural system this modified energy-based robustness metric is supposed to be better suitable for systems wherein the structural elements may fail simultaneously. In the proposed metric the energy between the global buckling load (alternatively limit load or ultimate load) and the collapse load, the energy reserve, is considered an indicator of structural robustness. A structural system with a large energy reserve is less sensitive to collapse, thus featuring a higher robustness. The robustness metric itself is a relation of the compared energy levels, thus giving a normalized result.

The *modified energy-based structural robustness metric* as relative measure, according to Da Cunha [69] is:

$$R_{EI,GB} = 1 - \frac{E_{GB}}{E_{CL}} \quad (3.21)$$

with the energy required for the global buckling event  $E_{GB}$  in relation to the energy required for the collapse event  $E_{CL}$ , and  $0 \leq R_{EI,GB} < 1$ , while “non-robustness” equals zero and “perfect robustness” equals one. As the energy reserve measures the insensitivity of the structural collapse due to a local failure. Due to the strong similarity of the mechanical behavior (buckling behavior) of stiffened shells and the booms used in the here investigated GosSSS type, this approach is considered well applicable to the booms system. Analogously the structural robustness can also be evaluated through the calculated area under the load-shortening curve using the different load limits. However, Da Cunha [69] applies this robustness metric only to a panel, that he considers the system, while in GosSSS the boom system is just a subsystem. Since other subsystems fail and behave in a different fashion, other additional robustness metrics are deemed necessary.

A measure of robustness in the field of probabilistic risk assessment during the decision making process is proposed by Baker [65] as “Index of Robustness”  $I_{Rob}$  with equation (3.22). Aiming to quantify structural robustness it measures the relative risk due to indirect consequences of damage, thus relating direct risks  $R_{Dir}$  (direct consequences of potential system damage) and indirect risks  $R_{Ind}$  (risk of a secondary failure of a damaged system) to the structure. Robustness values are between 1 and 0, while the first indicates complete robustness with no risk due to indirect consequences and second no robustness with all arising risks due to indirect consequences. However, indirect risks should be kept as low as possible.

*Risk-based robustness metric* according to Baker [65]:

$$I_{Rob} = \frac{R_{Dir}}{R_{Dir} + R_{Ind}} \quad (3.22)$$

Already accounting for both probabilities and consequences of failure, Baker [65] suggested to include sensing and detection as well in order to increase robustness. Thus, combining typical results of an FMECA (Failure Modes, Effects and Criticality Analysis) with a robustness metric, this approach is also considered worthwhile for a Gossamer Structural Space System, as damage probabilities from e.g. MMOD impacts can pose a high risk. Furthermore, this approach provides conditional robustness (based on probability), that is also apparent GosSSS, as some subsystems or component might trigger cascading failure (e.g. failure of two booms), while others may not (e.g. failure of one sail membrane).

Similarly Frangopol et al. [70, 71] consider probabilistic indices to measure structural redundancy, as robustness measure, based on the relationship between damage probability and system failure probability.

The redundancy index  $RI$ , proposed by Fu and Frangopol [71], is defined by equation (3.23), with the probability of damage occurrence to a component  $P_{f(dmg)}$  and the failure probability of the system  $P_{f(sys)}$ . Thus, this index (the difference between  $P_{f(dmg)}$  and  $P_{f(sys)}$ ) is indicating the reserve strength of a system i.e. the residual strength of a system that has sustained damage. Hence, a structural system is considered non-redundant if  $P_{f(dmg)}$  equals  $P_{f(sys)}$ .

*Probability-based robustness (redundancy) metric* according to Frangopol and Curley [70]:

$$RI = \frac{P_{f(dmg)} - P_{f(sys)}}{P_{f(sys)}} \quad (3.23)$$

Alternatively Frangopol and Curley [70] consider deterministic safety factors to measure redundancy in a systems-reliability approach. They defined the redundancy factor  $\beta_R$ , as expressed with equation (3.24). Here  $\beta_{intact}$  is the reliability index of the intact system and  $\beta_{damaged}$  is the reliability index of the damaged system. The index varies between 0 and  $\infty$ , with 0 indicating a failed structure and  $\infty$  representing a very robust structure.

*Reliability-based robustness metric* according to Fu and Frangopol [71]:

$$\beta_R = \frac{\beta_{intact}}{\beta_{intact} + \beta_{damaged}} \quad (3.24)$$

Redundancy in systems is closely related to the concept of robustness. However, it is worth noting that while redundant systems are generally believed to be more robust, there are additional methods of providing robustness that are not related to redundancy, as explained in section 3.2.2.

### 3.4 Chapter Conclusion

This chapter discusses the state-of-the-art Gossamer Structural Systems, their applications, deficiencies in robustness and basic elements, the standard design process in space engineering and design philosophies, as well as robustness approaches and metrics for structural systems. Argumentations and discussion is focusing on the most relevant aspects of the hypotheses.

Firstly, a definition and heritage of Gossamer Structural Space System (or short Gossamer) is provided in order to give a fundamental understanding of these specifically light, delicate and large structural systems. Further a classification along with a list of the most advanced GosSSS applications is derived. Encountered damages and failures, ascribed to a lack in robustness, are discussed on selected examples. Here the examples of deployable and flexible solar arrays on Hubble, ISS and an in-orbit demonstrator, clearly illustrate, what difficulties such lightweight and deployable structural systems might be facing. Issues occur mainly due to their low natural frequencies and low damping rates, low masses and delicate structures, accompanied by large thermal loads and strict orientation requirements causing disturbances. Moreover, the harsh space environment and the fact that these kinds of structures are hardly testable on ground, in a realistic environment, make these structural systems sensitive to disturbances and influences. This again shows that a special attention on robustness already in the design phase is essential for mission success and lowering costs when considering advanced GosSSS. It further demonstrates that safety factors alone might not grasp all effects that influence such structural systems. Thus, robustness is seen beneficial to be introduced in the design process, determined and eventually increased. For a deeper understanding of a GosSSS, basic design configurations and main elements, of the here investigated class of planar-tensioned (2D) systems are reviewed, as well as general requirements and characteristics. Here the need for paying attention to robustness, due to the strict requirements and high sensitivity becomes evident.

Secondly this chapter describes the standard development and design procedure of space structures, while discussing the most beneficial allocation of the proposed robustness assessment within the phases of the Space Flight Project Life Cycle, the Technical Readiness Levels (TRL) as well as in the standard design procedure according to standard VDI. The outcome of the discussion suggests incorporating robustness assessment as early as possible, as long as sufficient information, knowledge and design maturity are available. Further state-of-the-art design philosophies and principles in engineering such as safe-life, fail-safe damage tolerance and application of safety factors and reliability are reviewed and discussed in terms of how robustness is determined. The result that robustness not adequately considered separately supports the main hypothesis of this work.

In the last part of this chapter definition and understanding of robustness used in this thesis as well as robust design with its main aims is reviewed and refined in order to establish a common base of understanding. This is followed by categorization of robustness metrics as found in literature and rated towards their applicability to GosSSS. Further the most relevant robustness metrics like Taguchi's quality loss function and Signal-to-Noise Ratio, as well as metrics like the robustness radius, stiffness based, damage based, energy based as well as risk-based metrics, developed and applied by different authors are reviewed and discussed in regard to their advantages, disadvantages and their applicability to Gossamer structural systems. It can be summarized that each metric concentrates only on one aspect, namely variation of variables, sensitivity of output towards input, probability of damage and risk, energy or stiffness. Detection and sensing were brought up as a notion by different authors, however it has not yet been implemented. Further overall system robustness was determined as a whole from top-down, however an overall robustness metric emerging from several robustness metrics for sub-systems and components has not yet been considered. Another outcome of this chapter is the cognition that a combination of different aspects, including an assessment and weighting of different robustness, can be considered valuable and marks a knowledge gap. This could give engineers the opportunity to determine the robustness of lower level entities e.g. the subsystem they are responsible for, and in consequence the herein generated robustness as a result for the complete system as an overall robustness metric.



## 4. ROBUSTNESS ASSESSMENT — METHODOLOGY

This chapter presents the novel robustness assessment methodology for Gossamer Structural Space Systems. After discussing requirements this methodology is founded on, robustness quantification strategies are discussed and robustness metrics are developed. Here the robustness metrics and their relations at different levels of complexity on system, subsystem and component level are described mathematically in detail. It is further described how the robustness parameters, that are used to measure robustness, are brought into relation in order to find comparable and normalized robustness values. This robustness assessment is put into a framework and main tasks, which are described in detail, thus showing how the necessary data is acquired and processed. The chapter closes with a discussion about how to implement the proposed robustness assessment methodology in a spacecraft design process.

### *Robustness defined in this thesis*

Derived from findings and drawn conclusions of analyzing the existing robustness definitions and related methods in chapter 3, robustness, understood in this thesis incorporates sensitivity, as typically used in the field of robust design, but is advanced by performance reserves, typical for engineering design philosophies.

Thus, aspects of sensitivity are incorporated in terms of insensitivity towards variations and noise, like imperfections, variations of characteristic parameters and external disturbances, including probability of occurrence of such. Moreover, sensitivity regarded in the here defined robustness assumes that characteristic parameters assessed, suffice design requirements a priori.

Furthermore, reserves are accounted for in terms of exceeding functional performance, compared to requirements, similar to engineering principles of design regarding this with safety factors, margins of safety and reserves.

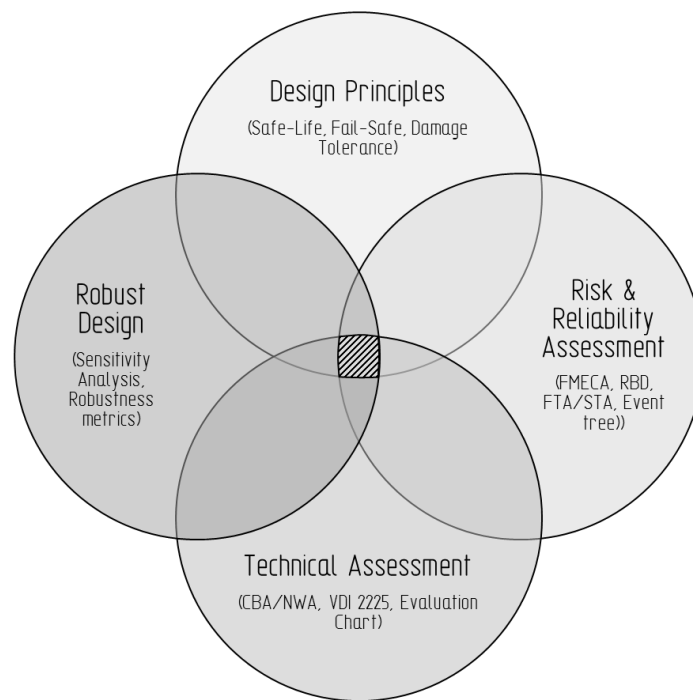
Therefore, robustness understood herein and further regarded is defined as follows:

*Robustness is a measure of insensitivity towards variations and performance exceedance of a system function at the same time.*

### 4.1 Requirements & Extent

The main objective to quantify robustness of GosSSS makes requirements and limitations necessary in order to develop a methodology that can serve this purpose.

As discussed in previous sections (see sections 3.2, 3.3 and Appendix B) each discipline in engineering design aims for increasing robustness independently in some sort. This is done by setting tolerances, safety factors, redundancy, segmentation/compartimentation and acceptable damage; by finding and assessing failures, its causes, probabilities of occurrence, severity and detectability; by quantifying, weighting, normalizing and rating system utility values; and by measuring specific robustness, in the disciplines Design Principles, Risk & Reliability Assessment, Technical Assessment and Robust Design, respectively. While each single discipline by its own lacks some aspects of robustness considerations, the aim in this thesis is to make use of a combination of the different approaches and strategies for quantification and understandings of robustness. They are combined in one methodology, as illustrated in Figure 4.1, much like a toolbox with different sets of tools. Thus, keeping the different possibilities given and existing experiences in mind, the requirements and the extent of application of the herein developed methodology is described in the following.



**Figure 4.1.** Multidisciplinary approach for robustness quantification

Studies in other areas of engineering regarding the quantification of structural robustness led to a synthesis of general requirements. In Starossek & Haberland [58], the authors develop along several robustness metrics on the progressive collapse of structural systems like buildings or truss like bridges a series of general requirements. From their findings and the one of others, they link validity and usefulness of measures of robustness to the following definition of requirements: Expressiveness, Objectivity, Simplicity, Calculability and Generality. As some of these requirements are also true for the here proposed methodology for GosSSS, some additional requirements are seen to improve the framework.

The following requirements are considered for the methodology assessing robustness of GosSSS (arranged by requirement headings):

- Expressiveness:*
- shall express all aspects of robustness in a single value
  - should allow clear distinction between robust and non-robust
- Objectivity:*
- assessment should be independent of end users decisions (not be biased)
  - expert knowledge and experience should be transferred into an objective value
  - values of measure should be reproducible under unchanged conditions
- Simplicity:*
- used measures and metrics should be as simple as possible (in order to gain acceptance with users and increased reproducibility)

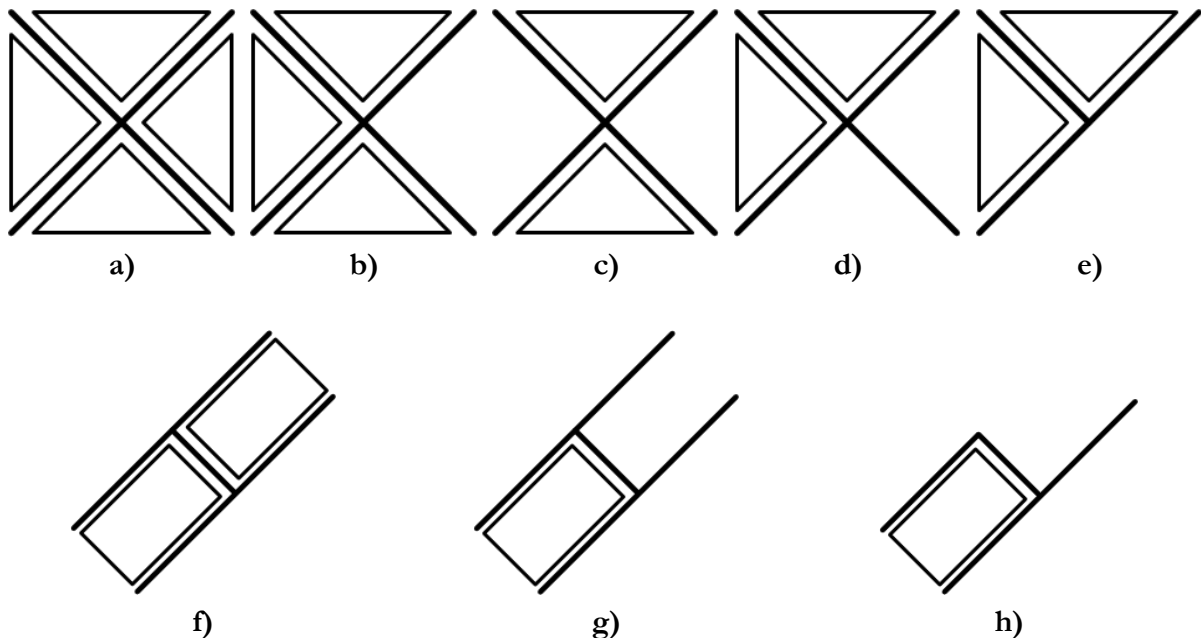
- Calculability:*
- shall be possible to derive measures/metrics from properties or behavior of the structural system (GosSSS)
  - all input parameters must be quantifiable (subjective parameters must be quantified)
  - calculations should be possible without excessive effort
- Applicability:*
- robustness measures and metrics should be applicable to any kind of GosSSS (as defined within this thesis)
  - robustness measures and metrics should be measurable in practice, on the according entity of a complexity level i.e. through testing of a subsystem
- Holistic (Multidisciplinary):*
- robustness should be determined from all engineering disciplines in a single complex result
  - single specific robustness values should be combined/interrelated to an overall robustness
  - for specific cases or when exceeding reasonable effort not all disciplines need to be consulted
- Setting Design Limits:*
- for all circumstances design objective and limits shall be defined in order to measure robustness against them

The described requirement classes consist of one or more requirements, that are defined according to the nomenclature in ECSS-E-AS-11C [39]. On one hand for some cases, requirements may partly be in conflict with each other and it may not be possible to fulfil them all to the same degree at the same time. On the other hand, some requirements seem to be repeated in different requirement headings. Within the requirement headings *Expressiveness* and *Holistic (Multidisciplinary)*, both in some way demand that all aspects and disciplines dealing with robustness and at the same time determine a single value as a result of robustness. However *Expressiveness* aims for a single quantified result value, while requirement in *Holistic (Multidisciplinary)* aims for generating results from different sub-results. Similarly, one could mistakenly assume redundancy of requirements within the headings *Objectivity* and *Calculability*. While on one hand the requirement under the heading *Objectivity* demands that subjective information such as expertise should be considered, while transferring it to objective information. On the other hand, under *Calculability* it is referred to the requirement that values generated from subjective information need to be in a format that can be processed within the robustness assessment.

## 4.2 Conditional System Robustness Considerations

When analyzing a GosSSS with its elements (subsystems and components) as described in 3.1.4 and considering the elements exhibiting different robustness, the overall system robustness can be assumed to be conditional. It is assumed that the overall system robustness depends on the case of lacking robustness and the application of the GosSSS. In Figure 4.2 several cases in which a lacking robustness of a subsystem is visualized by the absence of that subsystem. Visualized for a solar sail, drag sail of PV-array application, in a) all element can be considered robust. In Figure 4.2 b) a membrane subsystem (synonymous with an interface (I/F) connecting a membrane to another subsystem) is assumed to show a lack of robustness. Here conditional overall system robustness is assumed. This shows for a solar sail or drag sail application in which the overall system robustness would be considered insufficient as a functional sailing and attitude control cannot be accomplished. Nevertheless, this is the opposite for a PV array application in which the objective function could at least partially be provided, thus rendering an asymmetric structural robustness case critical. Another example is given in Figure 4.2 c). Here two membrane subsystems are lacking robustness. Due to the

symmetric robustness case for all applications (solar sail, drag sail and PV array) the system objective function could partially be provided as well as attitude control, thus considering a symmetric case (more) robust. This cannot be generally stated for the case in Figure 4.2 d), showing an asymmetric robustness case with two subsystems lacking robustness. Similar to the case presented in Figure 4.2 b) for a solar sail or drag sail application, the overall system robustness would be considered insufficient while for a PV array application the objective function could at least partially be provided, thus rendering this asymmetric structural robustness case critical depending on the systems objective function and application. In Figure 4.2 e) only one subsystem, a boom subsystem, is lacking robustness. However, this is causing the same asymmetric robustness case as in d), in which two membrane subsystems showed a lack of robustness. This demonstrates as well that robustness is consequently conditional on each subsystem robustness in a different extent. Here the robustness of a boom subsystem seems much more influential than the one of a membrane subsystem. Similar can be observed in the image series f) to h) of Figure 4.2. Considering all elements of the GosSSS robust in Figure 4.2 f), thus providing robustness for the overall system, in g) again the membrane subsystem lacks robustness, while the boom subsystem does. Conditionally on the application, a PV array may exhibit robustness as it fulfills at least partially its objective function, the same case for an antenna does not. Again, it becomes obvious that although the boom subsystem is robust, the system might not be, due to the greater influence of the membrane subsystem. Substantiating the theory of conditional robustness, the example given in Figure 4.2 h) considering the boom subsystem as non-robust, also considers the membrane subsystem to be non-robust, despite of the fact that the membrane system alone might feature sufficient robustness. This generic thought experiment shows that the found conditional relations of subsystem robustness are found in a hierarchical order. This contributes to the notion that weighting of robustness on each hierarchy level should be considered. Furthermore, it is assumed that an increasing number of components can increase robustness, as the objective function of an application can be distributed in a much greater fashion. Supporting these findings, Starossek et al. [44, 58] suggest to increase the amount of structural elements in system as well, as investigated for bridges and buildings. In this thesis the afore discussed conditional relationships are regarded especially in section 5.6 on the example of the Gossamer-1 solar sail demonstrator.



**Figure 4.2.** Exemplary cases of Conditional System Robustness on GosSSS applications

### 4.3 System Robustness — Bottom-up versus Top-down

Apart from being conditional towards cases, applications and subsystem hierarchy, overall system robustness is considered the result of the performance and the ability to evince robustness in some

sort for all elements defining the system. Overall system robustness is herein proposed to be quantifiable from two perspectives: bottom-up and top-down. A generic GosSSS is visualized in a building block scheme in Figure 4.3, displaying the different levels of complexity with its entities at each level of complexity, namely system, subsystem, component and coupon (material) with decreasing complexity, respectively.

In the top-down approach robustness is quantified using one system model that comprises all independent (DP, noise) and dependent variables (output response) of all levels of complexity. It observes the system from the top, without differentiating e.g. each subsystem robustness. The overall system robustness value is determined with only one model, thus resulting in the Top-Down System Robustness  $RO_{SysT}$ , as represented on the right of Figure 4.3. The advantages are that relations and dependencies of entities of each level e.g. between two subsystems or components, as well as across complexity levels are inherently considered, without knowing them. However, a disadvantage is that one must rely on the assumption that all physical characteristics are represented correctly in the model. Due to high computation power needed, simplifications are made to those models, thus introducing inaccuracy. Nevertheless, this approach is widely applied by several authors (see section 3.3.3). Starossek et al. [44, 58] apply this top-down approach on bridges and multistory buildings, while Lee [66, 72] and Da Cunha [69] use a top-down approach as they investigate thin-walled composite panels, considering a panel, with its skin and stringers, the structural system. Furthermore Göhler et al. [61, 73] and Baker & Faber [55, 65] apply a top-down view on several technical systems like a gas pedal system or generic systems. The Top-down System Robustness  $RO_{SysT}$  can be expressed as a function of all parameters, of any considered entity, (independent, dependent of all levels, as far as known) as given in equation (4.1).

$$RO_{SysT} = f\{y_i, \dots, y_n\} \quad (4.1)$$

With  $y$  being the variables considered of entity (subsystem, component, material)  $i$  to entity  $n$ .

The bottom-up approach follows the building blocks principle, as illustrated in Figure 4.3., and determines robustness separately for each entity of a complexity level. Thus, providing robustness for each coupon  $RO_{Matk}$ , component  $RO_{Compj}$  and subsystem  $RO_{Subi}$ , the overall system robustness  $RO_{SysB}$  however, is a composition of all lower level robustness. In principle the robustness of entities are cumulated to the robustness of the according next level of complexity, and finally to the “Bottom-up system robustness”. Since some parameters might not be considered in the lower level robustness i.e. as geometric parameters are not considered on the material level, all robustness of levels higher than material must consider additional parameters. Therefore, a robustness of an entity of a level depends on the robustness of the next lower level and according parameters as given in the equations (4.2), (4.3), (4.4) and (4.5). Hence, material robustness solely depends on parameters, due to the lowest possible level of complexity. One advantage of this approach is that robustness of lower level entities like subsystems, components or materials can be determined separately. This is often necessary since different groups of engineers might design them and need to make statements of their own. Cumulating these robustness components to an overall robustness value is one of the main advantages of this approach. Furthermore, the influence on the overall robustness of each lower level entity can be determined, thus providing information which entity needs to be improved. One drawback however is, that relations between robustness of different levels must be known or assumed.

*Bottom-up System Robustness:*

$$RO_{SysB} = f\{RO_{Subi}, \dots, RO_{Subn}; y_{Sysi}\} \quad (4.2)$$

Subsystem Robustness:

$$Ro_{Subi} = f\{Ro_{Compj}, \dots Ro_{Compn}; y_{Subj}\} \quad (4.3)$$

Component Robustness:

$$Ro_{Compi} = f\{Ro_{Matk}, \dots Ro_{Matn}; y_{Compj}\} \quad (4.4)$$

Material Robustness:

$$Ro_{Matk} = f(y_{Matk}, \dots y_{Matn}) \quad (4.5)$$

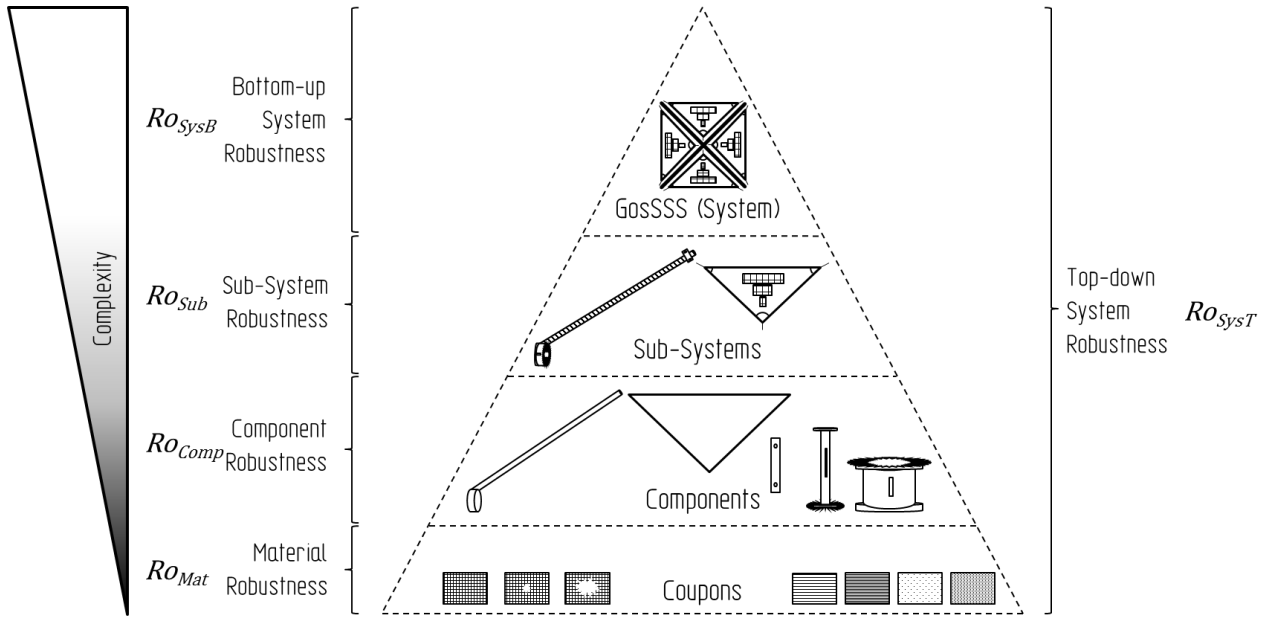


Figure 4.3. System robustness composition – Bottom-up versus Top-down

#### 4.4 Mathematical Robustness Approach

Pursuing a mixed approach in this thesis, each entity robustness can be considered a top-down robustness itself, as the according model contains all downwards variables, effects, influences and consequently robustness. The highest level a top-down robustness is determined at is the subsystem level, thus considered a system itself. Relations and conditions are then regarded on the overall system level by composing the overall system robustness.

##### 4.4.1 Composition of Overall System Robustness

On the theoretical example of a system comprising of four subsystems, six mathematical approaches of combining constituents to an overall term are studied and evaluated. The approaches in the example are evaluated by seven different cases (A to G), each comprising a set of four robustness value samples, and a set of weighting factors, constant over all cases and if applicable to the investigated approach, as listed in Table 4.1. The robustness values  $Ro_{Subi}$  represent the robustness for each theoretical subsystem, while  $w_{si}$  represents the according weighting factor (if applicable) of the  $i^{th}$  subsystem of  $n=4$  overall subsystems. The weighting factors and their generation are further explained in section 4.4.2., as weighting is considered beneficial as it considers importance and probability of failure or influence occurrence. Adopted from existing robustness approaches is that all robustness metric values are within a range of values between zero and one. The reason for this is to generate comparable and standardized robustness metrics, with unit less values. Furthermore, they are calibrated or normalized in order to obtain practical and plausible values. While a value of

one represents the maximum possible robustness (perfectly robust), a value of zero corresponds to a total lack of robustness (non-robust). Values in between are intended to be quantitative and expressive measures of robustness. Considering the overall robustness to be zero when one or more partial robustness is zero, accounts for the assumption that all regarded robustness constituents are essential for structural integrity of the system. This is considered true for all studied mathematical approaches independent of mathematical rules. Nevertheless, for demonstration such case is also investigated in the example.

The six mathematical approaches are discussed in comparison to one another by the result values for the overall system robustness they produce, and with respect to the subsystem robustness and weighting factors. These results can be followed in the heat map given in Figure 4.4, thus highlighting values according to their distance to one and zero, visualizing their conservatism. Furthermore, Figure 4.4 shows the formulas and the results of each approach for each studied case.

**Table 4.1.** Exemplary values of subsystem robustness and weighting factors

Case	Subsystem Robustness				Weighting Factors (Subsystem)			
	$Ro_{Sub1}$	$Ro_{Sub2}$	$Ro_{Sub3}$	$Ro_{Sub4}$	$w_{S1}$	$w_{S2}$	$w_{S3}$	$w_{S4}$
A	1	1	1	1	0.5	0.2	0.05	0.25
B	0	1	1	1	0.5	0.2	0.05	0.25
C	1	1	0.01	1	0.5	0.2	0.05	0.25
D	1	1	0.1	1	0.5	0.2	0.05	0.25
E	0.1	1	1	1	0.5	0.2	0.05	0.25
F	0.3	0.3	0.5	0.7	0.5	0.2	0.05	0.25
G	0.8	0.8	0.8	0.8	0.5	0.2	0.05	0.25

Case	Multiplicative System Robustness $Ro_{Mult} = \prod_{i=1}^n Ro_{Subi}$	Minimum System Robustness $Ro_{Min} = \min_i Ro_{Subi}$	Inverted Cumulative System Robustness $Ro_{Inv} = \frac{1}{\sum_{i=1}^n \frac{1}{Ro_{Subi}}} \cdot n$	Inverted Weighted Cumulative System Robustness $Ro_{wInv} = \frac{1}{\sum_{i=1}^n w_{si} \cdot \frac{1}{Ro_{Subi}}}$	Weighted Cumulative System Robustness $Ro_{wCum} = \sum_{i=1}^n w_{si} \cdot Ro_{Subi}$	Averaged System Robustness $Ro_{Av} = \frac{\sum_{i=1}^n Ro_{Subi}}{n}$
A	1.00	1.00	1.00	1.00	1.00	1.00
B	0.00	0.00	0.00	0.00	0.00	0.00
C	0.01	0.01	0.04	0.17	0.95	0.75
D	0.10	0.10	0.31	0.69	0.96	0.78
E	0.10	0.10	0.31	0.18	0.55	0.78
F	0.03	0.30	0.40	0.36	0.41	0.45
G	0.41	0.80	0.80	0.80	0.80	0.80

**Figure 4.4.** Conservatism heat map of example robustness using the investigated approaches

The first approach studied is the *Multiplicative* approach. It is adopted from a similar approach widely established as standard for reliability theory in systems engineering, also called Lusser’s Law, Lusser’s product law or the probability product law of series components. Developed by Robert Lusser to determine the overall reliability of missile systems, as reported by Woo [53], this term multiplies all constituents (individual reliabilities of subsystems or components) to the overall value, thus realizing the “weaker than the weakest link” principle. It eventually became the theoretical basis of the military standards MIL-HDBK-217 and MIL-STD-756. Acknowledging the benefits of a composite overall

value, Brett [74] applied this approach to determine the overall robustness and redundancy of truss structures in civil engineering. However, some restrictions apply, when adapting to robustness metrics. For the cases in which only one individual subsystem robustness is smaller one, while all others are equal to one, the law changes to “weakest link” instead of “weaker than the weakest link”. Applying this approach to the example cases, the determined overall robustness values produced are the most conservative values over all cases, as indicated in Figure 4.4. This represents results for the overall system robustness that are considered far too conservative and unrealistic. It further adversely eliminates weighting in a way that it has no effect on individual constituent values, and rather applies an overall factor.

Secondly, the *Minimum* approach is studied and evaluated. This approach is widely accepted for robustness quantification and applied by e.g. Starossek & Haberland [215], Lee [223] and other authors in civil engineering. It makes use of the principle of the “weakest link”, assuming that system robustness cannot be larger than the smallest individual robustness value determined for a parameter, component or subsystem, thus considering the minimal individual robustness to be the overall system robustness. As visualized by Figure 4.4, this approach is similarly conservative, underestimating the overall robustness over all cases. The fact that it does not allow a composition of constituent contributions to an overall value is another disadvantage. Moreover, it does only indirectly allow for the implementation of weighting, before determining the minimum value. In this case, the smallest value for robustness is not necessarily representing the robustness with the greatest impact on the system. The third and fourth approaches, the *Inverted Cumulative* and *Weighted Inverted Cumulative* approaches, respectively, are based on an analogy to electrical systems and are newly introduced to robustness assessment. As systems like GosSSS are made up of elements that are arranged in series or parallel, as well as in combinations, the analogy to electrical systems e.g. the arrangement of resistors lead to the idea of inverted cumulative system robustness as well as considering weighted to account for different importance or probabilities. Generally, in this type of approach the inverted of the sum of inverted partial robustness of individual constituents like subsystems determines the system robustness, as the formulas in Figure 4.4 show. For these approaches subsystem robustness values must be larger than zero in order to comply with mathematical rules. However, this disadvantage is eliminated by the assumption that the overall system robustness must be zero if one constituent is zero, as explained earlier. These approaches show less conservatism in general than the first two approaches. However, for case C both *Inverted Cumulative* and *Weighted Inverted Cumulative* approaches show a strong conservatism, especially when keeping in mind that the minor weighted subsystem robustness (implies less importance) is the reason for the low overall robustness. Another case of being overly conservative can be observed in case E, specifically for the weighted version of the approach. Here the low value of the major contributing subsystem robustness is overly penalized. Hence, this approach, in both versions, penalizes low values of constituents in the overall system robustness. This can result in overall robustness values that are too conservative. However, the advantage is the indication of low robustness of individual subsystems, forcing the engineer to improve the constituent in order to generate a satisfying overall robustness value.

The fifth approach is the *Weighted Cumulative* approach. It is known and applied in technical assessments e.g. when evaluating design variation during the design phase of a product. However, here it is proposed to be used for robustness basement. Since combining constituents to an overall robustness has only been done by Brett [74] with the first approach, the application of the *Weighted Cumulative* approach represents a new possibility to determine the overall robustness with a bottom-up strategy. Its simple mathematical term represents the sum of all individually weighted subsystem robustness, combined to an overall value. When comparing the results of the listed cases in Figure 4.4 this approach does show a moderate to low conservatism. Especially when comparing the results of the previous approaches for case C. Recapitulating that in this case a minor weighted, low subsystem robustness, with  $w_{s3}=0.05$  and  $RO_{Sub3}=0.01$  are combined with three higher weighted, maximum values for robustness, the *Weighted Cumulative* approach seems to be more realistic than all other approaches. It is more reasonable that a minor constituent value will provide still a high overall value, if specifically major constituent values are at their maximum. This is the case for the *Weighted*



*Cumulative* approach especially in comparison to the *Inverted Cumulative* and *Weighted Inverted Cumulative* approaches. The *Weighted Cumulative* approach has the advantage of being less conservative, while incorporating weighting and thus acknowledging the different importance and probabilities of each constituent.

Approach number six is the *Averaged* Approach. A common approach is the averaged approach, a term applied in many disciplines. It determines the overall robustness from the average of all subsystem robustness. Compared to the first four discussed approaches it is the least conservative approach. However, it is somewhat unprecise and ignores the different impacts of the constituents, since weighting cannot be implemented. This becomes obvious when studying cases D and E of Figure 4.4. Here case D represents a low subsystem robustness ( $RO_{Sub3}=0.1$ ) of the least important subsystem ( $w_{s3}=0.05$ ) and case E a low robustness ( $RO_{Sub1}=0.1$ ) of the most important subsystem ( $w_{s1}=0.5$ ), while all other constituents have a robustness value of one. One would expect to have a lower overall robustness in case D than in case E, due to the higher importance of subsystem Sub<sub>1</sub>. Nevertheless, the *Averaged* Approach gives identical results for both cases, and thus demonstrates its most significant disadvantage.

Applying the *Weighted Cumulative* approach is seen most beneficial to determine overall robustness from several constituents like subsystems. This approach is considered most promising and is used as the baseline within this thesis, providing just enough conservatism while regarding the different impacts of the constituents on the overall system in the most realistic manner. The general expression in equation (4.6) while the GosSSS specific expression with the subsystems defined previously in section 3.1.4 is given in equation (4.7). The overall robustness of a general system  $RO_{Sys}$  is expressed in equation (4.6) for a series of  $n$  subsystems, and the robustness of the  $i^{\text{th}}$  subsystem or component  $RO_{Subi}$  and the according weighting factors  $w_{si}$ . The overall robustness of a Gossamer Structural Space System  $RO_{GosSSS}$  expressed with equation (4.7) the robustness of the boom, membrane, interface and mechanism subsystem,  $RO_{Booms}$ ,  $RO_{Membranes}$ ,  $RO_{I/FS}$  and  $RO_{MechS}$  respectively, as well with the according weighting factors  $w_{si}$ .

The newly introduced *Weighted Inverted Cumulative* approach however is considered an adequate alternative whenever more conservatism is needed, especially when low robustness values of individual constituents shall be penalized. It will be used for comparison of final overall robustness results.

Weighted Cumulative Overall System Robustness:

$$RO_{Sys} = \sum_{i=1}^n w_{si} \cdot RO_{Subi} = w_{s1} \cdot RO_{Sub1} + w_{s2} \cdot RO_{Sub2} + \dots + w_{sn} \cdot RO_{Subn} \quad (4.6)$$

Weighted Cumulative Overall System Robustness for GosSSS:

$$RO_{GosSSS} = w_{s1} \cdot RO_{Booms} + w_{s2} \cdot RO_{Membranes} + w_{s3} \cdot RO_{I/FS} + w_{s4} \cdot RO_{MechS} \quad (4.7)$$

In Table 4.2 robustness metrics are associated with the severity of failure consequences in scales. Assigned are values of robustness to avoid a failure consequence with a certain level of severity. This is assumed useful in order to classify the degree of robustness of a GosSSS (system) or a subsystem. Different value ranges (scales) for system and subsystem robustness, calculated with equation (4.7) or equation (4.10), respectively, are assigned. This is due to the assumption that system robustness and subsystem robustness could have different scales as they are obtained by different mathematical principles, thus showing different conservatism. It is worth noting that the assigned values are assumed and need to agree with the specific objective of the specific Gossamer space application as well as in consensus with the overlooking authority. However, currently no scale values are available in any standard.

**Table 4.2.** Exemplary scale of robustness metrics associated with the severity of possible failure

Severity of Failure Consequence	Minimum Robustness Value $RO_{GosSSScrit}$	Minimum Robustness Value $RO_{Subcrit}$
Catastrophic	0 - 0.2	0 - 0.5
Critical	> 0.2 - 0.6	> 0.5 - 0.7
Major	> 0.6 - 0.8	> 0.7 - 0.9
Negligible	> 0.8 - 1	> 0.9 - 1

#### 4.4.2 Weighting Factors for System Robustness

Weighting factors here for the example of the previous section are generated from functionality, failure events, and redundancy of the according subsystem. For functionality the number of functions is viewed as benefit for the overall system function, presuming that each subsystem is essential for the overall system function. With failure events the consequence of a subsystem failure on the overall system are analyzed and rated. Redundancy is the third parameter regarded as level of redundancy for each subsystem or in terms of multiple parallel main components.

This is done in an evaluation chart in Figure 4.5 similar to an evaluation chart of scoring methods or FMECA (see appendix for information on assessment methods). However, in this case the weighting factors are to be determined instead of using them. Assessment is done on a scale from 0 to 10, while 10 marks the highest achievable score, for each category and subsystem. Firstly, for each subsystem the functionality number  $FuN$ , the failure number  $FN$  and the redundancy number  $RN$  are combined according to equation (4.8), thus resulting in the  $WN$  weighting number for each subsystem. The weighting factor  $w_{si}$ , one for each subsystem, is then determined with equation (4.9), as a ratio of a single weighting number and the sum of all weighting numbers. This results in the exact weighting factor with a value between 0 and 1. Hence, the sum of all weighting factors must be equal to 1, as commonly applied in standards. For simplification these factors are rounded to more perceivable values in the studied example. While in this example arbitrary numbers are used for illustration, section 5.6 applies subsystem weighting factors determination on an existing solar sail system.

Subsystem	Functionality Number $FuN$	Failure Number $FN$	Redundancy $RN$	$WN_i$	$w_{si}$	
					exact	rounded
Sub1	2	10	1	12,0	0,358	0,40
Sub2	1	7	1	8,0	0,239	0,20
Sub3	2	7	1	9,0	0,269	0,30
Sub4	1	7	2	4,5	0,134	0,10
$\Sigma$				33,50	1	1

**Figure 4.5.** Determination of subsystem weighting factors

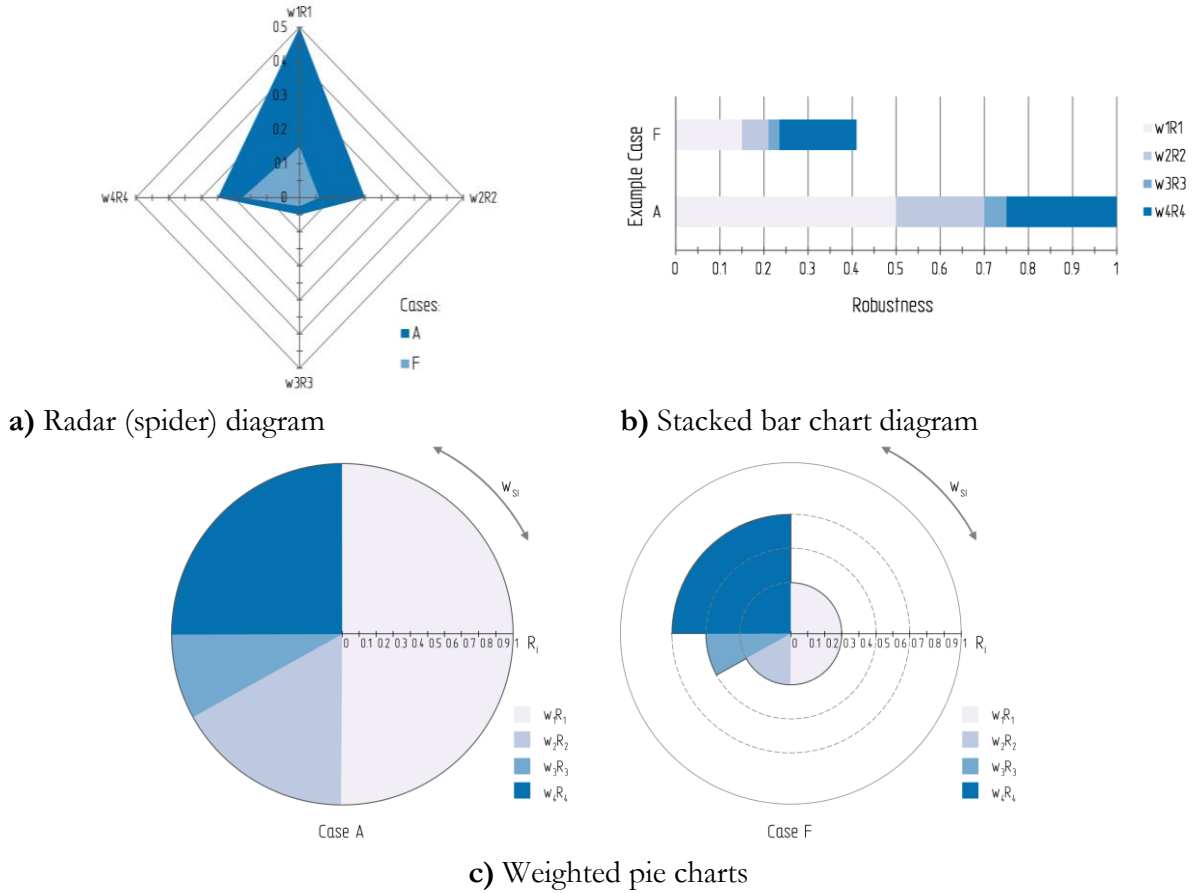
$$WN_i = FuN_i + \left( \frac{FN_i}{RN_i} \right) \quad (4.8)$$

$$w_{si} = \left( \frac{WN_i}{\sum_{i=1}^n WN_i} \right) \quad (4.9)$$

### 4.4.3 Visualization of overall Robustness Composition

Visualization of composition of overall system robustness, its constituents (robustness of subsystems) and the impact (weighting factors) is considered essential in the design process in order for the engineer to localizing deficiencies of robustness and finding appropriate measures. It provides knowledge about what subsystem needs to be improved and further which subsystem to be improved has the biggest impact. This is demonstrated on cases A and F of the studied generic example (see Table 4.1 and Table 4.2) using the baseline, the weighted cumulative approach, in Figure 4.6. Case A represents a combination of weighted subsystem robustness with a value of one, thus resulting in overall system robustness  $Ro_{SysA}=1$ , standing for a perfect robustness. Case F represents a typical combination of weighted values between zero and one for the subsystem robustness, resulting in a value of  $Ro_{SysF}=0.41$ . Two established and a new type of diagrams is discussed as shown in Figure 4.6. In this figure chart a), a common radar chart (spider chart), b) a stacked bar chart and in c) a newly introduced weighted pie chart are used to visualize the impact of each constituent ( $w_{si} \cdot Ro_{Subi}$ ) on the overall robustness and the overall robustness itself. While a) and b) are well known, the newly introduced weighted pie chart displays the subsystem robustness on its axis, while the weighting factor on each constituent is displayed as the according circular segment circumference. Summarizing the different types of visualization all chart types display both overall robustness and its constituents. While the weighted subsystem robustness can easily be distinguished in b) and c), in a) it is harder to grasp at once for the human eye. However as acknowledged in data science, aerial chart types, like a) and c), might be misleading the perception of impacts of individual constituents due to the quadratic scale. On the other hand, linear charts like the bar chart in b) are considered more explicit to human perception. The radar chart in Figure 4.6 a) gives an overview of overall robustness and its constituents, but is only suitable when displaying a few different constituents. Here the appearance of the chart and spanned areas differ with different order of the axes. Further comparing more than two cases is difficult to display due to overlaying of the charts. Additionally, multi-axes are misleading the perception especially when comparing to the maximum achievable robustness, due to its aerial nature. The stacked bar chart displays the overall robustness and its constituents in a linear fashion. This can be well perceived at once, thus enabling a clear assessment of the different cases. Further, weighting can be well distinguished, provided by the clear visualization on only one axis and many different cases can be displayed in one chart. The weighted pie charts in Figure 4.6. c) display the overall system robustness in comparison to the maximum achievable (unity), its constituents, as well as weighting factors. Here the composition is vocalized very clearly. However, the area sizes of the representative circular segments may somewhat exaggerate the impression of the effect of an individual subsystem, due to the quadratic nature of this chart type, which is true for all quadratic chart types. Although this chart type can only display one case at a time in a single diagram, it is the only chart from which values of individual subsystem robustness and weighting factors can be read out.

Concluding, all mentioned chart types are used where applicable within this thesis in order to visualize the composition of robustness, which also depends on the used mathematical approach.



**Figure 4.6.** Visualization of robustness composition for two example cases A and F

#### 4.4.4 Subsystem & Component Robustness Metrics

For each subsystem, as defined in section 3.1.4. for a GosSSS, the here proposed robustness metrics are developed in this section. As detailed knowledge, models and experimental/empirical results are available for each subsystem and component, dedicated relations are determined using a top-down approach at this level, as described in section 4.3. Each subsystem or component robustness is composed of several individual robustness metrics itself, further called partial robustness metrics, much like the before discussed overall subsystem robustness although on a lower level. However, the focus within this thesis is put on the boom subsystem. The developed robustness metrics are mostly a combination of partial robustness metrics that focus on parameters that influence the overall system function and therefore the overall system robustness. These partial robustness metrics are further composed of a combination of robustness parameters, that are widely compliant with the requirements set in section 4.1. Due to the different sensitivities and importance of each robustness parameter towards the overall system robustness, each individual robustness is weighted again. Regarding the mathematical findings in the previous sections, a weighted, cumulative approach is assumed most suitable to determine a subsystem robustness  $RO_{Subi}$ , as expressed with the general equation (4.10):

*Weighted, cumulative* Subsystem Robustness:

$$RO_{Subi} = \sum_{i=1}^n w_i \cdot RO_i \tag{4.10}$$

with the robustness of the  $i^{th}$  parameter  $RO_i$  and  $n$  the number of considered parameter robustness. Accounting for the different influences robustness parameters pose on each partial robustness metric of a subsystem, individual weighting factors  $w_i$  are introduced. While the explicit robustness metrics for each subsystem as well as the determining robustness parameters are described in detail in

the following, the influences and value ranges for robustness parameters are identified in chapter 5, derived from experiments in chapter 6 and applied in chapter 7.

Following robustness as defined in this thesis by regarding sensitivity as well as performance reserves, two types of partial robustness for a parameter can be used separately or in combination.

A sensitivity related partial robustness, given exemplary in Equation (4.11), is relating influenced values (after degradation or damage) to ideal (non-influenced, before damage) values of a robustness parameter. However, this is only assumed to be valid under the condition that an influence is always detrimental to function fulfillment, representing a state after damage. This ensures the compliance with the postulation of  $0 \leq Ro_i \leq 1$ .

A reserve related partial robustness sets required values in relation to achieved values of a robustness parameter. Here, two variants are distinguished, one that sets a maximum requirement into relation, represented exemplary by Equation (4.12), thus comparing with a requirement that must not be exceeded, while the second sets a minimum requirement into relation, represented exemplary by Equation (4.13), comparing with a requirement that must be at least satisfied. Nevertheless, both types of partial robustness should incorporate the probabilistic aspect of value variations where possible, thus determining robust as a minimum from a set of values.

*Sensitivity-related* partial robustness:

$$Ro_i = \min_i \left( \frac{\text{influenced}}{\text{ideal}} \right), \quad 0 \leq Ro_i \leq 1 \quad (4.11)$$

*Reserve-related* partial robustness:

$$Ro_i = \min_i \left( 1 - \frac{\text{achieved}}{\text{Max requirement}} \right), \quad 0 \leq Ro_i \leq 1 \quad (4.12)$$

$$Ro_i = \min_i \left( 1 - \frac{\text{Min requirement}}{\text{achieved}} \right), \quad 0 \leq Ro_i \leq 1 \quad (4.13)$$

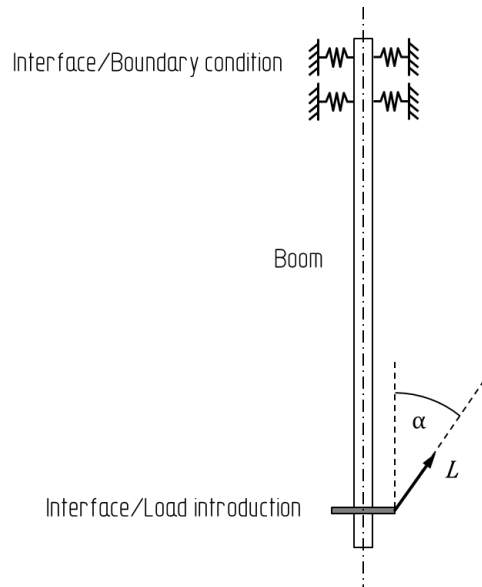
Although GosSSS are studied in their deployed configuration in this thesis, the deployment itself is essential in order to serve their fundamental function. Being deployed only once in its operational environment these structural systems show some similarity to “one-time use products” like airbags or missile systems, with high numbers of test samples while applying no or low repeatedly tests on the same sample or system in reliability testing. On the other hand common reliability testing and verification in standards such as ECSS-E-10-C [75] and ECSS-E-10-02C [76], usually demand medium to high repeatedly testing (test cycles) of standard mechanical deployment systems on the same system under test. This demands a GosSSS to be deployed several times before launch, proving its functionality. Due to the delicate build of the structural components and the associated higher risk of damage, a very high number of repeatedly test cycles on one system is considered critical and opposing to the effort of an ultra-light-weight design. Nevertheless, it is clear that a GosSSS must function within its limits after a given number of deployments with a given probability. This should be resembled in the here proposed robustness metrics as well. It is proposed to incorporate probability of functioning (reliability  $R_i$ ) with certain robustness after a given number of deployments, by multiplying the partial robustness with the according reliability  $R_i$  as expressed with equation (4.14). Nonetheless, this option can only be applied if reliability data is available. Although this approach is not further pursued within this work, it is recommended to do so in future research.

*Weighted, cumulative* Subsystem Robustness incorporating reliability:

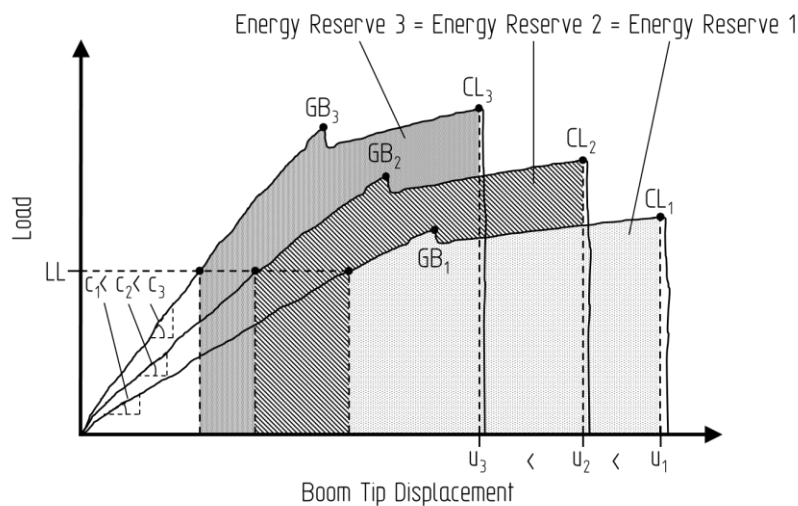
$$Ro_{SubiR} = \sum_{i=1}^n w_i \cdot Ro_i \cdot R_i \quad (4.14)$$

### *Boom Subsystem Robustness*

Robustness of a boom subsystem is based on its mechanical behavior and can be determined using characteristic parameters and curves. Similar to a load shortening curve providing the basis for a robustness metric as investigated for composite panels by Da Cunha [69] and Lee [66] (cf. section 3.3.3), the typical behavior of a boom subsystem is represented in a load-displacement curve. Such exemplary curves, extracted from mechanical bending tests on a boom subsystem (visualized in Figure 4.7), showing the applied load over the displacement of the boom tip, the load is introduced at, are displayed in Figure 4.8. Both types, load-shortening-curves of composite panels (see DaCunha [69]) and load-boom-tip-displacement curves show similar features such as: load over displacement, a linear slope leading to global buckling (GB), followed by a non-linear range (post buckling area) that consequently leads to a collapse (collapse load CL), ending in a sudden load drop. A reasonable approach for determining the robustness of buckling structures is proposed by Da Cunha and earlier by Starossek et al. [58] with an energy based robustness metric. However, this approach applied to a GosSSS does not satisfy all requirements, especially expressiveness and applicability, defined in section 4.1. This circumstance and the here suggested approach are explained in the following, while visualized in Figure 4.8. In this diagram three cases are represented by three different curves for applied loads on three boom subsystems. According to DaCunha [69] robustness based on energy is determined by the energy reserve between i.e. the global buckling (*GB*) and collapse load (*CL*), that is represented by the area underneath a curve. Specifically, the ratio of both energy levels as well as the energy reserve itself are considered metrics that quantify robustness, at least for composite panels. While the example curves in Figure 4.8 exhibit equal sizes of energy reserves (area under curve), that can be interpreted as equal robustness according to DaCunha, different stiffness ( $c_1$ ,  $c_2$  and  $c_3$ ), different collapse and global buckling loads, *GB* and *CL* respectively, and different boom tip displacements  $u$  are also evident and indicating otherwise. Hence, the interpretation of only one factor may mislead to the assumption of equal robustness. Moreover, is this single factor approach not complying with the requirement expressiveness. Furthermore, does an energy-based robustness metric incorporating stiffness, loads and displacement (shortening) in a combined single value not provide an advantage to a boom subsystem. More expressive and applicable for GosSSS is a separate robustness determination of stiffness, characteristic loads and boom tip displacement, especially when determining robustness on existing hardware. To do so such parameters can be obtained in practical tests, e.g. boom bending tests as discussed in chapter 7, or even while operating in-orbit [77].



**Figure 4.7.** Load introduction into boom subsystem (boom bending test)



**Figure 4.8.** Comparison of characteristic parameters as measure of robustness ( $c$  - stiffness,  $u$  - boom-tip displacement,  $LL$  - limit buckling load,  $GB$  - global buckling load,  $CL$  - collapse load)

Therefore, this thesis proposes the robustness of the boom subsystem  $RO_{Booms}$  to be determined from three partial robustness metrics combining a stiffness-based, a load-based and a displacement-based robustness in an additive manner, with  $RO_{\kappa}$ ,  $RO_L$  and  $RO_u$  respectively. Accounting for the different impacts of the characteristic parameters of the subsystem, explained in section 5.2, on the overall system as well as the influences the according parameters are altered by, for each partial robustness metric an individual weighting factor ( $w_{\kappa}$ ,  $w_L$ ,  $w_u$ ) is derived, with the sum of all weighting factors equal to one. The developed weighted and additive robustness metric  $RO_{Booms}$  is thus expressed in equation (4.15). It incorporates the different importance/impacts of the partial robustness as a cumulative, weighted function. Furthermore all three partial robustness metrics satisfy the requirements defined for the here developed methodology. However, additionally and if data is available,  $RO_{Booms}$  shall also consider the reliability of successfully deploying the subsystem with a required robustness and as proposed with equation (4.14).

Boom Subsystem Robustness:

$$Ro_{Booms} = w_{\kappa} \cdot Ro_{\kappa} + w_L \cdot Ro_L + w_u \cdot Ro_u \quad (4.15)$$

The stiffness-based partial robustness metric  $Ro_{\kappa}$  is derived in conjunction to Starossek & Haberland [58]. However, it adopts the bending stiffness of a boom subsystem as robustness parameter. Robustness is here represented by the minimum of the ratio of all stiffness variations and the nominal stiffness (lower limit) given by design. This is expressed exemplarily in equation (4.16), in a sensitivity related robustness, with the bending stiffness  $\kappa_0$  of the intact/undisturbed structural subsystem in relation to the structural subsystem stiffness  $\kappa_i$  after being influenced by noise and variation. Note that the investigated bending stiffness  $\kappa$ , can either be a beam bending stiffness  $c$  or a flexural rigidity  $EI$ , depending on the free boom length.

*Sensitivity-Stiffness-based* partial robustness:

$$Ro_{\kappa} = \min_i \left( \frac{\kappa_i}{\kappa_0} \right), \quad 0 \leq Ro_{\kappa} \leq 1 \quad (4.16)$$

Similar, but giving the minimum of a ratio of characteristic loads, is the second partial robustness metric  $Ro_L$ . This load-based robustness metric is expressed in equation (4.17), in a sensitivity related form. Here the collapse load  $L_{Bcrit}$  of the intact/undisturbed boom subsystem is brought into relation with the collapse load  $L_{Bi}$  of the boom subsystem after being influenced by noise and variation. However, the characteristic load itself is exchangeable and can be selected to be the collapse or global buckling load,  $CL$  or  $GB$  respectively, depending on the overall system and the perception of damage tolerance. Thus, a reserve related relation can be applied, interchangeably, as given by equation (4.17). Here the minimum required collapse load  $L_{Breq}$  for the boom subsystem is brought into relation with the collapse load  $L_{Bi}$  of the boom subsystem after being influenced by noise and variation. Aiming for robustness quantification, thus reducing safety factors and consequently mass, a limit load is considered suitable when starting a new design. The ultimate load however, that includes one or more safety factors and sometimes tends to be over dimensioned, is recommended to be used when analyzing existing systems. However, when using this approach loads must be available, defined or measurable.

*Sensitivity-Load-based* partial boom robustness:

$$Ro_L = \min_i \left( \frac{L_{Bcrit}}{L_{Bi}} \right), \quad 0 \leq Ro_L \leq 1 \quad (4.17)$$

*Reserve-Load-based* partial boom robustness:

$$Ro_L = \min_i \left( 1 - \frac{L_{Bi}}{L_{Breq}} \right), \quad 0 \leq Ro_L \leq 1 \quad (4.18)$$

The third partial robustness metric that comprises the boom subsystem robustness, the displacement-based robustness metric  $Ro_u$ , considers the boom tip displacement. Such displacements consider boom tip displacements caused by loads as well as boom tip displacements caused by plastic deformation of some kind. Being the minimum of a ratio as well, this partial robustness metric puts the nominal/acceptable boom tip displacement  $u_0$  into relation with the boom tip displacement of the influenced/disturbed boom system  $u_i$ , as expressed in equation (4.19). Penalizing of this metric depending on the application should be accounted for as expressed in equation (4.20) with a minimum function using an decadal logarithmic penalizing term. A drag sail might accept small deviations of boom tip displacement from the nominal. For an antenna however, only very small displacements might be acceptable due to the stronger influence of small variations in shape/geometry towards its main function. Furthermore, the boom tip displacement  $u_i$  is presumed a sum of different



displacement components, having their cause in different influences as expressed with equations (4.21) and (4.22). These components are the boom tip displacement caused by mechanical loads, by dimensional and shape imperfections (imprinted, plastic deformations), as well as by thermal loads, denoted  $u_{mech}$ ,  $u_{imperfections}$  and  $u_{thermal}$  respectively. Going onto the most detailed level on which boom tip displacements can independently be measured, the displacements caused by imperfections are presumed to consist of creep and manufacturing induced displacements,  $u_{creep}$  and  $u_{manufacturing}$ , respectively. While each displacement component can be of positive or negative value in regard to a set coordinate system of the subsystem, the overall displacement will be considered a positive value in order to make use of the penalty term. Therefore, the assumption is made, that an overall boom tip displacement in positive direction results in the same robustness reducing effects as a boom tip displacement in a negative direction.

*Displacement-based* partial boom robustness:

$$Ro_u = \min_i \left( 1 - \frac{u_i}{u_0} \right), \quad 0 \leq Ro_u \leq 1 \quad (4.19)$$

Penalized *Displacement-based* partial boom robustness:

$$Ro_{u,penalized} = \min_i \left[ 1 - 10 \cdot \log_{10} \left( \frac{u_i}{u_0} \right) \right], \quad 0 \leq Ro_u \leq 1, \quad \frac{u_i}{u_0} > 0 \quad (4.20)$$

Composition of boom tip displacement:

$$u_i = |u_{mech} + u_{imperfections} + u_{thermal}| \quad (4.21)$$

with:

$$u_{imperfections} = u_{creep} + u_{manufacturing} \quad (4.22)$$

### *Membrane Subsystem Robustness*

The robustness of the membrane subsystem  $Ro_{Membranes}$  consists of three partial robustness metrics, additively combined. These are reflectivity-based, shape-accuracy-based and a load-based robustness, with  $Ro_{RS}$ ,  $Ro_{SRMS}$  and  $Ro_{LM}$  respectively. Note that reflectivity, here is expressive for the performance of a solar sail or a reflective antenna and can be substituted by other parameters like the generated power of an PV array, depending on the application under investigation. Considering the different impacts of the characteristic robustness parameters for a membrane subsystem on the overall system, that are exemplary described in section 0, weighting factors are again introduced. For each partial robustness metric the individual weighting factors  $w_{RS}$ ,  $w_{SRMS}$  and  $w_{LM}$  are derived. Expressed in equation (4.23) the developed robustness metric for a membrane subsystem  $Ro_{Membranes}$  as well as all three partial robustness metrics satisfy the requirements set for the here developed methodology. Especially expressiveness, simplicity and applicability are satisfied.

Electrical properties are not considered within this structural robustness approach. Such components are only regarded as structural parts or could in terms of increasing robustness by providing a certain detectability of consequences e.g. detecting reduced power generation of PV arrays. As recommended previously, additionally and if data is available,  $Ro_{Membranes}$  shall also consider the reliability of successfully deploying the subsystem as proposed with equation (4.14).

Membrane Subsystem Robustness:

$$Ro_{MembraneS} = w_{R_S} \cdot Ro_{R_S} + w_{S_{RMS}} \cdot Ro_{S_{RMS}} + w_{L_M} \cdot Ro_{L_M} \quad (4.23)$$

The first partial robustness for a membrane subsystem, the reflectivity-based robustness metric  $Ro_{R_S}$ , is represented by the minimum of the ratio of all variations in the reflectivity and the nominal reflectivity (lower limit) required by design, thus using reflectivity as robustness parameter. This is expressed in equation (4.24), with the sample reflectivity  $R_{S_0}$  of the intact/undisturbed membrane subsystem (required design reflectivity) in relation to the sample reflectivity  $R_{S_i}$  after being influenced by noise, degradation and variation. Hence, the sample reflectivity  $R_S$ , according to ECSS-Q-ST-70-09C [78], resembles the average reflectivity over 96 % of the total energy for the solar spectral range with wavelengths between 250 nm and 2500 nm. This makes reflectivity a good indicator for the robustness of thrust capabilities of a solar sail system. However, for applications other than solar sails, reflectivity might be substituted by the generated power or the power gain e.g. for deployable photovoltaic arrays or membrane antennas, respectively, as key performance indicators.

*Reflectivity-based* partial membrane robustness:

$$Ro_{R_S} = \min_i \left( \frac{R_{S_i}}{R_{S_0}} \right), \quad 0 \leq Ro_{R_S} \leq 1 \quad (4.24)$$

The second partial robustness metric for the membrane subsystem is the shape-accuracy-based robustness  $Ro_{S_{RMS}}$ . It assumes that a defined shape and dimensions provide a defined functionality. Deviations and variations from this defined shape or dimensions (e.g. nominal geometry, dimensions, and flatness) are influencing the intended function of the membrane subsystem. This is acknowledged and expressed in equation (4.25), with the minimum of the ratio of the required shape accuracy value  $S_{RMS_0}$  of the intact/undisturbed membrane subsystem (required shape accuracy e.g. flatness) and the measured or predicted shape accuracy value  $S_{RMS_i}$  after being influenced by noise, degradation and variation. Such influencing factors are identified and described in section 0.

It is understood that reflectivity and shape accuracy could be understood to be substitutable for one another. However, they are rather complementary in terms of robustness assessment. While reflectivity, being a material driven parameter, could exhibit high to perfect values, the thrust of a solar sail or gain of an antenna could still be reduced if the membrane shape is off limits, pointing in undefined directions or distorted in some detrimental way, thus featuring a low shape accuracy. Due to this consideration reflectivity and shape accuracy are introduced as separate robustness parameters.

Among the considered GosSSS, membrane antennae show the strongest dependency between physical shape and application performance. As investigated by Straubel [79, 80] for a SAR membrane antenna the radar performance is strongly linked to the physical dimensions of the antenna and the used operational frequency. Wrinkling, local distortion and deformation lower the RF (radio frequency) performance by deteriorating shape accuracy. In order to measure this, the RMS (root mean square) value is a common indicator for the shape accuracy of such membrane apertures. While expecting a high shape accuracy for reflector antenna surfaces, in the order of about 1 mm rms (according to Freeland et al. [81]), a solar sail will experience billowing in the order of several centimeters according to Seefeldt in [82]. Similar can be assumed for drag sails, while photovoltaic arrays are expected to show intermediate values. The difference to the previously determined reflectivity-based robustness however is, that shape accuracy is determined on macroscopic level, while reflectivity is on a microscopic level, although both contribute to the overall reflectivity of the complete GosSSS i.e. a solar sail.

*Shape-accuracy-based* partial membrane robustness:

$$RO_{S_{RMS}} = \min_i \left( \frac{S_{RMS0}}{S_{RMSi}} \right), \quad 0 \leq RO_{S_{RMS}} \leq 1 \quad (4.25)$$

The third partial robustness of this subsystem is the load-based robustness  $RO_{LM}$ , giving the minimum of the ratio of characteristic loads, as expressed in equation (4.26). Here the expected membrane limit load  $LL_{Mi}$  is set into relation with the critical membrane load  $L_{Mcrit}$  of the membrane subsystem.

*Load-based* partial membrane robustness:

$$RO_{LM} = \min_i \left( 1 - \frac{LL_{Mi}}{L_{Mcrit}} \right), \quad 0 \leq RO_{SL} \leq 1 \quad (4.26)$$

The  $L_{Mcrit}$  represents the threshold until which an influenced, degraded or damaged membrane subsystem is able to perform within the required limits. Exceeding this threshold will result in unacceptable performance and functionality loss. The membrane limit load  $LL_{Mi}$  is exchangeable and can resemble the tension load, necessary to appropriately tension the membrane in order to provide the intended function, or the deployment load that is needed to deploy the membrane. In order to illustrate the different characteristics of the tension load(s) for different applications, Figure 4.9 gives some simplified load cases. It demonstrates that membrane loads largely comprise of several load vectors, preferably in a symmetric manner. However, as both load types, tension and deployment loads, are transferred into connected subsystems, i.e. introduced into a I/F subsystem and from here into the boom subsystem or as reaction loads into the mechanism subsystem(s), thus they might cause interactions between all system elements. The question of whether using a limit load or ultimate load depends on the phase in development in which a robustness assessment is performed. In order to make the most use of robustness by preventing over dimensioning with large safety factors, and therefore saving mass, in an early design phase the limit load should be considered. However, when determining robustness of existing systems, the limit load should be replaced by the ultimate load, thus assessing robustness provided by the used safety factors. Loads however ought to be determined by simulations, measurements in ground tests, measurements in orbit during operation, thus rendering a load-based robustness metric to be expressive, objective, applicable and calculable. In spite of that, an alternative stress-distribution-based robustness, that is not considered here, representing the uniformity of stress distribution, can hardly be measured in practice on such thin films without influencing the film itself locally. This would limit a stress-based approach only to simulations and therefore not satisfy the applicability requirement.

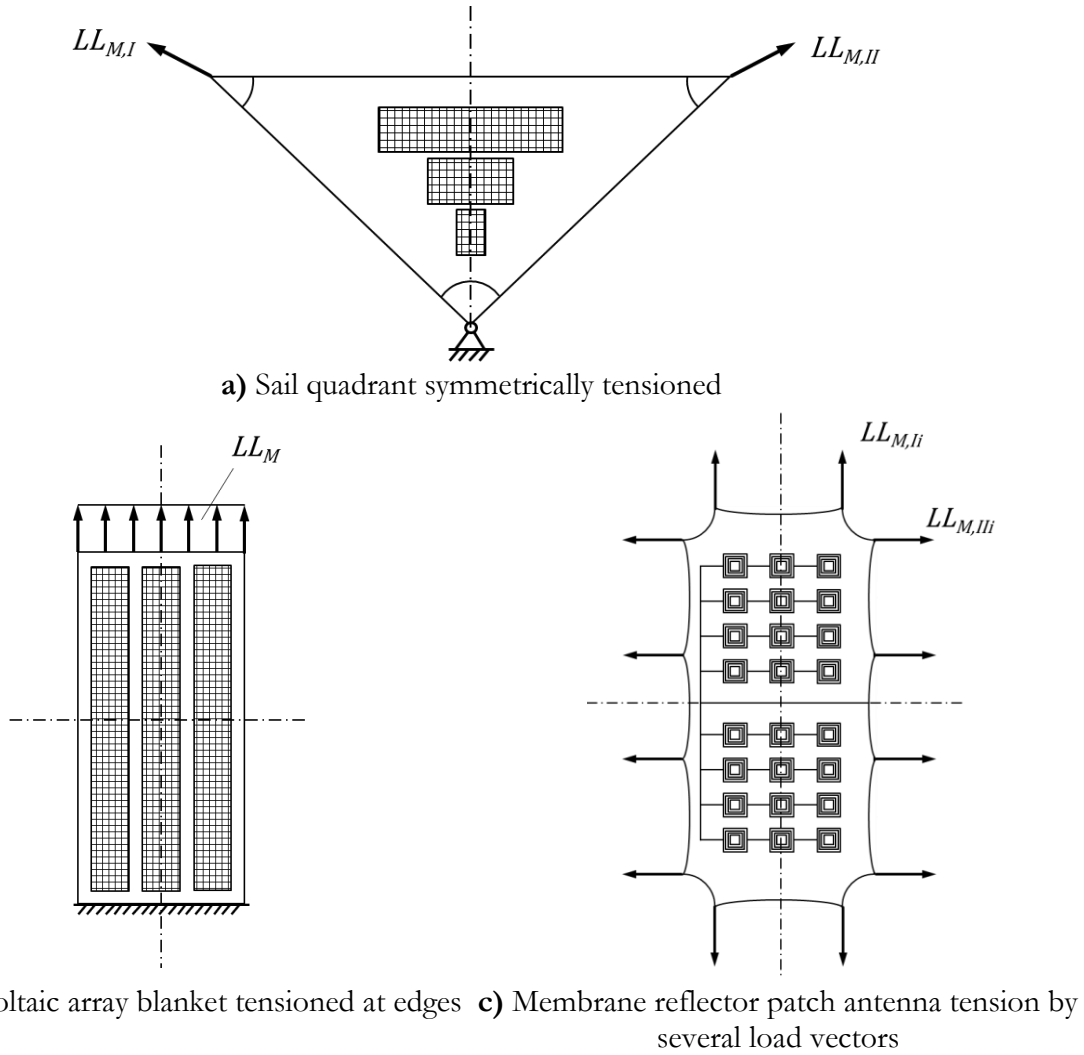


Figure 4.9. Symmetric membrane/tension loads of different applications

*Interface (I/F) Subsystem Robustness*

The I/F subsystem poses a special case. Since most I/F subsystems determine the boundary conditions of connected subsystems and unless providing their own functionality, they should rather be investigated as part of the subsystems connecting and interacting with, thus being handled as part of other subsystems. This is true for the I/F that connects the boom subsystem to the according mechanism or main structure (bus) as explained in the hardware description in section 5.1.2. It consequently is investigated within the boom subsystem as it determines the boundary conditions of the boom. However, for I/F subsystems with own functionality like a phalange of constant force springs or interface prone to damage like thin strings or more complex structures, robustness should be determined separately. The here proposed robustness for an I/F subsystem  $RO_{I/FS}$  is determined from two partial robustness metrics, a length-change-based partial robustness metric and a tensile load-based partial robustness,  $RO_{\Delta l}$  and  $RO_{L_t}$ , respectively. Considering the different impacts of the characteristic parameters of the subsystem as described in section 5.2, e.g. thermal expansion, the individual weighting factors  $w_{\Delta l}$  and  $w_{L_t}$  are derived. With this, the developed weighted and additive robustness metric  $RO_{I/FS}$  is thus expressed in equation (4.27). The first partial robustness metric  $RO_{\Delta l}$  gives the robustness of the subsystem in regard to the variation of length of the interface, expressed in equation (4.28). It gives the minimum of the ratio of the required interface length value  $l_0$  of the intact/undisturbed I/F subsystem and the measured or predicted interface length value  $l_i$

after being influenced by noise, degradation and variation. The second partial robustness of this subsystem, the tensile load-based robustness  $Ro_{L_t}$ , is based on the minimum required interface tensile limit load  $L_{ti}$  in relation to the critical tensile load  $CL_t$  of the I/F subsystem, as expressed in equation (4.29). The critical tensile load, however, is the threshold at which an interface might be damaged and therefore might not be able to fulfil its function anymore.

I/F Subsystem Robustness:

$$Ro_{I/FS} = w_{\Delta l} \cdot Ro_{\Delta l} + w_{L_t} \cdot Ro_{L_t} \quad (4.27)$$

*Length-change-based* partial I/F robustness:

$$Ro_{\Delta l} = \min_i \left( 1 - \frac{\Delta l}{l_0} \right), \quad \Delta l = |l_0 - l_1|, \quad 0 \leq Ro_{\Delta l} \leq 1 \quad (4.28)$$

*Tensile-load-based* partial I/F robustness:

$$Ro_{L_t} = \min_i \left( 1 - \frac{L_{ti}}{CL_t} \right), \quad 0 \leq Ro_{L_t} \leq 1 \quad (4.29)$$

### *Mechanism Subsystem Robustness*

The mechanism subsystem is not investigated in the same degree as the boom subsystem is, in this thesis. Nevertheless, a methodologic approach for quantifying robustness is proposed, considering the necessary parameters and influences. The mechanism subsystem itself are very similar to conventional mechanical subsystem or mechanism as found in other spacecraft. However, mechanism subsystems for GosSSS need to adhere to the special characteristics of the light-weight and deployable elements it interacts with. As it serves the purpose of storage and deployment and/or retraction (in rare cases) a robustness based on two partial robustness metrics is proposed.

The first  $Ro_{\tau}$  is based on the torque necessary for deploying the according element like boom or membrane. This partial robustness, as expressed with a “nominal the best” approach in equation (4.31), shall penalize force values exceeding or dropping below the nominal value. Further, the torque-based robustness resembles the minimum of the ratio of the generated torque  $\tau_i$  influenced by variation and noise, in relation to the nominal torque  $\tau_0$  required for the mechanism subsystem in order to deploy the connected subsystems. An inhomogeneous torque generating a inhomogeneous deployment or undesired dynamics should be penalized. This could be realized by penalizing high variance in torque values as well as large amplitude changes at low frequencies, provoked by e.g. over dimensioned leaf springs as brake components within the mechanism subsystem. Accounting for the actuation principle of using a co-coiled belt pulled out to deploy stowed booms, widely used in DLR developments, torque as a robustness parameter can be replaced by a spool-off force, thus resulting in a spool-off force-based partial robustness. This offers the advantage of easy measurements when testing the subsystem or assemblies. Nonetheless, in case of a directly driven spool for stowage torque as robustness parameter is considered more suitable.

The second partial robustness metric  $Ro_d$  resembles the robustness of the subsystem in regard to the variation of realized packaging diameter, as a measure of packaging density or packaging efficiency, of the stored element (boom or membrane). It is expressed as well with a “nominal the best” approach in equation (4.35). This gives the minimum of the ratio of the achieved packaging diameter (outer diameter)  $d_i$  of the mechanism subsystem influenced by noise, degradation in restraining forces and variation in design and material, in relation to the nominal packaging diameter value  $d_0$  of a boom or membrane rolled up on a spool of the undisturbed mechanism subsystem. Presuming the stored element (boom or membrane) itself is stowable/packageable to the demanded packaging diameter on the according spool, the mechanism subsystem is largely ruling the diameter (packaging efficiency) by its ability to maintain restraintment throughout different phases. Hence, the packaging-

based partial mechanism robustness reflects the ability of the mechanism subsystem to maintain storage quality past integration and handling, during and after launch, as well as during deployment. Individual weighting factors for each partial robustness  $w_\tau$  and  $w_d$ , considering the different impacts of the robustness parameters on the function of the subsystem, as described in section 5.2.2, are derived as well.

Concerning the requirements set for a robustness metric to be developed, the subsystem robustness as well as partial robustness are expressive, applicable, objective, holistic and calculable.

Similarly, as noted for the previously discussed subsystems the robustness of the mechanism subsystem would benefit from being extended by considering the reliability of the subsystem in future work.

Mechanism Subsystem Robustness:

$$Ro_{MechS} = w_\tau \cdot Ro_\tau + w_d \cdot Ro_d \quad (4.30)$$

*Torque-based* partial mechanism robustness:

$$Ro_\tau = \min_i \left( 1 - \frac{|\tau_i - \tau_0|}{\tau_0} \right), \quad 0 \leq Ro_\tau \leq 1 \quad (4.31)$$

*Spool-off-force-based* partial mechanism robustness:

$$Ro_{F_S} = \min_i \left( 1 - \frac{|F_{Si} - F_{S0}|}{F_{S0}} \right), \quad 0 \leq Ro_{F_S} \leq 1 \quad (4.32)$$

*Packaging-based* partial mechanism robustness:

$$Ro_d = \min_i \left( 1 - \frac{|d_i - d_0|}{d_0} \right), \quad 0 \leq Ro_d \leq 1 \quad (4.33)$$

### *Component Robustness*

Staying with the example of the boom subsystem, its components and component behavior are widely regarded as effects within the influence factors of subsystem robustness metrics. This is also true for other subsystems and their components in most cases. However, if an effect cannot be regarded in the subsystem model e.g. as simulation in a FE model, a separate robustness metric should be generated. This is the case for the example of the bearable axial compressive load of a boom after MMOD impact. In the here described example and within this thesis, such advanced FE model is not available, and the MMOD influence on the bearable axial load is determined by experiments. Since practical values can only be generated in experiments in hyper-velocity impact facilities, which are designed to house samples with small dimensions, the influence factor (impact damage size and shape) can only be established on short boom specimens, thus falling into the component category. Therefore, an according component robustness is established. This metric for MMOD impacts consequences on booms,  $Ro_{MMODC}$  (expressed in equation (4.34)), represents the minimum of the ratio of the limit load for axial compression  $LL_{ax}$  of the intact/undisturbed boom component and the achievable axial collapse load  $LL_{MMODax}$  of the boom component after being impacted by MMOD particles. Consequently, the robustness formula for the boom subsystem is extended by  $Ro_{MMODC}$  and the weighting factor  $w_{MMODC}$  as shown in equation (4.35). The additional weighting factor incorporates the probability of occurrence of the regarded MMOD impact, and therefore considers that such rare events should not be overrated or overpower other effects. Furthermore, all weighting factors in this case must be adjusted in order for the sum of all weighting factors to be equal to one.

*MMOD-based* component boom robustness:

$$Ro_{MMODC} = 1 - \frac{LL_{ax}}{L_{MMODax}}, \quad 0 \leq Ro_L < 1 \quad (4.34)$$

Extended Boom Subsystem Robustness:

$$Ro_{Booms} = w_k \cdot Ro_k + w_L \cdot Ro_L + w_u \cdot Ro_u + w_{MMODC} \cdot Ro_{MMODC} \quad (4.35)$$

As stated before, the lowest level of robustness assessment is regarded the sub-system level, with the here described exception. However, further component robustness metrics are not determined, as all relevant effects, variations and noise are regarded as influence factors.

## 4.5 Framework of Robustness Assessment and Quantification

In the following the proposed methodology for robustness assessment and quantification is described. This sequence of tasks and sub tasks, as schematically illustrated in Figure 4.10, starts with a given initial design, depending on the stage of complexity, at system, subsystem or component level (compare with Figure 4.14). It ends, at least for the iteration slope at present, with consigning the information if the robustness of an entity achieved an acceptable value or not. The main outcome of this sequence are quantified values of robustness for each considered parameter and a total robustness value that enables the engineer to decide if a design modification is necessary. All sub-steps and methodical tools applied are described in detail in dedicated subsections following, while a summary of the main tasks is given below.

*Summary of main tasks – Robustness Assessment and Quantification:*

1.	Identification of Parameters
----	------------------------------

This task focuses on the analysis of the system, subsystem or component with the goal to find all applicable parameters that might influence or determine the robustness of an entity. Several sub-steps are to be performed using analytic and intuitive methods to do so.

*Output:* List of all applicable parameters influencing/determining robustness

2.	Classification of Parameters
----	------------------------------

Classifying the found parameters in Signal, Control and Noise parameters and giving an overview of the entity of subject to robustness assessment is the main task. This is realized in several sub-steps using well-established methods of structuring.

*Output:* Classified parameter groups

3.	Selection of relevant Parameters
----	----------------------------------

Selecting and systemically rating the most relevant parameters with the estimated largest impact on a robust behavior from the before acquired parameter groups is the main objective of this task. This is important in order to reduce the effort of robustness assessment, thus providing a feasible and efficient method on hand for the engineer using the here proposed method. Furthermore, interactions between individual parameters are detected.

*Output:* Relevant parameters; Parameter interactions

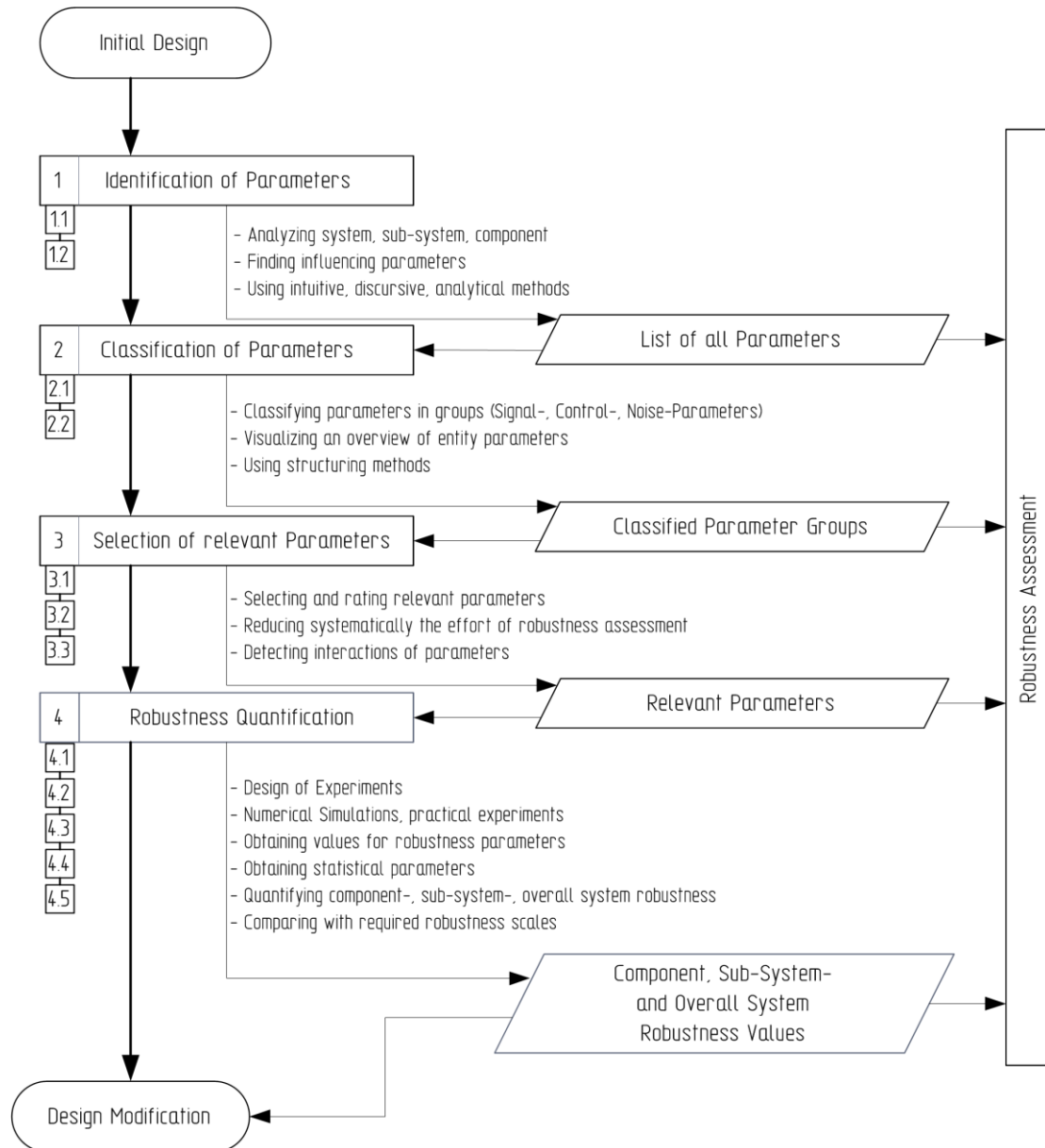
4.	Robustness Quantification
----	---------------------------

This task resembles the core work of the method of robustness assessment and quantification. It comprehensively includes the robustness evaluation and quantification of each relevant parameter using robustness functions, weighting, penalty and amplification coefficients if applicable, and systematic assessments of probabilities, and finally assesses and quantifies the total robustness of the investigated entity. This main result is then compared to required

robustness values or robustness parameters, thus providing explicit areas to be improved in design.

*Output:*

Component and Subsystem Robustness Values, Total Robustness Value (System Robustness)



**Figure 4.10.** Main tasks of the robustness assessment method (sub-tasks are denoted with sub-numberings)

### Task 1. Identification of Parameters

Analyzing the system, subsystem or component with the goal to find all applicable parameters that might determine or influence the robustness of an entity is done in several subsequent sub-steps (sub-tasks) as described in the following:



*Sub-Task 1.1. Screening for Parameters*

In this first step, a screening for parameters that might determine or influence robustness is performed on the entity of the current level of complexity (system, subsystem, component). Here intuitive methods like brainstorming, method 635, Delphi method, gallery method or Synectics, as given in literature [41]; discursive methods like systematic physical studies, system search schemes, the use of design catalogues; or analytical methods in terms of analyzing existing design knowledge, measurements, standards and handbooks are used in order to gather the necessary information. The outcome is a brief unsorted list of parameters.

*Sub-Task 1.2. Relating Parameters*

By applying assessment methods like the Ishikawa's causal diagram, mind maps, event trees and FTA (failure tree analysis; see Appendix B for more information on methods), the found parameters are systemized and related to the investigated entity. This establishes hierarchical parameter structures and determines causes and effect directions with the outcome of a systematic parameter overview for an entity.

**Task 2. Classification of relevant Parameters**

Classifying the found parameters generally in signal, control and noise parameters, thus defining the input parameters, as well as identifying the output and response is the focus of this task. This gives an overview of the system under assessment of robustness and is realized in several sub-steps using well established methods of structuring as described below.

*Sub-Task 2.1. Sorting Parameters into Classes*

Classifying in this sub-step is realized by generally sorting the identified parameters into three classes: signal factors, control factors and noise factors, similar to the principle of dynamic systems theory. This principle is further adopted from the field of Quality Engineering based on the Robust Design Theory of Genichi Taguchi as described by Klein [64].

The three factors are defined herein as:

*Signal Factors:*

- parameters/factors set by the engineer as input with a range of settings (e.g. motor voltage of a deployment mechanism to change deployment speed)
- should cause desired effect of a product
- defines target value
- not present in static Robust Designs according to Taguchi

*Control Factors:*

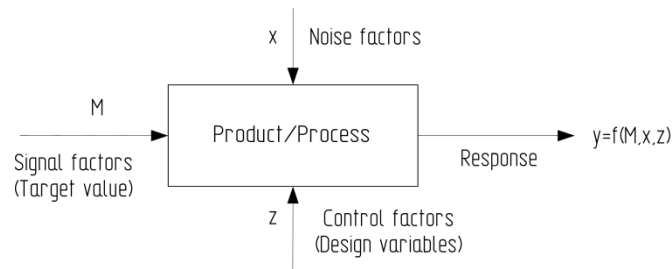
- free to choose by the engineer as functional design parameter
- used to optimize/control a product function
- can be fixed or adjustable
- examples are equipment settings, material used to manufacture the product, or product design features

*Noise Factors:*

- parameters/factors cause output variations
- often environment factors
- difficult to control
- examples are ambient temperature or humidity

*Sub-Task 2.2. Visualizing classified Parameter Groups on Entity*

In order to visualize the parameter groups assigned to the entity, a parameter diagram, as displayed for a general case of a product or a process in Figure 4.11, is generated. This allows the necessary and comprehensive understanding of the entity and its parameters it interacts with.



**Figure 4.11.** Parameter-Diagram (P-Diagram)

### Task 3: Selection of relevant Parameters

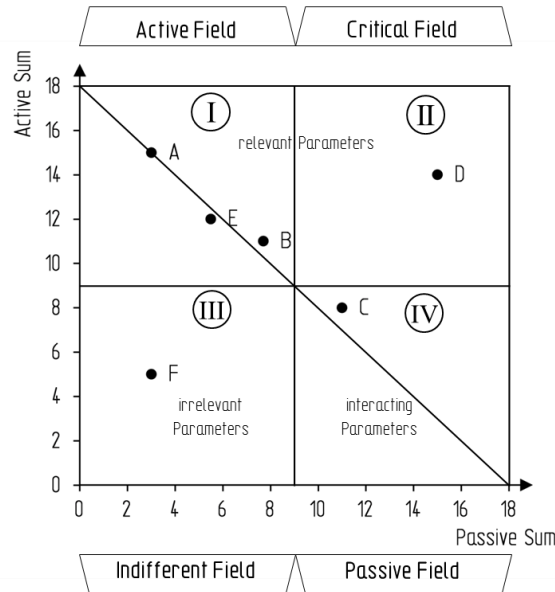
In Task 3 the focus is on systemically ranking and selecting the most relevant parameters with the estimated largest impact on a robust behavior. This is important in order to reduce the effort of overall robustness assessment and keep it within feasible limits in terms of cost, time and resources. A ranking of parameters with a subsequent deeper evaluation of parameter relevancies give the basis for the final selection at the end of this task.

#### *Sub-Task 3.1. Ranking Parameter Relevance*

Within this sub-step, prioritizing of parameters by assessing their influence on the objective function and ranking them is the main task. The goal is to find the parameters with the highest influence on the objective function. Ranking itself is realized with a pairwise comparison of parameters, based on qualitative weighting thru e.g. a Preference Matrix or Intensity-Relation Matrix (see section Appendix B), with active and passive sums. Here experts and engineers use the available information gathered before in Task 1. The generated rank list is used to down select only the most influential parameters, suggested in Robust Design Theory according to Klein 6-10 parameters [64], that are further regarded in the robustness assessment. This helps to keep the effort of the overall assessment within feasible limits in terms of cost, time and resources.

#### *Sub-Task 3.2. Assessing Parameter Relevance*

Profoundly evaluating the relevance of each parameter and visualizing the dependencies and effects of each parameter are the tasks of this sub-step. Determining evaluation scores for each parameter is done with the acquired data from sub-step 3.1. Each active and passive sum for a parameter is transferred into an analysis scheme e.g. a GRID-Analysis as portfolio diagram as shown in the generic example of Figure 4.12. The parameters A to B, shown in the figure are placed according to their active and passive sums into four fields that determine the influence of a parameter on the objective function of a system. In this scheme field I (active field) contains strong main effects, field II (critical field) medium/weak main effects, field III (indifferent field) low/no effects and field IV (passive field) interacting effects between single parameters. In general, one can state that parameters with main effects can be found in a decreasing order on the diagonal of the scheme.



**Figure 4.12.** GRID-Analysis in a portfolio scheme

*Sub-Task 3.3. Selecting Parameters for further assessment*

This sub-step consists of the selection of 6-10 parameters with the highest relevance, determined by the scores in task Sub-Task 3.2. These selected parameters are handed over to the next task 4.

## Task 4. Robustness Quantification

Resembling the core work of robustness assessment with five sub-steps, task 4 comprehensively includes all steps necessary for a robustness evaluation and quantification of each relevant parameter using robustness metrics on different levels.

This is herein explained exemplary on the boom subsystem, and can be followed in Figure 4.13. After handing over the selected and relevant robustness parameters sub-task 4.1 establishes the designs of experiments with two parallel paths, sub-task 4.1a) for a simulation and sub-task 4.1b) for a test campaign. In sub-task 4.2 the two parallel paths are continued each with 4.2a and 4.2b, by performing a finite element analysis and an experiment, respectively, both with the outcome of a load-displacement curve. The following sub-task 4.3 assesses the load displacement curves from FEA and experiments, thus determining robustness parameters like stiffness, characteristic points like collapse load or displacement at collapse (see also section 4.4.2). Further, in this sub-task basic statistical parameters are determined. In sub-task 4.4 the partial robustness metrics are determined according to equations (4.16), (4.17) and (4.19). Finally, in sub-task 4.5 the subsystem robustness metric is calculated using equation (4.15), followed by a comparison with the required robustness values (c.f. Table 4.2). Then, the overall system robustness can be determined from all calculated subsystem robustness metrics according to equation (4.7). These main results are then compared to required overall robustness levels (if available), thus giving the essential value for decision making in the overall design process if the system, subsystem or component is robust (enough) or not. If the results are deemed unsatisfactory, a design modification or optimization, that is not included in this thesis, might be performed and robustness be reiterated.

*Sub-Task 4.1.a) Design of Experiment for Simulation*

Design of experiments (DoE) is planned for a finite element simulation, based on the design variables (control factors) and the influence parameters (noise, inherent variation, environmental factors, obtained in section 4). For each simulative experiment a sample is planned for evaluation, while the sample size is based on trade-off between acceptable run time of each numerical model

and error. For each design of the sample a finite element model (FEM) is established and the input for the finite element model is generated.

*Sub-Task 4.1.b) Design of Experiment for Testing*

Design of experiments (DoE) for this sub-task is planned for practical experiments such as boom bending tests. These are based on test parameters (e.g. dimension of sample, aim of test) and the influence parameters (noise, inherent variation, environmental factors, obtained in section 4) that need to be regarded in the test sample or subsystem under test. For each practical experiment a sample is planned for testing, while the sample size is decided on the trade-off between effort of testing, generating the specimens and the necessary output for valid results. Inherent variations are already included in the sample by default or might be introduced for an isolated investigation separately. Thus, for each design of the sample a test setup is generated.

*Sub-Task 4.2.a) Performing Finite Element Analysis (FEA)*

In this branch of the sub-task, a three stepped finite element analysis (buckling analysis) is carried out for each sample. Firstly, a linear, static analysis to imprint imperfections using an eigenvalue analysis is performed; secondly a linear buckling analysis to obtain the characteristic boom deformation and thirdly a non-linear, static buckling analysis to derive the failure load. Further, inherent variations of design parameters are introduced to the simulation models through random number generators (Monte-Carlo simulation). Finally, load as well as boom-tip displacement data is obtained as output.

*Sub-Task 4.2.b) Performing Experiment*

This second branch of sub-task 4.2 contains the whole process of testing, including setting up the test stand and equipment as well as installing necessary sensors and their calibration. However, carrying out the tests and acquiring test data embodies the main process.

*Sub-Task 4.3. Result Assessment and Statistical Analysis*

In this sub-task, the acquired data from simulation and/or experiments is analyzed and post processed. This is done as a load-displacement curve is generated for each numerical model and/or test sample. Further, robustness parameters, here characteristic load points (local buckling, global buckling, and collapse load) as well as stiffness and boom tip displacement at e.g. collapse load are determined. Following this, a statistical analysis is carried out to obtain basic statistical parameters (mean, standard deviation, coefficient of variance) and to compute reliability.

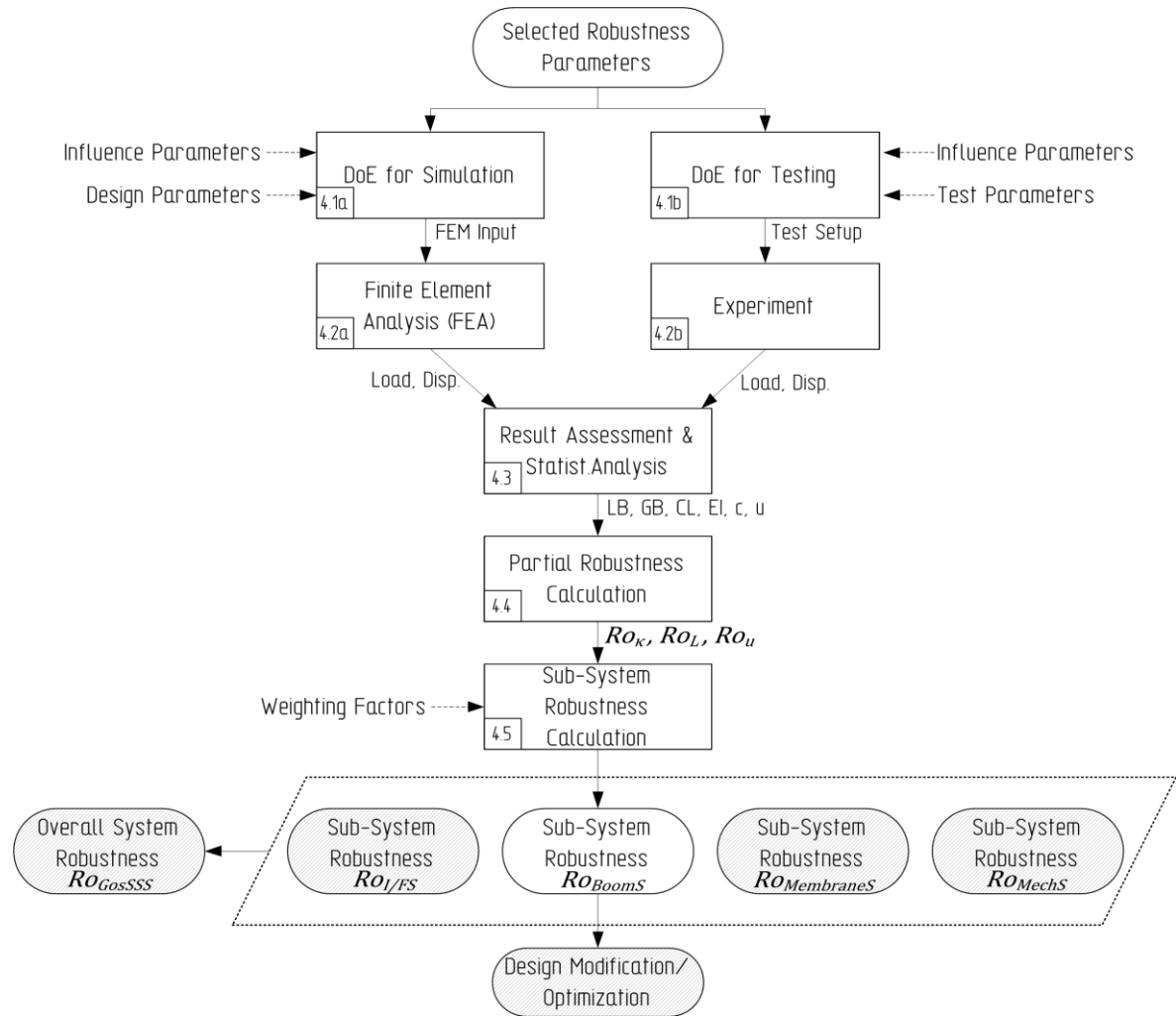
*Sub-Task 4.4. Partial Robustness Metric Calculation*

In this sub-task the partial robustness metrics are calculated from the determined robustness parameters using equations (4.16), (4.17) and (4.19).

*Sub-Task 4.5. Subsystem Robustness Calculation*

Using the obtained partial robustness metrics and the previously defined weighting factors that regard the impact of consequences for each robustness parameter, the according subsystem robustness is calculated. Following this, the obtained values for the robustness metrics are compared to the predefined scale values (Table 4.2) and the subsystem can be evaluated robust enough or not. If not satisfying a design modification or an optimization can take place, followed by another iteration of robustness assessment.

Finally, determining the overall robustness value of the investigated system with equation (4.7) and comparing this as well as the subsystem or component robustness to required robustness value ranges (as assumed in Table 4.2) gives the information if an entity is robust (enough) or not. This and all information acquired throughout the whole robustness assessment is handed over as input to the overall design process, at the according level of complexity, as described in section 4.6.



**Figure 4.13.** Strategy for robustness quantification – exemplary on the boom subsystem

#### 4.6 Implementation in the Design Process

Analyzing design and robustness of a complete GosSSS requires analyzing and optimizing its sub-systems, components and materials as well, including the relations and interactions between these entities. A general implementation of the robustness assessment methodology in the design process of such systems is given in Figure 4.14. Robustness assessment is introduced for all levels of complexity. The primary input is the initial design, derived from the overall spacecraft system design. It is based on the secondary input, such as mission definition and mission goal, mission constraints and requirements, objective function, defined overall robustness aimed for, and design rules for Gossamer structural space systems, being a possible condensation of the findings of this thesis. The aspired overall output is the final and robust design of the GosSSS. Starting with a system design process that considers the identified robustness parameters and details the initial design of the structural system, the procedure is carried out in a cascading manner subsequently over all levels of complexity. Robustness assessment is initiated with what can be summarized as risk and sensitivity analysis, earlier described as tasks 1 to 3 in section 4.5, considering the specific mission risks and Gossamer technology risks, described in section 0. Following is the robustness quantification, the core task, thus delivering the value of the according robustness metrics. On each level, the calculated robustness values are compared to required robustness values and a decision process is initiated. Generally, if the analyzed level entity achieves the required robustness, its design is fed back into the next upper level of complexity. Otherwise, iterations are repeated and design modifications are made until a robust design is achieved, that can be transferred to the next upper level.

Two strategies of methodology application, as discussed earlier in section 4.3, are identified: a top-down and a bottom-up strategy. In the top-down strategy, robustness is determined at the first iteration, preferably at the highest level. The next lower level is only investigated if robustness is not satisfying or the system design is reiterated directly. This however presumes that e.g. the system model considers all major effects, interactions and component behavior. In case this information is known entirely and in detail from e.g. previous designs and design heritage, this top-down strategy can be applied to save time but demands large resources in order to predict robustness accurately and to find an optimal final robust design. On the other hand, this strategy might provide results with lower accuracy, due to missing or unknown information on subsystems, components, their interactions or effects.

The bottom-up strategy considers more details, and establishes models (e.g. FE models or experiments) on each level. Here the process is pursued through all levels, down to the lowest one. Further, during the first iteration all decisions are bypassed with “NO” (not robust). In this way the procedure is taken directly to the lowest and most detailed level, thus starting the whole assessment at the lowest complexity. However, it is assumed that an entity model (e.g. subsystem model) contains all characteristics of each lower level entity (components). In this strategy, the next lower level is approached, if robustness of a level entity is not satisfying the required robustness, instead of reiterating on the same level, as done in the top-down strategy. Nevertheless, this strategy relies on detailed and complete analysis at each level, thus providing a maximum accuracy in predictions and results. However, this is also very time consuming.

Within this thesis an intermediate strategy is applied. The process is biased until subsystem level, consequently starting robustness assessment here, since almost all identified influencing parameters can be incorporated within a model at this point. Assuming a detailed knowledge base, the next lower level is only approached if an effect or influence cannot be acknowledged at subsystem level. The robustness assessment methodology is applied in the development phases A to C, as defined by ECSS [37], in order to make design changes. However, determining robustness by the proposed robustness assessment methodology is also valuable in later phases. This provides control of robustness throughout service life and can even give valuable information about robustness during in-orbit operation. Within design phases the here developed methodology is located in the embodiment design of phases II and III in regard to the German industrial standard VDI 2221 [40].

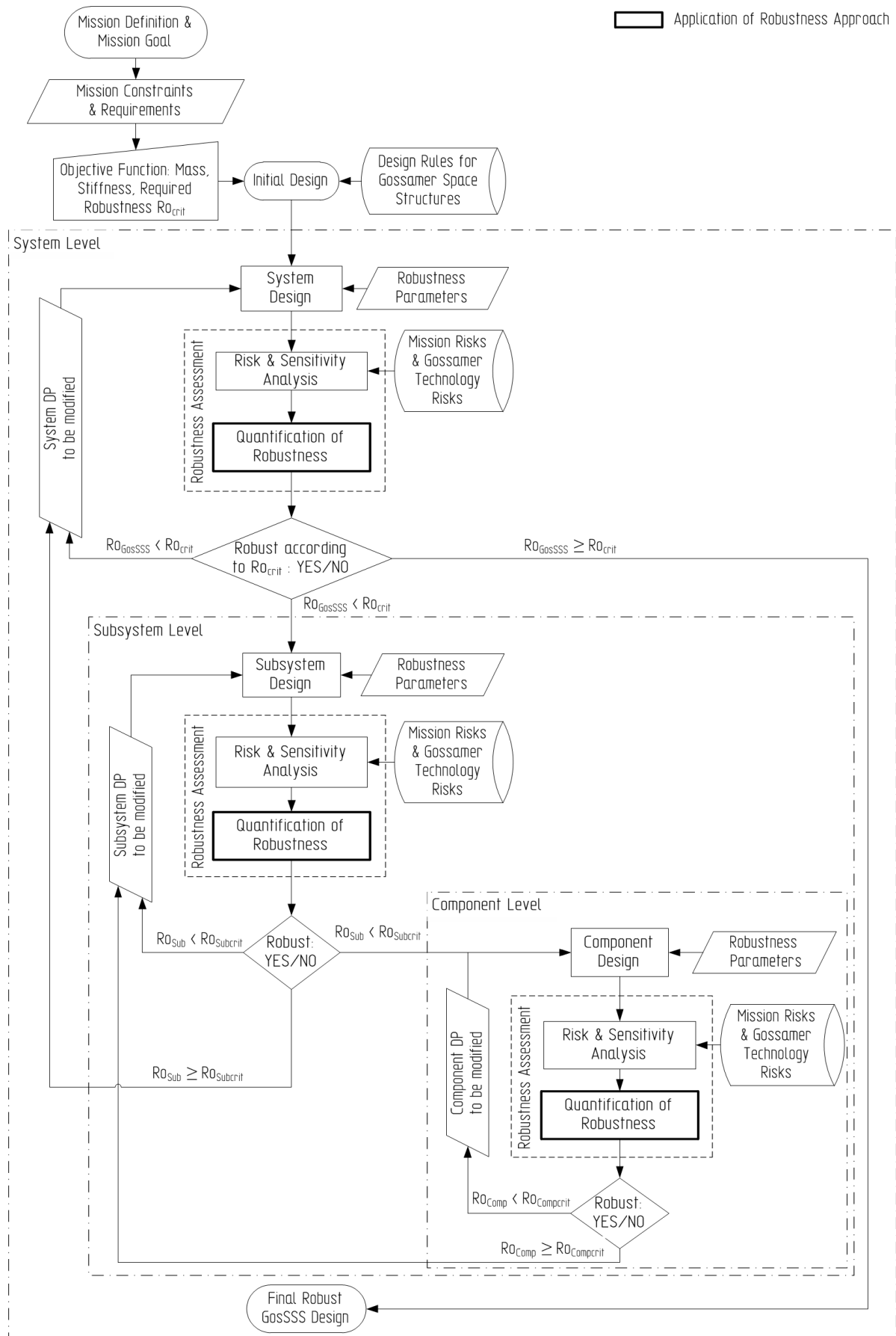


Figure 4.14. Design process with the implemented robustness assessment methodology – over all levels of complexity

## 4.7 Chapter Conclusion

This chapter provides and discusses a novel robustness assessment methodology for Gossamer Structural Space Systems, based on the proposed hypotheses (cf. chapter 2). This methodology regards a combination of different disciplines like design principles, risk & reliability assessment, technical assessments and robust design, as lacking aspects of each discipline by its own can thus be compensated. Furthermore, requirements are set and formulated into the classes: expressiveness, objectivity, simplicity, calculability, applicability, holistic and setting design limits, thus giving guidance for defining robustness metrics. Considerations on conditional robustness are discussed in order to make aware of how robustness on a level might affect the overall system robustness. While different strategies to approach system robustness, in form of top-down or bottom-up strategy are identified, they are discussed along with the advantages and disadvantages of each, with the outcome that an intermediate strategy should be chosen to determine the robustness of GosSSS within this thesis. As a main result, this chapter makes robustness measures available on all levels of complexity, with the specific quantification of robustness for GosSSS being a novelty in this regard. Mathematical approaches are generated, compared and expressed by relations of robustness parameters for system, subsystems and exemplary for a component. Furthermore, the cumulative approach is seen most useful, thus providing less conservatism, enabling effective weighting and supporting the main hypothesis (cf. chapter 2). Additionally, the framework of how to assess robustness is introduced. Firstly, the necessary tasks and sub-tasks to pursue a robustness assessment are provided. Secondly, the quantification strategy is scrutinized, explaining its steps and application. Here parallel paths, regarding numerical simulation as well as practical experiments, are joined in the process to provide characteristic robustness parameters e.g. buckling loads of the boom subsystem, and consequently generate the robustness values on all levels of complexity. Finally, a discussion is given about the implementation of the proposed robustness methodology in a design process, as well as in the context of space and industry standards.



## 5. SENSITIVITY, RISK AND SYSTEM ANALYSIS – CASE STUDY

### 5.1 The selected Gossamer Structural Space System

Mainly a solar sail demonstrator serves as practical framework and case study for this thesis and is investigated regarding robustness. Additionally, at some points within this thesis, hardware provided by other projects is inserted for discussion. Nevertheless, the two applications described in the following provide the main context of robustness investigation.

The first application is the solar sailing technology demonstrator Gossamer-1, a DLR project. The spacecraft for this application is aimed to apply and augment Gossamer technology of DLR in terms of CFRP boom & mechanism technology, thin foil technology and space system competence. Planned as technology demonstration mission it is the first step of originally three, of the “Gossamer Roadmap” of DLR and ESA [83], developed in 2009 and aimed for the development of ultra-light weight deployable technology, scalable in size and complexity. The roadmap consists of the three steps: In the first step, Gossamer-1, a planar 5 m x 5 m, 3-axis stabilized, squared in-orbit deployment demonstrator, serving as space qualified and scalable technology basis, should be realized and deployed in a 700 km (initially 320 km) orbit. An advanced 20 m x 20 m demonstrator (termed Gossamer-2) with a limited orbit and full attitude control, to be deployed in a 500 km orbit, should follow this. In the third step, a 50 m x 50 m fully functional solar sail (termed Gossamer-3) should be realized, ready for being deployed in a full-scale solar sail mission at an orbit altitude of over 10,000 km. Although the road map has not exceeded development and ground qualification of Gossamer-1, it served as a valuable research and development base, and contributes major knowledge and data to this thesis.

The second application partially discussed in this case study is the ESA-GSTP funded drag sail (de-orbiting sail) ADEO (Architectural Design and Testing of a De-orbiting Subsystem), DLR participated as the contributor of booms, sails and basic deployment technology. Facilitating a passive principle, the ADEO subsystem is a scalable drag augmentation device that uses Earth’s residual atmosphere present in low Earth orbit. This very light-weight drag sail is deployed at EOL (End of Life) of the satellite in order to generate an altitude decay of the satellite followed by its burn up in the atmosphere when deorbiting. ADEO features a 25 m<sup>2</sup>, truncated, pyramidal drag sail, with a squared projected area and uses four deployable thin shell CFRP booms that deploy four triangular membrane sails simultaneously. ADEO is mainly based on Gossamer-1 technology; however, its subsystems have been adapted and further developed for this drag sail application.

#### 5.1.1 Mission envelope and objectives

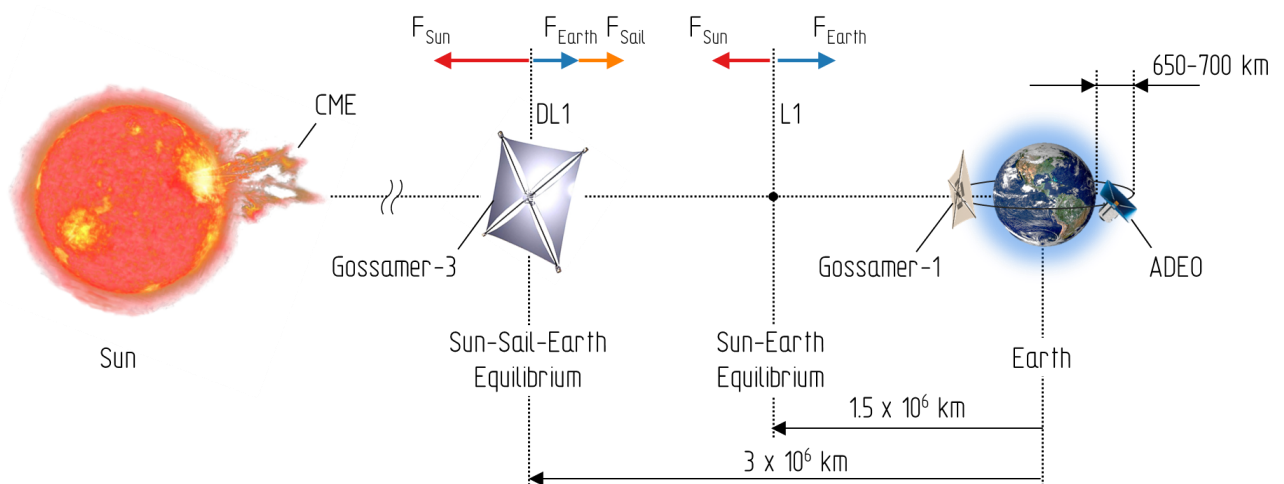
The missions described in the following section provide the basic information for the sensitivity and risk analysis in the course of this chapter as well as the background for determining the influence factors in chapter 6. The different missions are used to generate an envelope of environmental effects, influences, constraints and requirements that determine structural robustness. Following in chapter 6, the influences of all missions are investigated, since the structural system should be scalable and applicable to all missions considered. Furthermore, the derived mission design envelope is graphically represented in Figure 5.1, in terms of orbital positioning.

Attaining a space qualified basis of solar sail technology that proved its ability to deploy in-orbit is the focus of Gossamer-1. It should be launched within an international network of 50 CubeSats for multi-point, in-situ measurements in the lower thermosphere and re-entry research (EC FP7 Project QB50). In addition to the CubeSats, Gossamer-1 had been selected as an in-orbit demonstration mission (IOD mission) within QB50. Gossamer-1 was intended to be operated as a free flyer in a circular Low Earth Orbit (LEO) at an altitude of 700 km. Mission duration of this demonstrator was envisioned to be several weeks to several months. Decommissioning by drag forces by residual atmosphere in LEO was intended. The major aims for the Gossamer-1 mission are: The successful and controlled boom and sail deployment; the proof of functionality of thin-film photovoltaics on

thin film sails; monitoring sail and boom deployment, and transmitting data and overall space qualifying the system. The in-situ determination and monitoring of boom loading, structural dynamic behavior like Eigenmodes and Eigenfrequencies, attitude estimation and estimation of the acting gravity and atmospheric drag. Further mission details and mission phases can be found literature [84–87].

An interplanetary solar sail mission for space weather warning, station keeping at a sunwards displaced Lagrange point DL1 (also referred to Sub L1), as described by McInnes et al [88], may use the largest development stage of DLR’s solar sails with 65 m x 65 m (Gossamer-3 technology). The mission’s goal is to double the warning time of space weather events, like coronal mass ejections (CME), compared to conventional space weather missions like the ACE (Advanced Composition Explorer) mission of NASA and NOAA, located at Lagrange point L1 (see Figure 5.1), according to McInnes [88]. By exploiting solar radiation, the solar sail delivers artificial equilibria (of gravitational forces) to the enhanced space weather mission in a restricted three-body problem (Sun-Solar Sail-Earth). This allows the sail craft to be located sunwards of the classical L1 point, at DL1, as illustrated in Figure 5.1, where it shall be deployed after Earth escape. The mission will provide space weather data for a period of about 10 years.

As ADEO is designed with the intension of being an additional module of satellites, its mission is following subsequently a typical commercial satellite mission in LEO, augmenting drag forces as a drag sail and thus deorbiting the satellite. In order to initiate the de-orbit maneuver a large membrane surface is deployed which multiplies the drag effective surface of the satellite. The aim of ADEO is to increase drag forces and thereby causing an accelerated decay in orbit altitude of the satellite for decommissioning after service. De-orbiting itself however shall not exceed 25 years, while the booms have to be typically stored for 20 years until the deployment is initiated. This period includes 5 years of on ground stowage before launch and 15 years of on orbit stowage during service life of the satellite. Selecting the reference mission was done in such a way that the carrying satellite would fit on the European VEGA launcher as well as being operated in LEO, as this is currently the region that is most critical regarding space debris mitigation. This led to a generic satellite with a mass of about 1000 kg, operating on a 650 km orbit. Complying with ESA’s Space debris legislation to de-orbit satellites in LEO within 25 years, the drag sail area of ADEO was determined to be 25 m<sup>2</sup>. Furthermore, the ADEO system design aims for passive attitude stabilization with its pyramidal shaped drag sail design, thus making active attitude control during de-orbiting expandable. Further information on this project and mission can be found in Sinn et al [89–91].

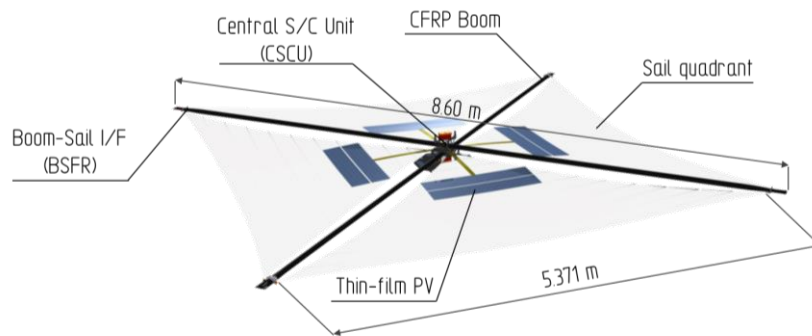


**Figure 5.1.** Considered mission design envelope (CME- coronal mass ejection, L1- Lagrange point 1, DL1-Displaced Lagrange point 1)

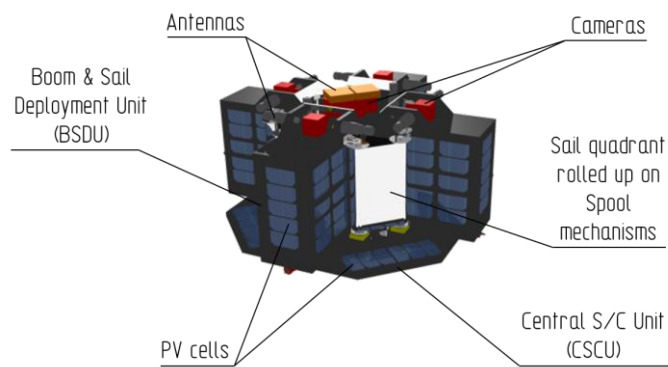
### 5.1.2 Overall Structural System Architecture of Gossamer-1

The fully deployed, squared and planar solar sail demonstrator Gossamer-1, as displayed in Figure 5.2 a), is about 5.3 m x 5.3 m (6 m x 6 m measured from boom tips) in size, thus realizing a total sail area of about 27.5 m<sup>2</sup>. Gossamer-1 uses two thin shell CFRP boom assemblies of 8.6 m in length, configured in a cross-like arrangement, with a vertical offset. Once fully deployed, the booms span four identical triangular polyimide sail membranes. In stowed configuration, as displayed in Figure 5.2 b), the spacecraft is as compact as 790 mm in diameter and 500 mm in height. Comprising of several subsystems and components, the structural system is categorized according to the methodology proposed in chapter 4, in the boom subsystem, the membrane subsystem, the mechanism subsystem and the interface subsystem, and the non-GosSSS central bus. While all subsystems, typical for deployable planar GosSSS, are described in detail in the following sections, the central bus system, termed Central S/C Unit (CSCU), is not. It is considered a regular space structure that could also be found in non-deployable spacecraft. However, it connects all subsystems and hosts components, equipment and electrical subsystems like the DLR developed bus CLAVIS, batteries, PV cells, cameras, antennae.

Deploying the sail craft is realized in a boom tip deployment, by simultaneously unrolling the booms out of the remotely controlled and electrically driven Boom & Sail Deployment Units (BSDUs), that in consequence unfurl the four sail quadrants. Here a unique sail stowage concept is facilitated in which each sail quadrant is stored on two different sail spools of two adjacent BSDUs. In Figure 5.3 all stages of the deployment sequence for the spacecraft are depicted. The sequence starts in stowed configuration (a), with a compact size of 790 mm in diameter and 500 mm in height, featuring a mass of about 30 kg. Deploying all four booms tips and all four sail quadrants simultaneously with the deployment units results in an increase of functional area. Following an intermediate stage with the booms and sail quadrants partially deployed (b), the sail quadrants are then fully deployed, while the boom tips are still partially rolled up in the BSDU over a short length, thus keeping the BSDU attached to the spacecraft (c). In the next stage the BSDUs proceed deploying the boom tips, followed by being jettisoned away, while the sails are already taut and fixed to the according boom sail interfaces (d). This leaves the sail craft fully deployed in sailing configuration (e) with a considerable mass reduction, consequently increasing the resulting thrust. The functional sail now features a size of 5.3 m x 5.3 m (27.5 m<sup>2</sup>), and a much lower mass of about 3.5 kg. Ideally the booms are under constant axial pressure load while the sail quadrants are mainly in a tensioned condition, during the complete deployment sequence. However, in reality loads deviate and a combination of axial compression and bending moments is apparent, demanding certain robustness from the involved subsystems.



a) Fully deployed sailing configuration



b) Stowed configuration

Figure 5.2. Overall design of Gossamer-1

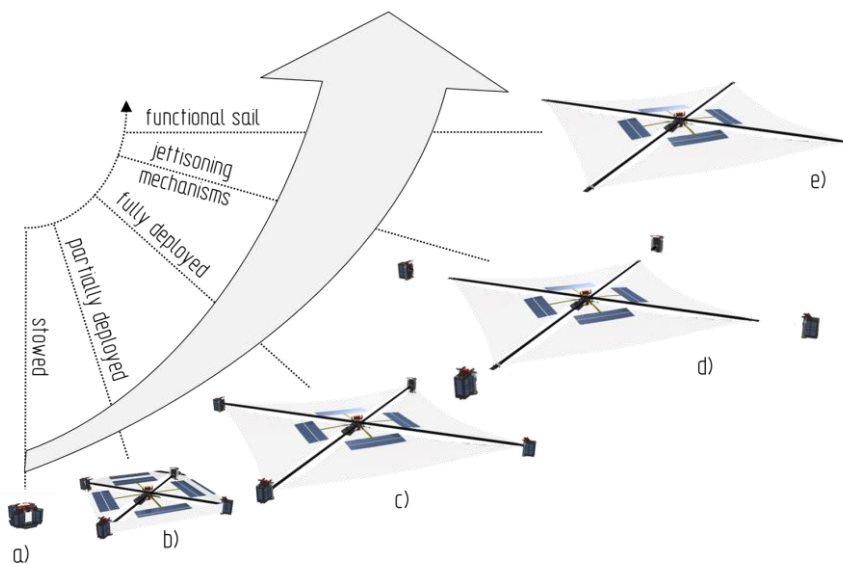
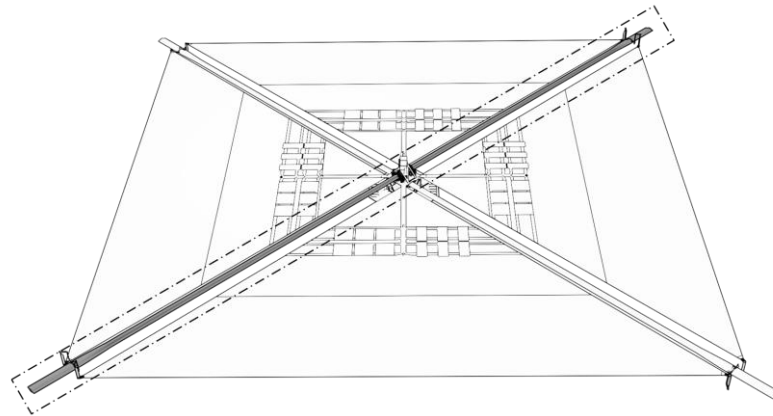


Figure 5.3. Deployment sequence of Gossamer-1

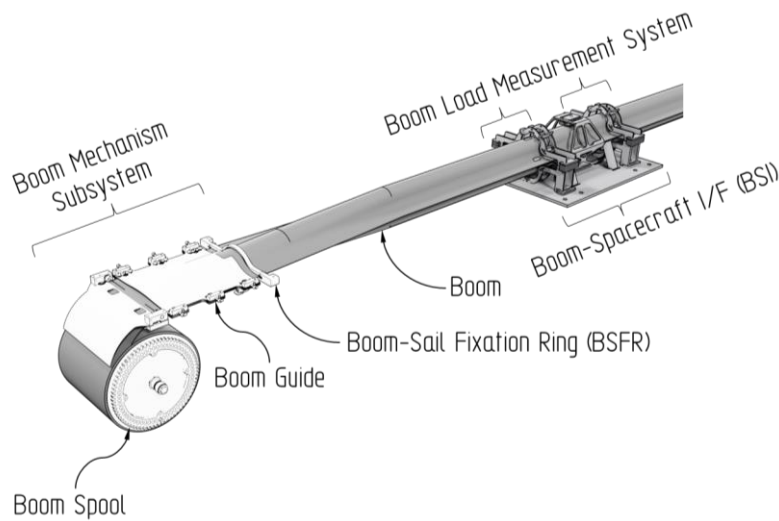
### 5.1.3 Boom Subsystem

The boom subsystem, highlighted in Figure 5.4 a) thus locating it in the overall system, comprises several components. However, the whole Gossamer-1 system features two identical boom subsystems in a cross-like arrangement in order to achieve the intended functional dimensions of 5 m x 5 m for the solar sail. For simplification and in the light of robustness assessment a boom subsystem is investigated on one-half due to its symmetrical design. The main components and elements of the boom subsystem as highlighted (gray) in Figure 5.4 b) and c) are: the deployable boom, the boom load measurement system, the boom spacecraft interface (BSI), as well as the stop wings and one

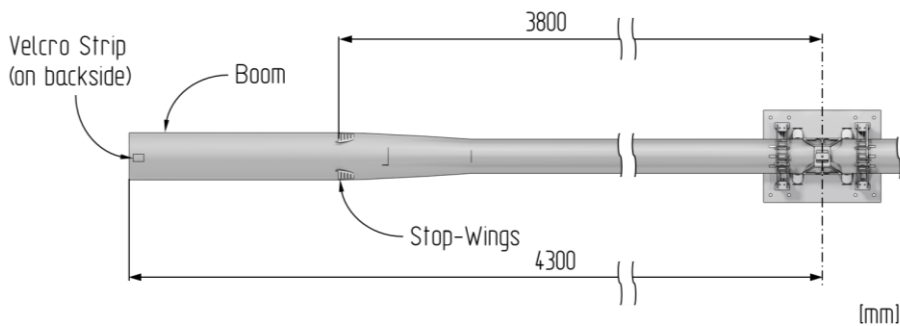
counterpart of a Velcro® strip. Nevertheless, components of connected subsystems (left white in Figure 5.4 b), like the boom storage spool and the boom guide shell of the mechanism subsystem or the boom sail fixation ring (BSFR) as part of the interface subsystem determine boundary conditions and the load introduction of the boom subsystem for large parts. Further the main dimensions of the investigated symmetrical half of the boom subsystem with 4.3 m and 3.8 m for the fully deployed and functional boom length, respectively, are given in Figure 5.4 c).



a) Boom subsystem located in the structural system Gossamer-1



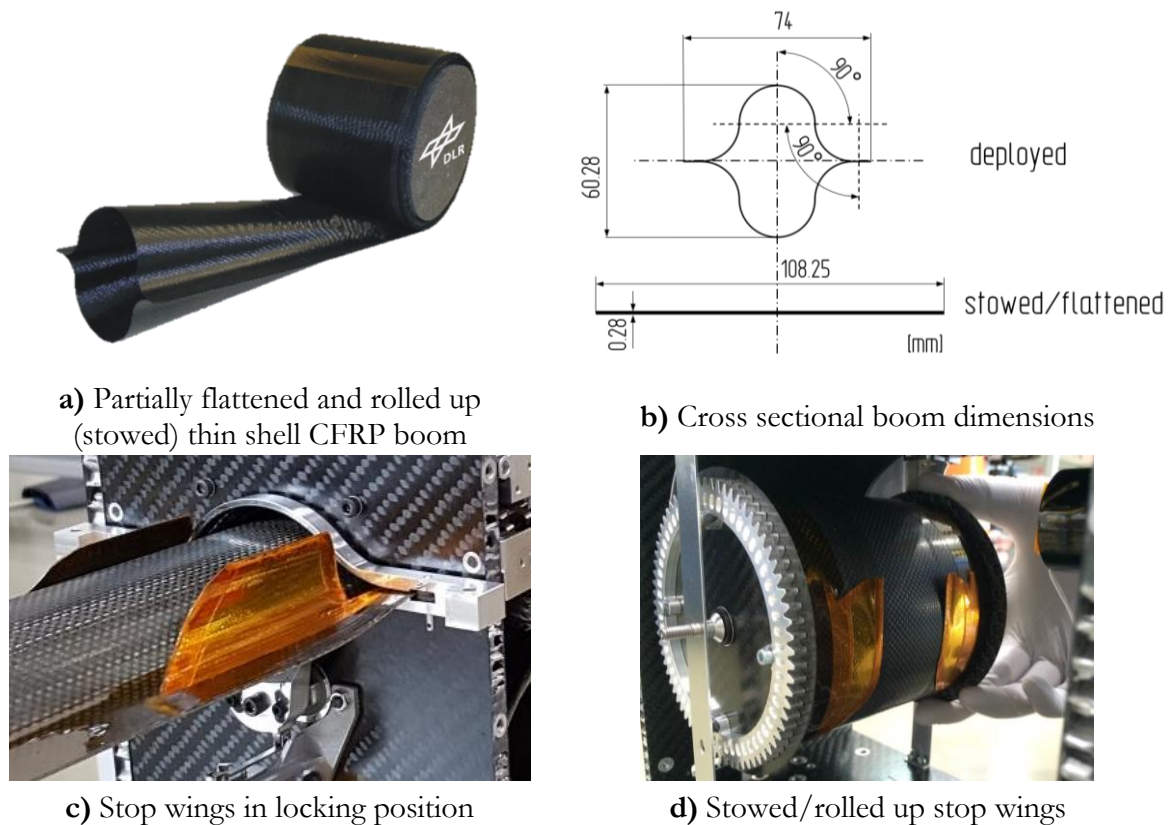
b) Main elements and components (gray)



c) Main length dimensions

Figure 5.4. Boom subsystem of Gossamer-1

The used thin shell, deployable CFRP booms are collapsible (flattened in cross section) and rolled up at their tip on storage spools (boom spools) with 100 mm in diameter, as displayed in Figure 5.4 b). Such boom type can generally be considered as collapsible tube mast (CTM [92]). Featuring a closed double  $\Omega$ -shaped cross section when deployed, also referred to as lenticular, the boom is fabricated from a  $0^\circ/90^\circ$  one-layer plain weave fabric ( $0^\circ$  resembles the longitudinal boom axis) with a nominal shell thickness of only 0.14 mm when cured. Each boom further consists of two CFRP half shells that are symmetrically bonded along their flanges (flat region of the booms cross section). The material's elasticity and the dedicated double  $\Omega$ -shaped cross section enable the boom to be flattened out over the whole length and rolled up on the cylindrical boom spool inside each deployment unit for stowage, as shown exemplarily in Figure 5.5 a). Within this process the cross-section transitions, according to Figure 5.5 b), from a nominal height of 60 mm and a width of 74 mm (deployed dimensions) to a flattened state with a nominal height of about 0.37 mm (thickness at flanges) and a width of 108.25 mm. These dimensions are the smallest possible values that allow coiling of the boom without reaching critical stress levels in the shell material and bonding layers. Dimensioning, however, is not a subject of the here studied robustness. Once deployed a specific mass of about 36 g/m is achieved for such a boom. By joining two 4.3 m boom components the full subsystem length of 8.6 m is achieved. Nevertheless, the remaining length between the functional length of 3.8 m (see Figure 5.4 c), at which a sail quadrant is ankered to, measured from the subsystem center, and the total length of one boom subsystem is used for jettisoning the deployment mechanisms (BSDU) by pushing themselves off the boom tip. As illustrated in Figure 5.5 c) the ankering point on the boom is equipped with two stop wings that lock the sail interface ring (BSFR – Boom Sail Fixation Ring) to the boom and thus fix the sail corner at the functional deployed length. During deployment the stop wings slide through the boom guide shells of the deployment units and the boom sail fixation ring, and erect by the intrinsic stored strain energy much like a tape spring. In this way the sail corners are kept from sliding back inwards and thus fixed the tensioned sail quadrants. For stowage, however, the stop wings are coiled up along with the boom as depicted in Figure 5.5 d). In order to transfer deployment loads in the phase of jettisoning a Velcro® strip is attached to the boom tip, connecting it to the actuator belt that is part of the mechanism subsystem and described in section 5.1.5.



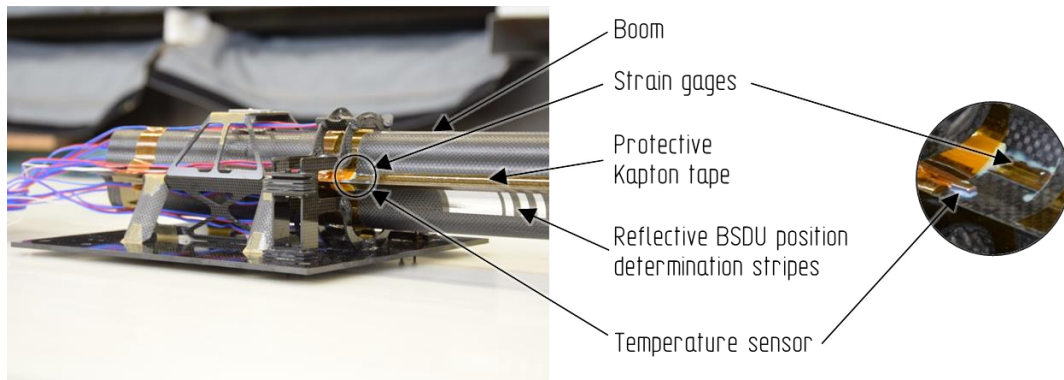
**Figure 5.5.** Gossamer-1 boom cross sectional dimensions and principle

Further features are reflective, incremental indicator stripes, a boom load measurement system, as well as protective Kapton tapes. As shown in Figure 5.6 a) two reflective stripes on each boom serve in combination with an optical sensor in the deployment mechanism subsystem as optical position measuring system for the deployed length. It facilitates increments to determine the exact position of the deployment unit on the deployed boom.

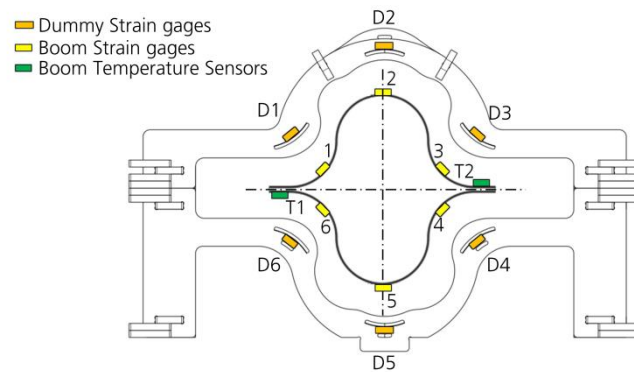
As part of the boom load measurement system, that detects mechanical loads acting on the booms during deployment and operation, six strain gages are accommodated around the circumference, near the root, on each side of the joined booms. This arrangement is shown in Figure 5.6 a) and schematically illustrated in Figure 5.6 b). Besides general load monitoring, this sensor system is also used to detect boom overloading, thus giving essential information to trigger an emergency stop and additional FDIR (Fault Detection, Isolation and Recovery). In order to measure mechanical loads reliably under changing temperatures in orbit, a parallel strain gage system that is mechanically decoupled from the boom is introduced. This almost identical arrangement, termed Temperature Compensation Dummy, facilitates the Active Dummy Method (or Active Strain Gage method), in which strains generated by thermal expansion are cancelled out, thus sensing only the relevant strains due to mechanical deformation of the boom. Realizing this is done by so-called dummy strain gages that are applied onto boom material samples (substrates) fixed in a frame and are free from mechanical boom loads. At the same time, they experience identical temperature conditions as the strain gages directly on the boom do. Electrically the dummy and boom strain gages are connected to adjacent sides of a Wheatstone bridge of the boom loading measurement system. The complete schematic arrangement of the boom loading measurement system is depicted in Figure 5.6 b).

Additionally, two temperature sensors, one on each boom flange of a boom, positioned close to the subsystem center are applied, giving valuable on-orbit information about temperature peaks and changes. For further protection of the boom surface as well as for reduction of friction, four Kapton tape stripes are applied on each boom component along the whole boom length.





a) Sensors and components of the equipped qualification model

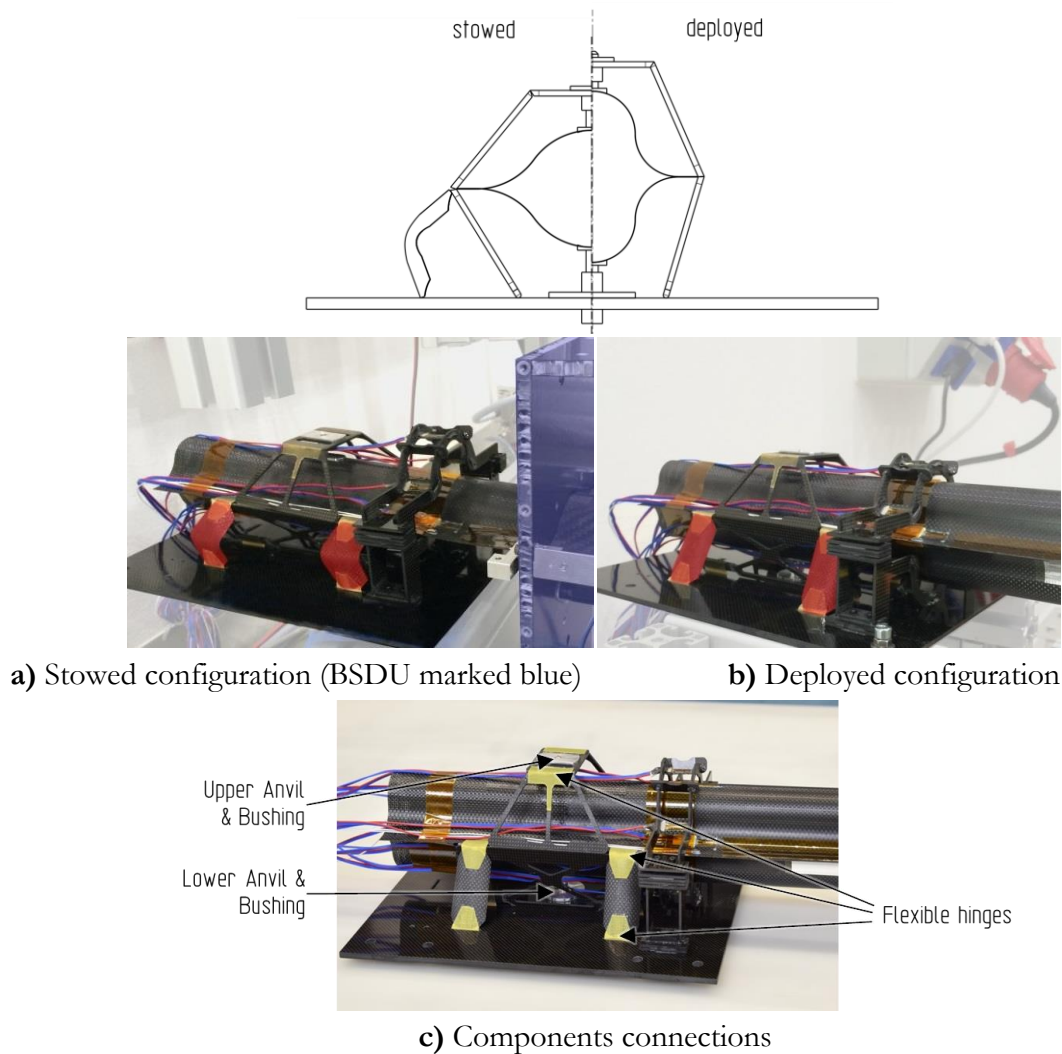


b) Scheme of sensor arrangement

**Figure 5.6.** Sensors and equipment of the boom subsystem

Another major assembly of the boom subsystem is the boom spacecraft interface (BSI). Although it could be viewed as an interface subsystem itself, it is here considered an integral structural part of the boom subsystem since it is predominantly determining the boundary conditions of the boom root and inseparably connected to the boom assembly. Its main purpose is to fix the boom to the spacecraft bus structure, while enabling an adaptation to the changing cross-sectional shape of the boom when transitioning from stowed to deployed configuration. At the same time, it must ensure sufficient stiffness in order to redirect occurring boom loads. These crucial features make stowage in the deployment units possible and consequently prevents the boom from being damaged during deployment or folding. In order to account for the transition from an intermediate cross section (stowed) to the full size (deployed), the BSI performs an articulated movement and is somewhat flexible. This principle of folding is illustrated in the images a) and b) of Figure 5.7, comparing stowed and deployed configurations. In contrast, to the full cross-sectional dimensions, for stowage the cross-sectional height of the boom is reduced while its width increases. An elastic self-actuation is realized with a foldable frame assembly in combination with CFRP tape springs to spring back and lock into the final position as shown in the images a) and b) of Figure 5.7. Further connection points between boom and BSI are two pin-like parts (anvil) that are bonded one on the upper and one on the lower shell of the joined booms. They are freely sliding in bushings, mounted in the upper plate like part and in the lower interface plate of the BSI. This enables a free cross-sectional extension of the boom height, while inhibiting shear movements caused by lateral bending of the boom. Connecting all adjacent parts of the BSI as well as the joined boom to the BSI is realized using custom made, flexible Aramid hinges as shown in Figure 5.7.c).



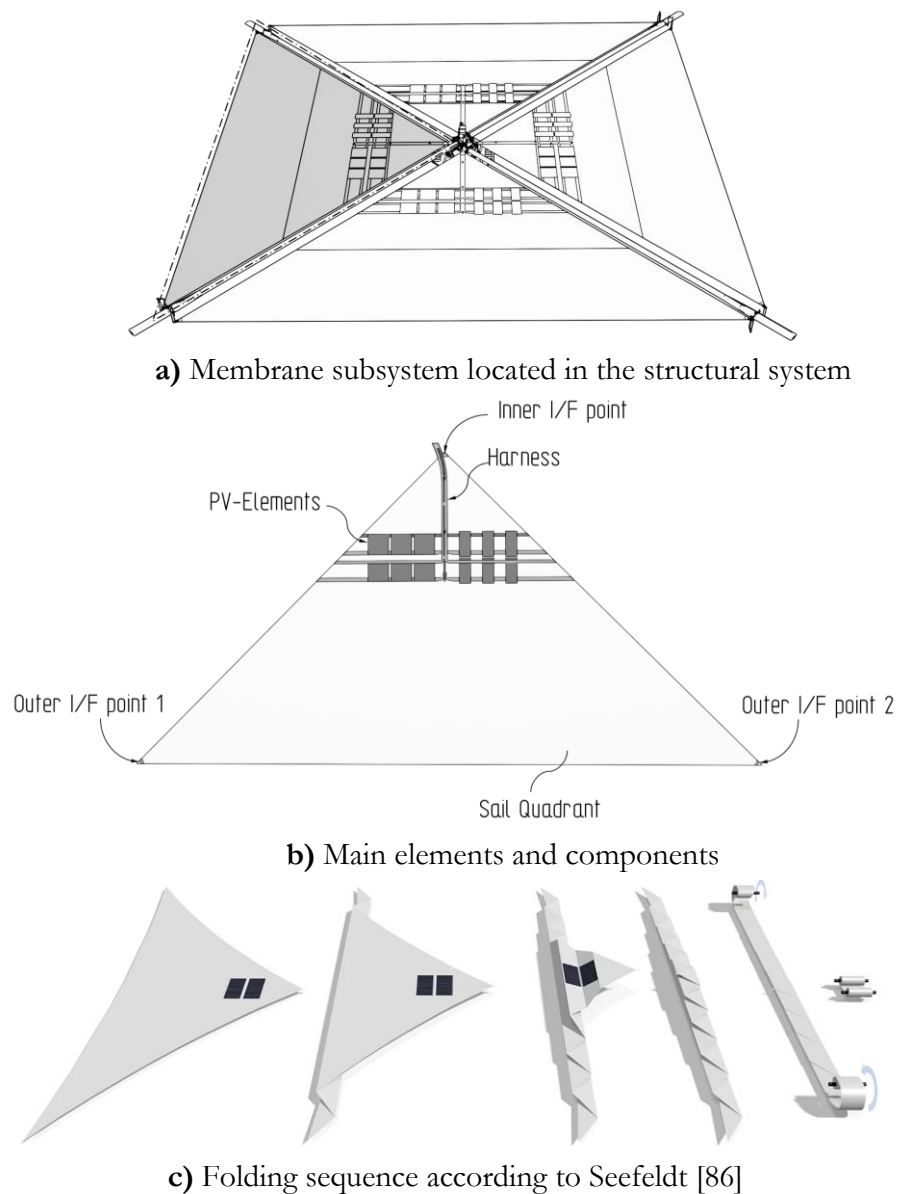


**Figure 5.7.** Boom spacecraft interface (BSI)

#### 5.1.4 Membrane Subsystem

The full Gossamer-1 system comprises four identical membrane subsystems as depicted in Figure 5.8 a), highlighting one of such subsystems. These subsystems, each a triangular sail quadrant, are spanned by the two boom subsystems to a total sail area of about  $27.5 \text{ m}^2$ . However, they are further equipped with several components and features. The main elements and components of a membrane subsystem are: the polyimide sail quadrant, photovoltaic arrays, harnesses for electrically connecting the PV arrays as well as measuring currents, and different attachments for the interfaces at the sail corners. These main components are summarized in Figure 5.8 b). Folding of the membrane subsystem is realized with a combination of frog leg (zig zag) folding followed by coiling the two ends of the resulting elongated package on adjacent spools (of BSDU), as shown in Figure 5.8 c), and has been developed by Seefeldt [86]. This folding methodology is chosen to be best suited regarding packaging efficiency and venting capability, and is key for a controlled deployment of the sails in the configuration of Gossamer-1. In this way solely the minimal required amount of sail area is uncoiled from the sail spools thus keeping the deployed part of the sail taut throughout the whole deployment process, without allowing a large slack.

The information given in the following, describing the membrane subsystem, are reduced to the most important aspects. Further and more detailed information regarding the sail design, materials and their development are described by Seefeldt et al in [82, 85–87].

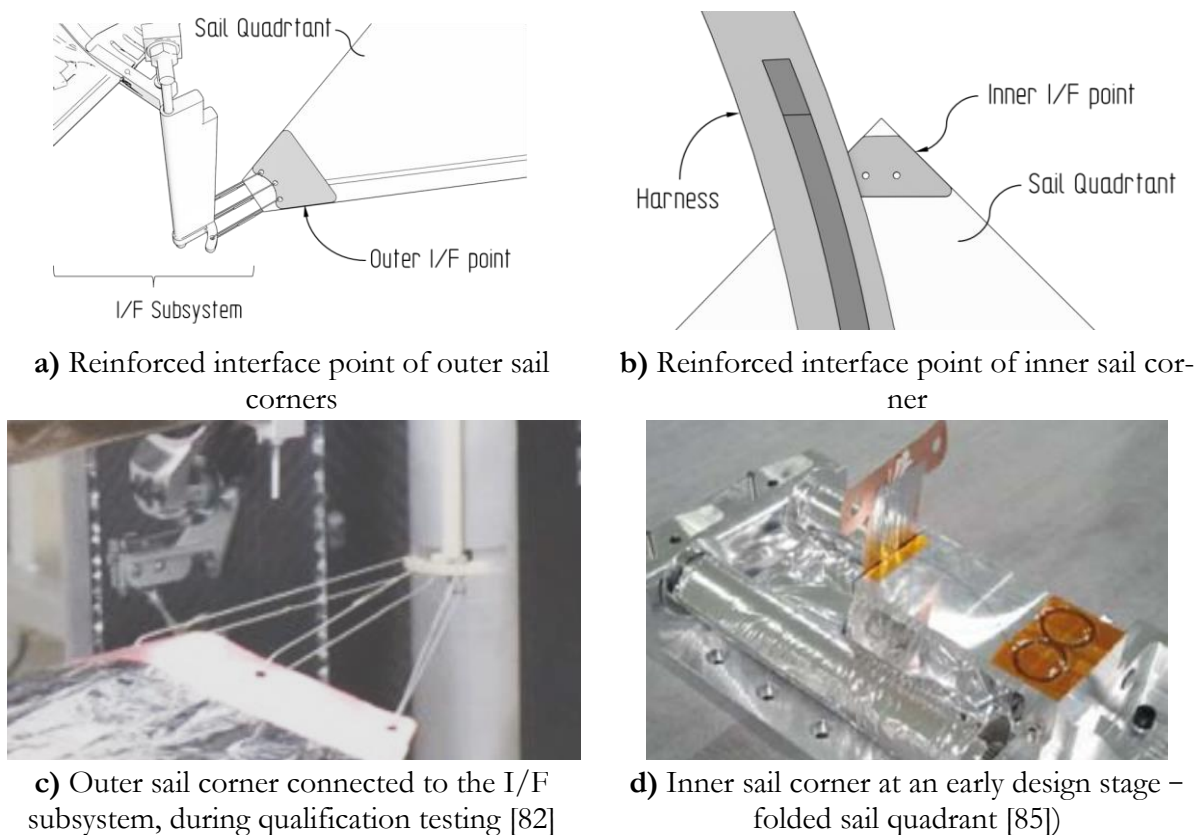


**Figure 5.8.** Membrane Subsystem of Gossamer-1

The mentioned triangular sail quadrants are manufactured of the polyimide film UP ILEX-S® (by UBE Industries Ltd.), featuring a thickness of  $7.5 \mu\text{m}$  and  $100 \text{ nm}$  vacuum deposited aluminum coating on both sides. Each quadrant is composed of four sheet segments that are joined with an adhesive transfer tape, thus featuring some rip stop reinforcement at the seams. Moreover, the sail edges are reinforced by folding them over and bonding them with an adhesive as well. Enabling trapped air to be vented off, in order to prevent the packaged sail from expanding in space and thus being damaged, is realized by using foil patches with venting holes every  $100 \text{ mm}$  along the sail edges.

An assembled sail quadrant, however not yet equipped with additional features like bonded thin film PV modules (CIGS cells) and harnesses, undergoing ground deployment testing for evaluation of its mechanical functionality is described and visualized by Seefeldt in [85]. The pv modules are located at the inner corners of each sail quadrant, while electrically contacted with a flexible PCB (Printed Circuit Board) harness (main harness) that is running along the centerline of the triangular sail quadrant.

The sail quadrants are attached at three points to the overall structural system. While the inner sail corner is attached (bolted) to the structure of the central spacecraft unit (CSCU), the outer sail corners are attached to the interface subsystem, thus connecting the sail and the booms. However, these sail interface points are reinforced with a thicker copper coated polyimide foil, similar to the one of the flexible PCB substrate of the harness, and are featuring holes for the connection with bolts and thin stainless steel ropes, for the inner and the outer sail corners respectively. These reinforced interface points of the sail quadrant are shown in Figure 5.9 a) and b) schematically, while the images c) and d) of Figure 5.9 display the built interface points that have been tested in diverse experiments.

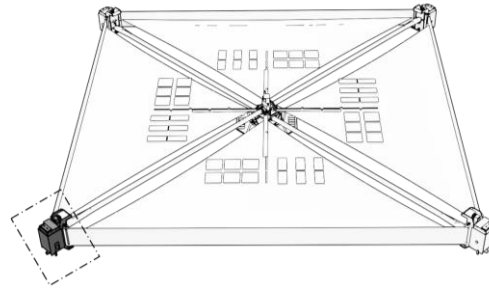


**Figure 5.9.** Features of the membrane subsystem

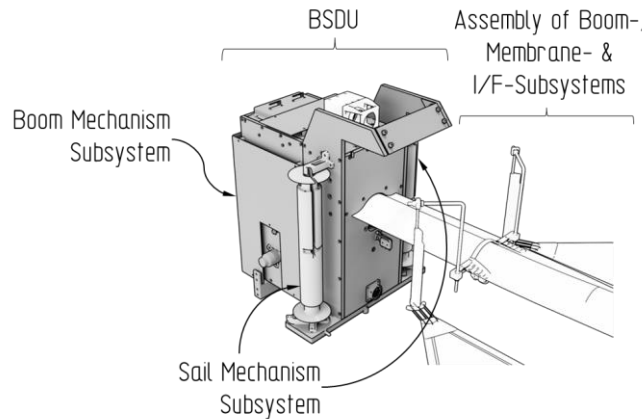
### 5.1.5 Mechanism Subsystem

The before described boom and membrane subsystems are stored in and on four boxlike units as highlighted in Figure 5.10 a), the Boom & Sail Deployment Units (BSDU). They are holding the rolled-up ends of the booms and the coiled up sail packages. Moreover, two slightly different types of BSDUs are used, in order to compensate for the vertical offset of the arranged booms in the center of the spacecraft. Nevertheless, all BSDUs have identical components and are therefore considered identical in this thesis, specifically when regarding robustness assessment. They enable a motorized, simultaneous and controlled deployment of all booms and sails. Additionally, they carry all necessary mechanisms, power supply, antennas as well as cameras, to realize an autonomous deployment in orbit. Such deployment unit comprises the two mechanism subsystems, the boom mechanism subsystem and the sail mechanism subsystem. Both mechanism subsystems, as an assembly (BSDU), are located in the overall Gossamer-1 system as depicted in Figure 5.10 a). Providing a view on the combination of both mechanism subsystems to the overall deployment unit, however, is given Figure 5.10 b). Overall deployment is driven by the BSDUs that are moving away from the CSCU as described in section 5.1.2 and illustrated by Figure 5.3, while booms and sail quadrants are deployed simultaneously. In stowed configuration, all four BSDUs are locked to the central spacecraft unit.

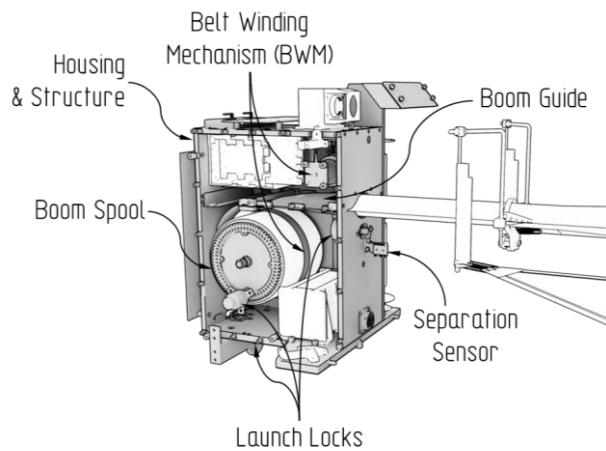
The boom mechanism subsystem, as shown in Figure 5.10 c), consists of several components like the housing and structure, the belt winding mechanism (BWM), the boom spool (hub) including a brake and a boom guide, as well as launch locks. The housing and structure is made from CFRP sandwich panels with aluminum honeycomb core material, providing a high stiffness at a low weight. It connects the two mechanism subsystems to form the boom and sail deployment unit (BSDU). The boom is stored and coiled on the boom spool (sometimes referred to as boom hub), a rotatable CFRP cylinder, with an outer diameter of 100 mm and a width of 110 mm. The diameter is derived from the minimum radius a Gossamer-1 boom can be coiled on safely. The belt winding mechanism (BWM) reels in a stainless steel belt that is coiled along with the boom on the boom spool and therefore uncoils the boom as well. In this way, the boom pushes the BSDU away from the CSCU, thus unfurling the sail quadrants. Actuation is realized using an electric motor, while a counter acting brake system on the boom spool (boom spool brake) ensures a constant tension on the belt, a controlled boom deployment and restrains the boom to a compact package thus preventing blossoming to occur. This makes the boom mechanism subsystem an actively actuating subsystem. The deployment of the 3.8 m functional boom length is realized in this way in about 7.5 min. In order to realize the jettisoning function of a BSDU, the Velcro® strip at the tip of a boom and its counterpart on the belt connects the two components, thus transferring shear loads in this last phase of deployment. Detaching the two Velcro® parts and consequently separating boom and belt is accomplished when the Velcro® strip passes a pulley and is peeled apart. Further components of this subsystem include the boom guides that lead the boom into the intended direction when deploying it out of the BSDU and three launch locks. One launch lock, a pin puller, restrains rotation of the boom spool for launch by a conical pin that locks into according holes of a gear wheel mounted on one sidewall of the boom spool. Once the destined orbit is reached the launch lock and therefore the boom spool is released, giving free rotation for deployment. Another launch lock, the non-explosive Ejection and Release Mechanism (ERM 250®, TiNi AEROSPACE, Inc., USA), separates the boom sail fixation ring (BSFR, see also section 5.1.5) from the BSDU, once it is interlocked into its final position on the boom and a separation sensor indicates this event. This enables the BSDU to continue moving and deploying the rest of the boom length to speed up for jettisoning, while the sail is fixed to the boom. The third launch lock of this subsystem secures the complete BSDU to the spacecraft structure (CSCU) for launch and is realized with a shape memory alloy actuator (Frangibolt®, TiNi AEROSPACE, Inc., USA) on the lower front side of the BSDU. Further information on this subsystem, in specific detailed descriptions of design, development and testing as well as electronic components, are given by Straubel & Zander [93], Straubel et al. [94] and Sprowitz et al. [84].



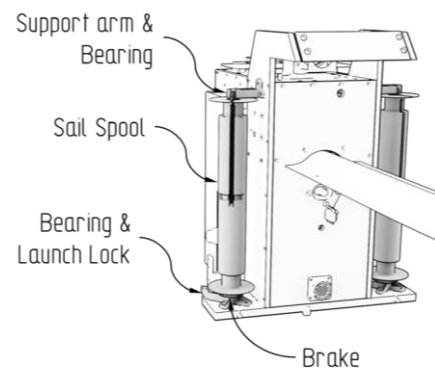
a) Membrane subsystem located in the structural system



b) Mechanism Subsystems (gray) assembled to the BSDU



c) Boom mechanism subsystem



d) Membrane mechanism subsystem

**Figure 5.10.** Mechanism Subsystems and components

The second mechanism subsystem, the membrane mechanism subsystem, as depicted in Figure 5.10 d), is a passive subsystem that stores one half of a sail quadrant while it inhibits the part of the sail that is rolled up from unpurposely unfurling. This also provides a certain sail tension throughout the complete process of deployment. Each deployment unit (BSDU) features two of such subsystems, thus resulting in eight sail mechanism subsystem in the overall Gossamer-1 system. Its main components are: the sail spool, support arms featuring ball-joint bearings, a brake and a launch lock. As described afore each sail quadrant is folded and coiled onto two sail spools. However, each of the slender, cylindrical sail spools, made of sintered aluminum alloy, holds one-half of an adjacent sail quadrants. This means that the two sail mechanism subsystems of a BSDU store the halves of two different sail quadrants. Additionally, the sail spool stores the part of the interface subsystem (insert) that attaches to the sail corner inside. It further features an axial groove and one perpendicular in

order to release the stored interface once the sail quadrant is fully deployed, the full functional boom length is reached and the interface subsystem is locked onto the boom. Until this event, the sail spool rotates around the mentioned interface part in order to uncoil the sail quadrant. Rotation however is enabled by ball-joint like bearings at the bottom and top of each sail spool. In order to prevent an uncontrolled or self-triggered sail deployment a brake mechanism facilitating a leaf spring that engages a gear wheel at the lower shoulder of the sail spool is used. This enables the sail to be kept taut throughout deployment and operation and adds a maximum break torque of about 0.035 Nm, according to Seefeldt [82]. It also allows a complete halt within the deployment process while providing a safe and taught sail stowage. For locking the sail mechanism, subsystem and its rotating parts for launch a form-fitting element on the spacecraft's central structure (CSCU) locks into the same gear wheel that is used by the sail spool brake, thus securing this subsystem. Once in orbit, this launch lock is released and deployment is initiated.

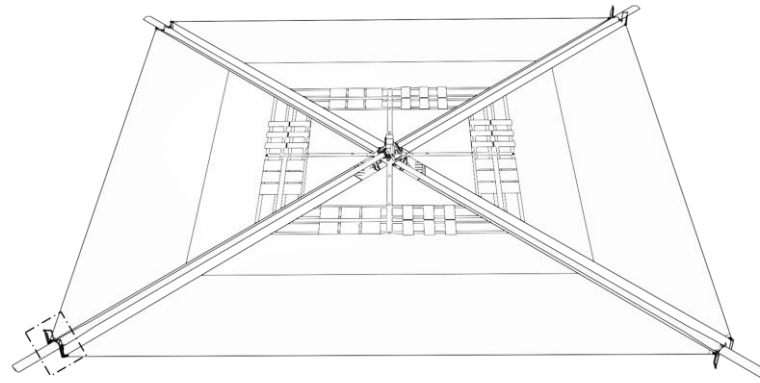
Further details on the sail mechanism subsystem, its components, their development as well as performed testing is described by Seefeldt [82, 85, 86] and Sprowitz et al. [84].

### 5.1.6 Interface (I/F) Subsystem

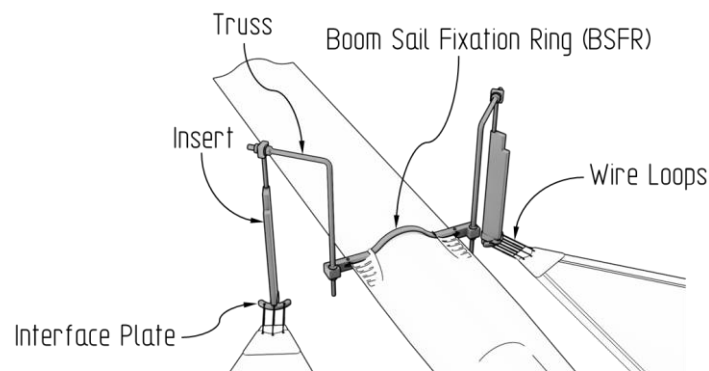
The interface subsystem further referred to as I/F subsystem is here defined as a subsystem that connects two other subsystems. Such a subsystem becomes necessary whenever other subsystems cannot be coupled directly, thus requiring additional functions and interfaces. The overall Gossamer-1 system comprises four identical I/F subsystems, as depicted in Figure 5.11 a) highlighting one of such subsystems. The I/F subsystem connects the boom subsystem to two adjacent membrane subsystems in operational configuration (deployed) and the mechanism subsystems to both the boom and the membrane subsystem, when stowed and during deployment. It comprises of the boom sail fixation ring (BSFR) as mentioned before, a symmetrical truss structure with inserts and interface plates and three redundant steel wire loops on each side. In order to connect the two adjacent sail corners to the boom, the BSFR, an aluminum ring featuring the cross sectional contour of the semi-deployed boom, interlocks with the flexible stop wings that erect on the boom, once the functional deployed boom length is reached (see also section 5.1.3). This in consequence fixes the sail quadrants to the boom. Initiating separation of the BSFR from the deployment unit (BSDU) is done at this point, indicated by the separation sensor. However, during deployment and while deploying (extruding) the boom out of the deployment unit, the BSFR is fixed to the BSDU with the boom running through it. The mechanical connection of the sail corners and the boom sail fixation ring is realized with an arm like truss structure featuring an insert with an interface plate and three steel wire loops attached at each side, as depicted in Figure 5.11 b). These loops run thru holes in the plate of the insert and thru the holes of the reinforced corners of the sail quadrant, thus connecting boom and membrane subsystems. The loops are made of  $\varnothing$  0.45 mm steel wires and are closed by crimping their ends with metal sleeves.

Enabling a special and necessary function, the insert of the truss is stored inside the sail spool during deployment and can rotate along with the unfurling sail quadrant. Furthermore, when the functional boom length is reached and the BSFR is locked onto the boom, the insert is pulled out of the sail spool thru the vertical groove, thus separating it from the sail mechanism subsystem. Illustrating this crucial feature in the images of Figure 5.11 c), the I/F subsystem during deployment (stored insert) and at the event of separation, are displayed from left to right, respectively.

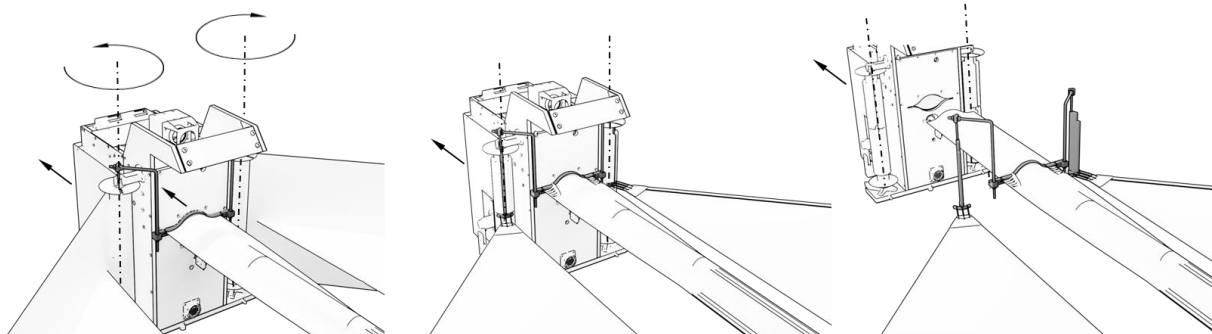
Further details regarding this subsystem and its components can be found in Seefeldt [82, 85, 86] as well as in Straubel & Zander [93].



a) Interface subsystem located in the structural system



b) Main elements and components (gray)



c) Separation sequence of the interface during deployment (from left to right)

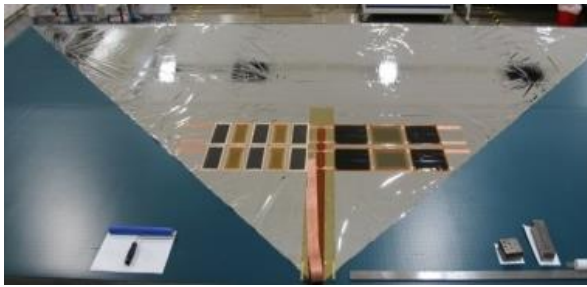
**Figure 5.11.** Interface subsystem of Gossamer-1

### 5.1.7 Realized Gossamer-1 Hardware

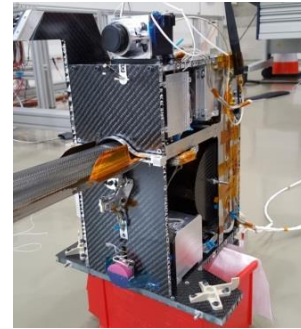
The Gossamer-1 system was realized in an Engineering Qualification Model (EQM), a quarter model of Gossamer-1, and tested in a qualification campaign. This model comprises of the flight representative main components (depicted in Figure 5.12) namely the CSCU test adapter; two Sail quadrants equipped with photovoltaics and dummies, representing the membrane subsystem, one fully equipped BSDU with sensors, actuators, antennas and electronics, representing the mechanism subsystems; the central flight electronics representing the bus system of the spacecraft and one boom subsystem attached to the according interfaces and fully equipped with sensors. In ground deployment tests, this reduced configuration is extended by linear units simulating adjacent BSDUs and the CSCU test adapter, made of aluminum, structurally simulating the CSCU, thus providing a representative system. Individual subsystems and components were realized as engineering and qualification models and in different stages of development. These subsystems and components have been



tested in different test campaigns over the project duration ranging from mechanical characterization of booms, sail manufacturing and folding studies, to characterization and functional testing of individual mechanisms and finally system qualification tests, as described in several publications [84–86, 93, 95]. This included vibration testing, venting tests, thermal vacuum testing, partial deployment and full deployment testing. Further aiming for TRL 5 for the main technologies, testing was performed under representative environmental conditions. It proved to be well designed for all occurring launch, deployment and operational loads as described by Seefeldt et al in [86], thus finishing the Gossamer-1 project with an TRL level of 5 and providing qualified technology for subsequent projects and.



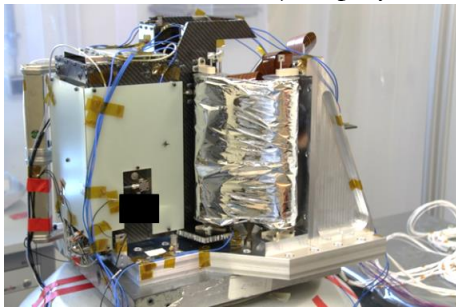
a) Membrane subsystem prepared for integration



b) Mechanism subsystem partially integrated



c) Deployed Boom subsystem in clean room



d) Stowed Overall system before vibration testing



e) Deployed (built) overall system during deployment testing

**Figure 5.12.** Built and tested Gossamer-1 system model (EQM)

## 5.2 Identification of Functions, Robustness Parameters and associated Weighting Factors

This subsection provides a systematic breakdown of the Gossamer-1 structural system as well as its main functions. Furthermore, the robustness parameters that determine partial robustness metrics for each subsystem are derived specifically for Gossamer-1 while following the general methodology



proposed in section 4.4.4. Finally, the associated weighting factors that influence the impact of each robustness parameter, the partial robustness weighting factors, are determined by rating the degree of function fulfillment. This section is sought to investigate **2. Work Hypothesis**, that demands realistic and measureable parameters that define robustness.

### 5.2.1 System Structure and Functions Analysis

The structure and functions analysis are a vital part of the overall analysis steps. This can be considered as steps of a Failure, Mechanisms, Effects and Criticality Analysis (FMECA). In the following, the structural analysis performed with the aim to determine all elements of the Gossamer-1 system and visualized their connections and hierarchy. Facilitating a structural breakdown of the Gossamer-1 system visualizes its elements and gives an overview, as shown in Figure 5.13. Here the system is analyzed on different levels of complexity as granularity increases from system, subsystem, assembly to component level. While each element is arranged and connected according to its relation to the next higher element in hierarchy, some subsystems feature no assembly level, like the Membrane Mechanism and the I/F Subsystem, as they are built up from components directly, due to their moderate complexity. For subsystems that do feature assemblies, their components are clustered at the lowest level of complexity for better visibility, along with the components that are directly and additionally making up a subsystem. On every level, each element is given an element code and element name as an identifier for the subsequent analysis. Coding is done following the hierarchy throughout the different levels. Starting at the subsystem level with capital letters on each level an individual number or letter is added resulting in a unique identifier for each element. As defined before in section 5.1 the subsystems are: The Membrane Subsystem, the Boom Mechanism Subsystem, the Membrane Mechanism Subsystem, the Boom Subsystem and the Interface Subsystem, coded A, B, C, D and E, respectively. The CSCU is not included in the study since it is rather considered a regular structure than a characteristic element of a GosSSS. However, for completion it is listed in Figure 5.13 as well. As stated, before the focus in this thesis is put on the Boom Subsystem and its inferior elements as marked out in Figure 5.15, and is scrutinized more closely further analysis specifically in chapters 6 and 7.

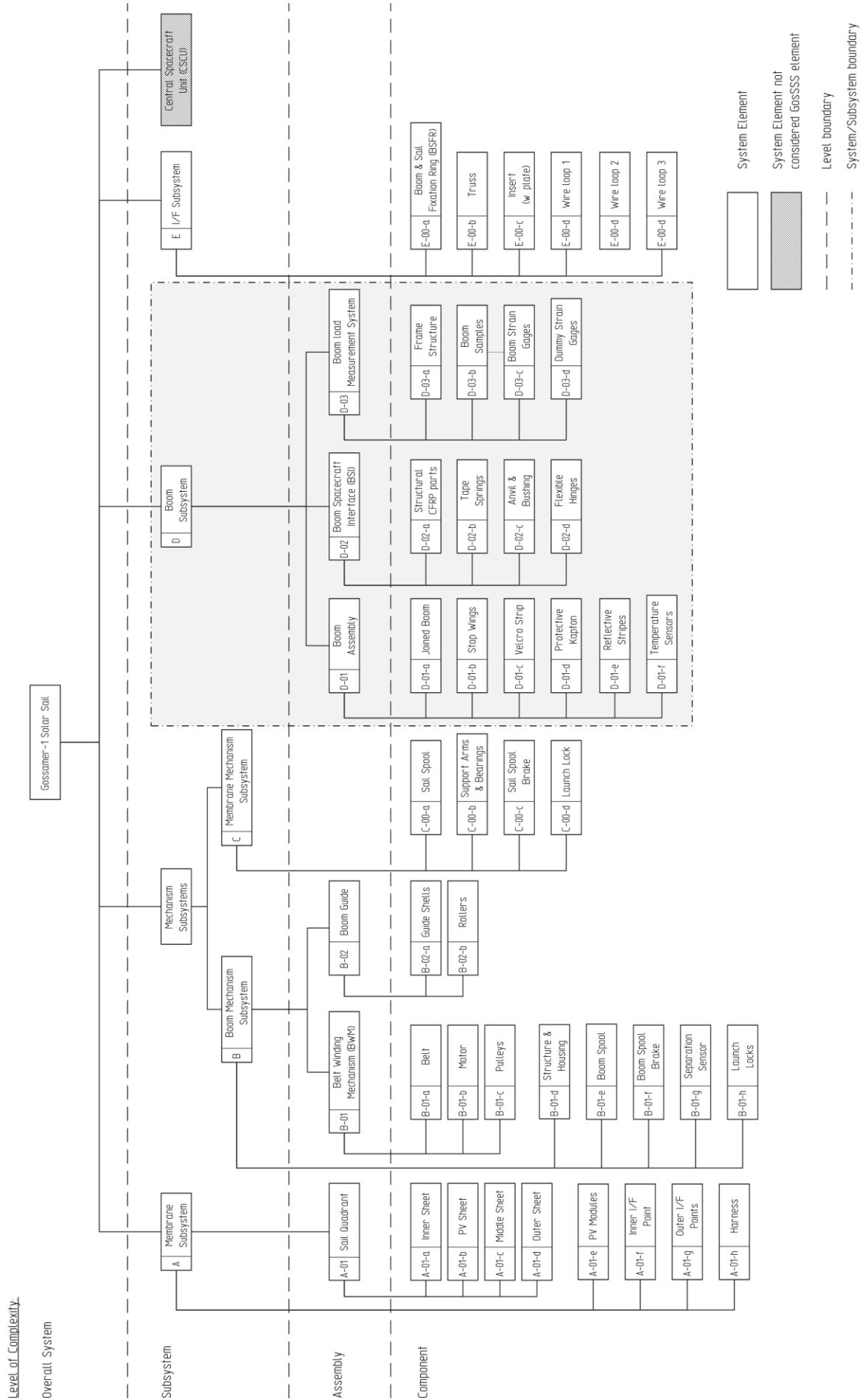


Figure 5.13. System structure breakdown and coding of Gos-1

Followed by the structural breakdown of the system the most crucial functions of each element from component up to subsystem level, over all subsystems are analyzed. This is done in order to subsequently identify the relevant robustness parameters for each main function of a subsystem in section 5.2.2. While all main functions of each Gossamer-1 subsystem are given and described in the following, a complete list describing all functions on every level of complexity down to component level is given in Table C. 1 of appendix Appendix C. Note that functions which cannot directly be associated with the structural subsystems e.g. those of electronics or information subsystems are not considered here. In the following paragraphs the system and subsystem main functions, their identifier as well as a description is given. The coding principle mentioned before is continued here as well.

### *System Main Function:*

*Function 1: Provide propulsion/thrust to spacecraft*

The primary function of the Gossamer-1 solar sail system is to convert mainly solar radiation pressure, by reflection and by a small fraction through absorption and emission, into propulsive thrust for a spacecraft.

Analogously, in ADEO, the system is used to decelerate a spacecraft by drag augmentation of the residual atmosphere.

### *Boom Subsystem Main Functions:*

*Function 1: Transfer loads and provide stiffness*

(D-F1) The Boom Subsystem as a whole serves the function of transferring loads, originated in the solar radiation pressure exerted on the membranes (sails) and in deployment forces when unfurling the membranes, into the spacecraft.

To do so the loads must be transferred from the sails through and by several components of the boom subsystem, while certain stiffness must be provided.

*Function 2: Deploy Membranes*

(D-F2) Secondly, the Boom Subsystem serves the function of deploying the membranes as it is deployed itself as a major structural element of the system. This function is coupled to the first function, as load transfer is necessary in to deploy the membranes.

*Function 3: Span membranes to intended dimensions and orient them into intended direction*

(D-F3) The third function is spanning the membranes to the intended dimensions and area needed for solar sailing. It further serves to orient the membrane area into the intended direction as this defines the impulse direction exerted by solar radiation pressure.

***Membrane Subsystem Main Functions:******Function 1: Reflect solar radiation***

(A-F1) The primary function is to physically reflect the incident photons of the solar radiation pressure, while also absorbing and emitting a small fraction. This involves several components of the Membrane Subsystem, as the sail quadrant must be sufficient in materials, size and shape.

***Function 2: Transfer solar radiation loads into mechanical loads/propulsion***

(A-F2) This function consists of transferring the impulse by solar radiation pressure and its reflection into mechanical loads of the structural system for spacecraft propulsion. It is realized mechanically by the sail quadrant and interface points at the sail corners as they transfer impulse loads thru its membrane structure into the adjacent I/F and Boom Subsystem.

***Function 3: Generate electrical power***

(A-F3) Thirdly, the function of generating electrical power by the pv modules, arranged on the sail quadrant, and the connected harnesses needs to be fulfilled. This represents a secondary function as it is realized mainly to power auxiliary electrical systems and for research of facilitating thin film photovoltaics.

***I/F Subsystem Main Functions:******Function 1: Transfer loads between adjacent subsystems and connect***

(E-F1) Serving the purpose of transferring loads between the Membrane Subsystem and the Boom Subsystem, this function enables the necessary load path into the spacecraft, in order to generate thrust. This function can simply be viewed as providing connection between Membrane and Boom subsystems during operation, after separation.

***Function 2: Provide accurate membrane dimensions, tension and orientation***

(D-F2) The second function consists of providing to the accurate dimensions, membrane tension as well as orientation of the deployed Membrane Subsystem, ruled by the geometric properties of the I/F Subsystem. This function is realized by all components of the I/F Subsystem, along with the Boom Subsystem.

***Boom Mechanism Subsystem Main Functions:****Function 1: Store booms*

(B-F1) This essential function represents the storage of the thin shell CFRP booms that are flattened and reeled up on the boom spool for this purpose. The co-reeled belt of the BWM and one part of the Velcro strip on the boom spool further ensure a tightly and securely stored boom with high packaging density. This function further ensures secure stowage by restraining the boom and inhibiting blossoming or unwanted self-deployment.

*Function 2: Deploy booms in a controlled manner*

(B-F2) Deploying the booms in a controlled manner, with a controlled speed and deployed length, and in a predefined extrusion direction is realized with this function using the BWM, sensors as well as the boom guide. This function consequently deploys the sail quadrants, while it further drives the BSDU away from the CSCU (spacecraft) and thus enables the jettisoning action.

*Function 3: Hold and Support Mechanism Subsystems and I/F Subsystem*

(B-F3) The third function consist of providing the structure, and therefore stiffness and load transfer, to hold and support the Membrane Mechanism Subsystem and the I/F Subsystem, while latter only is the case during deployment, prior to separation. This function also provides the fixation of all subsystems to the spacecraft by the launch locks during launch.

***Membrane Mechanism Subsystem Main Functions:****Function 1: Store Membrane Subsystem (sail)*

(C-F1) Storing the zig-zag folded sails (membrane subsystem) securely reeled up on the sail spool is represented by this function. As explained before one membrane subsystem is stored on two sail spools of two BSDU, each holding one half. A defined storage is considered the essential part of this function. The sail spool in combination with launch locks and the spool brake ensure a tightly and securely stored Membrane Subsystem aiming for a high packaging density. This function further provides secure stowage by inhibiting blossoming and unwanted unfurling of the Membrane Subsystem during launch and deployment.

*Function 2: Dispense/deploy sail quadrants in a controlled manner*

(C-F2) The second function consists of controlling the sail (membrane subsystem) deployment. More precisely controlled dispensing of the sail under a defined tension and speed is realized by this function, as the sail spool brake generates a braking torque counteracting to the forces exerted by the deploying booms.

## 5.2.2 Derived Robustness Parameters and Determination of Partial Robustness Weighting Factors

As proposed in the previous chapter, it can be said that system robustness of a GosSSS is generally determined from a combination of subsystem robustness metrics that comprise several partial robustness metrics. A partial robustness metric as proposed in section 4.4.4 is determined by robustness parameters specific for each subsystem or component mostly as a ratio of undisturbed versus influenced values and the according partial robustness weighting factors. The robustness parameters are derived from two aspects to be considered, the requirements that have been set for robustness itself in section 4.1, and the main functions each subsystem has to fulfill. The according weighting

factors are determined by preferring the robustness parameters for each function. This is exemplary described for the subsystems of Gossamer-1 in the following.

### *Boom Subsystem Robustness Parameters*

Recapitulating section 4.4.4, the general boom subsystem robustness  $Ro_{Booms}$  is determined from three partial robustness metrics: stiffness-based robustness  $Ro_{\kappa}$ , load-based robustness  $Ro_L$  and displacement-based robustness  $Ro_u$ , given in the equations (4.16), (4.17) and (4.19) respectively. This is adopted to the boom subsystem of Gossamer-1. As proposed, the robustness parameters that determine the three partial robustness metrics are stiffness (bending stiffness), the characteristic buckling load and the boom tip displacement. Stiffness can either be the flexural rigidity  $EI$  or the bending stiffness  $c$  that are typical measures in the characterization of boom structures. The characteristic buckling load itself is exchangeable and can be selected to be the collapse  $CL$  or global buckling load  $GB$ , as described before. However, for simplification at this point the characteristic buckling load is generally denoted by  $L$  and stiffness by  $\kappa$ . Both robustness parameters comply with the requirements that have been set in section 4.1. for robustness itself. They are expressive and applicable for GosSSS as well as measureable metrics, especially when determining robustness on existing hardware. Here stiffness and characteristic buckling load can be measured in practical tests as scrutinized in chapter 7, in boom bending tests on the boom subsystem and the boom component. Another important aspect is the compliance of the derived robustness parameters with the main functions of a subsystem. For the Gossamer-1 Boom Subsystem the stiffness  $\kappa$  and the characteristic buckling load  $L$  indicate the fulfillment of the main functions D-F1 and D-F2. For D-F1 that serves the function of transferring loads and providing certain stiffness, stiffness  $\kappa$  and the characteristic buckling load  $L$  are well suited to be used as direct measures and involve all assemblies. The boom assembly with all its components as well as the BSI serve as the main contributing assemblies, while the Boom Load Measurement System detects the loads on orbit. Both robustness parameters  $\kappa$  and  $L$  of the Gossamer-1 Boom Subsystem are further suited to represent main function D-F2, although in an indirect way, as stiffness and a certain load needs to be provided in order to reach necessary membrane deployment loads and the associated restraining and control loads. They can also be associated with function D-F3 as boom bending stiffness in consequence affects the membrane dimensions and orientation and certain load levels are necessary to span the sail quadrants and keep them taught and under tension.

The robustness parameter boom tip displacement, here generally denoted by  $u$ , is presumed a sum of different displacement components, having their cause in different influences, as described in section 4.4.4. It considers the boom tip displacement caused by mechanical loads, thermal loads and by dimensional and shape imperfections mainly of the boom assembly and in combination with the BSI and partially the boom guide. Such imperfections are imprinted or plastic deformations originated in creep as well as manufacturing induced as practically determined as influence factors in chapter 6. As a robustness parameter the boom tip displacement complies with the requirements set in section 4.1., expressiveness, objectivity, calculability and applicability. Moreover,  $u$  is measureable as done on the Gossamer-1 Boom Subsystem in boom bending tests and the boom component in chapter 7. In terms of measuring functional fulfillment it complies well with main function D-F3. Here  $u$  is facilitated as a measure that determines the intended sail dimensions and orientation of the spanned membrane, as the sail corners are connected via components of the I/F Subsystem to the boom tip. It is further indirectly contributing to the fulfillment of D-F1 as it partially determines the bending stiffness of the boom subsystem.

### *Membrane Subsystem Robustness Parameters*

Robustness of the membrane subsystem  $Ro_{Membranes}$ , as generally proposed in section 4.4.4, consists of three partial robustness metrics:  $Ro_{RS}$ ,  $Ro_{SRMS}$  and  $Ro_{LM}$ , that are reflectivity-based, shape-accuracy-based and a load-based, respectively. This approach is adopted to the Membrane Subsystem of Gossamer-1, as the subsystem and partial robustness metrics satisfy the requirements, set in

section 4.1, for the developed methodology. Thus, the robustness parameters for the Gossamer-1 membrane subsystem comprise the robustness parameters reflectivity, shape accuracy and membrane load.

Reflectivity, here denoted by  $R_S$ , is considered a good indicator for the thrust capabilities of a solar sail system, as Gossamer-1 obtains propulsion mainly from the reflection of radiation. It is mainly determined by the material surface property of the sheets of the sail quadrant e.g. the aluminum coating in combination with the polyimide substrate foil. This robustness parameter is considered a direct measure of the subsystem main function A-F1 and thus fully resembles it in the according partial robustness metric.

The robustness parameter shape accuracy, denoted by  $S_{RMS}$ , is based on the assumption that a defined shape and dimensions provide a defined functionality, here reflection of radiation. Shape accuracy represents e.g. flatness and dimensions the sail quadrant and its different sheets it is assembled of and affects the fulfillment of the Membrane Subsystem main functions. It contributes mainly to the fulfillment of A-F1 since the global shape e.g. flatness needs to feature a certain accuracy in order to provide the demanded reflection for a large area. For the main function A-F2 the shape accuracy is rather a result of a successful load transfer than the reason. Hence it could be seen as an indirect measure and indicator for this function. However, when considering the dimensions of the sail quadrant, it certainly affects the load distribution. In a minor way this robustness parameter affects also function A-F3, as the pv modules need to be oriented towards the light source, which is ruled by the shape accuracy and orientation of the membrane subsystem. The fulfillment of all main functions of the Gossamer-1 Membrane Subsystem is affected by deviations and variations from the defined shape or dimensions on a macroscopic scale. Such deviations might show in creases, local distortion or large deformations, as Gossamer-1 might experience sail billowing in the order of several centimeters according to Seefeldt [82].

The third robustness parameter of this subsystem is the load  $L_M$  of the membrane subsystem. It resembles the tension load when the sail quadrant is spanned and is further transferred via the sail quadrant and interface corners into the I/F Subsystem and from there into the boom subsystem. A load below the necessary value will result in unacceptable performance and functionality loss, while exceeding a certain threshold may provoke damage and functionality loss. Hence, this robustness parameter fully represents and affects the fulfillment of A-F2. Additionally, and in order to incorporate a robustness parameter specifically for function A-F3, the voltage generated by the pv modules  $V_M$  is proposed for future work on this topic. Since this thesis concentrates solely on structural elements that are specific to GosSSS, this parameter is not further considered.

### *I/F Subsystem Robustness Parameters*

The generally proposed robustness for an I/F subsystem  $RO_{I/FS}$  is determined from two partial robustness metrics: a length-change-based partial robustness metric and a tensile-load-based partial robustness,  $RO_{\Delta l}$  and  $RO_{L_t}$ , respectively. This is adopted to the I/F Subsystem of the Gossamer-1 system.

The length of the interface subsystem, denoted by  $l$ , is derived as robustness parameter. In the according robustness metric this is represented by the deviation of the measured or predicted interface length value  $l_i$  after being influenced by noise, from the required interface length value  $l_0$  (see equation (4.28)). This robustness parameter largely represents function E-F2 and is considered a direct measure of its fulfillment, as the accuracy of the spanned sail quadrant dimensions directly depend on the length of the interface it is connected to. While  $\Delta l$  is determined for the complete I/F Subsystem, the wire loops are considered to contribute the most to length variations.

The second robustness parameter is the tensile I/F load, denoted by  $L_t$ . It resembles the load that has to be transferred by the I/F Subsystem between the Membrane and Boom Subsystems. It is transferred from a tensile load in the wire loops that are connected to the sail corner interfaces to a combined load vector at the boom sail fixation ring, resulting in transversal and axial load components in the boom assembly. The truss and insert are the components that transfer the load type.

The tensile I/F load as robustness parameter fully represents function E-F1 and contribute directly to its fulfillment. It further represents indirectly function E-F2, as it contributes partially to its fulfillment by introducing the I/F tensile load in order to span the membrane subsystem to its dimensions, shape and orientation.

### *Boom Mechanism Subsystem Robustness Parameters*

The general proposal that a mechanism subsystem robustness consists of two partial robustness metrics, based on the robustness parameters: torque, necessary for deploying, and the packaging diameter of the according element (boom or membrane), is principally adopted to the Boom Mechanism Subsystem of Gossamer-1.

However, since torque is not directly applied for boom deployment in Gossamer-1 and instead the co-coiled belt of the Belt Winding Mechanism (BWM) is pulled out to deploy the stowed booms generating a spool-off force, torque is replaced by the robustness parameter  $F_{SB}$ , the spool-off force, thus introducing the spool-off-force based partial robustness  $RO_{F_{SB}}$ , as given in equation (4.32). A large advantage is the practical measurement of the spool-off force when testing this mechanism subsystem or its assemblies. In regard to function B-F1, the spool-off force is only an indirect measure of its fulfillment since it must overcome the restraining force that keeps the boom tightly packaged. Nevertheless, a spool-off force of too low or too high amplitude can indicate a faulty storage or packaging. On the other hand it fully represents function B-F2 and is a direct measure of its fulfillment since variation in load values show the controllability of the deployment while the amplitude measures the restraining and friction forces to be overcome for deployment.

The second robustness parameter for this subsystem is the boom packaging diameter  $d_B$ . This is the outer diameter of the stored boom, rolled up on the boom spool, resembling the packaging density/packaging efficiency of the stored boom. Presuming the stored boom itself can be rolled up onto the boom spool without exceeding material strain and strength limits, the Boom Mechanism Subsystem largely rules the packaging diameter (packaging efficiency) by its ability to maintain restraintment throughout different phases. It further reflects the ability of the Boom Mechanism Subsystem, in specific the BWM assembly, the boom spool and boom spool brake, in combination with the boom guide assembly, to maintain storage quality past integration and handling, during and after launch, as well as during deployment. The boom packaging diameter fully represents function B-F1 and contributes largely to its fulfillment, while it is also a direct measure of the function. In order to provide a robustness parameter that represents main function B-F3, a dynamic load e.g. a load value the structure must sustain during launch or vibration testing is here proposed to be introduced in a future work. Since the thesis focuses solely on structural elements that are specific to GosSSS, this parameter is not further investigated.

### *Membrane Mechanism Subsystem Robustness Parameters*

Similar to the above described robustness parameters for the Boom Mechanisms Subsystem, the Membrane Mechanisms Subsystem for Gossamer-1 also adopts the general proposal that a mechanism subsystem robustness consists of two partial robustness metrics facilitating one robustness parameter each.

Again, torque is replaced by a spool-off force robustness parameter, here denoted by  $F_{SM}$ , since the Membrane Subsystem of Gossamer-1 is spooled off the sail spool by pulling rather than by direct torque application. With this circumstance a spool-off-force based partial robustness  $RO_{F_{SM}}$  is introduced, as given with the general equation (4.32). The practical measurement of the spool-off force when testing the Membrane Mechanism Subsystem or its assemblies is again a considerable advantage. Hence, this robustness parameter determines inhomogeneity, detrimental dynamics and exceeding loads limits of the sail deployment. In regard to function C-F1,  $F_{SM}$  is only an indirect measure of its fulfillment since it must overcome the restraining force that keeps the sail package tightly packed, and therefore might indicate proper storage. However, fully representing function C-F2, the membrane spool-off force is considered a direct measure of its fulfillment. While variations in load values indicate the controllability of the deployment, the amplitude indicates the restraintment,



provided by the sail spool brake, and friction forces, generated by the bearings and internally by the folds of the sail, to be overcome for deployment.

The second robustness parameter for the Gossamer-1 membrane mechanism subsystem is the membrane packaging diameter  $d_M$ , similar to that of the Boom Mechanism Subsystem. It represents the outer diameter of the stored sail that is folded and rolled up on the sail spool, resembling the packaging density/packaging efficiency of the stored sail. Presuming the fold lines of the sail assembly are optimally arranged to reach a minimal packaging diameter, the Membrane Mechanism Subsystem largely rules the packaging diameter (packaging efficiency) by its ability to maintain restraint. It further reflects the ability of the Membrane Mechanism Subsystem to maintain storage quality past integration and handling, during and after launch, as well as during deployment. This specifically involves the interaction of the sail spool, sail brake, launch locks and bearings, with the moving BSDU. The membrane packaging diameter as robustness parameter fully represents main function C-F1 and contributes largely to its functional fulfillment. It can also be seen as a direct measure of the function. A direct relation to main function C-F2 is not apparent.

### Determination of Partial Robustness Weighting Factors for Boom Subsystem

Following the developed assessment methodology, described in chapter 4, for each robustness parameter a weighting factor is determined. The procedure and the results are explained in the following section. In order to determine values for the according weighting factors, a scoring method is facilitated to generate these values in an assessment. Assessed are the robustness parameters in terms of their contribution to the fulfillment of main functions of the according subsystem.

Rating is performed by asking the following questions for each robustness parameter under investigation:

1. *How well does the robustness parameter represent the considered function?*
2. *How much is the robustness parameter contributing to the fulfillment of the considered function?*
3. *To what extent is the robustness parameter a measure of function fulfillment?*

Further each robustness parameter is rated with an ordinal scale ranging from zero to ten. Here, zero resembles a parameter that is “not representing” or that provides “no contribution” to the fulfillment of the according main function, while a rated value of ten for a robustness parameter is deemed “fully representative” or “fully contributing” to the fulfillment of the according main function. All rating values for a robustness parameter are cumulated to a partial sum, which is then normalized based on the sum over all robustness parameters for a subsystem. This results in a weighting factor for each robustness parameter. Applying the scoring method at this point, as discussed in detail among other methods in Appendix B, requires that the overall sum of all weighting factors of a set of evaluated parameters, here all robustness parameters for a subsystem, must be equal to one. The value determination of the partial robustness weighting factors can be followed on the example of the Gossamer-1 Boom Subsystem, in the score matrix of Figure 5.14. For all other subsystems of Gossamer-1 the according score matrices as well as the reasoning for the rating can be found in Appendix C. Moreover, a comprehensive list of determined partial robustness weighting factors is given below in

Table 5.1, while the following sections describe the reasoning for each rating.

*Rating Boom Subsystem robustness parameters*

- Stiffness*
  - considered a direct measure of D-F1 and is therefore rated very high for this main function
  - medium rated in regard to the function fulfillment of D-F2, since it is necessary to realize deployment and contributes to it
  - for D-F3 fulfillment rated medium high, although a high stiffness contributes to fulfilling dimensional requirements; it is not a direct measure.
  
- Characteristic load*
  - is contributing in a high degree to main function D-F1 as it resembles the maximum possible load that can be transferred before the structure collapses; considered a direct measure of the load transfer
  - medium rated to contribute to the fulfillment of main function D-F2 since the achievable buckling load during deployment is required for a successful membrane deployment; is not a direct measure in this regard
  - medium rated for contribution to main function D-F3, as loads are necessary to span the membrane subsystems and keep them taught and under tension
  
- Boom Tip Displacement*
  - is indirectly contributing to the fulfillment of D-F1, since it is embodied in the stiffness
  - not considered to represent the fulfillment of main function D-F2
  - rated high in regard to representing the fulfillment of function D-F3, due to the fact that the boom-tip displacement largely determines the dimensions, pointing and orientation of the spanned sail quadrant

No.(i)	Robustness Parameter	Rating Main Function			Partial Sum	$w_i$
		D-F1	D-F2	D-F3		
$\kappa$	Stiffness	10	6	8	24	0.421
$L$	Characteristic Load	10	6	6	22	0.386
$u$	Boom Tip Displacement	2	0	9	11	0.193
Sum					57	1.0

**Figure 5.14.** Partial robustness weighting factors determined for the Boom Subsystem

**Table 5.1.** Overview determined partial robustness weighting factors

Subsystem	Partial Robustness Weighting Factor $w_i$	Value
Boom Subsystem	$w_{\kappa}$	0.421
	$w_L$	0.386
	$w_u$	0.193
Membrane Subsystem	$w_{RS}$	0.256
	$w_{SRMS}$	0.308
	$w_{LM}$	0.436
I/F Subsystem	$w_{\Delta l}$	0.417
	$w_{L_t}$	0.583
Boom Mechanism Subsystem	$w_{FSB}$	0.550
	$w_{dB}$	0.450
Membrane mechanism Subsystem	$w_{FSM}$	0.550
	$w_{dM}$	0.450

### 5.3 Mission Phases & Relevance

The Gossamer-1 solar sail demonstrator mission is aiming to prove controllable, autonomous and reliable deployment of Gossamer structural space system as described before in section 5.1. It further aims to demonstrate power generation with thin film photovoltaics as well as to obtain in-situ scientific data of the structural behavior and attitude characteristics. This subsection further pursues to account for conditionality of robustness, as presumed by the **4. Work Hypothesis**, relating functionality and consequently robustness to the different mission phases, requirements and conditions.

The mission key characteristics that provide the frame of action to realize these aims are the following:

Operational orbit:	700 km; circular sun-synchronous
Orbits per day:	8-7
Inclination:	98.1°
Launch vehicle:	Cyclone-4
Mission duration:	6-12 weeks

The course of the mission is divided into nine phases, as illustrated in Figure 5.15 and explained in the following.

#### *Phase 1: Launch and Separation*

The Gossamer-1 spacecraft is launched and inserted into the target orbit, followed by the separation from the launcher, followed by activation (power on).

#### *Phase 2: Initial Boot*

Still stowed, the central spacecraft unit (CSCU) with its board computers and S-Band communication systems are booted. The first contact to ground station is acquired and test images of the on board cameras (on the CSCU) are downlinked. About two ground contacts are established during this phase.

#### *Phase 3: BSDU power on and boot*

Still in stowed configuration, the deployment units (BSDU) are activated and booted. Then on board, wireless communication is activated and a blue tooth connection between central spacecraft unit and deployment units, in order to command deployment, is established. Network charging of deployment unit is initialized and sensor data and test images of the cameras on the deployment units are transmitted to the ground station, thus realizing three to four ground contacts during this phase. At the end of this phase, the spacecraft is declared ready for deployment.

#### *Phase 4: Deployment*

Starting this phase via time tagged command, in full sunlight and between ground contacts, initiates the deployment process and unlocks the deployment units (Boom Mechanism Subsystem) and sail spool mechanisms (Membrane Mechanism Subsystem). Both booms (Boom Subsystem) and sails (Membrane Subsystem) are deployed simultaneously, while wireless communication between deployment units and central S/C unit remain established. During the whole phase, images are taken by all nine cameras and sensor data of the deployment position are acquired. As soon, as the deployment, units have reached their separation position, the I/F Subsystem and consequently the sail corners are fixed via BSDFR to the booms. The phase duration is planned to 10 to 15 min with no ground contact throughout the whole phase.

*Phase 5: I/F Separation*

In this phase the S/C operations continue autonomously, separating the boom-sail-fixation rings (BSFR) of the I/F Subsystem from the Boom Mechanism Subsystem, and releasing the insert of the I/F Subsystem from the sail spools of the Membrane Mechanism Subsystem by further moving (deploying) the BSDUs away from the spacecraft for a few centimeters. At this stage, the BSDUs are still attached to the boom and have some remaining boom length stored. This phase has a duration of a few minutes with no ground contact.

*Phase 6: Data Downlink*

The data acquired during the previous deployment phases are downlinked to the ground station. This is estimated to take about ten ground contacts (downlinks) over the complete phase 6. Over the phase duration of a few days Gossamer-1 goes into sleep mode (power saving mode) in between ground contacts, in order to save energy.

*Phase 7: Intermediate Monitoring Phase*

For the Gossamer-1 spacecraft, this phase largely takes place in the energy saving sleep mode. Its systems autonomously wake up (time tagged) for science measurements of e.g. the photovoltaics experiment, boom load measurements, and measurements of accelerations and magnetic fields, at times of high sun light incidence. The phase duration ranges from a few days to several weeks depending on scientific measurements, with only limited ground contact.

*Phase 8: BSDU jettisoning & Solar Sailing*

All deployment units (BSDU) are jettisoned by pushing themselves off the boom tips. This is recorded by the central S/C unit taking images of the departing deployment units, while the deployment units take images as well, record data and transfer them to the central S/C unit. This jettisoning action converges Gossamer-1 into the fully deployed solar sail configuration. However, due to the character of in-orbit technology demonstration, a controlled solar sailing is not executed, due to the lack of attitude control at this TRL. Phase 8 ends whenever wireless contact between deployment units and CSCU cannot be established. During the several hours lasting phase ground, contacts and downlinks are established sporadic, depending on the necessity of data transfer.

*Phase 9: Final monitoring & Decommissioning*

In this final phase monitoring and acquiring science data e.g. of photovoltaics experiment, boom loading is performed, as Gossamer-1 is operating in solar sailing mode. These tasks are recurrently interrupted by times in sleep mode and autonomous wake ups of the system, while offering limited ground contact and downlinks. The mission ends with a passive (not actively controlled) decommissioning and de-orbiting of Gossamer-1. Nevertheless, system activities and monitoring is kept up as long as possible.

Structurally relevant for the here proposed methodology, specific for GosSSS and further considered in this thesis are phases 4, 5 and 8. In these phases, marked grey in Figure 5.15, all subsystem main functions of the structural system are performed that are crucial for mission success. While Phase 4 and Phase 5 deal with all functions related to deployment and stowage, Phase 8 deals with a further boom deployment, jettisoning of BSDUs as well as the solar sailing, resembles the operating phase. For other applications, this may be the phase of antenna operation or drag augmentation and spacecraft deceleration. Phase 1 is not specific to GosSSS, as every spacecraft, independently of its specialty, must go through. However, launch vibrations in combination with the light-weight built and stowage principle, may cause the rolled up booms and sails to blossom (unintentionally unravel) and thus pose a special threats to GosSSS.

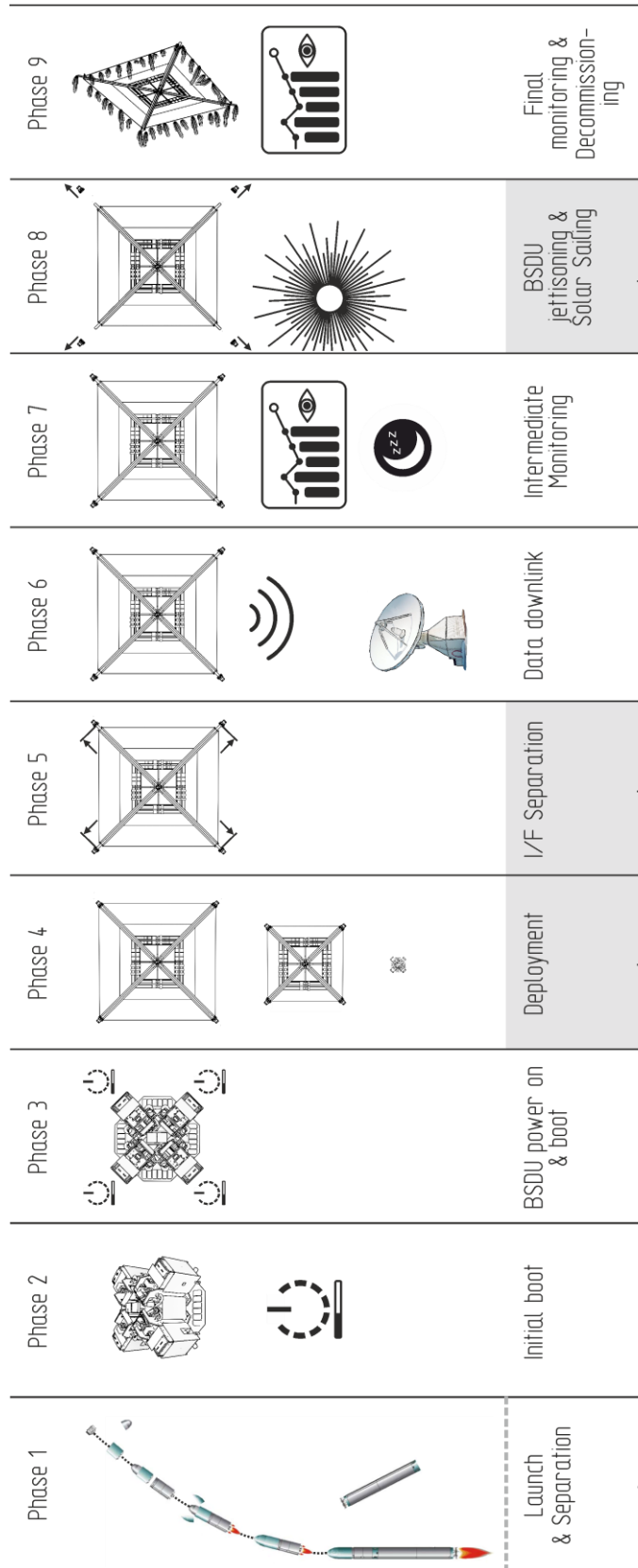
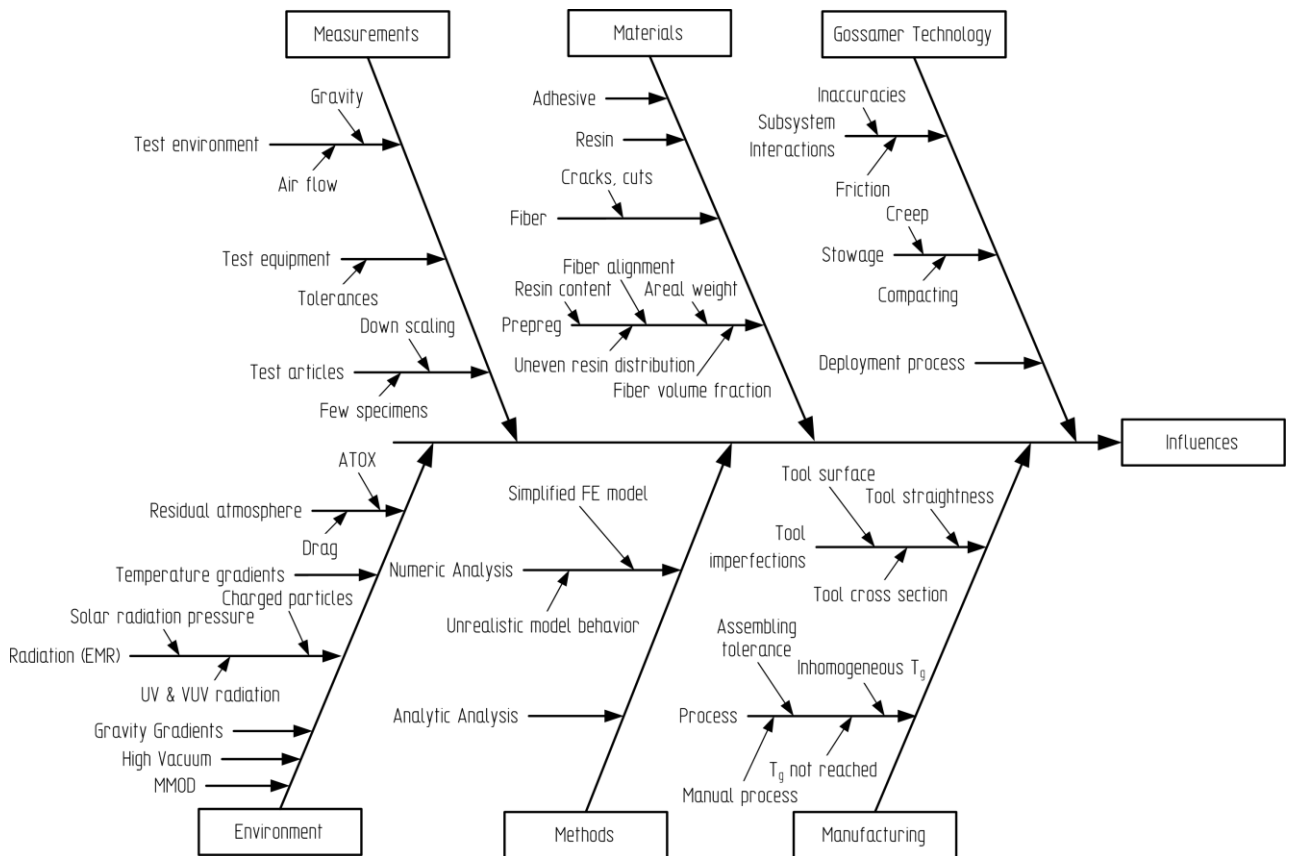


Figure 5.15. Mission phases of Gossamer-1

### 5.4 Identification of Influence Factors and Detrimental Effects

Influences, their causes and consequences generally occurring for GosSSS are identified and examined for the Gossamer-1 system in this section, as proposed in the **3. Work Hypothesis**. Here the effects of the influences on subsystems and their functions is discussed. Moreover, the application of derived influence factors is shown exemplary, while influences are categorized by type.

This section scrutinized possible causes for influences, influences itself that affect functions and robustness of subsystems and Gossamer Structural Space Systems in general, while pointing out specific circumstances for the addressed mission envelop (Gossamer-1, ADEO and Gossamer-2) and described hardware (Gossamer-1). Facilitating a cause-effect diagram (also known as Ishikawa diagram), all causes are categorized in main categories as depicted in Figure 5.16. Here the main cause categories are identified as: Environment, Measurements, Methods, Materials, Manufacturing and Gossamer Technology. These categories contain specific causes leading to influences affecting the subsystems and their functions. This, the specific influences, causes and consequences are discussed in detail in the following, while Figure 5.19 provides a summary of the identified influences, generally for the viewed type of GosSSS. Furthermore, in Figure 5.20 the resulting consequences on subsystem and system level in the Gossamer-1 case is summarized.



**Figure 5.16.** Categorized causes for occurring influences on GosSSS

#### 5.4.1 Environment related Influences

##### *Residual Atmosphere caused influences*

Atomic oxygen (ATOX, AO) is the dominant gaseous environmental effect in LEO, produced by the photo dissociation of molecular oxygen by energetic photons in the Vacuum Ultraviolet (VUV) range (1000 ~ 2000 Å). This form of oxygen mainly reacts with organic materials including thin films, paints, and composites, causing erosion and resulting in material degradation, while metallic materials are less affected. A prominent example of erosion caused by ATOX is the solar array wings

of the ISS, as described before in section 3.1.3. Atomic oxygen fluxes for LEO are given in the left diagram of Figure 5.17, by Rooij [96], resulting in an flux at an orbit of 700 km altitude of about  $9 \times 10^{12} \text{ cm}^{-2} \text{ s}^{-1}$ . Requirement levels regarding atomic oxygen flux have been studied for membrane materials by Seefeldt [82], giving some calculated values for Gossamer-1. Altering optical and thermal properties as a result of changes in surface morphology have been observed. Inert to atomic oxygen reactions are silicone coatings applied e.g. on the sail quadrants. Nevertheless, on cuts and edges of the membrane without coating, due to cutting sail segments after metallization, or at impact craters, atomic oxygen can erode material, which is critical especially for longer mission durations. The unprotected components of the Boom Subsystem, I/F Subsystem and the Mechanism Subsystems on Gossamer-1 are affected as well and alter mechanical properties. However, due to the higher wall thickness of most of these structural elements the possible damage could be relatively low, although over a long period of time atomic oxygen can be critical and must be considered. For Gossamer-1, atomic oxygen could be considered uncritical due its short mission duration. Nevertheless, as Gossamer-1 is regarded to demonstrate the capabilities of the later solar sailing technology, atomic oxygen should be regarded as well. For the ADEO mission, atomic oxygen is considered critical as well due to its long mission duration in LEO. For solar sailing in interplanetary space, like Gossamer-3, atomic oxygen is considered uncritical when operating in interstellar space due to the absence of oxygen at  $DL_1$ . However, during GTO (geosynchronous transfer orbit) phase the influences due to atomic oxygen might have an impact and need to be considered. Summarizing the influences due to atomic oxygen, material degradation and erosion can cause *optical properties changes*, *material (thermal) properties changes* as well as *mechanical properties changes* for thin structures.

Aerodynamic drag occurs due to the spacecraft's traveling velocity and atmospheric density, dependent on the altitude. While the resulting drag effect is useful for de-orbiting systems like the described ADEO, it is critical especially for large GosSSS due to a resulting decrease of altitude or unwanted dynamic effects as Sickinger simulated on a solar sail in [35]. The resulting atmospheric density can be as high as  $8 \times 10^{-12} \text{ kg/m}^3$  for an altitude of 700 km, at solar maximum according to Rooij [96]. For Gossamer-1, the residual atmosphere is considered uncritical due to its small size and short mission duration. However, the atmospheric drag could produce influences like *structural deformations* to some extent, due to additional loads. For Gossamer-3 in the  $DL_1$ -mission, the residual atmosphere needs to be considered only during Earth escape at GTO perigee, where the orbit altitude and escape velocity might be affected. Further *changes of loads* associated with this cause are inertial bending forces acting on the deployed booms exerted by rotation of the spacecraft. This has its origin in a passive attitude control and the so-called windmill effect in which aerodynamic drag in LEO, and in a minor fashion radiation pressure, spin up the spacecraft.

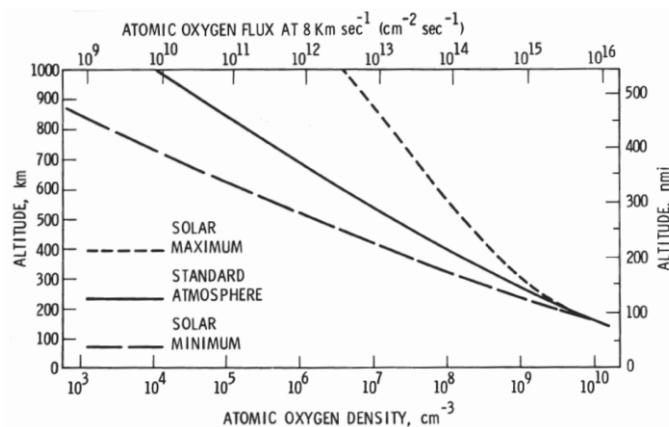


Figure 5.17. Atomic oxygen flux in Low Earth Orbits according to Rooij [96]

### *Radiation caused influences*

Components of radiation causing detrimental effects are electromagnetic radiation (EMR) and charged particles originated in the solar wind, solar flares, Earth's radiation belts and cosmic rays. Electromagnetic radiation, as defined in ECSS-Q-ST-70-06C [97], that is relevant for materials in space is in the spectrum of ultra violet light (UV) and specifically in combination with vacuum (VUV).

Generally, all organic materials are prone to degradation e.g. embrittlement by VUV. Polymers used in LEO, here especially for the sheets of the sail quadrant are susceptible to VUV radiation of high intensity as discussed by Seefeldt [82]. Nevertheless, structural parts can suffer from degradation as well. Exposure to intense VUV can therefore lead to influences like *changed mechanical properties* as well as to *changed optical properties* like reflectivity of exposed parts. In VUV range, here especially important for the DL<sub>1</sub>-mission, radiation energy is sufficient to break chemical bonds in the exposed materials, resulting in possible decomposition. Although appropriate shielding facilitating metal or ceramics coating or the use of multi-layer insulation (MLI) can generally protect an exposed surface to a certain degree, for such thin and delicate structural elements like the sail quadrant or a boom a direct protection needs to be applied. Still, not all exposed areas can be protected and rather should provide some robustness.

Charged particle fluxes (protons and electrons) emitted by the sun, specifically low energy protons can cause material degradation as addressed in ECSS-Q-ST-70-06C [97]. Due to the absorbed dose through the depth of the material, mainly surface degradation is prevalent. This makes especially ultra-thin structures like membranes susceptible to damage. Such polymeric films, as used for the Membrane Subsystem of Gossamer-1, are prone to material degradation in the form of blister generation on its surface due to absorbed and trapped protons underneath its protective metal coating as described by Sznajder [98]. This negatively *changes (decreases) optical properties* like the reflectivity of the sail or may even cause material erosion and thus have a structural influence like *mechanical properties changes*. Polymers as used in the resin of CFRP parts as the booms, structures like the central spacecraft unit, sail material and adhesives are as well degrading at their surfaces when unprotected. However due to the relatively large structural thickness this is expected to be negligible. The solar radiation pressure used as design load and being the fundamental requirement for realizing a solar sail, accompanied by the much smaller pressure exerted upon the solar wind (flux of charged particles), may also vary and therefore cause influences like *changes in loads* during sailing operation.

Another aspect specifically for the Membrane Subsystem and generally thin polymeric films is the buildup of electrostatic potential leading to an effect of clinging between folded membranes. This problem particularly occurs when a metal coating and a bypass for discharging between two surfaces like the sail front and back side is missing as discussed by Jenkins [3] and experienced within deployment testing of uncoated breadboard models, as reported by Hillebrandt et al. [99]. The caused influences are *increases of deployment loads* that can lead to damages of the membrane like tearing, to deployment failures due to underpowered actuators or to boom buckling. Further investigations of electro static influences and quantified values for the such requirements for Gossamer-1 are discussed by Seefeldt [82].

While degradation by charged particles and EMR depend on exposure time and exposure intensity and therefor the distance to the source (here sun), short term missions like Gossamer-1 with a mission duration of several weeks are less critical and shielding/protection of the materials might not be critical to mission success. Nevertheless, since the technology is also aimed to be applicable for long term missions like ADEO and Gossamer-3, lasting over years or decades, the adverse influences need to be accounted for in design.

### *High Vacuum caused influences*

The high vacuum is known to cause outgassing of materials, resulting in contamination of instruments or building an artificial spacecraft atmosphere that is negative for measurements. While outgassing is usually prevented by standardized procedures before launch, an accidental inflation of



entrapped air within packaged Membrane Subsystem folds might occur in vacuum. This could lead to a volume increase of the packaged membrane that in consequence influences or prevents a controlled deployment by blocking the Membrane Mechanism Subsystem, damages the membrane itself thus *changing mechanical properties*, or *increases necessary deployment loads* by preventing folds to be released due to billowing. Furthermore, high vacuum, when seen as absence of matter, increases the influences of potentially harmful causes like UV radiation and atomic oxygen.

### *Temperature gradients caused influences*

Regarding the thermal environment of space, all components of an any spacecraft need to withstand high temperature gradients and thermal cycling. The impacting electromagnetic radiation is mostly converted into thermal energy, from direct and indirect solar radiations, radiation from earth or other celestial bodies. Extreme temperature gradients according to Binet [100], that can change due to eclipses or changing spacecraft orientation, between 393.15 K for a sun facing side and 2.7 K on the outer space facing side can occur. Thermal effects on the material include cold cracking, change in stiffness or flexibility, optical effects, aging and degradation, while thermal expansion and contraction are of main concern.

While all materials for Gossamer-1 have to be thermally stable, Seefeldt [82] determines hot and cold cases that define the occurring temperature on the membrane surface depending on the coating, and therefore set design requirements for the temperature resistance of the used material combination for the Membrane Subsystem. A low temperature resistance of the used material could result in *changes of mechanical properties*.

For components with large dimensions, specifically thermal effects due to linear expansion (depending on the CTE) causing curvature or length changes can be critical. While thermal expansion of membranes may *change geometric dimensions*, resulting in changed membrane tension and deficiencies in flatness or the profile of the sail surface thus reducing reflectivity of the sail, thermally induced *changes in geometric dimensions* of the booms may result in curvature or torsion, thus introducing more *changes in dimensions* to the Membrane Subsystem.

However, for the Membrane Subsystem the necessity of high tensioning for better reflectivity and hence a better photon thrust is not proved satisfactorily as Barnes addresses in [101] as the Sunjammer space weather warning solar sail relies in billowing sails with slack (booms feature metal coating to prevent thermal deformation). Nevertheless, the *change (decrease) of optical properties* (reflectivity) by thermal deformation is an influence to be addressed for the robustness of a GosSSS.

Geometric changes in terms of thermally induced deformations on CFRP booms is investigated by Sickinger [35] in simulations as he determines the possible boom tip deflections of a 30 m long boom under high thermal gradients, resulting in about 105 mm tip deflection. Illustrating the impact of such influences the Hubble Space Telescope experienced adverse deformations on its flexible solar arrays as reported by Gerlach [22], and described in section 3.1.3, making a replacement mission necessary. Further deformations on booms caused by thermal expansion were observed and predicted by Stohlman [102, 103]. Here the used rigid metallic tape spring booms, metallic triangular rollable and collapsible (TRAC) booms, of the Near-Earth Asteroid Scout (NEA Scout), a NASA deep space CubeSat deployable solar sail, experienced substantial thermal warping as much as 0.2 to 0.5 m of tip displacement in a 4 m boom, measured in sunspot chamber experiments. Due to the harmful influence on both structural performance and surface shape, accuracy a redesign of the sail craft was deemed necessary as the center of pressure very far displaced from the spacecraft center of mass, producing a torque on the system that would eventually become uncorrectable.

Furthermore, Stohlman et al. [102, 103] identified thermo-dynamic behavior as the boom developed torsional oscillations, that are suspected to be thermal flutter. Another well-known example are the detrimental dynamic effects of the STEM booms of the flexible solar array wings of Hubble (see in details in section 3.1.3.), that have been analyzed by Blandino [104]. The influence associated with these dynamic causes are identified as *changes in dynamic-mechanical behavior*, although they are considered to have a larger influence on instruments rather than on the main function of a GosSSS itself, with the exception of a deployable antennae or reflectors.

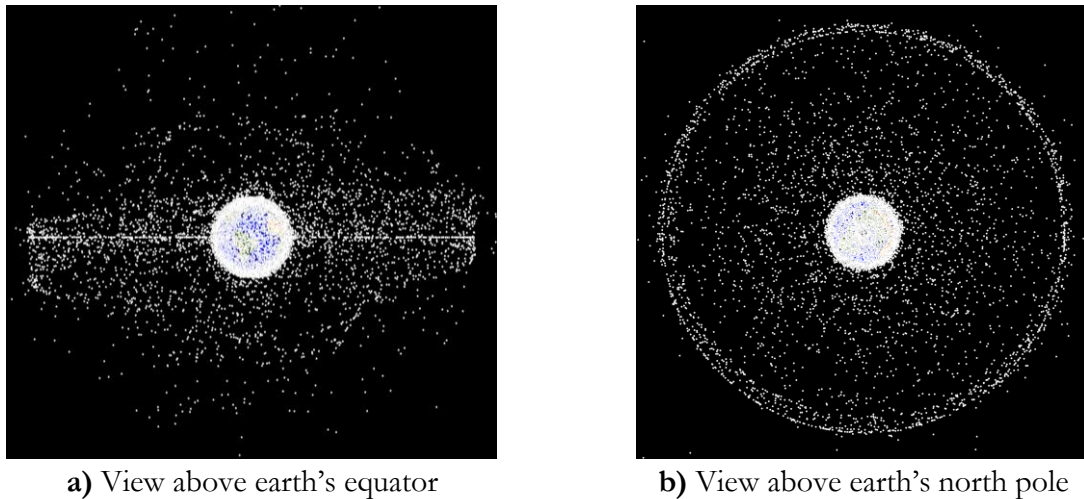
Additionally, very low temperatures may impose some influences increased deployment forces due to material stiffening in the stowed state. This may specifically concern the folded Membrane Sub-system.

For a relatively small demonstrator like Gossamer-1, facilitating CFRP booms with a low CTE, the influences associated with thermal causes is of minor impact. However, for large size structures as planned for Gossamer-3, with growing boom sizes and limited heat conduction, small *geometric changes* will eventually add up to large deformations of the booms and membranes, and have more severe impact. For high accuracy GosSSS such as the SAR-antennae, with high membrane tension, high assumed specular reflectivity the deformations are more critical than for low accuracy GosSSS like a drag sail like ADEO with low membrane tension and lower assumed diffuse reflectivity.

### *Micrometeoroids and orbital debris (MMOD) caused influences*

Micrometeoroids and orbital debris (MMOD) are solid particles of natural and artificial (space flights) origin in Earth orbit and in interplanetary space. They might cause minor to severe damages to GosSSS. The chances of a spacecraft to be hit by natural objects are rather small, except from cyclically recurring meteoroid showers like the Perseids and Leonids, due to the higher intensities by a factor of 100 compared to the annual average [105]. However, the chance of a spacecraft being hit by an artificial object is much higher. According to ESA's Space Debris Office the number of debris objects estimated by statistical models to be in orbit (from LEO to GEO) range from 34,000 objects >10 cm, 900,000 objects from greater than 1 cm to 10 cm, to 128 million objects from greater than 1 mm to 1 cm. [106]. Although such objects are regularly tracked by the US Space Surveillance Network and maintained in their catalogue, covering objects larger than about 5 to 10 cm in LEO and 30 cm to 1 m at geostationary altitudes, even very small particles in the submillimeter range can cause severe damage when hitting a spacecraft at speeds in excess of 11 km/s. An illustration of debris population in the orbits around Earth is given in Figure 5.18. Because at extremely high velocities, spacecraft can travel, collisions with even small pieces of matter can have disastrous consequences. The application of commonly used multiple layer shielding mechanisms (Whipple shield), which are based on the fragmentation of impacting objects and conversion of kinetic into thermal energy are not applicable to thin structures such as GosSSS. Expected damages to film materials range from minute surface degradations, penetration of the coating without significant damage through the thickness, to complete puncturing and cratering of the film and coatings leading to crack opening and crack propagation [3]. After all crack propagation on only on film samples ideally stressed has been investigated. For large membranes with realistic non-ideal stresses, practical tests are lacking. Of special interests is the load carrying structural parts such as booms and interfaces. The effects on partial or total destruction of single or several components are part of the research within this thesis. Some examples of damages experienced on GosSSS are given in section 3.1.3.

For the Gossamer-1 mission and the ADEO micro meteoroids and orbital debris are of special interest due to their low Earth orbits. Furthermore, for longer mission durations damages will accumulate and are more critical, as it is the case for ADEO with its mission duration of more than 20 years, the influence of *changed mechanical properties* resulting in reduced load carrying capability needs to be accounted for. For Gossamer-3, MMOD is seen similarly critical, due its transfer maneuver from GTO perigee and its large area, although it will be operating in interstellar space. Summarizing the major influences are local *changes in mechanical properties and behavior*, resulting in reduced load carrying capability (reduced collapse loads or reduced membrane rupture loads), and *changes in optical properties*.



**Figure 5.18.** Illustration of tracked debris objects in LEO and GEO (image source: NASA ODPO 2019 [107])

### *Gravity gradients caused influences*

The cause gravity gradients are an effect that occurs and is noticeable on spacecraft in the proximity of a celestial body like Earth or moon. It is purposely used for passive stabilization of a spacecraft in a fixed orientation facilitating especially very long booms or tethers as gravity differs at one end of the spacecraft compared to the other, thus generating a moment upon. It is made use of the spacecraft's mass distribution and the gravitational field as Earth's gravity decreases with the inverse square. In order to expand a spacecraft's mass distribution, the long axis perpendicular to the orbit is increased using very long booms or tethers, commonly equipped with a tip mass. While the lower (attitude wise) part of body mass of the orbiting structure experiences higher gravity attraction than the upper one, the spacecraft or satellite will tend to align its axis to the minimum moment of inertia along the vertical axis, thus keeping the spacecraft aligned in the desired orientation. Nevertheless, for very large GosSSS this effect may also be experienced unintentionally causing adverse influences on the spacecraft and its components.

As reported by Staugaitis [108] a boom bending moment due to the gravity gradient effect becomes significant for very long booms, as in the case of the 229 m booms on the RAE satellite. As the experiences a combination of the gravitational and centrifugal gradients, the magnitude of the bending moment changes continuously because of orbit eccentricity and the variations in boom orientation. The derived influence can be summarized as *increased loads* and *geometric changes* mainly on the boom subsystem. However, the GosSSS and mission envelop considered in this thesis with Gossamer-1, ADEO or Gossamer-2 do not show such large dimension and a noticeable gravity gradient effect is unlikely.

## 5.4.2 Measurements related Influences

### *Test environment, Test equipment & Test articles caused influences*

The presence of gravity constraints the realistic testing and influences measurements. Structural ground testing poses the necessity to apply gravity compensation devices to simulate weightlessness, which in response influences the structure by itself and therefore the test results, as done with helium filled balloons as described by Leipold et al. in [109]. Horizontal mechanical boom tests may generate smaller bearable buckling loads, while vertical test configurations might produce increased loads due to the acting gravity. Furthermore, large enough facilities to resemble space environment are rare and expensive, while facilities for real size Gossamer structures e.g. a 65 m x 65 m solar sail, do not exist. This imposes risks due to lacking knowledge of the structural behavior of a very large ultra-

light structure in a realistic environment and size. Moreover, thin membranes are prone to air flow and gravity since folded sail packages may fall out or roll off their compartment or sail spool instead of being dispensed in a controlled manner due to the acting gravity, while air flow may influence force measurements during deployment due to the small loads necessary. The fore the associated influences can be considered inaccuracies in terms of *variability of deployment loads* and *variability of bearable loads (buckling loads)*.

Similar influence may occur due to inaccuracies in the test equipment itself or due to the small number of specimens or small size as large ultra-light structures are usually tested as subscale models, reduced specimen size or in a simplified manner.

### 5.4.3 Methods related Influences

Computer models are necessary to simulate large structures like GosSSS in order to predict structural behavior, acceleration, impact probability or similar parameters of interest. These numeric models are commonly based on verifications with real test data, that many times cannot be acquired for full size ultra-light and large structures like booms, sails or complete systems. To solve this problem, small scale tests are used as verification basis and computer models are scaled up to represent the real size spacecraft or component, presuming the correctness of the model. Furthermore, due to simplifications in FE models that represent the investigated subsystem or component, model behavior and boundary conditions might not fully resemble reality. Such an example of influence is considered by Sickinger et al. [5,106,107] in terms of geometric changes like the geometrical amplitude of imperfections applied to the used FE model in a buckling analysis. These causes can lead to *variability in predicted loads*, displacements, stresses, strains or other mechanical output.

The same is true for used analytical models as they simplify and restrict applied cases.

### 5.4.4 Materials related Influences

Variability and imperfections in properties of the used materials like adhesives, films, resins and fibers can cause influences like changes in mechanical behavior of the regarding component or subsystem. Furthermore, flaws in raw material like fiber cracks and cuts, or in semi-finished products like prepregs, especially causes like variability in areal weight, resin content, fiber volume fraction or fiber misalignment and uneven resin distribution, may lead to *changes in mechanical properties* like stiffness or in reduced load carrying capability (reduced collapse loads). Used membrane materials might exhibit *changes in mechanical properties* in the form of thickness gradients leading to a reduced load carrying capability (reduced rip/rupture loads). Further material properties change like the varying CFRP layout of the boom shell as applied by Sickinger et al. [5,106,107] in terms of design parameter variations can be considered a relevant influence. Thus, imperfections of material and semi-finished products for example flaws of the CFRP prepreg material used for booms or membrane materials can lead to overall performance loss that need to be resembled in a robustness metric.

### 5.4.5 Manufacturing related Influences

Causes for manufacturing related influences can be found in the manufacturing tool and the manufacturing process. The boom manufacturing tool may exhibit geometric imperfections in the form of variations in surface quality, straightness, gapping tool joints and cross-sectional deviations leading to influences like *changes in boom dimensions* and changes in mechanical properties with the result of a reduced load carrying capability. These influences may express in the boom as straightness deviations like an imprinted curvature (radius of a boom  $< \infty$ ), flaws in the shell surface (kinking) or deviations in cross sectional dimensions. Moreover, sail quadrants might exhibit variability in dimensions or interface components deviations in length dimensions. These influences may in consequence impact the subsystem and overall system functions.

Imperfections due to the manufacturing processes caused by deviating process parameters like inhomogeneous temperature or pressure fields, or low temperatures and pressure values (caused by

insufficient insulation and leakage) may lead to inhomogeneous glass transition temperatures over the boom length thus evoking *changes in mechanical and material properties* of the boom.

Due to a manual manufacturing process itself, imperfection e.g. during the assembling of the sail quadrant of different film sheets or the joining of boom components may cause geometric imperfections, and in consequence to *changes in geometry and dimensions*.

In literature manufacturing caused geometric changes are considered as varying design parameters by Sickinger et al. [5,106,107] in terms of a varying shell thickness and cross-sectional dimensions of the designed booms.

#### 5.4.6 Gossamer Technology related Influences

##### *Stowage caused influences*

Compact stowage is crucial to GosSSS, also to Gossamer-1. In combination with high compacting, long term stowage and high temperatures creep will eventually cause changes of geometry and dimensions on the stowed components.

For the booms of the Boom Subsystems, these influences are similar to the ones related to manufacturing causes. Occurring *changes in geometry and dimensions* of a boom e.g. curvature, kinks in the shell surface or deviations in cross sectional dimensions (reported by Fernandez [110]) may result in reduced bending stiffness and bearable buckling loads.

On the stowed sail quadrants creep might induce wrinkles and deep fold lines as reported by Seefeldt in [82], thus resulting in thermal hot spots, thermally damaging the film material, cracks in the protective coating with subsequent damages, and in consequence cause a *change (decreasing) in optical properties* or *increase deployment loads* due to stretching out the fold lines. Consequences on the system could be a reduced thrust due to geometric changes or even subsystem failures due to overloading. However, occurring creep of rolled up CFRP booms or folded membranes are difficult to predict for long mission durations. Testing has to be accelerated in order to simulate a long-time span within a reasonable testing period, while correlation of accelerated testing with real storage and mission operation time is unknown, resulting in risks to be considered. This is partially addressed in chapter 6 and in dedicated studies e.g. by Meyer & Zander [111]. While for Gossamer-1, the stowage related influences might not be critical due to the short mission duration, for long duration space flights especially when being stowed over months or years like in ADEO or when operating with affected components over a long period like anticipated for Gossamer-3, the impact is critical and need to be considered in robustness assessment.

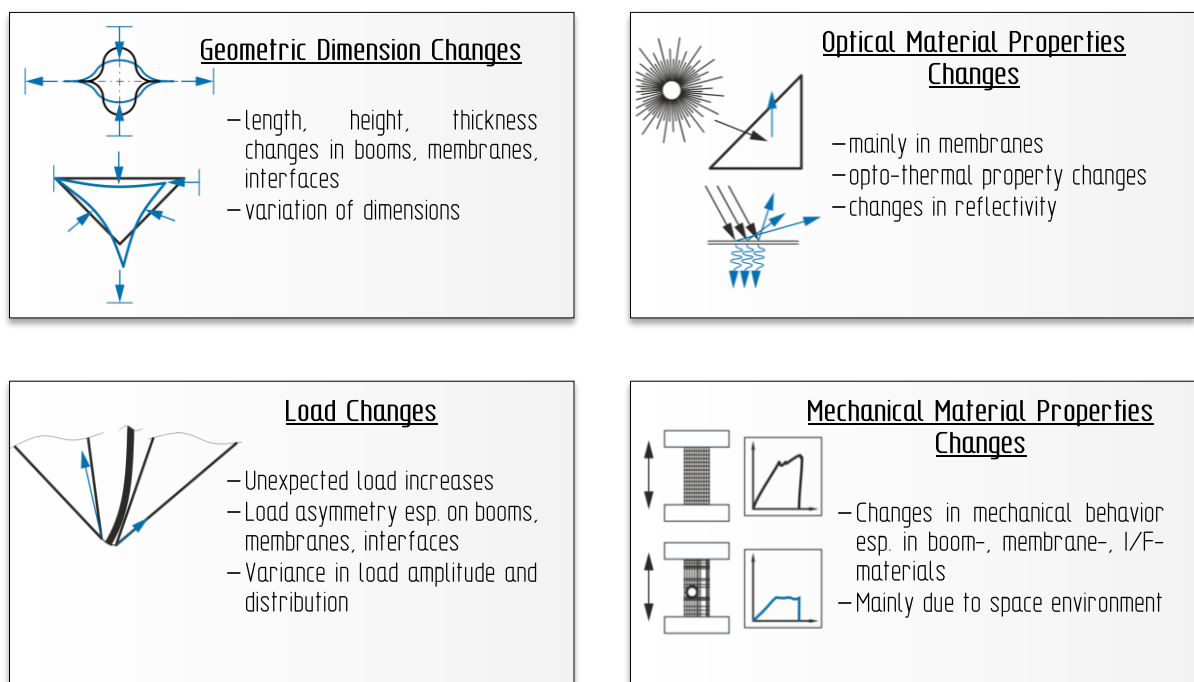
##### *Subsystem interaction caused influences*

Inaccuracies (variance) and effects at points of interactions of subsystems with one another cause influences on robustness parameters. For example, do the interactions of the Gossamer-1 Boom Subsystem and the Boom Mechanism Subsystem cause pointing deviations of the boom guided by the boom guide shell and thus cause a change in geometry of the whole structural sail system. It further causes friction between boom and boom guide shells that are not accounted for when looking at the mechanism subsystem alone. Hence, an increase of deployment loads introducing adverse dynamic-mechanical behavior or overloading of structural components may rise. Further examples are the interactions between BSFR and boom causing friction or the release and locking of mechanisms. Here chain interactions are evident. This becomes obvious as the boom loading for example is affected by the loads exerted by the Membrane Mechanism Subsystem onto the Membrane Subsystem via the I/F Subsystem. A load exceeding the designed threshold altering at any point of the chain will influence the whole structural system in terms of geometric deviations leading to an overall performance loss. Influences on robustness parameters in the light of structural robustness are mainly *geometric changes* of subsystems and *load changes (increased introduced loads)* over subsystem borders due to interactions. Similar Gossamer Technology caused load changes in literature are described by Sickinger [109] as load eccentricities as result of cross section distortion due to nominal loading direction at the boom tip.

### *Deployment process caused influences*

The deployment process is crucial to the mission success of a Gossamer spacecraft. Depending on potential single points of failure such as deployment mechanisms, deployment testing and validation is mandatory. However, ground deployment tests for functional approval directly can only be performed with limited deployment cycle numbers for testing a subsystem and even more limited for system. This has different reasons: Once due to the effort the mostly manual and complex folding and packaging processes. In specific packaged sails might differ slightly from packaging process to packaging process as they are manually folded. Secondly, the ground deployed sail might experience damage just by handling due to its delicate composition and can commonly not be used for the actual mission, thus limiting empirical data and repeatability. This makes such a subsystem or component impractical to be tested and later used for mission operation, similar to airbags used in other applications. Furthermore, delicate structural systems like GosSSS cannot be tested as required for common space structures. Occurring damages at high cycling will limit the total number of cycles for deployment testing of subsystems like the Membrane Subsystem or the Boom Subsystem. Moreover, the effort producing realistic test articles and testing itself limits test schemes. Apart from that, the large size of such deployed structural systems or subsystems many times poses problems of providing test equipment, area and appropriate environment. The resulting influences that are identified in this regard are *increased introduced loads* for deployment due to uncertainty, *changes in subsystem and system geometry* due to asymmetric deployment (tolerances), and *changes of load distribution* e.g. unsymmetrical load distribution at the four boom tips.

Analyzing the identified and discussed influences, they can be generally systemized in four types for 2d-planar GosSSS as given in Figure 5.19. These are: Geometric dimension changes that mainly concern booms, membranes and interfaces in terms of length, height and thickness changes as well as variations; optical material property changes mainly involve changes of opto-thermal behavior and reflectivity of membranes; load changes including unexpected load increases, load introduction asymmetry as well as variations, for structural subsystems like booms, membranes and interfaces; and changes of mechanical material properties predominantly driven by the harsh space environment.



**Figure 5.19.** Identified influence types in GosSSS

### 5.4.7 Overview of Influences on Gossamer-1 Subsystems and System

The previously described influences and their causes are summarized in Figure 5.20.

Here the subsystems applicable, derived influences, the impacted robustness parameters and the consequence for the according subsystem are given. This provides an overview thus linking possible influences and consequences to the according subsystems and robustness parameters. Furthermore, resulting consequences arising at system level of Gossamer-1 are given.

The resulting consequences on the Gossamer-1 system can be summarized with:

- 1) *Loss in total thrust*
- 2) *Inaccuracy of thrust direction* caused by a resulting displacement of center of pressure relative to the center of mass, thus compromising attitude control
- 3) *Detrimental rotation* (windmill torque) causing sail system to spin, thus inducing adverse dynamic effects making attitude control difficult or impossible or evoking a loss of spacecraft

The derived consequences on the Gossamer-1 system are in accordance with findings in similar solar sail systems. Stohlman, Chamberlain, Zander & Wilkie [112] structurally analyzed the squared solar sail Hipersail, a mission anticipated by NASA as DL<sub>1</sub>-mission for space weather warning, featuring an edge length of 21 m, using four 16 m CFRP booms stored on a single central deployment spool. However, the authors concentrate on a single type of influence, that can be identified according to the scheme presented in this thesis as geometric dimension changes caused by manufacturing. Sickinger et al. [35, 113, 114] consider some influences in terms of design parameters at subsystem and system level in their probabilistic design approach for a 40 m x 40 m solar sail, being the ancestral design of Gossamer-1 and Gossamer-2, using the similar CFRP booms. Here on system level the FE model considers Environment caused increases in loads due to drag initiated by the residual atmosphere at a 300 km LEO altitude. Further consequences on the subsystem or system performance or robustness are not considered. Both examples mainly show the use of influences as varying design parameters on single subsystems and the overall system. However, influences and their consequences were not used to assess robustness or its quantification in any way.


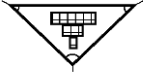
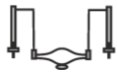
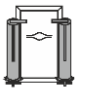
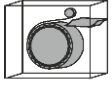

System/Subsystem		Influence	Influenced Robustness Parameter	Consequence
	Boom Subsystem	geometric dimension changes mechanical properties changes material properties changes	$\kappa$ $u$	Boom curvature Changed cross section Boom root angle deviations (pointing deviations)
		increased introduced loads variability in predicted loads variability of bearable loads	$L$	Stiffness reduction Changed deployed boom length Collapse load (buckling load) reduction Introduced dynamic-mechanical behavior reduced load carrying capability
	Membrane Subsystem	optical properties changes material properties changes (thermal) mechanical properties changes	$R_S$	Variation of sail shape Planarity insufficient (billowing)
		geometric dimension changes (flatness or profile of a surface) mechanical properties changes	$S_{RMS}$	Reflectivity insufficient (wrinkles, sail fold creases) Load introduction disturbed (stiff corners/rigid body area)
		increased introduced loads mechanical properties changes variability in predicted loads variability of bearable loads	$L_M$	Ripping/rupture (crack propagation) Reduced load carrying capability
	Interface Subsystem	geometric dimension changes mechanical properties changes	$l$	Interrupted load transfer Asymmetric load transfer
		increased introduced loads variability in predicted loads variability of bearable loads	$L_t$	Stiffness reduction Reduced load carrying capability
	Membrane Mechanism Subsystem	mechanical properties changes increased introduced loads variability in deployment loads	$F_{SM}$	Uncontrolled deployment (self-deploying membrane) Increased deployment loads
		geometric dimension changes mechanical properties changes	$d_M$	Interrupted load transfer (dynamics) Asymmetric load distribution
	Boom Mechanism Subsystem	mechanical properties changes increased introduced loads variability in deployment loads	$F_{SB}$	Uncontrolled deployment (boom blossoming) Increased deployment loads (friction)
		geometric dimension changes mechanical properties changes	$d_B$	Interrupted load transfer (dynamics) Asymmetric load distribution
System		Consequences on Gossamer-1 System		
	Gossamer-1 Structural System	<ol style="list-style-type: none"> <li>1. Loss in total thrust</li> <li>2. Inaccuracy of thrust direction (by displacement of center of pressure versus center of mass)</li> <li>3. Detrimental rotation (windmill torque, causing sail to spin)</li> </ol>		

Figure 5.20. Influences and consequences on subsystem and system level of Gossamer-1

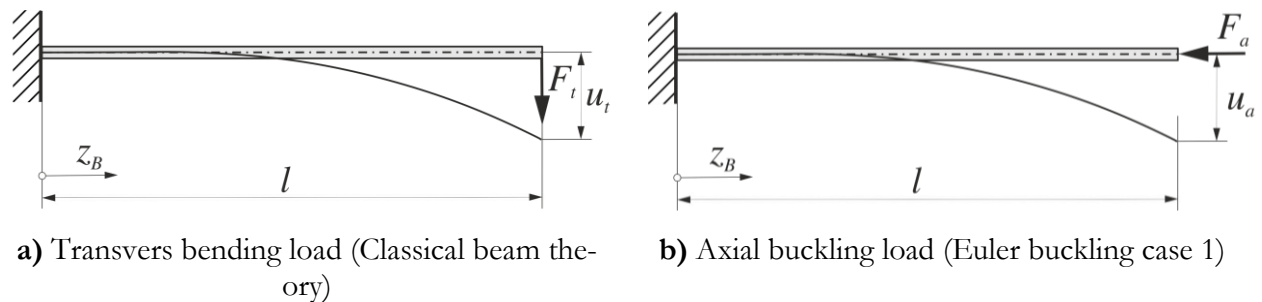


## 5.5 Application of Influence Factors – An Example

In this section it is demonstrated how influence factors are principally applied, on a theoretical and simplified analytical example of the Boom Subsystem.

As discussed in the previous section, influence factors are factors that represent the impact of an influence and its cause, and determine how much an influence is affecting certain robustness parameters and their components. Moreover, influence factors can be considered as knock down factors. Their application is demonstrated in principle on two analyses on the example of the Boom Subsystem, in a simplified manner. Therefore, a symmetrical half of the Boom Subsystem is considered as simple cantilever beam, that is fixed at one end, representing the boom root fixed to the spacecraft, and experiencing a load (force) at the free end, representing the boom tip with the attached sail subsystems. The two investigated cases, as illustrated in Figure 5.21, represent two typical load scenarios of a boom:

a) a transversal force acting on the boom tip representing a worst load case scenario for a boom, in a classical beam theory (Bernoulli beam theory) scheme; and b) an axial force acting on the boom tip representing an ideal load case scenario, in a classical Euler buckling scheme (Euler case 1). Due to the nature of the boom with its beam like geometry, load case a) with its transversal load ( $F_t$ ) can be considered the worst-case scenario due to its strong asymmetric load introduction that is elevated by the boom length ( $l$ ) as a leverage arm. It represents the most adverse loading type e.g. whenever only one Membrane Subsystem is deployed or stretched. The axial load ( $F_a$ ) case b) is considered much more beneficial leading to higher loads achievable e.g. used as loads for deploying and stretching the Membrane Subsystems, due to its symmetric load introduction. However, in reality a combination of both load scenarios usually occurs.



**Figure 5.21.** Load cases on boom example for analytical influence factors application

### *Applied Influence factors and resulting Boom dimensions*

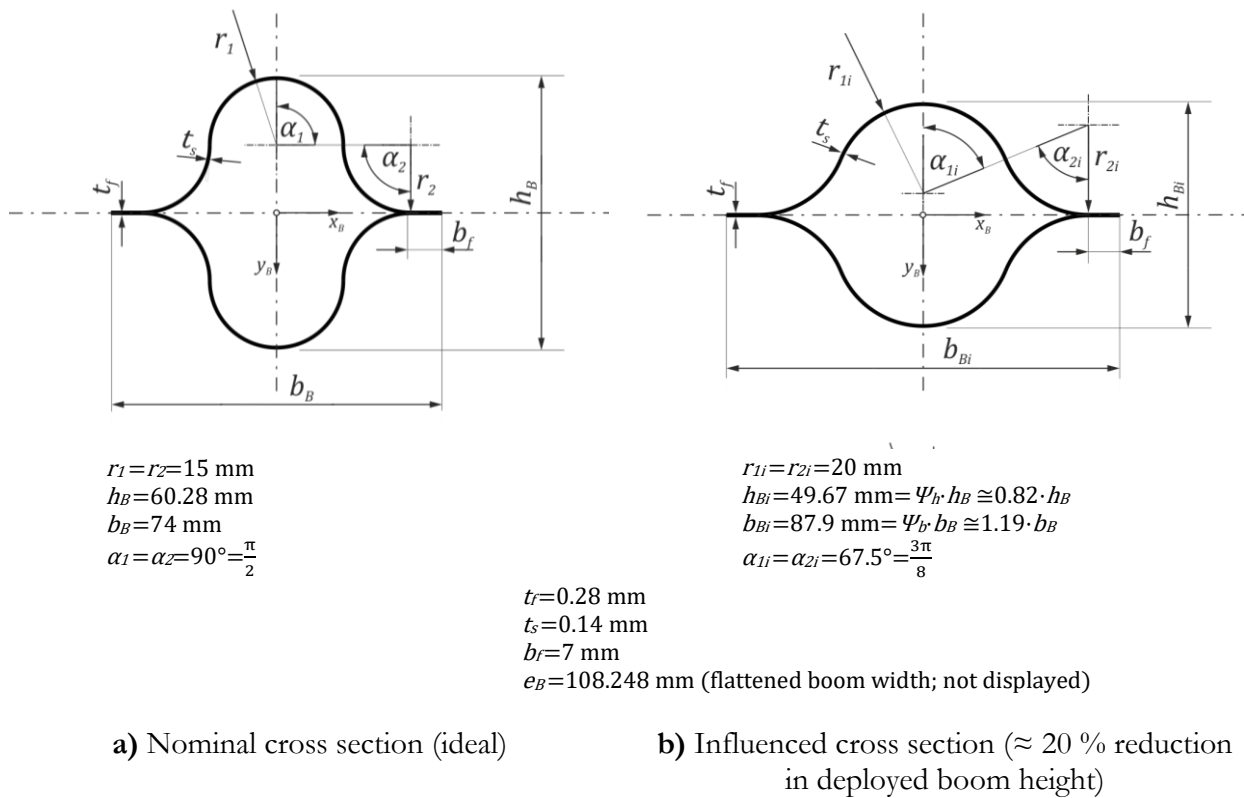
In the following the application of certain influence factors to the robustness parameters *Stiffness*, *Boom tip displacement* and *Characteristic load* are demonstrated in a simple bending stiffness analysis and in a Euler buckling analysis. The considered influences *geometric changes* and *material changes* are originating in different causes as described in section 0. Each influence is applied as a factor that is multiplied with the according metric. The *geometric changes* considered are cross sectional changes e.g. caused by shrinkage during manufacturing and creep and a change in boom length. Here a change in cross sectional boom height  $h_B$  by a factor of  $\Psi_h = 0.67$  results in a by a third reduced boom height  $h_{Bi}$ . This could be a realistic case after long term stowage under high temperatures. Similar is done with the further influence factors  $\Psi_b$ , representing a change of boom width, and  $\Psi_l$ , representing a change in boom length. Material property changes are considered in the reduction of the Young's modulus of the boom material e.g. resulting from prepreg fiber misalignment, impact damage, resin degradation by atomic oxygen and VUV radiation, in the factor  $\Psi_E$ . While the factors are chosen arbitrarily, they can be considered realistic in amplitude.

Applied values for each influence factors are:

boom height factor	$\Psi_h = 0.82$
boom width factor	$\Psi_b = 1.19$
boom length factor	$\Psi_l = 0.9993$
Young's Modulus factor	$\Psi_E = 0.8$

These factors lead to the geometry of the boom cross section under investigation, displayed in Figure 5.22, showing the nominal geometry in a) and the influenced geometry in b). While the nominal geometry is given by default design from Gossamer-1, the influenced geometry, denoted by the index  $i$ , is derived under the assumptions of:

An existing general symmetry of the nominal and influenced cross sections; curvatures are circular radii, while the determining radii  $r_{1i}$  and  $r_{2i}$  are equal in size; subtended angles  $\alpha_{1i}$  and  $\alpha_{2i}$  are equal size; and certain dimensions remain constant and uninfluenced like flange thickness  $t_f$ , the shell thickness  $t_s$ , flange width  $b_f$  as well as the overall flattened boom width  $e_b$ . These assumptions allow for constructing an influenced boom cross section using simple geometric elements, with the according dimensional values for each cross section, as given in Figure 5.22 as well.



**Figure 5.22.** Cross sectional geometry of the studied boom example

### Second moment of area

In order to calculate the characteristic physical quantities for transversal bending and axial buckling it is necessary to determine the second moment of area for both the nominal and the influenced boom cross section. This is done by dividing each cross section into sub-areas as shown in Figure D. 1 of Appendix D. Then the second moment of area is determined for each sub-area. This and all necessary calculations and sub results can be followed in Appendix D. Given that the second moment of area about each axis of a cross section is a compound from all sub areas of a type, its calculation is done according to equations (5.1) and (5.2) for the nominal cross section, and with equations (5.3) and (5.4) for the influenced cross section. Here again the parameters for the

influenced geometry are denoted by the index  $i$ . As expected from the from the cross-sectional dimension changes of the influenced boom, the second moment of area is also reduced in one direction, while increased in the perpendicular.

Second moments of area for nominal boom geometry:

$$I_{x_B x_B} = 2I_{x_B x_B1} + 4I_{x_B x_B2} + 2I_{x_B x_B3} = 8946.83 \text{ mm}^4 \quad (5.1)$$

$$I_{y_B y_B} = 2I_{y_B y_B1} + 4I_{y_B y_B2} + 2I_{y_B y_B3} = 11684.15 \text{ mm}^4 \quad (5.2)$$

Second moments of area for the influenced boom geometry:

$$I_{x_B x_B i} = 2I_{x_B x_B1i} + 4I_{x_B x_B2i} + 2I_{x_B x_B3i} = 6131.86 \text{ mm}^4 \quad (5.3)$$

$$I_{y_B y_B i} = 2I_{y_B y_B1i} + 4I_{y_B y_B2i} + 2I_{y_B y_B3i} = 17916.61 \text{ mm}^4 \quad (5.4)$$

### *Transversal Boom bending*

Characteristic robustness parameters for the Boom Subsystem like *stiffness* and *boom tip displacement* are determined in this example by facilitating the classical beam theory, as explained before. In doing so an asymmetric load introduction by a transversal force causing a bending moment and a boom tip displacement is realized. In reality this could happen during deployment or in operation e.g. when the boom is only loaded by one sail deploying or stretching in-sail-plane or due to an out-of-plane off-set between boom plane and sail attachment plane. Both directions are viewed separately about each axis. The robustness parameters *stiffness* is herein determined in terms of flexural rigidity  $EI$ , derived from the general Equation (5.5), and alternatively the bending stiffness  $c$ , derived from the general Equation (5.6), as the latter is easily measurable in boom bending tests. Further the robustness parameter *boom tip displacement* is determined from the beam deflection at its end with  $u$ , derived from the general Equation (5.7).

Exemplary showing the application of influence factors, Equation (5.8) is given for the boom tip displacement about the x-axis for the influenced boom. Here the implementation of the cross-sectional influence factors is included in the second moment of area and thus not obvious in the given equations. An isotropic and homogeneous Young's Modulus of  $E = 48000$  MPa is assumed for simplification, while assuming a transversal force of  $F_t = 1$  N and a boom length of  $l = 4200$  m (corresponding to the free length in experiments of this type in section 7.1.2). However, material strength considerations are not done at this point.

Flexural Rigidity of a beam:

$$E \cdot I = \text{flexural rigidity} \quad (5.5)$$

Bending stiffness of a beam:

$$c = \frac{F_t}{u_t} = \frac{3 \cdot EI}{l^3} \quad (5.6)$$

Beam displacement:

$$u_t = \frac{l^3 \cdot F_t}{3 \cdot EI} \quad (5.7)$$

Boom displacement about x-axis for the influenced boom:

$$u_{tx_B x_B i} = \frac{(\Psi_l \cdot l)^3 \cdot F_t}{3 \cdot (\Psi_E \cdot E \cdot I_{x_B x_B i})} = \frac{l_i^3 \cdot F_t}{3 \cdot E_i \cdot I_{x_B x_B i}} \quad (5.8)$$

### Euler buckling load

The *Characteristic Load*  $L$ , as robustness parameter for the Boom Subsystem, is calculated according to Euler buckling (case 1) in terms of a buckling load, as given generally with Equation (5.9). This load case represents an ideal load case with a symmetric load introduction, as one could theoretically expect when the sails are equally tensioned during deployment and specifically at its end. While for the nominal boom, nominal parameters are used, for the influenced boom the influence factors are directly and indirectly applied in the same manner as done previously for the boom tip displacement. Both is done about the two axes of the boom's cross section.

Euler buckling load:

$$F_c = \frac{\pi^2 \cdot EI}{(2 \cdot l)^2} \quad (5.9)$$

### Results

The results for both load cases are summarized in Table 5.2 for comparison. As expected from the changes in the second moments of area, the influenced boom loses performance about the x-axis and gains about the y-axis. These changes are given in percentage, while functional performance loss is marked blue in Table 5.2. Here a negative influence on the Boom Subsystem's function is represented by a loss in stiffness, while for the boom tip displacement a gain shows an adverse effect. Comparing the losses and gains for each robustness parameter and axis, it becomes obvious that adverse changes are of greater amplitude than beneficial ones. However, due to the used equations, values  $EI$ ,  $c$  and  $F$  are in a linear relationship and therefore show the same relative changes. The here obtained results would further be used, in the process of robustness assessment, in Equations (4.16), (4.17), (4.19) and finally in Equation (4.15), thus determining the Boom subsystem robustness. Furthermore, the obtained nominal results serve as analytical reference in section 7.

**Table 5.2.** Comparison of nominal and influenced robustness parameter results

Relevant Robustness Parameter	Stiffness $\kappa$				Boom Tip Displacement $u$		Characteristic Load $L$	
	$EI_{x_B x_B}$ [ $\times 10^6 \text{ N}\cdot\text{mm}^2$ ]	$EI_{y_B y_B}$ [ $\times 10^6 \text{ N}\cdot\text{mm}^2$ ]	$c_{x_B x_B}$ [N/mm]	$c_{y_B y_B}$ [N/mm]	$u_{tx_B x_B}$ [mm]	$u_{ty_B y_B}$ [mm]	$F_{cx_B x_B}$ [N]	$F_{cy_B y_B}$ [N]
Nominal boom	430	561	0.0174	0.0227	57.5	44	60	78.5
	$E_i I_{x_B x_B i}$ [ $\times 10^6 \text{ N}\cdot\text{mm}^2$ ]	$E_i I_{y_B y_B i}$ [ $\times 10^6 \text{ N}\cdot\text{mm}^2$ ]	$c_{x_B x_B i}$ [N/mm]	$c_{y_B y_B i}$ [N/mm]	$u_{tx_B x_B i}$ [mm]	$u_{ty_B y_B i}$ [mm]	$F_{cx_B x_B i}$ [N]	$F_{cy_B y_B i}$ [N]
Influenced boom	250	731	0.0102	0.0297	98.5	33.7	35	102.4
Change due to Influence [%]	-41	+30.3	-416	+30.6	+71.3	-23.4	-416	+30.5

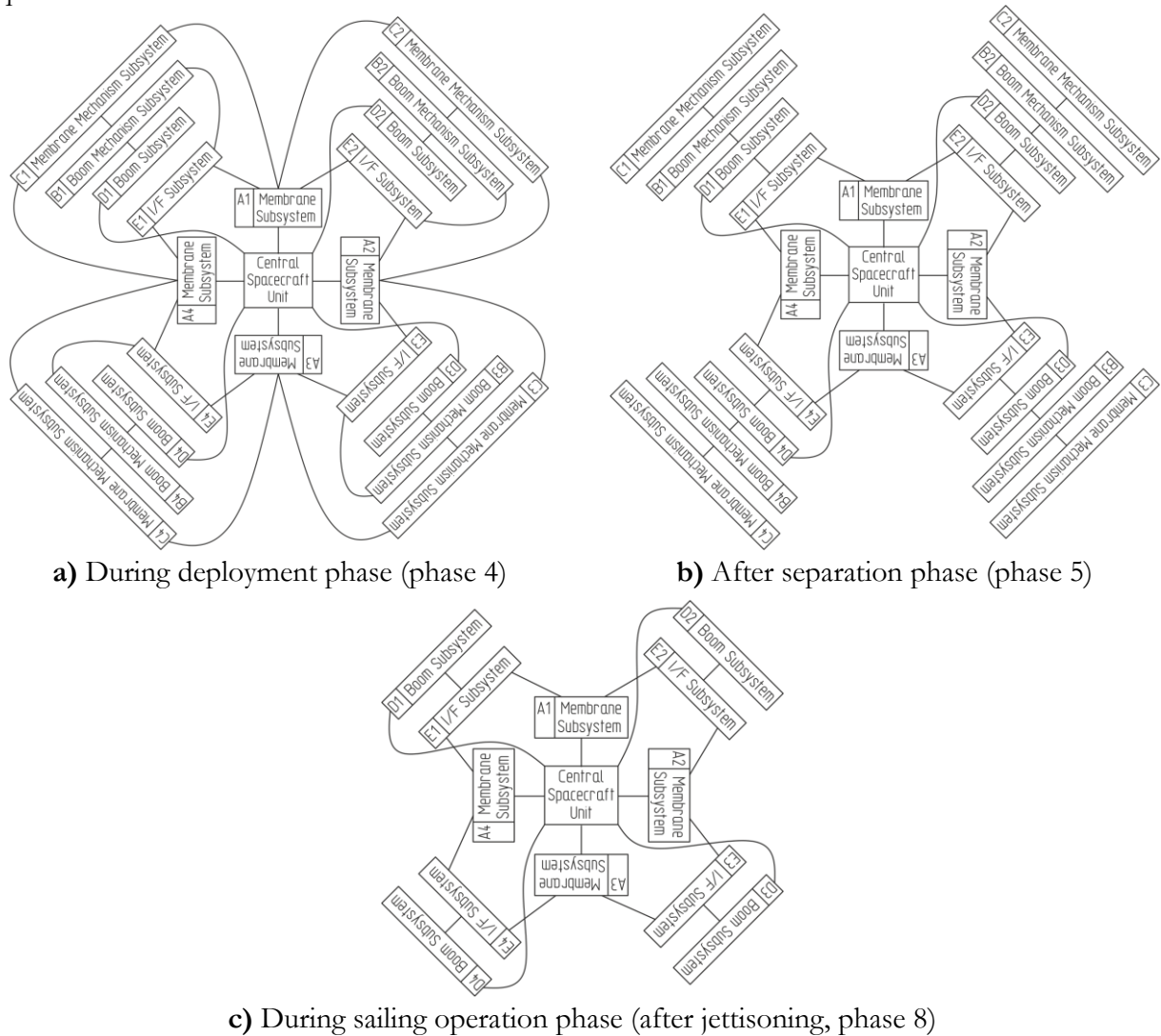
Adverse changes in regard to robustness parameter marked grey

Although this analytical example gives some descriptive results, there are some aspects that an analytical approach cannot do. It can be used for simplification. However, several influences cannot be implemented without increasing the effort enormously or cannot be implemented at all. Such influences are e.g. curvature of the boom or angle variations of the interface or effects like local buckling and preexisting shell imperfections. However, this can be considered in a numerical approach using an appropriate model (FE model). This in combination with probabilistic modelling is further enables to include parameter variance. Such a numeric analysis is performed in terms of linear and non-linear buckling analysis on the Boom Subsystem of Gossamer-1 discussed in section 7.

### 5.6 Subsystem Weighting Factors – Conditions and Determination

In this subsection weighting factors, one for each subsystem, are determined for the studied Gossamer-1 structural system. These factors shall weight each subsystem robustness in terms of system function fulfillment for the mission with a functionality number  $F_{\mu N}$ , consequences of subsystem failure for the system state with a failure number  $FN$  and redundancy with a redundancy number  $RN$ . This subsection therefore investigates the **4. Work Hypothesis**, that assumes a conditional relationship of robustness.

In order to do so interactions of the Gossamer-1 subsystems and consequently their physical connections between another are essential to know. For assessing these interactions, a scheme resembling the system, that is made up of subsystem blocks, is developed. For Gossamer-1 such block schemes are shown in Figure 5.23 for different phases within the mission. Displaying the connections with a) during the deployment phase, b) after interface separation and c) in operation phase (cf. phase 4, 5 and 8 respectively in Figure 5.15), the images indicate that connections and interactions are conditional and depend on the phase the system is viewed at. The graphics of Figure 5.23 also reveal that a simple differentiation in logical series and parallel connections is difficult. Moreover, the schemes illustrate that robustness should be considered conditional, also depending on the phase Gossamer-1 is viewed at, and extends the general considerations made in section 4.2. However, at this point the graphics are mainly used to provide an overview and help to determine failure sequences.



**Figure 5.23.** Conditional physical connections and interactions of Gossamer-1 (structural system)

### *Failure numbers*

Before the failure number can be determined the failure sequences are analyzed in an event tree chart, as shown for Gossamer-1 in Figure 5.24. Here the consequence of a subsystem failure on the overall system are analyzed, while the question is asked “what if subsystem X fails”. In the displayed case the sequence of subsystems starts according to the schemes of Figure 5.23 from inside at the Membrane Subsystem and proceeds outwards. Failure is here considered as total loss of function, while success resembles a complete function fulfillment.

Figure 5.24. lists each identified subsystem type as a chart, to be read from left to right, starting with an initiating interruptive event. If a subsystem is robust and fulfills its function(s), it is further proceeded with success, and the next subsystem is analyzed. If a subsystem fails, it is considered a complete loss of functionality. Thus, each subsystem is analyzed according to the identified connections and order found in Figure 5.23, with the focus put on failures. For each subsystem type of Gossamer-1 the logical combinations of failure of subsystem elements is given, as the system comprises four subsystems of each type. For the Boom Subsystem four identical symmetric halves are considered one subsystem each. Failure rating is performed with a value of ten for failure and value a five for a conditional success. These values are summed up and scaled for each subsystem with a maximum value of ten, to comply with rating scale of 0 to 10. Results are the failure number  $FN$  for each subsystem, while redundancy is regarded separately.

System failure of Gossamer-1 is considered for failure combinations as discussed in section 4.2 for conditional robustness, for the asymmetric cases b), d) and e) of Figure 4.2, as they are assumed to cause spacecraft tumbling in orbit and therefore deter the main functions of sail propulsion and power generation and with an unstable attitude. This means that for subsystems D, B and C a failure of a single subsystem element already causes the overall system to fail, as expressed with the logical combination, e.g.  $D1 \wedge D3 \wedge D2 \wedge D4$ . For subsystems A and E failure of the subsystem can result in a system failure or in a conditional success of the system. Here conditional success (a partial system failure) is a result of a condition in which a certain combination of failing subsystem elements does not directly lead to a system failure, but instead provide some essential functionality of the system. Such cases can be found in the image of Figure 4.2 c), as discussed for conditional robustness earlier in section 4.2. If for example only one, two adjacent, three or all of the four subsystem elements of the membrane subsystem fail, the system fails. This is due to asymmetric sailing loads leading to uncontrollable tumbling and therefore system loss. However, if two opposite membrane subsystem elements fail, the system can still be considered operable, at least partially. This condition can be expressed with the logic combination  $A1 \wedge A3 \vee A2 \wedge A4$ . Here symmetry enables a stable attitude of the spacecraft, thus possibly providing a reduced sailing functionality, power generation and science operations. Similar is considered true for the I/F subsystem. Continuing the process of calculating the failure number a rating of ten is assigned to a system failure, while a rating of five is for conditional robustness. After normalizing the resulting failure number can be transferred to determine the subsystem weighting factors in Figure 5.26.

Initiating Event ( <i>I/E</i> )	Membrane Subsystem $A_i$	I/F Subsystem $E_i$	Boom Subsystem $D_i$	Boom Mechanism Subsystem $B_i$	Membrane Mechanism Subsystem $C_i$	System State	Failure rating	Failure Number $FN$
						Success	-	-
			Success	Success	Success	Failure	10	7
			Failure	Failure	Failure	Failure	10	7
	Success		Failure	Failure	Failure	Failure	10	7
	Failure		Success	Success	Success	Cond. Success	5	10
	Failure		Success	Success	Success	Failure	10	
	Failure		Success	Success	Success	Cond. Success	5	10
	Failure		Success	Success	Success	Failure	10	

Figure 5.24. Determination of failure numbers  $FN$

**Functionality numbers**

The number of functions a subsystem performs is rated and regarded in the weighting factor in terms of a functionality number (see Figure 5.25). The number of functions is viewed as benefit for the overall system function, presuming that each subsystem is essential for the overall system function. The more functions (primary and secondary) that are performed, the higher the weight of a robustness, due to its higher impact on the overall system. For each subsystem the amount of fulfilled functions is listed. Each number is normalizing to a maximum value of 10, resulting in the functionality number. The resulting values (between 0 and 10) are then assigned as functionality numbers  $FuN$  to the determination chart, as shown in Figure 5.26.

Subsystem	Number of fulfilled functions	Functionality Number $FN$
Boom Subsystem D	3	10.0
Membrane Subsystem A	3	10.0
I/F Subsystem E	2	6.7
Boom Mechanism Subsystem B	3	10.0
Membrane Mechanism Subsystem C	2	6.7

Figure 5.25. Determination of functionality numbers  $FuN$

**Redundancy**

Redundancy as described in section 3.2.2 are here understood as e.g. two parallel and identical (in build or function) subsystems or main components that might be used for alternative load paths in case of damage or failure. In Gossamer-1 this is case in the I/F subsystem, as the wire loops, that connect the interface to the sail quadrant corner, are in triplicate on each side. All other subsystems feature no redundancy in structural parts or components. While no redundancy is indicated by a redundancy number ( $RN$ ) of 1, a simple (doubled) redundancy is assigned a 2 and triplicate a 3.

**Subsystem Weighting factors**

The subsystem weighting factors are then generated from the three evaluation numbers functionality number, failure number and redundancy number, for each subsystem, as done for Gossamer-1 in Figure 5.26 in an evaluation chart. Firstly, the evaluation numbers are combined according to equation (4.8), thus resulting in the weighting number  $WN$  for each subsystem. Assessment is then done on an ordinal scale ranging from zero to ten, while ten marks the highest achievable score, for each

category and subsystem. Each weighting factor  $w_{si}$ , is determined with equation (4.9), with the ratio of the single weighting number for each subsystem to the overall sum of weighting numbers. This results in the weighting factors for each of the subsystems of Gossamer-1.

Subsystem	Functionality Number $F_{iN}$	Failure Number $F_N$	Redundancy $R_N$	$WN_i$	$w_{si}$
Boom Subsystem D	10.0	7	1	17.0	0.163
Membrane Subsystem A	10.0	10	1	20.0	0.192
I/F Subsystem E	6.7	10	3	36.7	0.352
Boom Mechanism Subsystem B	10.0	7	1	17.0	0.163
Membrane Mechanism Subsystem C	6.7	7	1	13.7	0.131
$\Sigma$				104.40	1

**Figure 5.26.** Determination of subsystem weighting factors for Gossamer-1

## 5.7 Chapter Conclusion

Within this chapter, a mission envelope on a case study with the focus on the Gossamer-1 system was studied. As the system architecture was investigated, subsystems are identified and described by function and design, as well as their realized hardware. These four major subsystems are the Boom Subsystem, the Membrane Subsystem, the Mechanism Subsystem and the Interface Subsystem. Additionally, to the subsystem structure, its components as well main functions of each subsystem was identified and described.

In order to be able to determine the partial robustness and consequently subsystem robustness factors for each subsystem have been derived. With the major robustness parameters for the Boom Subsystem further scrutinized within this thesis, such as the characteristic load  $L$ , stiffness  $\kappa$ , and Boom Tip Displacement  $u$ , this approach is supporting the **2. Work Hypothesis**.

Furthermore, the according weighting factors, that determine the impact of contribution of a robustness parameter to the subsystem robustness, were determined by analyzing subsystem functions, thus supporting **1. Work Hypothesis**. By analyzing the mission scenario for Gossamer-1, the most relevant phases could be identified, thus providing conditional relations of functional fulfillment for each phase and consequently for robustness, as proposed with the **4. Work Hypothesis**.

As robustness is largely impacted by internal and external factors, influences, detrimental effects, and their associated causes were identified and studied, as another crucial step in the proposed robustness assessment methodology. Moreover, the causes were categorized into groups like measurements, materials, Gossamer Technology, environment, methods and manufacturing related, while induced influences relevant for each subsystem are elaborated and discussed for GosSSS in general and the studied mission envelope in specific, thus supporting **3. Work Hypothesis**.

Following, four main influence types for GosSSS were synthesized, namely: geometric dimension changes, load changes, optical material properties changes and mechanical material properties changes, and applied on the example of the Gossamer-1 boom under lateral bending load and axial compression. Here the impact of applied influences in terms of geometric changes e.g. cross-sectional height reduction on the quantifiable robustness parameters such as bending stiffness, flexural rigidity, boom tip displacement were demonstrated, thus also indicating an impact on robustness.

Finally, the conditional aspect of robustness in terms of subsystem and component interaction within a system has been scrutinized in connection graphs, while subsystem-weighting factors, incorporating failure, function fulfillment and redundancy were determined, complying with the **3. Work Hypothesis**.



## 6. EXPERIMENTAL DETERMINATION OF INFLUENCE FACTORS ON THE BOOM SUB-SYSTEM

In order to incorporate influences in robustness assessment, as identified in section 0, the influence itself or an appropriate factor, representing its impact, ought to be quantified. This is done with a variety of experiments and test campaigns for the Boom Sub-System, its main component and material, as defined in section 5.1 for the case study of Gossamer-1, and partially for ADEO, as both mission cases share the same boom component. Within the scope of this thesis two major types of influences for GosSSS are investigated, geometric dimension changes and mechanical property changes (cf. Figure 5.19).

### 6.1 Geometric Dimension Changes induced Influence Factors

Changes of geometric dimensions of the boom and the Boom Subsystem are identified being a major type of influences in the previous section 0. These and their results are determined in several experiments, described in the following subsections. While mainly focusing on manufacturing and stowage induced influences, quantified influence factors are obtained for cross sectional changes, curvature, deviation from straightness and resulting boom tip deflection.

#### 6.1.1 Stowage induced Influences – on short Boom Specimens

Aiming to determine stowage induced influences shape deviations like cross sections, straightness and waviness of stowed boom specimens are investigated.

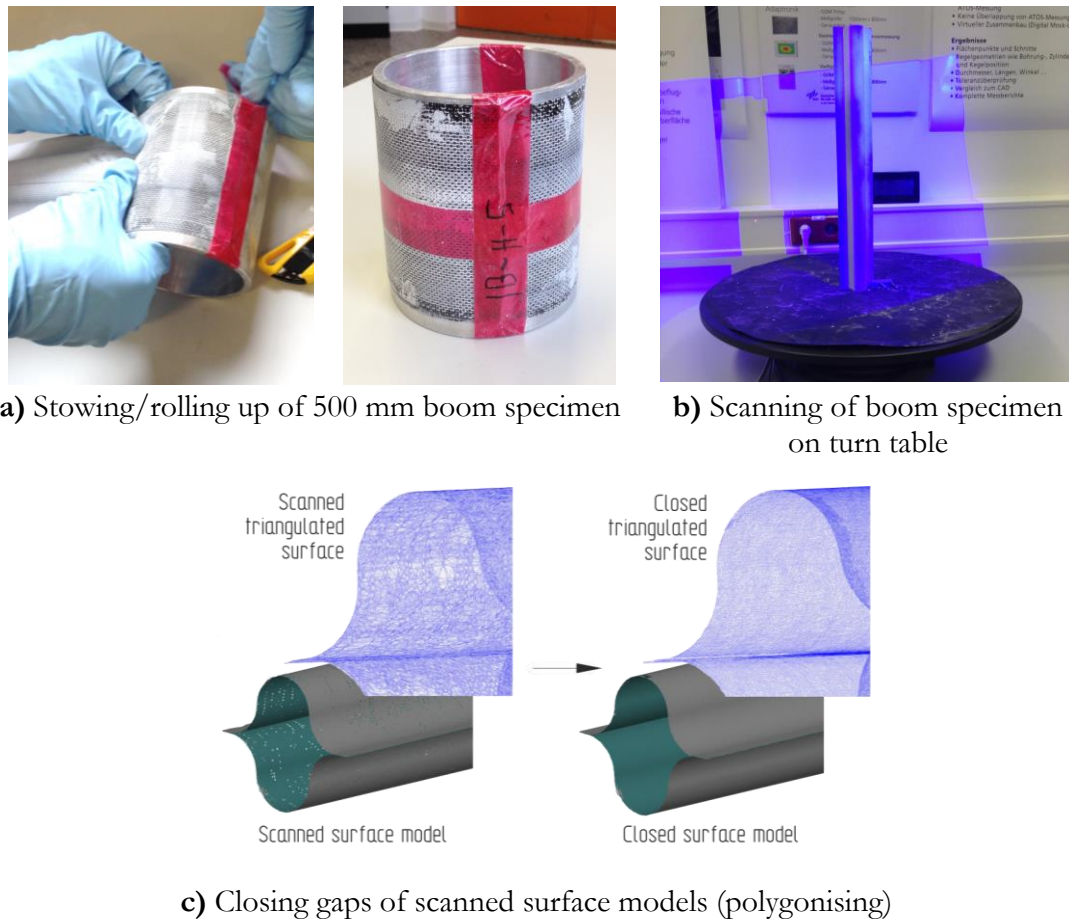
Twelve specimens of Gossamer-1 booms, each 500 mm in length, are stored rolled up on aluminum cylinders ( $\varnothing 100$  mm), as depicted in Figure 6.1 a), for a duration of 194 days. Measurements on day 1 represent the pristine condition as of manufacturing, before being rolled up and stowed for the first time, while measurements on day 98 represent the last day of specimen stowage on the cylinders. Following day 98, all specimens were stored in deployed configuration, lying flat under controlled environmental lab conditions at room temperature ( $23^{\circ}\text{C}$ ) and 50% rel. humidity for relaxation. On the last day of the campaign, on day 194, all specimens were scanned once again, aiming to measure the impact of relaxation

For storage in stowed condition, one set of six specimens was stored at room temperature at  $23^{\circ}\text{C}$  (50% rel. humidity), in lab environment, and another set of six at elevated temperatures of  $80^{\circ}\text{C}$ , in a vented heat chamber. Every 14 days each specimen is taken out of its stowed condition, unreeled and left 30 min to acclimate to lab conditions, followed by being scanned using a GOM ATOS Triple Scan 3D scanning system, that provides an accuracy of 0.003 mm.

Surface scanning is performed, with the boom specimen standing in an upright position on a rotation table. A stepwise rotation of about  $45^{\circ}$  after each of the eight still scans per specimen results in capturing the complete surface area (see Figure 6.1 b) and sweeping over  $360^{\circ}$ . For scanning and storing the same orientation of each specimen is maintained by applying tape marks as well as fixating the specimen to the rotation table by the weight of a metal clamp. This ensures that each specimen is always reeled up at the same side and starting at the same specimen end, resulting in a consistent test regime over the observed period. Specimen preparation also included coating each specimen before every scan with titanium dioxide in order to provide a non-reflecting surface.

Post-scan processing, that followed, consists of closing surface gaps, caused by the perforated nature of the boom material in the scanned model, thus refining the triangulated surface model for analysis (see Figure 6.1 c), as well as positioning the scanned surface model in a defined coordinate system along with a nominal CAD model of the specimen in the analysis software (ATOS Professional $\text{\textcircled{C}}$ ). Moreover, different inspection sections are introduced at which cross section, longitudinal deformations (straightness) are analyzed as described in the following subsections.

Further information on the analysis procedure, sections and finding appropriate coordinate systems can be found in [115].



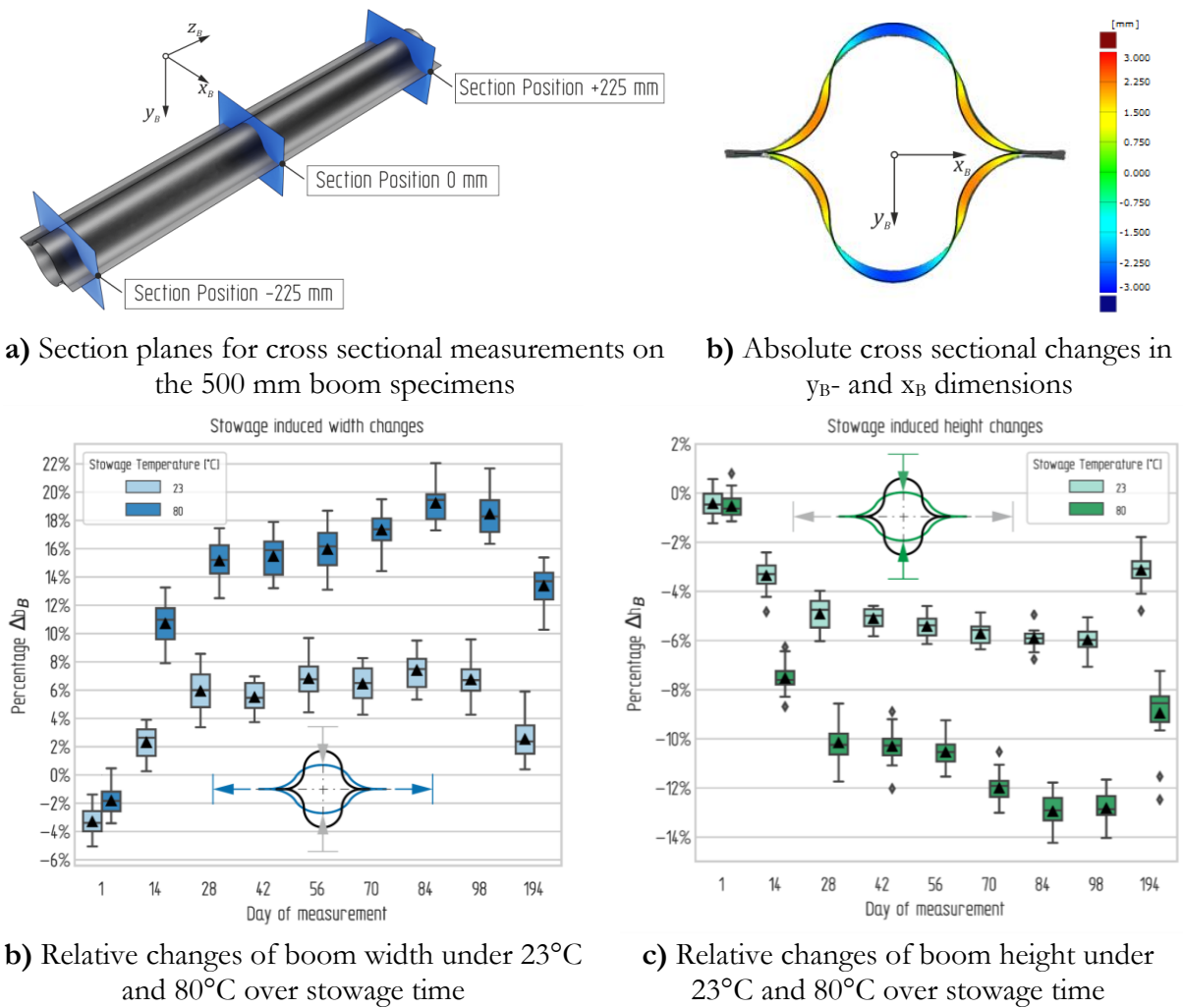
**Figure 6.1.** Process of specimen surface scanning and model preparation for analysis

#### 6.1.1.1 CROSS SECTIONAL CHANGES

Cross sectional dimensions are measured at three section planes perpendicular to the boom specimen axis, at the center (0-position), at -225 mm and at +225 mm, as illustrated in Figure 6.2 a). In this way, deviations from the nominal cross section are determined in the  $y_B$ - $x_B$ -plane, as shown in Figure 6.2 b), as a difference between scanned surface and aligned CAD model.

Test results are summarized in box and whiskers plots, as given in Figure 6.2 c) and d), providing median, mean, upper and lower quartile as well as outliers with one box representing the measurements of each set of six specimens and three section measurements each, incorporating eighteen data points in total. As presumed for the theoretical example in section 5.5, the boom width is increased, while the height is reduced over stowage time. A near linear quasi-kinematic relationship between width increase and height decrease is immanent, although the change in height is smaller than the one of boom width. This is assumed to have its reason in expansion losses by additional distortions of the cross section. By analyzing the acquired data, several different results can be obtained.

Measurements on day 1, representing deviations due to manufacturing, indicate an average width reduction of about 3%, while at the same time an average height reduction of about 0.5%. While width reduction is assumed to be the result of tolerance due to cutting the flange edges to size, height reduction can be linked to tolerances caused by the manufacturing process equipment. Specifically the thermal expansion of the used steel tooling can be related to this effect, as this and the processed CFRP prepreg exhibit a thermal expansion mismatch.



**Figure 6.2.** Change of boom cross section caused by stowage

Another effect investigated is the creep effect due to stowage time span and temperature on the thermoset CFRP material (cured at 130°C,  $T_g=160^\circ\text{C}$ ). Analyzing width, it increases asymptotically over stowage time, until day 98, and is about four to five times higher for specimens stored at elevated temperature (80°C), compared to width changes of specimens at room temperature (see Figure 6.2 c). Vice versa is true for height reductions as displayed in Figure 6.2 d). Here height decreases asymptotically until day 98. Outliers in measurements of boom specimen height can be attributed to the discrete measurements at the three sections, and with small local buckles or digitally filled prepreg gaps occurring at this position. Moreover, errors of measurement are contributing, as measured values are in the millimeter to sub-millimeter range.

The effect of relaxation becomes visible when comparing day 98 and day 194, for both temperature regimes in Figure 6.2 c) and d). Storing the specimens in a relaxed (unstressed) state, in a deployed configuration reversed some of the maximum width and minimum height changes by roughly one half to three quarters in average, as one can follow in Table 6.1.

Finally resulting influence factors for cross sectional changes can be derived from absolute values, and percentage of change for width and height, as given in Table 6.1., while complete result data is provided in Table E. 1 of Appendix E. This data also shows that maximum changes can be found on days 84 and 98, at the longest time of stowage. The derived influence factors, for boom width with  $\Psi_b$  and boom height with  $\Psi_h$ , as theoretically discussed before in section 5.5, represent the relative resulting dimensions and are conditional on the temperature regime and stowage time. These are provided in Table 6.1 as well.

**Table 6.1.** Cross sectional changes of boom specimens

Temperature regime	Day	Width changes $\Delta b_B$			Height changes $\Delta h_B$		
		Mean (mm)	Percentage Change	Influence Factor $\Psi_b$	Mean (mm)	Percentage Change	Influence Factor $\Psi_h$
23 °C	1	-1,98	-3,3 %	0,967	-0,31	-0,4 %	0,996
	14	1,40	2,3 %	1,023	-2,47	-3,3 %	0,967
	28	3,59	6,0 %	1,060	-3,63	-4,9 %	0,951
	42	3,33	5,5 %	1,055	-3,76	-5,1 %	0,949
	56	4,13	6,9 %	1,069	-4,00	-5,4 %	0,946
	70	3,90	6,5 %	1,065	-4,22	-5,7 %	0,943
	84	4,48	7,4 %	1,074	-4,37	-5,9 %	0,941
	98	4,08	6,8 %	1,068	-4,41	-6,0 %	0,940
	194	1,54	2,6 %	1,026	-2,31	-3,1 %	0,969
80 °C	1	-1,08	-1,8 %	0,982	-0,38	-0,5 %	0,995
	14	6,47	10,7 %	1,107	-5,56	-7,5 %	0,925
	28	9,14	15,2 %	1,152	-7,51	-10,1 %	0,899
	42	9,34	15,5 %	1,155	-7,62	-10,3 %	0,897
	56	9,64	16,0 %	1,160	-7,79	-10,5 %	0,895
	70	10,46	17,3 %	1,173	-8,87	-12,0 %	0,880
	84	11,60	19,2 %	1,192	-9,57	-12,9 %	0,871
	98	11,14	18,5 %	1,185	-9,48	-12,8 %	0,872
	194	8,07	13,4 %	1,134	-6,61	-8,9 %	0,911

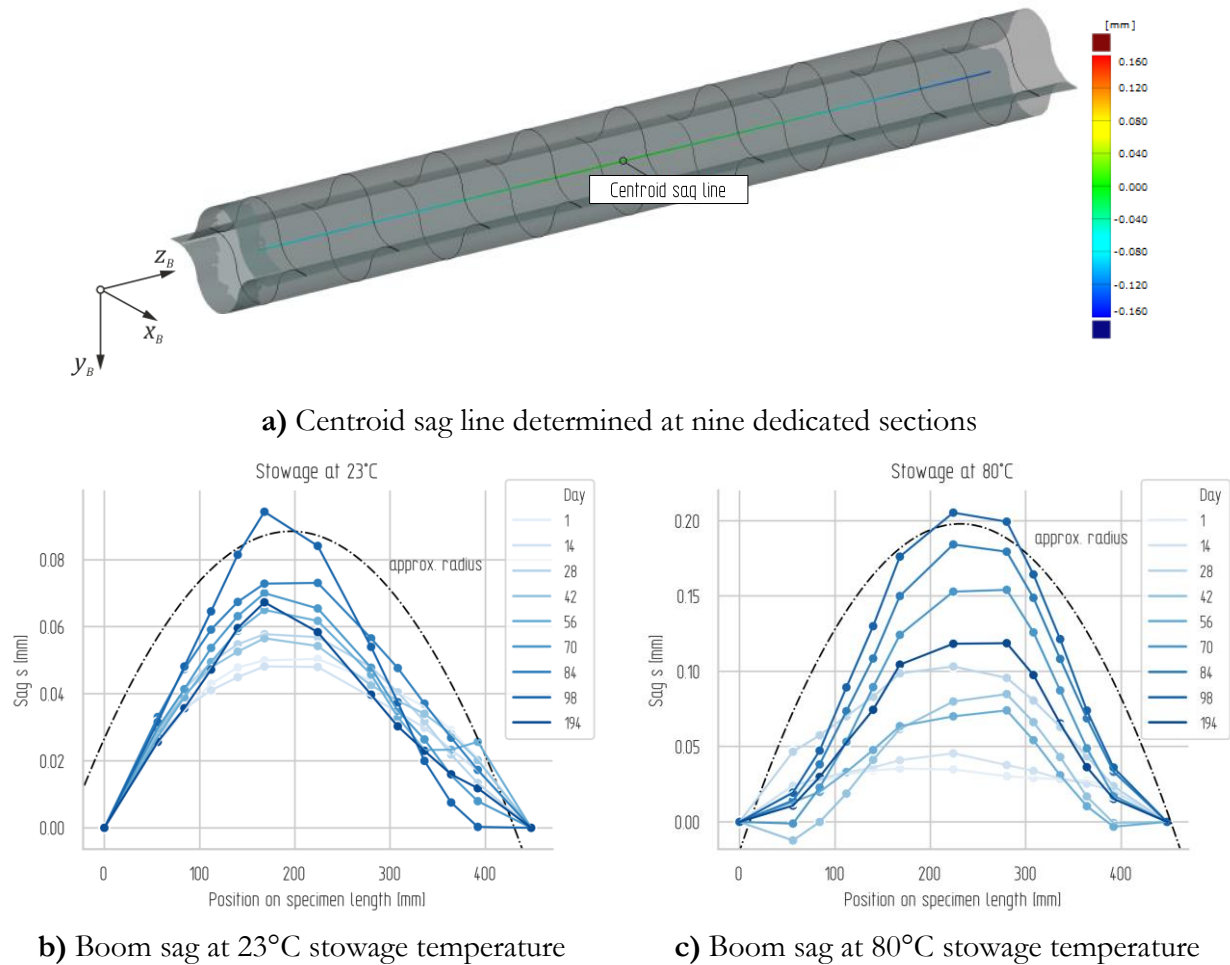
### 6.1.1.2 STRAIGHTNESS

Deviation from ideal boom straightness is determined on the same test data for the two temperature regimes, described before. Analysis is done in two ways and compared herein.

With one method, the acquired surface models are analyzed by determining the centroid sag line, the center deflection of a curved beam, at discrete points along the specimen length. The second method analyzes the continuous contour of the tensioned side of the boom specimen as well as the compressed side. The tensioned side is the outwards facing side when the specimen is reeled onto its cylinder, thus being under tension, while the compressed side is the side that is always facing towards the cylinder when reeled up on the storage cylinder (inner side), thus being compressed when stowed. Due to superposition of dimensional changes like cross sectional changes, axial curvature, sag and local buckling the two methods and the herewith obtained results are compared.

### Applying the Discrete Analysis Method

Curvature and sag are determined at nine discrete sections along the length of the 500 mm boom specimen, as illustrated in Figure 6.3 a). Here the centroid sag is determined at each section plane, resulting in a sag line over length. This is done for all specimens, at each temperature (23°C and 80°C) and for each day. The obtained results are shown in diagrams of sag over the position of measurement, representing the curvature of the specimens. These diagrams are given for the two temperature regimes in Figure 6.3 b) and c), providing a curve for each day of observation. The generated curves capture the change in sag over stowage time and represent the average curvature of a specimen set. Furthermore, approximated radii are given exemplary for day 98, the day with the largest sag. Nevertheless, the graphs indicate specimen curvature of higher order to be more realistic.



**Figure 6.3.** Centroid boom sag of 500 mm specimens for 23°C and 80°C temperature regime (approx. radius displayed for day 98)

Results for pristine condition (after manufacturing) show very low sag values of about 0.05 mm at day 1, with an approximated average radius of 495554 mm (0.5 km), indicating almost no curvature. Creep induced by stowage, however, is visible in the change of radii and sag values over time and increasing with higher temperature. The maximum deformation is reached at day 98 for stowage with a maximum sag, for both temperature regimes. With such increasing deformation, the approximated radius becomes smaller and smaller until day 98, thus indicating an increase in curvature. For the 80°C regime, however the smallest radius of 122878 mm (0.1 km) is determined at day 194, after relaxation. The reason for this is assumed to be in errors due to the measurements at discrete points on the specimen length and the short specimen length, compared to a full-size boom.

The according results can be found in Table 6.2.

In order to derive influence factors the change in radius with reference to the pristine radius, exhibited after manufacturing, is given in percentage. This shows a maximum decrease of radius at day 98 of about -83% for stowage at 80°C. Finally, the influence factors are determined as the residual as given in Table 6.2. However, these small resulting values and the superposition of local measuring error, local buckles, closed gaps and cross-sectional changes can only give an estimation for geometric changes of a boom.

**Table 6.2.** Results of discrete curvature and sag measurements

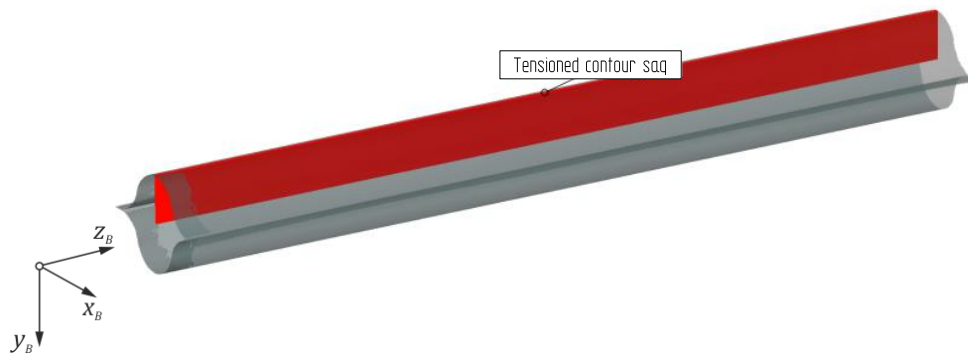
Temperature regime	Day				
		Sag $s$ (mm)	Radius $r_B$ (mm)	Percentage Change in Radius	Influence Factor $\psi_{rB}$
23 °C	1	0,050	495554	0,0 %	1,000
	14	0,048	538940	8,8 %	1,088
	28	0,058	438388	-11,5 %	0,885
	42	0,057	473041	-4,5 %	0,955
	56	0,065	444294	-10,3 %	0,897
	70	0,070	398288	-19,6 %	0,804
	84	0,073	355887	-28,2 %	0,718
	98	0,094	310180	-37,4 %	0,626
	194	0,067	440409	-11,1 %	0,889
80 °C	1	0,035	732837	0,0 %	1,000
	14	0,046	609613	-16,8 %	0,832
	28	0,103	208697	-71,5 %	0,285
	42	0,085	245167	-66,5 %	0,335
	56	0,074	307250	-58,1 %	0,419
	70	0,154	345568	-52,8 %	0,472
	84	0,184	163441	-77,7 %	0,223
	98	0,205	139389	-81,0 %	0,190
	194	0,119	122878	-83,2 %	0,168

accuracy of sag measurement: 3  $\mu\text{m}$ 

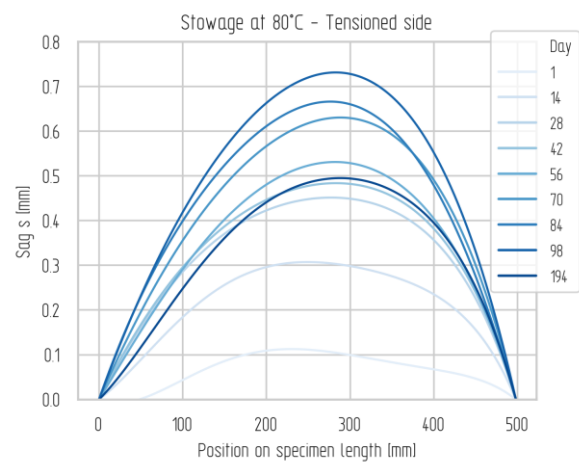
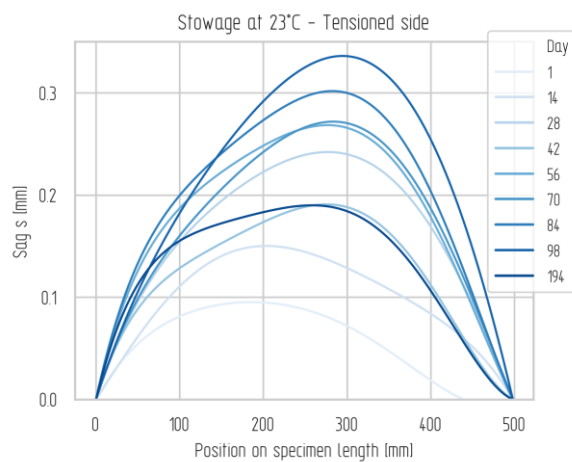
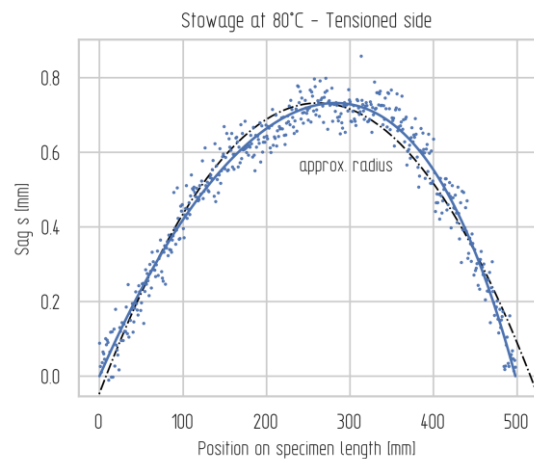
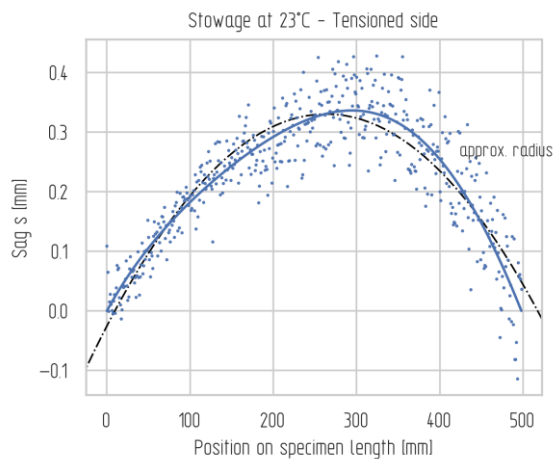
### Applying the Continuous Analysis Method

Using the continuous analysis method, the two sides of a specimens, one tensioned and compressed when reeled up, are analyzed separately. For both sides the scanned model is analyzed along its axis, at a center contour line section, providing continuous data (about 6000 data points) over the whole specimen length. Such longitudinal contour section is displayed for the tensioned side and the compressed side in Figure 6.4 a) and Figure 6.5 a), respectively. With this method results like sag of a specimen, curvature of higher order, approximated radii and statistical analysis data can be obtained. The results (see Table 6.3) for the tensioned side in pristine condition, right after manufacturing, show the smallest sag values, thus indicating small deformations. The average sag for all twelve specimens, determined from a 5<sup>th</sup> order linear polynomial regression curve, is about 0.1 mm. However, measurements of pristine sag differ between both specimens sets. This is due to the specimens resembling each a section of a long boom as they are cut from one. Such long boom however features more a multi-valley curve than a circular radius, as discussed following in subsection 6.1.2. Nevertheless, the approximated radius of 338326 mm (338 m) and a radius of 255959 mm (255 m) are estimated for day 1 of the 20°C and 80°C specimen sets, respectively.





a) Contour sag line determined at tensioned side

b) Boom sag at 23°C stowage temperature determined by a 5<sup>th</sup> order polynomial regressionc) Boom sag at 80°C stowage temperature determined by a 5<sup>th</sup> order polynomial regression

d) Exemplary polynomial curvature (sag), raw measured data points and approximated radius for day 98 at 23°C

e) Exemplary polynomial curvature (sag), raw measured data points and approximated radius for day 98 at 80°C

**Figure 6.4.** Curvature and sag of tensioned side of the 500 mm specimens for 23°C and 80°C temperature regime

Creep induced deformation is found to increase with stowage time and temperature leading to the largest sag at day 98 with 0.336 mm for 23°C and 0.732 mm for 80°C. The results also show that maximum sag is less centered at in early day of storage, assumed to be due to the specimen cut from a large boom, inheriting its curvature. Comparing maximum sag, found at day 98, for both temperature regimes, show that elevated temperature seems to cause values about twice as high. As

deformations grow, this is accompanied by a reduction of radius (increase of curvature). The radius at 80°C for example is reduced by about 83%, compared to the initial radius in pristine condition (day 1), while for 20°C the radius is only reduced by 71%, at the end of stowage (day 98).

Furthermore, the effect of relaxation is visible by an increase of radius, by 8% points, to a radius reduction of about 75%, compared to the initial one, for the 80°C regime. At 23°C, the radius relaxes from 71% to only 50% radius decrease, compared to the initial radius after manufacturing (day1).

Data analysis and results quality can be viewed in Figure 6.4 d) and e). The diagrams displayed show exemplary the acquired data points with sag over specimen length, the 5<sup>th</sup> order polynomial curvature and the approximated radius. Generally, curvature here, determined by a 5<sup>th</sup> order polynomial regression, adhere closely to the circular curvature (radius), although scatter in data points is present as one can observe. The quality of regression and radius is given complementary with the R value, RISE and the residual error radius determination in Table E. 2, in Appendix E, but not further discussed.

The here determined influence factor of curvature, indicating a diminishing straightness, can directly be applied to an FE model with boom radius  $r_B$ , used for partial robustness assessment.

**Table 6.3.** Overview curvature results – tensioned specimen side

Temperature regime	Day	Tensioned Side		
		Sag $s$ (mm)	Radius $r_B$ (mm)	Percentage Radius Change
23 °C	1	0,095	338326	0,0 %
	14	0,150	219004	-35,3 %
	28	0,242	132706	-60,8 %
	42	0,191	164906	-51,3 %
	56	0,269	120659	-64,3 %
	70	0,272	117571	-65,2 %
	84	0,302	107553	-68,2 %
	98	0,336	97539	-71,2 %
	194	0,190	168796	-50,1 %
80 °C	1	0,113	255959	0,0 %
	14	0,307	103607	-59,5 %
	28	0,452	72715	-71,6 %
	42	0,484	67874	-73,5 %
	56	0,531	60300	-76,4 %
	70	0,631	51714	-79,8 %
	84	0,666	47909	-81,3 %
	98	0,732	44072	-82,8 %
	194	0,495	64958	-74,6 %

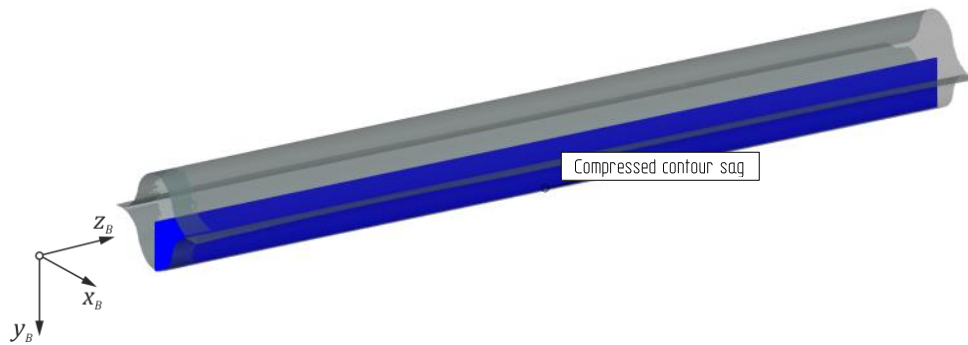
accuracy of sag measurement: 3  $\mu$ m

The results for the compressed side in pristine condition, right after manufacturing, show very similar results for both sets of specimens. The average sag for all twelve specimens, determined from a fifth order regression curve, is again about 0.1 mm. The approximated radius of 301566 mm (301 m) and a radius of 4389682 mm (4389 m) are found for day 1 at 23°C and 80°C specimen sets respectively, a difference by one magnitude. These results are given in Table 6.4.

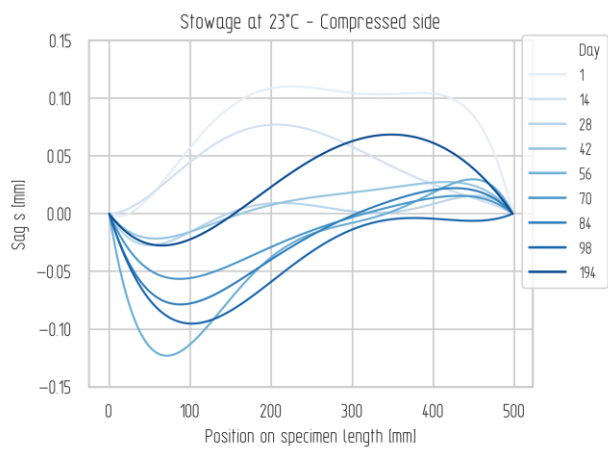
Creep induced deformation increases with stowage time and temperature. As visible in Figure 6.5 b) and c) curvature is of higher order and sag is increasing for some cases, while decreasing for following cases, thus resulting in wavy curves, here determined by a 5<sup>th</sup> order linear regression. Until day 28, deformation behavior induced by creep seems unpredictable. For the room temperature, the overall radius increases, indicating the boom specimen to become straighter over stowage time, which is in contrast to the expected behavior. Comparing maximum sag, found at day 98, for both temperature regimes, values at elevated temperature are about twice as high. Nevertheless, local deformations



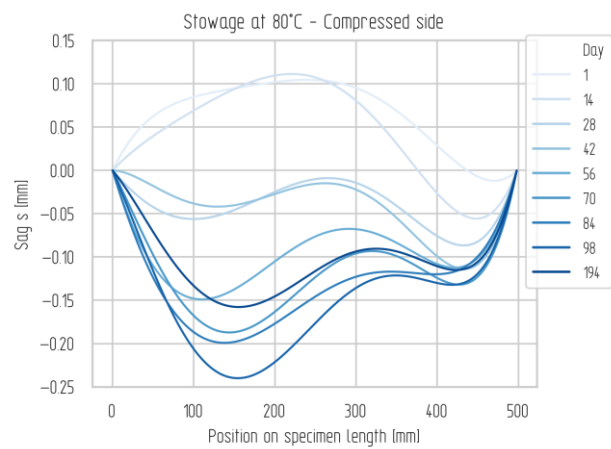
grow over stowage time in one or the other direction. Relaxation is visible by a reduction of absolute sag, e.g. for 80°C, by about 78% points, compared to the initial sag.



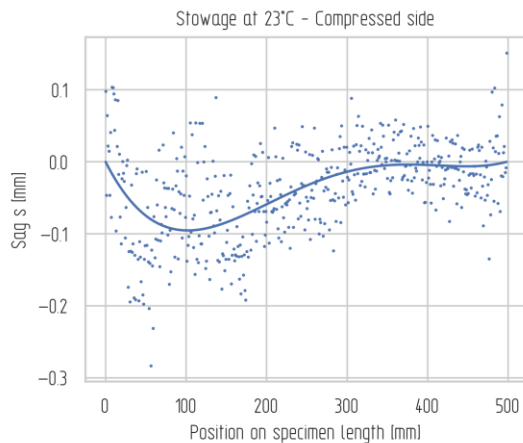
a) Contour sag line determined at compressed side



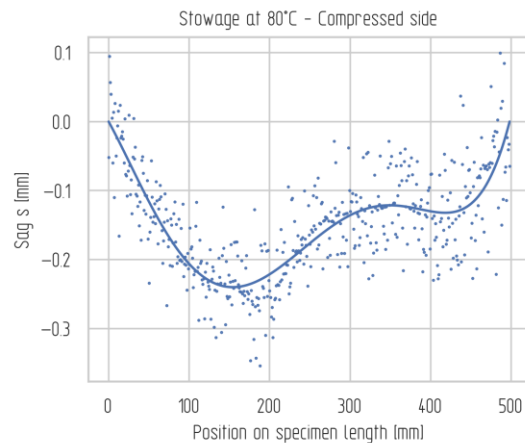
b) Boom sag at 23°C stowage temperature determined by a 5<sup>th</sup> order polynomial regression



c) Boom sag at 80°C stowage temperature determined by a 5<sup>th</sup> order polynomial regression



d) Exemplary polynomial curvature (sag), raw measured data points and approximated radius for day 98 at 23°C



e) Exemplary polynomial curvature (sag), raw measured data points and approximated radius for day 98 at 23°C

**Figure 6.5.** Curvature and sag of compressed side of the 500 mm specimens for 23°C and 80°C temperature regime

In Figure 6.5 d) and e), diagrams show exemplary the acquired data points with sag over specimen length and the fifth order polynomial curvature. Generally, the curvature does not adhere closely to a circular radius, as data points exhibit larger scatter. The quality of regression and radius is given

with the R value, RISE and the residual error radius determination in Table E. 4, to be found in Appendix E.

Overall, it must be concluded that data of the compressed specimen side alone does not give sufficient information about the overall specimen curvature. Here a superposition of global curvature, waviness and possibly local buckling, are the reason for the ambiguity of these results

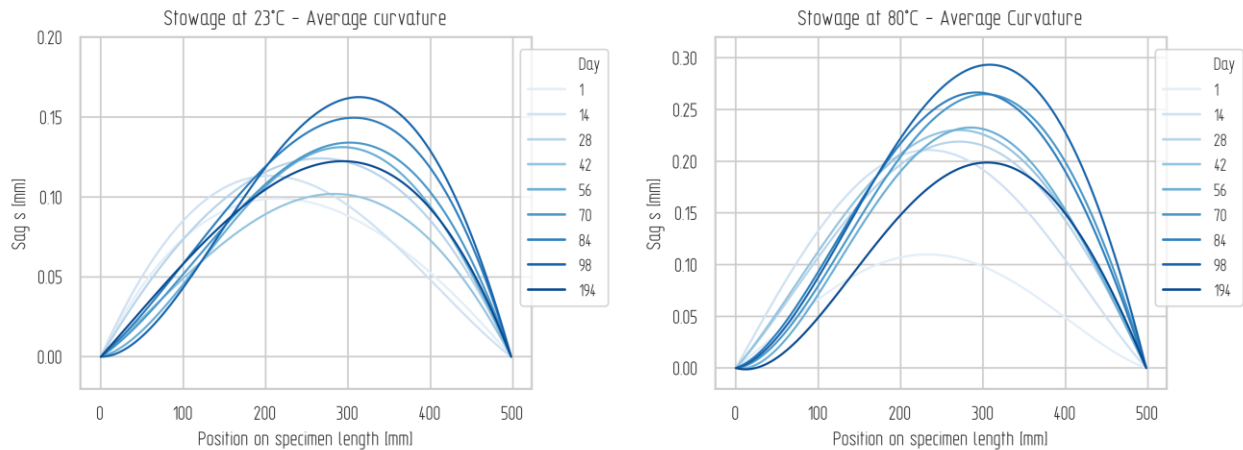
**Table 6.4.** Overview curvature results – compressed specimen side

Temperature regime	Day	Compressed Side			
		Sag $s$ (mm)	Radius $r_B$ (mm)	Percentage Radius Change	Influence Factor $\Delta r_B$
23 °C	1	0,109	301566	0,0 %	1,000
	14	0,076	390508	29,5 %	1,295
	28	-0,008	3637339	1106,2 %	12,062
	42	0,021	2497258	728,1 %	8,281
	56	-0,086	2262757	650,3 %	7,503
	70	-0,049	1428693	373,8 %	4,738
	84	-0,069	2159442	616,1 %	7,161
	98	-0,095	1256037	316,5 %	4,165
	194	0,068	586436	94,5 %	1,945
80 °C	1	0,105	4389682	0,0 %	1,000
	14	0,111	227950	-94,8 %	0,052
	28	-0,087	1064679	-75,7 %	0,243
	42	-0,114	1146992	-73,9 %	0,261
	56	-0,149	3551352	-19,1 %	0,809
	70	-0,187	5334988	21,5 %	1,215
	84	-0,199	281560	-93,6 %	0,064
	98	-0,240	214847	-95,1 %	0,049
	194	-0,158	349417	-92,0 %	0,080

accuracy of sag measurement: 3  $\mu\text{m}$

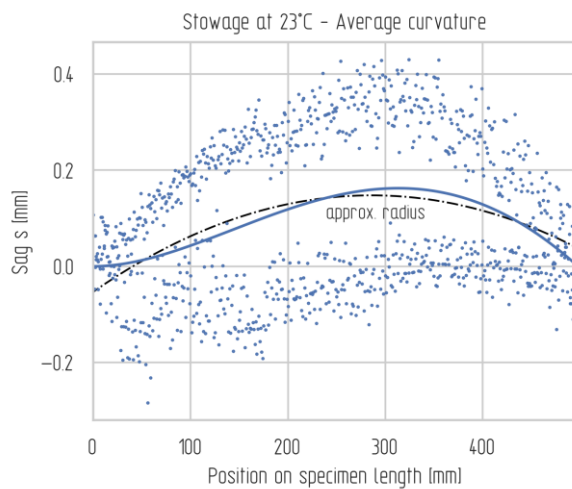
While the results of the separate measurements of each specimen side are revealing some interesting behavior, they are alone not suitable to provide estimations for the boom as a whole. Therefore average values from tensioned and compressed side are analyzed as a whole for each temperature regime and day of measurement.

The averaged results in pristine condition show the smallest sag values, indicating small deformations induced by manufacturing. Again, the average sag is determined from a 5<sup>th</sup> order regression curve, with about 0.1 mm. Here, the average value of the pristine sag does not differ largely between both specimens sets (temperature regimes). However, the approximated radius of 321907 mm (312 m) and of 266445 mm (266 m) for day 1 of the 20°C and 80°C specimen sets, differ somewhat. Approximation and measurement errors are assumed the cause of this. Overall, results are given in Table 6.5, while sag and curvature are visualized in Figure 6.6 a) and b) for 20°C and 80°C stowage temperature, respectively.

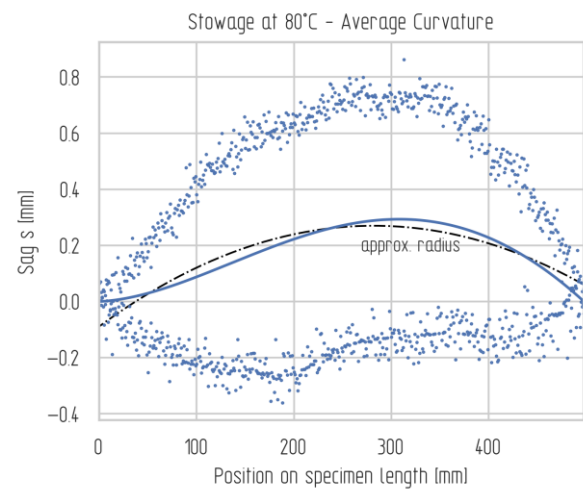


a) Boom sag at 23°C stowage temperature determined by a 5<sup>th</sup> order polynomial regression

b) Boom sag at 80°C stowage temperature determined by a 5<sup>th</sup> order polynomial regression



c) Exemplary polynomial curvature (sag), raw measured data points and approximated radius for day 98 at 23°C



d) Exemplary polynomial curvature (sag), raw measured data points and approximated radius for day 98 at 23°C

**Figure 6.6.** Averaged sag and curvature over both sides (tensioned, compressed)

Deformation induced by creep is evident by increased sag with stowage time and temperature leading to the largest sag at day 98 with 0.163 mm for 23°C and 0.293 mm for 80°C. A comparison of maximum sag, found at day 98, show that the sag at elevated temperature is higher by factor of about 1.8. Alongside with sag increase, radius reduction and therefore an increase of curvature is evident. Citing as example, the average radius reduction at 80°C is about -58%, compared to the initial radius in pristine condition (day 1). For 23°C the radius is only reduced by 37% averaged over tensioned and compressed side, at the end of stowage (day 98).

Relaxation is evident by an increase of radius, by 18% points, to a radius reduction of about -40.2%, compared to the initial one, for the 80°C regime. For 23°C, the radius relaxes from -37% to only -18% radius decrease, compared to the initial radius after manufacturing (day 1), thus almost halving creep deformations in terms of radius. In Figure 6.6 c) and d), diagrams show exemplary the acquired data points with sag over specimen length, the curvature and the approximated radius.

Generally, curvature here, determined by a 5<sup>th</sup> order polynomial regression, adheres closely to the circular curvature (radius). Moreover, as curvatures of tensioned and compressed sides differ strongly, scatter between the bands of data points is present. The quality of regression and radius is given with the R value, RMSE and the residual error radius determination in Table E. 5, to be found in Appendix E.

However, the resulting radii and influence factors are favored over the discrete section analysis and an analysis viewing tensioned and compressive sides separately. The averaged sag and radius values provide higher confidence due to the continuous data points instead of viewing discrete ones, while also considering global curvature of both sides. In terms of application to robustness assessment, the obtained radii  $r_B$  can directly be applied to an FE model, thus considering curvature due to manufacturing and stowage. An influence factor  $\Psi_{rB}$  can be applied as relative factor to the initial radius a boom exhibits.

**Table 6.5.** Overview curvature results – Averaged curvature

Temperature regime	Day	Averaged Curvature			
		Sag $s$ (mm)	Radius $r_B$ (mm)	Percentage Radius Change	Influence Factor $\Psi_{rB}$
23 °C	1	0,099	321907	0,0 %	1,000
	14	0,113	280457	-12,9 %	0,871
	28	0,124	251661	-21,8 %	0,782
	42	0,102	305910	-5,0 %	0,950
	56	0,131	235315	-26,9 %	0,731
	70	0,134	241100	-25,1 %	0,749
	84	0,150	220115	-31,6 %	0,684
	98	0,163	203814	-36,7 %	0,633
	194	0,122	262200	-18,5 %	0,815
80 °C	1	0,110	266445	0,0 %	1,000
	14	0,211	141570	-46,9 %	0,531
	28	0,219	137798	-48,3 %	0,517
	42	0,230	131012	-50,8 %	0,492
	56	0,233	127069	-52,3 %	0,477
	70	0,265	119882	-55,0 %	0,450
	84	0,267	115544	-56,6 %	0,434
	98	0,293	110763	-58,4 %	0,416
	194	0,199	159286	-40,2 %	0,598

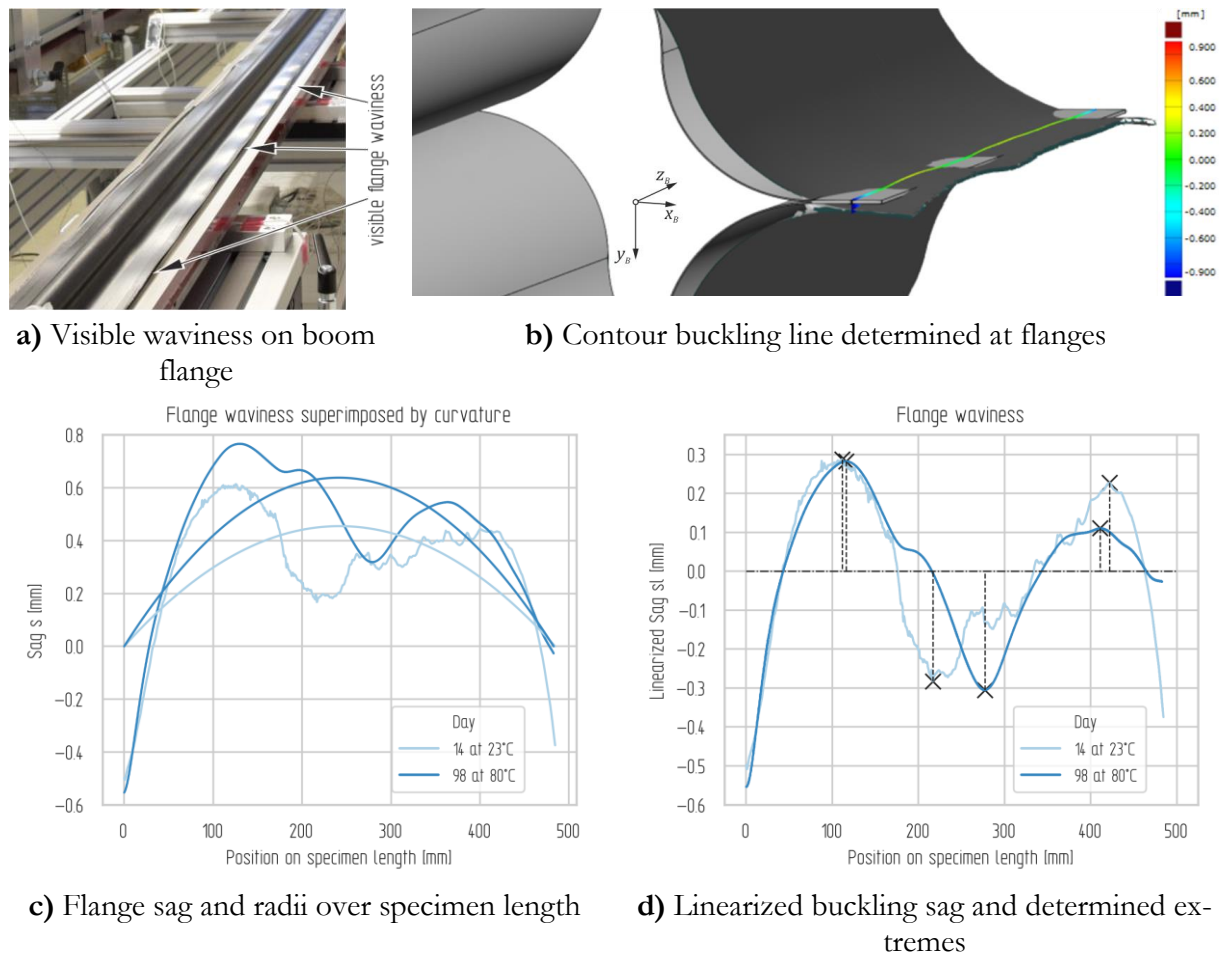
accuracy of sag measurement: 3  $\mu\text{m}$

### 6.1.1.3 WAVINESS OF BOOM FLANGES

Waviness of boom flanges is observed, as buckles are visible under certain light circumstances on the flanges, as depicted in Figure 6.7 a). While these deformations are assumed to have an impact on boom buckling stability, and ultimately on the boom subsystem robustness, this effect is further investigated and quantified herein. For this, continuous section planes are analyzed along the boom specimen flanges, at  $\pm 35$  mm in  $x_B$ -axis of the boom coordinate system (cf. Figure 5.22 for coordinate system), as depicted in Figure 6.7 b). The surface displacements out-of-plane of the scanned model are measured and compared to the nominal boom geometry, at the flange region.

With this sag and curvature are obtained as well as shallow buckles, representing the waviness of the flange. However, the analysis is limited to two points in time at day 14 for 23°C and day 98 for 80°C, thus representing the two cases of short and long storage in stowed condition. Data is still considered representative as day 14 is near to the beginning of stowage and day 98 represents the last day of stowage.

The results of sag and radius, as curves illustrate in Figure 6.7 c), are compared in Table 6.6. While the difference in maximum sag is only 7%, the difference in approximated radius is about -29%, marking a decrease of radius for the elevated temperature, hence an increase of global flange curvature. In general, radii are about one order of magnitude smaller compared to the previously determined for the contour centerlines, thus indicating a higher curvature than the mid-section of the boom.



**Figure 6.7.** Sag, curvature and buckles of the flange of two 500 mm boom specimens stowed at 23°C and 80°C and over different periods of stowage

Waviness is determined by linearizing (normalizing) the sag curves by the according approximated radius, thus providing a linearized buckling profile, as depicted for both cases in Figure 6.7 d). This eliminated the superposition of global curvature and local waviness or buckles. A pairwise comparison of minima and maxima linearized sag of both cases, as done in Table 6.7. show that the effect of creep induced deformation cannot clearly be distinguished as the change in linearized sag  $\Delta s_l$  differs between 8% and -51%.

However, due to the very small values in submillimeter range, results can also be affected by measuring errors of the system, providing an accuracy of 0.003 mm. It is further assumed that the found waviness and buckles, are predominantly generated by manufacturing and less affected by stowage, since the flange is less strained compared to tensioned or compress shell sides. With this assumption, a mean value for the linearized sag  $s_l = 2.49$  mm is considered the quantified influence, that can be directly used as input to model flange waviness as preexisting imperfection in a FE model and therefore in the design process regarding robustness.

**Table 6.6.** Flange curvature and sag

Temperature regime	Day	Flange Curvature							
		Sag $s$ (mm)	Percentage Sag Change	$R^2$ (mm)	RMSE (mm)	Radius $r_B$ (mm)	Residual (mm)	Percentage Radius Change	Influence Factor $\Psi r_B$
23°C	14	0.893	0.0 %	3.4E-02	1.93E-01	64490	1.68E-10	0.0 %	1,000
80°C	98	0.956	7.0 %	2.32E-01	1.78E-01	45640	1.58E-09	-29.2 %	0,708

accuracy of sag measurement: 3  $\mu$ m

**Table 6.7.** Flange waviness

Temperature regime	Day	Averaged Curvature				Difference [%]	
		Extremum type	Linearized sag $s_l$ (mm)	Position on specimen length $z$ (mm)	$\Delta s_l$	$\Delta z_B$	
23°C	14	Max	0,288	112	-1,8	4,1	
80°C	98	Max	0,282	116			
23°C	14	Min	-0,283	217	8,1	27,9	
80°C	98	Min	-0,305	277			
23°C	14	Max	0,227	422	-51,4	-2,6	
80°C	98	Max	0,110	411			
Mean:			0,249				

### 6.1.2 Manufacturing & Stowage induced Influences – on a full-size Gossamer-1 Boom

One full size Gossamer-1 boom (also used in ADEO), with a length of 4300 mm, was scanned using the before mentioned ATOS scanning system, in pristine condition, after manufacturing, and after stowage on a 100 mm aluminum cylinder for 98 days. The boom was scanned lying flat, placed on one of the used manufacturing tool halves as depicted in Figure 6.8 a). Alternatively, the boom was also scanned supported by two long aluminum profiles, without any noticeable difference in results. Therefore, analysis in the following is done with data of the boom placed directly on the tool. Nevertheless, for both types of support gravity cannot be cancelled out. For comparison and to determine the amplitude of transferred imperfections by the manufacturing process and equipment the according tool halves are scanned as well (see Figure 6.8 b).

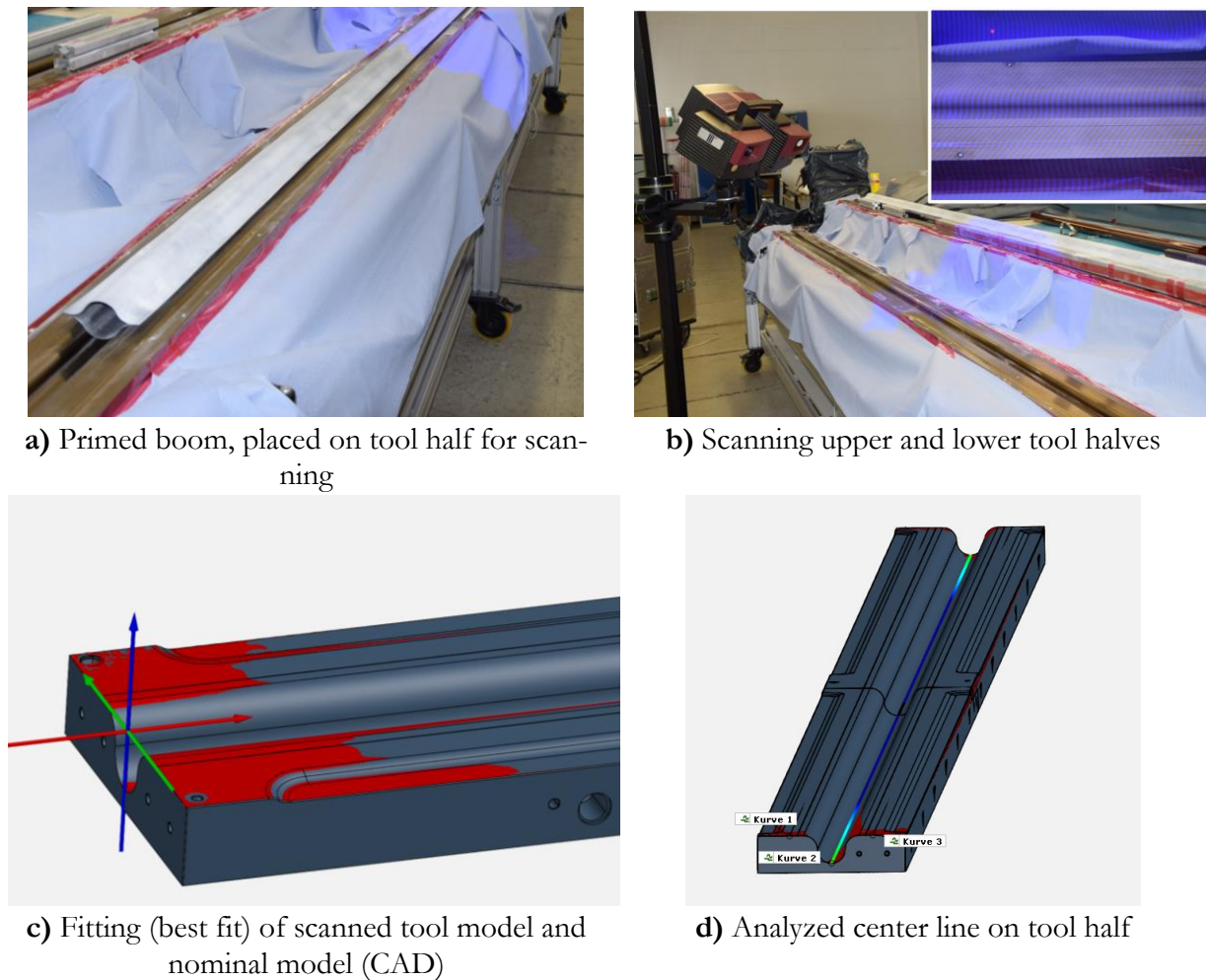
The tool itself consists of two stainless steel tool halves, a lower half and an upper half, that are separately equipped with prepreg material layup and joined for curing in an integral manufacturing process (see also patent [116]). Note that the upper tool half is not in its final manufacturing position when scanned. Instead it is upside down positioned for layup placement and later rotated about its longitudinal axis and lowered onto the lower tool half (tool is closed) and further prepared for evacuating and curing. Here the lower half is supported by a frame, carrying the complete weight of the assembled tool and layup. More precisely, the lower tool half is supported at eight pair wise floating slides, for positioning under the upper tool half, thus enabling unconstrained thermal expansion. Carrying the complete weight of the closed and assembled tool, the lower tool half is further considered as reference.

While the positioned boom can only be scanned at one side at the time, target markers on the tool increase scanning accuracy and enable subsequent assembling of scanned surface models to a complete boom surface model, to be analyzed. In contrast to this the two tool halves can be scanned in a single instance, as both are placed mold surface facing up.

For analysis preparation two steps are taken. Firstly, the scanned surface models of the boom sides are aligned by best-fit at their flange planes in a shared coordinate system. Secondly, as done previously, the according nominal CAD model is aligned by best-fit to the scanned and assembled surface model, in a shared analysis coordinate system. Similar is done for the tool, although only the second step was performed, as both tool halves are analyzed separately. Figure 6.8 c) illustrates such analysis preparation as a surface model of a tool half is aligned to its nominal CAD model.

Analysis is done on a continuous center contour line of the digitally assembled boom and the tool halves, similar to analyzing the short boom specimens discussed previously (see Figure 6.8 d). As defined prior to scanning and stowing, the upper boom side, represents the side that is molded into the upper tool half and at the same time the tensioned side when stowed. The lower boom side therefore represents the side molded into the tool lower tool half and the compressive side when stowed.



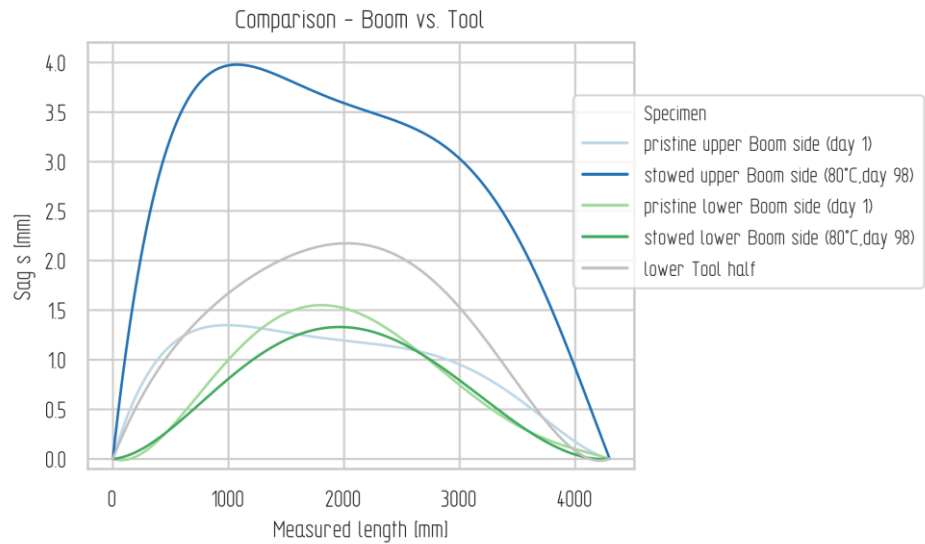


**Figure 6.8.** Scanned and analyzed 4300 mm Gossamer-1 boom and tool halves

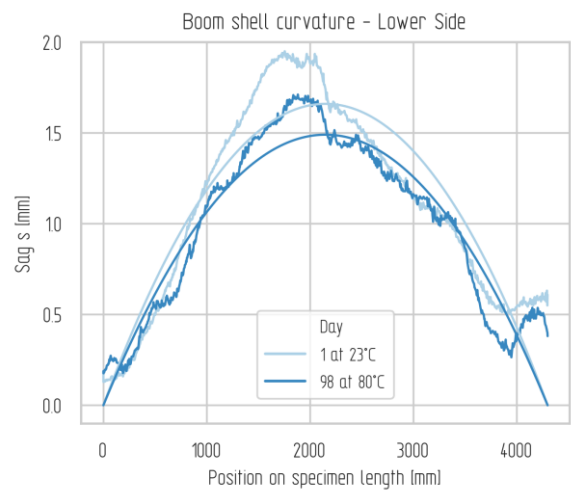
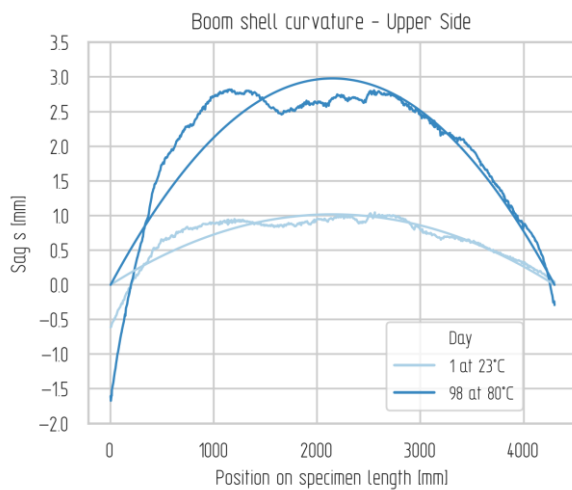
Acquired results are analyzed using diagrams and tables. In Figure 6.9 a) sag values are compared for the upper and lower boom side, in pristine condition (day 1, before stowage) and after stowage at 80°C (day 98), as well as for the lower boom tool. The displayed curvatures are determined by a linear 5<sup>th</sup> order linear polynomial regression from the acquired data points at the continuous center line. As sag increases due to stowage for the upper side (tensioned side) by 192% compared to values at pristine condition, contrarily sag values of the lower side (compressed side) seem to decrease with stowage, although by only -10%, as given with Table 6.8. These values are still smaller compared to that of the lower tool half, thus indicating that tool deformations are not fully passed on to the boom. Detailed results can also be compared when looking at Table E. 6 in Appendix E.

The approximated radii, shown in Figure 6.9 b) and c), superimposed with their according data points, decrease for the upper boom side by -68% and contrarily increase for the lower side by 11% with stowage time. The reason for this is assumed to be the nature of stress as one boom side is tensioned while the other is compressed during stowage. When analyzing the inherited sag of the according tool side, the upper boom half only inherits about one third, while the lower boom side about one half, by manufacturing.

Waviness is determined once more by linearizing by the approximated radius. As visible in Figure 6.9 d) for the upper side, waviness increases with stowage, while for the lower side, as depicted in Figure 6.9 e), stowage seems not to have such a large impact on waviness. This is consistent with findings for the short boom specimens. The results can further be followed by analyzing selected minima and maxima and their changes due to stowage with  $\Delta s_l$  and  $\Delta z_B$ , in amplitude and longitudinal position on the specimen, as given in Table E. 7, in Appendix E.

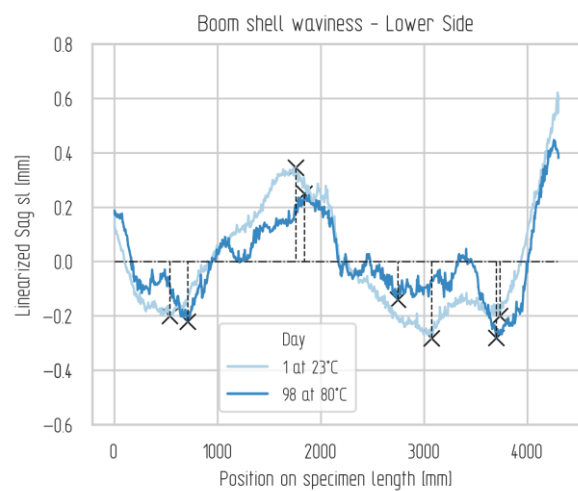
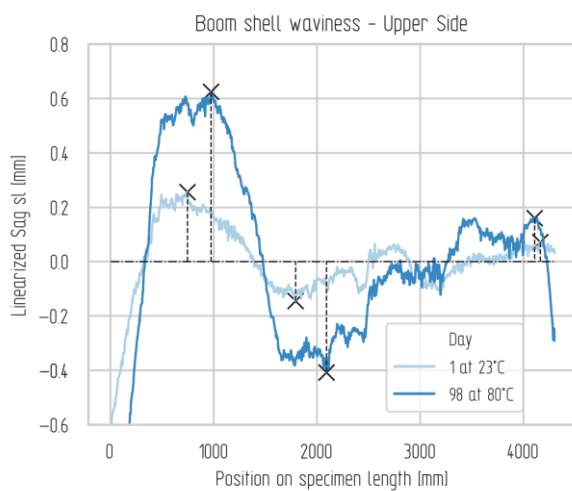


a) Comparison of curvature and sag of boom sides and tool at different stowage regimes



b) Sag and radius of upper boom side at 23°C and 80°C

c) Sag and radius of lower boom side at 23°C and 80°C



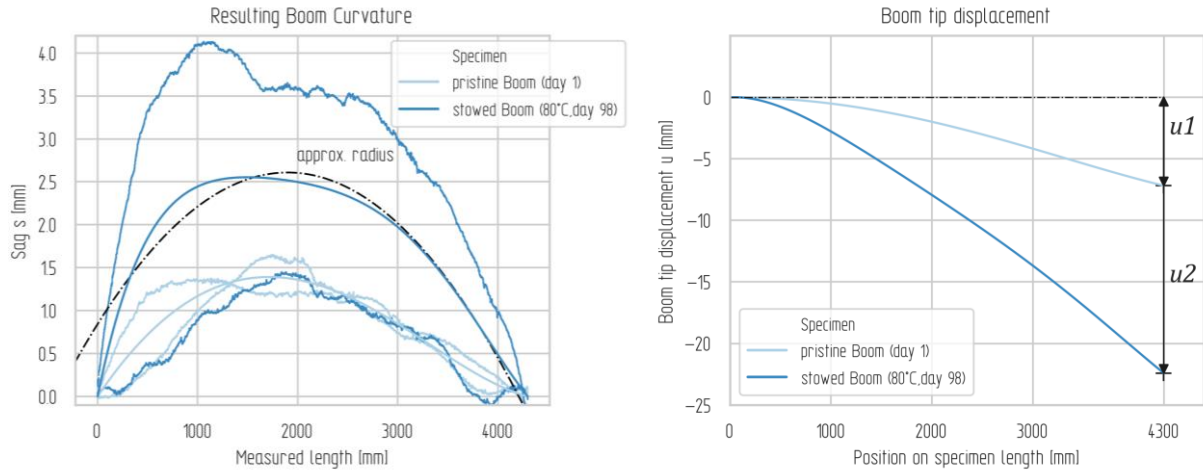
d) Linearized local buckling (waviness) of upper boom side at 23°C and 80°C (5<sup>th</sup> order polynomial regression)

e) Linearized local buckling (waviness) of lower boom side at 23°C and 80°C (5<sup>th</sup> order polynomial regression)

Figure 6.9. Sag, curvature and waviness – 4300 mm boom and tool



In order to provide a statement of the overall boom behavior the resulting curvature, sag and radius are determined as average value for upper and lower boom side, for each condition (pristine, stowed). In Figure 6.10 a) sag data is grouped by day and an average curvature is determined by linear polynomial regression (5<sup>th</sup> order) for each case. Additionally, the according radii are approximated, as displayed exemplary for day 98 in the graph. When comparing the determined curvature of both cases, boom curvature increases with stowage as expected while the radius decreases.



a) Averaged boom sag in pristine and stowed conditions (5<sup>th</sup> order polynomial regression)      b) Averaged boom tip displacement in pristine ( $u_1$ ) and stowed conditions ( $u_2$ )

**Figure 6.10.** Resulting boom curvature and sag of boom in pristine and stowed conditions

Furthermore, overall boom tip displacement, as a direct constituent of the robustness parameter  $u$  (cf. section 5.2.2), is determined. This is displayed in Figure 6.10 b), comparing pristine and stowed cases. The boom tip displacement is determined from curvature (5<sup>th</sup> order linear regressed), while generically assuming the first 100 mm boom length to be used for root fixation, being tangential to the nominal boom axis. Consequently, the displacements at the boom tip for the stowed (at 80°C) and pristine conditions are determined with  $u_1 = 7.2$  mm and  $u_2 = 22.4$  mm respectively, as provided in Table 6.9. Presuming an acceptable upper limit of boom tip displacement of 1% of the present boom length (4300 mm), further referred to as percentage limit of length, the pristine boom exhibits a percentage of length of 0.17% while under stowed condition it exhibits about 0.52%. Moreover, the partial displacement-based robustness, given with Equation (4.20), can be determined for each condition with  $Ro_{u\text{manufacturing}} = 0.83$  and  $Ro_{u\text{creep}} = 0.48$ , for the pristine (post manufacturing) and the stowed boom, respectively. These metrics can directly be incorporated in the proposed assessment method for robustness.

**Table 6.8.** Gossamer-1 boom curvature and sag

Condition	Day	Sag $s$ (mm)	Percentage Sag Change	$R^2$ (mm)	RMSE (mm)	Radius $r_B$ (mm)	Residual (mm)	Percentage Radius Change	Influence Factor $\Psi_{rB}$
Upper Boom Side									
pristine (23°C)	1	1,018	0,0 %	8,3E-03	1,32E-01	2269851	1,12E+02	0,0 %	1,000
stowed (80°C)	98	2,979	192,8 %	6,46E-02	3,73E-01	775256	1,08E+03	-65,8 %	0,342
Lower Boom Side									
pristine (23°C)	1	1,661	0,0 %	7,3E-03	2,00E-01	1390261	2,70E+02	0,0 %	1,000
stowed (80°C)	98	1,491	-10,2 %	4,55E-01	1,45E-01	1548933	1,56E+02	11,4 %	1,114
Average (resultant curvature)									
pristine (23°C)	1	1,391	0,0 %	1,3E-01	1,88E-01	1715992	6,23E+02	0,0 %	1,000
stowed (80°C)	98	2,553	83,5 %	4,76E-02	1,15E+00	1020424	2,04E+04	-40,5 %	0,595

accuracy of sag measurement: 3  $\mu$ m**Table 6.9.** Determined Gossamer-1 boom tip displacements

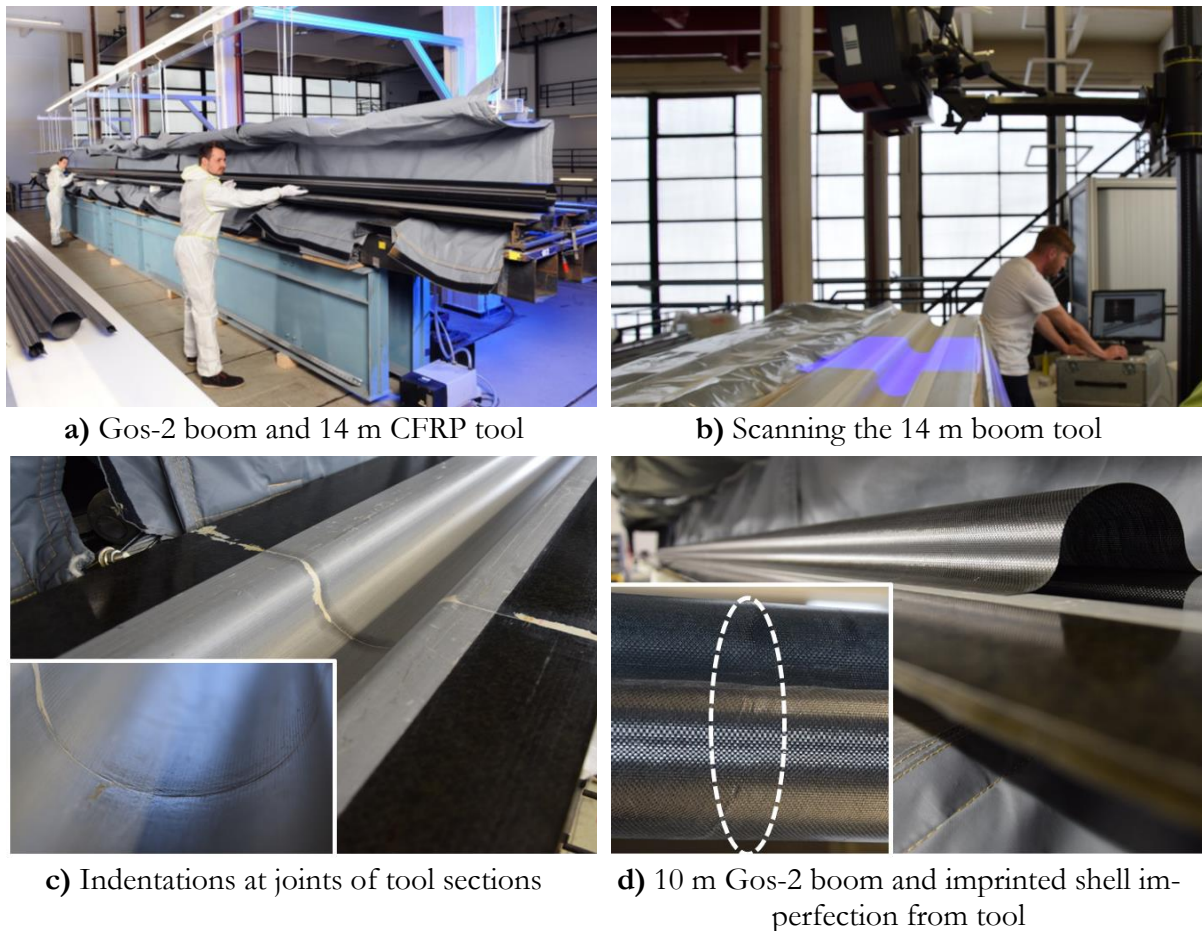
Condition	Day	Boom tip Displacement $u$ (mm)	Percentage of Length	Partial robustness $Ro_u$
pristine	1	7,2	0,167 %	0,833
stowed (at 80°C)	98	22,4	0,521 %	0,479

### 6.1.3 Manufacturing induced influences – on a 10 m Gossamer-2 Boom

For analyzing influences induced by manufacturing on a large-scale boom, a Gossamer-2 boom with 10 m in length, is scanned and analyzed, as well as its 14 m long manufacturing tool made of CFRP, as shown in Figure 6.11 a). For scanning further described in [117], the boom is placed in the mold tool as shown in Figure 6.11 b). In contrast to the integral manufacturing used for the previously discussed smaller boom of Gossamer-1, the Gossamer-2 boom is assembled from two separately cured half shells (sides), that are bonded together at their flanges. Therefore, only one tool half is used for manufacturing and scanned.

While the two boom sides are scanned separately, the obtained surface models are assembled in the analysis software and aligned by a best fit option to the nominal CAD model. The purpose of this analysis is to scrutinize the imperfections like sag, curvature, radius, waviness of boom and tool. Since the long tool is assembled by several sections, the butt joints feature some indentions as depicted in Figure 6.11 c) of unknown depth. Further it is of interest if and by how much imperfections inherent to the tool surface are transferred to the boom by the manufacturing process, as small imprinted buckles on the boom shell indicate so (see Figure 6.11 d).

From measurements, sag, curvature and radii are determined for the two scanned boom sides and tool as well as a resultant boom curvature, approximated from the two sides. Figure 6.12 a) displays sag and curvature for both boom sides, tool and the resultant boom, while the approximated radius is exemplary depicted for the resultant boom. Hence that the separate boom sides are displayed as scanned (both shells facing up), while the resultant boom considers the two sides in the symmetric orientation, with the shells facing opposite sides, as assembled during manufacturing.

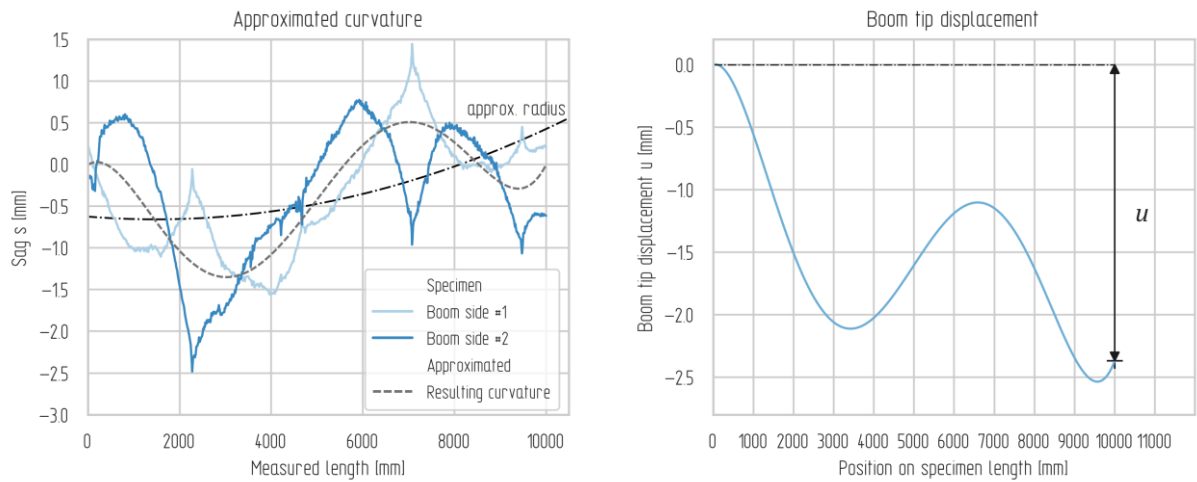


**Figure 6.11.** Scanned Gos-2 10 m boom and 14 m tool

For this long boom, sag is determined from 8<sup>th</sup> order polynomial linear regression curves, that represent the higher order curvature. As analyzed data show in Table 6.10, the maximum tool sag is almost 4 mm while the inherited sag of the resultant boom is about 66% less in comparison. This circumstance can be explained with the symmetric orientation of the assembled boom halves and their imperfections facing in opposite direction, thus balancing out curvature in regard to the resultant boom.

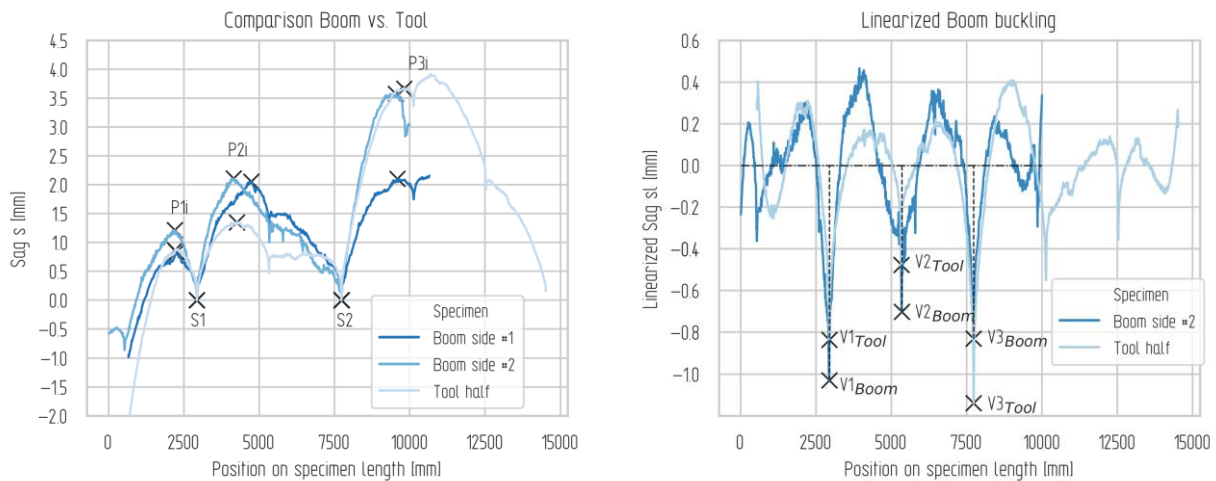
However, each side shows larger amplitudes of imperfection, closer to the one of the tool. Although an increasing sag indicates a reduced curvature that is inherited, the decreased radius of the resultant boom implies the opposite. Such conflicting results are based on the nature of higher order curvature that makes simplifications on sag and radius somewhat inaccurate.

More explicit and directly applicable to the here proposed method of robustness assessment is the overall boom tip displacement. It is determined from the resultant boom curvature (8<sup>th</sup> order linear polynomial regression) and gives a clear result independent from sag or order of curvature. For its determination, again the first 100 mm of boom length are generically assumed to be used for root fixation and to be tangential to the nominal boom axis. The outcome for the resultant boom determined in this way is visualized in Figure 6.12 b), and is quantified with the a tip deflection  $u = 2.4$  mm. Additionally Table 6.11 summarizes the results. With a presumed acceptable boom tip displacement of 1% of the boom length (10000 mm), the percentage of length only exhibits about 0.024%, indicating a good value for straightness. By applying Equation (4.20), the partial displacement-based robustness (cf. section 4.4.4), can be determined for the Gossamer-2 boom with  $Ro_{manufacturing} = 0.976$ , showing a high robustness in regard to manufacturing imperfections.



a) Curvature and sag of both boom sides; resulting boom curvature (8<sup>th</sup> order polynomial regression) and approximated boom radius

b) Resulting boom tip displacement of the 10 m Gos-2 boom



c) Comparison of deformations (sag) between boom sides (halves) and tool; normalized on support points S1 and S2

d) Exemplary comparison of linearized local buckling (here valleys displayed) of boom side #2 and tool

**Figure 6.12.** Sag, curvature and local buckling of 10 m boom specimen and 14 m tool

In order to investigate waviness, measured data of the two boom sides and tool are normalized by two shared support points (S1, S2), found as valleys and identified as indentations of the tool section joints. For this comparison boom side data is inversed at longitudinal axis, as they represent the positive of the mold tool. This is displayed in Figure 6.12 c) showing a good correlation of curves and indicating a significant transfer of surface profile by manufacturing. A further comparison of the selected peak points, however show some deviation in sag, as can be followed by the relative difference to the tool, in Table E. 8. This data is then linearized by the before determined curvature, thus providing waviness as displayed in Figure 6.12 d). Here the exemplary selected valleys of boom side #2 and the tool are analyzed and compared (values provided in Table E. 9).

In conclusion, the viewed minima are in the same range of amplitude, when compared pairwise, indicating a significant transfer of imperfections also for waviness. In terms of robustness assessment, waviness can be incorporated indirectly, by applying it as imperfection to structural models, that are used for robustness quantification.

**Table 6.10.** Gossamer-2 boom and tool curvature and sag

Condition	Sag $s$ (mm)	Percentage Sag Change	$R^2$ (mm)	RMSE (mm)	Radius $r_B$ (mm)	Residual (mm)	Percentage Radius Transfer	Influence Factor $\psi_{rB}$
Boom Side #1	2,340	-41,7 %	3,7E-01	1,65E-01	28397488	9,14E+02	-33,5 %	
Boom Side #2	3,650	-9,2 %	2,8E-02	2,50E-01	79650222	2,02E+03	86,5 %	
Resultant boom curvature	1,350	-66,4 %	1,4E-01	4,35E-01	33431382	3,02E+03	-21,7 %	0,783
Tool	4,018	0,0 %	2,6E-02	2,13E-01	42717180	4,52E+03	0,0 %	

accuracy of sag measurement: 3  $\mu\text{m}$ **Table 6.11.** Determined Gossamer-2 boom tip displacements

Specimen	Boom tip Displacement $u$ (mm)	Percentage of length	Partial robustness $Ro_u$
Resultant boom	2,4	0,024 %	0,976

#### 6.1.4 Long term Stowage induced Influences – on Boom material specimens

Influences of long-term storage of a stowed boom is imperative to know for robustness assessment and determined for the use case of ADEO, which is stored for 20 years until deployment (after satellite decommissioning), including 5 years of previous on-ground storage and 15 years stored in orbit during satellite operation. In addition, the discussed influence considerations are also applicable to Gossamer-1, that shares the same boom component and operates in the same vicinity.

Stowage is very demanding on the boom material due to the thermal loading under flexural stress.

Besides the direct geometric changes as described in the previous subsections, the goal here is to predict the degradation of the relaxation modulus after 20 years of storage in stowed configuration, thus providing material behavior under creep. This in turn is dependent on the duration of storage, the temperature the material is exposed to during storage, and the emerging stress, caused by boom stowage (flattening and reeling up).

The experiments are performed on flat boom material samples, 80 mm x 20 mm in size, that are stowed onto cylinders of seven different diameters (shown in the upper image of Figure 6.13 a) and four temperature regimes (-20°C, 23°C, 80°C, 100°C) in a controlled lab environment, as reported by Meyer & Zander in [111]. With three specimens stowed on a cylinder at a time, sets of 21 specimens for each temperature are stored and analyzed, leading to 84 specimens in total. While each set is stored for 127 days, it is followed by a period of relaxation of 14 days, adding up to overall observation duration of 141 days.

During the period of storage, the specimens are measured every four weeks. They are removed from the cylinders, placed on a holder and scanned with a 3D measuring system (ATOS Triple Scan) in climate controlled lab environment at ambient temperature conditions (see Figure 6.13 a)

Following each scan, the specimens are reeled back on their according cylinder, in their marked orientation, and stored again in the according environment. After the last day of storage (day 127), the specimens are stored flat for two weeks for relaxation in their according environment, and scanned again, in order to measure the residual plastic deformation. Flat reference specimens that have not been stowed were scanned for direct comparison. After post processing, aligning and generating surface models from the specimen scans, the measured data is analyzed. Geometric relations are analyzed and the resulting radius of each specimen is determined using the Pythagorean Theorem, measuring cord and height of the scanned specimen, as illustrated in Figure 6.13 b). As one would expect radii decrease with smaller stowage diameters and increasing temperature, while for the -20°C regime no significant change can be observed. However, the extend in which the radius contributes to the viscoelastic behavior is not further discussed at this point and can be found in [111].

More interesting in regard to robustness is the creep compliance and the relaxation modulus of the material. Resulting creep compliance curves are determined one for each temperature and radius. Generally, they are determined by applying a constant stress, while measuring strain. However, in this case strain is kept constant and time depended stress is determined according to [111] by:

*Time dependent stress of stowage:*

$$\sigma(t) = E_0 \cdot \left( \frac{z}{r_{cyl}} - \frac{z}{r(t)} \right) \quad (6.1)$$

With the coordinate  $z$  in specimen thickness normal direction,  $r_{cyl}$  the radius of the stowage cylinder,  $r(t)$  the measured specimen radius and  $E_0$  the initial Young's modulus of the boom material. The relaxation modulus is determined from the occurring stress  $\sigma(t)$  and total strain  $\epsilon_{total}$  (radius measurements and bending strain, [111]):

*Relaxation modulus:*

$$E(t, \sigma, T) = \frac{\sigma(t)}{\epsilon_{total}} \quad (6.2)$$

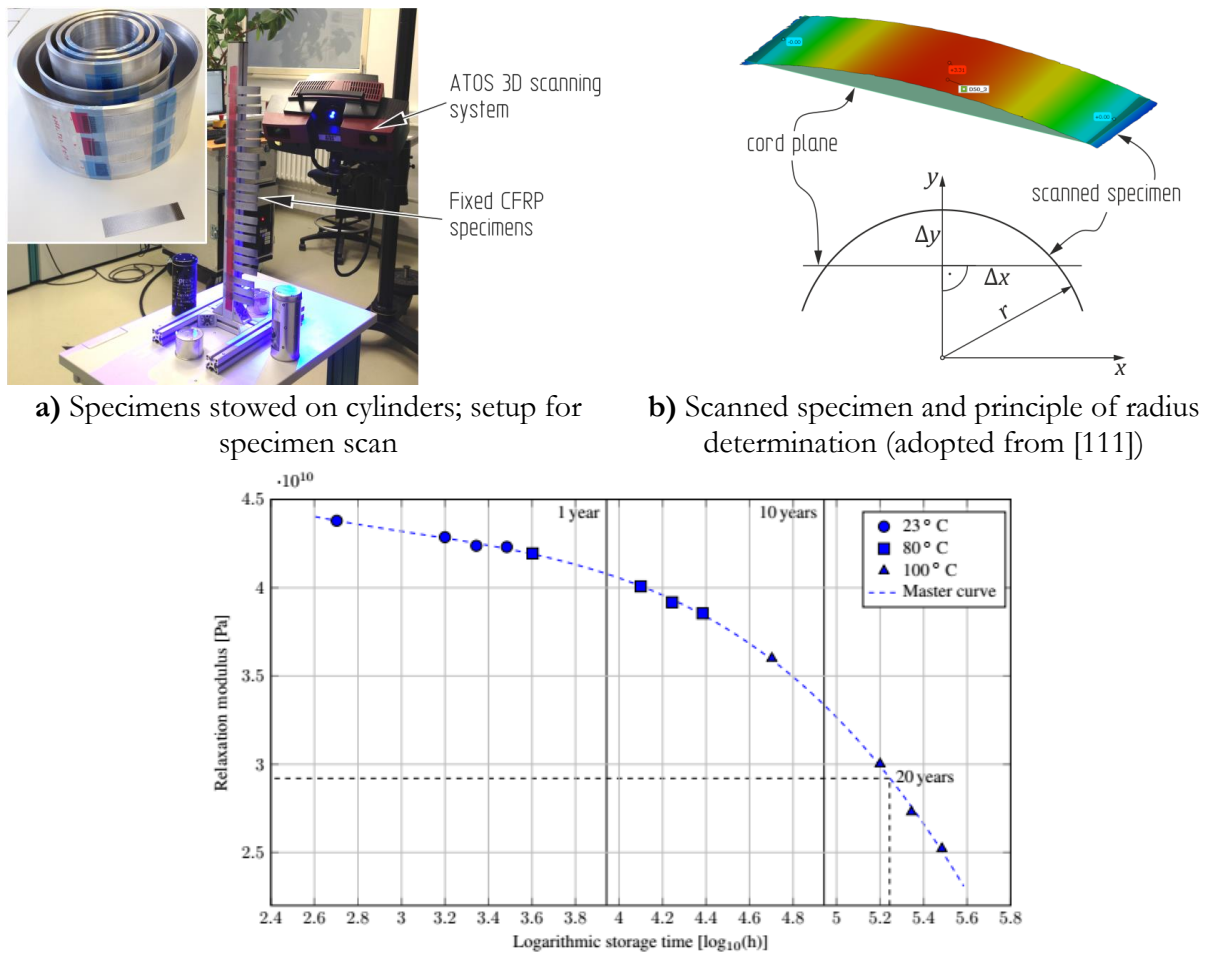
In contrast to the real time of storage of 20 years, 147 days are a comparably short period of observation. Instead of long-term storage, several short time storage tests are performed in the here presented case. However, by facilitating the time-temperature superposition method, stress relaxation curves can be determined for each regime at elevated temperatures for a short time span, by superimposing them to generate a master curve for the relaxation modulus.

This is done by manually shifting the separate relaxation curves of the elevated temperature regimes to the right on a logarithmic time axis, in relation to a selected reference curve, as shown in Figure 6.13 c) on the example of the 100 mm stowage diameter specimen set. With the 23°C isothermal relaxation curve as reference, the resulting master curve builds up as shown in this graph.

While the point of interest at 20 years of storage in stowed configuration gives an estimate of about 29.2 GPa, the resulting degradation of modulus is about 40%, considering the initial Young's modulus to be 48.5 GPa.

In terms of robustness this result can be interpreted as an influence factor that reduces the Young's modulus of a boom by storing it in stowed configuration over 20 years with  $\Psi_{Creep} = 0.6$ . In simplification, this factor could be implemented in an FE model used for robustness prediction. Nevertheless, the issue of creep and its impact on boom geometry, especially in terms of predicting long-term behavior, needs to be addressed in detail in the future work.



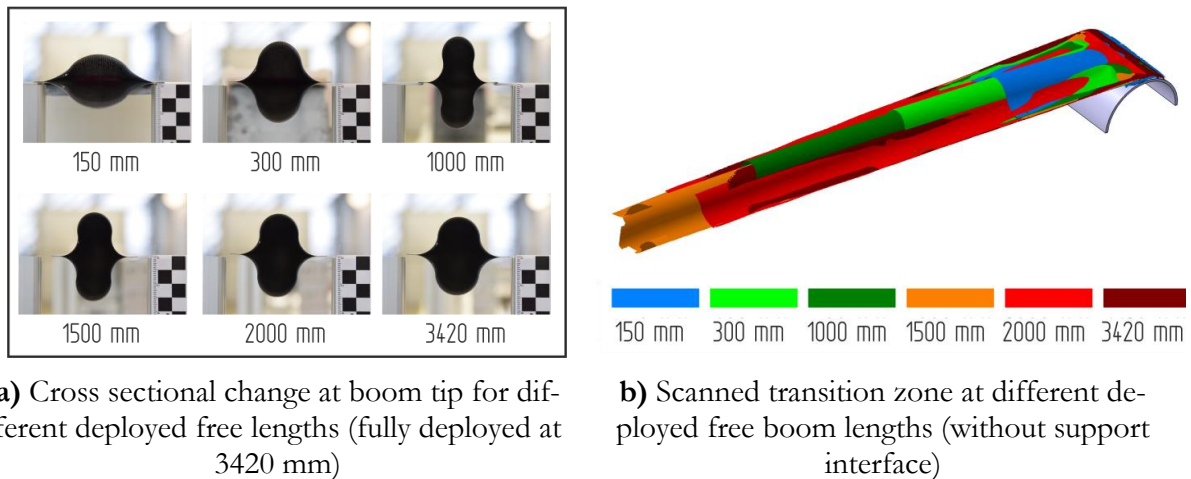


**Figure 6.13.** Creep testing of boom material specimens for estimating long-term stowage behavior

### 6.1.5 Interaction induced Influences – caused by Interfaces

As a boom deploys from its stowage hub or cylinder a transitional zone forms between the flattened to the fully deployed boom cross section. The partially flattened cross section, specifically at the boom root, provides only a reduced second moment of area and therefore a reduced local stiffness, while at the same time facing the highest bending moments due to its leverage. As this is addressed by using a mechanically guide & support device, stiffness can be maintained to some degree and boom deployment can be guided in the destined pointing direction. By doing so, the interaction between guide & support device and boom, influences its buckling behavior, buckling load capacity, stiffness and consequently robustness.

Additionally, the transition zone is changing in cross sectional shape throughout deployment, as visualized in Figure 6.14 a). It displays the changing cross section of the boom tip, captured at different free deployed lengths. Figure 6.14 b) displays the scanned transition zone of a Gossamer-1/ADEO boom deploying from its hub at different free lengths, illustrating that a rigid support device cannot be optimal for all working points and interacts differently with variation in boom length. As described by Zander et al. in [118] this is investigated under lateral bending and combined loads on three boom guide & support concepts, for the boom subsystem of the ADEO drag sail (cf. section 5.1). Further information on the concept design generation is described in [119].



**Figure 6.14.** Boom transition zone and its change with changing deployed length

Testing is performed in two configurations: one resembling different states during deployment at different lengths and angles of attack, the Deployment Configuration, and the second resembling the fully deployed state, the De-orbiting Configuration. Experiments are carried out in a vertical arrangement, with the boom mounted hanging in a test stand, as described generally for this type of performed test in chapter 7. A simulated membrane load is applied at the boom tip under a certain angle of attack, while measuring boom tip deflection and applied forces in in-flange-plane and out-of-flange-plane, thus acquiring typical load-displacement curves.

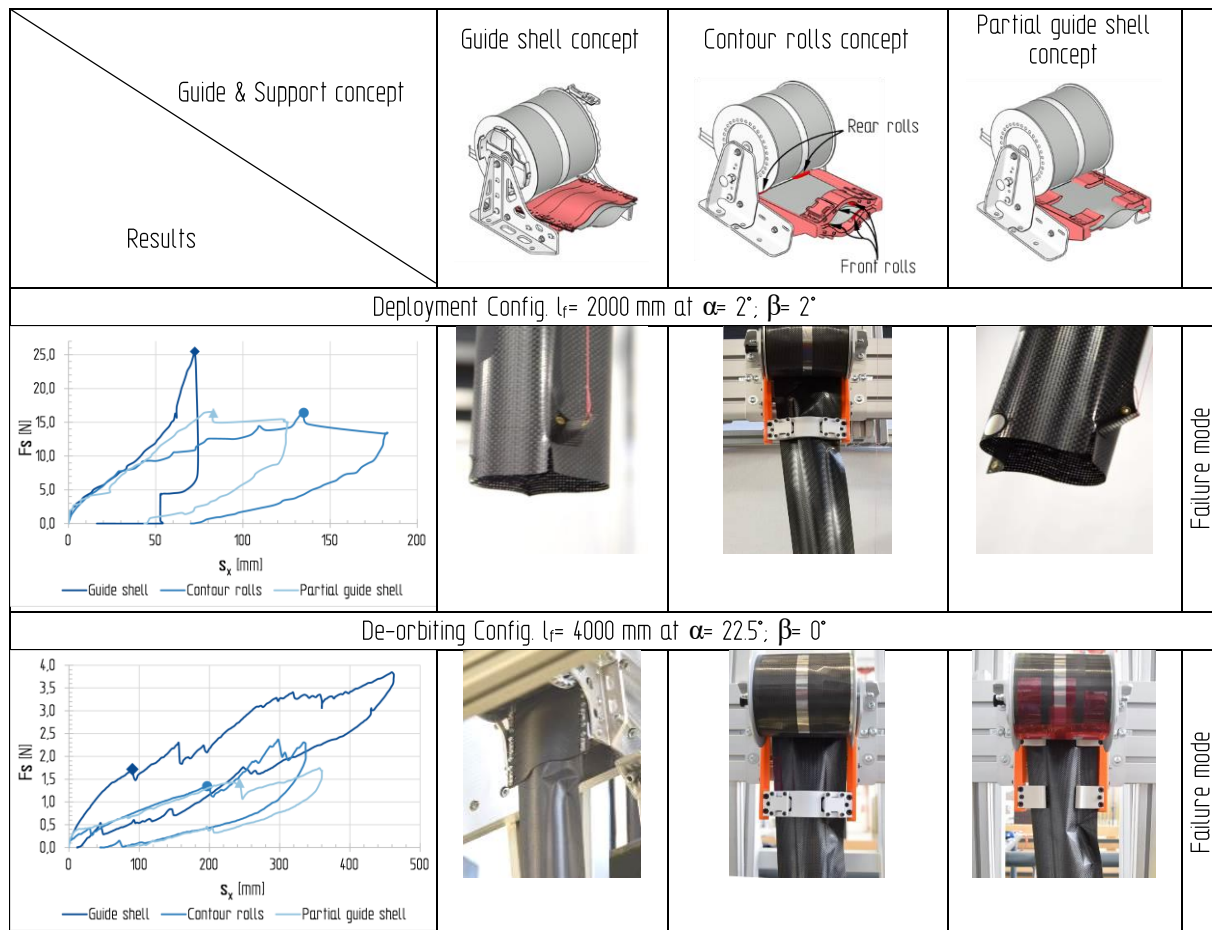
An overview of selected results is given in Figure 6.15, comparing all three guide & support concepts for each configuration. Here results are given in load-displacement curves, while providing images of the failure modes as well. Although buckling is expected to occur near the end of the guide & support device for all concepts, different failure modes are observed, as explained in the following. The examples of the Deployment Configuration exhibit a quasi-axial load under very small angles of attack in both directions. As a result, the guide shell concept delivers the highest failure load, although all three concepts show a similar stiffness (slope) in the linear region at low tip displacements. While the guide shell concept and partial guide shell concept exhibit a failure mode of tearing/shearing off the flange, the contour rolls concept in contrast exhibits buckling failure near the support device. Furthermore, the guide shell concept exhibits a sudden failure, while the other two concepts fail gradually, as apparent in the load-displacement graph.

The tested concepts in the de-orbiting configuration exhibit mainly lateral bending under  $22.5^\circ$ , in-flange-plane, without an out-of-flange-plane component. All concepts show a similar failure mode, with buckling at the end of the guide & support device. When considering the load-displacement graphs, a gradual buckling with large post-buckling zones is apparent, while the guide shell concept shows a higher stiffness (slope). Overall, the results illustrate that while different concepts might behave and fail in one configuration very similar, for another configuration this may vary greatly.

They also demonstrate that interactions of the boom with the guide & support device influences failure mode, failure loads and boom tip displacement.

How are these findings meaningful to robustness assessment or robust design? This example demonstrates the influences of interaction between boom and deployment mechanisms and their interfaces. It further shows that a “one for all” solution is hard to obtain, and that the most critical cases should be considered, and therefore robustness should be determined for the most critical configurations, while maintaining at least acceptable robustness for other cases, strongly supporting that robustness is conditional (4. Work Hypothesis). One influence factor that bears general validity cannot be determined due to the specific character of each interface, thus solely demonstrating the influence itself at this point. However particular results of boom bending tests for Gossamer-1 are used in section 7 to determine robustness in comparison to numerical simulations.





**Figure 6.15.** Influence comparison of boom-I/F-interaction on load carrying capability and failure mode under lateral bending

## 6.2 Mechanical Property Changes induced Influence Factors

In the following sections, influences and the according factors, causing mechanical property changes as identified in the previous chapter 5, are determined for material variations, space environment effects like atomic oxygen and MMOD, as well as effects by test method and equipment.

### 6.2.1 Material Property Variations

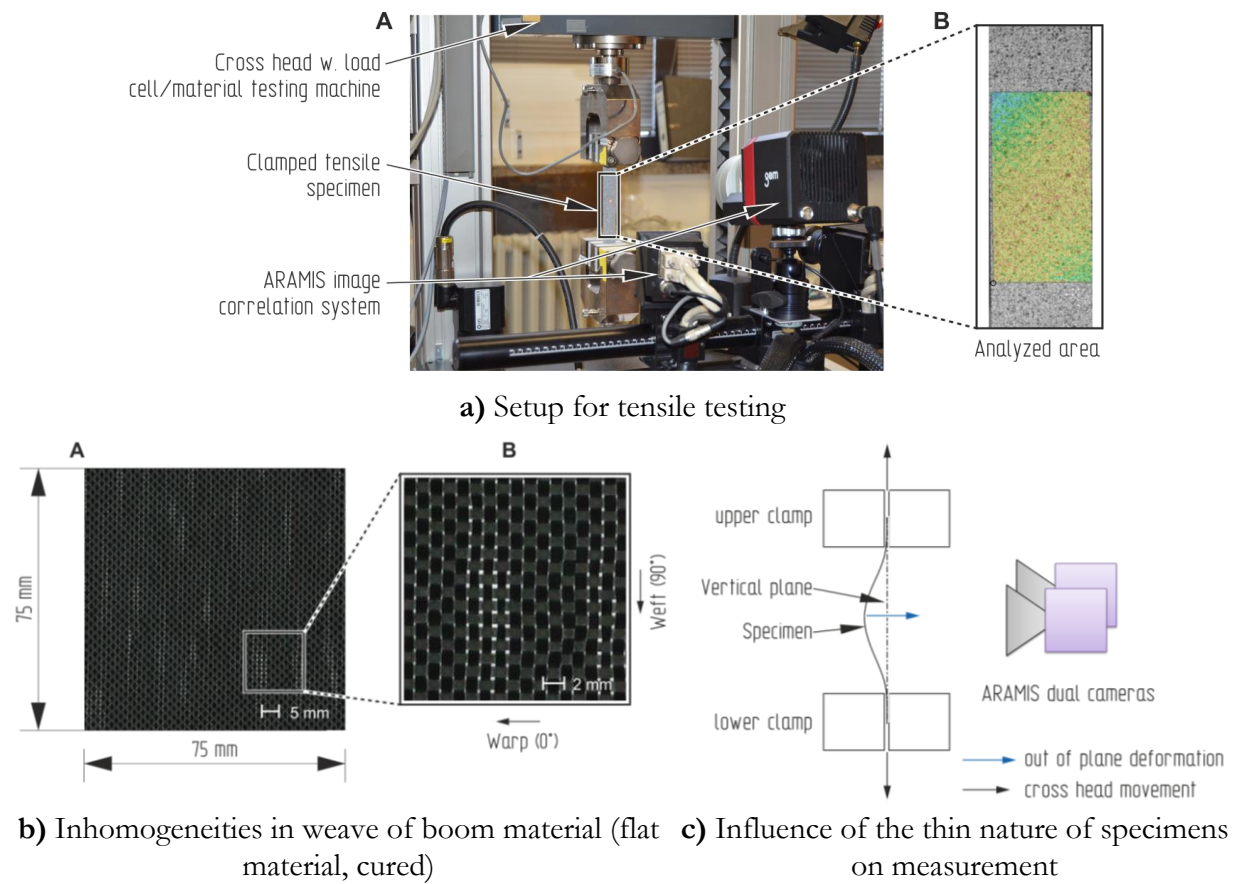
In the following material property variations caused by different influences such as influences of material inhomogeneity and influences induced by test equipment/test method are discussed. Influences induced by material inhomogeneity's are addressed by comparing mechanical characteristics of warp and weft of the boom material (cf. section 5.1.3), while influences induced by test equipment/test method are addressed by comparing results obtained by a 3-dimensional and 2-dimensional measurement setup in tensile testing.

Inhomogeneity like misalignment of rovings, gaps or displacements can be eminent in the plain weave fabric of the boom material ( $0^\circ/90^\circ$  plain weave prepreg). Such imperfections, observable in the boom material displayed in Figure 6.16 b), can render mechanical properties and therefore robustness. Here warp direction, also referred to as  $0^\circ$ -direction, falls in the  $z_B$ -axis of the boom coordinate system (cf. section 5.5), while weft direction ( $90^\circ$  direction) is equal to the  $x_B$ -axis of boom coordinate system (cf. section 5.5), and is determined boom design and manufacturing. Although such imperfections may not have a large impact on structures made up of multiple layers, they have on the mechanical characteristics of a boom with shells of only one layer.

Therefore, testing is carried out on one layer material specimens in order to specify material properties, although not complying with most standards that demand more than one layer or a larger

minimal thickness. Previous measurements of density on one layer and multilayer samples (2 mm of thickness, complying with standard) of this material support this approach. Such tests (see [120]) show that density of multilayer specimens is about 10% lower in average than density of one layer specimens, despite using the same material and manufacturing process. Expanding these findings, the Young’s modulus of warp and weft as well as shear modulus and Poisson’s ratio are determined as described in the following.

Commonly, in standard tensile tests mechanical properties are obtained using applied strain gages. Yet, as influences of local stiffening/strengthening of these thin specimens due to the bonded strain gages cannot be omitted, measurements are carried out using an image correlation system (GOM ARAMIS), analyzing the stochastic speckle pattern applied, as depicted in Figure 6.16 a). Testing routine and setup is done according to the standards DIN-EN-ISO-527-4 for E-moduli and according to DIN-EN-ISO-14129 for the shear modulus. Post-processing and analysis is performed using the GOM-Correlate software and scripted analysis routines (see [121] for details).



**Figure 6.16.** Determining material property influences – Tensile testing

Awareness of the influence by test setup and equipment arose when analyzing results obtained with 2D-measurements, a common test setup for flat samples. Contrarily to the mechanics these results partially featured negative Poisson’s ratios, indicating a transversal expansion instead of contraction, as expected. This effect was observed although precautions were taken as a pre-tensioning force of 2 N is applied after clamping the samples, to avoid out-of-specimen plane shape deviations during testing. Nevertheless, specimens billow, partially move and distort out-of-vertical plane, as illustrated in Figure 6.16 c) in this setup.

While 2D-measurements capture the speckles on a specimen and track their relative movement as well as expansion, both in vertical plane, the tracked speckles move out-of-plane towards the camera, as the specimen billows or un-billows. Consequently, the system falsely determines strain from this optical change and therefore an influenced and false Poisson’s ratio.

However, this effect can be observed until reaching higher tensile loads that straighten out the specimen and eventually suppress out-of-plane distortion. This 2D-setup effect also affects E-Moduli in both directions. In consequence a 3D-setup is applied, thus cancelling out this influence and providing more accurate values.

Compared to the 3D setup, which is recommended for further use, the 2D-measurement setup generates about 19% higher values for the E-Modulus in 0°-direction and 2.6% lower values in 90°-direction, provided as summary in Table 6.12. Note, that results are determined using the effective thickness of 0.1 mm (determined from areal weight and density), while the measured specimen thickness is larger with of 0.17 mm, due the porous single layer of the weave. Further the shear modulus determined with the 2D-setup is about 7% higher than the mean value determined with the 3D-setup, thus demonstrating the influence of test method and setup. The influence induced by material inhomogeneity can be assessed when comparing warp (0°) and weft (90°) results, as done in Table 6.12. Here the E-Moduli for warp and weft, measured in 3D-setup, differ by about 6%, with a higher mean value for the warp direction. Results obtained with the 2D-setup show an even larger discrepancy, of about 23%, again with higher values for the warp direction.

But what do these findings mean in terms of robustness assessment? Robustness determined with or based on obtained mechanical specifications that are influenced by the test method or equipment may result in an overrated robustness (regarding too optimistic material values), or on the other hand in underrated robustness when obtained specifications are lower than in reality. This undermines the effort of assessing and quantifying a realistic robustness, as measurements should be obtained with the highest accuracy possible.

**Table 6.12.** Result comparison of 3D- and 2D-setup

Measurement Setup	Young's Modulus E <sub>0°</sub> (MPa)			Young's Modulus E <sub>90°</sub> (MPa)			Shear Modulus G (MPa)		
	Mean	SD	ΔE <sub>0°</sub> (3D basis)	Mean	SD	ΔE <sub>90°</sub> (3D basis)	Mean	SD	ΔG (3D basis)
3D	47950	1564	19,1 %	45038	284	-2,6 %	2839	69	6,7 %
2D	57088	4195		43860	7842		3028	237	
Comparison 0° vs. 90° 3D:			→ -6,1 % ←						
Comparison 0° vs. 90° 2D:			→ -23,2 % ←						

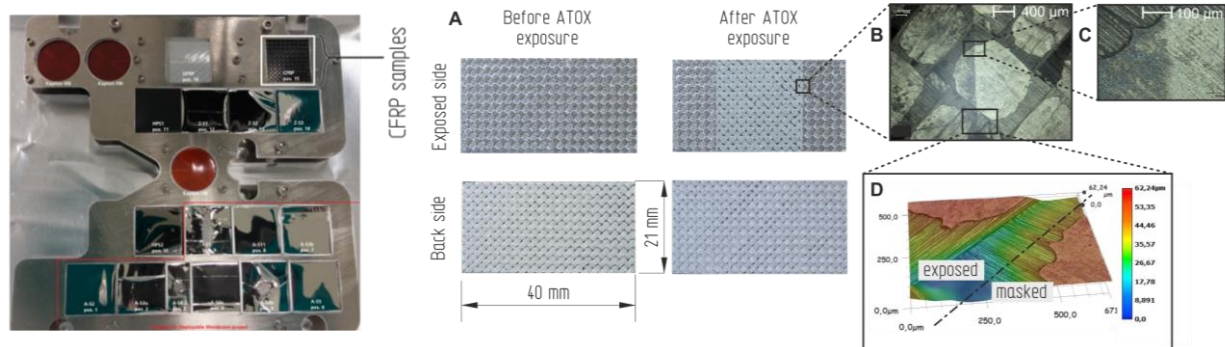
### 6.2.2 Atomic Oxygen exposure induced Influences

With the objective to determine the influence of atomic oxygen exposure on a boom and its material characteristics, a set of material samples were exposed to such ATOX environment, followed by measurements of mass, an optical surface analysis, and a subsequent mechanical test series, determining the shear modulus.

Due to the limited capacity within the test campaign only three flat boom material samples were exposed, as shown in Figure 6.17 a) with the equipped sample tray prepared for exposure in the atomic oxygen simulator at ESA ESTEC. This test campaign was carried out to simulate 20 years of ATOX exposure in LEO (700 km altitude) with an O-atom fluence of  $1 \cdot 10^{21} \frac{\text{atoms}}{\text{cm}^2}$ , as partially described in [91].

The optical analysis is carried out before and after ATOX exposure on a macroscopic and microscopic level, in order to detect any surface changes of the material. As the image collection A in Figure 6.17 b) illustrates, the exposed area can clearly be distinguished from the area masked by the sample tray. The surface on the exposed side appears dull in daylight, while a change of optical properties on the backside cannot clearly be determined. However, since atomic oxygen is not a radiation and rather free atoms, the backside was exposed as well, perhaps seeing a smaller dose.

When scrutinized under a microscope the border between exposed and masked surface area is clearly visible, with the exposed area appearing darker, shown at a magnification of 100x in image B of Figure 6.17 b). However, material ablation as one would expect is not observable. Instead a minor surface oxidization along with deposited matter of other specimens, tested in the same campaign, might be a reasonable explanation. Even when analyzing resin aggregations (due to manufacturing process at warp-weft crossings) on the exposed specimen surface at a magnification of 500x (see image C of Figure 6.17 b), no surface changes or anomalies except from the darkening can be observed. By further scrutinizing surface changes, the specimen profile is measured under the opto-digital microscope, comparing exposed and masked areas of resin aggregation at the very border, as shown in image D of Figure 6.17 b). However, no height difference is apparent.



a) Specimens on tray for ATOX exposure testing

b) A: Specimens before and after exposure; B and C: Dark area (left): ATOX exposed, bright area (right): unexposed (masked); D: Profile comparison along boundary of exposure

Figure 6.17. Microscopic images of ATOX exposed specimens

Table 6.13. Mass loss due to ATOX exposure

ATOX exposure	Mean Sample Mass (mg)	SD	Mass loss (mg)	Percentage Change
Before	124.05	0,0015	-0,83	-0,67 %
After exposure	123,22	0,0179		

As standard analysis step for ATOX exposure testing, the sample mass is measured before and after exposure under lab conditions. Summarizing the outcome of mass measurements, provided in Table 6.13, the mass loss over the simulated 20 years of exposure is very small, with only about 0.7% loss compared to pre-exposure.

Further scrutinizing the influence of ATOX exposure, mechanical tensile testing is performed, in the same manner as previously described section 6.2.1, applying the 3D-setup. The three ATOX-exposed specimens and eight non-exposed specimens as reference were tested, determining the shear modulus. As ATOX is assumed to predominantly reacting with the resin, a change in shear modulus is considered to provide the most substantial result. While generally complying with the standard DIN-EN-ISO-14129 for the shear modulus measurements, the tested samples are smaller in size than recommended (see Figure 6.17 a). This induces the effect of stiffening the specimens as the measured area is affected by clamping, and results in shear modulus values about 25% higher (see Table 6.14) than those of standard specimens of the same material (compare with Table 6.12). Nevertheless, a relative comparison between ATOX-exposed and reference specimens of the same size can be made. Consequently, the results show a reduction of shear modulus by only 1.13%. This can be translated to an ATOX influence factor for shear modulus loss of  $\Psi_{ATOX} = 0.989$ , for implementation in models for robustness assessment.

For a wider database however, a larger sample size as well as larger specimen dimensions are vital to determine robustness accurately in the future.

**Table 6.14.** Result comparison – shear modulus of ATOX-exposed vs. reference (pristine)

Measurement Setup	Shear Modulus G			
	Mean G (MPa)	SD	Percentage Change	Influence Factor $\Psi_{ATOX}$
Reference	3623,2	202,9	-1,13 %	0,989
ATOX exposed	3582,3	170,8		

### 6.2.3 MMOD induced Influences

In order to investigate the influence of micro meteoroid and orbital space debris on Gossamer-1/ADEO booms and its robustness, hyper velocity impact tests on boom samples have been carried out within the ADEO project [91]. Followed by an optical analysis of the occurring impact damage, a mechanical characterization by compression after impact (CAI) testing is performed subsequently, aiming to determine the remaining load carrying capability of a MMOD-damaged boom.

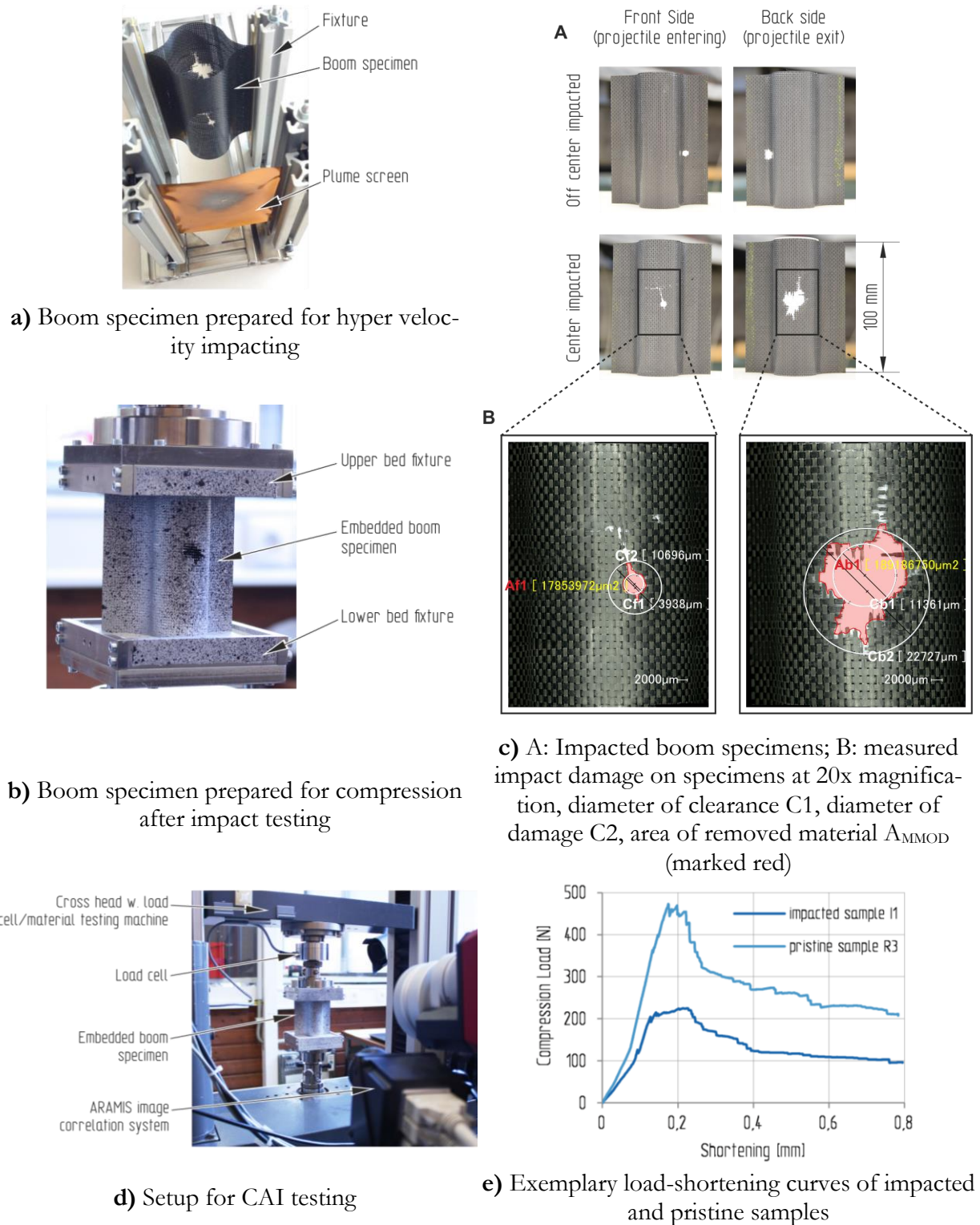
Impacting has been carried out on 100 mm boom samples with the Electrothermal Accelerator of the Institute of Astronautics of the Technische Universität München. The impact projectile, a nylon cylinder, 4 mm in diameter and 2 mm in length, simulates a typical debris particle in LEO, and is shot at a specimen with a velocity of 4 km/s, thus generating about 224 J impact energy.

During impacting, the boom samples are mounted in a fixture as displayed in Figure 6.18 a). Moreover, the boom specimen is shielded by a plume screen from gaseous gusts generated by the plasma gun that accelerates the projectile. Overall four specimens were impacted, three of which were penetrated at their center and one off-center near the boom flange, as displayed for comparison in image A of Figure 6.18 b).

Following impacting, the degree of damage caused by the projectile entering and exiting a specimen is measured under an opto-digital microscope. As expected, damage is larger at the specimen's back shell (back side), at which the projectile exits, than at the front side where the projectile enters. While penetrating the front and leaving sharp damage edges about the size of the diameter of the impact object itself, the projectile carries along fragments of the front shell that disperse over the travel distance and hit the back shell causing more severe impact damages.

In the optical analysis three measures are taken at each side of a specimen, the diameter of clearance C1, by best fitting a circle into the damage opening, the diameter of damage C2, by best fitting a circle enclosing most part of the damage opening (not regarding cracks), and the area of removed material  $A_{MMOD}$  by precisely measuring the area along the edges of the damage opening, including smaller break-outs. This is illustrated in image B of Figure 6.18 b). While the diameters exhibit a ratio of front-to-back side of about 1/2, the exact measurement of the removed shell area exhibits a ratio of 1/6, as results indicate in Table E. 10 in Appendix E. Furthermore, the exact measurement of the removed area is one magnitude larger than the approximated diameter measurements. Due to the higher accuracy, it should further be used. Regarding the relation between entrance and exit damage, the removed area of the entrance damage is about the four times the size of that of the projectile diameter, while the exit damage is almost 25 times its size.





**Figure 6.18.** Impact, optical analysis and compression after impact (CAI) testing of boom specimens

In preparation of the subsequent compression after impact testing, specimens are embedded to provide clear boundary conditions and a fixation to the material testing machine as shown in Figure 6.18 c). The test setup with the specimen mounted in the testing machine, as depicted in Figure 6.18 d), also comprised the image correlation system ARAMIS, in order to record and measure buckling patterns. This, however, is not analyzed at this point, but provides data for future research. While all four impacted specimens were tested, nine pristine specimens were tested for reference as well, generating the results provided in Table 6.15. Additionally, an example of buckling curves is

given in Figure 6.18 e) for comparison of both specimen types. It can be seen that on average, the impacted specimens achieve a lower limit load at buckling failure of about 291 N, while the pristine reference specimens achieve a limit load of about 385 N. Hence, the remaining load carrying capability of the impacted specimen is about 75% of that of the pristine one. In consequence an influence factor for the boom can therefore be determined with  $\Psi_{MMOD} = 0.756$ , regarding the loss by impact damage, although limited to an axial compression load case.

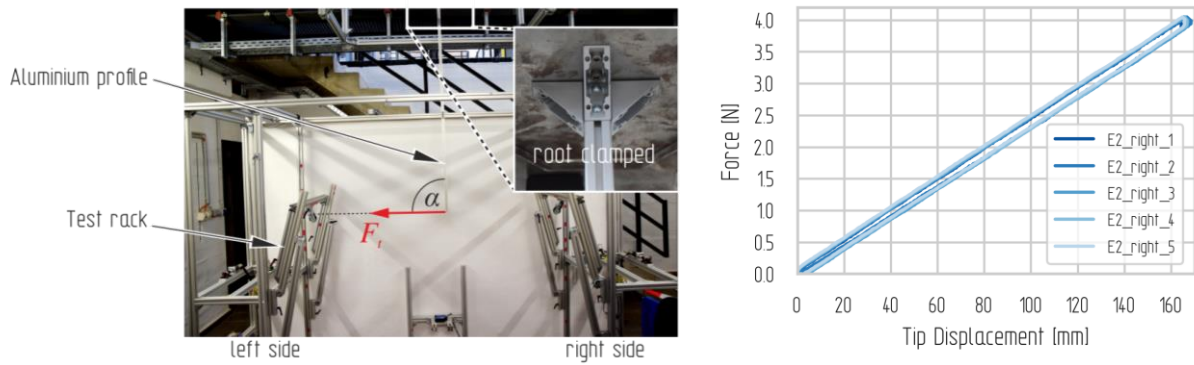
**Table 6.15.** Buckling load of impacted Gos-1/ADEO boom specimens

Sample	Limit Load $F_L$ (N)	SD	Mean $F_{Lmean}$ (N)	Remaining Load carrying capability	Influence Factor $\Psi_{MMOD}$
R1	340,4	43,2	384,9	75,6 %	0,756
R2	404,5				
R3	472,9				
R4	362,9				
R5	366,5				
R6	360,4				
R7	406,0				
R8	412,8				
R9	338,0				
I1	224,6	59,0	290,9		
I2	298,2				
I3	274,1				
I4	366,5				

#### 6.2.4 Test Equipment induced Influences

In an effort to determine the influence on mechanical results, acquired with the boom test stand (described in section 7), and on robustness in consequence, a standard aluminum profile beam (20 mm x 20 mm, 3900 mm in length) was tested analogously to booms. The profile beam is mounted in the boom test stand vertically hanging, while its root is clamped, as illustrated in Figure 6.19 a). Stiffness measurements are carried out by deflecting the profile tip at a 90° angle of attack, relative the its vertical axis. For comparison, the beam's bending stiffness is analytically calculated in parallel for a cantilever beam case, with its Young's Modulus and second moment of area provided by the manufacturer's data sheet.

As generally done in boom testing, tip displacement is performed in the two main directions used in the test stand, to the left and to the right. For each side 10 repeated runs are carried out. Presuming a linear relationship for small displacements and staying within the region of elastic deformation, tip displacement is limited to about 160 mm, while not exceeding a force of 4.1 N. With the obtained load-displacement curves, the linear behavior echoes, as shown in Figure 6.19 a). However, as expected in reality the curves show hysteresis when reversing displacement (relaxing). This is assumed to arise due to inner losses by friction and the pulley-string system of test stand itself.



a) Test setup – aluminum profile mounted in test rack b) Transversal force over tip displacement – stiffness determination

**Figure 6.19.** Determining influence factor and error of the boom bending test stand with a reference aluminum profile beam

As mentioned before the influence of the test equipment and test method is quantified by comparing the analytical solution with test results for bending stiffness. These results are summarized in Table 6.16. However, since measurements of stiffness and limit loads are obtained from the positively deflecting branch of a load-displacement curve, the reversing one (relaxation) is only qualitatively analyzed and is not further discussed at this point, but can be found in [117].

While the results show small standard deviations (SD), thus implying good accuracy of repeated test runs, the measured stiffness mean values show some deviation from the analytical solution.

This difference over all test runs and both sides tested, is  $2.45 \times 10^{-2}$  N/mm in absolute values, thus translating to an -3.8% error. As one would expect, measurements with the boom test stand are generally lower in reality. However, quantified influences need to be derived from them in order to incorporate this influence in robustness when using these measurements.

From these results an influence factor  $E_{equip}=0.962$  can be derived, to be applied when generating results with the according equipment for robustness assessment.

**Table 6.16.** Result overview aluminum beam - Measured vs. analytical bending stiffness

Load case		Spring stiffness C					Influence Factor $\Psi_{equip}$
		Mean C (N/mm)	SD (N/mm)	SD [%]	Difference to analytics (N/mm)   %		
analytical		2,55E-02	-	-	-	-	0,962
pos. deflection	Right	2,40E-02	9,42E-06	0,039 %	-1,48E-03	-5,8	
	Left	2,50E-02	1,15E-05	0,046 %	-4,44E-04	-1,7	
	Overall	2,45E-02	1,05E-05	0,043 %	-9,60E-04	-3,8	

### 6.3 Chapter Conclusion

Concluding this chapter, it demonstrates realistic influences on the performance of a boom and its material, and consequently the robustness derived from this data. It therefore supports **1. Work Hypothesis** and **3. Work Hypothesis** with measured and quantified influences. In specific geometric dimension, changes and mechanical property changes were investigated. Influences of long-term storage in stowed condition and manufacturing influences were studied on short boom samples stored at 23°C and 80°C. Here cross-sectional changes lead to a reduction in height and an increase in width over time and increasingly with elevated temperatures. Sample straightness was determined in terms of sag, curvature, radius and waviness, showing an increasing influence with storage time span and temperature, and a noticeable difference in behavior between tensioned and compressed



sides. Influences induced by manufacturing and long-term storage on full size booms were measured in terms of straightness and waviness of a 4 m Gossamer-1 boom and a 10 m Gossamer-2 boom. Full size booms are showing some differences in curvature compared to short samples, as they provide a full picture with the complete boom length. Additionally, manufacturing tools were analyzed in order to determine the extent of imperfection transfer to the manufactured booms. Moreover, influences induced by space environment like atomic oxygen and hypervelocity impacts of MMOD, as well as influences induced by test equipment and setup were investigated by determining characteristic mechanical metrics. Under the aspect of the here proposed robustness assessment method, this chapter providing essential constituents in terms of major factors for influences of the herein studied Boom Subsystem.

## 7. METHOD APPLICATION – CASE STUDY

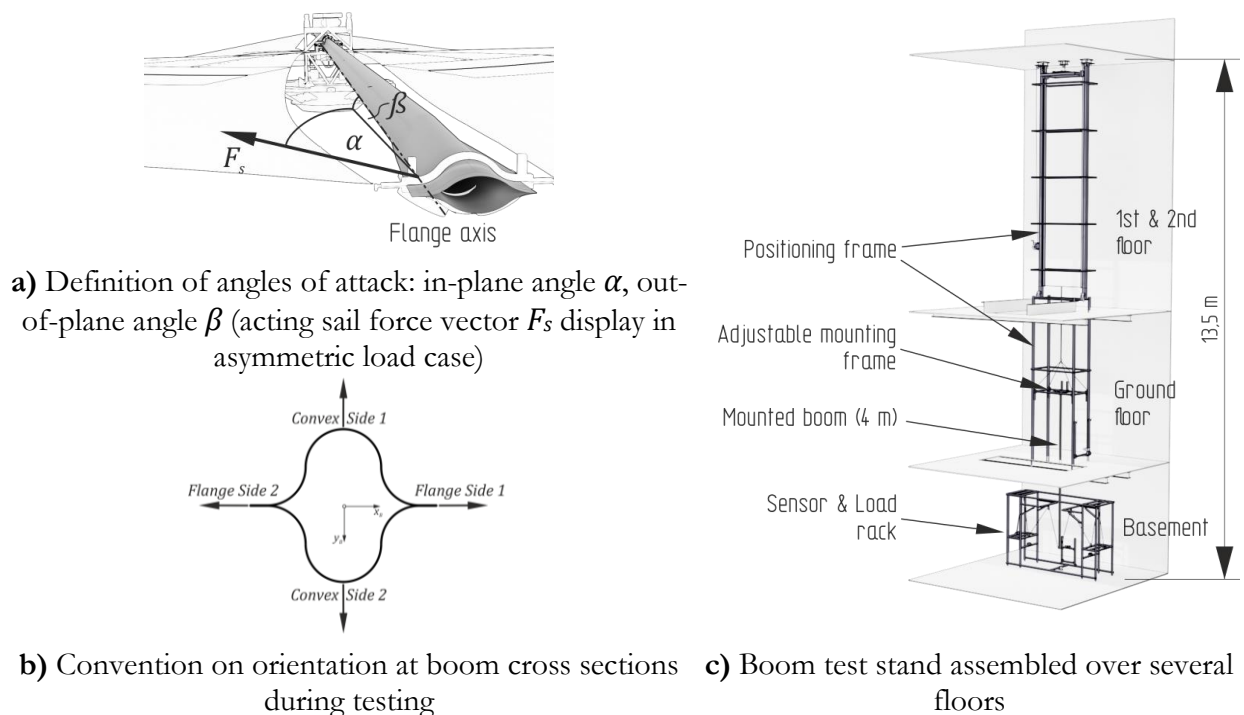
This chapter applies the before developed method for robustness assessment to the case study of the Gossamer-1 Boom Subsystem and boom component. It further determines the necessary robustness parameters in boom bending tests and applies the found influences and influence factors within a predictive finite element analysis. Moreover, robustness is quantified and compared for the investigated subsystem.

### 7.1 Assessment in mechanical Boom Tests

This sub-section describes the practical realization of several sub-tasks within the strategy for robustness quantification (cf. Figure 4.13.) as described in section 4.5, with the execution of experiments in sub-task 4.1b, result assessment (sub-task 4.3), the calculation of partial robustness (sub-task 4.4) and sub-system robustness (sub-task 4.5).

#### 7.1.1 Boom Test Stand & Test Principle

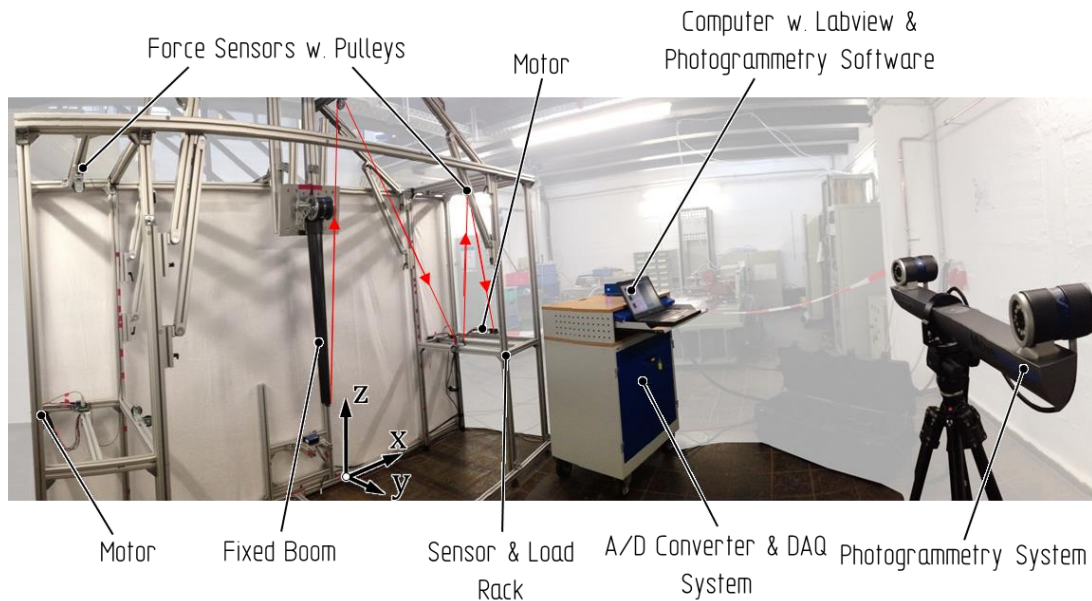
The objective of mechanically testing the booms can generally be described as characterizing the mechanical behavior of a boom or boom subsystem, including interfaces and partially deployment mechanisms. With this, typical load cases, such as bending, axial compression and combinations of both, are applied and measured. Applying known load cases exerted on a boom or boom subsystem, as described for following example of Gossamer-1, as well as generic load cases that provide a basis for comparison over all boom subsystem independent of the aspired application, are commonly applied. However, in mission related testing mostly worst-case scenarios are tested. Test data in terms of boom tip displacement and applied string load is generated, thus providing load-displacement curves and metrics like buckling failure load, stiffness and tip displacement, representing the identified robustness parameters (cf. section 5.2.) characteristic load  $L$ , stiffness  $\kappa$  and boom tip displacement  $u$ , respectively. Overall, this test stand may provide quantified data to determine performance and derive robustness, serve as realistic comparison for finite element or analytic models, and consequently data for further design developments of boom subsystem and other related subsystems.



**Figure 7.1.** Boom test stand and conventions

While the Membrane Subsystem and Interface Subsystem exerts a force vector into the Boom Subsystem, as described for Gossamer-1 in section sections 5, this vector is oriented by two different angles of attack defined with regard to the theoretical membrane plane, depending on the application. For Gossamer-1, one is defined as in-flange plane with angle  $\alpha$  while the other reaches perpendicular to that out-of-flange-plane with angle  $\beta$ , as illustrated in Figure 7.1 a). In the test stand, in- and out-of-plane angles are consistently applied in the same orientation, lengthwise in the Sensor & Load Rack and perpendicular, respectively. It can distinguish in two major load cases to be tested: an asymmetric load case, ruled by lateral bending, and a symmetric load case, ruled by axial compression. In an ideally loaded sail craft, the force vectors of adjacent sail segments generate a symmetric load introduction causing the boom to be loaded mainly in axial direction, exhibiting axial compression. While this type of loading is most favorable for booms, resulting in the highest load values in axial direction, reality imposes asymmetry in load distribution over the different structural system elements. In the space application (GosSSS), bending during deployment, operation, and e.g. spanning the sails, may occur due to friction in mechanisms and the non-uniform membrane deployment due to folding, seen in an asymmetric manner. Therefore, worst-case scenarios with an asymmetric load introduction, thus leading to bending or a combined load with bending as main component are necessary to investigate.

In order to determine mechanical properties regarding for a Boom Subsystem or boom component holistically, tests in all four cross sectional directions are performed. For this, conventions of applied load directions in regard to the boom's cross section are established, to enhance clarity within different test scenarios. These directional conventions are displayed in Figure 7.1 b) with in-flange plane applied force directions: flange side 1 and 2 (FS1, FS2), and with directions perpendicular to the flange plane, referred to as in direction of convex sides, with convex side 1 and 2 (CS1, CS2).



**Figure 7.2.** Boom test stand – Sensor & Load Rack (load string marked red; visual load adapter on boom tip not displayed)

The used test stand is a vertical multi-load test stand and is designed to mechanically characterize the thin shell CFRP booms with different sizes under a variety of load cases. For testing, booms are mounted vertically hanging in the test stand, with the boom tip facing downwards as depicted in Figure 7.1 c), and consequently fixed on the structure of the surrounding building. The test stand itself reaches over two floors of the building, from the basement up to the second floor, enabling a free boom test length of up to 13.5 m, depending on the necessary root fixture. It consists of three main elements (see Figure 7.1 c): The sensor & load rack, hosting force sensors, laser sensors,

redirection pulleys and actuators (motors), including a mobile photogrammetry system; the height adjustable mounting frame on which the boom is mounted to (at its root via interface) and can be positioned according to the required free boom length; and the positioning frame that is fixed to the surrounding building, guiding the positioning table and consequently holding the boom and its fixture.

Measuring the mechanical characteristics of a mounted boom, the sensor & load rack as depicted in Figure 7.2., is the central element of the boom test stand. The load is applied by a string-pulley-system to the boom tip, with one string end connected to the boom tip, a specific test interface (Visual/Load Adapter) or a realistic boom tip interface and the other end being reeled up with two electrical motors. The applied boom tip deflection results in the string reaction forces in the according direction. By positioning the adjustable pulleys on swivel arms, angles of attack in the test stand can be accommodated, with  $\alpha$  from  $0^\circ$  to  $90^\circ$  and  $\beta$  from  $0^\circ$  to  $10^\circ$ , to the needs of the investigated load case. This enables symmetrical as well as asymmetrical load conditions. Note that in-plane angle  $\alpha$  is applied within the x-z-plane of the test stand coordinate system, while out-of-plane angle  $\beta$  is in the y-z-plane. Super positioning of both angles is applied for load combinations.

Occurring boom tip displacements are measured with a photogrammetry system (AICON Move Inspect HR) in all 6 degrees of freedom at an accuracy of  $25\ \mu\text{m}$ , facilitating two five-mega pixel resolution cameras in stereo. A Visual/Load Adapter fixed at the boom tip serves as an optical tracking target, while transferring the applied string load into the boom structure at the same time. Complementary, three laser triangulation sensors are used for measuring very small displacements if needed. The occurring tensile forces in the load applying strings are measured by two load sensors integrated in the pulley system, one at each side. This is illustrated in the schematic of the Sensor & Load Rack in Figure 7.3. and further provides an overview of all components and their interactions. Throughout testing, a synchronous process of measuring is realized by triggering all sensors in the same frequency of 9 Hz. Furthermore, all sensor and measured data is gathered in, while motors and triggering are controlled by a single data acquisition system using a customized LabVIEW© environment.

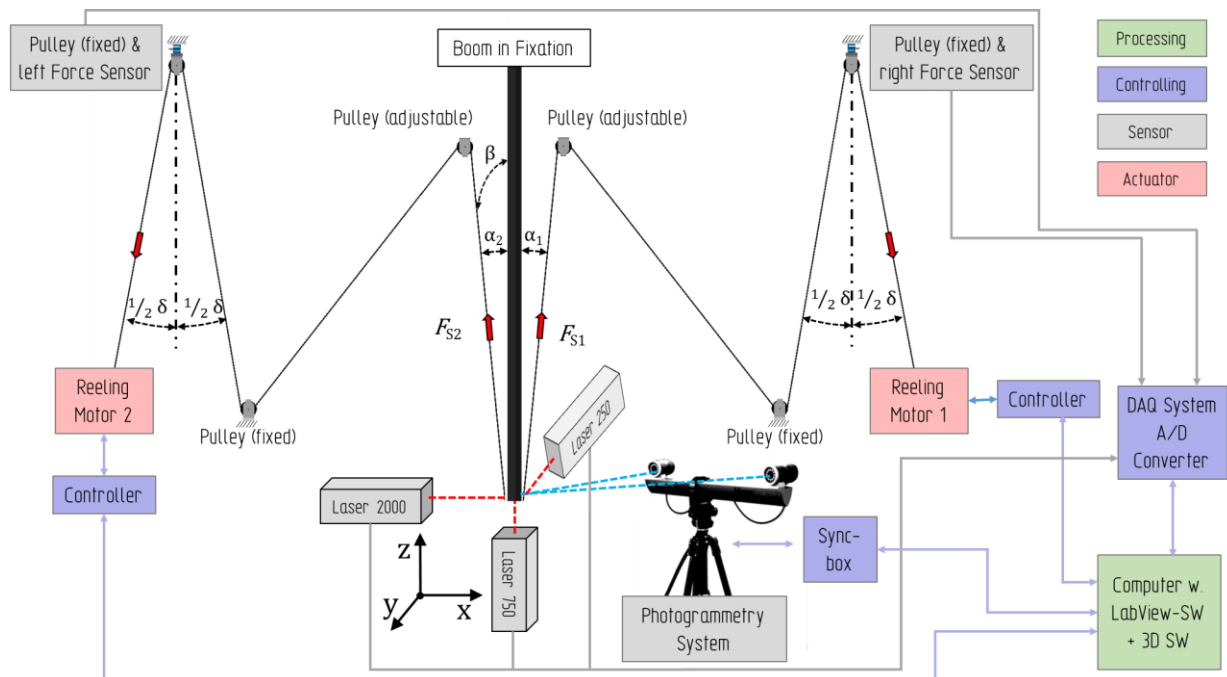


Figure 7.3. Boom test stand – Scheme

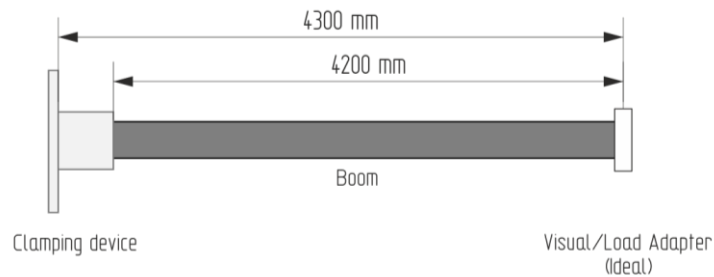
### 7.1.2 Testing Gossamer-1 Boom Subsystem and Boom Component

Within the here described test campaign 3 Gossamer-1 Boom Subsystems and 3 booms, with a free test length of 3800 mm (4300 mm overall length) and 4300 mm respectively, each were tested. For simplification, both are further referred to as boom. While two main load cases are applied, lateral bending under different angles of attack and axial compression, two main configurations are investigated, an ideal configuration, clamping the boom root and testing the boom component, and a realistic configuration with the boom mounted in its interface (BSI, cf. section 5.1.3), thus testing the Boom Subsystem. Both configurations and their differences in dimensions are illustrated in Figure 7.4, while the different components used for fixation and load introduction are described in the following subsections.

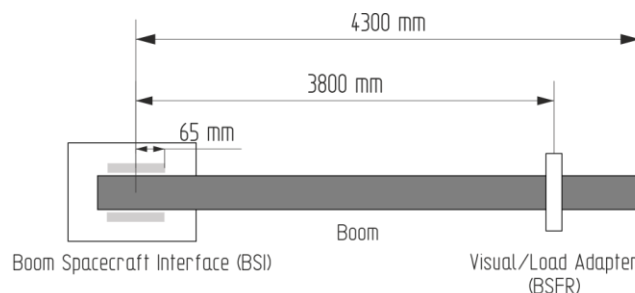
Furthermore, it should be noted that each boom was tested multiple times, in different test scenarios, due to the effort of manufacturing CFRP booms. However, with the knowledge from past boom testing, showing that buckling due to lateral bending almost always occurs near the boom root fixation [35, 109, 113, 122], both ends of a boom and both sides were tested, without fearing large impacts on measurements. This was realized with one boom end deflected in the direction of both flange sides, while the other end was deflected in the direction of both convex sides. Under axial compression, only one boom end per boom was tested, since in most cases Euler buckling is observed resulting in buckling (snapping in) at the boom's mid-section. Overall 40 test runs for all load types and configurations were performed, providing the base of the analyzed data.

#### Tested configurations:

*Ideal (Clamped)-Configuration* – A boom “ideally” clamped at its root, and using a Visual/Load Adapter that keeps the fully deployed cross sectional shape of the boom tip



*Real (Spacecraft)-Configuration* – A boom mounted in a spacecraft interface at its root, and using a Visual Load Adapter that simulates the boom-sail interface (BSFR) of Gossamer-1



**Figure 7.4.** Dimensions of tested configurations

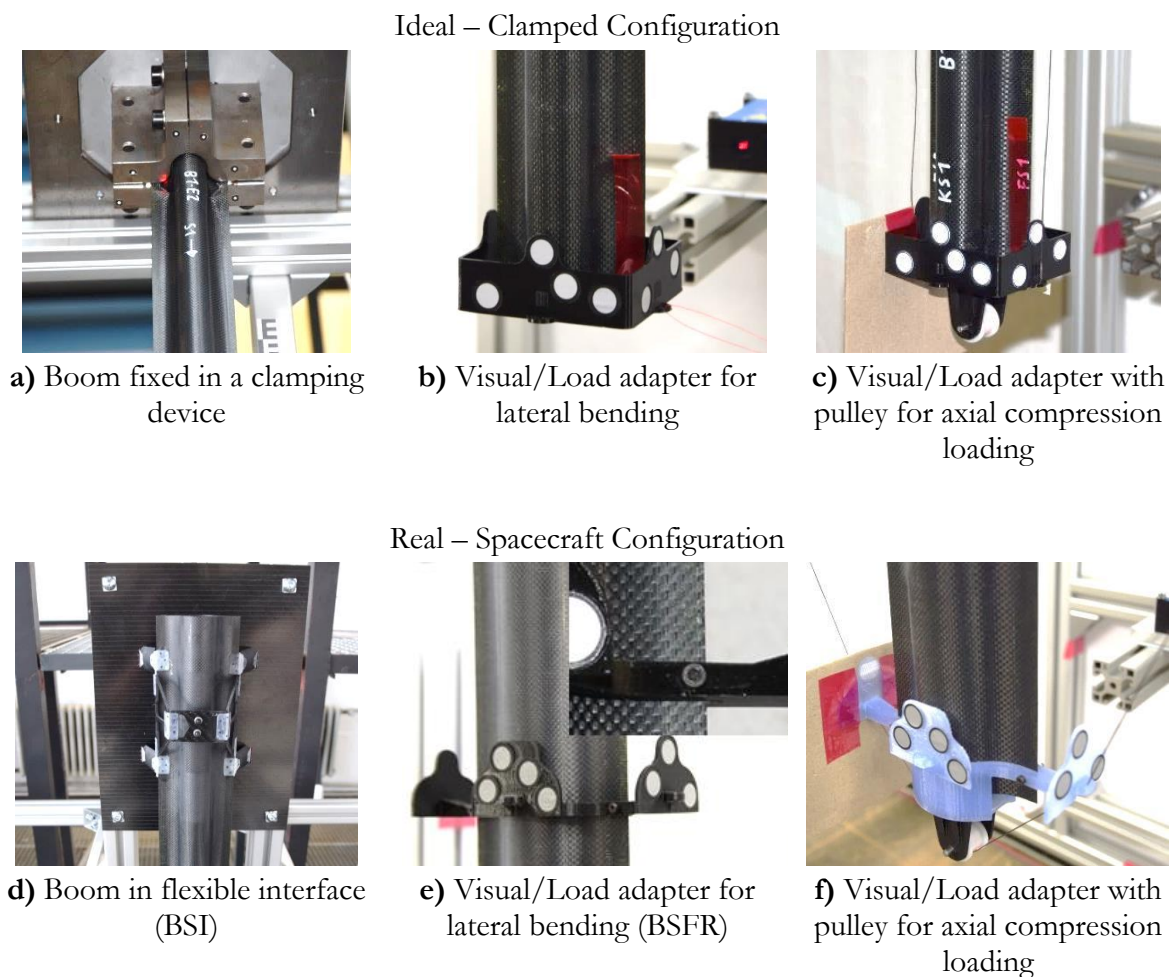
### Load Application and Boundary Conditions

While the boom/Boom Subsystem is mounted in the test stand in the two test configurations, certain boundary condition at the fixed boom root and the freely movable boom tip need to be established.



Hanging upside down, in both configurations, the boom tip is able to realize translation and rotation in all 6 degrees of freedom, while the load is introduced by a Visual/Load Adapter. In the ideal “clamped-configuration”, the boom root is fixed over length of 100 mm with a clamping device, featuring four clamps and metal core, inhibiting all degrees of freedom as shown in Figure 7.5 a). The used Visual/Load Adapter for this configuration constraints its boom tip by keeping the cross section the fully deployed state, somewhat like an end cap with optical targets applied (see Figure 7.5 b). It maintains the full cross section throughout load application and tip displacement. The load applying string is attached via eyelets at the according side of testing. For axial loading the adapter is equipped with an additional pulley (see Figure 7.5 c), guiding the string while transferring the symmetrical load into the boom tip in axial direction as a resultant load.

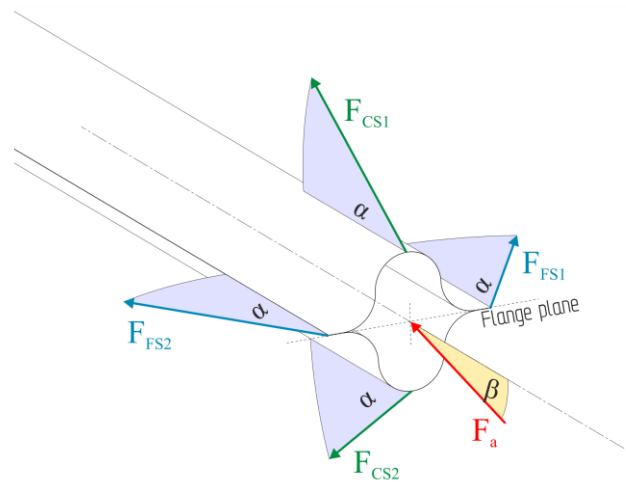
For the “spacecraft-configuration”, further referred to as real configuration, the boom is assembled to its flexible boom-spacecraft-interface (BSI) as described in section 5.1.3, and mounted by its plate to the test stand, as illustrated in Figure 7.5 d). This interface somewhat allows for cross sectional deformations in the root area, due to its folding function. The used Visual/Load Adapter for this configuration resembles an early version of the boom spacecraft interface of Gossamer-1 (BSFR, cf. section 5.1.6), equipped with optical targets, as depicted in Figure 7.5 e). As this is used for lateral bending with the load string attached to an eyelet at the according side to be tested, another version of the Visual/Load Adapter, featuring a pulley, is used for symmetrical testing and applying axial loads, as displayed in Figure 7.5 f).



**Figure 7.5.** Boundary conditions of ideal and real test configurations

Throughout testing, the angles of attack are referring to the Sensor & Load Rack. For testing the different boom sides, a boom is rotated in order to have the according sides in line with the test rack

and the fore with the load strings and pulley system. While the angle of attack  $\alpha$  is always in-test-rack plane, the second angle of attack  $\beta$ , only applicable for symmetric axial compression, is out-of-test-rack plane. Thus,  $\alpha$  is always applied in-plane, with the boom oriented sides accordingly, as illustrated in Figure 7.6. Lateral bending, as a main load case, is introduced as asymmetric load and applied under an angle of attack of  $\alpha = 15^\circ$ ,  $45^\circ$  and  $90^\circ$  in the clamped-configuration and with  $\alpha = 22.5^\circ$ ,  $45^\circ$  and  $90^\circ$  in the spacecraft-configuration. The out-of-test-plane angle is not applied kept with  $\beta = 0^\circ$  for lateral bending. Load application is further realized by attaching the load to only one side of the Visual/Load Adapter at a time. For axial compression, loads are realized with a symmetrical load introduction, by guiding the load string over a pulley at the Visual/Load Adapter, as described before, thus applying a resultant axial load by two load vectors, on at each side of the boom's cross section. For this load case an angle of attack of  $\alpha = 3^\circ$  and  $\beta = 0^\circ$  is applied for the ideal configuration, while for the real configuration a representative load case for the Boom Subsystem with  $\alpha = 22.5^\circ$  and  $\beta = 3^\circ$  is realized in a combined manner.



**Figure 7.6.** Orientation of angles of attack for each tested boom side

#### 7.1.2.1 LATERAL BENDING TESTS

In the here described tests three four constituents of the relevant robustness parameters are quantified. The characteristic load is determined in terms of the critical buckling load  $F_{scrit}$ , the maximum load achievable by a boom. Furthermore, the residual load carrying capacity of a boom is considered representative for robustness, and therefore the achievable buckling loads after the second and third time of repeated failure (collapse) are determined. Stiffness is quantified in terms of bending stiffness  $c$  and flexural rigidity  $EI$ , while boom tip displacement is provided for all observed cases as well. Lateral bending is analyzed on a limited set of cases tested for both configurations and for both boom sides tested, namely under  $\alpha = 90^\circ$  ( $\beta = 0^\circ$ ), considered the worst case in a theoretical scenario, and  $\alpha = 22.5^\circ$  ( $\beta = 0^\circ$ ) being considered the worst case in a realistic scenario of Gossamer-1.

### Mechanical Buckling Behavior and Failure Modes

The mechanical buckling behavior under this type of load is represented by acquired load-displacement curves, showing the applied force  $F_s$  versus displacement of the boom tip  $s_x$ . Such characteristic graphs are given exemplary for the here assessed cases of both configurations in the images of Figure 7.7. Further graphs for comparison of configurations and tested cases, and under different angles of attack, at flange side and convex side, are provided in Appendix F with Figure F. 1. Additional test results, exceeding the here discussed cases, also for larger and smaller boom sizes and different interfaces, can be found in [77, 93, 118, 123–125].

While the load-displacement curves generally start with a linear or near-linear behavior slope, for the ideal configuration, with the flange side (FS) loaded, this linear course continues until reaching the

peak load  $F_{scrit}$ , that is considered the failure load (maximum achievable load), thus marking global buckling, as shown in Figure 7.7 a). Following a load drop from this maximum, the curve continues with a smaller slope, being identified as post buckling region.

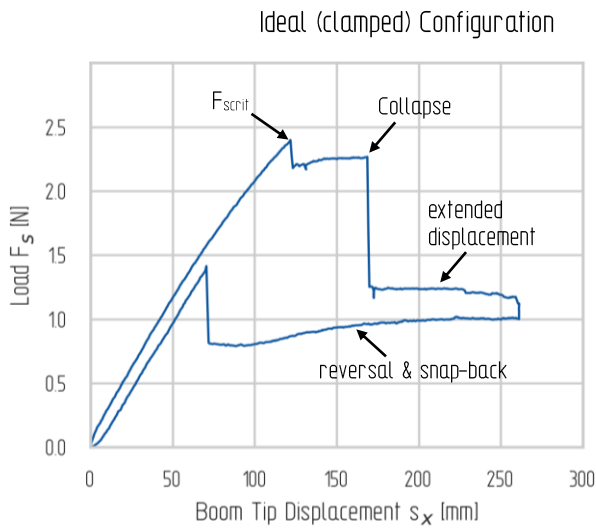
This suddenly ends with a more significant load drop and the collapsing of the boom, eventually. Although this behavior is similar to findings discussed by e.g. Da Cunha or Lee [66, 69, 72] for cylinders, robustness determination in terms of energy difference between global buckling and collapse over the post-buckling region is not considered most adequate here (cf. section 4.4.4), since convex side (CS) load cases (see Figure 7.7 b) do not feature such region, and global buckling ( $F_{scrit}$ ) and collapse coincide. Here instead the linear curve section continues undisturbed until reaching the maximum bearable load  $F_{scrit}$ , directly followed by a sudden load drop and collapse, as Figure 7.7 c) illustrates.

Subsequently to the event of collapse and in consequence, some oscillating dynamics of the boom tip can be observed, while boom tip displacement is extended for some further distance. After reeling in of the string is finally stopped, displacement is reversed and string is given. In this phase, the boom shell “unbuckles” as local buckles form back. Eventually, the boom snaps back to its initial shape, while the curve returns to a near-linear slope, at a certain point of displacement reduction. A test run and the associated load-displacement curve end, whenever the boom tip displacement is reduced to its initial value and the string tension is down to zero. Hysteresis is assumed due to energy dissipation by internal friction and buckling, visible by the gap when comparing the two parallel linear sections of a curve.

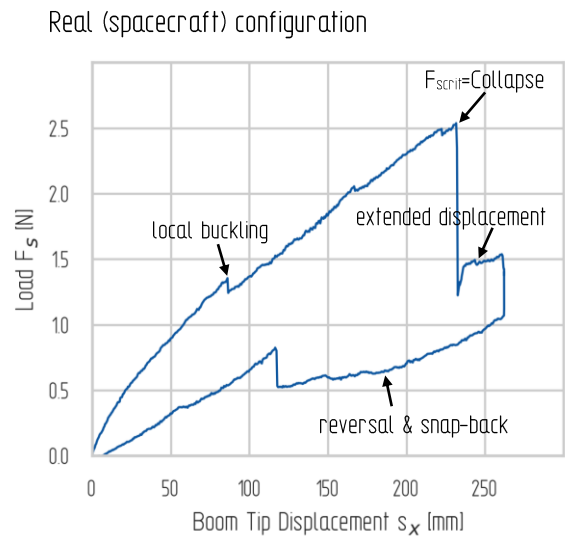
Along with the different load-displacement curves exhibited for varying angles of attack and loaded sides, failure modes and buckling patterns differ as well. For the compressively loaded flange side, the boom shows a sine like buckling wave pattern along the flanges before reaching failure  $F_{scrit}$ , as shown in Figure 7.8 a). As this is an expectable behavior, its location of occurrence, frequency in waviness and amplitude may be associated with the manufacturing induced influence of flange waviness, as investigated in section 6.1.1.3. Moreover, these sine like waves are assumed to initiate flange buckling followed by failure, serving as disturbance of geometry. Once a certain boom tip displacement is reached the sine wave like buckles transform into a larger single buckle at the flange, as depicted in Figure 7.8 b), consequently leading to the collapse of the boom. This indicates a flange failure under compressive loads. While the convex side, when loaded, shows a regular buckling pattern at the clamped fixation for large angles of attack e.g.  $90^\circ$ , as depicted in Figure 7.8 c), for some cases with smaller angles of attack buckling occurs further away from clamping, thus resulting in failure as depicted in in Figure 7.8 d). Imperfections in the convex area of the boom shell e.g. as material inhomogeneity as investigated in section 6.2.1, are assumed the reason. Further result data of failure location at a boom under test is listed for each specimen and test run in Figure F. 2 of Appendix F.

For the real (spacecraft) configuration, load-displacement curves acquired for the assessed cases are given exemplary in Figure 7.7 d), e) and f). The courses of the graphs again start with a near-linear behavior, with increasing force and displacement, although small load drops can already be observed. These can be associated to local buckling on the boom shell, while additionally some yielding of the flexible interface (BSI), specifically at the tape springs, is observed. In most cases for the flange side buckling failure load  $F_{scrit}$  coincides with collapse, as depicted in Figure 7.7 d). However, for the convex side, as depicted in Figure 7.7 e), the peak load at buckling  $F_{scrit}$  is followed by a small post-buckling region, resulting in collapse subsequently. The dynamic behavior of the oscillating boom after collapse is again present. When reversing displacement and reducing boom tip deflection, a snapping back to near-linear behavior, after some unforming of smaller local buckles, is only observed for flange-loaded cases. Curves of the convex side case do not indicate a return to linear behavior, as shown in Figure 7.7 e). Furthermore, a significant residual deflection value is eminent, after fully relaxing the string and boom tip. This and a larger hysteresis compared to the ideal configuration is assumed to arise due to setting processes in the assembled flexible interface and its components e.g. tape springs, anvil and elastic joints, as well as due to the failure modes involved.

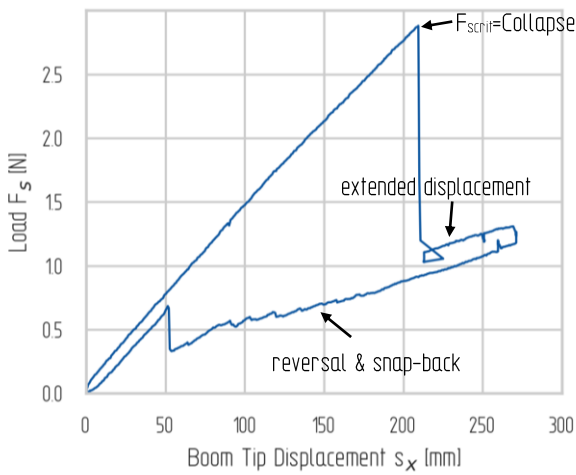




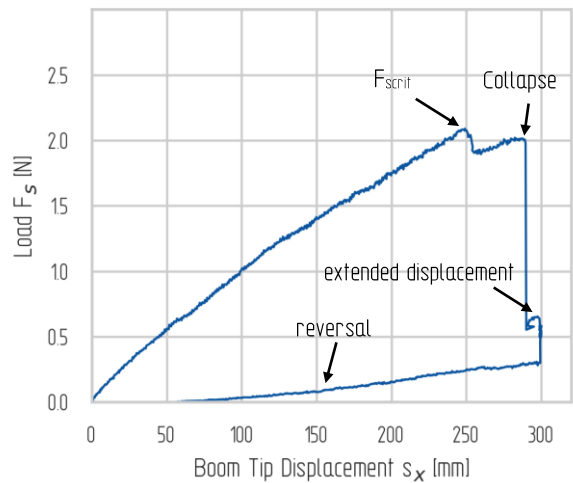
a) Ideal configuration, flange side (FS) loaded under  $\alpha = 90^\circ, \beta = 0^\circ$



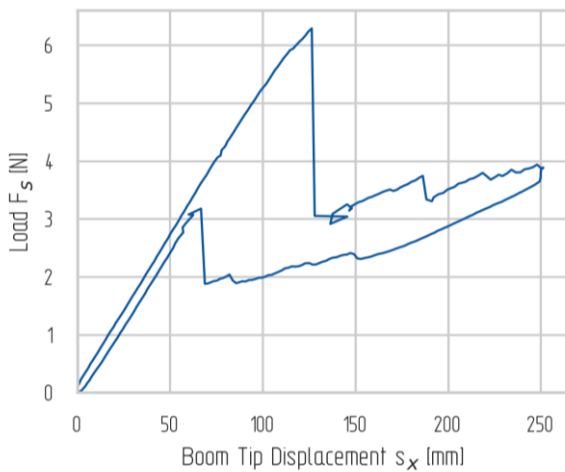
d) Real configuration, flange side (FS) loaded under  $\alpha = 90^\circ, \beta = 0^\circ$



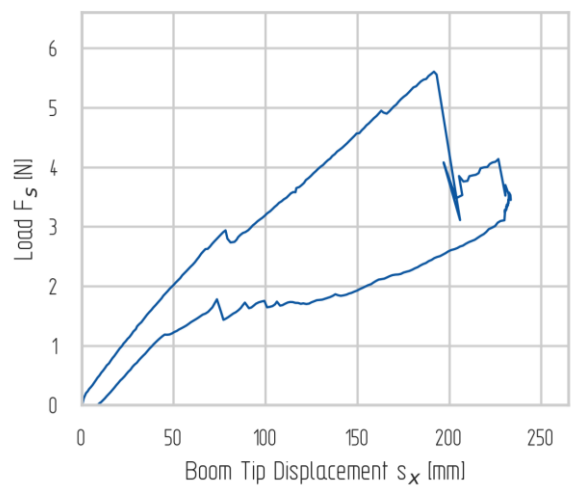
b) Ideal configuration, convex side (CS) loaded under  $\alpha = 90^\circ, \beta = 0^\circ$



e) Real configuration, convex side (CS) loaded under  $\alpha = 90^\circ, \beta = 0^\circ$



c) Ideal configuration, flange side (FS) loaded under  $\alpha = 22.5^\circ, \beta = 0^\circ$

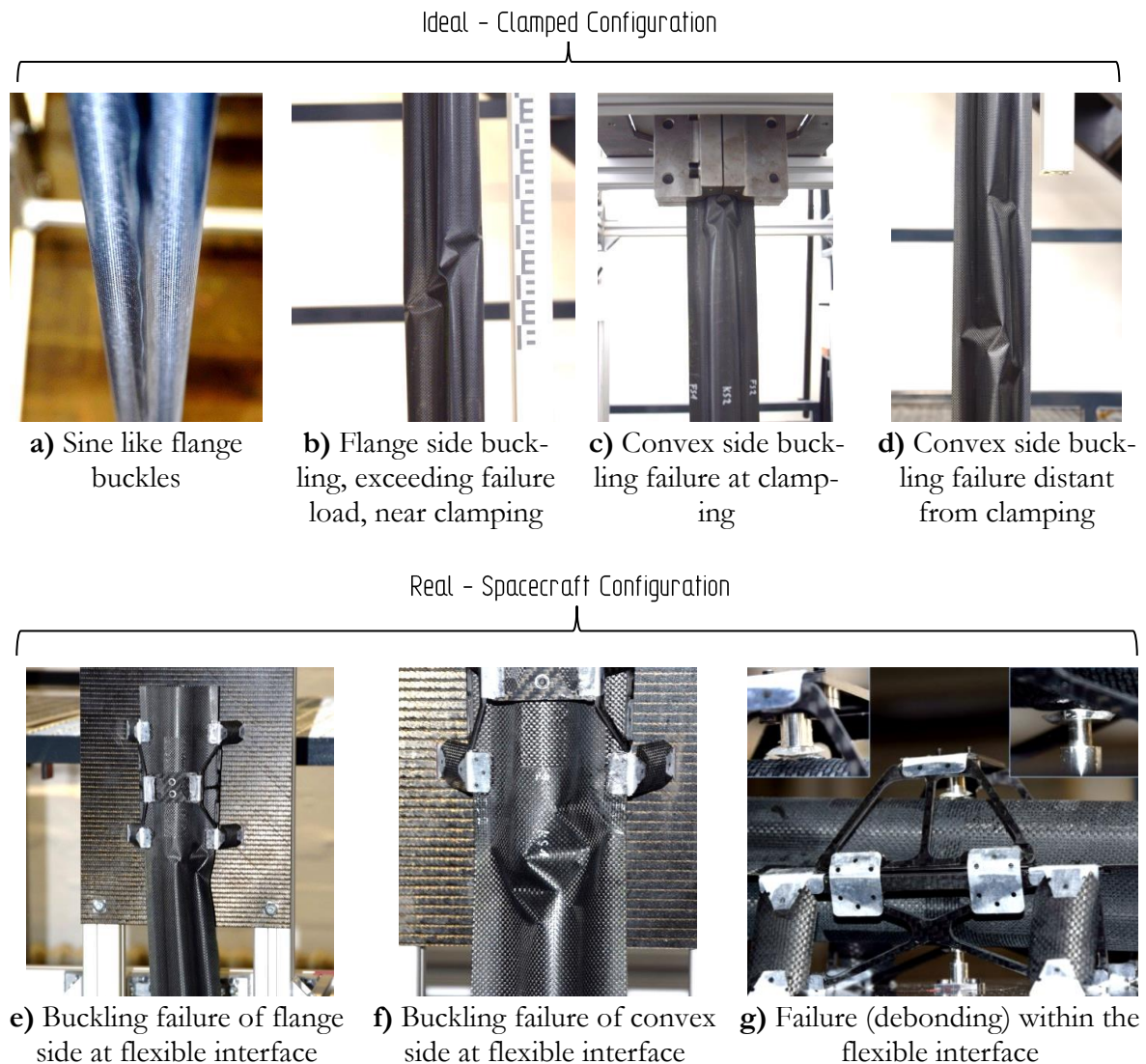


f) Real configuration, flange side (FS) loaded under  $\alpha = 22.5^\circ, \beta = 0^\circ$

accuracy of force measurement: 0,05 N

Figure 7.7. Observed buckling behavior in ideal (clamped) and real (spacecraft) configurations under lateral bending

For the real configuration, there are three main failure modes present. Flange failure close to the interface as depicted in Figure 7.8 e) occurs, following sine wave like buckling when loading the flange side. Here, in some cases yielding of the interface's tape springs lead to small load drops, although ultimate failure occurred on the boom shell at the end of the interface. For the convex side, regular buckling patterns at the convex shell are observed leading to a failure near the interface, as shown in Figure 7.8 f). However, specific to the real interface with its complex assembly is the failure of some components when testing convex side cases. Thus, in six out of nine test runs a debonding (breakage) of upper or lower anvil and boom shell lead to failure within the interface, as depicted in Figure 7.8 g). Generally, one can state that for this kind of test smaller angles of attack lead to a higher maximum critical buckling load  $F_{scrit}$ , as the axial load compound increases relatively. For larger angles of attack, as shown on cases for  $\alpha = 90^\circ$  in both configurations, flange sides and convex sides experience different behaviors in terms of post buckling regions, while for small angles of attack they behave very similar, with no post-buckling region and coinciding global buckling ( $F_{scrit}$ ) and collapse loads. Increasing bearable loads after collapse and while extending tip displacement may occur due to a stabilizing effect of the strongly buckled boom shell. At this point, the boom is strongly buckled and partially damaged, and the tip displacement shows values above an acceptable level for a structure like a solar sail.



**Figure 7.8.** Failure modes of ideal (clamped) and real (spacecraft) configuration under lateral bending

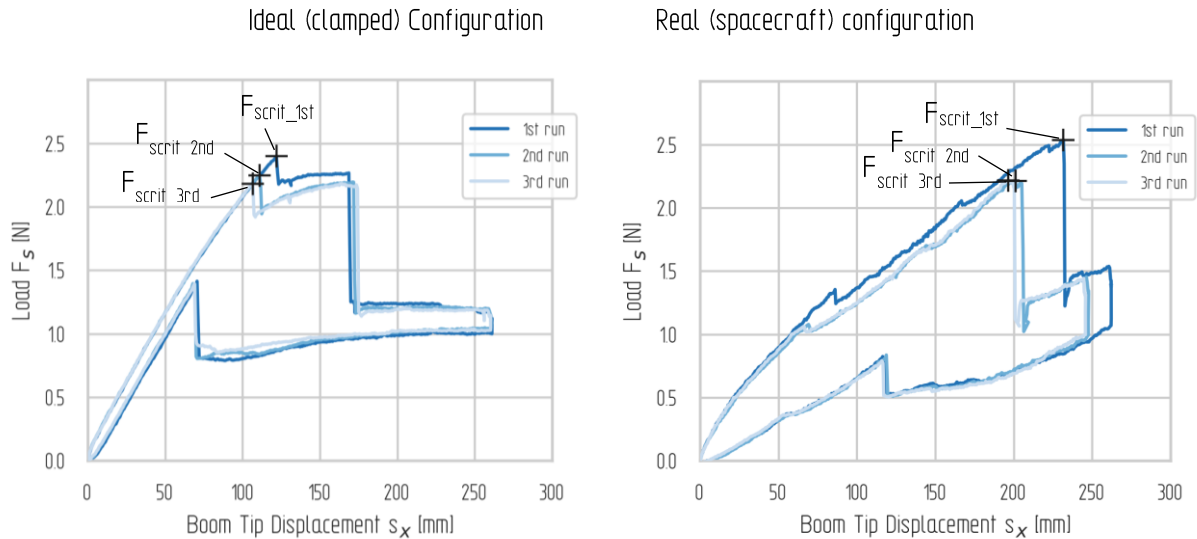
## Buckling Load and Residual Load Carrying Capacity

The results for both tested configurations, ideal (clamped) and real (spacecraft) configuration, sorted by load cases, are summarized in the tables of Figure F. 2 and Figure F. 3, respectively, given in Appendix F. Here the critical buckling load  $F_{scrit}$ , the maximum value achievable at which a boom fails due to buckling, and the occurring boom tip deflection  $s_x$  at which the boom buckles as well as the failure position on the boom specimen's z-axis can be compared. Furthermore, for each test scenario both convex and flange sides were tested, given in averaged values over both sides. An exception is inherent in the spacecraft configuration with its flexible interface. Here only one convex side could be tested due to the lack of space towards the interface-plate for deflecting the boom.

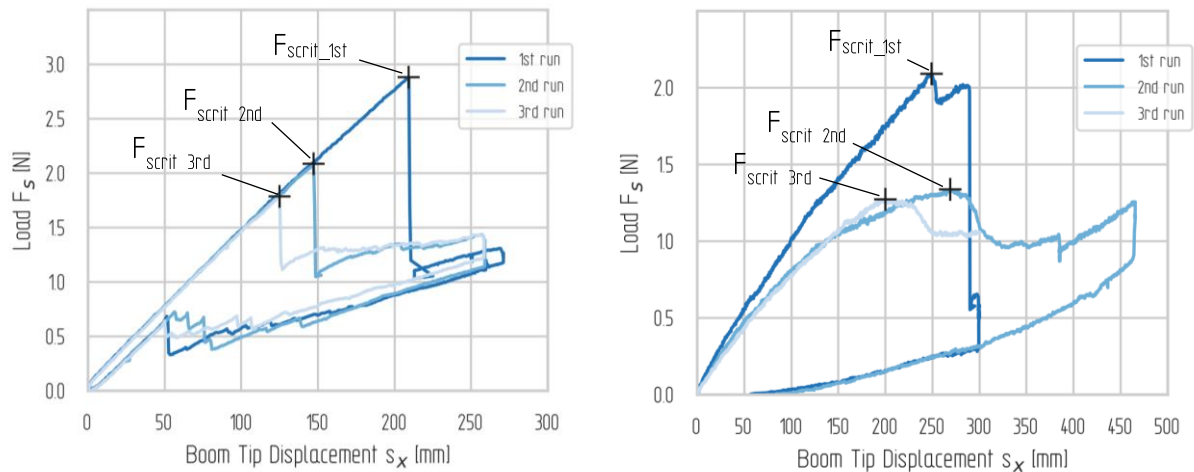
In the ideal configuration the acquired critical buckling loads exceed the required one of  $F_{sReq}=2$  N, defined within Gossamer-1. For the application case with an in-plane angle of attack  $\alpha = 22.5^\circ$ , the critical load achieved  $F_{scrit}=6.54$  N, exceeds the requirement by about a factor of 3. For the theoretical cases of  $90^\circ$  in flange and convex side, values for  $F_{scrit}$  of 2.2 N and 2.76 N are achieved, respectively. Although, the requirement was not defined for this load case, values for the critical buckling load achieved, exceed the required value. When comparing flange (FS) and convex sides (CS) for  $\alpha = 90^\circ$ , the convex side achieves a slightly higher buckling load on average, however still in the same range.

For the real configuration, the application case at  $\alpha = 22.5^\circ$  exceeds the requirement of  $F_{sReq}=2$  N, with an average of  $F_{scrit}=5.33$  N by a factor of 2.6. The theoretical cases with  $\alpha = 90^\circ$  in flange and convex side achieve values for  $F_{scrit}$  of 2.48 N and 2.10 N, respectively, thus showing similar values for both sides. When comparing according load cases of ideal and real configuration at least for the work case with  $\alpha = 22.5^\circ$ , the ideal configuration achieves higher values, while for the theoretical cases with  $\alpha = 90^\circ$ , values are in the same range and do not differ significantly. However, due to the small sample size in terms of number of booms tested, it is difficult to clearly determine a trend. Overall, results for the flange sides of both configurations show that with smaller angles of attack, higher values of the critical buckling force  $F_{scrit}$  are reached, while this effect is not consistent for the maximum displacements  $s_x$ .

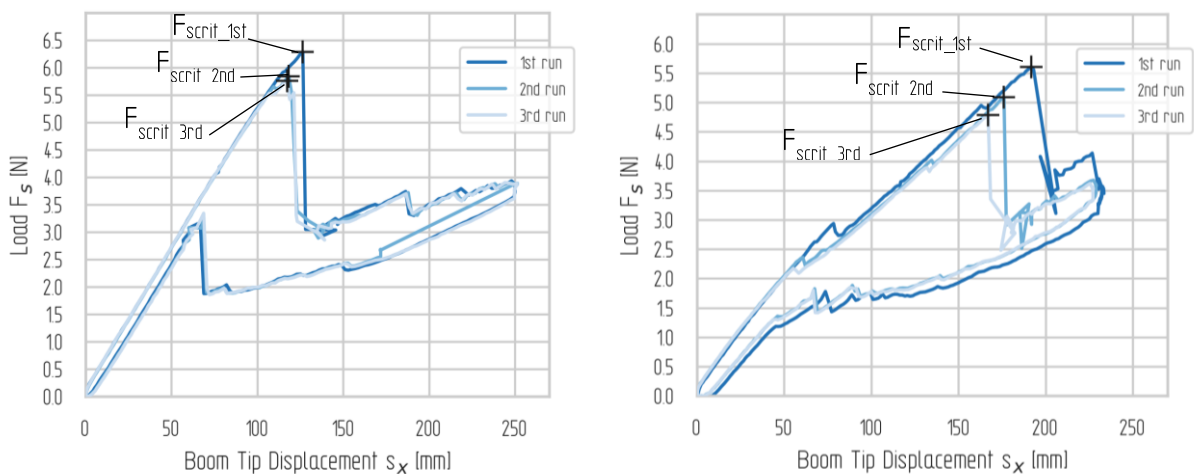
Values for boom tip displacement are expressed in positive numbers (see tables in Figure F. 2 and Figure F. 3) for better readability, therefore not indicating the direction of boom tip deflection within the test stand coordinate system. The boom tip displacements  $s_x$  are in general higher for the spacecraft configuration than for the clamped configuration, for all tested scenarios, having its origin in the beneficial flexibility of the spacecraft interface. However, the lower maximum loads for the flange side can be explained with the resulting buckling pattern, exhibiting sine wave like buckles along a loaded flange. Further comparisons can be drawn in the graphs of Figure 7.9 and Figure 7.10, although these figures serve the purpose to illustrate subsequent and repeated failure and residual load carrying capacity.



a) Ideal configuration, flange side (FS) loaded under  $\alpha = 90^\circ, \beta = 0^\circ$       d) Real configuration, flange side (FS) loaded under  $\alpha = 90^\circ, \beta = 0^\circ$



b) Ideal configuration, convex side (CS) loaded under  $\alpha = 90^\circ, \beta = 0^\circ$       e) Real configuration, convex side (CS) loaded under  $\alpha = 90^\circ, \beta = 0^\circ$



c) Ideal configuration, flange side (FS) loaded under  $\alpha = 22.5^\circ, \beta = 0^\circ$       f) Real configuration, flange side (FS) loaded under  $\alpha = 22.5^\circ, \beta = 0^\circ$

accuracy of force measurement: 0,02 N

Figure 7.9. Observed buckling loads of subsequent and repeated testing, exceeding collapse

In order to determine the residual load carrying capacity each test scenario with its specific angle of attack comprises of three subsequent test runs. Here critical buckling load and collapse are repeatedly exceeded, thus simulating a failure of the boom multiple times, including the damage eventually occurs. For each of the here discussed and assessed cases a graph displaying the load-displacement curves of subsequent test runs, with the achieved critical buckling loads, are given in Figure 7.9. The graphs show good repeatability of the tested cases for all three runs, as the curves match very closely, with the exception of the case displayed in Figure 7.9. e), in which the failure mode differs between runs, as the interface failed. Generally, it can be observed that a subsequent and repeated test run produces a smaller critical buckling load than its predecessor, thus indicating some degeneration due to damage. However, a residual load carrying capacity even after three subsequent test runs with the boom collapsing is apparent and implies some robustness, although different load cases show different buckling behavior, as discussed before. The decreasing values for the critical buckling load  $F_{scrit}$ , over repeated testing can be explained with occurring damages in the boom's CFRP shells and the bond lines of the flanges, as observed, when overloading the boom (collapse). Therefore, damages like cracks and delamination, visible and invisible, are assumed to lead to this effect, as one would expect.

As the first test run can be considered to be without damages it  $F_{scrit}$  can be considered the maximum achievable load, while subsequent test runs show decreased values. Given as percentage of the initially achieved critical buckling load (1<sup>st</sup> run), the residual load carrying capacity is illustrated for each load case assessed in Figure 7.10. Here the initial critical buckling load  $F_{scrit\_1st}$  is taken as bases and compared to the two subsequent runs.

For the work load case and each flange side loaded under  $\alpha = 22.5^\circ$ , the residual load carrying capacity of the ideal configuration can be quantified for the 2<sup>nd</sup> test run with  $F_{scrit\_2nd} = 5.78$  N reaching 77 %, compared to the 1<sup>st</sup> test run with  $F_{scrit\_1st} = 6.54$  N (base equals 100 %), while in the 3<sup>rd</sup> test run with  $F_{scrit\_3rd} = 5.61$  N still achieves 76 % of the initial value.

For the real configuration an even higher residual load carrying capacity is reached in the 2<sup>nd</sup> test run with  $F_{scrit\_2nd} = 5.09$  N reaching 90%, and after the 3<sup>rd</sup> test run  $F_{scrit\_3rd} = 4.97$  N still achieving 93%, compared to the initial value with the 1<sup>st</sup> test run with  $F_{scrit\_1st} = 5.32$  N (100%). These results further show that even after the boom specimen failing and collapsing three times subsequently, the requirement of  $F_{sReq} = 2$  N is still over-fulfilled by a factor of about 2.5.

For the theoretical case of  $\alpha = 90^\circ$ , both configurations produce similar residual load carrying capacities. When loading the convex sides residual load carrying capacities between 64 % and 66 % for the 2<sup>nd</sup> and between 58 % and 60 % for the 3<sup>rd</sup> run are achieved. The cases when loading the flange side achieves results between 85 % and 90 % for the 2<sup>nd</sup> and 85 % to 87 % for the 3<sup>rd</sup> run, thus indicating a smaller robustness for the convex side than for the flange side. However, a tendency cannot clearly be distinguished as the two configurations exhibit very similar results for the residual load carrying capacity.

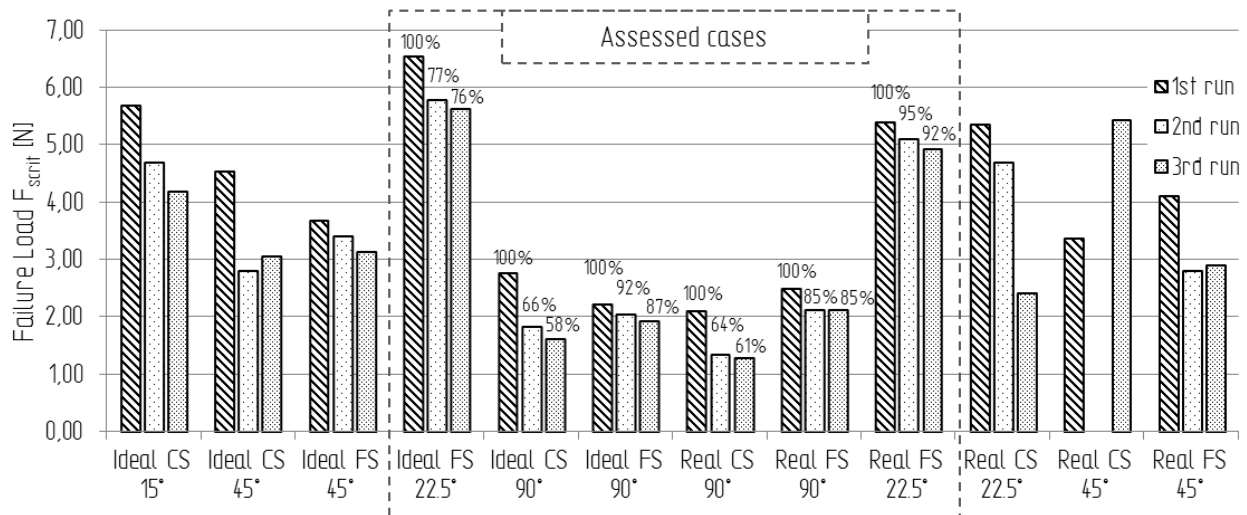


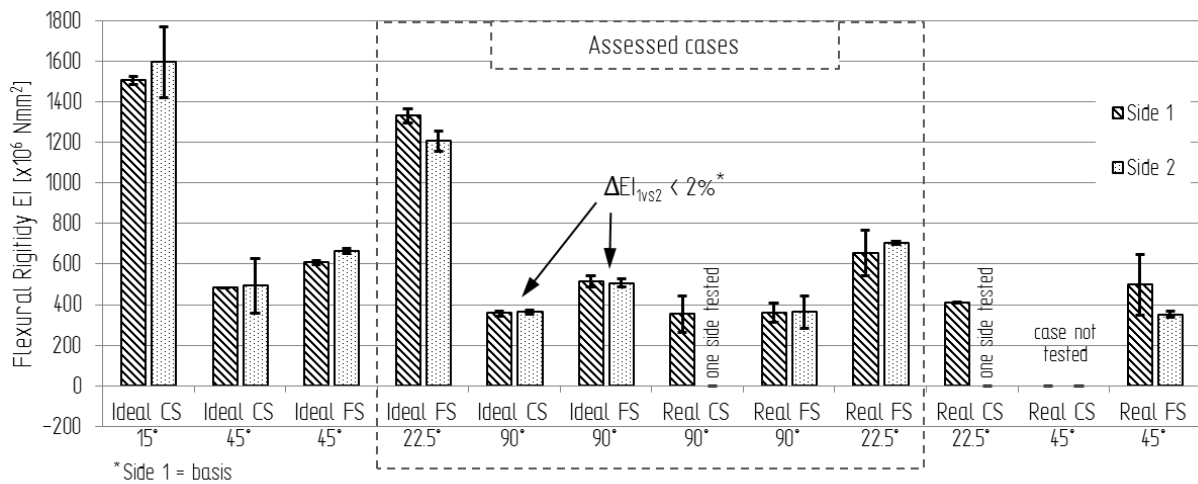
Figure 7.10. Residual load carrying capacity of assessed cases

### Stiffness

For each case and configuration, at each boom side type (convex side type, flange side type), for each of the two sides (side 1 and side 2) tested per side type, about 10 repeated test runs, below  $F_{scrit}$ , at up to 1 N were performed. This is done in order to remain in the elastic region without inducing local or global buckling, by keeping boom tip deflections small. The acquired near-linear curves are assessed by a linear polynomial regression of second order for data points between 10-90% of the overall tip displacement, thus determining the slope and therefore stiffness in the forms of bending stiffness  $c$  and flexural rigidity  $EI$ , according to the basic Equation (5.5) and Equation (5.6). The obtained results are given in detailed tables in Figure F. 2 and Figure F. 3, in Appendix F. For analysis, flexural rigidity  $EI$  results are compared in Figure 7.11 in a pairwise manner for the tested sides.

In the theoretical case of  $\alpha = 90^\circ$ , for ideal configuration, test runs exhibit a standard deviation that is very low, thus allowing to assume a good repeatability of tests runs and high quality of results. Furthermore, the difference between the two sides of a side type (convex side type, flange side type) are found to be below 2%, implying that both sides are of equal stiffness, thus implying the influence of the apparent curvature from manufacturing to be neglectable. However, results for tested stiffness are generally below the analytically determined values (cf. section 5.5). In average the flange side provides a flexural rigidity of  $EI_{FS} = 510$  N/mm and the convex side with  $EI_{CS} = 362$  N/mm when tested, while the according analytically determined values are higher with  $EI_{FS\_analytical} = EI_{yByB} = 561$  N/mm and  $EI_{CS\_analytical} = EI_{xBxYB} = 430$  N/mm, although in the same range. Moreover, flexural rigidity for the flanges sides is closer to analytically results than convex side results, thus either implying less imperfections/influences being present, being less affected by existing influences (higher robustness) or both, for the flange side of a boom. Results of the real configuration show flange side and convex side results being equal in size with  $EI_{FS} = 362$  N/mm and  $EI_{CS} = 352$  N/mm.

Furthermore, the results for  $EI$  of the real configuration are generally much lower than in ideal configuration and analytical results. This can be explained by the significant influence of the realistic interface assembly (BSI) that provides some flexibility by design. In the work case of Gossamer-1 with  $\alpha = 22.5^\circ$  applied on the flange side, flexural rigidity of the ideal configuration is almost twice as high with  $EI_{FS\_ideal} = 1269$  N/mm compared to the real configuration with  $EI_{FS\_real} = 679$  N/mm. Assuming again the impact of the somewhat flexible interface, this observation further indicates that steeper angles of attack, thus an increased axial load component, increases the influence on stiffness.



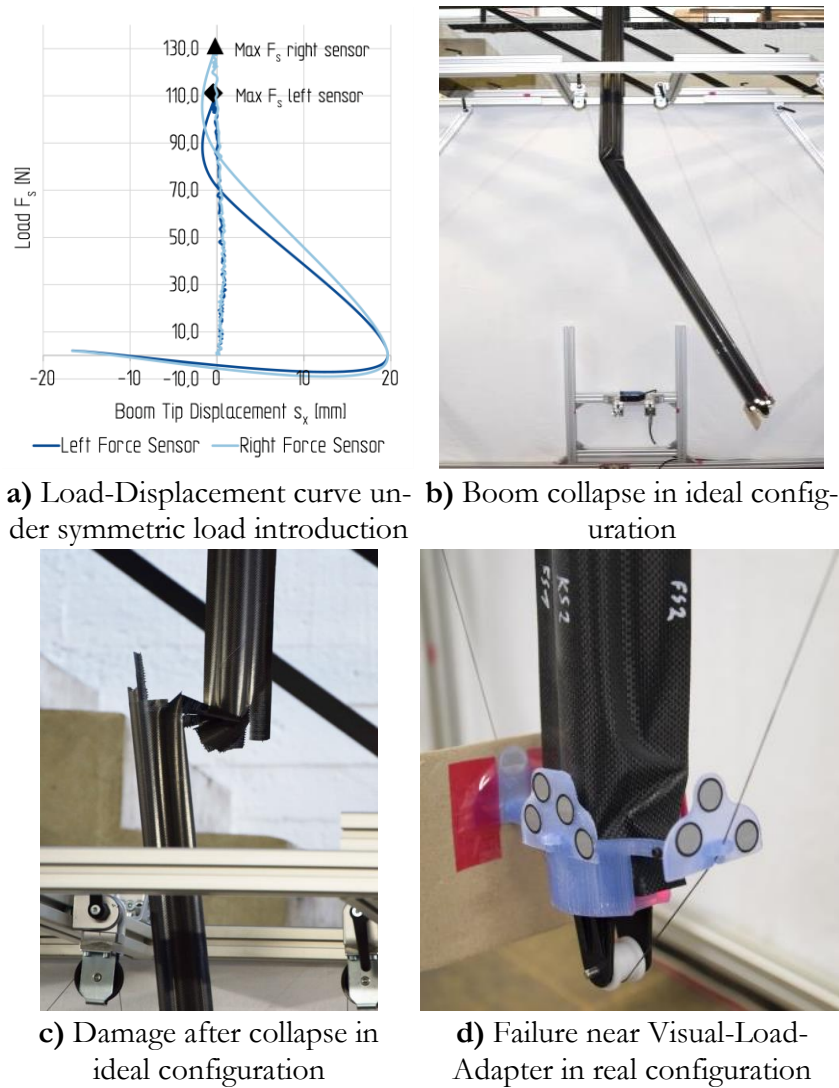
**Figure 7.11.** Flexural rigidity (stiffness) and standard deviation (whiskers) of assessed load cases under lateral bending

### 7.1.2.2 QUASI-AXIAL COMPRESSION TESTS

#### Mechanical Buckling Behavior and Failure Modes

Load displacement diagrams as used afore to analyze lateral bending are not applied in this case, due to the very small boom tip displacements present. Such graphs are only used to visualize the quality of load introduction in terms of symmetry as exemplary shown in Figure 7.12. Here the curves under an angle of attack of  $\alpha=3^\circ$  to each side are displayed for each of the sensors. Starting at the initial zero position of displacement, small oscillations around the zero value occur with increasing force values, due to providing self-stabilizing its center position by the pulley. This continues until each curve reaches its maximum, at which the boom suddenly fails and collapses. At this point, the two sensors show different maxima of  $F_{scrit}$ , assumed due to deviations from symmetry. The dropping force values along with increasing and followed declining displacement values represent the uncontrolled swinging of the boom part that is broken away. Nevertheless, this graph shows a good symmetry in load introduction, although the maximum values measured by the two sensors differ. While in Figure 7.12 image a) illustrates this load-displacement behavior, image b) demonstrates the according failure event (collapse) observed. Furthermore, to determine quality of load introduction a relative load off-set between the two loaded sides is determined. The determined load symmetry off-set, using  $F_{scritFS1}$  as basis, ranges between 12% and 18% for the ideal, and between 0% and 8% for the real configuration, thus indicating an acceptable quality for axial load introduction. The deviations from symmetric load introduction are assumed to occur due to friction in the string pulley system in interaction with the Visual-Load-Adapter and due to misalignments in the test setup or boom tip adapter. Albeit the varying symmetry, the occurring failure modes can be identified as global buckling and column buckling, at least for tests with the ideal configuration, as displayed in Figure 7.12 b) and c), respectively. However, the real configuration fails under the applied quasi-axial load near its Visual-Load-Adapter (BSFR), by local buckling.





accuracy of force measurement: 0,2 N

**Figure 7.12.** Failure modes of ideal (clamped) and real (spacecraft) configuration under quasi-axial compression

### Buckling Load and Residual Load Carrying Capacity

In the following, the resulting axial load  $F_{ares}$  is discussed. For the ideal configuration this load derives from the symmetrically applied load vectors under  $\alpha=3^\circ$  at each flange side, in an in-plane case, according to Equation (7.1). However, the resulting axial load for the real configuration is derived from a load vector on each flange side under an in-plane angle of attack  $\alpha=22.5^\circ$  and an out-of-plane angle  $\beta=3^\circ$ , according to Equation (7.2). The summarized results for the booms tested in ideal and real configuration are provided in Figure F. 4 and Figure F. 5, respectively, in Appendix F.

Resulting axial force in ideal configuration:

$$F_{ares} = (F_{scritFS1} + F_{scritFS2}) \cdot \cos \alpha \quad (7.1)$$

Resulting axial force in real configuration:

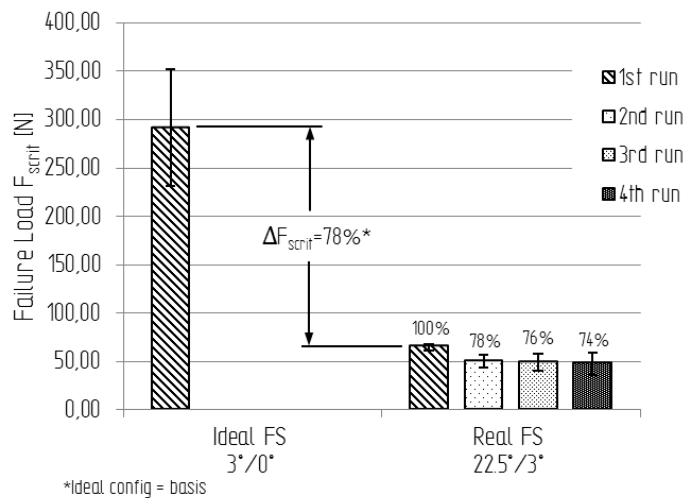
$$F_{ares} = \sqrt{\frac{F_{scritFS1}^2}{(\tan \beta)^2 + (\tan \alpha)^2 + 1}} + \sqrt{\frac{F_{scritFS2}^2}{(\tan \beta)^2 + (\tan \alpha)^2 + 1}} \quad (7.2)$$



When studying the acquired results the ideal configuration reaches much higher buckling loads for axial loading with an average of  $F_{ares}=252$  N, as displayed in the bar chart of Figure 7.13. Compared to this, the average maximum value for the real configuration of  $F_{ares}=65$  N, is about 78% lower, assumed due to the different boundary conditions. However, the variation of tests results is much lower for real configuration than for the ideal configuration, as illustrated in Figure 7.13. Nevertheless, with a sample size of only three specimens no conclusive statistical analysis can be drawn, and is herein not further discussed.

The residual load carrying capacity is again determined in subsequent and repeatedly test runs exceeding the critical buckling load and collapse, in this case the resulting maximum axial buckling load  $F_{ares}$ . Nevertheless, this could only be performed for the real configuration, due to the fatal damages and destructive buckling caused during the first test run in the in the ideal configuration.

Four subsequent test runs in the real configuration resulted in an average residual load carrying capacity of 78% for the second, 76% for the third and 74% for the fourth subsequent and repeated test run, as illustrated for comparison in Figure 7.13. A comparison of all samples tested, for both configurations, in terms of maximum achievable and residual axial loads can be done in Figure 7.14. Here again, the large difference of achieved critical buckling loads between ideal and real configurations is immanent. Both configurations indicate some robustness, although of two different types, as introduced in section 4.4.4. While the high critical buckling loads achieved with the ideal configuration exceed the required 4 N minimum axial buckling load (derived from requirement of 2 N at each side using Equation (7.1)) by a factor of 126, it could represent a reserve-related robustness. The repeatedly achieved buckling loads for subsequent failure in the real configuration, on the other hand can be interpreted as sensitivity-related robustness. Which presumptive robustness is of higher impact and how these types are included in a subsystem robustness is discussed in the following section.



**Figure 7.13.** Comparison of averaged maximum buckling loads under quasi-axial loading (standard deviation represented by whiskers)

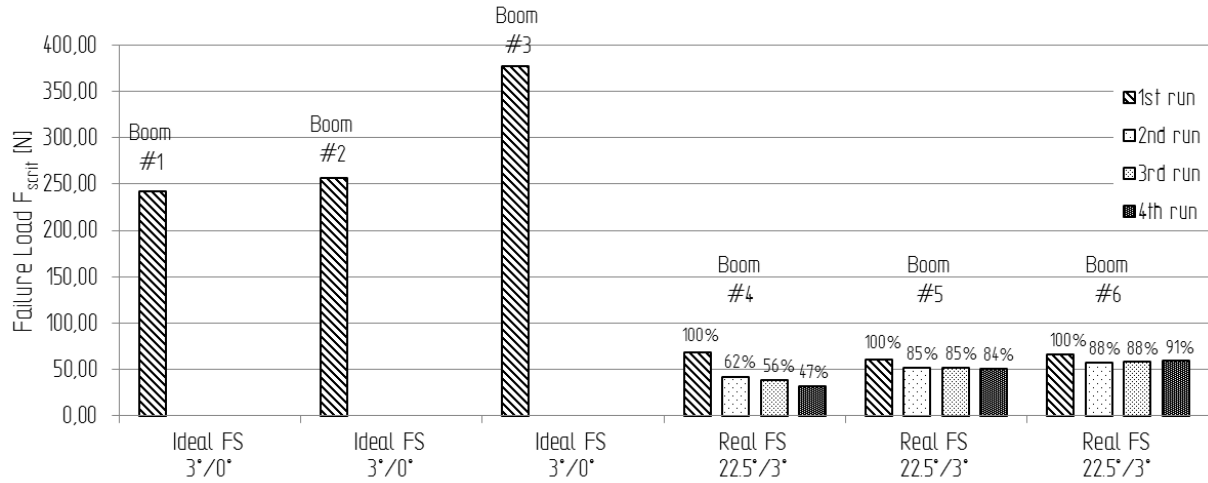


Figure 7.14. Residual load carrying capacity of tested booms under axial compression (angles given as  $\alpha/\beta$ )

### 7.1.3 Robustness Assessment of Experimental Results

In order to obtain the subsystem robustness for the boom  $Ro_{Booms}$  according to Equation (4.15), as developed in section 4.4.4., three partial robustness metrics need to be determined and combined with the partial robustness weighting factors provided in

Table 5.1, as determined in section 5.2.2. These three partial robustness metrics, namely *Stiffness-related* partial robustness, *Load-related* related partial robustness and *Displacement-related* partial robustness are assessed in the following. Robustness assessment and quantification is done for three cases, two theoretical cases with the ideal configuration and the real configuration under  $\alpha=90^\circ$ , and an application case with the real configuration under  $\alpha=22.5^\circ$ . Seeking for comparability and yet including all acquired data that make up the subsystem robustness, partial robustness metrics are determined using the same principle equations given in the following with Equation (7.3), (7.4) and (7.5). Each constituents in a partial robustness metric is a quantified value obtained from tests, experiments and analytical calculations and is provided for each case studied in Table G. 1, of Appendix G. Probabilistic considerations are not explicitly undertaken as test data is limited. However, the used constituent values represent minimum values achieved, if more than one value is available, and thus complying with the idea of robustness assessment in a conservative way.

The stiffness-based partial robustness  $Ro_k$  is determined from two weighted constituent metrics, that are representing the sensitivity of flexural rigidity. Given in Equation (7.3),  $EI_{FS}$  and  $EI_{CS}$  each represent the achieved flexural rigidity (minimum principle used) in testing at the flange side and convex side respectively. These values are brought into relation to the according analytically determined flexural rigidity about the same axis,  $EI_{yByB}$  and  $EI_{xBxB}$ . Hence, these relations quantify the impact of influences on the existing boom or boom subsystem, compared to theoretical expectations. For the case of the real configuration under an angle of attack of  $\alpha=22.5^\circ$ , the analytical flexural rigidity is substituted by a comparative flexural rigidity  $EI_{FScom}$  and  $EI_{CScom}$ , since only for the flange side a value has been determined in experiments. The according value for the convex side  $EI_{CScom}$  is calculated with Equation (G. 1), assuming the same stiffness relation of flange versus convex side as found in analytical calculations. The weighting factors  $w_{k1}$  and  $w_{k2}$  are arbitrary chosen in this example, however both to be equal in size.

*Stiffness-based* partial robustness:

$$RO_{\kappa} = \underbrace{w_{\kappa 1} \cdot \frac{EI_{FS}}{EI_{y_B y_B}} + w_{\kappa 2} \cdot \frac{EI_{CS}}{EI_{x_B x_B}}}_{\text{Flexural rigidity Sensitivity}} \quad (7.3)$$

The second component, the load-based partial robustness  $RO_L$ , comprises of several metrics that are derived from different relations of constituents. It incorporates the residual lateral load carrying capacity in terms of sensitivity, axial load and lateral bending as reserves, and the residual axial load carrying capacity in terms of sensitivity, as formulated in Equation (7.4). Each metric's importance is regarded in terms of dedicated weighting factors, here arbitrary chosen for demonstration (see Table G. 1, in Appendix G).

For each tested side type, flange side (FS) and convex side (CS), the achieved loads in the first test run  $F_{FS1st}$  and  $F_{CS1st}$ , are brought into relation to the loads achieved in the second test run with  $F_{FS2nd}$  and  $F_{CS2nd}$ , therefore providing the residual lateral load carrying capacity after collapse/failure.

The next term sets the required resulting axial load,  $F_{aResReq}$ , in relation to the achieved resulting axial load during the first test run  $F_{aRes1st}$ , and therefore to the maximum achievable value, thus representing the axial load reserve. The required resulting axial load is derived from the  $F_{FSReq}=2$  N required per side, under an symmetric load introduction at  $\alpha=22.5^\circ$ , as found in the application case. This same requirement is used in the theoretical case under  $\alpha=90^\circ$  angle of attack.

Similar to this, the third sub-component, the lateral load reserve, sets the required lateral bending load for each side,  $F_{FSReq}$  for flange and  $F_{CSReq}$  convex side, in relation the critical buckling load for lateral bending that is reached in the first test run with  $F_{FS1st}$  and  $F_{CS1st}$ , for flange and convex side respectively.

In the fourth load related component, the residual axial load carrying capacity, the resulting axial critical buckling load achieved in the first run  $F_{aRes1st}$  is set into relation to the critical axial buckling load achieved in the second test run  $F_{aRes2nd}$ , thus resembling the sensitivity of a boom or boom subsystem after repeated collapse/failure, including influences by occurring damages.

*Load-based* partial boom robustness:

$$RO_L = \underbrace{w_{L1} \cdot \frac{F_{FS2nd}}{F_{FS1st}} + w_{L2} \cdot \frac{F_{CS2nd}}{F_{CS1st}}}_{\text{Residual lateral load carrying capacity (sensitivity)}} + \underbrace{w_{L3} \cdot \left(1 - \frac{F_{aReq}}{F_{aRes1st}}\right)}_{\text{Axial load reserve}} + \underbrace{w_{L4} \cdot \left(1 - \frac{F_{FSReq}}{F_{FS1st}}\right) + w_{L5} \cdot \left(1 - \frac{F_{CSReq}}{F_{CS1st}}\right)}_{\text{Lateral bending load reserve}} + \underbrace{w_{L6} \cdot \frac{F_{aRes2nd}}{F_{aRes1st}}}_{\text{Residual axial load carrying capacity (sensitivity)}} \quad (7.4)$$

The displacement-based partial robustness  $RO_u$  is determined from two weighted constituents, in terms of a reserve. One is bringing the achieved boom tip displacement under symmetric axial loading at a nominal load value of 2 N, for the flange side  $u_{aFS_{2N}}$ , in relation to the overall limit for boom tip displacement during operation  $u_{limit}$  (1% of the boom length, cf. section 6.1.2). The second represents the according displacement for the convex side at a nominal load value of 2 N  $u_{aCS_{2N}}$ , adding

the boom tip displacement imprinted by manufacturing  $u_{manuf}$  as determined in section 6.1.2, in relation to the overall limit for boom tip displacement  $u_{limit}$ . More displacement constituents can be added, if data is available and if demanded by the studied case e.g. stowage or thermal deformations. However, manufacturing induced deformation was only measured for the convex side, as it is the side that is most likely influenced by tooling, and reeled up for stowage.

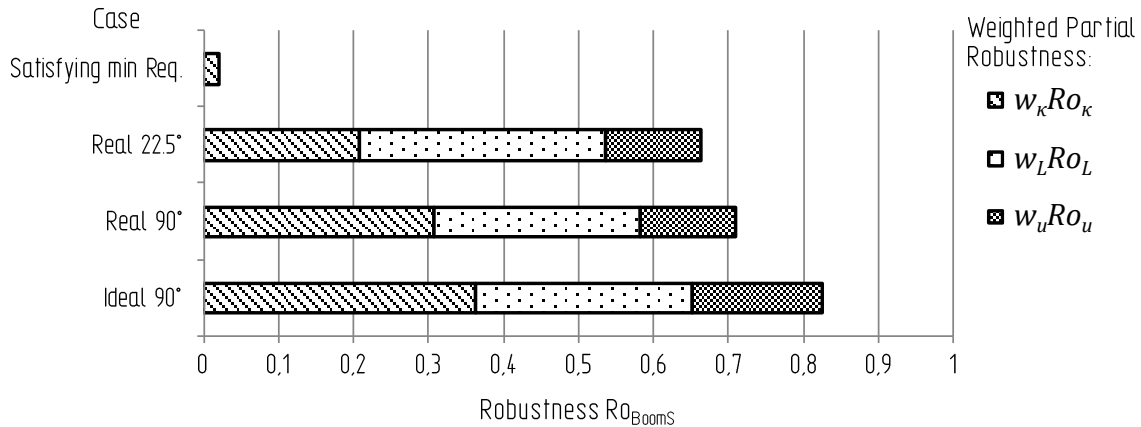
*Displacement-based* partial boom robustness:

$$Ro_u = 1 - \underbrace{\left( w_{u1} \cdot \frac{u_{aFS2N}}{u_{limit}} + w_{u1} \frac{u_{aCS2N} + u_{manuf}}{u_{limit}} \right)}_{\text{Boom tip displacement reserve}} \quad (7.5)$$

While the results for the partial robustness metrics and the Boom Subsystem robustness are summarized in Table 7.1, the proportions of contribution by the partial robustness metrics are illustrated for comparison in Figure 7.15, for the here assessed cases. Robustness for ideal configuration case at  $\alpha=90^\circ$  is  $Ro_{Booms\_Ideal90}=0.826$ , for real configuration case at  $\alpha=90^\circ$   $Ro_{Booms\_Real90}=0.709$  and for configuration case at  $\alpha=22.5^\circ$   $Ro_{Booms\_Real22.5}=0.663$ . Here the quantified robustness, generated with the proposed assessment methodology show that the ideal (clamped) configuration reaches higher robustness than the real (spacecraft) configuration, while the real configuration under the theoretical case of  $\alpha=90^\circ$  achieves a higher robustness than under the application case of  $\alpha=22.5^\circ$ . Partial robustness based on stiffness and load contribute major portions, as this is driven by the chosen weighting factors and the achieved performance. Although, e.g. robustness for case of the real configuration under  $\alpha=22.5^\circ$  seems to be low, one should keep in mind that a robustness of nearly zero, meaning all partial robustness metric are zero, except for the stiffness-related one that can only be very small, would still mean that all requirements are met, however without any reserve, margin or insensitivity. This case, only satisfying the minimum requirements, is added in the bar chart displayed in in Figure 7.15, for comparison. But, this circumstance also demonstrates a drawback of the here proposed robustness assessment methodology, at least for the here presented examples. Robustness cannot be zero, since at least some stiffness needs to be provided in order for the GosSSS to have any functionality. Although the here presented demonstration of robustness quantification is limited, the **Basic Hypothesis** is demonstrated on subsystem level to be valid and applicable. As more combinations of robustness parameters for characteristic load  $L$ , stiffness  $\kappa$  and boom tip displacement  $u$ , using further data in terms of measurement or simulation results are implemented, better accuracy of robustness can be made.

**Table 7.1.** Quantified Boom Subsystem robustness from experiments

Case	Partial Robustness			Weighted Partial Robustness			Subsystem Robustness
	$Ro_\kappa$	$Ro_L$	$Ro_u$	$w_\kappa Ro_\kappa$	$w_L Ro_L$	$w_u Ro_u$	$Ro_{Boom}$
Ideal 90°	0.864	0.745	0.906	0.364	0.288	0.175	0.826
Real 90°	0.73	0.716	0.651	0.307	0.276	0.126	0.709
Real 22.5°	0.493	0.855	0.651	0.208	0.330	0.126	0.663



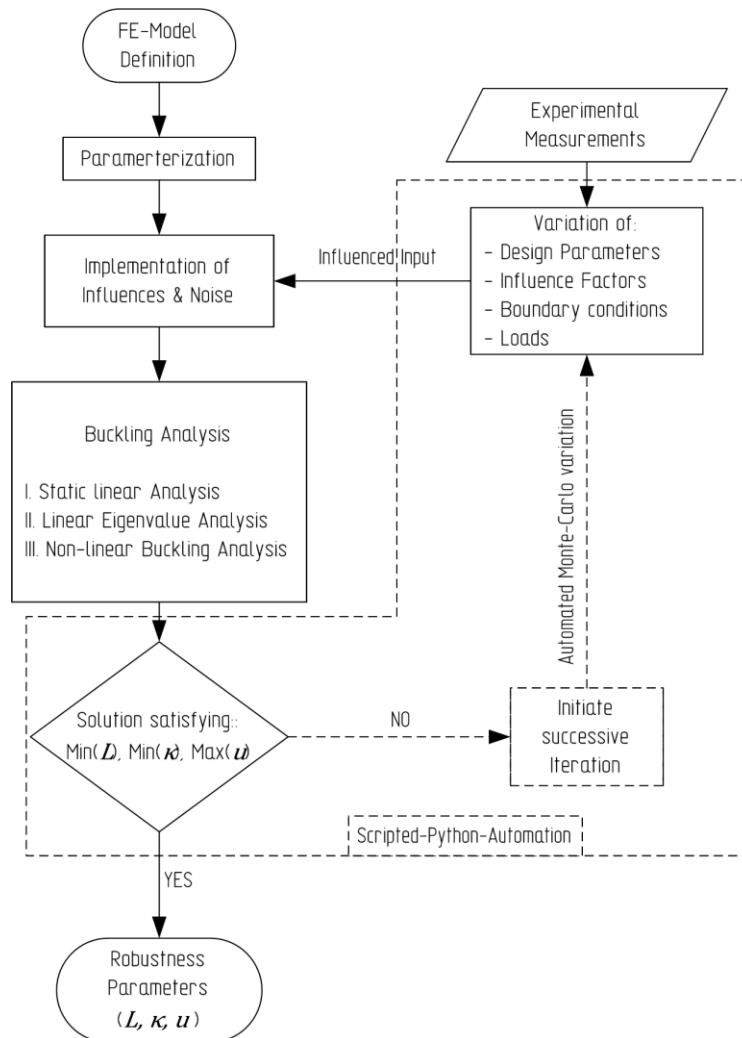
**Figure 7.15.** Comparison of Boom Subsystem robustness for exemplary cases

## 7.2 Finite Element Analysis of Case-Study Structural System

In the following the practical realization of a finite element analyses (FEA) is performed within the case study of a Gossamer-1 boom subsystem with the goal of predicting mechanical behavior, robustness parameters and consequently robustness under before quantified influences. Thus, numeric simulations provide a tool to predict mechanical behavior in cases that have not been tested or cannot be tested due to the enormous effort of applying the relevant influences on large scale. The following tasks can be located in the developed strategy for robustness quantification (cf. Figure 4.13.), described in section 4.5, as sub-task 4.1a, sub-task 4.3, result assessment, sub-task 4.4, calculation of partial robustness, and sub-task 4.5, calculation of the sub-system robustness.

FE-Analysis as implemented in the robustness assessment with sub-task 4.1a and realized as illustrated in the scheme of Figure 7.16. Beginning with a model definition of geometry, sectioning and meshing, parameterization of e.g. geometric and material metrics in order to access them in an automated manner and according to the DoE is performed. Next, influences and noise that act on the studied component or subsystem are implemented. This is done as influenced input values are used as parameters for the analysis. Such input is obtained from e.g. experimental measurements as done in the previous section 7.1 and chapter 6, from analytical calculations and data sheets. The input consists of influenced design parameters (geometric and material parameters), boundary conditions and loads rendered by influences and noise, as well as obtained influence factors. For implementation of probability, these parameters are varied within the DoE using an automated Monte-Carlo simulation, taking place using a scripted Python automation. However, at this point the automation is not applied within the here presented thesis, although it has been realized to a basic functional level. The FEA continues with the core procedure, the buckling analysis. It is divided into three subsequently run sections, the static linear analysis, a linear Eigenvalue analysis and non-linear buckling analysis. The linear static analysis obtains a pre-stressed model, by a small applied boom tip displacement, a fraction of what is necessary for the boom to buckle, in the directions of loading. With the following linear Eigenvalue buckling analysis mode shapes of buckling are generated and forwarded as imprinted geometric imperfections into the model of the third step. In this last step, the non-linear buckling analysis, the imprinted deformations of the boom shell model enable in most cases the model to buckle and therefore to determine a buckling failure load, boom tip displacement at failure and stiffness prior to buckling. Furthermore, perturbation loads or displacements are used if necessary in order to trigger buckling, as an implicit solver is used for the analysis. With the characteristic load, stiffness and boom tip displacement obtained, robustness parameters and in consequence robustness with FE-based data is determined. In an automated design process FE-results are then checked for satisfying minimum requirements of the characteristic load and stiffness, and maximum requirement for the boom tip displacement. This complies with the general assumption of robust

assessment to consider the worst-case achievable values to determine robustness in a conservative manner. If the solution does not satisfy the requirements, another iteration is initiated followed by an automated parameter variation using the Monte-Carlo method in Python. However, in the here applied FE analysis a deterministic solution is performed, using the least favorable input values obtained through experiments. The final out put are the robustness parameters  $L$ ,  $\kappa$  and  $u$  in their specific form and type, that are further used within the robustness assessment process.



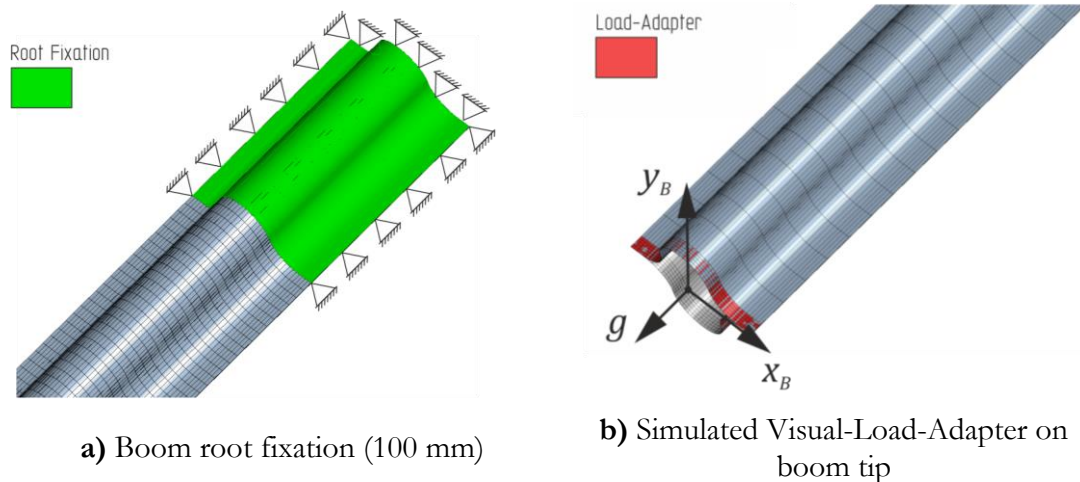
**Figure 7.16.** Finite Element Analysis – Procedure and implementation of influenced parameters

## 7.2.1 FE-Model, Cases and Results

### Model, boundary conditions and load introduction

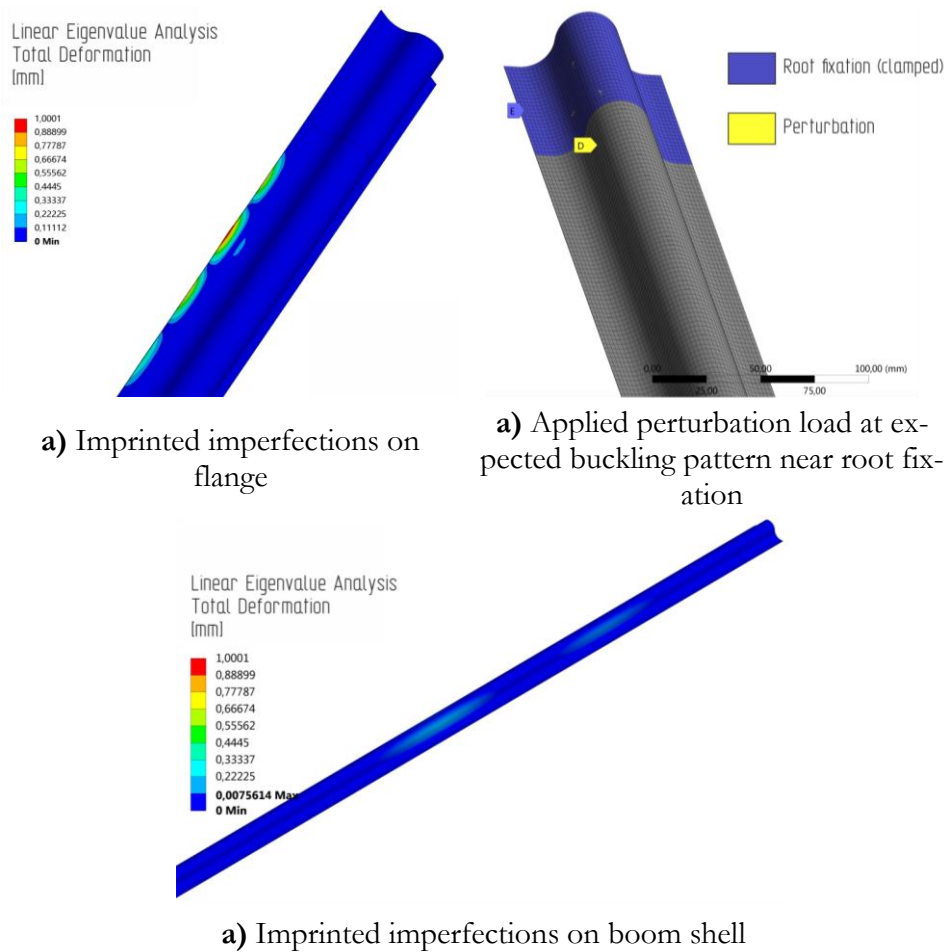
With the purpose to predict the impact of influences on mechanical performance and robustness, a Gossamer-1 boom is modeled in the finite element analysis software ANSYS Workbench (2019 R3). This is done by using eight-node solid shell elements of the type SOLSH190, combining the advantage of shell elements that demand a lower solution effort with the advantage of easy CAD modelling of a solid (volume) element. With the boom model exhibiting a total length of 4300 mm, thus representing the boom tested in experiments in section 7.1., meshing results in a total element number of about 60000. The boundary conditions are set at the boom root over a length of 100 mm in

a fixed condition, as illustrated in Figure 7.17 a), simulating the clamped boom root of the experiments. Load is applied at the considered boom side under investigation as a directional displacement of the boom tip, perpendicular to the boom length axis, thus realizing an angle of attack of  $\alpha=90^\circ$ , while keeping the out-of-plane angle to  $\beta=0$ . Introducing the load into the boom tip is realized by simulating the Visual-Load-Adapter. This is done by inhibiting cross sectional changes of the last 6 mm length on the boom tip, as displayed in Figure 7.17 b), and connecting it to a remote point that is displaced, while free rotation is enabled.



**Figure 7.17.** Boundary and load conditions on the boom model

Furthermore, gravity is enabled ( $g$ ), thus considering the mass of the boom and the adapter (approximately 20 g), although both are small. Influenced material parameters e.g. degraded moduli by atomic oxygen and differences in warp and theft directions are regarded in the material parameter sets for each case simulated. Further imperfections due to influences are introduced in terms of flange waviness and pre-existing boom tip displacement, as well as cross-sectional deviation from nominal. The size of the boom tip displacement in the static analysis, in order to obtain local sine-like buckling patterns along the flange, as shown in Figure 7.18 a), is about 5 mm in flange side direction of the boom (in  $x_B$ -boom axis). This results in a buckle amplitude of about 1 mm, in the linear Eigenvalue buckling analysis, which is transferred as geometric imperfection into the non-linear buckling analysis by a factor of 1.5, in order to initiate buckling eventually. Straightness deviations of the boom, as determined in scans in section 6.1.2, are simulated by additional boom tip displacements in one convex side direction (in  $y_B$ -boom axis), in the static analysis, and provided as a pre-stressed state to the linear Eigenvalue analysis if applicable for the simulated case. The resulting deformed geometry is then forwarded to the final non-linear buckling analysis as influenced geometry, illustrated in Figure 7.18 c). Furthermore, reduced cross sectional dimensions as measured in scans in section 6.1.1.1, are regarded in the cross-sectional model geometry generation for the according case. Mostly necessary for some cases in which the boom's convex side is simulated, a perturbation load (1 mm nodal displacement) in the region of the expected buckling pattern, near the fixation, is applied (see Figure 7.18 b), thus providing some additional imperfection to initiate buckling at some point. The solution of the non-linear buckling analysis is performed using an implicit solver, generating results within 10-100 sub steps, at an applied boom tip displacement of 300 mm, thus exceeding the expected displacement known from experiments. Obtained results are reaction forces and applied boom tip displacements, while local displacements and maximum principle strains are reviewed as well.

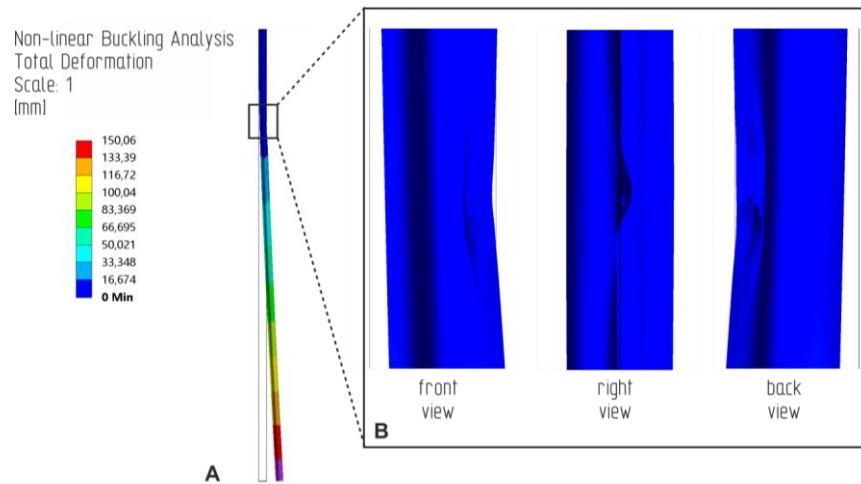


**Figure 7.18.** Imperfections applied to the FE boom model

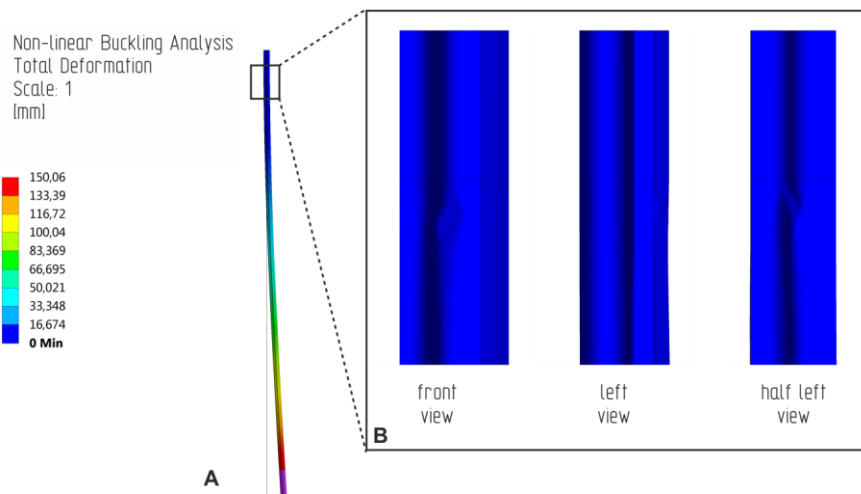
### Simulated cases, Solution and Results

Three cases are simulated and analyzed: a “nominal” case representing nominal geometry and material specifications without any influences, a “manufactured” case with realistic material parameters and according manufacturing imperfections, and a “stowed” case, resembling a boom after long term storage in stowed condition under 80°C, with cross sectional and shape deviations, and an assumed exposure to atomic oxygen, as analyzed in the experiments in chapter chapter 6. The according geometric dimensions, influence factors and material properties are applied to the model via design parameters and imperfections. However, all cases are modeled in ideal configuration with an applied angle of attack of  $\alpha=90^\circ$ , and  $\beta=0^\circ$ , thus applying a simple one directional load vector. Similar to the tests in the previous sections, both boom sides (FS, CS) are loaded and analyzed for each case separately, while only the influenced side, e.g. featuring the imprinted imperfections, is simulated. While the FE model in this thesis serves the purpose of predicting the impact of influences on the mechanical behavior of a boom, further finite element analyzes on the realistic configuration for Gossamer-1 has been presented by Straubel and Zander in [93].





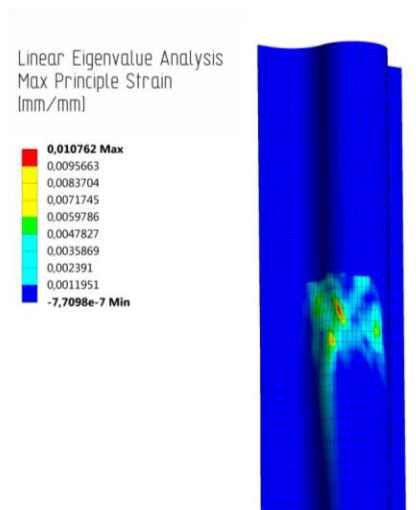
a) Flange side (FS) - Resulting deformations: A: Global buckling, B: Local buckling of flange and shell



b) Convex side (FS) - Resulting deformations: A: Global buckling, B: Local buckling of shell

**Figure 7.19.** Resulting buckling patterns at failure

In the final step of simulation, the non-linear buckling analysis, a load is simulated by displacing the tip of the boom by 300 mm, in the direction of interest. Although convergence over the full applied displacement is not always achieved as solving is being stopped, buckling failure is assumed to occur as follows. It is distinguished between a numerical and a physical origin for the end of convergence. Three criteria that are assumed to prove a structural buckling stability failure of boom shell are assumed: A local buckling e.g. of the flange and approximate area exceeding reasonable deformations, similar to observations in experiments for the event of collapse; reaction forces and boom tip displacement levels similar to those found for failure in experiments, at the same time; and local principle strains reaching critical levels of the material at the failure position. Examples of global boom buckling with local failure and forming buckling patterns at the expected failure position are given in Figure 7.19, with a) displaying the typical failure when loading the flange side, and b) for loading the convex side. While both patterns comply with what has been seen in the experiments, the convex side often demands an additional perturbation in order for it to buckle (fail). Here the second last load step before non-convergence is assumed to represent buckling failure. Additionally, to the assumption from load steps, boom tip displacements and local buckling patterns, local strain reaching the theoretical maximum material strain (0.01 mm/mm) is used as another indicator for buckling, as shown for a buckled convex side case in Figure 7.20.



**Figure 7.20.** Principle strain at local buckling failure at convex side loading

The results acquired represent values of the second last step in a solution or when a load significantly and suddenly drops and are given in **Table 7.2**. All critical buckling failure loads, directly obtained from reaction forces, are very close to loads achieved in experiments. When comparing the “Manufactured” case, loaded at its flange side, to the equivalent of the experiments (“Ideal-90°”), the achieved loads in FE are at the same general level, with values above 2 N, but slightly higher by about 13 %. In contrast to this, the FE results of convex side exhibit values about 30 % lower compared to experimental results.

Another observation is that with larger influences the critical buckling load is not necessarily impacted in an adverse manner, as seen for the “stowed” case compared to the “nominal” one. However, this may have its reason in the FE model, in which some influences are underrepresented or not modelled at all.

The boom tip displacement is directly read out as displacement in the second last sub step of the solution. Acquired results for the boom tip displacement at failure are very similar to experimental results for both flange and convex sides, when comparing the equivalent “manufactured” cases. As one could expect boom tip displacement decreases with increasing stiffness. Furthermore, the failure positions on boom length axis are comparable to what is seen in experiments of both tested sides. Stiffness is determined as a secant stiffness, here the slope between two sub step results, that can be allocated to be within the linear region of the load-displacement curve. In the “Nominal” case stiffness, best seen on flexural rigidity EI in both directions, can be verified by the analytical results obtained in section 5.5. When comparing these results FEA-stiffness in flange direction (FS) is off by about -1.25 % compared to the analytical stiffness, and in convex side direction (CS) FEA-stiffness deviates from analytical stiffness by about 1 %. This demonstrates a close correlation between the FE and analytical model, and therefore verifies the FE-model. When comparing stiffness for the “Manufactured” case with the experimental results (“Ideal-90°”, see **Figure F. 2** in Appendix F), stiffness in flange side direction in FEA is about 4 % and in convex side direction about 11 % higher than found in experiments. Comparing the “Stowed” case to the simulated “Manufactured” case the impact of the regarded influences becomes apparent. As the flange side shows an increase of about 68 % in stiffness for the “Stowed” case, an increase in width of only 19% was applied as influence. This demonstrates that geometric changes due to influences cannot generally be assumed to have a linear impact. However, the convex side shows a decrease of about -16% compared to the manufactured case, at a boom height decrease of -13%, demonstrating that cross sectional changes may result in different impacts although experiencing the same influences.

**Table 7.2.** Acquired results from FEA

Case	in-plane Angle of attack $\alpha$ [°]	Flange Side FS					Convex Side CS								
		$F_{scrit}$ [N]	$u$ [mm]	at $F_{scrit}$	Failure Position $z$ [mm]	at $F_{scrit}$	Bending stiffness $c$ [N/mm]	Flexural rigidity $EI$ [ $\times 10^6$ Nmm <sup>2</sup> ]	$F_{scrit}$ [N]	$u$ [mm]	at $F_{scrit}$	Failure Position $z$ [mm]	at $F_{scrit}$	Bending stiffness $c$ [N/mm]	Flexural rigidity $EI$ [ $\times 10^6$ Nmm <sup>2</sup> ]
Nominal	90	2,55	150,4		866		0,0224	554	1,884	162,3		118		0,0172	425
Manufactured	90	2,51	153,8		897		0,0214	529	1,89	172,0		114		0,0162	401
Stowed	90	2,60	95,0		296		0,0360	890	1,833	242,5		166		0,014	335

## 7.2.2 Robustness Assessment of FEA results and comparison to Experiments

Considering the same components of subsystem robustness with the stiffness-based, load-based and displacement-based partial robustness as done before, their constituents differ since the number of robustness parameters determined with the FEA is reduced. Subsystem robustness is determined for three cases: the stowed case (“Stowed-FEA”) and the manufactured case (“Manufactured-FEA”) determined in FEA, and for comparison robustness is again determined with a reduced set of robustness parameters for the ideal configuration under  $\alpha=90^\circ$  from the experiments in section 7.1.2, as “Manufactured-Experiment” case. This allows to draw a comparison between strongly influenced and pristine cases, as well as between FEA and experimental results for robustness.

As done previously stiffness-based partial robustness is determined by bringing the achieved flexural rigidity of the influenced structure ( $EI_{FS}$  and  $EI_{CS}$ ) into relation to the flexural rigidity of the uninfluenced structure, here the nominal results ( $EI_{FSnom}$  and  $EI_{CSnom}$ ) for each side of the boom. As provided with Equation (7.6) this is done for the cases “Manufactured-FEA” and “Manufactured-Experiment” with terms that represent the flexural rigidity sensitivity. For the case “Stowed-FEA” however partial robustness is made up of two different types of terms, a reserve and a sensitivity term, as shown in Equation (7.7). This is due to the postulation for the here proposed method claiming robustness to be between zero and one ( $0 \leq Ro_i \leq 1$ ; see chapter 4), thus leading to the requirement for each term that its numerator must always be smaller than the denominator. In consequence each term types change has to be adjusted to the specific case. As this circumstance may decrease comparability, it might also increase the effort of robustness assessment, and is seen as a drawback of the proposed method.

*Stiffness-based* partial robustness – “Manufactured-FEA” case, “Manufactured-Experiment” case:

$$Ro_\kappa = w_{\kappa 1} \cdot \frac{EI_{FS}}{EI_{FSnom}} + w_{\kappa 2} \cdot \frac{EI_{CS}}{EI_{CSnom}} \quad (7.6)$$

}  
 Flexural rigidity Sensitivity

*Stiffness-based* partial robustness – “Stowed-FEA” case:

$$RO_{\kappa} = \underbrace{w_{\kappa 1} \cdot \left(1 - \frac{EI_{FS_{nom}}}{EI_{FS}}\right)}_{\text{Flexural rigidity reserve}} + \underbrace{w_{\kappa 2} \cdot \frac{EI_{CS}}{EI_{CS_{nom}}}}_{\text{Flexural rigidity sensitivity}} \quad (7.7)$$

Again similar to robustness assessment for experiments done in section 7.1, load-based partial boom robustness is determined by relating required critical buckling loads ( $F_{FS_{Req}}$  and  $F_{CS_{Req}}$ ) to achieved buckling loads at failure ( $F_{FS_{1st}}$  and  $F_{CS_{1st}}$ ), and uninfluenced buckling load results ( $F_{FS_{nom}}$  and  $F_{CS_{nom}}$ ) to the achieved buckling loads at failure. Note that for experimental data values of the first test runs for the achieved buckling loads are chosen, while FEA provides only one run. Additionally, and due to the lack of axial load data, a reduced number of terms is used to determine partial robustness. Again, the requirement of a smaller numerator leads to different terms used in the three cases, as shown in Equations (7.8) and (7.9). Thus, Equation (7.9) is valid for both “manufactured” cases, while the “stowed” case demands a different combination of terms.

*Load-based* partial boom robustness –, “Stowed-FEA” case:

$$RO_L = \underbrace{w_{L1} \cdot \left(1 - \frac{F_{FS_{Req}}}{F_{FS_{1st}}}\right) + w_{L2} \cdot \left(1 - \frac{F_{CS_{Req}}}{F_{CS_{1st}}}\right)}_{\text{Lateral bending load reserve}} + \underbrace{w_{L3} \cdot \frac{F_{FS_{1st}}}{F_{FS_{nom}}} + w_{L4} \cdot \frac{F_{CS_{1st}}}{F_{CS_{nom}}}}_{\text{Lateral bending load sensitivity}} \quad (7.8)$$

*Load-based* partial boom robustness – cases “Manufactured-FEA”, “Manufactured-Experiment”:

$$RO_L = \underbrace{w_{L1} \cdot \left(1 - \frac{F_{FS_{Req}}}{F_{FS_{1st}}}\right) + w_{L2} \cdot \left(1 - \frac{F_{CS_{Req}}}{F_{CS_{1st}}}\right) + w_{L3} \cdot \left(1 - \frac{F_{CS_{nom}}}{F_{CS_{1st}}}\right)}_{\text{Lateral bending load reserve}} + \underbrace{w_{L4} \cdot \frac{F_{FS_{1st}}}{F_{FS_{nom}}}}_{\text{Lateral bending load sensitivity}} \quad (7.9)$$

The displacement-based partial robustness is determined for all cases with a separate equation, due to the before mentioned requirement of the numerator to be smaller than the denominator in a term. Following this, Equation (7.10), Equation (7.11) and Equation (7.12) determine partial robustness for the “Manufactured-FEA”, the “Manufactured-Experiment” and the “Stowed-FEA” cases, respectively. Here the achieved boom tip displacements at failure ( $u_{FS}$  and  $u_{CS}$ ), are related to the simulated nominal boom tip displacements ( $u_{FS_{nom}}$  and  $u_{CS_{nom}}$ ), thus comparing influenced value with uninfluenced. As seen in the second term of the displacement –based equations the preexisting displacement due to influences (manufacturing and stowage) are added to the convex side values, since the FE-determined values are relative to the starting point of tip displacement when loading.

*Displacement-based* partial boom robustness – “Manufactured-FEA” case:

$$RO_u = \underbrace{w_{u1} \cdot \frac{u_{FS_{nom}}}{u_{FS}} + w_{u2} \cdot \left(\frac{u_{CS_{nom}}}{u_{CS} + u_{infl}}\right)}_{\text{Boom tip displacement sensitivity}} \quad (7.10)$$

Displacement-based partial boom robustness – “Manufactured-Experiment” case:

$$Ro_u = w_{u1} \cdot \frac{u_{FSnom}}{u_{FS}} + w_{u2} \left( 1 - \frac{u_{CS} + u_{infl}}{u_{CSnom}} \right) \quad (7.11)$$

Boom tip displacement sensitivity

Displacement-based partial boom robustness – “Stowed-FEA” case:

$$Ro_u = w_{u1} \cdot \frac{u_{FS}}{u_{FSnom}} + w_{u2} \left( \frac{u_{CSnom}}{u_{CS} + u_{infl}} \right) \quad (7.12)$$

Boom tip displacement sensitivity

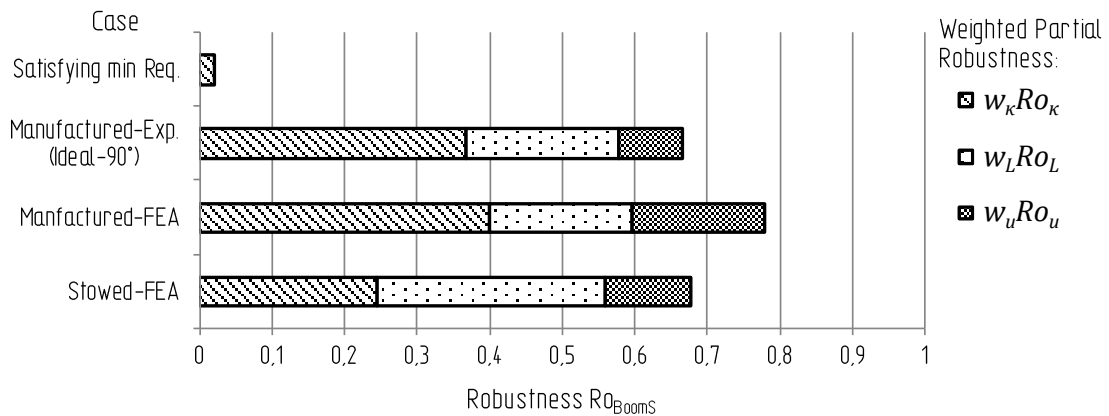
With the input values from FEA, experiments and weighting factors, provided in an overview in Table G. 2 of Appendix G, the equations are solved. Note that weighting factors are chosen to represent a general application of a boom and is done for demonstration at this point. An overview of the results for partial and subsystem robustness is given with Table 4.1, while the contribution by each of the partial robustness metrics to subsystem robustness is illustrated for all studied cases in Figure 7.21. When comparing all three cases, quantified subsystem robustness exhibits similar values, which can be explained by the similar results from FEA, with robustness for the “Stowed-FEA” case with  $Ro_{BoomS_{stow-FEA}}=0.678$ , for the “Manufactured-FEA” case with  $Ro_{BoomS_{Man-FEA}}=0.78$  and for the “Manufactured-Experiment” case with  $Ro_{BoomS_{Man-Exp}}=0.665$ .

However, both simulated cases (“Stowed-FEA”, “Manufactured-FEA”) achieve higher robustness compared to the tested case (“Manufactured-Experiment”). Additionally, when comparing robustness of the tested case facilitating the reduced results set of the FEA (“Manufactured-Experiment”), with the robustness facilitating the extended results set obtained directly in the experiments (“Ideal-90°” in subsection 7.1), the reduced set-based robustness is lower. This shows that a more precise selection of robustness parameters with greater availability, therefore incorporating more effects and influences, may lead to a higher precision of robustness quantification.

**Table 7.3.** Resulting Robustness based on FEA

Case	Partial Robustness			Weighted Partial Robustness			Subsystem Robustness
	$Ro_K$	$Ro_L$	$Ro_u$	$w_K Ro_K$	$w_L Ro_L$	$w_u Ro_u$	$Ro_{Boom}$
Stowed-FEA	0.583	0.812	0.622	0.245	0.313	0.12	0.678
Manufactured-FEA	0.949	0.511	0.942	0.4	0.197	0.182	0.78
Manufactured-Exp.	0.875	0.547	0.445	0.368	0.211	0.086	0.665

As Figure 7.21 provides a graphical illustration and comparison of the achieved subsystem robustness for each case under investigation, it further illustrates the proportions of contribution by each partial robustness metric. Partial robustness based on stiffness and load are again major contributors, as this is driven by the chosen weighting factors and the achieved performance. When comparing the two cases of the manufactured boom, it becomes obvious that partial contribution differs and stiffness contributes more in the FEA-based cases. Due to the identical stiffness and load terms this can be attributed to the higher values in achieved robustness parameters.



**Figure 7.21.** Comparison of Boom Subsystem robustness for exemplary cases simulated in FEA

### 7.3 Chapter Conclusion

In conclusion this chapter applies the proposed robustness assessment method by quantifying robustness parameters and consequently robustness in practical experiments and finite element simulations. It mainly resembles main task 4, robustness quantification, of the proposed robustness assessment method in section 4.5.

In detail this chapter describes mechanical experiments on the Boom Subsystem and boom component. It firstly introduces the boom test stand that is used to generate essential and characteristic mechanical data of the boom in bending and buckling experiments. It further explains the load and boundary conditions as well as testing principle. The experiments were executed on a Gossamer-1 boom under ideal clamped conditions and on the Boom Subsystem of Gossamer-1 with its spacecraft-realistic interfaces and boundary conditions, in the so called ideal and real configuration respectively. The characteristic load cases studied were lateral bending, as worst case asymmetric load case, and symmetric quasi-axial loading, representing a nominal load case. The different mechanical buckling behaviors observed are illustrated in typical load-displacement Diagrams, with most cases exhibiting a linear followed by a non-linear post buckling behavior. However, buckling failure is indicated mostly by the event of collapse, or for some configurations as sharp load drop following a maximum load. The obtained and discussed results are critical buckling load, stiffness in terms of boom bending stiffness and flexural rigidity, boom tip displacement and residual load carrying capacity.

In finite element simulations, resembling the same conditions as found in the mechanical experiments, several cases were studied, aiming to predict the mechanical buckling behavior. This was done especially with the goal to obtain robustness parameters for settings that cannot be realized in practical tests without enormous effort, such as incorporated influences in very long booms by long term storage in stowed state and space environmental influences. Three cases are simulated in the ideal configuration: a nominal (uninfluenced) case, a pristine case (after manufacturing), and a stowed case, after long-term storage in stowed state at elevated temperatures. Influences were incorporated in terms of geometric and material imperfections, in a three stepped simulation, featuring a static analysis, a linear buckling analysis and a final non-linear buckling analysis. The resulting reaction forces, stiffness and boom tip displacements are extracted and further used to determine partial and subsystem robustness, as those resemble the robustness parameters.

Nevertheless, some drawbacks of the proposed method were pointed out. One is that robustness cannot be zero by the here postulated definition, since at least some requirement e.g. stiffness needs to be provided in order for a GosSSS to have any functionality. Another drawback is the fact that mathematical terms need to be in such manner that a term's numerator is smaller than its denominator. This requirement renders comparability somewhat, as different terms must be used that might generate different outcomes. It may also increase the effort of finding the correct term. Nonetheless,

a thorough selection of mathematical terms is necessary for each application and is therefore considered a reasonable effort in order to obtain a realistic and quantifiable robustness value.

Overall, in the experiments and in the FE-simulations, it is demonstrated that partial robustness can be determined by combination and weighting of reserve and sensitivity terms, made up of specific metrics of robustness parameters, thus quantifying partial and subsystem robustness. This consequently approves the **2. Work Hypothesis** and **1. Work Hypothesis 3. Work Hypothesis**, while it supports the **Basic Hypothesis** as well.

## 8. SUMMARY, CONCLUSION AND OUTLOOK

With the overall goal to develop a methodology that can be used to assess robustness of Gossamer Structural Space Systems, several intermediate targets are pursued. One of them is to identify and derive metrics that characterize robustness, for a component, a subsystem, and consequently for the overall system. However, such metrics must be quantifiable and measurable, as they are required to be determined objectively by e.g. experiments, numerical simulations or analytical calculations. With the assumption that the overall system robustness can be viewed as a composition of several partial robustness values, different subsystems or components contribute in a different degree as they vary with conditions, relations and functions. Therefore, robustness differs with conditions and conditional states, relying on the mission phases and the constellation of system elements in terms of relations, first and foremost of mechanical nature. It is therefore essential to elaborate on such relations, conditions and contributions of robustness at lower levels of complexity e.g. on subsystem and component level, as well as to identify and determine them. Another goal is set to determine influences that affect robustness of Gossamer Structural Space Systems. Such influences are of external and internal origin e.g. imperfections, noise or environmental effects, and need to be quantified as well.

To do so, occurring problems and boundary conditions of existing Gossamer Structural Space systems as well as approaches, methods and principles in regard to robustness and robust design are analyzed. Existing GosSSS are categorized and examples of operating GosSSS applications are analyzed for occurring deficiencies in robustness and detrimental effects. Based on the 2D-planar type of GosSSS this thesis is concentrating on, focus is put on basic elements of a subsystem. Their functions are analyzed and general requirements and characteristics in regard to robustness are derived. Moreover, standard design approaches and principles in aerospace industry and engineering are scrutinized, the most suitable application of robustness assessment within the general design process is localized, and established design philosophies and principles like Fail-Safe, Safe-Life and Robust design are discussed. Within the review, existing robustness approaches are found in a variety of fields each defining robustness differently. Overall several approaches of robustness assessment are studied and discussed, with the goal to find basic principles that are applicable and adoptable to GosSSS.

Building on this, a new methodology is proposed by firstly defining requirements and the extend, as existing requirements on robustness for general structural systems are adopted, modified and extended. Theoretical considerations are made on the conditionality of robustness in terms of element failure, function fulfillment and severeness for different constellations of subsystem failures resulting in a system failure. Furthermore, two of the most common approaches of system view, the bottom-up and the top-down strategies, are discussed in the light of GosSSS, thus providing the principle base for the herein generated methodology. As mathematical relations have to be developed, the composition of the overall system robustness, made up of terms, is elaborated and discussed on simplified and theoretical examples. Here minimum principles as well as a variety cumulative approaches are developed, compared and further discussed. Moreover, the importance of using weighting factors and the reasoning behind it, as well as their application and determination, are elaborated and studied on simplified examples. In order to answer one of the main questions, component and subsystem robustness are principally developed for a generic 2D-planar GosSSS, while following the approaches of the two identified main robustness types, sensitivity-related robustness and reserve-related robustness. For each of the major subsystems which are determined for such GosSSS, namely Boom Subsystem, Membrane Subsystem, Mechanism Subsystem and Interface Subsystem, robustness is defined to be a composition of robustness, incorporating the specific characteristics of each subsystem with their robustness parameters and the fundamental metrics that make up a specific robustness. With the principal methodology of robustness in place, the main tasks of robustness assessment as well sub-tasks and their sequence are developed and transferred into a framework for robustness assessment that is an integral part of the design process. Additionally, a strategy for robustness quantification, showing how to practically incorporate simulations and experiments for metric (value) generation is created and outlined. Moreover, the implementation of



robustness assessment in a typical design process of a Gossamer Structural Space System is demonstrated to provide a tangible guideline for its application.

In order to expand the methodology development and to determine necessary constituents in a case study sensitivity, risk and the system itself (a 2D-planar GosSSS) are analyzed. Within a mission envelope and mission objective set for this case study, based on the solar sail demonstrator Gossamer-1 and to some extent on aspects of similar applications (ADEO, Gossamer-2), the overall and subsystem architecture is scrutinized. For each of the four subsystems of Gossamer-1, namely boom subsystem, membrane subsystem, mechanism subsystem and interface subsystem, essential functions, characteristic robustness parameters and associated weighting factors are determined. By analyzing the system's structure, main functions and their contributions to the overall system function are identified. Based on these functions, robustness parameters are derived, while according weighting factors are determined based on function fulfillment and conditionality of robustness in regard to the different mission phases. Moreover, different influences, their causes, consequences and quantifiable influence factors are identified and derived. They are further demonstrated along with the developed robustness parameters on an analytical example of a boom component with influenced geometry being loaded at its tip in the two main directions of its cross section. With a reduced cross-sectional height and an increased width compared to nominal, both by about 20 % change due to expected creep effects when stowing a boom for a long period of time, as well as an additional decrease of the material's Young's modulus induced by e.g. atomic oxygen influence, the bending stiffness and the achievable characteristic load deteriorates starkly in one direction while it is less impacted in the other main direction of loading. This demonstrates on one hand the exemplary application of influence factors within this thesis and on the other hand the necessity of quantifying these influences as they may be greatly impacting structural performance and consequently the function fulfillment of the component, subsystem and system. For the further use of the proposed robustness approach weighting factors, that are characteristic for each GosSSS subsystem, are determined from functionality numbers, failure numbers and redundancy numbers, thus demonstrating the relations and interactions between the different subsystems seen as a whole.

As influences are determining robustness in large parts, the major influences are measured in experiments in a case study on the boom subsystem of the solar sail demonstrator Gossamer-1 the drag sail ADEO, with the goal of providing quantified influence factors. This includes the determination of geometric dimension changes in several experiments with short boom samples and full-size booms of Gossamer-1. In specific manufacturing and stowage induced changes of cross-sectional dimensions as well as shape deviations e.g. axial curvature and waviness are extensively studied, while stowage induced creep behavior of the build material and influences of interactions are scrutinized in further experiments. Furthermore, material property variations due to material inhomogeneity as well as effects on material characteristics induced by space environment like atomic oxygen and micrometeoroids and orbital space debris are measured, thus providing a whole set of quantified influence factors. As influences within the process of measuring itself and induced by the used test equipment and principle are assumed, their impact on the measured performance metrics are investigated as well.

Aiming to give proof of the proposed method for robustness assessment, it is applied in a case study on the hardware of the Gossamer-1 solar sail demonstrator. In order to acquire quantified robustness values, the boom subsystem and boom component are tested in different configurations and load cases, in a specific boom test stand developed for this purpose. An ideal configuration with ideal boundary conditions, with a clamped boom root and a Visual-Load-Adapter that inhibits cross sectional deformations at the boom tip is compared to a realistic configuration that resembles the boundary conditions and load introduction of the spacecraft, thus providing robustness parameter values that are influenced by external and internal factors. These robustness parameters are obtained for stiffness in terms of flexural rigidity and bending stiffness, for characteristic loads in terms of maximum achieved critical buckling loads at which a boom fails, and for the residual load carrying capacity as well as for boom tip displacements. Subsequently, robustness assessment is performed using the robustness parameter values determined in the tests, in the here proposed approach. This

is done by combining parameters to different metrics that resemble two types of robustness constituents: Reserve-related terms, bringing achieved and required values into relation, and sensitivity-related terms, bringing influenced or achieved values into relation to theoretical achievable (uninfluenced) values or previously achieved values (pristine condition). When looking at the resulting robustness one can say that higher performance and robustness values are achieved for ideal conditions, although in some constellations the real configuration provides nearly equal results, thus expressing a good robustness. However, it should be noted that the performed tests with ideal and therefore less complex boundary conditions provide higher accuracy with lower standard deviations of the measurements, thus indicating also higher result accuracy. In order to further scrutinize the proposed robustness assessment approach, a finite element analysis is performed within this case study. This is done with the goal of predicting mechanical behavior, as basis for robustness parameters and consequently robustness, on influenced structural elements and subsystems, that cannot be tested in practice e.g. for very large sizes or harsh environmental conditions, but need to be investigated within the design process. The applied finite element analysis facilitates a three stepped analysis, starting with a static structural analysis that implements basic influences, followed by an intermediate linear Eigenvalue buckling analysis that provides a pre-deformed model with imperfections and finishes with the final non-linear buckling analysis that calculates the buckling behavior. The analysis focuses on three cases, a “nominal” case representing nominal geometry and material specifications without any influences, a “manufactured” case with realistic material parameters and according manufacturing imperfections, and a “stowed” case, resembling a boom after long term storage in stowed condition under 80°C, with cross sectional and shape deviations, and an assumed exposure to atomic oxygen. The model itself represents a boom in ideal configuration, while theoretical load cases under an angle of attack of 90° is simulated for each side of the boom cross section. With the obtained values for critical buckling load at failure, boom tip displacement and flexural rigidity as well as the determined weighting factors, robustness parameters, partial robustness as well as subsystem robustness are quantified using the developed equations and are compared over the studied cases. Moreover, robustness values determined in experiments are compared to the results from FEA, as well as single robustness components. Some requirements are becoming visible when applying the proposed method. One is that robustness cannot be zero by the here postulated definition, since at least some requirement e.g. stiffness needs to be provided in order for a GosSSS to have any functionality. In for the proposed approach to work properly the mathematical terms need to be in such manner that a term’s numerator is smaller than its denominator. This requirement renders comparability somewhat, as different types of terms deliver different outcomes, while it may also increase the effort of finding the correct term. After a thorough selection of mathematical terms is done, realistic and quantifiable robustness values for each studied case are provided, thus demonstrating the capability to quantify robustness for GosSSS with the here proposed approach.

## Conclusion

Supporting the **1. Work Hypothesis** connections and interactions of GosSSS subsystems are successfully captured in mathematical terms, leading to robustness, in theoretical examples comparing mathematical approaches with the outcome of using a cumulative approach that facilitates weighting factors for the here presented thesis. The proposed weighted cumulative approach enables the use of a composition that is made up of several robustness components, in accordance to the hardware system that is analyzed, and is sufficiently conservative without over estimating single components. This strongly supports the **1. Work Hypothesis**, and therefore is considered to be approved. Moreover, the finding that robustness is conditional and depending on the mission phase and the according constellation of subsystems including its interactions, further supports this hypothesis as well as it approves the **4. Work Hypothesis**.

Within the case study of the solar sail demonstrator Gossamer-1 all subsystems are analyzed down to the component level. While the main functions are identified and formulated into robustness parameters for each subsystem, the according partial robustness weighting factors are determined

and discussed on the explicit example of the boom subsystem. The variety in identified functions thus leads to different robustness parameters that determine the overall robustness. It is shown that robustness of a system or subsystem strongly depends on the fulfilment of its main function(s), as this poses the reason for building the system in the beginning. The function fulfilment in consequence, and as considered the bases of robustness parameters, is most useful when determined objectively and realistically. It therefore needs to be measurable, as provided with the approach discussed in this thesis instead of subjective. In essence robustness parameters and partial robustness weighting factors are derived from measurable values that represent function fulfilment, thus leading to consider the **2. Work Hypothesis** to be approved.

As influences and detrimental effects on hardware and its functions are identified, their causes and consequences are studied as well. By demonstrating the application of influence factors on a theoretical example, it is shown that influences, regarded as factors provide a realistic behavior of an influenced structure e.g. in terms of reducing factors for geometric dimensions, material properties or loads. Moreover, occurring influence factors are determined and quantified in experiments on CFRP booms, boom samples, material specimens and test equipment, on the boom subsystem and its components of Gossamer-1. With this successful application of realistic influence factors, as part of the here proposed robustness assessment method, the **3. Work Hypothesis** is therefore be considered approved as well.

Overall, the approach of system robustness as a composition is developed and demonstrated on the boom subsystem in the case study of Gossamer-1, although real data was limited to this subsystem. Moreover, robustness determined with the proposed methodology proves to be quantifiable and objective. This however, should be seen within the limitations that not all existing details on connections, relations and influences between components and subsystems can be incorporated in reality, due to a reasonable effort. Nevertheless, the proposed method generates a somewhat relative measure, since quantitative benchmarks and thresholds for nominal/optimal robustness parameters are necessary, as they are used for comparison in the developed mathematical robustness terms. This becomes clear when generating a case without any robustness, that is still satisfying requirements without any margin, however still providing very low robustness values, depending on the mathematical relations used in the defining robustness terms. Concluding one can consider the **Basic Hypothesis**, stating that the overall system robustness of a GosSSS can be quantified as a composite of single subsystem robustness, largely approved, however with some open ends for further discussions and work as given with the outlook.

## Outlook

In future design processes the here proposed approach should be applied from the beginning when developing a GosSSS. However, along with the application the proposed robustness assessment ought to be refined. When applying the here proposed methodology this should be addressed as robustness parameters and partial robustness need to be determined and quantified for all subsystems in order to provide robustness for the whole GosSSS. Moreover, the identified influences and detrimental effects should be explored and quantified for every subsystem as well. Concerning a better comparability and for tracking robustness improvements, benchmarks for robustness values of a subsystem are necessary, need to be established and used as an evaluation scale within the robustness assessment, while for the optimal choice of mathematical terms for each partial robustness a guideline is seen worthwhile to be implemented. In order to improve early predictions of robustness, the applied FE-model should be advanced and extended in terms of accuracy, automation and considered influences, as it currently does not include all addressable influences and imperfections. In specific using a scripted Python automation that varies input parameters e.g. influences factors with a Monte-Carlo-Simulation within the DoE, as described earlier, is considered promising. Moreover, an overall system model e.g. a representative FE beam-membrane model that predicts overall mechanical system behavior should be established in order to compare robustness terms and

different designs. This would also provide a viable tool to predict mechanical behavior in cases that have not been tested or cannot be tested due to the enormous effort of applying the relevant influences on large scale. Overall, an increased number of test samples and the extension of the here presented test program e.g. extended by VUV exposure and longer durations of stowage as well as extended functional testing of whole subsystems is recommended in order to provide a wider data base for the determination of robustness values.

## REFERENCES

1. Jenkins CHM (2006) Recent Advances in Gossamer Spacecraft, Vol. 212, Progress in Astronautics and Aeronautics Series, 212. AIAA. pp. 191–258
2. Jenkins CHM (ed) (2005) Compliant structures in nature and engineering. Design and nature, vol 5. WIT Press, Southampton. pp. 203–246
3. Jenkins CHM (2001) Gossamer Spacecraft: Membrane and Inflatable Structures Technology for Space Applications. In: Zarchan P (ed) Progress in Astronautics and Aeronautics, vol 191. American Institute of Aeronautics and Astronautics Inc, pp. 449–586
4. Chmielewski AB, Jenkins CHM (2005) Gossamer spacecraft: Chapter 10. In: Jenkins CHM (ed) Compliant structures in nature and engineering, vol 1. WIT Press, Southampton, pp. 203–243
5. European Cooperation for Space Standardization, ESA (2009) ECSS-E-ST-32-10C - Space Engineering: Structural factors of safety for spaceflight hardware (ECSS-E-ST-32-10C)
6. European Cooperation for Space Standardization, ESA (2010) ECSS-E-HB-32-24A - Space Engineering: Buckling of Structures (ECSS-E-HB-32-24A), Handbook
7. European Cooperation for Space Standardization, ESA (2011) ECSS-E-HB-32-20 Part 3A - Space Engineering: Structural materials handbook - Part 3: Load transfer and design of joints and design of structures (ECSS-E-HB-32-20 Part 3A), Handbook
8. Hillebrandt M (2019 / 2020) Conceptual Design of Deployable Space Structures. Dissertation, Technische Universität Carolo-Wilhelmina zu Braunschweig
9. NASA - National Aeronautics and Space Administration (1971) NASA SP 8065 - Tubular Spacecraft Booms (extendible, reel stored), Technical Report
10. Garcia M (2017) About the Space Station Solar Arrays. [https://www.nasa.gov/mision\\_pages/station/structure/elements/solar\\_arrays-about.html](https://www.nasa.gov/mision_pages/station/structure/elements/solar_arrays-about.html). Accessed 19 Jun 2019
11. Mansfield CL (2006) Spread Your Wings, It's Time to Fly. [http://www.nasa.gov/mision\\_pages/station/behindscenes/truss\\_segment.html](http://www.nasa.gov/mision_pages/station/behindscenes/truss_segment.html). Accessed 17 May 2018
12. NASA (2000) Shuttle Press Kit: Endeavour: Delivering solar Arrays to the International Space Station - STS-97. [http://www.jsc.nasa.gov/history/shuttle\\_pk/pk/Flight\\_101\\_STS-097\\_Press\\_Kit.pdf](http://www.jsc.nasa.gov/history/shuttle_pk/pk/Flight_101_STS-097_Press_Kit.pdf). Accessed 20 Jul 2012
13. Boeing (2012) International Space Station: Solar Power. [http://www.boeing.com/boeing/defense-space/space/spacestation/systems/solar\\_arrays.page](http://www.boeing.com/boeing/defense-space/space/spacestation/systems/solar_arrays.page). Accessed 20 Mar 2019
14. Kauderer A (2006) STS-116 Shuttle Mission Imagery: S116-E-05789
15. Mansfield CL (11.13.07) STS-120: Winning Team Completes Challenging Mission: Mission Overview. Accessed 17 May 2018
16. Kauderer A (2007) STS-120 Shuttle Mission Imagery: ISS016-E-008875
17. Banks BA, Groh KK de, Miller SK (2004) Low Earth Orbital Atomic Oxygen Interactions with Spacecraft Materials. MRS Proc 851: p. 103. <https://doi.org/10.1557/PROC-851-NN8.1>
18. Banks BA, Lenczewski M, Demko R (2002) Durability Issues for the Protection of Materials from Atomic Oxygen Attack in Low Earth Orbit. Paper IAC-02–1.5.02. In: IAF International Astronautical Federation (ed) 53rd International Astronautical Congress IAC. IAC 2002: The World Space Congress. Houston, TX, United States. 10-19 Oct. 2002
19. Christiansen E (2018) Micro-Meteoroid and Orbital Debris (MMOD) Protection Overview. <https://ntrs.nasa.gov/search.jsp?R=20190001193&q=Nm%3D4294930040%7CAuthor%7CChristiansen%2C%2520Eric%26N%3D0>. Accessed 20 Jan 2019
20. Christiansen E (2014) Micrometeoroid and Orbital Debris (MMOD) Risk Overview. In: NASA Johnson Space Center (ed) NASA In-Space Inspection Technology Workshop (ISIW 2014). ISIW 2014. Houston, Texas, USA. 15 –16 July 2014

21. Foster CL, Tinker ML, Nurre GS et al. (1995) Solar-array-induced disturbance of the Hubble Space Telescope pointing system. *Journal of Spacecraft and Rockets* 32: pp. 634–644. <https://doi.org/10.2514/3.26664>
22. Lothar Gerlach (2010) How Hubble got its Wings. [http://www.esa.int/Our\\_Activities/Space\\_Engineering/How\\_Hubble\\_got\\_its\\_wings](http://www.esa.int/Our_Activities/Space_Engineering/How_Hubble_got_its_wings). Accessed 08 Jan 2019
23. Moussi A, Drolshagen G, McDonnell J et al. (2005) Hypervelocity impacts on HST solar arrays and the debris and meteoroids population. *Advances in Space Research* 35: pp. 1243–1253. <https://doi.org/10.1016/j.asr.2005.03.060>
24. Kearsley AT, Drolshagen G, McDonnell J et al. (2005) Impacts on Hubble Space Telescope solar arrays: Discrimination between natural and man-made particles. *Advances in Space Research* 35: pp. 1254–1262. <https://doi.org/10.1016/j.asr.2005.05.049>
25. Lindberg Christensen L (2002) Hubble's solar arrays - behind the scenes. <https://www.spacetelescope.org/news/heic0203/>. Accessed 09 Dec 2018
26. NASA Hubble Site: Image - Hubble as Shuttle Columbia Approaches (2002). <http://hubble-site.org/image/4525/spacecraft>. Accessed 19 Jun 2019
27. Loff S (2015) Hubble Space Telescope Reaches Orbit. <https://www.nasa.gov/content/hubble-space-telescope-reaches-orbit>. Accessed 19 Jun 2019
28. NASA (1994) STS-61 Mission Highlights - YouTube: Resource Tape Pt.#1. <https://www.youtube.com/watch?v=ubKRN5G6Dzc>. Accessed 19 Jun 2019
29. ESA - European Space Agency Hubble: Impacts seen on returned solar arrays: averaging four holes per square metre. [http://www.esa.int/spaceinimages/Images/2010/12/Impacts\\_seen\\_on\\_returned\\_solar\\_arrays\\_averaging\\_four\\_holes\\_per\\_square\\_metre](http://www.esa.int/spaceinimages/Images/2010/12/Impacts_seen_on_returned_solar_arrays_averaging_four_holes_per_square_metre). Accessed 19 Jun 2019
30. ESA - European Space Agency (2010) Hubble: Piano-wire-like hinge pins observed moved out of position. [http://www.esa.int/spaceinimages/Images/2010/12/Piano-wire-like\\_hinge\\_pins\\_observed\\_moved\\_out\\_of\\_position](http://www.esa.int/spaceinimages/Images/2010/12/Piano-wire-like_hinge_pins_observed_moved_out_of_position). Accessed 19 Jun 2019
31. Chamberlain MK, Kiefer SH, Banik JA (2018) On-Orbit Structural Dynamics Performance of the Roll-Out Solar Array. In: AIAA American Institute of Aeronautics and Astronautics (ed) AIAA Spacecraft Structures Conference 2018. AIAA SciTech Forum 2018. Curran Associates Inc, Red Hook, NY. Kissimmee, Florida, USA. 8-12 January
32. NASA (2019) ROSA - Space Station Gallery. [https://www.nasa.gov/mission\\_pages/station/research/experiments/explorer/Investigation.html?#id=1876](https://www.nasa.gov/mission_pages/station/research/experiments/explorer/Investigation.html?#id=1876). Accessed 23 Jun 2019
33. NASA (2014) NASA - James Webb Space Telescope. <http://jwst.nasa.gov/index.html>. Accessed 23 Jun 2019
34. Arianespace (October/2016) ARIANE 5 User's Manual, Issue 5, Revision 6
35. Sickinger C (2009) Verifikation entfaltbarer Composite-Booms für Gossamer-Raumfahrtsysteme. Dissertation, Technische Universität Carolo-Wilhemina zu Braunschweig
36. European Cooperation for Space Standardization (2009) ECSS-M-ST-40C Rev. 1 - Space project management: Configuration and information management (ECSS-M-ST-40C Rev. 1)
37. European Cooperation for Space Standardization (2009) ECSS-M-ST-10C Rev. 1 - Space project management: Project planning and implementation (ECSS-M-ST-10C Rev. 1)
38. Hirshorn SR, Voss LD, Bromley LK (2017) Nasa Systems Engineering Handbook - Nasa Sp-2016-6105: Design Test Integrate Fly. NASA/SP-2016-6105 Rev 2, HQ-E-DAA-TN38707, Rev 2
39. European Cooperation for Space Standardization, ESA (2014) ECSS-E-AS-11C - Space engineering: Adoption Notice of ISO 16290, Space systems - Definition of the Technology Readiness Levels (TRLs) and their criteria of assessment (ECSS-E-AS-11C)
40. Verein Deutscher Ingenieure e.V. (2019) Design of technical products and systems: Model of product design - Part 1 ICS 03.100.40 (VDI 2221:2019-11)
41. Pahl G, Beitz W, Feldhusen J et al. (2007) *Engineering Design*. Springer London, London. pp. 249-263

42. Biondini F, Frangopol DM, Restelli S (2008) On Structural Robustness, Redundancy, and Static Indeterminacy. In: Anderson D, Ventura C, Harvey D et al. (eds) *Crossing Borders. Structures Congress 2008*. ASCE, pp. 1–10. Vancouver, British Columbia, Canada. April 24–26, 2008
43. Frangopol DM, Klisinski M (1989) Weight-strength-redundancy interaction in optimum design of three-dimensional brittle-ductile trusses. *Computers & Structures* 31: pp. 775–787. [https://doi.org/10.1016/0045-7949\(89\)90212-5](https://doi.org/10.1016/0045-7949(89)90212-5)
44. Starossek U, Haberland M (2012) Robustness of structures. *IJLCPE* 1: p. 3. <https://doi.org/10.1504/IJLCPE.2012.051279>
45. U.S. Department of Defense (2016) UFC 4-023-03 Design of Buildings to Resist Progressive Collapse, with Change 3 | WBDG - Whole Building Design Guide: Design of Buildings to Resist Progressive Collapse (UFC 4-023-03). <https://www.wbdg.org/ffc/dod/unified-facilities-criteria-ufc/ufc-4-023-03>. Accessed 23 Oct 2019
46. Belvin W, Zander ME, Sleight D et al. (2012) Materials, Structures and Manufacturing: An Integrated Approach to Develop Expandable Structures. In: AIAA American Institute of Aeronautics and Astronautics (ed) *53rd AIAA/ASME/ASCE/AHS/ASC Structures, Structural Dynamics and Materials Conference*. AIAA American Institute of Aeronautics & Astronautics, Reston, VA, United States. Honolulu, Hawaii, USA. 23 - 26 April
47. Zander ME, Belvin WK (2012) Concept-Development of a Structure Supported Membrane for Deployable Space Applications- From Nature to Manufacture and Testing. In: ESA, DLR, CNES (ed) *12th European Conference on Spacecraft Structures, Materials and Environmental Testing*. ECSS 2012, vol 691, p. 124. Noordwijk, The Netherlands. 20-23 March
48. Lind NC (1995) A measure of vulnerability and damage tolerance. *Reliability Engineering & System Safety* 48: pp. 1–6. [https://doi.org/10.1016/0951-8320\(95\)00007-0](https://doi.org/10.1016/0951-8320(95)00007-0)
49. Agarwal J, Blockley D, Woodman N (2001) Vulnerability of 3-dimensional trusses. *Structural Safety* 23: pp. 203–220. [https://doi.org/10.1016/S0167-4730\(01\)00013-3](https://doi.org/10.1016/S0167-4730(01)00013-3)
50. NASA - National Aeronautics and Space Administration NASA-STD-5001B W/CHANGE 2: Structural design and test factors of safety for Spaceflight hardware, NASA Technical Standard. <https://standards.nasa.gov/standard/nasa/nasa-std-5001>. Accessed 03 Sep 2019
51. Doorn N, Hansson SO (2011) Should Probabilistic Design Replace Safety Factors? *Philosophy & Technology* 24: pp. 151–168. <https://doi.org/10.1007/s13347-010-0003-6>
52. Elishakoff I (2004) *Safety Factors and Reliability: Friends or Foes?* Springer Netherlands, Dordrecht. pp. 118-152
53. Woo S (ed) (2017) *Reliability Design of Mechanical Systems - Reliability design of mechanical systems: A Guide for Mechanical and Civil Engineers - A guide for mechanical and civil engineers*. Springer International Publishing; Springer, Cham. pp. 61-100
54. NASA - National Aeronautics and Space Administration (2002) *Fault Tree Handbook with Aerospace Applications (Version 1.1)*. [https://elibrary.gsfc.nasa.gov/\\_assets/doclib-Bidder/tech\\_docs/25.%20NASA\\_Fault\\_Tree\\_Handbook\\_with\\_Aerospace\\_Applications%20-%20Copy.pdf](https://elibrary.gsfc.nasa.gov/_assets/doclib-Bidder/tech_docs/25.%20NASA_Fault_Tree_Handbook_with_Aerospace_Applications%20-%20Copy.pdf)
55. Faber MH, Maes MA, Straub D et al. (2006) On the Quantification of Robustness of Structures. In: American Society of Mechanical Engineers (ed) *Proceedings of the 25th International Conference on Offshore Mechanics and Arctic Engineering - 2006*. OMAE 2006. ASME, New York, NY, pp. 79–87. Hamburg, Germany. 4 – 9 June
56. Stewardson D (2001) *Robust Engineering*, Taguchi G, Chowdhury S, Taguchi S, McGraw-Hill, New York, 2000. Hard-Bound, Number of pages: 241. ISBN 0 07 134782 8. *Qual Reliab Engng Int* 17: pp. 141–142. <https://doi.org/10.1002/qre.382>
57. Park G-J, Lee T-H, Lee KH et al. (2006) Robust Design: An Overview. *AIAA Journal* 44: pp. 181–191. <https://doi.org/10.2514/1.13639>
58. Starossek U, Haberland M (2011) Approaches to measures of structural robustness. *Structure and Infrastructure Engineering* 7: pp. 625–631. <https://doi.org/10.1080/15732479.2010.501562>

59. Brett C, Lu Y (2013) Assessment of robustness of structures: Current state of research. *Frontiers of Structural and Civil Engineering* 7: pp. 356–368. <https://doi.org/10.1007/s11709-013-0220-z>
60. Slotine J-JE, Li W (1991) *Applied nonlinear control*. Prentice Hall, Englewood Cliffs, NJ. pp. 196-204
61. Moritz Göhler S, Eifler T, Howard TJ (2016) Robustness Metrics: Consolidating the Multiple Approaches to Quantify Robustness. *J Mech Des* 138: p. 111407. <https://doi.org/10.1115/1.4034112>
62. Taguchi G, Chowdhury S, Taguchi S (2000) *Robust engineering: Learn how to boost quality while reducing costs & time to market*. McGraw-Hill, New York, NY. pp. 1-33
63. Phadke MS (1989) *Quality engineering using robust design*. Prentice Hall, Englewood Cliffs, NJ. pp. 1-10
64. Klein B (2014) *Versuchsplanung - DoE: Einführung in die Taguchi/Shainin-Methodik*. [http://www.degruyter.com/search?f\\_0=isbnissn&q\\_0=9783110343847&searchTitles=true](http://www.degruyter.com/search?f_0=isbnissn&q_0=9783110343847&searchTitles=true)
65. Baker JW, Schubert M, Faber MH (2008) On the assessment of robustness. *Structural Safety* 30: pp. 253–267. <https://doi.org/10.1016/j.strusafe.2006.11.004>
66. Lee MC, Kelly DW, Degenhardt R et al. (2010) A study on the robustness of two stiffened composite fuselage panels. *Composite Structures* 92: pp. 223–232. <https://doi.org/10.1016/j.compstruct.2009.07.009>
67. McPhail C, Maier HR, Kwakkel JH et al. (2018) Robustness Metrics: How Are They Calculated, When Should They Be Used and Why Do They Give Different Results? *Earth's Future* 6: pp. 169–191. <https://doi.org/10.1002/2017EF000649>
68. Ruefer H (2019) *Living Without Mathematical Statistics: Accurate Analysis, Diagnosis, and Prognosis Based on the Taguchi Method*. Springer International Publishing, Cham. pp. 507148
69. da Cunha FRS (2014) *Robustness-based design strategy for thin-walled composite structures exploiting the postbuckling regime*. Dissertation, Technische Universität Carolo-Wilhemina zu Braunschweig
70. Frangopol DM, Curley JP (1987) Effects of Damage and Redundancy on Structural Reliability. *Journal of Structural Engineering* 113: pp. 1533–1549. [https://doi.org/10.1061/\(ASCE\)0733-9445\(1987\)113:7\(1533\)](https://doi.org/10.1061/(ASCE)0733-9445(1987)113:7(1533))
71. Fu G, Frangopol DM (1990) Balancing weight, system reliability and redundancy in a multi-objective optimization framework. *Structural Safety* 7: pp. 165–175. [https://doi.org/10.1016/0167-4730\(90\)90066-X](https://doi.org/10.1016/0167-4730(90)90066-X)
72. Lee MC, Mikulik Z, Kelly DW et al. (2010) Robust design – A concept for imperfection insensitive composite structures. *Composite Structures* 92: pp. 1469–1477. <https://doi.org/10.1016/j.compstruct.2009.09.054>
73. Göhler SM, Husung S, Howard TJ (2016) The Translation between Functional Requirements and Design Parameters for Robust Design. *Procedia CIRP* 43: pp. 106–111. <https://doi.org/10.1016/j.procir.2016.02.028>
74. Brett CJ (2014) *Quantification of structural redundancy and robustness*. Dissertation, The University of Edinburgh
75. European Cooperation for Space Standardization, ESA (2012) ECSS-E-10-03C - Space Engineering: Testing (ECSS-E-10-03C)
76. European Cooperation for Space Standardization (2018) ECSS-E-ST-10-02C Rev.1 - Space engineering: Verification (ECSS-E-ST-10-02C)
77. Zander ME, Sinapius M, Hühne C (2014) Preliminary experiments for an on-orbit detection system to monitor load and deflection states of thin shell CFRP Booms for the solar sail demonstrator Gossamer-1. In: ESA/DLR/CNES (ed) 13th European European Conference on Spacecraft Structures, Materials and Environmental Testing 2014. ECSSMET 2014, 16th edn. Braunschweig, Germany. 1-4 April



78. European Cooperation for Space Standardization (2008) ECSS-Q-ST-70-09C - Space product assurance: Measurements of thermo-optical properties of thermal control materials (ECSS-Q-ST-70-09C), Standard
79. Straubel M (2012) Design and Sizing Method for Deployable Space Antennas. Dissertation, Otto-von-Guericke-Universität
80. Straubel M, Sickinger C, Langlois S (2008) Trade-Off on Large Deployable Membrane Antennas. In: ESA - European Space Agency (ed) 30th ESA Antenna Workshop, Noordwijk, The Netherlands. Noordwijk, The Netherlands. 2008
81. Freeland RE, Bilyeu CD, Steiner MD (1997) Large Inflatable Deployable Antenna Flight Experiment Results. *Acta Astronautica* 41: pp. 267–277
82. Seefeldt P (2018 / 2018) Development and qualification of deployable membranes for space applications. Dissertation, Universität Bremen
83. Geppert URME, Biering B, Lura F et al. (2011) The 3-step DLR–ESA Gossamer road to solar sailing. *Advances in Space Research* 48: pp. 1695–1701. <https://doi.org/10.1016/j.asr.2010.09.016>
84. Spröwitz T, Seefeldt P, Grundmann JT et al. (2017) Design of the Gossamer-1 Deployment Demonstrator. In: JAXA Japan Aerospace Exploration Agency (ed) The Fourth International Symposium on Solar Sailing 2017. Kyoto, Japan. 17th–20th January
85. Seefeldt P, Spietz P, Sproewitz T et al. (2017) Gossamer-1: Mission concept and technology for a controlled deployment of gossamer spacecraft. *Advances in Space Research* 59: pp. 434–456. <https://doi.org/10.1016/j.asr.2016.09.022>
86. Seefeldt P, Spröwitz T (2016) Qualification Testing of the Gossamer-1 Deployment Technology. In: ESA/DLR/CNES (ed) 14th European Conference on Spacecraft Structures, Materials and Environmental Testing. ECSSMET 2016. ESA/DLR/CNES. Toulouse, France. 27–30 September 2016
87. Seefeldt P, Spietz P, Spröwitz T (2014) The Preliminary Design of the Gossamer-1 Solar Sail Membrane and Manufacturing Strategies: Part I Flight Programs. In: Macdonald M (ed) *Advances in Solar Sailing*. Springer-Verlag, pp. 133–151
88. McInnes CR, Bothmer V, Dachwald B et al. (2014) Gossamer Roadmap Technology Reference Study for a Sub-L1 Space Weather Mission: Part II Mission Applications. In: Macdonald M (ed) *Advances in Solar Sailing*. Springer-Verlag, pp. 227–242
89. Sinn T, Tiedemann L, Riemer A et al. (2017) ADEO passive de-orbit subsystem activity leading to a dragsail demonstrator: Conclusion and next steps. In: IAF International Astronautical Federation (ed) 68th International Astronautical Congress (IAC) - 2017. IAC 2017. Adelaide, Australia. 25–29 September 2017
90. Sinn T, Seefeldt P, Riemer A et al. (2016) Design, Analysis and Testing of the ADEO passive De-Orbit Subsystem Demonstrator. In: ESA/DLR/CNES (ed) 14th European Conference on Spacecraft Structures, Materials and Environmental Testing. ECSSMET 2016. ESA/DLR/CNES. Toulouse, France. 27–30 September 2016
91. Sinn T, Tiedemann L, Riemer A et al. (2019) Results of the deployable Membrane & ADEO passive de-orbit subsystem activities leading to a dragsail demonstrator. In: ESA - European Space Agency (ed) 7th European Conference on Space Debris. Darmstadt, Germany. 18–21 April 2019
92. Rennie BB (1967) New Closed Tubular Extendible Boom. In: NASA Jet propulsion Laboratory (ed) 2nd Aerospace Mechanisms Symposium. JPL Technical Memorandum 33-355, pp. 163–169. Santa Clara, California. May 4–5 1967
93. Straubel M, Zander ME, Hühne C (2014) Design and Sizing of the Gossamer Boom Deployment Concept: Part III Technology Activities. In: Macdonald M (ed) *Advances in Solar Sailing*. Springer-Verlag, pp. 593–608
94. Straubel M, Seefeldt P, Spietz P et al. (2015) The Design and Test of the Gossamer-1 Boom Deployment Mechanisms Engineering Model. In: AIAA American Institute of Aeronautics

- and Astronautics (ed) 2nd AIAA Spacecraft Structures Conference 2015. AIAA SciTech Forum 2015. Curran, Red Hook, NY. Kissimmee, Florida, USA. 5 - 9 January 2015
95. Seefeldt P (2017) A stowing and deployment strategy for large membrane space systems on the example of Gossamer-1. *Advances in Space Research* 60: pp. 1345–1362. <https://doi.org/10.1016/j.asr.2017.06.006>
  96. Rooij A de (2010) Corrosion in Space. In: Blockley R, Shyy W (eds) *Encyclopedia of aerospace engineering*, vol 26. John Wiley & Sons, Ltd, Hoboken, NJ, p. 371
  97. European Cooperation for Space Standardization (2008) ECSS-Q-ST-70-06C - Space product assurance: Particle and UV radiation testing for space materials (ECSS-Q-ST-70-06C), Standard
  98. Sznajder M, Geppert URME (2014) H<sub>2</sub> blister formation on metallic surfaces – a candidate for degradation processes in space: Part III Technology Activities. In: Macdonald M (ed) *Advances in Solar Sailing*. Springer-Verlag, pp. 559–572
  99. Hillebrandt M, Meyer S, Zander ME et al. (2015) Deployment Testing of the De-Orbit Sail Flight Hardware. In: AIAA American Institute of Aeronautics and Astronautics (ed) 2nd AIAA Spacecraft Structures Conference 2015. AIAA SciTech Forum 2015. Curran, Red Hook, NY. Kissimmee, Florida, USA. 5 - 9 January 2015
  100. Binet G (2006) Space Specifications Check List: Technical Note. In: ESA - European Space Agency (ed) *ESA – Innovation Triangle Initiative: Technical Notes*. ESA
  101. Derbes WC, Lichodziekewski D (2006) Propulsive Reflectivity and Photoflexibility: Effects on Solar Sail Performance and Control. In: AIAA American Institute of Aeronautics and Astronautics (ed) 42nd AIAA/ASME/SAE/ASEE Joint Propulsion Conference & Exhibit. Sacramento, California, USA. 09-12 July 2006
  102. Stohlman O, Loper E, Lockett T (2017) Temperature-Driven Shape Changes of the Near Earth Asteroid Scout Solar Sail. In: JAXA Japan Aerospace Exploration Agency (ed) *The Fourth International Symposium on Solar Sailing 2017*. Kyoto, Japan. 17th-20th January
  103. Stohlman OR, Loper E (2016) Thermal deformation of very slender TRAC booms. In: AIAA American Institute of Aeronautics and Astronautics (ed) 3rd AIAA Spacecraft Structures Conference 2016. AIAA SciTech Forum 2016, p. 895. San Diego, California, USA. 4-8 January
  104. Blandino JR (2015) Analysis of Thermal-Mechanical Interactions of STEM Booms. In: AIAA American Institute of Aeronautics and Astronautics (ed) 2nd AIAA Spacecraft Structures Conference 2015. AIAA SciTech Forum 2015. Curran, Red Hook, NY, pp. A6. Kissimmee, Florida, USA. 5 - 9 January 2015
  105. Ley W, Wittmann K, Hallmann W (2009) *Handbook of Space Technology*. John Wiley & Sons
  106. ESA - European Space Agency Space debris by the numbers: The latest figures related to space debris, provided by ESA's Space Debris Office at ESOC, Darmstadt, Germany. [http://www.esa.int/Safety\\_Security/Space\\_Debris/Space\\_debris\\_by\\_the\\_numbers](http://www.esa.int/Safety_Security/Space_Debris/Space_debris_by_the_numbers). Accessed 09 Mar 2020
  107. Eileen K. Stansbery (2020) ARES - Orbital Debris Program Office: Photo Gallery. <https://orbitaldebris.jsc.nasa.gov/photo-gallery/>. Accessed 09 Mar 2020
  108. Staugaitis CL, Predmore RE (1970) Mechanical properties of advanced gravity gradient Booms. <https://ntrs.nasa.gov/archive/nasa/casi.ntrs.nasa.gov/19700031329.pdf>. Accessed 23 Jan 2018
  109. Leipold M, Eiden M, Garner CE et al. (2003) Solar sail technology development and demonstration. *Acta Astronautica* 52: pp. 317–326. [https://doi.org/10.1016/S0094-5765\(02\)00171-6](https://doi.org/10.1016/S0094-5765(02)00171-6)
  110. Fernandez JM, Rose G, Stohlman OR et al. (2018) An Advanced Composites-Based Solar Sail System for Interplanetary Small Satellite Missions. In: AIAA American Institute of Aeronautics and Astronautics (ed) AIAA Spacecraft Structures Conference 2018. AIAA SciTech Forum 2018. Curran Associates Inc, Red Hook, NY, p. 163. Kissimmee, Florida, USA. 8-12 January

111. Meyer S, Zander ME, Hühne C (2016) Preliminary Creep Test for estimating the long term stowage behavior of DLR's CFRP booms. In: ESA/DLR/CNES (ed) 14th European Conference on Spacecraft Structures, Materials and Environmental Testing. ECSSMET 2016. ESA/DLR/CNES. Toulouse, France. 27-30 September 2016
112. Stohlman O, Chamberlain M, Zander ME et al. (2019) Structural modeling of a composite-boom-deployed solar sail with realistic part variability. In: FH Aachen University of Applied Sciences (ed) 5th International Symposium on Solar Sailing. Aachen, Germany. 30 July – 2 August 2019
113. Sickinger C, Herbeck L, Breitbach E (2006) Structural engineering on deployable CFRP booms for a solar propelled sailcraft. *Acta Astronautica* 58: pp. 185–196.  
<https://doi.org/10.1016/j.actaastro.2005.09.011>
114. Sickinger C, Herbeck L, Ströhlein T et al. (2004) Lightweight Deployable Booms: Design, Manufacture, Verification, and Smart Materials Application. In: IAF International Astronautical Federation (ed) 55th International Astronautical Congress IAC. IAC 2004. Vancouver, Canada. 5. Oct. 2004
115. Miranda de Leon D, Zander ME (2018) Untersuchung von bleibenden Verformungen von aufgerollten FVK-Booms unter verschiedenen Temperaturen
116. Hillebrandt M, Zander ME, Meyer S et al. (2019) Verfahren zum Herstellen eines Faserverbund-Hohlbauteils und Faserverbund-Hohlbauteil (DE 10 2018 105 765 A1 2019.09.19)
117. Schmidt F, Zander ME (2018) Untersuchung des Stabilitätsverhaltens von dünnwandigen aufrollbaren Schalenmasten in Faserverbundbauweise für ultra-leichte Raumfahrtanwendungen
118. Zander ME, Kottke G, Meyer S et al. (2015) Design, Test and Comparison of mechanical support principles to increase the robustness of deployable thin shell CFRP Booms of the de-orbiting device ADEO. In: IAF International Astronautical Federation (ed) 66th IAC International Astronautical Congress 2015. IAC 2015. IAF International Astronautical Federation. Jerusalem, Israel. 12-16 Oct. 2015
119. Kottke NG (2016) Entwicklung und experimenteller Vergleich eines Führungssystems für entfaltbare, dünnwandige CFK-Masten in Wurzel-Entfaltungskonfiguration ultraleichter Raumfahrtanwendungen. Studienarbeit, Technische Universität Carolo-Wilhelmina zu Braunschweig
120. Früh D (Agust 2014) Implementierung, Inbetriebnahme und Versuche an einem Biegeversuchsstand für ultraleichte CFK-Masten für Weltraumanwendungen. Bachelorarbeit, TU Berlin
121. Hoven Y, Zander ME (2019) Erstellung, Verifizierung und Validierung eines generischen Finite Elemente Modells für entfaltbare, dünnwandige CFK-Masten, unter simulierten Lasten und der Berücksichtigung von Imperfektionen. DLR-Interner Bericht
122. Sickinger C, Fischer C (2002) Solar Sail CFRP-Booms - Probabilistisches Strukturdesign entfaltbarer CFK-Masten. DLR-internem Bericht
123. Meyer S, Zander ME, Straubel M et al. (2015) Environmental Testing and Analysis of a Boom Deployment Mechanism for Gossamer-2. In: IAF International Astronautical Federation (ed) 66th IAC International Astronautical Congress 2015. IAC 2015. IAF International Astronautical Federation. Jerusalem, Israel. 12-16 Oct. 2015
124. Zander ME, Hillebrandt M, Sinapius M et al. (2015) Mechanical characterization of deployable thin shell CFRP Booms for the Cubesat “De-Orbit Sail”. In: IAF International Astronautical Federation (ed) 66th IAC International Astronautical Congress 2015. IAC 2015. IAF International Astronautical Federation. Jerusalem, Israel. 12-16 Oct. 2015
125. Zander ME, Wilken A, Sinapius M et al. (2016) Mechanical testing of deployable thin shell CFRP Booms in ideal and realistic interfaces for the Solar Sail demonstrator Gossamer-1. In: ESA/DLR/CNES (ed) 14th European Conference on Spacecraft Structures, Materials and Environmental Testing. ECSSMET 2016. ESA/DLR/CNES. Toulouse, France. 27-30 September 2016

126. NASA (2019) Cygnus - Space Station Gallery. <https://www.nasa.gov/sites/default/files/thumbnails/image/iss059e025268.jpg>. Accessed 23 Jun 2019
127. Northrop Grumman Space Components Deployables (2019) Ultra Flex Solar Array Systems: Fact sheet. [https://www.northropgrumman.com/Capabilities/SolarArrays/Documents/UltraFlex\\_Factsheet.pdf](https://www.northropgrumman.com/Capabilities/SolarArrays/Documents/UltraFlex_Factsheet.pdf). Accessed 03 Jul 2019
128. Northrop Grumman Space Components Deployables (2018) MegaFlex Solar Array Fact sheet. [http://www.northropgrumman.com/Capabilities/SolarArrays/Documents/MegaFlex\\_Solar\\_Array.pdf](http://www.northropgrumman.com/Capabilities/SolarArrays/Documents/MegaFlex_Solar_Array.pdf). Accessed 20 Apr 2018
129. Banik J, Kiefer S, LaPointe M et al. (2018) On-orbit validation of the roll-out solar array. In: IEEE Institute of Electrical and Electronics Engineers (ed) 2018 IEEE Aerospace Conference. IEEE, Piscataway, NJ, pp. 1–9. Big Sky, MT. 3-10 March 2018
130. Carpenter B, Banik J, Hausgen P (2017) Roll-Out Solar Arrays (ROSA): Next Generation Flexible Solar Array Technology. In: AIAA American Institute of Aeronautics and Astronautics (ed) AIAA Space and Astronautics Forum and Exposition 2017. Curran Associates Inc, Red Hook, NY, p. 782. Orlando, Florida, USA. 12-14 September 2017
131. Chamberlain MK, Kiefer SH, Banik J (2019) Photogrammetry-Based Analysis of the On-orbit Structural Dynamics of the Roll-Out Solar Array. In: AIAA American Institute of Aeronautics and Astronautics (ed) AIAA Scitech 2019 Forum, p. 215. San Diego, California. 7-11 January 2019
132. Chamberlain MK, Kiefer SH, Banik J (2019) Structural Analysis Methods for the Roll-Out Solar Array Flight Experiment. In: AIAA American Institute of Aeronautics and Astronautics (ed) AIAA Scitech 2019 Forum, p. 215. San Diego, California. 7-11 January 2019
133. Harbaugh J (2017) Changing How Solar Power Rolls. [https://www.nasa.gov/mision\\_pages/station/research/news/changing-how-solar-power-rolls](https://www.nasa.gov/mision_pages/station/research/news/changing-how-solar-power-rolls). Accessed 03 Oct 2019
134. Cadogan DP, Lin JK, Grahne Ms (1999) Inflatable Solar Array Technology. In: AIAA American Institute of Aeronautics and Astronautics (ed) 37th Aerospace Sciences Meeting and Exhibit, Reston. Reno, Nevada, USA. 11-14 January 1999
135. Grahne Ms, Cadogan DP (1999) Inflatable Solar Arrays: Revolutionary Technology? In: SAE Society of Automotive Engineers (ed) 34th Intersociety Energy Conversion Engineering Conference. IECEC 1999. Vancouver, British Columbia, Canada. 2-5 August 1999
136. Lichodziejewski D, Veal G, Helms R et al. (2003) Inflatable Rigidizable Solar Array for Small Satellites. In: AIAA American Institute of Aeronautics and Astronautics (ed) 44th AIAA/ASME/ASCE/AHS/ASC Structures, Structural Dynamics, and Materials Conference. AIAA American Institute of Aeronautics & Astronautics, Reston, Virginia. Norfolk, Virginia. 07 - 10 April 2003
137. Hillebrandt M, Zander ME, Christian H (2018) Conceptual Design of the deployable Booms for the GoSolAr-Satellite. In: ESA/DLR/CNES (ed) 15th European Conference on Spacecraft Structures, Materials and Environmental Testing. ECSSMET 2018. Noordwijk, The Netherlands. 28 May - 1 June 2018
138. Sprowitz T, Grundmann JT, Haack F et al. (2019) GoSolAr – A Gossamer Solar Array Concept for High Power Spacecraft Applications using flexible Photovoltaics. In: IEEE Institute of Electrical and Electronics Engineers (ed) 2019 IEEE Aerospace Conference. 2019 IEEE Aerospace Conference, pp. 1–14. Big Sky, MT, USA. 2. - 9. March
139. Sprowitz T, Grundmann JT, Haack F et al. (2018) GoSolAr – A Gossamer Solar Array Concept for High Power Spacecraft Applications using flexible thinfilm Photovoltaics. In: IAF International Astronautical Federation (ed) 69th International Astronautical Congress (IAC). 69th International Astronautical Congress (IAC). Bremen, Germany. 1-5 October
140. Carr JA, Boyd D, Martínez AE et al. (2016) The Lightweight Integrated Solar Array and Transceiver (LISA-T). In: AIAA American Institute of Aeronautics and Astronautics / Utah State University (ed) 30th Annual AIAA/USU Conference on Small Satellites: 2016 - Pioneering an Industry. Logan, Utah USA. 6-11 August 2016

141. Johnson CL, Carr J, Fabisinski L et al. (2015) Lightweight Integrated Solar Array (LISA): Providing Higher Power to Small Spacecraft. AIAA 2015-3896. In: AIAA American Institute of Aeronautics and Astronautics (ed) 13th International Energy Conversion Engineering Conference. Orlando, FL, USA. 27-29 July 2015
142. Johnson L, Carr JA, Boyd D (2017) The Lightweight Integrated Solar Array and Antenna (LISA-T) – Big Power for Small Spacecraft. In: IAF International Astronautical Federation (ed) 68th International Astronautical Congress (IAC) - 2017. IAC 2017. Adelaide, Australia. 25-29 September 2017
143. Lockett TR, Martinez A, Boyd D et al. (2015) Advancements of the Lightweight Integrated Solar Array and Transceiver (LISA-T) Small Spacecraft System. In: IEEE Institute of Electrical and Electronics Engineers (ed) 42nd Photovoltaic Specialist Conference (PVSC). PVSC 2015, pp. 1–6. New Orleans, Louisiana, USA. 14-19 June 2015
144. Bernasconi MC (2006) Chemically Rigidized Expandable Structures (CRES) for Space Application. *Tensinews* 10: p. 6
145. B. Defoort, V. Peypoudat, M.C. Bernasconi et al. (2005) Recent Advances in the Rigidization of Gossamer Structures. In: Oñate E, Kröplin B (eds) *Textile Composites and Inflatable Structures*, 3rd edn. Springer Netherlands
146. Roederer AG (2012) 7 Historical Overview of the Development of Space Antennas: Space Antenna Handbook. In: Imbriale WA, Shichang Gao S, Boccia L (eds) *Space Antenna Handbook*. Wiley, pp. 250–307
147. Freeland R, Bard S, Veal G et al. (1997) Inflatable Antenna Technology with preliminary Shuttle Experiment Results and potential Applications. <https://trs.jpl.nasa.gov/bitstream/handle/2014/26491/96-1367.pdf?sequence=1>. Accessed 20 Jun 2018
148. Steiner M, Freeland B, Veal G (1997) Spartan 207/Inflatable Antenna Experiment Flown on STS-77: Preliminary Mission Report
149. L.Garde Inc. (2019) Antennas. <http://www.lgarde.com/antennas-2/>. Accessed 06 Oct 2019
150. ILC Dover Inflatable and Deployable Antennas - SAR. <http://www.ilcdover.com/SAR/>. Accessed 20 Jun 2012
151. Huang J (2001) The development of inflatable array antennas. *Antennas and Propagation Magazine* 43: pp. 44–50
152. NASA JPL (2016) SMAP Reflector Deployment Test Anomaly (Design and Test of Large, Complex Deployables). <https://llis.nasa.gov/lesson/16501>. Accessed 26 Jun 2019
153. Northrop Grumman Space Components Deployables (2013) Data sheet AstroMesh™ Reflector Parametrics. <http://www.northropgrumman.com/BusinessVentures/AstroAerospace/Products/Documents/pageDocs/Parametrics.pdf>. Accessed 20 Apr 2018
154. Northrop Grumman Space Components Deployables (2013) Flight Heritage AstroMesh. [http://www.northropgrumman.com/BusinessVentures/AstroAerospace/Products/Documents/pageDocs/Flight\\_Heritage.pdf](http://www.northropgrumman.com/BusinessVentures/AstroAerospace/Products/Documents/pageDocs/Flight_Heritage.pdf). Accessed 04 Jun 2018
155. Northrop Grumman Space Components Deployables (2013) Data sheet JPL SMAP (AM-Lite). <http://www.northropgrumman.com/BusinessVentures/AstroAerospace/Products/Documents/pageDocs/SMAP.pdf>. Accessed 20 Apr 2018
156. Thomson MW (2002) AstroMesh Deployable Reflectors for Ku and Ka Band Commercial Satellites. In: AIAA (ed) 20th AIAA International Communication Satellite Systems Conference and Exhibit. Montreal, Quebec, Canada. 12-15 May 2002
157. Thomson MW (1999) The AstroMesh deployable Refelctor. In: IEEE Institute of Electrical and Electronics Engineers (ed) *Antennas and Propagation Society International Symposium*, vol 3. Orlando, FL, USA. 11-16 July 1999
158. Harris Corporation (2013) Data sheet Unfurlable Antenna Solutions. [http://download.harris.com/app/public\\_download.asp?fid=463](http://download.harris.com/app/public_download.asp?fid=463)
159. Harris Corporation (2010) Mobile User Objective System (MUOS) Satellite Unfurlable Mesh Reflectors. <http://govcomm.harris.com/solutions/products/defense/muos.asp>. Accessed 03 Apr 2018

160. Harris Corporation (2009) Harris Corporation Antenna Reflector for TerreStar Communications Satellite Successfully Deployed. [http://harris.com/view\\_pressrelease.asp?pr\\_id=2809](http://harris.com/view_pressrelease.asp?pr_id=2809). Accessed 15 Sep 2019
161. Lockheed Martin Corporation (2013) MUOS Status Updates. <http://www.lockheedmartin.com/us/products/mobile-user-objective-system-muos-/muosstatus.html>. Accessed 03 Apr 2018
162. Williams WD, Collins M, Hodges R et al. (2007) High-Capacity Communications From Martian Distances: Technical Memorandum
163. LightSquared (2013) Data sheet LightSquared-Satellite-Services-Information. <http://www.lightsquared.com/wp-content/themes/lightsquared/pdf/LightSquared-Satellite-Services-Information.pdf>. Accessed 20 May 2015
164. Boeing Space & Intelligence Systems (2013) Factsheet: Mexican Satellite System (MEXSAT)
165. Meguro A, Shintate K, Usui M et al. (2009) In-orbit deployment characteristics of large deployable antenna reflector onboard Engineering Test Satellite VIII. *Acta Astronautica* 65: pp. 1306–1316. <https://doi.org/10.1016/j.actaastro.2009.03.052>
166. Tibert G (2002) Deployable Tensegrity Structures for Space Application. Dissertation, KTH Royal Institute of Technology
167. NASA (2013) Tracking and Data Relay Satellite - TDRS-K Launch. [http://www.nasa.gov/mission\\_pages/tdrs/launch/index.html](http://www.nasa.gov/mission_pages/tdrs/launch/index.html). Accessed 02 Feb 2017
168. Williams DR RAE-B/Explorer 49 - Spacecraft - Details. NSSDCA/COSPAR ID: 1973-039A. <https://nssdc.gsfc.nasa.gov/nmc/spacecraft/display.action?id=1973-039A>. Accessed 09 Oct 2019
169. Staugaitis CL, Predmore RE (1973) Thermal static bending of deployable interlocked Booms. <https://ntrs.nasa.gov/archive/nasa/casi.ntrs.nasa.gov/19730012188.pdf>. Accessed 23 Jan 2018
170. Leipold M, Garner CE, Freeland RE et al. (1999) ODISSEE — A proposal for demonstration of a solar sail in earth orbit. *Acta Astronautica* 45: pp. 557–566. [https://doi.org/10.1016/S0094-5765\(99\)00176-9](https://doi.org/10.1016/S0094-5765(99)00176-9)
171. Barnes NC, Derbes WC, Player CJ et al. (2014) Sunjammer: A Solar Sail Demonstration: Part I Flight Programs. In: Macdonald M (ed) *Advances in Solar Sailing*. Springer-Verlag, pp. 115–126
172. Chafer CM (2014) Commercial Solar Sail Applications: Overview and Update on NASA's Sunjammer Mission: Part I Flight Programs. In: Macdonald M (ed) *Advances in Solar Sailing*. Springer-Verlag, pp. 127–132
173. Eastwood JP, Kataria DO, McInnes CR et al. (2015) Sunjammer. *Weather* 70: pp. 27–30. <https://doi.org/10.1002/wea.2438/pdf>
174. Greschik G, Mikulas MM (2002) Design Study of a Square Solar Sail Architecture. *Journal of Spacecraft and Rockets* 39: pp. 653–661. <https://doi.org/10.2514/2.3886>
175. Johnson L, Young RM, Montgomery EE, IV (2007) Recent advances in solar sail propulsion systems at NASA. *Acta Astronautica* 61: pp. 376–382. <https://doi.org/10.1016/j.actaastro.2007.01.047>
176. Alhorn DC, Casas JP, Agasid EF et al. (2010) NanoSail-D: The Small Satellite That Could! In: AIAA American Institute of Aeronautics and Astronautics / Utah State University (ed) 24th Annual Conference on Small Satellites. Utah State University. Logan, Utah, USA. 9-12 August 2010
177. Banik JA, Murphey TW (2010) Performance Validation of the Triangular Rollable and Collapsible Mast. In: AIAA American Institute of Aeronautics and Astronautics / Utah State University (ed) 24th Annual Conference on Small Satellites. Utah State University. Logan, Utah, USA. 9-12 August 2010
178. Johnson L, Whorton M, Heaton A et al. (2011) NanoSail-D: A solar sail demonstration mission. *Acta Astronautica* 68: pp. 571–575. <https://doi.org/10.1016/j.actaastro.2010.02.008>

179. Johnson L, Young R, Barnes NC et al. (2012) Solar Sails: Technology And Demonstration Status. *International Journal of Aeronautical and Space Sciences IJASS* 13: pp. 1687–1694. <https://doi.org/10.5139/IJASS.2012.13.4.421>
180. Johnson L, Young R, Montgomery E et al. (2011) Status of solar sail technology within NASA. *Advances in Space Research* 48: pp. 1687–1694. <https://doi.org/10.1016/j.asr.2010.12.011>
181. Murphey TW, Banik JA Triangular Rollable and Collapsible Boom (US7895795B1)
182. NASA (2011) NASA's Nanosail-D 'Sails' Home - Mission Complete. [http://www.nasa.gov/mission\\_pages/smallsats/nanosaild.html](http://www.nasa.gov/mission_pages/smallsats/nanosaild.html). Accessed 02 Feb 2017
183. Hillebrandt M, Meyer S, Zander ME et al. (2016) The Boom Design of the De-Orbit Sail Satellite. In: ESA/DLR/CNES (ed) 14th European Conference on Spacecraft Structures, Materials and Environmental Testing. ECSSMET 2016. ESA/DLR/CNES. Toulouse, France. 27-30 September 2016
184. Stohlman OR, Lappas V (2013) Deorbisail: a deployable sail for de-orbiting. In: AIAA American Institute of Aeronautics and Astronautics (ed) 54th AIAA/ASME/ASCE/AHS/ASC Structures, Structural Dynamics, and Materials Conference, p. 1687. Boston, Massachusetts, USA. April 8-11 2013
185. Stohlman OR, Lappas V (2014) Development of the Deorbisail flight model. In: AIAA American Institute of Aeronautics and Astronautics (ed) Spacecraft Structures Conference 2014. AIAA SciTech Forum 2014. Curran, Red Hook, NY, p. 31. National Harbor, Maryland, USA. 13 - 17 January
186. Stohlman OR, Fernandez JM, Lappas V et al. (2013) Testing of the Deorbisail drag sail subsystem. In: AIAA American Institute of Aeronautics and Astronautics (ed) 54th AIAA/ASME/ASCE/AHS/ASC Structures, Structural Dynamics, and Materials Conference, p. 1687. Boston, Massachusetts, USA. April 8-11 2013
187. Bidy C, Svitek T (2012) LightSail-1 Solar Sail Design and Qualification. In: 41st Aerospace Mechanisms Symposium. Pasadena, California. May 16-18 2012
188. The Planetary Society LightSail: Flight by Light for CubeSats. <http://www.planetary.org/explore/projects/lightsail-solar-sailing/#the-spacecraft>. Accessed 07 Oct 2019
189. Johnson L, Castillo-Rogez J, Dervan J (2017) Near Earth Asteroid Scout: NASA's Solar Sail Mission to a NEA. In: IAF International Astronautical Federation (ed) 68th International Astronautical Congress (IAC) - 2017. IAC 2017. Adelaide, Australia. 25-29 September 2017
190. McNutt L, Johnson L, Kahn P et al. (2014) Near-Earth Asteroid (NEA) Scout. In: AIAA American Institute of Aeronautics and Astronautics (ed) SPACE Conferences and Exposition, p. 697. San Diego, CA, USA. 4-7 August 2014
191. Harbaugh J (2018) NASA Tests Solar Sail that Will Study Near-Earth Asteroid. <https://www.nasa.gov/launching-science-and-technology/solar-sail-test-will-study-near-earth-asteroid>. Accessed 07 Oct 2019
192. Stohlman OR (2018) Coupled radiative thermal and nonlinear stress analysis for thermal deformation in large space structures. In: AIAA American Institute of Aeronautics and Astronautics (ed) AIAA Spacecraft Structures Conference 2018. AIAA SciTech Forum 2018. Curran Associates Inc, Red Hook, NY. Kissimmee, Florida, USA. 8-12 January
193. Fernandez JM (2017) Advanced Deployable Shell-Based Composite Booms for Small Satellite Structural Applications Including Solar Sails. In: JAXA Japan Aerospace Exploration Agency (ed) The Fourth International Symposium on Solar Sailing 2017. Kyoto, Japan. 17th-20th January
194. Mori O, Shirasawa Y, Mimasu Y et al. (2014) Overview of IKAROS Mission: Part I Flight Programs. In: Macdonald M (ed) *Advances in Solar Sailing*. Springer-Verlag, pp. 25–43
195. Kawaguchi J (2014) Overview of solar sail related activities at JAXA: Part I Flight Programs. In: Macdonald M (ed) *Advances in Solar Sailing*. Springer-Verlag, pp. 3–14

196. Lewis D How a Russian Space Mirror Briefly Lit Up the Night. <https://www.smithsonianmag.com/smart-news/how-russian-space-mirror-briefly-lit-night-180957894/>. Accessed 07 Oct 2019
197. Syromiatnikov V Space Regatta Consortium - Znamya 2 demonstration flight experiment. [http://src.space.ru/page\\_30e.htm](http://src.space.ru/page_30e.htm). Accessed 09 Mar 2016
198. Clampin M (2008) The James Webb Space Telescope (JWST). In: Elsevier (ed) *Advances in Space Research: The Official Journal of the Committee on Space Research (COSPAR), an interdisciplinary scientific committee of the International Science Council (ISC).*, Volume 41, vol 41. Elsevier, pp. 1984–1991
199. Ewing AP, Back JM, Schuettpelez BM et al. (2009) James Webb Space Telescope Sunshield Membrane Assembly. In: AIAA American Institute of Aeronautics and Astronautics (ed) 50th AIAA/ASME/ASCE/AHS/ASC Structures, Structural Dynamics, and Materials Conference. Scitech 2009. Palm Springs, California, USA. 04–09 May
200. Fellini R, Kropp YL (2008) James Webb Space Telescope Sunshield: Challenges in Analysis of Gossamer Structures. *Technology Review Journal Spring/Summer*: pp. 17–44
201. Gardner J, Mather J, Clampin M et al. (2006) The James Webb Space Telescope. *Space Science Reviews* 123: pp. 485–606. <https://doi.org/10.1007/s11214-006-8315-7>
202. Gutro R (2008) Super-Tough Sunshield to Fly on the James Webb Space Telescope. [http://www.nasa.gov/topics/universe/features/jwst\\_toughshield.html](http://www.nasa.gov/topics/universe/features/jwst_toughshield.html). Accessed 03 Jul 2019
203. Jenner L (2015) NASA's Webb Sunshield Stacks Up to Test! <https://www.nasa.gov/content/goddard/nasas-webb-sunshield-stacks-up-to-test>. Accessed 07 Oct 2019
204. Pereira C, Urgoiti E, Pinto I (2012) The Structure of the Gaia Deployable Sunshield Assembly. In: ESA, DLR, CNES (ed) 12th European Conference on Spacecraft Structures, Materials and Environmental Testing. ECSS 2012. Noordwijk, The Netherlands. 20–23 March
205. Sener Aeroespacial (2013) Press Release: Sener in Gaia. [http://www.sener-aero-space.com/EPORTAL\\_DOCS/GENERAL/SENERV2/DOC-cw52a5993caa7b9/sener-in-gaia-uk.pdf](http://www.sener-aero-space.com/EPORTAL_DOCS/GENERAL/SENERV2/DOC-cw52a5993caa7b9/sener-in-gaia-uk.pdf). Accessed 12 Apr 2016
206. Sener Aeroespacial (2013) Press Release: Successful deployment of Sener's sunshield in the Gaia satellite. [http://www.sener.es/EPORTAL\\_DOCS/GENERAL/SENERV2/DOC-cw52b2fded4f4de/successful-deployment-of-sener-sunshield-in-the-gaia-satellite.pdf](http://www.sener.es/EPORTAL_DOCS/GENERAL/SENERV2/DOC-cw52b2fded4f4de/successful-deployment-of-sener-sunshield-in-the-gaia-satellite.pdf). Accessed 01 Dec 2013
207. Urgoiti E, Pinto I, Appolloni M et al. (2012) GAIA Deployable Sunshield Qualification Testing. In: ESA, DLR, CNES (ed) 12th European Conference on Spacecraft Structures, Materials and Environmental Testing. ECSS 2012. Noordwijk, The Netherlands. 20–23 March
208. NASA Exoplanet Program: Starshade Technology Development. <https://exoplanets.nasa.gov/exep/technology/starshade/>. Accessed 14 Oct 2019
209. NASA - National Aeronautics and Space Administration (2019) Starshade to Enable First Images of Earth-sized Exoplanets | Science Mission Directorate. <https://science.nasa.gov/technology/technology-stories/starshade-enable-first-images-earth-sized-exoplanets>. Accessed 14 Oct 2019
210. Siegler N, Ziemer J (2017) Starshade Technology Development Status. In: SPIE, The international society for optics and photonics (ed) *SPIE Mirror Technology Workshop 2017*. SPIE Mirror Technology Workshop 2017. Redondo Beach, USA. 16 November
211. Webb D, Hirsch B, Bach V et al. (2016) Starshade Mechanical Architecture & Technology Effort. In: AIAA American Institute of Aeronautics and Astronautics (ed) 3rd AIAA Spacecraft Structures Conference 2016. AIAA SciTech Forum 2016, p. 68672. San Diego, California, USA. 4–8 January
212. Willems P (2018) Starshade to TRL5 (S5) Technology Development Plan. [https://exoplanets.nasa.gov/internal\\_resources/1033/](https://exoplanets.nasa.gov/internal_resources/1033/). Accessed 14 Oct 2019
213. Pappa RS, Giersch LR, Quagliaroli JM (2001) Photogrammetry of a 5 m inflatable space antenna with condumer-grade digital cameras. *Experimental Techniques* 25: pp. 21–29. <https://doi.org/10.1111/j.1747-1567.2001.tb00028.x>



- 
214. Pappa RS, Lassiter JO, Ross BP (2003) Structural Dynamics Experimental Activities in Ultralightweight and Inflatable Space Structures. *Journal of Spacecraft and Rockets* 40: pp. 15–23. <https://doi.org/10.2514/2.3934>
  215. Smalley KB, Tinker ML, Taylor WS (2001) Structural Modeling of a five-meter thin film inflatable Antenna/Concentrator with rigidized support Struts. In: AIAA American Institute of Aeronautics and Astronautics (ed) 42nd AIAA/ASME/ASCE/AHS/ASC Structures, Structural Dynamics, and Materials Conference and Exhibit, AIAA-2001-1412. Seattle, WA, USA. 16-19 April 2001
  216. Wong WA (2002) Operation of a Thin-Film Inflatable Concentrator System Demonstrated in a Solar Thermal Vacuum Environment
  217. Gelderloos CJ, Assad C, Balcewicz PT et al. (2000) Characterization testing of Hughes 702 solar array. In: IEEE Institute of Electrical and Electronics Engineers (ed) 28th IEEE Photovoltaic Specialists Conference - 2000. Anchorage, AK, USA. 15-22 Sept. 2000
  218. Stribling R (1988) Hughes 702 concentrator solar array. In: IEEE Institute of Electrical and Electronics Engineers (ed) 20th IEEE photovoltaic specialists conference. Las Vegas, Nevada, USA. 26-30 September 1988
  219. The BOEING Company (2013) Factsheet: BOEING 702HP Fleet - Galaxy and PAS. <http://www.boeing.com/boeing/defense-space/space/bss/factsheets/702/702fleet.page>. Accessed 09 Mar 2016
  220. Jones JA (2001) Inflatable Robotics for Planetary Applications. [http://www2.jpl.nasa.gov/adv\\_tech/balloons/Baln\\_ppr/jj01.pdf](http://www2.jpl.nasa.gov/adv_tech/balloons/Baln_ppr/jj01.pdf). Accessed 23 Jun 2018
  221. Jones JA (2012) Big Wheels Inflatable Rover Design Concept. [http://www2.jpl.nasa.gov/adv\\_tech/rovers/bigwheel.htm](http://www2.jpl.nasa.gov/adv_tech/rovers/bigwheel.htm). Accessed 23 Jun 2018
  222. Jones JA (2012) Big Wheels Inflatable Rover Design Concept - Field Testing. [http://www2.jpl.nasa.gov/adv\\_tech/rovers/bgwh\\_test.htm](http://www2.jpl.nasa.gov/adv_tech/rovers/bgwh_test.htm). Accessed 23 Jun 2018
  223. Behar A, Carsey F, Matthews J et al. (2004) An antarctic deployment of the NASA/JPL tumbleweed polar rover. In: IEEE Institute of Electrical and Electronics Engineers (ed) World Automation Congress 2004. Seville, Spain. 28 June-1 July 2004
  224. Behar A, Matthews J, Carsey F et al. (2004) NASA/JPL Tumbleweed Polar Rover. In: IEEE Institute of Electrical and Electronics Engineers (ed) 2004 IEEE Aerospace Conference, vol 1. Big Sky, MT, USA. 6-13 March 2004
  225. Godwin N, West P (2004) Tumbleweed Rover Goes on a Roll at South Pole. <http://www.jpl.nasa.gov/news/news.php?release=78>. Accessed 20 Mar 2018
  226. Antol J, Hajos GA (2012) A new Paradigm for Planet Exploration - The Mars Tumbleweed Rover. In: Lunar and Planetary Institute (ed) Concepts and Approaches for Mars Exploration Meeting 2012. Houston, Texas, USA. June 12-14 2012
  227. Antol J, Harris SB, Hajos GA et al. (eds) (2006) Wind Tunnel Tests of Evolved Mars Tumbleweed Concepts, vol 1. AIAA
  228. Kuhlman KR, Behar A, Jones J et al. (2012) Tumbleweed: A New Paradigm for Surveying Mars for In Situ Resources. In: Lunar and Planetary Institute (ed) Concepts and Approaches for Mars Exploration Meeting 2012. Houston, Texas, USA. June 12-14 2012
  229. Antol J, Chattin RL, Copeland BM (2006) The NASA Langley Mars Tumbleweed Rover Prototype. In: AIAA American Institute of Aeronautics and Astronautics (ed) 44th AIAA Aerospace Sciences Meeting and Exhibit, vol 1. AIAA American Institute of Aeronautics & Astronautics. Reno, Nevada, USA. 9–12 January 2006
  230. Antol J, Kolacinski R, Minton D et al. (2003) Low Cost Mars Surface Exploration: The Mars Tumbleweed. <https://ntrs.nasa.gov/api/citations/20030068113/downloads/20030068113.pdf>. Accessed 20 Mar 2019
  231. Claycomb JS, DeJarnette FR, Mazzoleni AP (2006) Development and Construction of a Prototype Mars Tumbleweed Rover. In: AIAA American Institute of Aeronautics and Astronautics (ed) 44th AIAA Aerospace Sciences Meeting and Exhibit. AIAA American Institute of Aeronautics & Astronautics. Reno, Nevada, USA. 9–12 January 2006

232. Flick JJ, Toniolo MD (2005) Preliminary Dynamic Feasibility and Analysis of a Spherical, Wind-Driven (Tumbleweed), Martian Rover. In: AIAA American Institute of Aeronautics and Astronautics (ed) 43rd AIAA Aerospace Sciences Meeting and Exhibit. Reno, Nevada, USA. 10-13 January 2005
233. Rose SE, Moody CB, James DL et al. (2005) Drag Measurement and Dynamic Simulation of Martian Wind Driven Sensor Platform Concepts. In: AIAA American Institute of Aeronautics and Astronautics (ed) 43rd AIAA Aerospace Sciences Meeting and Exhibit. Reno, Nevada, USA. 10-13 January 2005
234. ILC Dover (2013) Factsheet: Mars Pathfinder & Mars Exploration Rover Airbags. <http://www.ilcdover.com/Mars-Pathfinder-Exploration-Rover-MER/>
235. NASA JPL (1999) Mars Pathfinder - Entry Descent and Landing. <http://mars.jpl.nasa.gov/MPF/mpf/edl/edl1.html>. Accessed 20 Mar 2017
236. NASA JPL (1999) Mars Pathfinder Airbags. <http://mars.jpl.nasa.gov/MPF/mpf/mpfairbags.html>. Accessed 20 Mar 2017
237. NASA JPL (1999) NASA Facts Mars Pathfinder. [http://www.jpl.nasa.gov/news/fact\\_sheets/mpf.pdf](http://www.jpl.nasa.gov/news/fact_sheets/mpf.pdf). Accessed 20 Mar 2017
238. Stein J, Sandy C, Wilson D et al. (2003) Recent Developments in Inflatable Airbag Impact Attenuation Systems for Mars Exploration. In: AIAA American Institute of Aeronautics and Astronautics (ed) 44th AIAA/ASME/ASCE/AHS/ASC Structures, Structural Dynamics, and Materials Conference. AIAA American Institute of Aeronautics & Astronautics, Reston, Virginia. Norfolk, Virginia. 07 - 10 April 2003
239. ESA - European Space Agency (2013) Mars Express - Beagle 2 Lander. [http://www.esa.int/Our\\_Activities/Space\\_Science/Mars\\_Express/Beagle\\_2\\_lander](http://www.esa.int/Our_Activities/Space_Science/Mars_Express/Beagle_2_lander). Accessed 09 Mar 2018
240. ILC Dover (2013) Factsheet: Beagle 2 Airbags. <http://www.ilcdover.com/Beagle/>
241. Wright IP, Sims MR, Pillinger CT (2003) Scientific objectives of the Beagle 2 lander. *Acta Astronautica* 52: pp. 219–225. [https://doi.org/10.1016/S0094-5765\(02\)00160-1](https://doi.org/10.1016/S0094-5765(02)00160-1)
242. Hughes SJ, Cheatwood FM, Calomino AM et al. (2011) Hypersonic Inflatable Aerodynamic Decelerator (HIAD) Technology Development Overview. In: AIAA American Institute of Aeronautics and Astronautics (ed) 21st AIAA Aerodynamic Decelerator Systems Technology Conference and Seminar. Dublin, Ireland. 23-26 May 2011
243. Jurewicz D, Lichodziejewski L, Tutt B et al. (2013) Application of Inflatable Aeroshell Structures for Entry Descent and Landing. In: IEEE Institute of Electrical and Electronics Engineers (ed) 2013 IEEE Aerospace Conference. Big Sky, Montana, USA. 2-9. March 2013
244. NASA (2004) Fact Sheet: HIAD-IRVE-3 -NASA Successfully Demonstrates Inflatable Heat Shield. [http://gcd.larc.nasa.gov/wp-content/uploads/2013/07/FS\\_HIAD\\_IRVE-3\\_Fact\\_Sheet.pdf](http://gcd.larc.nasa.gov/wp-content/uploads/2013/07/FS_HIAD_IRVE-3_Fact_Sheet.pdf). Accessed 20 Jun 2016
245. Cadogan D, Scheir C, Dixit A et al. (2006) Intelligent Flexible Materials for Deployable Space Structures (InFlex). In: AIAA American Institute of Aeronautics and Astronautics (ed) 47th AIAA/ASME/ASCE/AHS/ASC Structures, Structural Dynamics and Materials Conference. 47th AIAA/ASME/ASCE/AHS/ASC Structures, Structural Dynamics, and Materials Conference. AIAA American Institute of Aeronautics & Astronautics, Reston, VA. Newport, Rhode Island. 01 - 04 May
246. Henry K (2007) Camping on the Moon Will Be One Far Out Experience. <http://www.nasa.gov/exploration/home/inflatable-lunar-hab.html>. Accessed 06 Jul 2019
247. Hinkle J, Sharpe G, Lin J et al. (2010) Intelligent Flexible Materials for Space Structures: Expandable Habitat Engineering Development Unit
248. Spampinato P (2010) Overview of ILC Dover Habitat Programs and Technology: Inflatable Space Habitats, Shelters & Enclosures. FISO Colloquium. In: Future In-Space Operations (FISO) Telecon Presentations. Future In-Space Operations (FISO) Telecon Presentations. Online. July

- 
249. NASA (2010) NASA eClips - NASA LAUNCHPAD: Lunar Habitats - Home on the Moon. [http://www.nasa.gov/pdf/472967main\\_LP5-LunarHabitats\\_508.pdf](http://www.nasa.gov/pdf/472967main_LP5-LunarHabitats_508.pdf). Accessed 09 May 2019
  250. Dismukes K, Petty JI (2003) TransHab Concept. <http://spaceflight.nasa.gov/history/station/transhab/index.html>. Accessed 12 Jul 2018
  251. ILC Dover (2018) Transhab. <http://www.ilcdover.com/Transhab/>
  252. Bigelow Aerospace GENESIS I. <http://www.bigelowaerospace.com/genesis-1.php>. Accessed 10 Jun 2018
  253. Bigelow Aerospace GENESIS II. <http://www.bigelowaerospace.com/genesis-2.php>. Accessed 10 Jun 2018
  254. Bigelow Aerospace BEAM - Bigelow Expandable Activity Module. [http://www.bigelowaerospace.com/beam\\_media\\_brief.php](http://www.bigelowaerospace.com/beam_media_brief.php). Accessed 10 Jun 2018
  255. NASA NASA to Test Bigelow Expandable Module on Space Station. [http://www.nasa.gov/mission\\_pages/station/news/beam\\_feature.html](http://www.nasa.gov/mission_pages/station/news/beam_feature.html). Accessed 04 Mar 2018
  256. Goldberg BE, Everhart K, Stevens R et al. (Dec 1994) System Engineering "Toolbox" for Design-Oriented Engineers: NASA Reference Publication 1358. NASA-RP-1358, M-768, NAS 1.61:1358, Washington, United States
  257. Breiing A, Knosala R (1997) Bewerten technischer Systeme: Theoretische und methodische Grundlagen bewertungstechnischer Entscheidungshilfen. Springer Berlin Heidelberg, Berlin, Heidelberg, s.l. pp. 227-256
  258. U.S. Nuclear Regulatory Commission (1981) Fault Tree Handbook (NUREG-0492). <https://www.nrc.gov/docs/ML1007/ML100780465.pdf>
  259. SaRS - The Safety and Reliability Society (2018) Applied R&M Manual for Defence Systems: GR-77 Issue 2011. Third edition, Issue 2011
  260. Wang JX, Roush ML (2000) What Every Engineer Should Know About Risk Engineering and Management. Taylor & Francis. pp. 46-76
  261. NASA - National Aeronautics and Space Administration (1966) Procedure for Failure Mode, Effects, and Criticality Analysis (FMECA): Apollo Program

## Appendix A EXAMPLE LIST OF GOSSSS APPLICATIONS

**Table A. 1.** Examples of advanced GosSSS applications, main characteristics and references






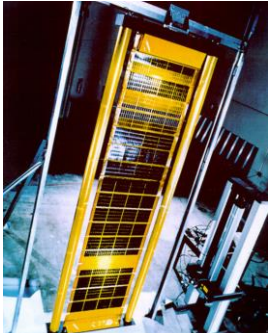
Solar Arrays			
Example		Specifications	Literature/Reference
ISS Solar Array Wings		Size: 35 m x 12 m (deployed wing), 0.51 m (height) x 4.57 m (stowed, wing), 73 m wing-span TRL (estimated): 9 Power output: 32 kW (per wing) Flown/used: in service since 2005, today in full complement of eight solar array wings Stowage: z-folded Deployment: by truss masts	Banks [17, 18] Boeing [13] Christiansen [19, 20] Garcia [10] Kauderer [14, 16] Mansfield [11, 15] NASA [12]
Hubble's flexible Solar Arrays		Size: 12.9 m x 2.9 m (deployed wing) TRL (estimated): 9 Power output: approx. 4.4 kW Flown/used: 2 sets in service on HST from 1990 to 2002 Stowage: Rolled-up Deployment: by stainless steel bi-stem booms	ESA [29, 30] Foster [21] Gerlach [22] Kearsley [24] Loff [27] Moussi [23] NASA [26, 28]
Ultra Flex Solar Array		Size: $\varnothing$ 2.1 m (on Phoenix, Insight), $\varnothing$ 3.8 m (on Cygnus), $\varnothing$ 9. m (Megaflex) TRL (estimated): 9 Power output: approx. > 103 W/kg Flown/used: in service since 2004 Stowage: circular z-folded Deployment: fanlike pivoting around hub	NASA [126] Northrop Grumman [127, 128]
ROSA Roll-Out Solar Array		Size: 5.4 m x 167 m TRL (estimated): 6 Flown/used: 2017 deployment experiment in space from ISS Stowage: Rolled-up Deployment: by CFRP bi-stem booms	Banik [129] Carpenter [130] Chamberlain [131, 131, 132] NASA [132, 133]
Teledesic Inflatable Solar Array		Size: 10 m x 3 m TRL (estimated): 4 Flown/used: full scale prototype demonstration in deployment trials, late 1990's Stowage: folded Deployment: by 3 inflatable booms	Cadogan [134] Grahne [135]
Inflatable Torus Solar Array Technology (ITSAT)		Size: 3.25 m x 1 m (deployed), 0.16 m x 0.21 m x 1.13 m (stowed) TRL (estimated): 6-7 Power output: approx. 275 W Flown/used: full scale protoflight model, ground tested, late 1999/2002 Stowage: accordion-folded Deployment: by inflatable booms	Chmielewski [4] Lichodziejewski [136]

Table A. 1 continuing

Gossamer Solar Array (GoSolAr)		Size: 5 m x 5 m (deployed; envisioned scale 20 m x 20 m), 60 cm x 60 cm x 48 cm (stowed) TRL (estimated): 4 Power output: approx. 2 x 140 W Flown/used: downscaled breadboard ground tested, 2018 Stowage: double z-folded Deployment: by CFRP CTM booms	Hillebrandt [137] Sprowitz [138, 139]
Lightweight Integrated Solar Array and Transceiver (LISA-T)		Size (estimated): 75 cm x 93 cm (wing main dimensions), 1.96 m x 1.96 m (deployed planar config), 10 cm x 10 cm x 5 cm (stowed planar config), 10 cm x 10 cm x 10 cm (stowed omnidirectional config), 1.7 m <sup>2</sup> (4 wings) TRL (estimated): 6 Power output: approx. 125-250 W Flown/used: prototype ground qualification testing, 2016 Stowage: z-folded/rolled Deployment: by elgiloy c-booms (tape springs)	Carr [140] Johnson [141, 142] Lockett [143]
Mars Rover Inflatable Solar Array		Size: ø150 cm (major) diameter 16-sided inflatable torus TRL (estimated): 3-4 Power output: approx. 20 W Flown/used: full scale prototype ground tested, late 1990's Stowage: folded Deployment: by inflatable torus and column	Cadogan [134] Grahne [135]
Power Sphere Solar Array		Size: ø0.5-1 m TRL (estimated): 3-4 Power output: approx. 20-50 W Flown/used: full scale prototype built Stowage: folded Deployment: by inflatable sphere	Chmielewski [4] Grahne [135]
Space Antennas & Reflectors			
Example		Specifications	Literature/Reference
Inflatable Space Rigidizable Reflector (LOAD-1 to 10)		Size: ø1-12 m (build in different sizes) TRL (estimated): 6 Surface accuracy: 0.7-2.66 mm RMS Operation frequ.: L-band, 80 MHz Flown/used: 8 full scale prototypes ground tested, 1979-1992 Stowage: folded Deployment: by inflatable torus	Bernasconi [144] Defoort [145] Roederer [146]

Table A. 1 continuing







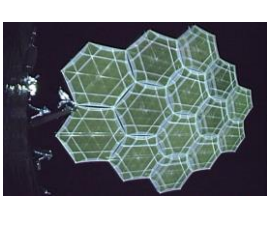
Inflatable Antenna Experiment (IAE)		Size: $\varnothing$ 14 m x 28 m TRL (estimated): 7-8 Surface accuracy: few mm RMS Flown/used: tested in-orbit, 1996 on Spartan-207 Stowage: folded Deployment: by inflatable booms (struts)	Freeland [81, 147] Steiner [148] L.Garde Inc. [149]
Synthetic Aperture Radar (SAR) Membrane Antenna with rigidizable Booms		Size: 3.3 m x 1 m TRL (estimated): 7-8 Operation frequ.: L-band, 80 MHz Flown/used: Subscale prototype ground tested Stowage: roll-up Deployment: by inflatable booms	Jenkins [3] ILC Dover Inc. [150] Huang [151]
SAR Membrane Antenna with CFRP-Booms		Size: 6 m x 1.3 m, 7.8 m <sup>2</sup> (envisioned 40 m <sup>2</sup> ) TRL (estimated): 3 Operation frequ.: L-band, 1.25 GHz Flown/used: Subscale prototype built Stowage: roll-up Deployment: by CFRP double-omega booms	Straubel [79, 80]
AstroMesh™ Mesh Antenna Reflector		Size: $\varnothing$ 3 m- $\varnothing$ 22 m TRL (estimated): 9 Operation frequ.: L-, Ka-band Flown/used: in service on 8 satellites, since 2000 Stowage: folded Deployment: by deployable ring truss & cable	NASA [152] Northrop Grumman [153-155] Thomson [156, 157]
Rigid & Folding Rib Mesh Reflector		Size: $\varnothing$ 4.8-18 m TRL (estimated): 9 Operation frequ.: S-, L-, Ku, UHF-band Flown/used: in service since 1983 Stowage: umbrella folding Deployment: by ribs & catenary	Harris Corp. [158-160] Lockheed Martin Corp. [161] Williams [162]
Hoop Truss Mesh Reflector		Size: $\varnothing$ 22 m TRL (estimated): 9 Operation frequ.: L-, Ku-band Flown/used: in service since 2011 Stowage: umbrella fold Deployment: by deployable ring truss	Williams [162] Harris Corp. [158-160] Lightsquared Inc. [163] The Boeing Company [164]
Large Deployable antenna reflectors (LDR)		Size: 19 m x 17 m (14 modules, $\varnothing$ 5 m each) TRL (estimated): 7 Surface accuracy: $>$ 2.4 mm RMS Operation frequ.: S-band Flown/used: in-orbit test in 2006 Stowage: rolled modules Deployment: by deployable truss structure & cable network	Meguro [165]



Table A. 1 continuing


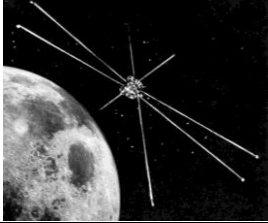
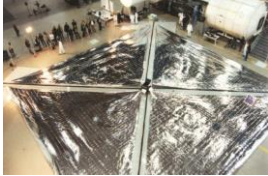
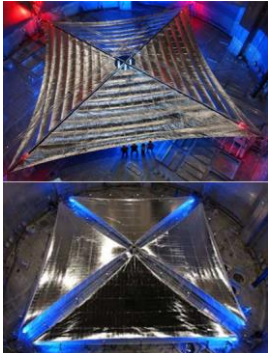


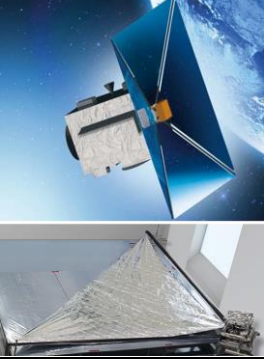
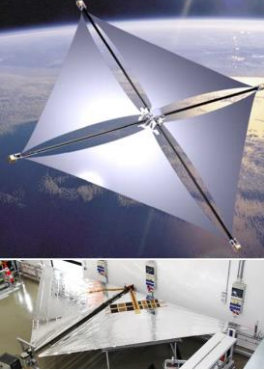
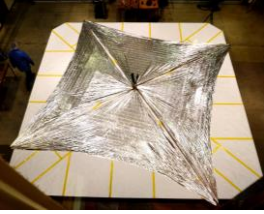
Spring-Back Antenna (SBA)		Size: 6.8 m ( $r_1$ ) x 5.25 m ( $r_2$ ) (elliptical; deployed), 4.9 m x $\varnothing$ 3 m (stowed) TRL (estimated): 9 Surface accuracy: $>2.4$ mm RMS Operation frequ.: up to Ka-band (27 GHz) Flown/used: in service since 1996 Stowage: taco rolled Deployment: by stored elastic strain energy of integrated lattice of ribs and hoop	Tibert [166] Williams [162] NASA [167]
Boom antennas of Explorer 49/RAE-B		Size: 229 m (deployed) TRL (estimated): 9 Operation frequ.: 25 kHz-13.1 MHz Flown/used: in-orbit experiment Explorer-B, 1973 Stowage: rolled Deployment: by metal stem booms	NASA [168] Staugaitis [108, 169]
Solar & Drag Sails			
Example		Specifications	Literature/Reference
DLR/ESA Solar Sail Ground Demonstrator (ODISSEE)		Size: 20 m x 20 m, 330.5 m <sup>2</sup> (deployed, envisioned 40 m x 40 m), 0.19 m <sup>3</sup> (stowed) TRL (estimated): 4-5 Sail type: Rigid Squared Solar Sail Areal density: 48.4 g/m <sup>2</sup> ; 30.5 g/m <sup>2</sup> achieved for sail & booms Flown/used: bread board ground deployed, 1999 Stowage: folded, rolled booms Deployment: by 4 CFRP booms (14 m)	Leipold [109, 170] Sickingler [35, 113, 122]
Sunjammer Solar Sail & predecessors		Size: 20 m x 20 m, 400 m <sup>2</sup> (deployed; envisioned 1200 m <sup>2</sup> ), 0.5 m <sup>3</sup> (stowed) TRL (estimated): 5-6 Sail type: Rigid Squared Solar Sail Areal density: 7 g/m <sup>2</sup> (approximated) Flown/used: 2 competing prototypes ground tested, 2005-2015 Stowage: folded Deployment: by 4 inflatable booms/ 4 coilable truss booms)	Barnes [171] Chafer [172] Eastwood [173] Greschik [174] Johnson [175]
NanoSailDeorbit (NanoSail-D & NanoSail-D2)		Size: 3.16 m x 3.16 m, 10 m <sup>2</sup> (deployed), 10 cm x 10 cm x 20 cm (stowed; 2U not including bus) TRL (estimated): 7-8 Sail type: Rigid Squared Drag Sail Areal density: - Flown/used: deployed in-orbit, 2011 Stowage: folded Deployment: by 4 elgiloy TRAC booms (2.5 m)	Alhorn [176] Banik [177] Garcia [10] Johnson [178-180] Murphey [181] NASA [182]

Table A. 1 continuing

DeorbitSail		<p>Size: 4 m x 4 m, 10 m<sup>2</sup> (deployed), 10 cm x 10 cm x 20 cm (stowed; 2U not including bus)          TRL (estimated): 6-7          Sail type: Rigid Squared Drag Sail          Areal density: –          Flown/used: launched, 2015, deployment failed due to motor failure          Stowage: folded          Deployment: by 4 CFRP double-omega booms (2.95 m)</p>	<p>Hillebrandt [99, 183]          Stohlman [184-186]          Zander [124]</p>
ADEO (Architectural Design and Testing of a De-orbiting Subsystem)		<p>Size: 5 m x 5 m, 25 m<sup>2</sup> (deployed), 23.4 cm x 46.2 cm x 46.2 cm (stowed)          TRL (estimated): 6          Sail type: Rigid Squared Drag Sail          Areal density: 60 g/m<sup>2</sup> (approximated)          Flown/used: segment breadboard ground tested/qualified, 2017          Stowage: folded/rolled          Deployment: by 4 CFRP double-omega booms (4.3 m)</p>	<p>Meyer [111]          Sinn [89-91]          Zander [118]</p>
Gossamer-1		<p>Size: 5 m x 5 m, 25 m<sup>2</sup> (deployed), 79 cm x 79 cm x 50 cm (stowed)          TRL (estimated): 6          Sail type: Rigid Squared Solar Sail          Areal density: –          Flown/used: breadboard ground tested/qualified, 2015          Stowage: folded/rolled          Deployment: by 2 crossing CFRP double-omega booms (8.6 m) + 4 mechanisms (jettisoned after deployment)</p>	<p>Seefeldt [85-87, 95]          Sprowitz [84]          Straubel [94]          Zander [77, 125]</p>
LightSail 1 & 2		<p>Size: 5.6 m x 5.6 m, 32 m<sup>2</sup> (deployed), 10 cm x 10 cm x 30 cm (stowed; 2U)          TRL (estimated): 9          Sail type: Rigid Squared Drag Sail          Areal density: –          Flown/used: deployed in-orbit, 2015/2019          Stowage: folded          Deployment: by 4 elgiloy TRAC booms (4 m)</p>	<p>Biddy [187]          The Planetary Society [188]</p>




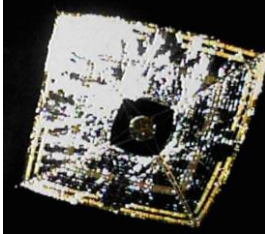
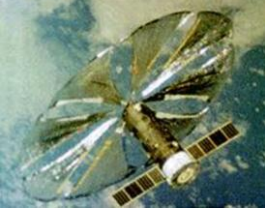



Near Earth Asteroid Scout (NEA)		Size: 9.3 m x 9.3 m, 86 m <sup>2</sup> (deployed), 20 cm x 10 cm x 30 cm (stowed, 6U) TRL (estimated): 4–5 Sail type: Rigid Squared Solar Sail Areal density: – Flown/used: breadboard ground tested/qualified, 2018 Stowage: folded Deployment: by 4 CFRP CTM booms (7.2 m); initially 4 elgiloy TRAC booms (7.3 m)	Johnson [189] McNutt [190] NASA [191] Stohlman [102, 103, 192] Fernandez [110, 193]
Interplanetary Kitecraft Accelerated by Radiation Of the Sun (IKAROS)		Size: 13.56 m x 13.56 m, 200 m <sup>2</sup> (deployed), ø16 m x 0.8 m (stowed, cylindrical) TRL (estimated): 8 Sail type: Spin-stabilized Solar Sail Areal density: 1550 g/m <sup>2</sup> Flown/used: tested in-orbit, 2010 Stowage: folded/rolled Deployment: by 4 tip masses + tethers	Mori [194] Kawaguchi [195] JAXA [195]
Znamya 2 and 2.5		Size: ø20 m (Znamya 2, deployed), ø25 m (Znamya 2.5 deployed) TRL (estimated): 6–8 Sail type: Spin-stabilized Solar Sail Areal density: – Flown/used: deployed prototype in-orbit, 1993/1999 Stowage: rolled Deployment: by centrifugal forces	Lewis [196] Syromiatnikov [197]
Solar Shades			
Example		Specifications	Literature/Reference
Sunshield Membrane Assembly (SMA) of James Webb Space Telescope (JWST)		Size: 212 m x 142 m (deployed, 5 layers) TRL (estimated): 7–8 Flown/used: full size ground deployed, 2017 Stowage: z-folded Deployment: by boom and cable deployment system	Clampin [198] Ewing [199] Fellini [200] Gardner [201] Gutro [202] NASA [33, 203]
Deployable Sunshield Assembly (DSA) of GAIA		Size: ø102 m (deployed) TRL (estimated): 7–8 Flown/used: in service since 2013 Stowage: umbrella-folded Deployment: by rectangular truss frames	Pereira [204] SENER [205, 206] Urgoiti [207]
Deployable Sunshield Assembly (DSA) of GAIA		Size: ø34 m (deployed) TRL (estimated): 4 Flown/used: ø10 m breadboard tests since 2015 Stowage: rolling-folding/folding collapsing (2 variations) Deployment: by complex truss & frames structure/petals	NASA [208, 209] Siegler [210] Webb [211] Willems [212]

Table A. 1 continuing

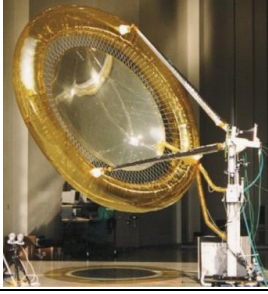
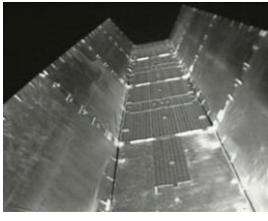









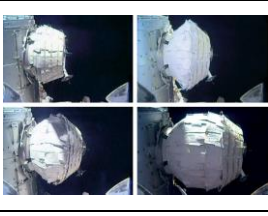
Solar Concentrators			
Example		Specifications	Literature/Reference
NASA's Thin Film Inflatable Solar Concentrator		Size: $\phi$ 6.5 m (assembly, deployed), $\phi$ 5 m (reflector, deployed) TRL (estimated): 6 Surface accuracy: 15 mm RMS Flown/used: prototypes ground tested, 1996 Stowage: folded Deployment: by inflation of reflector, torus & struts	Pappa [213, 214] Smalley [215] Wong [216]
Hughes 702 Solar Array Concentrator		Size: 34 m (deployed) TRL (estimated): 9 Surface accuracy: 15 mm RMS Power amplification: 14-15 times Flown/used: in service since 2000 Stowage: folded Deployment: by spring loaded hinges and tether system	Gelderloos [217] Stribling [218] The Boeing Company [219]
Entry, Descent Landing (EDL) & Surface Exploration			
Example		Specifications	Literature/Reference
Big Wheels Inflatable Mars Rover		Size: $\phi$ 15 m (deployed) TRL (estimated): 3-4 Flown/used: Breadboard ground tested in 2001 Stowage: folded Deployment: by inflation	Jones [220-222]
Inflatable Tumbleweed Rover		Size: $\phi$ 15 m (deployed) TRL (estimated): 3-4 Flown/used: Breadboard field tested in 2003 Stowage: folded Deployment: by inflation	Behar [223, 224] Godwin [225]
Inflatable Tumbleweed Rover		Size: $\phi$ 0.9-3 m (deployed) TRL (estimated): 3-4 Flown/used: Breadboard ground tested in 2002-2005 Stowage: folded Deployment: by hoops	Antol [226-230] Claycomb [231] Flick [232] Rose [233]
Mars Pathfinder (MPF) and Mars Exploration Rover (MER) Impact Attenuation Systems		Size: $\phi$ 5.2 m (assembly, 18 m (per sphere)) TRL (estimated): 9 Flown/used: Mars landing 1997, 2004 Stowage: folded Deployment: by inflation spheres	ILC Dover [234] NASA [235-237] Stein [238]

Table A. 1 continuing

Beagle 2 Airbag System		Size: $\varnothing$ 1.93 m (assembly) TRL (estimated): 7-9 Flown/used: flight qualified, launched 2003 Stowage: folded Deployment: by inflation of segments	ESA [239] ILC Dover [240] Wright [241]
Hypersonic Inflatable Aerodynamic Decelerator (HIAD; IRVE-3)		Size: $\varnothing$ 3-6 m (outer torus) TRL (estimated): 7-8 Flown/used: flown on sounding rocket, ground tested in 2003 Stowage: folded, wrapped Deployment: by inflation of structural tori	Hughes [242] Jurewicz [243] NASA [244]
Human Habitats			
Example		Specifications	Literature/Reference
InFlex-Lunar Habitat		Size: $\varnothing$ 3.65 x 5.18 m (main compartment) TRL (estimated): 6 Flown/used: prototype ground tested in 2007 Stowage: folded Deployment: by inflation	Cadogan [245] Henry [246] Hinkle [247] ILC Dover [248] NASA [249]
TransHab-Space Habitat		Size: $\varnothing$ 8.2 m x 11 m, 339.8 m <sup>3</sup> (deployed), $\varnothing$ 4.3 m (stowed) TRL (estimated): 6 Flown/used: prototype tested in vacuum chamber 2007 Stowage: folded Deployment: by inflation	Dismukes [250] ILC Dover [251]
Genesis I and II Space Habitats		Size: $\varnothing$ 2.4 m x 4.3 m (deployed) TRL (estimated): 8 Flown/used: prototypes tested in space 2006/2007 Stowage: folded Deployment: by inflation	Bigelow Aerospace [252, 253]
Bigelow Expandable Activity Module (BEAM)		Size: $\varnothing$ 3.23 m x 4.01 m, 16 m <sup>3</sup> (deployed), $\varnothing$ 2.36 m x 2.16 m, 14 m <sup>3</sup> (stowed) TRL (estimated): 8 Flown/used: prototype tested in space since 2016 Stowage: folded Deployment: by inflation	Bigelow Aerospace [254] NASA [255]

## Appendix B SURVEY OF ASSESSMENT METHODS

Assessment, evaluation and rating of technical systems or of their properties and behavior follows a similar path in all fields e.g. when assessing technology, risk and reliability. Commonly an approach from top down, breaking a system down to its smallest members, or following a bottom up approach, starting investigation at the least complex members of a system, working the way up towards a higher complexity, and ending up at the system, is realized. Similar to a system view a top down approach in applying methodology is considered a deductive principle, applying a method to a general application first, then following to the next lower and detailed level. In contrast, the bottom up approach can be considered an inductive principle from a methodological perspective. Here the starting point of method application is the most detailed level e.g. a specific investigation of an effect or when analyzing empirical data. In the following, the described methods are viewed from a methodological point of view.

In order to establish an appropriate rating method for robustness, the most common evaluation methods, with their characteristics, commonly applied in other fields like technical assessment (TA), risk assessment and reliability assessment are reviewed and compared. These methods are: Trend Extrapolation, Relevance Tree-Analysis, Cross-Impact Analysis, Risk Analysis, Scoring Method, Preference Matrix, Failure-Modes and Effects Analysis (FMEA, FMECA, FMEDA), Fault Tree Analysis (FTA) & Success Tree Analysis (STA), Reliability Block Diagram (RBD), Event Tree. Their main characteristics and differences are summarized in Table B. 5, while the most promising methods, providing some suitable approaches for a robustness rating, are discussed in detail. Even more methods of the different domains can be found in the systems engineering summary of Goldberg [256].

All methods have the objective to give quantified comparable results, from a qualitative and quantitative input.

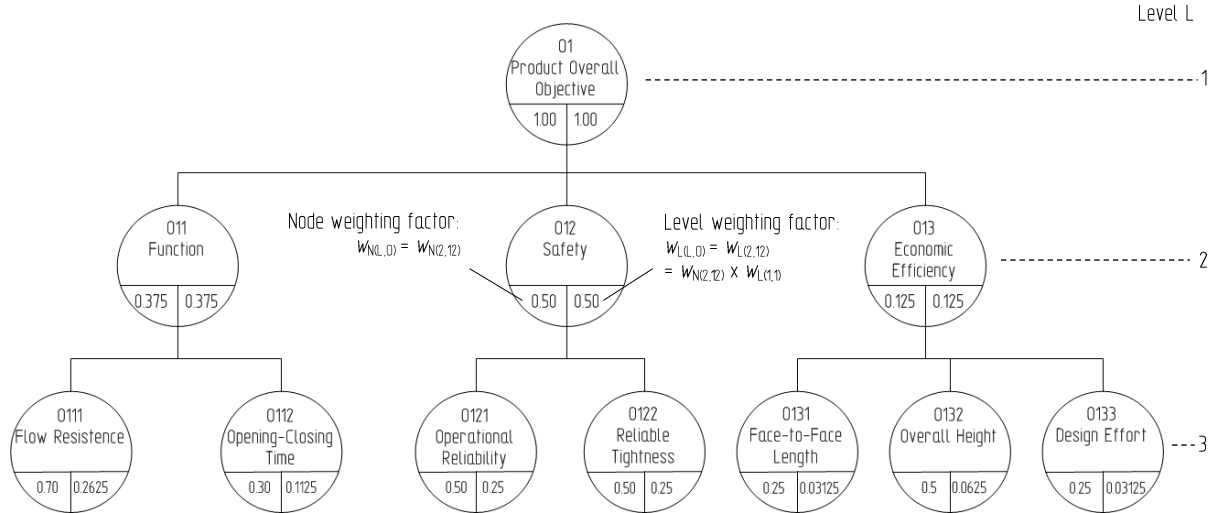
### Scoring Methods

In general, scoring methods are inductive methods that rate different alternatives or solutions by a scoring system assigning a score to each chosen criterion. By systemizing this approach in a typical matrix, the evaluation chart, where rows contain the alternatives (partial solutions) and columns the rating criteria, each entity in the matrix will be assigned a value by a benefit function. Scoring methods can be used for quantitative and qualitative criteria, while all aims must be independent from another [257].

Two main methods are commonly used in engineering, the Cost-Benefit Analysis (CBA) [41] (in German industry and engineering also known as “Nutzwertanalyse” – NWA according to Zangemeister) and the combined technical and economic evaluation technique (in some literature called trade studies [256]), firstly introduced by Kesselring, specified in the guideline of German industry standard VDI 2225. The Cost-Benefit Analysis referred to in this work features a technical focus while in economics this method and the similar Cost-Utility Analysis (CUA) predominantly focuses on economic and monetary metrics. In the following, the terms Cost-Benefit Analysis (CBA) and VDI 2225 are used to indicate the according method.

Mainly the following steps are to be taken when applying a scoring method:

1. Defining Objective Criteria (according to requirements; independent from one another)
2. Determining weighting factors (in VDI 2225 only in rare cases)
3. Determining Partial Utility Values and Weighted Partial Utility Values
4. Summation of Partial Utility Values or Weighted Partial Utility Values to an Overall Utility Value



**Figure B. 1.** Objectives tree to determine weighting factors of a valve design

In the Cost-Benefit Analysis, a systemized objective system is established with vertically organizing objective levels of decreasing complexity and horizontally objective areas that are hierarchically ordered in a so-called objectives tree. Such tree is depicted in Figure B. 1 giving the example of a new valve design for e.g. the life support system of the International Space Station. The evaluation criteria (objective criteria) are derived from the objective level of lowest complexity, here on level 3. Evaluation itself proceeds systematically from a level of higher complexity to the next lowest level. Each evaluation criterion is weighted according e.g. to its importance, priority or severity. Such factor  $w_i$  must lie between 0 and 1 or 0 % and 100 %. The importance of an objective in relation to the objective of the next higher level is expressed in Node weighting factors  $w_{N(L,O)}$ , while the sum of all Node weighting factors at each level  $L$  of all evaluation criteria that are related to the next higher objective, must result in 1 or 100 %:

$$\sum_{i=L_1}^{L_n} w_{N(L+1,O)} = 1 \tag{B.1}$$

The Level-weighting factor  $w_{L(L,O)}$  gives the absolute importance of the objective in the relevant level as product of Node weighting factor and Level weighting factor of the next higher level with

$$w_{L(L,O)} = w_{N(L,O)} w_{L(L-1,O)} \tag{B.2}$$

as it can be followed in of Figure B. 1. The sum of all Level weighting factors for each level must always be equal to 1.[41, 257]

In contrast to this, the industry standard VDI 2225 does not use a hierarchical order of objective areas. The evaluation criteria are directly derived from the technical requirements list while most commonly for VDI 2225, a weighting of evaluation criteria is not performed. Nevertheless, in cases of strongly different importance, a weighting can be considered. Due to the primarily un-weighted standard procedure, VDI 2225 in this work is considered a non-weighting method. This however assumes an equal significance of all evaluation criteria.

In the next step, similar in both methods, all determined evaluation criteria and weighting factors for each alternative are systemized into an evaluation chart as shown in Figure B. 2. For each evaluation criterion a qualitative or, in case parameter magnitudes are available, a quantitative rated measure, the Partial Utility Value  $p_i$ , is generated. In an ordinal scale ranging from 0 to 10 (VDI 2225 uses a scale of 0 to 4) such Partial Utility Value is assigned. For quantitative measures a linear or non-linear

value function might determine the assignment of points of the scale [41]. Here 0 represents a solution that is “of no use or unsatisfactory” and 10 (4 in VDI 2225) a solution that is deemed “ideal/very good”. Each partial utility value is then multiplied by the weighting factor of the according evaluation criterion resulting in a Weighted Partial Utility Value  $w_i p_i$  for each evaluation criterion and alternative. By summation of all Weighted Partial Utility Values (in VDI 2225 unweighted), an Overall Utility Value  $v_w$  (for each solution/alternative) can be determined according to

$$v_w = \sum_{i=1}^n w_i p_i \quad (\text{B.3})$$

as demonstrated in Figure B. 2. A following normalization of all acquired overall utility values provides a rank list, in order to ease the comparison of the different alternatives.

Evaluation Criteria	Weighting Factor $w_i = w_L$	Alternatives					
		A1 Ball Valve		A2 Gate Valve		A3 Butterfly Valve	
		$p_{i1}$	$w_{i1} p_{i1}$	$p_{i2}$	$w_{i2} p_{i2}$	$p_{i3}$	$w_{i3} p_{i3}$
Flow resistance	0.2625	8	2.100	6	1.575	4	1.050
Opening - Closing time	0.1125	7	0.788	4	0.450	3	0.338
Operational Reliability	0.25	7	1.750	7	1.750	5	1.250
Reliable Tightness	0.25	6	1.500	6	1.500	6	1.500
Face-to-Face Length	0.03125	7	0.219	6	0.188	7	0.219
Overall Height	0.06250	8	0.500	3	0.188	2	0.125
Design Effort	0.03125	6	0.188	5	0.156	5	0.156
Utility Value $v_w$			7.044		5.806		4.638
normalized Utility Value			1.000		0.824		0.658
Rank			1		2		3

**Figure B. 2.** Evaluation chart of a valve design example facilitating the Cost-Benefit Analysis

Furthermore, in order to provide a better comparability between different alternatives/solutions, a relation between the achieved and a maximum reachable (theoretically ideal) overall utility value, the Technical Value  $x_t$ , can be applied:

$$x_t = \frac{\sum_i^n p_i}{n \cdot p_{max}} \quad (\text{B.4})$$

This value might incorporate the found weighting factors as well. In the here described example however, the technical value was not applied.

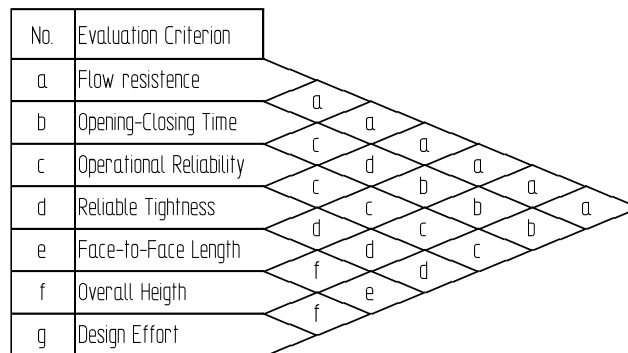
### *How can the principles of a scoring method be utilized for a robustness evaluation?*

The method of finding evaluation criteria and the weighting factors in a systematized manner is seen favorable also for finding robustness criteria and weighting factors of robustness. The here discussed hierarchical principle is also seen applicable to robustness criteria and weighting factors. Finding weighting factors on the lowest level of complexity seem to be well applicable to the robustness of each robustness criterion (evaluation criterion). In addition, the principle stating that the sum of level weighting factors equals one might also be transferred to a robustness evaluation. However, weighting factors solely as a product, as found in a CBA, might not depict the whole set of interactions between levels of hierarchy, since the relation to the next higher level might be inverted proportional according to **1. Work Hypothesis**. On the other hand, an ordinal scale of 0 to 10 (or a 0 to 4 scale) is seen well applicable for rating robustness criteria, as well as specific functions for

magnitudes of values for each evaluation criterion (robustness criterion). An evaluation chart as seen in Figure B. 2, in which each evaluation criterion is rated is also assumed well applicable for robustness, at least for determining a Weighted Partial Robustness Value (Weighted Partial Utility Value in CBA) for each criterion. Although a plain summation to determine the Overall Utility Value is considered appropriate in Cost-Benefit Analysis, it might not in a Robustness Evaluation, due to the assumption of the **1. Work Hypothesis** that partial robustness values are not necessarily related by addition.

**Preference Matrix**

Another method used to evaluate or rate technical solutions is the Preference Matrix (sometimes referred to as Dominance Matrix). It is an inductive method mainly focusing to determine weighting factors. After all relevant evaluation criteria have been determined; the method starts with associating every criterion with a code letter. The core principle of this method is a pairwise comparison of all evaluation criteria, one by one, with one another in a preference matrix, as shown in Figure B. 3 on the example of the shut-off valve of ISS’ life support system. The higher ranked criterion of a tuple is preferred and filled in the matrix, while a ranking of equal importance cannot be realized with this method. Determining the rank of each evaluation criteria itself is performed by ranking the frequency of each criterion. Criteria and frequency of occurrence are then listed as depicted in Figure B. 4, while the normalized frequency of occurrence provides the weighting factor for each criterion. With such procedure, subjective rating (of the evaluator) can be reduced and an objective decision (evaluation) can be realized [257]. Hence, in contrast to the Scoring Method (Cost-Benefit Analysis) the sum of all weighting factors is not limited by 1 or 100 %.



**Figure B. 3.** Preference Matrix example

Evaluation Criterion	a	b	c	d	e	f	g
Frequency	6	3	5	4	1	2	0
normalized Weighting Factor	1.00	0.50	0.83	0.67	0.17	0.33	0.00

**Figure B. 4.** Determining weighting factors from frequency of preferences

Moving forward in the evaluation process, the weighting factors are then filled into a general evaluation chart (see Figure B. 5). As it becomes obvious when going through the column of weighting factors, the less important evaluation criterion (Design Effort) obtains a weighting factor of  $w_i = 0$ , thus providing a special situation. Despite the supposedly unimportance of this evaluation criterion, indicated by the weighting factor, it has originally been chosen to be an important criterion that needs to be considered, and therefor will be listed in the evaluation chart. Here evaluation is performed as described before for the scoring methods. For the shown example each criterion is rated directly and qualitatively with the measure  $p_i$  (Partial Utility Value, un-weighted), in an ordinal scale ranging from 0 to 10. By multiplying the Partial Utility Value  $p_i$  with the weighting factor of the according evaluation criterion, the Weighted Partial Utility Value  $w_i p_i$  for each evaluation criterion, and by summing up these values, the Overall Utility Value  $v_w$  for each alternative is determined



following equation (B.3). Normalizing all acquired overall utility values  $v_{Nw}$  provides a rank list, for comparison of the different alternatives [257].

When comparing the evaluation results of the preference matrix method (Figure B. 5) and the results of the scoring methods (Figure B. 2) the same ranking of alternatives is achieved. The normalized overall utility values  $v_{Nw}$  however differ as well as the overall utility values  $v_w$  between the two methods. Furthermore, the preference matrix is considered useful for small and less complex systems, while the hierarchical nature of the Cost-Benefit Analysis provides well-structured and clear procedures for complex systems. Another drawback of the preference matrix is the fact that evaluation criteria can be underrated, with a weighting factor of zero, as shown in the example.

Evaluation Criteria	Weighting Factor $w_i$	Alternatives					
		A1 Ball Valve		A2 Gate Valve		A3 Butterfly Valve	
		$p_{11}$	$w_{11}p_{11}$	$p_{12}$	$w_{12}p_{12}$	$p_{13}$	$w_{13}p_{13}$
Flow resistance	1.00	8	8.000	6	6.000	4	4.000
Opening - Closing time	0.50	7	3.500	4	2.000	3	1.500
Operational Reliability	0.83	7	5.810	7	5.810	5	4.150
Reliable Tightness	0.67	6	4.020	6	4.020	6	4.020
Face-to-Face Length	0.17	7	1.190	6	1.020	7	1.190
Overall Height	0.33	8	2.640	3	0.990	2	0.660
Design Effort	0.00	6	0.000	5	0.000	5	0.000
Utility Value $v_w$			25.160		19.840		15.520
Normalized Utility Value			1.000		0.789		0.617
Rank			1		2		3

**Figure B. 5.** Example of an evaluation chart using normalized weighting factors determined with a preference matrix

### *How can the principles of a preference matrix be utilized for a robustness evaluation?*

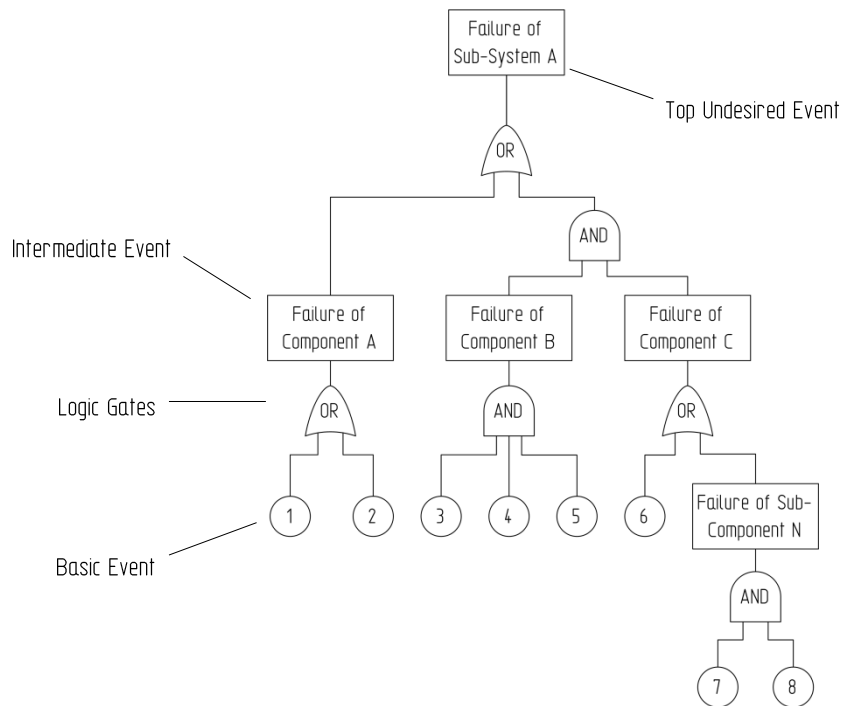
The Preference matrix cannot be used to find or determine evaluation or robustness criteria. Nonetheless, the preference matrix provides, with given evaluation criteria that are compared one by one in a pairwise manner, a good overview of preferences (importance) of the evaluation criteria. This is considered well applicable to robustness criteria and their evaluation. However, for a robustness evaluation weighting factors of zero are not considered useful, since it can falsely indicate unimportance. Similar to the scoring methods, also the plain summation to determine the Overall Utility Value, used in the general evaluation following the preference matrix, is not considered sufficient for a Robustness Evaluation, due to the assumption of the **1. Work Hypothesis**, stating that partial robustness values are not necessarily related by addition.

## Fault Tree Analysis (FTA) & Success Tree Analysis (STA)

The Fault Tree Analysis (FTA) is a deductive, top-down (backwards) method looking into the past, and can be allocated in the Safety I area of Reliability engineering, asking the question “What could cause the unwanted effect?”. It searches and quantifies the severity and probability of occurrence of a failure. Furthermore, FTA is a top-down method analyzing an “undesired State/Event” or a “system failure condition” of a system. The main goals are showing how a system can fail, identifying the best ways to reduce a risk and to determine event rates of failure and probabilities of failure, and consequently reducing the likelihood of failure through an improved system design. In a hierarchical order, FTA maps the relationship between faults, subsystems and reduced safety design elements with a diagram of the overall system based on Boolean logic, the fault tree, as shown in Figure B. 6. The top event represents the undesired event (failure) of a system or subsystem. Going top-down, intermediate events, e.g. the failure of a certain component, are identified. Basic events are the termination points of such analysis and provide the boundary of the model as well as the input of



external events. They may resemble a specific failure (or failure mechanism) of a component or sub-component, at the lowest level of the method’s hierarchical structure [54].



**Figure B. 6.** Example of a Fault-Tree

For quantification with this method, it is crucial to be able to assign a value for example a probability or frequency to these items. Making use of the Boolean logic, basic events are combined by gates thus forming “super-events” or “cut sets” (minimal cut sets) and connecting basic events leading to the top event. Representing reliability dependency, OR gates function as a series relation:

$$P(A \text{ or } B) = P(A \cup B) = P(A) + P(B) - P(A \cap B) \tag{B.5}$$

, while AND gates represent redundancy and function as parallel relation:

$$P(A \text{ and } B) = P(A \cap B) = P(A) \times P(B) \tag{B.6}$$

For specific cases, e.g. when failure probabilities are small, an OR gate connects the probabilities of two basic events with

$$P(A \text{ or } B) \approx P(A \cup B) \approx P(A) + P(B), \text{ if } P(A \cap B) \approx 0 \tag{B.7}$$

In case only one input or the other occurs with an output for an exclusive OR gate, probabilities are connected as follows:

$$P(A \times \text{or } B) = P(A) + P(B) - 2P(A \cap B) \tag{B.8}$$

Commonly all events are considered to be independent. If they are not independent, specific software approaches provide a solution, working with cut sets, thus increasing the effort of performing

a FTA drastically. A single fault tree can be used to analyze only one top event (undesired event). However, a fault tree may be fed into another fault tree as a basic event [54, 258].

Summarizing, the following steps are performed within a FTA:

1. Defining the Undesired Event
2. Understanding the system, identifying probabilities of occurrence and causing effects
3. Constructing a Fault Tree
4. Evaluation of Fault Tree (hazards, possible improvements)
5. Control identified hazards (decrease probability of occurrence)

As inversion of the FTA, a Success Tree Analysis (STA) is looking into the future in order to identify what is needed to achieve success for a system. Moreover, a conversion of a fault tree into a success tree and vice versa can be achieved by applying de Morgan's theorem, as Boolean logic is inverted [54].

### *How can the principles of a FTA/STA be utilized for a robustness evaluation?*

The hierarchical nature of a FTA/STA provides a structured procedure to analyze a system from top-down. This is assumed well applicable for an analysis of robustness of a system, due to a similar initial situation regarding the system point of view. Furthermore, the principles of FTA/STA are considered applicable tools to find robustness criteria, at the lowest hierarchy level. Similar to "undesired events" and failure probabilities in a FTA, robustness criteria or partial robustness are assumed to be connected in a similar way, by parallel and series connections, thus complying with **1. Work Hypothesis**. Robustness as stated in section 3.3.2 is also a function of probability of an event. This is found in the FTA/STA as well, leading to the assumption that the mathematic principles can be transferred to robustness assessment, at least for probability considerations.

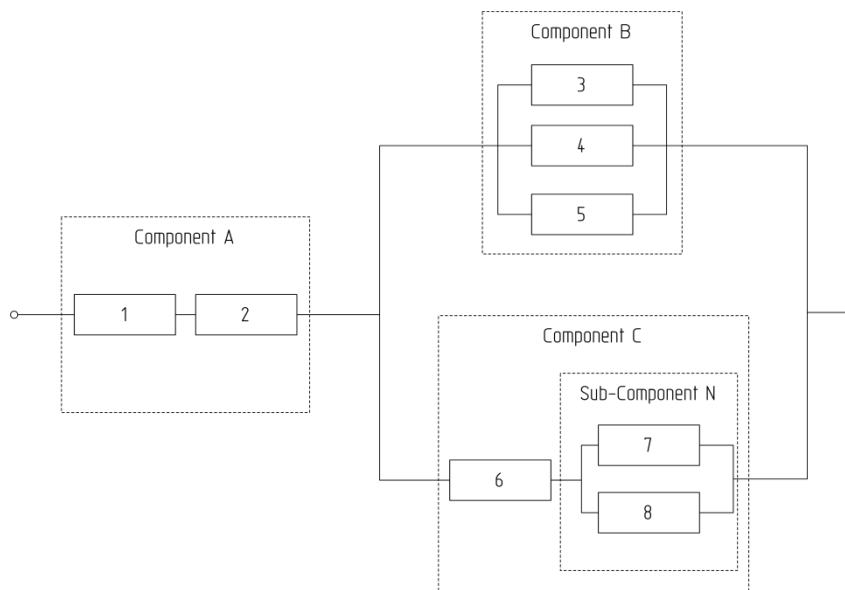
### **Reliability Block Diagram**

The Reliability Block Diagram (RBD; also known as Dependence Diagram) is a deductive, top-down (backwards) method that identifies how component reliability contributes to the failure or success of a complex system [54, 259]. It gives a graphical representation of the functional relations between the elements that comprise a system and the existing Boolean expressions. Here blocks are connected in parallel or in series, while each block represents one component or function of a system with a failure rate. Nevertheless, this method aims to produce a systematic overview for a function in a particular operating state rather than for a piece of hardware. Thus, an RBD indicates which sub functions must operate successfully in order for the system to accomplish its intended main function. As blocks may also be represented by switches (closed= working component, open= failed component), parallel paths indicate redundancy (active or standby; not all elements are required to be up for a successful operation of the system). When connected in series however the whole system might fail in case one or more components fail. In this way, groups of elements in series or a number of groups with redundancy (group parallel elements) are connected in series, as illustrated in Figure B. 7. Note that the here depicted system is identical with its components and functions to the one used in the fault tree of Figure B. 6. Due to the relation of elements and their associations to the overall system using Boolean logic, an RBD may be converted into a Success Tree (series converted into AND, parallel converted into OR). De Morgan's Theorem however, may then convert the Success Tree into a Fault Tree. Quantification using a RBD can be achieved by calculating System Reliability, Availability, Mean Time to Failure (MTTF), Mean Time Between Failures (MTBF) or Mean Time to Repair (MTTR) for each element and consequently for the system. Mathematical principles, based on Boolean logic, used are identical to the ones facilitated for the FTA, given in the equations (B.5), (B.6), (B.7) and (B.8) [54, 259].

The general procedure to derive a Reliability Block Diagram can be summarized with the following steps.

Steps of generating a Reliability Block Diagram:

1. Definition of functions the system performs (operating states)
2. Specification of minimum functions that are required for successful operation of the system
3. Drawing of system RBD of system functions
4. Specify elements required to perform system function
5. Drawing of system RBD of system elements
6. Simplify RBD



**Figure B. 7.** Exemplary Reliability Block Diagram

Generally, all blocks and components are assumed statistically independent from another. However, since an item might have more than one failure mode, the effect a failure inflicts on a system might therefore depend upon which failure mode occurs. Moreover, constellations might occur in which elements are not independent of each other, thus making operation and failure of each element conditional. In this case a system or equipment might require more than one RBD and a dynamic RBD must be performed, requiring much more effort. Although giving a structured overview of systems functions, a RBD cannot accurately depict operational phases e.g. where a system failure may or may not be affected by a component, depending on the phase or operational requirements at the time [259].

### *How can the principles of a Reliability Block Diagram be utilized for a robustness evaluation?*

Similar to the hierarchical nature of a FTA/STA, the Reliability Block Diagram provides a structured procedure to analyze a system from top-down. Identifying the functions that contribute and are necessary to accomplish the main function, ought to be very similar to relating partial robustness to an overall robustness, and is considered a well applicable procedure for a robustness evaluation. Moreover, the similar initial situation regarding the system point of view is assumed well applicable to pursue an analysis of robustness of a system. Parallel and series connections are also assumed part of the relations between robustness criteria or partial robustness, thus complying with **1. Work Hypothesis**.

Robustness as stated in section 3.3.2 can be expressed as a function of probability of an event and as quantified values exceeding requirements or expectations. Such values are used in a Reliability

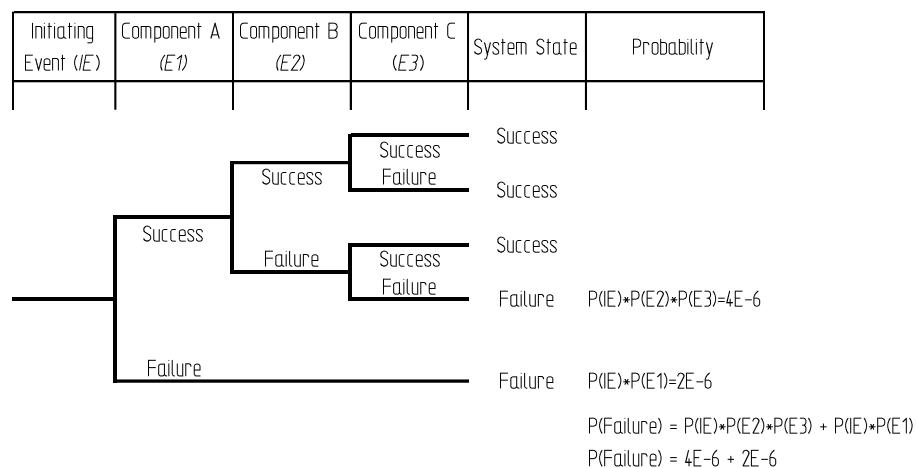
Block Diagram i.e. System Reliability, Availability, Mean Time to Failure (MTTF), Mean Time Between Failures (MTBF) or Mean Time to Repair (MTTR). This and the mathematic principles found in the RBD are supporting the assumption that the principles of an RBD can be transferred to a robustness assessment, at least partially.

## Event Tree

The Event Tree (ETA) is a graphical representation of an inductive and investigatory method (forward, bottom-up), which can be applied in a qualitative and quantitative manner (see Figure B. 8). It is represented in an analytical diagram, used to examine a chronological series of subsequent events or consequences. These are determined by how an accident's (initiating event) progression is affected by subsequent failure of other components or subsystems. Furthermore, this method helps to identify the sequence progression, sequence end states and sequence specific dependencies over time and is tracing forward in time or through a causal chain, contrary to the FTA that traces back in time or causal chain. As a forward tracing method it does not require a known hazard [260].

The procedure itself starts with the assumption that an initiating event, a failure or success, occurs. Each possible sequence of events that might result from the assumed initiating event is followed as its consequences propagate through the whole system. A quantified estimate such as the probability of occurrence is then assigned for each event and an overall probability of a sequence can be determined using Boolean logic as described with the equations (B.5), (B.6), (B.7) and (B.8).

All potentially dangerous or adverse events following the initial event are methodically identified and displayed as sequences of events by the event tree, as depicted in the example of Figure B. 8. This example is based on the identical system, including components and associations, previously discussed for the Fault Tree Analysis and the Reliability Analysis (see Figure B. 6 and Figure B. 7 for comparison). Here the linked events are forming a structure, much like the branches of a tree, following the Boolean logic. Each branch is evaluated to determine its own probability by multiplying the individual probabilities of the failure events occurring, given in Table B. 1. Event Tree Branch Probabilities with notional values for illustration. However, the overall probability (indicated as P Failure in Figure B. 8) in return is determined by a summation of all probabilities of a failure sequences (branches).



**Figure B. 8.** Example of an Event Tree

**Table B. 1.** Event Tree Branch Probabilities

<i>Event</i>	Description	Probability of Occurrence
IE	Initiating Event causing failure of system components (functions) e.g. electrostatic discharge, overloading, overflow	0.2 per year
E1	Failure of Functions 1 and 2 of Component A	1.00E-05
E2	Failure of Functions 3, 4 and 5 of Component B	2.00E-03
E3	Failure of Functions 6 or 7 and 5 of Component B	1.00E-02

### *How can the principles of an Event Tree be utilized for a robustness evaluation?*

The event tree facilitates a simple procedure following a path of events (causal chain). This could partially be applied to follow a path of components implying robustness and to determine robustness, similar to probabilities of the branches of an event tree. Finding robustness criteria are not thought to be possible with such procedure, although qualitative and quantitative values can be generated. Nevertheless, due to its relation to the FTA/STA and RBD, that are assumed to be well implemented into a robustness assessment, the procedure of the event tree is also considered to be at least a part of this analysis. Furthermore, parallel and series connections are assumed to be part of the relations between partial robustness, thus complying with **1. Work Hypothesis**. The principles of an event tree are considered transferrable, at least partially to a robustness assessment. This is supported by the stated definition section 3.3.2, in which robustness can be expressed as a function of probability of an event and as quantified values exceeding requirements or expectations.

### **Failure Modes, Effects (and Criticality) Analysis (FMEA/FMECA)**

The Failure Mode and Effects Analysis (FMEA), or Failure Modes, Effects and Criticality Analysis (FMECA), is an inductive, mainly subjective and bottom-up (forward) method that analyzes the effects of single components or function failures on equipment or subsystems. It is used as a design tool to assess and quantify risks and to identify failure modes and effects, thus asking the question “What if this happens; What can occur?”. This method is especially useful when comparing design concepts and for design refinement and can be found as established method for design analysis in the standards ECSS-Q-ST-30-02C, MIL-STD-1629A (cancelled, but still in wide use), MIL-HDBK-21F, RA-006-013-1A and as well as other literature like NASA’s System Engineering “Toolbox” [256], or NASA’s Apollo program [261]. Compared to FTA it does not consider external events, but in return identifies local effects and initial faults. FMEA analyzes the failure modes and failure effects, while FMECA additionally considers the criticality in its analysis. This analysis has the purpose to rank each potential failure mode identified in the FMEA according to the combined influence of the probability of occurrence and the severity of the failure effect, thus providing a rating of the criticality as well. Additionally detectability can be rated in the Failure Modes, Effects, Criticality and Detectability Analysis (FMEDA). [259] It is common to perform both FTA and FMEA in a Failure Modes, Effects Summary (FMES) [259] or in a cause-consequence analysis [256].

The following steps are commonly performed within a FMECA:

1. Identification of Failure Modes
2. Identification of Effects/Consequences & related System/Subsystem for each mode
3. Rate Severity (SN) of each effect
4. Identify potential Failure Causes for each failure mode
5. Rate Probability of Occurrence (PN) for each failure cause
6. Identify process controls and indicators
7. Rate Detectability (DN) of each failure mode/failure cause
8. Calculate Risk Priority Number (*RPN*) and criticality (*CN*)
9. Re-Assess Design (Re-design, modification)

Item	Failure Modes	Failure Effects	Failure Cause	Indicators/Controls	Severity <i>SN</i>	Prob. of Occurrence <i>PN</i>	Detectability <i>DN</i>	<i>CN</i> <sub>1</sub>	<i>RPN</i> <sub>1</sub>
Helmet light	Battery dead	Space Suit inoperable in dark	light left on other device left on end of life reached internal battery defect battery not charged	User notices helmet light off in dark; battery control lamp on; other electr. device do not turn on	3	2	1	6	6
	Broken wire	Space Suit inoperable in dark	mechanically overloaded (bent) electrically overloaded (fused thru)		3	1	3	3	9
	Bulb defect	Space Suit inoperable in dark	end of life reached Overcurrent (OC)	User notices helmet light off in dark	3	3	3	9	27
	Switch corroded	Space Suit inoperable in dark	sealing damaged exposed to inappr. environment short circuit (SC) end-of-life reached		3	1	3	3	9
	Switch broken	Space Suit inoperable in dark	mechanically overloaded end-of-life reached exposed to inappr. Environment	User notices helmet light off in dark; User notices mechanically unusual handling	3	2	2	6	12
	Short circuit in switch	Space Suit inoperable in dark	exposed to inappr. environment	User notices helmet light off in dark	3	1	3	3	9
Criticality <i>CN</i> <sub>1</sub>								30	
Risk Priority Number <i>RPN</i>									72

**Figure B. 9.** FMECA example

On the simplified example of the helmet light of an astronaut's spacesuit that is used by crewmembers of the International Space Station (ISS) for extravehicular activities (EVA) and out of order, a typical qualitative FMECA procedure is described in the following paragraphs.

Identifying the failure modes of the item under investigation ("helmet light") and assigning them to the appropriate columns in Figure B. 9 is followed by listing each identified effect and associated failure causes. The established failure causes are then rated (qualitatively by the expert) by probability of occurrence with a Probability Number (*PN*), degree of severity with a Severity Number (*SN*) and probability of detection with a Detectability Number (*DN*). Those are assigned according to scales, here in the range of 1 to 4, following the standard ECSS-Q-ST-30-02C, as listed in Table B. 2, Table B. 3 and Table B. 4. However, in other guidelines or standards the scales are often given with numbers ranging from 1 to 10.

**Table B. 2.** Severity categories and numbers (SN)

SN	Severity Category
4	Catastrophic
3	Critical
2	Major
1	Negligible

**Table B. 3.** Probability of Occurrence levels and numbers (PN)

PN	Level
4	Very likely
3	Likely
2	Unlikely
1	Extremely Unlikely

**Table B. 4.** Probability of Detection levels and numbers (DN)

DN	Level
4	Extremely Unlikely
3	Unlikely
2	Likely
1	Very Likely

One of the main results of a FMECA procedure is the criticality or Criticality Number ( $CN$ ), giving information about which failure mode or effect is more severe than others, and needs to be mitigated by design iteration. For each failure mode, a mode criticality number  $CN_i$  is determined by the multiplication of the according Severity Number and the Probability of Occurrence Number:

$$CN_i = SN_i \times PN_i \tag{B.9}$$

while the overall criticality number for an item  $CN_r$  is the sum of all mode criticality numbers:

$$CN_r = \sum_{i=1}^n C_i \tag{B.10}$$

The classification of a criticality for a failure mode can be surveyed in a criticality matrix (risk assessment matrix [256]) also known as , as depicted in Figure B. 10. Here the failure mode may be charted using severity code as one axis and probability level code on the other. It becomes obvious that a high severity combined with high probability of occurrence is leading to a high criticality. Numbers for  $CN_i$  greater or equal to 6, as well as failure consequences classified as catastrophic, are considered critical according to ECSS-Q-ST-30-02C (alternative classifications are given in MIL-STD-882C). However, this relation shows a linear character due the summation of numbers.

Severity Category	SNs	Probability Level			
		$10^{-5}$	$10^{-3}$	$10^{-1}$	1
		PNs			
		1	2	3	4
Catastrophic	4	4	8	12	16
Critical	3	3	6	9	12
Major	2	2	4	6	8
Negligible	1	1	2	3	4

**Figure B. 10.** Exemplary criticality matrix

In the example of Figure B. 9 the most critical failure mode (“Bulb defect”) shows a mode criticality number of 9, which must be, according to the given criticality matrix, considered critical. This enables engineers to take actions for the most critical, thus most severe and most probable failure modes and e.g. build in a redundant bulb. Nevertheless, the criticality number does not regard the probability of detecting a failure. In case two failure modes feature the same criticality number, as given for the failure modes “Battery dead” and “Switch broken” the one with the lower probability of detection should be taken action for first.

This circumstance can be identified with the second important result of a FMECA, the Risk Priority Number (*RPN*). Giving information about which failure mode or item needs to be payed the most attention to, due to high probability of occurrence and high severity combined with low detectability, the *RPN* provides a quantified measure of risk. The risk priority number for each failure mode (Mode Risk Priority Number) is determined with

$$RPN_i = SN_i \times PN_i \times DN_i \quad (\text{B.11})$$

By summation of all mode values, the overall Risk Priority Number for an item is determined with

$$RPN = \sum_{i=1}^n RPN_i \quad (\text{B.12})$$

Generally, one can say that for all results, such as criticalities and risk priority numbers, low values are aimed for. This supports the overall goal of this method to mitigate high risk and highly critical failures by changes in design. Finally, carrying out necessary design modifications for each iteration is followed by a last analysis, as proof of result, thus ensuring the achieved success.

A more quantitative FMECA assessment of criticality according to the standard MIL-STD-1629A, that had been cancelled but is still widely used, can be achieved by determining the modal criticality number  $CN_m$  (not to be confused with the mode criticality number  $CN_i$ ). It is calculated with equation (B.13) for each failure mode of an item. Here the criticality numbers are computed with the basic failure rate  $\gamma_p$ , the failure mode ratio  $\alpha_p$ , the conditional probability  $\beta_p$  and the mission phase duration  $t_m$ . However, these numbers are based on empirically data determined for each failure mode that are in most cases not available in structural design. The overall modal criticality number of an item  $CN_I$  is finally calculated by summation of all modal criticality numbers as shown in equation (B.14).

$$CN_m = \gamma_p \alpha_p \beta_p t_m \quad (\text{B.13})$$

$$CN_I = \sum_{n=1}^N (CN_m)_n \quad (\text{B.14})$$



### *How can the principles of a FMECA be utilized for a robustness evaluation?*

A qualitative and quantitative approach, as provided by FMECA, seems to be well suitable for robustness, since qualitative and quantitative data are available here as well. Especially the quantification of qualitative values is assumed to be applicable to a robustness evaluation. Rating failure modes and determining criticality and risk priority numbers can be considered very similar to rating robustness criteria or determining partial robustness. However, a simple summation to determine overall robustness is not considered sufficient for a Robustness Evaluation, especially when following the **1. Work Hypothesis**, stating that partial robustness values are not necessarily related by addition. In general, partially transferring principles of this method is seen useful as a support of a more hierarchical method, since finding failure modes is realized only in a less systemized manner in FMECA, compared to an FTA for example.

### **Summary and evaluation of surveyed assessment methods**

The following paragraphs give a brief summary of the essential principles found in the assessment methods that have been reviewed. Moreover, while giving an overview of the main characteristics of each surveyed method and a simple evaluation regarding the applicability to a robustness assessment in Table B. 5, the reasoning for the rating is shortly outlined as well.

The essential principles are:

#### *Structuring:*

Structuring an investigated system by its smallest parts (elements) like components and their linkage (association), and synthesizing them into a graphical representation provides an important overview of a system that is necessary for a profound evaluation. Finding these linkages is many times realized by evaluating the system's structure by its elements and functions. Furthermore, graphical representations can help to identify effects and consequences. Structuring a system and its elements is also considered beneficial concerning robustness. Especially identifying elements, functions and linkages is seen to provide an overview of partial robustness, effects and interactions within the system.

#### *Mathematical Associations:*

The mathematical base characterizing the associations of elements to be assessed are essential in order to determine the influence of the elements on one another and to find meaningful result values for an evaluation e.g. a utility value or a risk priority number. In the reviewed methods mostly Boolean logic, multiplications with factors or simple summation are building the core mathematical principles. Parallel and series associations, as inherent in Boolean logic, are compliant with the **1. Work Hypothesis** and are assumed to be connecting robustness criteria or partial robustness in a similar way. This leads to the assumption that these mathematical principles can be transferred to robustness assessment. Plain summation, however, as applied e.g. to determine the Overall Utility Value is not considered sufficient for a Robustness Evaluation, and might violate the **1. Work Hypothesis** saying that partial robustness values are not necessarily related by addition.

#### *Evaluation Criteria:*

Evaluation criteria are defined by the dedicated functions the elements should perform, which are determined according to the elements its selves or by system requirements. These criteria are specifically useful when e.g. different variations or alternatives of constructions must be evaluated and compared in order to find the best solution. The principle of evaluation criteria is assumed applicable very similar in a robustness evaluation. Here criteria can similarly be determined for an element, function or system requirement as robustness criteria.

### *Weighting Factors:*

Determining weighting factors is performed in order to differentiate between different levels of importance of evaluation criteria, functions or elements. These factors are generally multiplied in their generic or normalized form with rating values like partial utility values, thus resulting in a weighted rating value. This principle is considered promising to differentiate between levels of importance or impact of robustness criteria, and should be applied in a robustness evaluation.

### *Qualitative, Quantitative Principles and Quantification:*

Whenever no values e.g. measured data, are available, as apparent in the early concept phase of a design or many times in an FMECA, qualitative measures are used. They are mostly verbal expressions that are turned into quantified values (quantification) with an ordinal scale e.g. in a pairwise comparison of evaluation criteria with a following normalization (preference matrix) or by assigning values to each element in regard to the assessed field like probability of occurrence in a risk assessment. In addition, these qualitative principles are often used to establish an overview of a system's structure as realized in a fault tree. On the other hand, quantitative principles are using values that can, in a mathematical manner, directly be processed or compared such as dimensions, measures, specifications, probabilities or empirical values. However, for comparison with qualitatively based values or for determining overall evaluation values, quantitative values are transferred to a normalized form as well. This is especially practiced in methods for comparison like the scoring method or FMECA. Another principle of quantitative measures is the expression of probability of an event facilitated in some of the surveyed methods. Such measures might be System Reliability, Availability, Mean Time to Failure (MTTF), Mean Time Between Failures (MTBF) or Mean Time to Repair (MTTR). The mentioned principles of quantitative measures, qualitative measures and quantification are believed to be eligible to a robustness assessment, at least partially. This is supported by the definition of robustness stated in section 3.3.2, in which robustness can be expressed as a function of probability of an event and as quantified values exceeding requirements or expectations.

### *Objective and Subjective Input*

Some of the reviewed methods cope with both, objective input e.g. measured data, empirical values, specifications, dimensions, and with subjective input e.g. expert opinions, experiences, assumptions, and estimates. The surveyed methods show that if objective input is not available, subjective input is used specifically if new and unknown functions have to be evaluated.

For a robustness assessment, empirical data as well as estimations and experiences will provide the input for the evaluation and quantification, thus yielding to the need to adapt this principle.

### *Scales and Value Functions*

Assigning points for rating, using normalized ordinal scales for rating e.g. with VDI 2225, as well as ordinal scales of evaluation measures like levels of probability of occurrence, severity or detectability, are common principles in most of the reviewed methods. Latter scales are based on value functions that determine parameter magnitudes and their characteristic slope e.g. by mathematical relationships like increasing or decreasing linear, increasing or decreasing exponential, or logarithmic functions or many times by means of estimates.

Such scales and value functions are expected to be well applicable and necessary for evaluating robustness by robustness parameters and their characteristics. This is mainly due to the great similarity in nature of the robustness parameters expected and the ones used in the surveyed methods, and should be adapted to a robustness assessment as well.

### *Matrix like Evaluation Overview*

Matrix-like overviews, such as evaluation charts, illustrate and document the evaluation process with its components and steps. Additionally they are giving an overview of evaluation criteria, weighting factors, evaluation measures, quantitative and qualitative data as well as partial and overall evaluation results.

Adapting an evaluation chart to a process of robustness evaluation is considered a promising approach to give a good overview of all components and steps to be realized.

### *Combination of principles and methods*

As literature suggests, using deductive and inductive approaches in combination provide a higher level of confidence to find all elements and element connections/associations of a system. Therefore, combinations like FTA and RBD in a system assessment process are most common.

This is also considered true for the robustness assessment of a system, as developed within this work. Therefore, a combination of principles found in deductive and inductive methods is seen beneficial for a robustness assessment as well.

In Table B. 5 an overview of the reviewed assessment methods and their characteristics is given with four categories in the columns and methods clustered by the type in rows. This first category gives the type of method: deductive, inductive or a combination. The second category represents the field of application of each method, the third the name of each method, while the fourth category contains the inherent attributes to each method. Notably the last column of this category represents the result of rating each method, regarding its applicability of principles to a robustness assessment and if it can well be transferred.

The rating result of the methods with the lowest rated applicability derives as following:

Their principles are assumed not directly applicable to a robustness assessment, although some might be used to generate data. The Relevance Tree Analysis uses a search scheme for reliance, structures and illustrates relations between effort and value, while it quantifies the relevance of a resource. It is considered suitable to give only a brief overview of a system in a very normative manner, and is therefore rated with a low applicability. Risk Analysis searches for cause-effect, identifies, evaluates and manages risks, with a risk characterization using probability of occurrence of damage over damage severity. Its graphical illustration of risk in a risk matrix helps to visualize risk. The method in general is considered useful prior to the robustness assessment, in order to identify and quantify risks, which can be reduced/mitigated by higher robustness in the according field. Since its indirect applicability, it is rated low.

Trend Extrapolation can be applied prior and independently to the robustness assessment itself to predict or generate e.g. data for quantification from measures of deformations of a boom due to creep. Due its indirect usage is rated with a low applicability. The Cross-Impact Analysis is a technique for prognosis and tries to predict and analyze relations and cross impacts between future events in terms of probabilities. It is seen to be useful only when deriving a system structure and therefor rated with a low applicability.

The medium and high rated methods possess the advantage to be transferred directly or as principles of a method to a robustness assessment. This is true for most of the surveyed and relevant assessment methods described in detail before. Additionally, these methods or their essential principles comply largely with the **1. Work Hypothesis**. Detailed descriptions of the applicability, as discussed in the detailed surveys of the relevant methods before, are providing the basis for the rating result, shown in Table B. 5.

**Table B. 5.** Overview and evaluation of the surveyed assessment methods

Type	Field	Method	Attribute								
			Qualitative	Quantitative	Objective	Subjective	Structuring	Identification of Criteria	Weighting	Applicable Association Logic	Applicability to Ro-Business Assess-
Deductive	Technology	Relevance Tree-Analysis (discursive)	•	•	•	•	•				•
	Risk	Risk Analysis (risk matrix)	•	•	•	•		•	•	•	•
	Risk	Fault Tree Analysis (FTA) & Success Tree Analysis (STA)	•	•	•		•	•		•	•••
	Reliability	Reliability Block Diagram (RBD)	•	•	•		•	•		•	••
Inductive	Technology	Scoring Method (CBA, VDI 2225)	•	•	•	•		•	•	•	•••
	Technology	Preference Matrix	•			•		•	•	•	••
	Technology	Analytic Hierarchy Process (AHP/Saaty-Method)	•	•	•	•		•	•	•	••
	Risk	Failure-Modes, Effects and Criticality Analysis (FMEA, FMECA)	•	•	•	•		•	•	•	•••
	Risk	Event Tree	•	•	•		•	•		•	••
Combination	Technology	Trend Extrapolation		•	•						•
	Technology	Cross-Impact Analysis		•	•					•	•

• Low applicability; •• partially applicable; ••• good applicability

## Appendix C FUNCTIONS, PARAMETERS AND WEIGHTING FACTORS

**Table C. 1.** Main functions and functions of Gossamer-1 subsystems, assemblies and components

Level	Element Code	Element Name	Function Code	Function
Subsystem	D	Boom Subsystem	F1	– Transfer loads and provide stiffness
			F2	– Deploy Membranes
			F3	– Span membranes to intended dimensions and orient them into intended direction
Assembly	D-01	Boom Assembly		<ul style="list-style-type: none"> <li>– Deploy and therefore push deployment units outwards</li> <li>– Provide stiffness &amp; structural support for Membrane Subsystem</li> <li>– Transfer loads from sail corners into BSI</li> <li>– Provide accuracy for sail corner pointing/sail orientation</li> <li>– Enable jettisoning of Mechanism Subsystem</li> <li>– Provide measure of deployed length</li> </ul>
	D-02	Boom Spacecraft Interface (BSI)		<ul style="list-style-type: none"> <li>– Transfer loads from boom assembly into spacecraft (CSCU) (fix boom to spacecraft)</li> <li>– Provide sufficient stiffness for load transfer</li> <li>– Provide pointing accuracy for boom assembly</li> <li>– Self-adapt to changing cross sectional shape of the boom during deployment</li> </ul>
	D-03	Boom Load Measurement System		<ul style="list-style-type: none"> <li>– measure loads transferred through boom assembly</li> <li>– cancel out thermal effects</li> </ul>
Component	D-01-a	Joined Boom		<ul style="list-style-type: none"> <li>– provide bending and axial stiffness</li> <li>– provide functional length and spanned dimensions</li> <li>– provide pointing accuracy of sail corners</li> <li>– transfer sail loads and deployment loads into BSI</li> </ul>
	D-01-b	Stop Wings		<ul style="list-style-type: none"> <li>– lock Boom Sail Interface Ring (sail corner) to boom assembly at functional length</li> </ul>
	D-01-c	Velcro Strip		<ul style="list-style-type: none"> <li>– provide fixed positioning and fix boom tip to boom spool for tight stowage</li> <li>– transfer shear loads from belt (Boom Mechanism Subsystem) into boom during jettisoning</li> </ul>
	D-01-d	Protective Kapton		<ul style="list-style-type: none"> <li>– protect boom surface from being damaged</li> <li>– provide friction reduced tribological contact between boom guide shell and boom surface</li> </ul>
	D-01-e	Reflective Stripes		<ul style="list-style-type: none"> <li>– provide defined increment measure to determine deployed boom length</li> </ul>
	D-01-f	Temperature Sensor		<ul style="list-style-type: none"> <li>– provide temperature data of boom surface</li> </ul>
	D-02-a	Structural CFRP parts		<ul style="list-style-type: none"> <li>– provide stiffness</li> <li>– transfer mechanical boom loads into spacecraft</li> </ul>
	D-03-b	Tape springs		<ul style="list-style-type: none"> <li>– actively erect structural CFRP parts (BSI)</li> <li>– provide stiffness</li> <li>– transfer mechanical boom loads</li> </ul>
	D-03-c	Anvil & Bushing		<ul style="list-style-type: none"> <li>– provide lateral guidance/stiffness</li> <li>– transfer mechanical boom loads into spacecraft</li> </ul>

	D-03-d	Flexible Hinges		<ul style="list-style-type: none"> <li>– connects parts of BSI</li> <li>– transfer mechanical loads</li> </ul>
--	--------	-----------------	--	--

Table C. 1. continuing

Level	Element Code	Element Name	Function Code	Function
Subsystem	A	Membrane Sub-system	F1	– Reflect solar radiation
			F2	– Transfer solar radiation loads into mechanical loads/propulsion
			F3	– Generate electrical power
Assembly	A-01	Sail Quadrant		<ul style="list-style-type: none"> <li>– Transfer radiation loads (drag loads) into mechanical loads</li> <li>– Reflect radiation</li> <li>– Generate electrical current</li> </ul>
Component	A-01-a	Inner Sheet		<ul style="list-style-type: none"> <li>– Provide substrate for harness</li> <li>– Provide reflective area</li> </ul>
	A-01-b	PV Sheet		<ul style="list-style-type: none"> <li>– Provide substrate for PV modules and harness</li> <li>– Provide reflective area</li> </ul>
	A-01-c	Middle Sheet		– Provide reflective area
	A-01-d	Outer Sheet		– Provide reflective area
	A-01-e	PV Modules		– Generate electrical current
	A-01-f	Inner I/F Point		<ul style="list-style-type: none"> <li>– Connect inner sheet to spacecraft (CSCU)</li> <li>– Transfer mechanical loads</li> </ul>
	A-01-g	Outer I/F Point		<ul style="list-style-type: none"> <li>– Connect outer sheet to I/F subsystem</li> <li>– Transfer mechanical loads</li> </ul>
	A-01-h	Harness		– Conduct electrical current
Subsystem	B	Boom Mechanism Subsystem	F1	– Store booms
			F2	– Deploy booms in a controlled manner
			F3	– Hold and Support Mechanism Subsystems and I/F Subsystem
Assembly	B-01	Belt Winding Mechanism (BWM)		<ul style="list-style-type: none"> <li>– Pull out belt/Deploy boom</li> <li>– Control deployment</li> </ul>
	B-02	Boom Guide		– Guide extruding/deploying boom
Component	B-01-a	Belt		– Transfer motor torque via tensile force into boom spool torque
	B-01-b	Motor		– Generate torque
	B-01-c	Pulleys		– Redirect tensile force
	B-01-d	Boom Spool		– Store boom and belt
	B-01-e	Structure & Housing		– Provide stiffness and fixation

	B-01-f	Separation Sensor		– Detect event separation event
--	--------	-------------------	--	---------------------------------

Table C. 1. continuing

Level	Element Code	Element Name	Function Code	Function
	B-01-g	Boom Spool Brake		<ul style="list-style-type: none"> <li>– Provide counter torque to motor</li> <li>– Provide tension on belt</li> <li>– Restrain stored boom from unwanted self-deployment and blossoming</li> </ul>
Component	B-01-h	Launch Locks		<ul style="list-style-type: none"> <li>– lock boom spool rotation during launch and transfer phase</li> <li>– lock structure &amp; housing to spacecraft during launch and transfer phase</li> <li>– lock I/F subsystem (boom spool fixation ring) to structure &amp; housing until separation length (functional length) is reached</li> </ul>
	B-02-a	Guide Shells		– guide extruding boom out-of-sail plane
	B-02-b	Rollers		– guide extruding boom at flanges in-sail plane
Subsystem	C	MembraneMechanism Subsystem	F1	– Store Store Membrane Subsystem (sail)
			F2	– Dispense/deploy sail quadrants in a controlled manner
Component	C-00-a	Sail Spool		– Store sail quadrant
	C-00-b	Support Arms & Bearings		<ul style="list-style-type: none"> <li>– Provide positioning and stiffness to sail spool</li> <li>– Connect sail spool to Boom Mechanism Subsystem (structure &amp; housing)</li> <li>– Provide rotational degree of freedom to sail spool</li> </ul>
	C-00-c	Sail Spool Brake		<ul style="list-style-type: none"> <li>– Provide counter torque to tensile force pulling out the sail quadrant</li> <li>– Restrain stored sail quadrant from unwanted self-deployment</li> </ul>
	C-00-d	Launch Lock		– lock sail spool rotation during launch and transfer phase
Subsystem	E	I/F Subsystem	F1	– Transfer loads between adjacent subsystems and connect
			F2	– Provide accurate membrane dimensions, tension and orientation
Component	E-00-a	Boom Sail Fixation Ring (BSFR)		– Latch into stop wings of Boom Subsystem
	E-00-b	Truss		<ul style="list-style-type: none"> <li>– Connect BSFR to insert</li> <li>– Provide stiffness and redirect mechanical loads</li> </ul>
	E-00-c	Insert (w. plate)		<ul style="list-style-type: none"> <li>– Provide rotational degree of freedom during deployment</li> <li>– fit in sail spool</li> <li>– Connect wire loops to truss</li> </ul>

	E-00-d	Wire loop	<ul style="list-style-type: none"> <li>– Connect out I/F points of sail quadrant to insert</li> <li>– Provide distance between connection points of sail corner and insert plate</li> <li>– Transfer tension loads from sail quadrant to insert</li> </ul>
--	--------	-----------	--

*Rating Membrane Subsystem robustness parameters*

*Reflectivity*

- strongly represents function A-F1 and is rated very high; is a direct measure and fully contributes its fulfillment
- rated very-low in regard to main function A-F2; it does not represent it nor does it contribute to its fulfillment
- rated very-low in regard to main function A-F3; it does not represent it nor does it contribute to its fulfillment

*Shape*

*Accuracy*

- medium rated in regard to main function A-F1 as it represents reflection only indirectly, but contributes somewhat to the fulfillment of it, since global shape measures like flatness needs a certain accuracy in order to provide the demanded reflection for a large area
- low rated for function A-F2, representing it only in a minor way since an evenly flat stretched membrane can be considered a sign of good load transfer; it is more the result of a successful load transfer, hence it does not contribute to the function itself
- rated medium-low for function A-F3 as it does not represent the function directly; it contributes to the fulfillment somewhat since pv module orientation towards the light is partially ruled by the shape accuracy and orientation of the membrane subsystem

*Membrane*

*Load*

- rated very-low in regard to function A-F1, as it does not represent nor does it contribute directly to its fulfillment; it can be considered an indicator and requirement to realize sufficient reflection
- fully represents main function A-F2 and its fulfillment and is therefore rated very-high
- rated very-low in regard to function A-F3, since it does not represent nor does it contribute to its fulfillment.

No.(i)	Robustness Parameter	Rating Main Function			Partial Sum	$w_i$
		A-F1	A-F2	A-F3		
$R_S$	Reflectivity	10	0	0	10	0.256
$S_{RMS}$	Shape precision	7	2	3	12	0.308
$L_M$	Membrane Load	5	10	2	17	0.436
Sum					39	1.0

**Figure C. 1.** Assessment of partial robustness weighting factors for the Membrane Subsystem



*Rating I/F Subsystem robustness parameters**Change in length*

- does not represent or contribute to the fullfilment of function E-F1 and is rated very-low
- Very-high rated in regard to function E-F2 and largely represents it; is considered a direct measure of fullfilment, as the accuracy of the spanned membrane dimensions directly depend on the length of the interface it is connected to

*Tensile I/F Load*

- fully represents function E-F1 and contributes directly to its fullfilment; rated very-high
- represents only indirectly E-F2 and contributes somewhat the function fullfilment as the introduced I/F tensile loads are transfer loads that span the membrane to its dimensions, tension and orientation; medium-low

No.(i)	Robustness Parameter	Rating Main Function		Partial Sum	$w_i$
		E-F1	E-F2		
$\Delta l$	Change in length	0	10	10	0.417
$L_t$	Tensile I/F Load	10	4	14	0.583
Sum				24	10

**Figure C. 2.** Assessment of partial robustness weighting factors for the I/F Subsystem*Rating Boom Mechanism Subsystem robustness parameters**Boom Spool-off Force*

- rated very low in regard to function B-F1, as it does not represent this function; is only an indirect measure of the function fullfilment since too low or too high spool-off forces can indicate a faulty storage or packaging
- fully represents function B-F2 and is a direct measure of its fullfilment, since a varying load value indicates the controllability of the deployment and the amplitude indicates restraining and friction forces to be overcome for deployment; rated very-high
- Does not represent B-F3; does not contribute to the function fullfilment; rated very-low

*Boom Packaging Diameter*

- fully represents function E-F1 and contributes directly to its fullfilment; rated very-high
- represents only indirectly E-F2 and contributes somewhat the function fullfilment as the introduced I/F tensile loads are transfer loads that span the membrane to its dimensions, tension and orientation; rated medium-low

No.(i)	Robustness Parameter	Rating Main Function			Partial Sum	$w_i$
		B-F1	B-F2	B-F3		
$F_{SB}$	Boom spool-off force	1	10	0	11	0.550
$d_B$	Boom packaging diameter	9	0	0	9	0.450
Sum				20	10	

**Figure C. 3.** Assessment of partial robustness weighting factors of the Boom Mechanism Subsystem

*Rating Membrane Mechanism Subsystem robustness parameters*

*Membrane  
Spool-off  
Force*

- does not represent function C-F1; is only an indirect measure of the function fullfilment since it must overcome the restraining force that keeps the sail package tightly packed; too low or too high spool-off forces can indicate a faulty storage or packaging; rated very low
- fully represents function C-F2 and is a direct measure of its fullfilment since load value variations can indicate the controllability of the deployment, and amplitudes the restraintment and friction forces that have to be overcome for deployment; rated very-high

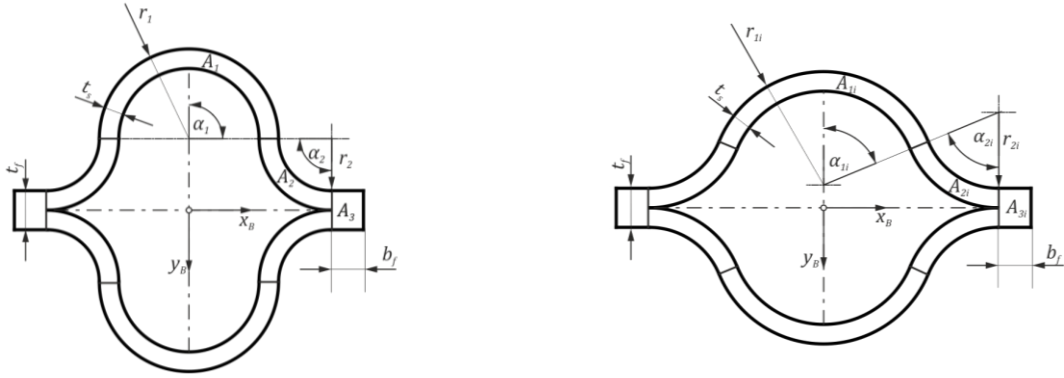
*Membrane  
Packaging  
Diameter*

- fully represents function C-F1 and contributes largely to the functional fullfilment; is a direct measure of the function; rated very-high
- does not represent C-F2 nor does it contribute to the function fullfilment; cannot be considered to be any measure; rated very-low

No.(i)	Robustness Parameter	Rating Main Function		Partial Sum	$w_i$
		C-F1	C-F2		
$F_{SM}$	Membrane spool-off force	1	10	11	0.550
$d_M$	Membrane Packaging diameter	9	0	9	0.450
Sum				20	1.0

**Figure C. 4.** Assessment of partial robustness weighting factors of the Membrane Mechanism Subsystem

## Appendix D ANALYTICAL CALCULATION OF BOOM SECOND MOMENT OF AREA



a) Nominal cross section (ideal)

b) Influenced cross section

**Figure D. 1.** Cross section divided into sub-areas for calculating the second moments of area

### Nominal Boom Cross Section

*Sub-Area  $A_1$  (convex section):*

Area:

$$A_1 = \alpha_1 \cdot [r_1^2 - (r_1 - t_s)^2] = 6.567 \text{ mm}^2 \quad (\text{D.15})$$

Local centroid:

$$x_{s1} = 0 \text{ mm} \quad (\text{D.16})$$

$$y_{s1} = \frac{2}{3} \cdot \frac{[r_1^3 - (r_1 - t_s)^3] \sin \alpha_1}{[r_1^2 - (r_1 - t_s)^2] \alpha_1} = 9.505 \text{ mm} \quad (\text{D.17})$$

Global centroid (in relation to boom coordinate system):

$$x_{s1B} = 0 \text{ mm} \quad (\text{D.18})$$

$$y_{s1B} = y_{s1} + r_2 + \frac{t_f}{2} = 24.645 \text{ mm} \quad (\text{D.19})$$

Local second moments of area:

$$I_{xx1} = \frac{\left[18\alpha_1 + 9 \sin(2\alpha_1) - 32 \cdot \frac{\sin^2 \alpha_1}{\alpha_1}\right]}{72} \cdot r_1^4 + \left(\frac{2}{3} \cdot \frac{r_1^3 \sin \alpha_1}{r_1^2 \alpha_1} - y_{s1}\right)^2 \cdot \alpha_1 r_1^2 \quad (\text{D.20})$$

$$- \frac{\left[18\alpha_1 + 9 \sin(2\alpha_1) - 32 \cdot \frac{\sin^2 \alpha_1}{\alpha_1}\right]}{72} \cdot (r_1 - t_s)^4 + \left(\frac{2}{3} \cdot \frac{(r_1 - t_s)^3 \sin \alpha_1}{(r_1 - t_s)^2 \alpha_1} - y_{s1}\right)^2 \cdot (-\alpha_1 (r_1 - t_s)^2) = 138.644 \text{ mm}^4$$

(D.21)

$$I_{yy1} = \frac{2\alpha_1 - \sin(2\alpha_1)}{8} \cdot r_1^4 + \left(\frac{2}{3}r_1 \cos \alpha_1 - x_{s1}\right)^2 \cdot \alpha_1 r_1^2 - \frac{2\alpha_1 - \sin(2\alpha_1)}{8} \cdot (r_1 - t_s)^4 + \left(\frac{2}{3} \cdot (r_1 - t_s) \cos \alpha_1 - x_{s1}\right)^2 \cdot (-\alpha_1(r_1 - t_s)^2) = 731.875 \text{ mm}^4$$

Global second moments of area (in relation to boom coordinate system):

$$I_{x_Bx_B1} = I_{xx1} + y_{s1B}^2 \cdot A_1 = 4126.95 \text{ mm}^4 \quad (\text{D.22})$$

$$I_{y_By_B1} = I_{yy1} = 731.875 \text{ mm}^4 \quad (\text{D.23})$$

*Sub-Area  $A_2$  (concave section):*

Area:

$$A_2 = \frac{1}{2} \alpha_2 \cdot [(r_2 + t_s)^2 - r_2^2] = 3.314 \text{ mm}^2 \quad (\text{D.24})$$

Local centroid:

$$x_{s2} = 9.594 \text{ mm} \quad (\text{D.25})$$

$$y_{s2} = \frac{2}{3} \cdot \frac{[(r_2 + t_s)^3 - r_2^3] \sin \alpha_2}{[(r_2 + t_s)^2 - r_2^2] \alpha_2} = 9.594 \text{ mm} \quad (\text{D.26})$$

Global centroid (in relation to boom coordinate system):

$$x_{s2B} = r_1 + r_2 - x_{s2} = 20.4 \text{ mm} \quad (\text{D.27})$$

$$y_{s2B} = r_2 + \frac{t_f}{2} - y_{s2} = 5.546 \text{ mm} \quad (\text{D.28})$$

Local second moments of area:

$$I_{xx2} = \left(\frac{\pi}{16} - \frac{4}{9\pi}\right) \cdot (r_2 + t_s)^4 + \left(\frac{2}{3} \cdot (r_2 + t_s) \cdot \frac{\sin^2 \frac{\alpha_2}{2}}{\frac{\alpha_2}{2}} - y_{s2}\right)^2 \cdot \frac{1}{2} \alpha_2 (r_2 + t_s)^2 - \left(\frac{\pi}{16} - \frac{4}{9\pi}\right) \cdot (r_2)^4 + \left(\frac{2}{3} \cdot r_2 \cdot \frac{\sin^2 \frac{\alpha_2}{2}}{\frac{\alpha_2}{2}} - y_{s2}\right)^2 \cdot \left(-\frac{1}{2} \alpha_2 r_2^2\right) = 71.29 \text{ mm}^4 \quad (\text{D.29})$$

$$I_{yy2} = \left(\frac{\pi}{16} - \frac{4}{9\pi}\right) \cdot (r_2 + t_s)^4 + \left(\frac{2}{3} \cdot (r_2 + t_s) \cdot \frac{\cos \frac{\alpha_2}{2} \sin \frac{\alpha_2}{2}}{\frac{\alpha_2}{2}} - x_{s2}\right)^2 \cdot \frac{1}{2} \alpha_2 (r_2 + t_s)^2 - \left(\frac{\pi}{16} - \frac{4}{9\pi}\right) \cdot (r_2)^4 + \left(\frac{2}{3} \cdot r_2 \cdot \frac{\cos \frac{\alpha_2}{2} \sin \frac{\alpha_2}{2}}{\frac{\alpha_2}{2}} - x_{s2}\right)^2 \cdot \left(-\frac{1}{2} \alpha_2 r_2^2\right) = 71.29 \text{ mm}^4 \quad (\text{D.30})$$

Global second moments of area (in relation to boom coordinate system):

$$I_{x_Bx_B2} = I_{xx2} + y_{s2B}^2 \cdot A_2 = 173.227 \text{ mm}^4 \quad (\text{D.31})$$

$$I_{y_B y_B 2} = I_{yy2} + x_{s2B}^2 \cdot A_2 = 1451.3 \text{ mm}^4 \quad (\text{D.32})$$

*Sub-Area  $A_3$  (Flange):*

Area:

$$A_3 = b_f \cdot t_s = 1.96 \text{ mm}^2 \quad (\text{D.33})$$

Local centroid:

$$x_{s3} = \frac{1}{2} b_f = 3.5 \text{ mm} \quad (\text{D.34})$$

$$y_{s3} = \frac{1}{2} t_f = 0.14 \text{ mm} \quad (\text{D.35})$$

Global centroid (in relation to boom coordinate system):

$$x_{s3B} = r_1 + r_2 - x_{s3} = 33.5 \text{ mm} \quad (\text{D.36})$$

$$y_{s3B} = \frac{t_f}{2} - y_{s3} = 0 \text{ mm} \quad (\text{D.37})$$

Local second moments of area:

$$I_{xx3} = \frac{b_f \cdot t_f^3}{12} = 0.012805 \text{ mm}^4 \quad (\text{D.38})$$

$$I_{yy3} = \frac{b_f^3 \cdot t_f}{12} = 8.003 \text{ mm}^4 \quad (\text{D.39})$$

Global second moments of area (in relation to boom coordinate system):

$$I_{x_B x_B 3} = I_{xx3} = 0.01281 \text{ mm}^4 \quad (\text{D.40})$$

$$I_{y_B y_B 3} = I_{yy3} + x_{s3B}^2 \cdot A_3 = 2207.613 \text{ mm}^4 \quad (\text{D.41})$$

*Overall cross section:*

Global second moments of area (in relation to boom coordinate system):

$$I_{x_B x_B} = 2 \cdot I_{x_B x_B 1} + 4 \cdot I_{x_B x_B 2} + 2 \cdot I_{x_B x_B 3} = 8946.833 \text{ mm}^4 \quad (\text{D.42})$$

$$I_{y_B y_B} = 2 \cdot I_{y_B y_B 1} + 4 \cdot I_{y_B y_B 2} + 2 \cdot I_{y_B y_B 3} = 11684.149 \text{ mm}^4 \quad (\text{D.43})$$

**Influenced Boom Cross Section**

*Sub-Area  $A_{1i}$  (convex section):*

Area:

$$A_{1i} = \alpha_{1i} \cdot [r_{1i}^2 - (r_{i1} - t_s)^2] = 6.567 \text{ mm}^2 \quad (\text{D.44})$$

Local centroid:

$$x_{s1i} = 0 \text{ mm} \quad (\text{D.45})$$

$$y_{s1i} = \frac{2}{3} \cdot \frac{[r_{1i}^3 - (r_{1i} - t_s)^3] \sin \alpha_{1i}}{[r_{1i}^2 - (r_{1i} - t_s)^2] \alpha_{1i}} = 15.629 \text{ mm} \quad (\text{D.46})$$

Global centroid (in relation to boom coordinate system):

$$x_{s1Bi} = 0 \text{ mm} \quad (\text{D.47})$$

$$y_{s1Bi} = 2 \cdot \left[ r_{1i} - r_{1i} \cdot \sin \left( \frac{\pi}{2} - \alpha_{1i} \right) \right] + \frac{t_f}{2} - (r_{1i} - y_{s1i}) = 20.462 \text{ mm} \quad (\text{D.48})$$

Local second moments of area:

$$\begin{aligned} I_{xx1i} = & \frac{\left[ 18\alpha_{1i} + 9 \sin(2\alpha_{1i}) - 32 \cdot \frac{\sin^2 \alpha_{1i}}{\alpha_{1i}} \right]}{72} \cdot r_{1i}^4 + \left( \frac{2}{3} \cdot \frac{r_{1i}^3 \sin \alpha_{1i}}{r_{1i}^2 \alpha_{1i}} - y_{s1i} \right)^2 \cdot \alpha_{1i} r_{1i}^2 \\ & - \frac{\left[ 18\alpha_{1i} + 9 \sin(2\alpha_{1i}) - 32 \cdot \frac{\sin^2 \alpha_{1i}}{\alpha_{1i}} \right]}{72} \cdot (r_{1i} - t_s)^4 \\ & + \left( \frac{2}{3} \cdot \frac{(r_{1i} - t_s)^3 \sin \alpha_{1i}}{(r_{1i} - t_s)^2 \alpha_{1i}} - y_{s1i} \right)^2 \cdot (-\alpha_{1i} (r_{1i} - t_s)^2) = 91.567 \text{ mm}^4 \end{aligned} \quad (\text{D.49})$$

$$I_{yy1i} = \frac{2\alpha_{1i} - \sin(2\alpha_{1i})}{8} \cdot r_{1i}^4 - \frac{2\alpha_{1i} - \sin(2\alpha_{1i})}{8} \cdot (r_{1i} - t_s)^4 = 913.838 \text{ mm}^4 \quad (\text{D.50})$$

Global second moments of area (in relation to boom coordinate system):

$$I_{x_B x_B 1i} = I_{xx1i} + y_{s1Bi}^2 \cdot A_{1i} = 2844.19 \text{ mm}^4 \quad (\text{D.51})$$

$$I_{y_B y_B 1i} = I_{yy1i} = 913.838 \text{ mm}^4 \quad (\text{D.52})$$

*Sub-Area  $A_{2i}$  (concave section):*

Area:

$$A_{2i} = \frac{1}{2} \alpha_{2i} \cdot [(r_{2i} + t_s)^2 - r_{2i}^2] = 3.3102 \text{ mm}^2 \quad (\text{D.53})$$

Local centroid:

$$x_{s2i} = 0 \text{ mm} \quad (\text{D.54})$$

$$y_{s2i} = \frac{2}{3} \cdot \frac{[(r_{2i} + t_s)^3 - r_{2i}^3] \sin \left( \frac{\alpha_{2i}}{2} \right)}{[(r_{2i} + t_s)^2 - r_{2i}^2] \frac{\alpha_{2i}}{2}} = 18.929 \text{ mm} \quad (\text{D.55})$$

Rotated local centroid:

$$x_{s2irot} = y_{s2i} \cdot \cos \left( \frac{\pi}{2} - \varphi \right) = 10.517 \text{ mm}, \quad \text{with } \varphi = \frac{\alpha_{2i}}{2} \quad (\text{D.56})$$

$$y_{s2irot} = y_{s2i} \cdot \sin \left( \frac{\pi}{2} - \varphi \right) = 15.739 \text{ mm}, \quad \text{with } \varphi = \frac{\alpha_{2i}}{2} \quad (\text{D.57})$$

Global centroid (in relation to boom coordinate system):

$$x_{s2Bi} = r_{1i} \cdot \sin \alpha_{1i} + r_{2i} \cdot \sin \alpha_{2i} - x_{s2irot} = 26.439 \text{ mm} \quad (\text{D.58})$$

$$y_{s2Bi} = r_{2i} + \frac{t_f}{2} - y_{s2irot} = 4.401 \text{ mm} \quad (\text{D.59})$$

Local second moments of area:

$$\begin{aligned} I_{xx2i} &= \frac{(r_{2i} + t_s)^4}{4} \cdot \left( \frac{\alpha_{2i}}{2} + \frac{\sin \alpha_{2i}}{2} \right) - \frac{4}{9} \cdot \frac{(r_{2i} + t_s)^4}{\frac{\alpha_{2i}}{2}} \cdot \sin^2 \left( \frac{\alpha_{2i}}{2} \right) \\ &+ \left( \frac{2}{3} \cdot (r_{2i} + t_s) \cdot \frac{\sin \left( \frac{\alpha_{2i}}{2} \right)}{\frac{\alpha_{2i}}{2}} - y_{s2i} \right)^2 \cdot \frac{1}{2} \alpha_{2i} (r_{2i} + t_s)^2 - \frac{r_{2i}^4}{4} \cdot \left( \frac{\alpha_{2i}}{2} + \frac{\sin \alpha_{2i}}{2} \right) \\ &- \frac{4}{9} \cdot \frac{r_{2i}^4}{\frac{\alpha_{2i}}{2}} \cdot \sin^2 \left( \frac{\alpha_{2i}}{2} \right) + \left( \frac{2}{3} \cdot r_{2i} \cdot \frac{\sin \left( \frac{\alpha_{2i}}{2} \right)}{\frac{\alpha_{2i}}{2}} - y_{s2i} \right)^2 \cdot \left( -\frac{1}{2} \alpha_{2i} r_{2i}^2 \right) \\ &= 3.39939 \text{ mm}^4 \end{aligned} \quad (\text{D.60})$$

$$I_{yy2i} = \frac{(r_{2i} + t_s)^4}{4} \cdot \left( \frac{\alpha_{2i}}{2} - \frac{\sin \alpha_{2i}}{2} \right) - \frac{(r_{2i})^4}{4} \cdot \left( \frac{\alpha_{2i}}{2} - \frac{\sin \alpha_{2i}}{2} \right) = 143.864 \text{ mm}^4 \quad (\text{D.61})$$

$$I_{xy2i} = 0 \text{ mm}^4 \quad (\text{D.62})$$

Rotated local second moments of area:

$$I_{\zeta\zeta2i} = \frac{1}{2} (I_{xx2i} + I_{yy2i}) + \frac{1}{2} (I_{xx2i} - I_{yy2i}) \cdot \cos(2\varphi) + I_{xy2i} \cdot \sin(2\varphi) = 46.755 \text{ mm}^4 \quad (\text{D.63})$$

$$\begin{aligned} I_{\eta\eta2i} &= \frac{1}{2} (I_{xx2i} + I_{yy2i}) - \frac{1}{2} (I_{xx2i} - I_{yy2i}) \cdot \cos(2\varphi) - I_{xy2i} \cdot \sin(2\varphi) \\ &= 100.508 \text{ mm}^4 \end{aligned} \quad (\text{D.64})$$

$$I_{\zeta\eta2i} = -\frac{1}{2} (I_{xx2i} - I_{yy2i}) \cdot \sin(2\varphi) + I_{xy2i} \cdot \cos(2\varphi) = 64.886 \text{ mm}^4 \quad (\text{D.65})$$

Global second moments of area (in relation to boom coordinate system):

$$I_{x_Bx_B2i} = I_{\zeta\zeta2i} + y_{s2Bi}^2 \cdot A_{2i} = 110.863 \text{ mm}^4 \quad (\text{D.66})$$

$$I_{y_By_B2i} = I_{\eta\eta2i} + x_{s2Bi}^2 \cdot A_{2i} = 2414.343 \text{ mm}^4 \quad (\text{D.67})$$

*Sub-Area  $A_{3i}$  (Flange):*

Area:

$$A_{3i} = b_f \cdot t_s = 1.96 \text{ mm}^2 \quad (\text{D.68})$$

Local centroid:

$$(\text{D.69})$$

$$x_{s3i} = \frac{1}{2} b_f = 3.5 \text{ mm}$$

$$y_{s3i} = \frac{1}{2} t_f = 0.14 \text{ mm} \quad (\text{D.70})$$

Global centroid (in relation to boom coordinate system):

$$x_{s3Bi} = r_{1i} \cdot \sin \alpha_{1i} + r_{2i} \cdot \sin \alpha_{2i} + \frac{b_f}{2} = 40.4552 \text{ mm} \quad (\text{D.71})$$

$$y_{s3Bi} = \frac{t_f}{2} - y_{s3i} = 0 \text{ mm} \quad (\text{D.72})$$

Local second moments of area:

$$I_{xx3i} = \frac{b_f \cdot t_f^3}{12} = 0.012805 \text{ mm}^4 \quad (\text{D.73})$$

$$I_{yy3i} = \frac{b_f^3 \cdot t_f}{12} = 8.003 \text{ mm}^4 \quad (\text{D.74})$$

Global second moments of area (in relation to boom coordinate system):

$$I_{x_Bx_B3i} = I_{xx3i} = 0.012805 \text{ mm}^4 \quad (\text{D.75})$$

$$I_{y_By_B3i} = I_{yy3i} + x_{s3Bi}^2 \cdot A_{3i} = 3215.782 \text{ mm}^4 \quad (\text{D.76})$$

*Overall cross section:*

Global second moments of area (in relation to boom coordinate system):

$$I_{x_Bx_Bi} = 2 \cdot I_{x_Bx_B1i} + 4 \cdot I_{x_Bx_B2i} + 2 \cdot I_{x_Bx_B3i} = 6131.859 \text{ mm}^4 \quad (\text{D.77})$$

$$I_{y_By_Bi} = 2 \cdot I_{y_By_B1i} + 4 \cdot I_{y_By_B2i} + 2 \cdot I_{y_By_B3i} = 17916.612 \text{ mm}^4 \quad (\text{D.78})$$



## Appendix E RESULTS OF INFLUENCE MEASUREMENTS

**Table E. 1.** Results overview – measured cross sectional changes of 500 mm boom specimens

Temperature regime	Day	Width changes $\Delta b_B$						Height changes $\Delta h_B$					
		Mean (mm)	Standard deviation (mm)	Max (mm)	Min (mm)	Percentage Change	Influence Factor $\Psi_b$	Mean (mm)	Standard deviation (mm)	Max (mm)	Min (mm)	Percentage Change	Influence Factor $\Psi_h$
23 °C	1	-1,98	0,60	-0,83	-3,05	-3,3 %	0,967	-0,31	0,42	0,42	-0,91	-0,4 %	0,996
	14	1,40	0,70	2,35	0,16	2,3 %	1,023	-2,47	0,46	-1,79	-3,57	-3,3 %	0,967
	28	3,59	0,86	5,16	2,03	6,0 %	1,060	-3,63	0,50	-2,94	-4,46	-4,9 %	0,951
	42	3,33	0,62	4,20	2,25	5,5 %	1,055	-3,76	0,29	-3,39	-4,31	-5,1 %	0,949
	56	4,13	0,85	5,84	2,67	6,9 %	1,069	-4,00	0,35	-3,40	-4,54	-5,4 %	0,946
	70	3,90	0,72	4,98	2,57	6,5 %	1,065	-4,22	0,33	-3,59	-4,70	-5,7 %	0,943
	84	4,48	0,80	5,73	3,21	7,4 %	1,074	-4,37	0,35	-3,66	-5,01	-5,9 %	0,941
	98	4,08	0,90	5,78	2,57	6,8 %	1,068	-4,41	0,41	-3,74	-5,23	-6,0 %	0,940
	194	1,54	0,88	3,56	0,24	2,6 %	1,026	-2,31	0,51	-1,32	-3,54	-3,1 %	0,969
80 °C	1	-1,08	0,64	0,28	-2,06	-1,8 %	0,982	-0,38	0,39	0,59	-0,85	-0,5 %	0,995
	14	6,47	0,86	7,99	4,76	10,7 %	1,107	-5,56	0,45	-4,63	-6,43	-7,5 %	0,925
	28	9,14	0,85	10,52	7,53	15,2 %	1,152	-7,51	0,57	-6,34	-8,69	-10,1 %	0,899
	42	9,34	0,90	10,78	7,96	15,5 %	1,155	-7,62	0,53	-6,58	-8,90	-10,3 %	0,897
	56	9,64	0,87	11,27	7,90	16,0 %	1,160	-7,79	0,44	-6,84	-8,54	-10,5 %	0,895
	70	10,46	0,77	11,75	8,69	17,3 %	1,173	-8,87	0,50	-7,79	-9,62	-12,0 %	0,880
	84	11,60	0,80	13,29	10,43	19,2 %	1,192	-9,57	0,49	-8,72	-10,53	-12,9 %	0,871
	98	11,14	0,91	13,07	9,85	18,5 %	1,185	-9,48	0,47	-8,63	-10,39	-12,8 %	0,872
	194	8,07	0,85	9,27	6,19	13,4 %	1,134	-6,61	0,95	-5,35	-9,23	-8,9 %	0,911

**Table E. 2.** Results overview – discrete curvature and sag measurements of 500 mm boom specimens

Temperature regime	Day	Curvature changes				
		Radius $r_B$ (mm)	Residual (mm)	Sag $s$ (mm)	Percentage Change in Radius	Influence Factor $\Delta r_B$
23 °C	1	495554	0,000058	0,050	0,0 %	1,000
	14	538940	0,000139	0,048	8,8 %	1,088
	28	438388	0,000302	0,058	-11,5 %	0,885
	42	473041	0,000230	0,057	-4,5 %	0,955
	56	444294	0,000822	0,065	-10,3 %	0,897
	70	398288	0,001017	0,070	-19,6 %	0,804
	84	355887	0,000535	0,073	-28,2 %	0,718
	98	310180	0,003194	0,094	-37,4 %	0,626
	194	440409	0,000995	0,067	-11,1 %	0,889
80 °C	1	732837	0,000129	0,035	0,0 %	1,000
	14	609613	0,000056	0,046	-16,8 %	0,832
	28	208697	0,004016	0,103	-71,5 %	0,285
	42	245167	0,000540	0,085	-66,5 %	0,335
	56	307250	0,004463	0,074	-58,1 %	0,419
	70	345568	0,002110	0,154	-52,8 %	0,472
	84	163441	0,008888	0,184	-77,7 %	0,223
	98	139389	0,008711	0,205	-81,0 %	0,190
	194	122878	0,010064	0,119	-83,2 %	0,168

**Table E. 3.** Results overview – tensioned side – continuous curvature and sag of, 500 mm boom specimen

Temperature regime	Day	Tensioned Side							
		Sag $s$ (mm)	Percentage Sag Change	$R^2$ (mm)	RMSE (mm)	Radius $r_B$ (mm)	Residual (mm)	Percentage Radius Change	Influence Factor $\Delta r_B$
23 °C	1	0.095	0,0 %	7,7E-01	3,25E-02	338326	0,58	0,0 %	1,000
	14	0.150	57,7 %	8,3E-01	2,91E-02	219004	0,45	-35,3 %	0,647
	28	0.242	154,2 %	7,6E-01	3,71E-02	132706	0,72	-60,8 %	0,392
	42	0.191	100,4 %	4,7E-01	2,60E-02	164906	0,37	-51,3 %	0,487
	56	0.269	181,8 %	3,1E-01	3,08E-02	120659	0,52	-64,3 %	0,357
	70	0.272	185,4 %	2,3E-01	3,46E-02	117571	0,66	-65,2 %	0,348
	84	0.302	216,8 %	1,7E-01	3,07E-02	107553	0,55	-68,2 %	0,318
	98	0.336	252,9 %	2,0E-01	4,52E-02	97539	1,17	-71,2 %	0,288
	194	0.190	99,5 %	7,6E-01	4,73E-02	168796	1,15	-50,1 %	0,499
80 °C	1	0.113	0,0 %	7,15E-01	2,79E-02	255959	0,43	0,0 %	1,000
	14	0.307	172,7 %	4,33E-02	3,47E-02	103607	0,64	-59,5 %	0,405
	28	0.452	300,7 %	5,50E-02	5,31E-02	72715	1,55	-71,6 %	0,284
	42	0.484	329,3 %	1,49E-01	3,95E-02	67874	0,96	-73,5 %	0,265
	56	0.531	371,3 %	2,27E-02	4,35E-02	60300	1,17	-76,4 %	0,236
	70	0.631	459,5 %	1,22E-01	5,36E-02	51714	1,82	-79,8 %	0,202
	84	0.666	491,1 %	1,07E-01	5,54E-02	47909	1,74	-81,3 %	0,187
	98	0.732	549,0 %	3,98E-02	4,24E-02	44072	1,29	-82,8 %	0,172
	194	0.495	339,3 %	5,32E-02	1,07E-01	64958	5,98	-74,6 %	0,254

**Table E. 4.** Results overview – compressed side – continuous curvature and sag of, 500 mm boom specimen

Temperature regime	Day	Compressed Side							
		Sag $s$ (mm)	Percentage Sag Change	$R^2$ (mm)	RMSE (mm)	Radius $r_B$ (mm)	Residual (mm)	Percentage Radius Change	Influence Factor $\Delta r_B$
23 °C	1	0.109	0,0 %	7,3E-01	3,16E-02	301566	0,51	0,0 %	1,000
	14	0.076	-30,4 %	9,0E-01	2,76E-02	390508	0,41	29,5 %	1,295
	28	-0.008	-107,3 %	8,6E-01	3,92E-02	3637339	0,79	1106,2 %	12,062
	42	0.021	-80,4 %	9,3E-01	2,89E-02	2497258	0,47	728,1 %	8,281
	56	-0.086	-179,0 %	6,1E-01	2,99E-02	2262757	0,64	650,3 %	7,503
	70	-0.049	-144,8 %	7,7E-01	3,21E-02	1428693	0,59	373,8 %	4,738
	84	-0.069	-163,5 %	3,9E-01	3,09E-02	2159442	0,65	616,1 %	7,161
	98	-0.095	-186,9 %	5,2E-01	5,28E-02	1256037	1,60	316,5 %	4,165
	194	0.068	-37,5 %	9,0E-01	3,52E-02	586436	0,75	94,5 %	1,945
80 °C	1	0.105	0,0 %	6,47E-01	2,96E-02	4389682	1,09	0,0 %	1,000
	14	0.111	6,3 %	4,46E-01	3,60E-02	227950	0,87	-94,8 %	0,052
	28	-0.087	-182,7 %	1,46E-01	5,98E-02	1064679	2,00	-75,7 %	0,243
	42	-0.114	-208,7 %	8,03E-02	5,04E-02	1146992	1,52	-73,9 %	0,261
	56	-0.149	-242,2 %	2,50E-02	3,97E-02	3551352	1,30	-19,1 %	0,809
	70	-0.187	-278,7 %	8,34E-02	4,98E-02	5334988	2,20	21,5 %	1,215
	84	-0.199	-290,2 %	2,09E-01	4,64E-02	281560	1,48	-93,6 %	0,064
	98	-0.240	-329,2 %	2,73E-02	4,79E-02	214847	1,85	-95,1 %	0,049
	194	-0.158	-250,7 %	9,06E-01	7,85E-02	349417	3,42	-92,0 %	0,080

**Table E. 5.** Results overview – Averaged curvature – continuous curvature and sag of, 500 mm boom specimen

Temperature regime	Day	Averaged Curvature							
		Sag $s$ (mm)	Percentage Sag Change	$R^2$ (mm)	RMSE (mm)	Radius $r_B$ (mm)	Residual (mm)	Percentage Radius Change	Influence Factor $\Delta r_B$
23 °C	1	0,099	0,0 %	7,0E-04	3,93E-02	321907	1,56	0,0 %	1,000
	14	0,113	14,3 %	1,1E-02	4,15E-02	280457	1,77	-12,9 %	0,871
	28	0,124	25,3 %	4,0E-03	9,69E-02	251661	9,36	-21,8 %	0,782
	42	0,102	2,9 %	1,7E-03	7,10E-02	305910	5,06	-5,0 %	0,950
	56	0,131	32,4 %	2,3E-02	1,22E-01	235315	14,94	-26,9 %	0,731
	70	0,134	35,3 %	1,5E-02	1,12E-01	241100	12,53	-25,1 %	0,749
	84	0,150	51,0 %	1,2E-02	1,27E-01	220115	16,23	-31,6 %	0,684
	98	0,163	64,0 %	2,4E-02	1,48E-01	203814	22,28	-36,7 %	0,633
	194	0,122	23,5 %	2,3E-03	7,47E-02	262200	5,61	-18,5 %	0,815
80 °C	1	0,110	0,0 %	8,48E-03	3,30E-02	266445	1,11	0,0 %	1,000
	14	0,211	92,0 %	2,31E-03	9,84E-02	141570	9,71	-46,9 %	0,531
	28	0,219	99,4 %	1,18E-03	1,99E-01	137798	39,60	-48,3 %	0,517
	42	0,230	109,5 %	9,69E-05	2,09E-01	131012	43,67	-50,8 %	0,492
	56	0,233	111,7 %	8,12E-03	2,45E-01	127069	60,30	-52,3 %	0,477
	70	0,265	141,1 %	6,47E-03	2,99E-01	119882	89,51	-55,0 %	0,450
	84	0,267	142,7 %	3,94E-03	3,17E-01	115544	100,37	-56,6 %	0,434
	98	0,293	167,1 %	6,49E-03	3,50E-01	110763	122,76	-58,4 %	0,416
	194	0,199	81,0 %	8,84E-03	2,53E-01	159286	64,17	-40,2 %	0,598

**Table E. 6.** Gossamer-1 tool - curvature and sag

Tool model	Sag $s$ (mm)	$R^2$ (mm)	RMSE (mm)	Radius $r_B$ (mm)	Residual (mm)
Upper tool half	3,919	3,1E-02	3,28E-02	577019	2,76E+01
Lower tool half	2,175	1,3E-01	4,30E-02	1010589	5,03E+01
Closed tool (averaged)	3,032	1,1E-03	1,88E-01	741709	2,25E+01

**Table E. 7.** Gossamer-1 Boom shell waviness

Temperature regime	Day	Extremum type	Linearized sag $s_l$ (mm)	Position on specimen length $z$ (mm)	Difference (%)	
					$\Delta s_l$	$\Delta z_B$
Upper side						
23°C	1	Max	0,255	741	145,2	30,9
80°C	98	Max	0,626	970		
23°C	1	Max	0,072	4161	122,0	-1,3
80°C	98	Max	0,160	4106		
23°C	1	Min	-0,144	1791	-183,4	16,6
80°C	98	Min	-0,408	2088		
Lower side						
23°C	1	Max	0,346	1755	-27,9	4,7
80°C	98	Max	0,250	1838		
23°C	1	Min	-0,201	533	-10,5	32,3
80°C	98	Min	-0,222	706		
23°C	1	Min	-0,282	3068	50,2	-10,6
80°C	98	Min	-0,140	2743		
23°C	1	Min	-0,200	3732	-40,3	-0,9
80°C	98	Min	-0,281	3697		

**Table E. 8.** Local sag deviation of Gos-2 boom shell sides and tool

Point	Specimen	Extremum type	Sag $s$ (mm)	Position on specimen length $z$ (mm)	Difference (%)	
					$\Delta s$	$\Delta z_B$
P1i	Boom Side #1	Max	0,837	2241	3,5	-2,1
	Boom Side #2	Max	1,217	2186	-40,2	0,4
	Tool	Max	0,868	2195	-	-
P2i	Boom Side #1	Max	2,060	4731	-52,4	-11,3
	Boom Side #2	Max	2,113	4138	-56,3	2,7
	Tool	Max	1,352	4252	-	-
P3i	Boom Side #1	Max	2,110	9578	42,5	2,3
	Boom Side #2	Max	3,580	9525	2,5	2,9
	Tool	Max	3,671	9808	-	-
S1	Support point 1	Min	0,000	2926	-	-
S2	Support point 2	Min	0,000	7727		

**Table E. 9.** Results - waviness comparison of boom side #2 and tool of Gos-2

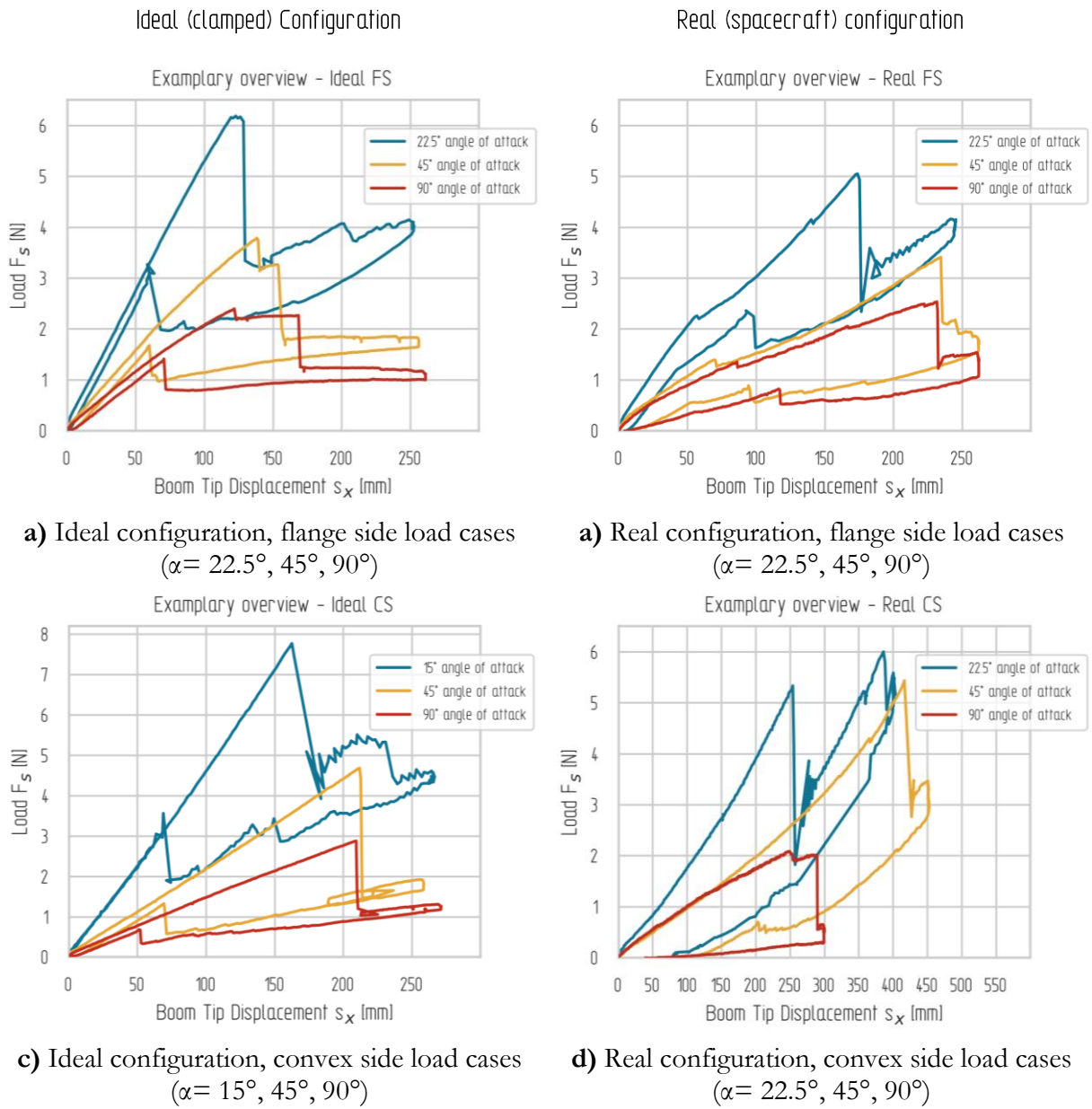
Point	Specimen	Extremum type	Linearized Sag $s_l$ (mm)	Position on specimen length $z$ (mm)	Difference [%]	
					$\Delta s$	$\Delta z_B$
V1i	Boom Side #2	Min	-1,029	2930	-23,3	0,0
	Tool	Min	-0,835	2929	-	-
V2i	Boom Side #2	Min	-0,701	5336	-47,1	-0,2
	Tool	Min	-0,476	5325	-	-
V3i	Boom Side #2	Min	-0,830	7729	27,2	0,0
	Tool	Min	-1,140	7728	-	-

**Table E. 10.** Areal damage measured on impacted Gos-1 boom specimens

Sample	Side	Diameter of Clearance C1 (mm)	Diameter of Damage C2 (mm)	Area of removed material $A_{MOD}$ (mm <sup>2</sup> )
#1	front	3,938	10,696	17,854
	back	11,361	22,727	189,187
#2	front	3,757	5,988	13,420
	back	5,785	14,944	72,732
#3	front	4,136	6,242	18,081
	back	5,518	9,604	39,614
#4 (off-center)	front	4,185	7,331	19,849
	back	7,839	19,609	131,737
Mean*	front	3,944	7,642	16,452
	back	7,555	15,758	100,511

\*determined for center impacted specimens

Appendix F RESULTS OF MECHANICAL BOOM TESTS



a) Ideal configuration, flange side load cases ( $\alpha= 22.5^\circ, 45^\circ, 90^\circ$ )

a) Real configuration, flange side load cases ( $\alpha= 22.5^\circ, 45^\circ, 90^\circ$ )

c) Ideal configuration, convex side load cases ( $\alpha= 15^\circ, 45^\circ, 90^\circ$ )

d) Real configuration, convex side load cases ( $\alpha= 22.5^\circ, 45^\circ, 90^\circ$ )

Figure F. 1. Overview of buckling behavior in exemplary load-displacement curves of different lateral load cases ( $\alpha=$  varying; at  $\beta=0^\circ$ ) for ideal and real configurations

Boom No	In-plane angle of attack $\alpha$ [°]	Run No.	Flange Side 1 FS1										Flange Side 2 FS2										Average (FS1 & FS2)																															
			F <sub>crit</sub> (N)	Residual Load Capacity (%)	s <sub>x</sub> (mm)	at F <sub>crit</sub>	Failure Position z (mm)	at F <sub>crit</sub>	Bending stiffness c (N/mm)	SD <sub>c</sub> (N/mm)	Flexural rigidity EI (x10 <sup>6</sup> Nmm <sup>2</sup> )	SD <sub>EI</sub> (x10 <sup>6</sup> Nmm <sup>2</sup> )	F <sub>crit</sub> (N)	Residual Load Capacity (%)	s <sub>x</sub> (mm)	at F <sub>crit</sub>	Failure Position z (mm)	at F <sub>crit</sub>	Bending stiffness c (N/mm)	SD <sub>c</sub> (N/mm)	Flexural rigidity EI (x10 <sup>6</sup> Nmm <sup>2</sup> )	SD <sub>EI</sub> (x10 <sup>6</sup> Nmm <sup>2</sup> )	Average F <sub>crit</sub> (N)	Residual Load Capacity (%)	Average s <sub>x</sub> (mm)	at F <sub>crit</sub>	Bending stiffness c (N/mm)	SD <sub>c</sub> (N/mm)	Flexural rigidity EI (x10 <sup>6</sup> Nmm <sup>2</sup> )	SD <sub>EI</sub> (x10 <sup>6</sup> Nmm <sup>2</sup> )																								
B1	22.5	1	6.29	-	126.4	960	0.054	1.43E-03	1331	3.5E-01	6.79	-	126.6	900	0.049	2.02E-03	1208	5.0E-01	6.54	-	126.5	0.051	1.72E-03	1269	4.3E-01	5.78	88.3	125.7	-	-	-	-	5.61	85.8	125.2	-	-	-	-															
		2	5.85	93.0	118.2	960	-	-	-	-	5.70	83.9	133.2	900	-	-	-	-	-	5.78	88.3	125.7	-	-	-	-	-	-	-	-	-	-	-	-	-	-	-	-																
		3	5.76	91.6	117.2	960	-	-	-	-	5.46	80.4	133.2	900	-	-	-	-	-	5.61	85.8	125.2	-	-	-	-	-	-	-	-	-	-	-	-	-	-	-																	
B2	45.0	1	3.60	-	146.4	660	0.025	4.67E-04	608	1.2E-01	3.75	-	139.3	650	0.027	5.50E-04	664	1.4E-01	3.68	-	142.8	0.026	5.08E-04	636	1.3E-01	3.12	86.7	115.9	660	-	-	-	-	3.41	92.7	123.7	-	-	-	-	3.13	91.8	116.6	-	-	-	-							
		2	3.12	86.7	115.9	660	-	-	-	-	3.69	98.4	131.4	650	-	-	-	-	-	3.41	92.7	123.7	-	-	-	-	-	-	-	-	-	-	-	-	-	-	-	-	-	-	-	-	-											
		3	2.78	77.2	111.8	660	-	-	-	-	3.47	92.5	121.5	650	-	-	-	-	-	3.13	91.8	116.6	-	-	-	-	-	-	-	-	-	-	-	-	-	-	-	-	-	-	-	-	-	-										
B3	90.0	1	2.01	-	142.4	850	0.021	1.07E-03	514	2.6E-01	2.40	-	121.9	1500	0.020	8.18E-04	505	2.0E-01	2.21	-	132.1	0.021	9.42E-04	510	2.3E-01	1.88	93.5	132.0	850	-	-	-	-	2.04	92.3	121.8	-	-	-	-	1.92	87.1	108.7	-	-	-	-	1.92	87.1	108.7	-	-	-	-
		2	1.88	93.5	132.0	850	-	-	-	-	2.19	91.3	111.7	1500	-	-	-	-	-	2.04	92.3	121.8	-	-	-	-	-	-	-	-	-	-	-	-	-	-	-	-	-	-	-	-	-	-	-	-	-	-						
		3	1.66	82.6	110.8	850	-	-	-	-	2.18	90.8	106.7	1500	-	-	-	-	-	1.92	87.1	108.7	-	-	-	-	-	-	-	-	-	-	-	-	-	-	-	-	-	-	-	-	-	-	-	-	-	-						

Boom No	In-plane angle of attack $\alpha$ [°]	Run No.	Convex Side 1 CS1										Convex Side 2 CS2										Average (CS1 & CS2)																															
			F <sub>crit</sub> (N)	Residual Load Capacity (%)	s <sub>x</sub> (mm)	at F <sub>crit</sub>	Failure Position z (mm)	at F <sub>crit</sub>	Bending stiffness c (N/mm)	SD <sub>c</sub> (N/mm)	Flexural rigidity EI (x10 <sup>6</sup> Nmm <sup>2</sup> )	SD <sub>EI</sub> (x10 <sup>6</sup> Nmm <sup>2</sup> )	F <sub>crit</sub> (N)	Residual Load Capacity (%)	s <sub>x</sub> (mm)	at F <sub>crit</sub>	Failure Position z (mm)	at F <sub>crit</sub>	Bending stiffness c (N/mm)	SD <sub>c</sub> (N/mm)	Flexural rigidity EI (x10 <sup>6</sup> Nmm <sup>2</sup> )	SD <sub>EI</sub> (x10 <sup>6</sup> Nmm <sup>2</sup> )	Average F <sub>crit</sub> (N)	Residual Load Capacity (%)	Average s <sub>x</sub> (mm)	at F <sub>crit</sub>	Bending stiffness c (N/mm)	SD <sub>c</sub> (N/mm)	Flexural rigidity EI (x10 <sup>6</sup> Nmm <sup>2</sup> )	SD <sub>EI</sub> (x10 <sup>6</sup> Nmm <sup>2</sup> )																								
B1	15	1	4.86	-	79.7	1370	0.061	7.81E-04	1504	1.9E-01	6.50	-	100.6	110	0.065	7.11E-03	1595	1.8E-02	5.68	-	90.1	0.063	3.94E-03	1550	9.7E-01	4.05	83.3	69.5	1370	-	-	-	-	4.68	82.3	74.1	-	-	-	-	4.17	73.3	66.5	-	-	-	-							
		2	4.05	83.3	69.5	1370	-	-	-	-	5.30	81.5	78.7	110	-	-	-	-	-	4.68	82.3	74.1	-	-	-	-	-	-	-	-	-	-	-	-	-	-	-	-	-	-	-	-	-	-	-	-	-	-	-					
		3	4.04	83.1	68.7	1370	-	-	-	-	4.29	66.0	64.2	110	-	-	-	-	-	4.17	73.3	66.5	-	-	-	-	-	-	-	-	-	-	-	-	-	-	-	-	-	-	-	-	-	-	-	-	-	-	-					
B2	45	1	4.61	-	131.9	1870	0.020	2.92E-05	484	7.2E-01	4.43	-	212.9	460	0.020	5.48E-03	494	1.4E-02	4.52	-	172.4	0.020	2.76E-03	489	6.8E-01	1.95	42.3	119.1	1870	-	-	-	-	2.80	61.9	140.8	-	-	-	-	1.90	42.0	104.5	-	-	-	-	1.90	42.0	104.5	-	-	-	-
		2	1.95	42.3	119.1	1870	-	-	-	-	3.65	82.4	162.5	460	-	-	-	-	-	2.80	61.9	140.8	-	-	-	-	-	-	-	-	-	-	-	-	-	-	-	-	-	-	-	-	-	-	-	-	-	-	-	-	-			
		3	1.85	40.1	113.2	1870	-	-	-	-	1.95	44.0	95.7	460	-	-	-	-	-	1.90	42.0	104.5	-	-	-	-	-	-	-	-	-	-	-	-	-	-	-	-	-	-	-	-	-	-	-	-	-	-	-	-				
B3	90	1	2.64	-	192.7	675	0.014	5.05E-04	356	1.2E-01	2.88	-	209.5	110	0.015	3.92E-04	362	9.7E-00	2.76	-	201.1	0.015	4.49E-04	362	1.1E-01	1.56	59.1	110.3	675	-	-	-	-	1.83	66.1	128.8	-	-	-	-	1.61	58.2	112.8	-	-	-	-	1.61	58.2	112.8	-	-	-	-
		2	1.56	59.1	110.3	675	-	-	-	-	2.09	72.6	147.3	110	-	-	-	-	-	1.83	66.1	128.8	-	-	-	-	-	-	-	-	-	-	-	-	-	-	-	-	-	-	-	-	-	-	-	-	-	-	-	-				
		3	1.42	53.8	100.3	675	-	-	-	-	1.79	62.2	125.2	110	-	-	-	-	-	1.61	58.2	112.8	-	-	-	-	-	-	-	-	-	-	-	-	-	-	-	-	-	-	-	-	-	-	-	-	-	-	-					

Figure F. 2. Test results – Lateral bending - Ideal (clamped) configuration

		Flange Side 1 FS1										Flange Side 2 FS2										Average FS1 & FS2									
Boom No	In-plane Angle of attack $\alpha(T)$	Run No.	$F_{crit}$ (N)	Residual Load Capacity (%)	$S_x$ (mm)	at $F_{crit}$	Failure Position z (mm)	at $F_{crit}$	Bending stiffness c (N/mm)	$SD_c$ (N/mm)	Flexural rigidity EI ( $10^6$ Nmm <sup>2</sup> )	Failure characteristic	$F_{crit}$ (N)	Residual Load Capacity (%)	$S_x$ (mm)	at $F_{crit}$	Failure Position z (mm)	at $F_{crit}$	Bending stiffness c (N/mm)	$SD_c$ (N/mm)	Flexural rigidity EI ( $10^6$ Nmm <sup>2</sup> )	Failure characteristic	Average $F_{crit}$ (N)	Residual Load Capacity (%)	Average $S_x$ (mm)	at $F_{crit}$	Bending stiffness c (N/mm)	$SD_c$ (N/mm)	Flexural rigidity EI ( $10^6$ Nmm <sup>2</sup> )	Failure characteristic	
B4	22.5	1	5.16	-	178.3	70	0.036	6.07E-03	655	1.1E-02	buckling	5.61	-	191.6	70	0.038	4.06E-04	704	7.4E+00	buckling	5.38	-	184.9	0.037	3.24E-03	679	5.9E+01	buckling			
		2	5.10	98.9	175.0	70	-	-	-	-	-	buckling	5.08	90.6	176.0	70	-	-	-	-	-	-	-	-	5.09	94.6	175.5	-	-	-	-
		3	5.04	97.8	173.8	70	-	-	-	-	-	buckling	4.78	85.2	166.9	70	-	-	-	-	-	-	-	-	4.91	91.2	170.3	-	-	-	-
B5	45.0	1	4.78	-	217.00	70	0.027	8.25E-03	497	1.5E+02	buckling	3.42	-	234.4	70	0.019	7.97E-04	351	1.5E+01	buckling	4.10	-	225.7	0.02	4.52E-03	424	8.3E+01	buckling			
		2	2.60	54.3	184.4	70	-	-	-	-	-	buckling	2.99	87.6	214.5	70	-	-	-	-	-	-	-	-	2.80	68.2	199.5	-	-	-	-
		3	-	-	-	-	-	-	-	-	-	buckling	2.90	84.8	208.7	-	-	-	-	-	-	-	-	-	2.90	70.6	208.7	-	-	-	-
B6	90.0	1	2.41	-	216.3	70	0.020	2.54E-03	360	4.6E-01	buckling	2.54	-	231.6	70	0.020	4.45E-03	363	8.1E+01	buckling	2.48	-	223.9	0.020	3.50E-03	362	6.4E+01	buckling			
		2	1.98	82.3	188.2	70	-	-	-	-	-	buckling	2.22	87.6	201.0	70	-	-	-	-	-	-	-	-	2.10	85.0	194.6	-	-	-	-
		3	1.99	82.4	187.2	70	-	-	-	-	-	buckling	2.23	87.9	196.5	70	-	-	-	-	-	-	-	-	2.11	85.2	191.9	-	-	-	-

		Convex Side 1 CS1										
Boom No	In-plane Angle of attack $\alpha(T)$	Run No.	$F_{crit}$ (N)	Residual Load Capacity (%)	$S_x$ (mm)	at $F_{crit}$	Failure Position z (mm)	at $F_{crit}$	Bending stiffness c (N/mm)	$SD_c$ (N/mm)	Flexural rigidity EI ( $10^6$ Nmm <sup>2</sup> )	Failure characteristic
B4	22.5	1	5.34	-	253.9	70	0.022	7.52E-05	411	1.4E+00	Anvil	
		2	4.68	87.8	340.7	70	-	-	-	-	-	Anvil
		3	2.39	44.9	195.9	3800	-	-	-	-	-	Adapter
B5	45	1	3.36	-	257.5	70	-	-	-	-	Anvil	
		2	9.68	288.1	544.1	90	-	-	-	-	-	buckling
		3	5.42	161.3	416.4	90	-	-	-	-	-	buckling
B6	90	1	2.10	-	248.8	70	0.019	4.85E-03	352	8.9E+01	Anvil	
		2	1.34	63.8	268.7	70	-	-	-	-	-	Anvil
		3	1.27	60.8	199.9	70	-	-	-	-	-	Anvil

Figure F. 3. Test results – Lateral bending -Real (spacecraft) configuration



Ideal (clamped) configuration								
Boom No.	In-plane Angle of attack $\alpha$ (°)	out-of-plane Angle of attack $\beta$ (°)	Run No.	$F_{axial FS1}$ (N)	$F_{axial FS2}$ (N)	Load symmetry off-set (%)*	$F_{axial}$ (N)	Failure Position z (mm)
B1	3	0	1	111,16	131,19	18,02	242,02	2600
B2	3	0	1	117,74	138,59	17,70	255,98	3120
B3	3	0	1	121,60	136,20	12,01	257,45	3770
			Mean	116,84	135,33	15,91	251,82	3163

\*FS1 = basis

Figure F. 4. Test results – axial compression – Ideal (clamped) configuration

Real (spacecraft) configuration									
Boom No.	In-plane Angle of attack $\alpha$ (°)	out-of-plane Angle of attack $\beta$ (°)	Run No.	$F_{axial FS1}$ (N)	$F_{axial FS2}$ (N)	Load symmetry off-set (%)*	$F_{axial}$ (N)	Residual Load Capacity (%)	Failure Position z (mm)
B4	22,5	3	1	37,72	36,11	-4,27	68,12	-	3730
			2	22,63	22,78	0,64	41,91	61,5	3730
			3	19,78	21,43	8,33	38,03	55,8	3730
			4	16,88	17,62	4,34	31,84	46,7	3730
B5	22,5	3	1	32,93	32,81	-0,37	60,67	-	3727
			2	27,89	27,90	0,04	51,48	84,9	3727
			3	27,87	27,91	0,15	51,47	84,8	3727
			4	27,51	27,52	0,04	50,78	83,7	3727
B6	22,5	3	1	36,14	35,16	-2,71	65,80	-	3728
			2	31,66	30,75	-2,87	57,58	87,5	3728
			3	31,84	31,00	-2,63	57,99	88,1	3728
			4	31,60	33,00	4,44	59,61	90,6	3728
			Mean 1st run	35,60	34,69	-2,45	64,86	-	3728
			Mean 2nd run	27,39	27,14	-0,73	50,32	78,0	3728
			Mean 3rd run	26,50	26,78	1,95	49,16	76,3	3728
			Mean 4th run	25,33	26,04	2,94	47,41	73,7	3728

\*FS1 = basis

Figure F. 5. Test results – axial compression – Real (spacecraft) configuration

## Appendix G INPUT VALUES – ROBUSTNESS ASSESSMENT

**Table G. 1.** Constituents for robustness assessment with experimental results

Case	Stiffness $\kappa$						Boom Tip Displacement $u$			
	$EI_{FS}$ [ $\times 10^6$ N·mm <sup>2</sup> ]	$EI_{CS}$ [ $\times 10^6$ N·mm <sup>2</sup> ]	$EI_{yByB}$ [ $\times 10^6$ N·mm <sup>2</sup> ]	$EI_{xBxB}$ [ $\times 10^6$ N·mm <sup>2</sup> ]	$EI_{FScomp}$ [ $\times 10^6$ N·mm <sup>2</sup> ]	$EI_{CScomp}$ [ $\times 10^6$ N·mm <sup>2</sup> ]	$u_{limit}$ (mm)	$u_{aFS2N}$ (mm)	$u_{aCS2N}$ (mm)	$u_{manuf}$ (mm)
Ideal 90°	505	356	561	430	-	-	42	0.63	0.05	7.2
Real 90°	360	352	561	430	-	-	38	18.2	1.16	7.2
Real 22.5°	655	411	561	430	1208	926	38	18.2	1.16	7.2
Case	Characteristic Load $L$									
	$F_{FS1st}$ (N)	$F_{CS1st}$ (N)	$F_{FS2nd}$ (N)	$F_{CS2nd}$ (N)	$F_{FSReq}$ (N)	$F_{CSReq}$ (N)	$F_{aResReq}$ (N)	$F_{aRes1st}$ (N)	$F_{aRes2nd}$ (N)	
Ideal 90°	2.01	2.64	188	156	1	1	3.7	242	-	
Real 90°	2.41	2.10	198	134	1	1	3.7	60.7	-	
Real 22.5°	5.16	5.34	5.10	4.68	2	2	3.7	64.86	50.32	
Case	Parameter weighting factors									
	$w_{\kappa 1}$	$w_{\kappa 2}$	$w_{L1}$	$w_{L2}$	$w_{L3}$	$w_{L4}$	$w_{L5}$	$w_{L6}$	$w_{u1}$	$w_{u2}$
Ideal 90°	0.5	0.5	0.35	0.35	0.1	0.1	0.1	-	0.5	0.5
Real 90°	0.5	0.5	0.35	0.35	0.1	0.1	0.1	-	0.5	0.5
Real 22.5°	0.5	0.5	0.3	0.3	0.1	0.1	0.1	0.1	0.5	0.5

Determination of comparative flexural rigidity :

$$EI_{CScomp} = \frac{EI_{xBxB}}{EI_{yByB}} \cdot EI_{FScomp} = 925.92 \times 10^6 Nmm^2 \quad (G. 1)$$

with  $EI_{FScomp} = EI_{FSideal22.5^\circ} = 1208 \times 10^6 Nmm^2$ , determined in mechanical boom testing for the flange side, loaded under an in-plane angle of attack  $\alpha=22.5^\circ$ , and  $EI_{yByB}$  and  $EI_{xBxB}$  determined as analytical values in section 5.5.

**Table G. 2.** Constituents for robustness assessment with FEA results

Case	Stiffness $\kappa$				Boom Tip Displacement $u$				
	$EI_{FS}$ [ $\times 10^6$ N·mm <sup>2</sup> ]	$EI_{CS}$ [ $\times 10^6$ N·mm <sup>2</sup> ]	$EI_{FSnom}$ [ $\times 10^6$ N·mm <sup>2</sup> ]	$EI_{CSnom}$ [ $\times 10^6$ N·mm <sup>2</sup> ]	$u_{FS}$ (mm)	$u_{CS}$ (mm)	$u_{FSnom}$ (mm)	$u_{CSnom}$ (mm)	$u_{infl}$ (mm)
Stowed-FEA	890	335	554	425	95	242.5	150.4	162.3	22.4
Manufactured-FEA*	529	401			153.8	172			7.2
Manufactured-Exp.	505	356			201.1	132.1			7.2
Case	Characteristic Load $L$								
	$F_{FS1st}$ (N)	$F_{CS1st}$ (N)	$F_{FSReq}$ (N)	$F_{CSReq}$ (N)	$F_{FSnom}$ (N)	$F_{CSnom}$ (N)			
Stowed-FEA	2.6	1833	1	1	2.55	1884			
Manufactured-FEA*	2.51	189							
Manufactured-Exp.	2.01	2.64							
Case	Parameter weighting factors								
	$w_{\kappa 1}$	$w_{\kappa 2}$	$w_{L1}$	$w_{L2}$	$w_{L3}$	$w_{L4}$	$w_{u1}$	$w_{u2}$	
Stowed-FEA	0.5	0.5	0.2	0.2	0.3	0.3	0.5	0.5	
Manufactured-FEA*									
Manufactured-Exp.									